Biological and Biomimetic Mineralization of Calcium Carbonate

Dissertation zur Erlangung des Doktorgrades
Dr. rer. nat.
an der Fakultät für Geowissenschaften
der Ludwig-Maximilians-Universität München

Vorgelegt von
Xiaofei Yin

München, 04.11.2020

Betreuer: Prof. Dr. Wolfgang. W. Schmahl

Erstgutachter: Prof. Dr. Wolfgang. W. Schmahl
Zweitgutachter: Prof. Dr. William D. Orsi

Promotionskommission: Prof. Dr. Wolfgang W. Schmahl
Prof. Dr. William D. Orsi
Prof. Dr. María Lourdes Fernández-Díaz
Prof. Dr. Stuart Gilder
Prof. Dr. Julia Pongratz
PD Dr. Sara Carena Ph.D. Princeton

Tag der mündlichen Prüfung: 08. März 2021

Abstract

Calcium carbonate is a common chemical substance that can be widely found in Nature. It is geologically present in rocks in large quantities as calcite and/or aragonite minerals (e.g. limestone, a type of sedimentary rock consisting mainly of calcite), or it biologically composes the main component of many marine organisms' endo- and exoskeletons as shells, spines, spicules etc. Organisms have evolved a remarkable ability to produce complex biominerals, which are mainly composite materials consisting of both biopolymers and minerals with sophisticated hierarchical structures and fascinating properties. Most of these materials are generally adapted as specific implements to the creatures, but these implements keep inspiring mankind on biomimetic imitation of Nature to solve critical challenges faced by humanity. The studies of biogenic carbonates and their calcification pathways are able to provide attractive alternative applications to produce synthetic materials at ambient pressures and temperatures. The control of crystal nucleation and growth is a key factor for a bottom-up approach to synthesis in material science. This dissertation presents findings from examples of biogenic calcium carbonate in the coccolithophore species *Emiliania huxleyi*, and three species of Rotalliid foraminifers, and it is supplemented by biomimetic calcium carbonate crystal growth experiments with hydrogels and bacterial extracellular polymeric substances (EPS) that serve as the organic matrix in the biologically inspired mineralization system.

Coccolithophores, a group of unicellular eukaryotic phytoplankton, are known as the largest phytoplankton contributors of the global calcium carbonate precipitation. Their exoskeletons are so-called coccospheres, and each coccolithophore is enclosed in its own collection of coccoliths, the calcified scales. The morphology of coccoliths are highly intricate, however, unlike extracellularly formed biological hard tissues, coccolith calcite is not a dense composite and its hierarchical microstructure is of a special category. To get insight into the calcification pathway of *E. huxleyi* coccoliths, intracrystalline nanostructure of the coccolith calcite and the cell ultrastructural were investigated. The diffraction and element analysis results confirm the pure calcite composition of the coccolith and prove the presence of planar defects and dislocations within the calcite crystals. This observation lacks any evidence for the current general paradigms that biominerals are assembled nanoparticles, however, the observation indicates a classical ion-by-ion crystal growth mechanism. Our cytological results suggest the presence of a new interorganelle junction, the “nuclear envelope junction”, and point to a new pathway of intracellular calcium transport into the coccolith vesicle. The formation of the coccolith utilizes the nuclear envelope – endoplasmic reticulum Ca^{2+}-store of the cell from the external medium to the coccolith vesicle, which also implies the coccolith calcite forms by ion-by-ion growth rather than by a nanoparticle accretion mechanism.

Foraminifera are a large phylum of unicellular calcifying eukaryotes. Most of them produce an elaborate shell-like outer protective layer (called a "test") which is often calcareous. The calcification of foraminifera holds a major role in marine biogeochemical cycles and their fossil counterparts are widely used for paleoceanographic reconstructions. To better understand the microstructure and texture of foraminiferal tests, three benthic rotaliid foraminifera *Amphistegina lobifera*, *Amphistegina lessonii* and *Ammonia tepida* are examined with electron backscatter diffraction. Our results show that the skeletal elements of the investigated foraminiferal tests are formed of mesocrystals, which have highly irregular dendritic-fractal morphologies and interdigitate strongly. Those mesocrystals can be grouped into two types: large (20–50 μm) frequently twinned ones and small (< 20 μm) usually untwinned ones. The twinning of large mesocrystals mainly follows the {001} twinning pattern, while a further unknown twin type is also observed. We identify the small untwinned mesocrystals with the inner calcitic layer, forming between the inner organic lamellipodial lining and the primary organic sheet, and the large and usually twinned dendritic mesocrystals within the outer calcitic layer between the primary organic sheet and the outer organic lamellipodial lining. The mixing of extremely pronounced mesocrystalline dendritic-fractal patchwork and the twin-law is a unique feature of benthic foraminiferal calcite. The formation of the dendritic-fractal mesocrystals must be related to calcite crystal growth in the presence of obstacles such as organic matrix molecules binding more strongly to the calcite than in other carbonate-shell forming organisms. In a broader perspective, we attempt to relate the different modes of calcite organization that we find in the tests to varying structural biomaterial formation processes and strategies. In addition, as the EBSD technique is widely established by now, we propose to develop crystal orientation measurements and analyses as a tool to distinguish between the different calcifying foraminiferal groups.

Organic components in biominerals have been proven to hold key functions in biomineralization. Biogenic minerals tend to be associated with mainly two kinds of biopolymers. Quantitatively, the majority are referred to as “framework macromolecules”, which are usually highly cross-linked, insoluble, and slightly hydrophobic and they act as a supporting matrix where the mineral parts can grow onto/into, and/or as substrate where other soluble and smaller biopolymers may interact with the mineral phase. The other set of the matrix elements are referred to as “control macromolecules”, which are soluble, could be unbound or adsorbed onto the framework, or even occluded within the mineral parts during the crystal growth process.

Hydrogels are adequate systems for investigating the biological structural material formation and to understand the process of biomineralization, as they are porous networks and show strikingly similar chemical features to the organic matrices. Previous projects within our research group focused on the impact of single-component hydrogel systems on calcium carbonate (calcite is the dominant phase in all the preceding studies), the growth of composite aggregates and their microstructure characteristics. To explore the influence of each single hydrogel component in gel mixtures on calcite aggregate formation, agarose/gelatin hybrid gel was prepared with three different solid contents as the growth medium. Since magnesium is a common element in exoskeletons of marine organisms, crystal growth experiments were conducted with and without Mg^{2+} dose. The increase of either gelatin or agarose in the gel content brings clear differences to the morphology, size, texture, and microstructure of the aggregates. The presence Mg^{2+} in the growth medium, in addition to the gel incorporation, strongly influences the local deformation within the aggregates.

Although hydrogels are chemically close to the organic matrices in biomineralization and provide volumetric confinement after gelation which is analogous to the confined environments where biomineralization often takes place, they are still synthetic chemicals and their native attributes are partially lost during the manufactoring process. Extracellular polymeric substances (EPS) is a broad term including a large variety of biopolymers secreted by microbial cells. Polysaccharides are the major component of most EPS, in which polypeptides, nucleic acids, phospholipids, and other polymeric compounds are often combined. As the characteristics of the bacterial EPS are chemically very close to that of the "control macromolecules" whereas the hydrogels may provide a suitable "framework" to support crystallization, the combination of these two elements could inspire a more appropriate system to mimic the biomineralization process as well as to understand the bacterial mediated calcification process. To explore the directing influence of native biopolymers on calcium carbonate mineralization, calcite/gel composite aggregates growth experiments were conducted with agarose hydrogel gels containing four different bacterial EPS of *Bacillus subtilis*, *Mycobacterium phley*, *Mycobacterium smagmatis*, and *Pseudomonas putida*, respectively. The further characterizations reveal that the aggregates containing EPS are reduced in size and show distinctive morphologies directed by the EPS of a specific bacterium, compared to the reference aggregates grown without EPS. Bacterial EPS changes mineral microstructure/texture in a species-specific manner, which is a characteristic that when developed further might be used as an identification tool for bacterial calcification in present/past environments.

Zusammenfassung

Calciumcarbonat ist eine einfache und häufige chemische Substanz, die in der Natur weit verbreitet ist. Es kommt geologisch in Gesteinen in großen Mengen als Calcit- und /oder Aragonit vor (z. B. Kalkstein, ein Sedimentgestein, das hauptsächlich aus Calcit besteht), oder es bildet biologisch den Hauptbestandteil der Endo- und Exoskelette vieler Meeresorganismen wie Schalen, Stacheln, Nadeln usw. Organismen haben eine bemerkenswerte Fähigkeit entwickelt, komplexe Biomineralien herzustellen, bei denen es sich hauptsächlich um Verbundwerkstoffe handelt, die sowohl aus Biopolymeren als auch aus Mineralen mit ausgefeilten hierarchischen Strukturen und faszinierenden Eigenschaften bestehen. Die meisten dieser Materialien sind im Allgemeinen als spezifische Werkzeuge der Organismen entwickelt; diese Objekte inspirieren die Menschheit immer wieder, biomimetische Ideen zu entwickeln, die die Natur imitieren, um die kritischen Herausforderungen der Menschheit zu lösen. Die Untersuchungen zu biogenen Karbonaten und ihren Mineralisationswegen bieten attraktive Alternativen zur Herstellung synthetischer Materialien bei gewöhnlichen Umweltbedingungen. Die Kontrolle der Kristallkeimbildung und des Kristallwachstums ist ein Schlüsselfaktor für den Bottom-up-Ansatz für Synthesen in den Materialwissenschaften. Diese Dissertation präsentiert die Ergebnisse von Beispielen von biogener Calciumcarbonat-Mineralisation in der Coccolithophoriden-Spezies *Emiliania huxleyi* sowie drei Spezies Rotalliider Foraminiferen. Diese Studien werden ergänzt durch sowie biomimetische Calciumcarbonat-Kristallwachstumsexperimente mit Hydrogelen und bakteriellen extrazellulären polymeren Substanzen (EPS), die als organische Matrix im biologisch inspirierten Mineralisierungssystem dienen.

Coccolithophoriden, eine Gruppe von einzelligem eukaryotischem Phytoplankton, sind als die größten Produzenten der globalen Calciumcarbonat-Ausfällung bekannt. Ihre Exoskelette sind sogenannte Coccosphären, und jede Coccolithophoriden-Zelle ist in einer eigenen Ansammlung von Coccolithen, der Coccosphäre, eingeschlossen. Die Morphologie von Coccolithen ist sehr kompliziert. Im Gegensatz zu extrazellulär gebildeten biologischen Hartgeweben ist Coccolith-Calcit jedoch kein kompakter Verbundwerkstoff seine hierarchische Mikrostruktur bildet eine eigene Kategorie. Um einen Einblick in die Mineralisation von *E. huxleyi*-Coccolithen zu erhalten, wurden die intrakristalline Nanostruktur des Coccolith-Calcits und die Zell-Ultrastruktur untersucht. Die Ergebnisse der Beugungs- und Elementanalyse bestätigen die reine Calcit Zusammensetzung des Coccolithen und belegen das Vorhandensein planarer Defekte und Versetzungen in den Calcit Kristallen. Die Beobachtungen liefern keine Evidenz für die gegenwärtigen allgemeinen Paradigmen, dass Biominerale nanopartikulär zusammengesetzt sind, und weisen dagegen auf einen klassi-schen Ion-für-Ion-Kristallwachstumsmechanismus hin. Unsere zytologischen Ergebnisse deuten auf das Vorhandensein einer neuen interorganellen Anbindung hin, der „*nuclear envelope junction*“ und weisen auf einen neuen Weg des intrazellulären Calciumtransports in das Coccolith-Vesikel hin. Die Bildung des Coccolithen nutzt die Ca^{2+} -Speicherung der Kernhülle - des endoplasmatischen Retikulums der Zelle vom externen Medium zum Coccolith-Vesikel, was ebenfalls impliziert, dass sich der Coccolith-Calcit eher

durch Ionenwachstum als durch einen Nanopartikel-Akkretion Mechanismus bildet.

Foraminiferen sind ein großes Phylum einzelliger kalkbildender Eukaryoten. Die meisten von ihnen bilden ein aufwändiges schalenartiges Gehäuse („Test“ genannt), das zum größten Teil aus Carbonatmineralen besteht. Die Kalk-Biomineralisation von Foraminiferen spielt eine wichtige Rolle in marinen biogeochemischen Kreisläufen, und ihre fossilen Gegenstücke werden häufig für paläozeanographische Rekonstruktionen verwendet. Um die Mikrostruktur und Textur von Foraminiferen-Gehäuse besser zu verstehen, werden drei benthische Rotaliid-Foraminiferen *Amphistegina lobifera*, *Amphistegina lessonii* und *Ammonia tepida* mit Elektronenrückstreuungsbeugung untersucht. Unsere Ergebnisse zeigen, dass die Skelettelemente der untersuchten Foraminiferen-Gehäuse aus Mesokristallen bestehen, die stark unregelmäßige dendritisch-fraktale Morphologien aufweisen und stark ineinandergreifen. Diese Mesokristalle können in zwei Typen eingeteilt werden: große (20–50 μm) häufig verzwillingte Kristalle und kleine (< 20 μm), normalerweise nicht verzwillingte Kristalle. Die Zwillingsbildung großer Mesokristalle folgt hauptsächlich dem Zwillingsmuster $\{001\}$, während ein weiterer unbekannter Zwillingstyp ebenfalls beobachtet wird. Wir identifizieren die kleinen, nicht verzwillingten Mesokristalle mit der inneren Kalzitlage, die sich zwischen der inneren organischen Lamellipodialauskleidung und der primären organischen Schicht bildet, und die großen und normalerweise verzwillingten dendritischen Mesokristalle mit der äußeren Kalzitschicht zwischen der primären organischen Schicht und der äußeren organischen Lamellipodialumgrenzung. Die Vermischung von extrem ausgeprägtem mesokristallinem dendritisch-fraktalem Patchwork und dem Zwillingsgesetz ist ein einzigartiges Merkmal von benthischem foraminiferalem Calcit. Die Bildung der dendritisch-fraktalen Mesokristalle muss mit dem Wachstum von Calcitkristallen in Gegenwart von Hindernissen wie organischen Matrixmolekülen zusammenhängen, die stärker an den Calcit binden als in anderen Karbonatschalen-bildenden Organismen. In einer breiteren Perspektive versuchen wir, die verschiedenen Arten der Calcitorganisation, die wir in den Gehäusen finden, mit unterschiedlichen strukturellen Prozessen und Strategien zur Bildung von Biomaterialien in Beziehung zu setzen. Da die EBSD-Technik mittlerweile weit verbreitet ist, schlagen wir außerdem vor, Kristallorientierungsmessungen und -analysen zu entwickeln, um zwischen den verschiedenen kalzifizierenden Foraminiferengruppen zu unterscheiden.

Es wurde nachgewiesen, dass organische Komponenten in Biomineralen Schlüsselfunktionen bei der Biomineralisation haben. Biogene Minerale neigen dazu, hauptsächlich mit zwei Arten von Biopolymeren assoziiert zu sein. Quantitativ werden die meisten als „Gerüstmakromoleküle“ bezeichnet, die üblicherweise stark vernetzt, unlöslich sowie leicht hydrophob sind und als Trägermatrix bzw. Substrat dienen, in bzw. auf der die Minerale wachsen können, wobei andere lösliche und kleinere Biopolymere mit der Mineralphase interagieren. Der andere Satz der biologischen Matrixelemente wird als „Kontrollmakromoleküle“ bezeichnet, die löslich sind, ungebunden oder am Gerüst adsorbiert oder sogar während des Kristallwachstumsprozesses in den Mineralteilen eingeschlossen sein können.

Hydrogele sind geeignete Systeme zur Untersuchung der Bildung von biologischem Strukturmaterial und zum Verständnis des Prozesses der Biomineralisation, da sie poröse Netzwerke sind

und auffallend ähnliche chemische Merkmale wie die organischen Matrices aufweisen. Frühere Projekte in unserer Forschungsgruppe konzentrierten sich auf Calciumcarbonatbildung in Ein-Komponenten-Hydrogel-Systemen (Calcit ist die dominierende Phase in allen vorhergehenden Studien), insbesondere das Wachstum von Komposit-Aggregaten und ihre Mikrostrukturmerkmale. Um den Einfluss jeder einzelnen Hydrogel Komponente in Gelmischungen auf die Bildung von Calcit Aggregaten zu untersuchen, wurde Agarose/Gelatine-Hybridgel mit drei verschiedenen Feststoffgehalten als Wachstumsmedium hergestellt. Da Magnesium ein häufiges Element in Exoskeletten mariner Organismen ist, wurden Kristallwachstumsexperimente mit und ohne Mg^{2+}-Dosis durchgeführt. Die Erhöhung des Gelgehalts von Gelatine oder Agarose führt zu deutlichen Unterschieden in der Morphologie, Größe, Textur und Mikrostruktur von Aggregaten. Das Vorhandensein von Mg^{2+} im Wachstumsmedium beeinflusst zusätzlich zum Gel-Einbau stark die lokale Kristallstruktur-Deformation innerhalb der Aggregate.

Obwohl Hydrogele bei der Biomineralisierung chemisch nahe an den organischen Matrices liegen und nach der Gelierung volumetrische Eingrenzung (*confinement*) bieten, die analog zu den eingegrenzten Umgebungen ist, in denen Biomineralisation häufig stattfindet, handelt es sich immer noch um synthetische Chemikalien, und ihre natürlichen Eigenschaften gehen während des Herstellungsprozesses teilweise verloren. Extrazelluläre polymere Substanzen (EPS) sind ein weit gefasster Begriff, der eine Vielzahl von Biopolymeren umfasst, die von mikrobiellen Zellen sekretiert werden. Polysaccharide sind der Hauptbestandteil der meisten EPS, in denen häufig Polypeptide, Nukleinsäuren, Phospholipide und andere polymere Verbindungen kombiniert werden. Da die Eigenschaften des bakteriellen EPS chemisch sehr nahe an denen der „Kontrollmakromoleküle“ liegen, während die Hydrogele ein geeignetes „Gerüst“ zur Unterstützung der Kristallisation darstellen können, könnte die Kombination dieser beiden Elemente ein geeigneteres System zur Nachahmung des Biomineralisierungsprozesses darstellen um den bakteriell vermittelten Mineralisationsprozess zu verstehen. Um den direkten Einfluss nativer Biopolymere auf die Calciumcarbonat Mineralisierung zu untersuchen, wurden Kristallwachstumsexperimente mit Calcit/Gel-Verbundaggregate in Agarose durchgeführt, die vier verschiedene bakterielle EPS von *Bacillus subtilis*, *Mycobacterium phley*, *Mycobacterium smagmatis* bzw. *Pseudomonas putida* enthielten. Die weiteren Charakterisierungen zeigen, dass die EPS-haltigen Aggregate verglichen mit den ohne EPS gewachsenen Referenzaggregaten verkleinert sind und unterschiedliche Morphologie aufweisen, die vom EPS eines bestimmten Bakteriums gesteuert werden. Bakterielles EPS verändert die mineralische Mikrostruktur/Textur auf speziesspezifische Weise. Dies ist ein Merkmal, das bei seiner Weiterentwicklung als Identifikationsinstrument für die bakterielle Mineralisation in rezenten bzw. Paläo-Umweltbedingungen verwendet werden kann.

List of Abbreviations

ACC	amorphous calcium carbonate
ACCI/pc-ACC	proto-calcite ACC
ACCII/pv-ACC	proto-vaterite ACC
ADF	annular dark field
Asn	asparagine
Asp	aspartic acid
ATPase	adenosine triphosphatase
BF	bright field
BSE	backscatter electron
CBED	convergent beam electron diffraction
CCD	charge-coupled device
CL	cathodoluminescence
CNT	Classical nucleation theory
COD	Crystallography Open Database
CPD	critical point drying
DF	dark field
EBSD	electron backscatter diffraction
EDX/EDS	energy-dispersive X-ray spectroscopy
EELS	electron energy loss spectroscopy
EM grids	electron microscopy grids
EPMA	electron probe microanalysis
EPS	extracellular polymeric substances
ER	endoplasmic reticulum
FE-SEM	field emission scanning electron microscopy
FET	field-effect transistor
FIB	focused ion beam

FT-IR	Fourier transform infrared spectroscopy
FWHM	full width at half maximum
Gln	glutamine
Glu	glutamic acid
GPA	a glutamine/proline/alanine-rich protein
HAADF	high-angle annular dark field
HRTEM	high-resolution transmission electron microscopy
ICDD	International centre for diffraction data
ICSD	Inorganic crystal structure database
MUD	multiple of uniform (random) distribution
PNCs	prenucleation clusters
POS	primary organic sheet
SAED	selected area electron diffraction
SDD	silicon drift detectors
SE	secondary electron
SEM	scanning electron microscopy
Ser	Serine
STEM	scanning transmission electron microscopy
TEM	transmission electron microscopy
WDX	wavelength dispersive X-ray spectroscopy
XRD	X-ray diffraction

Contents

1 Introduction

This dissertation focuses on calcium carbonate biominerals and the corresponding biomimetic calcite crystalline aggregates. Several exemplary carbonate biominerals formed by different organisms were investigated. Biomimetic experiments were performed to understand the crystallization process of the calcium carbonates in the presence of an organic matrix, as what is the case in biomineralization. The scientific results presented in the present work aim to expand the current knowledge of both biological and biomimetic mineralized calcium carbonates.

1.1 Processes of Biomineralization

The term *biomineralization* refers to the processes by which living organisms produce minerals (Mann 1988; Lowenstam & Weiner 1989). The produced biominerals are usually hierarchically structured and hold specific functional purposes for the organisms. Biomineralization is a multifarious and widespread phenomenon. Whether those beautiful corals, exquisite molluscs shells or vertebrate skeleton such as bones and teeth that also produced by our own species, all are epitomes of biominerals. It is reported that at least 64 different minerals are known to be formed by organisms to date (Lowenstam & Weiner 1989; Knoll 2003).

The processes of biomineralization are in principle distinguished into two fundamental categories based upon their degree of biological control. The concept of "*biologically induced mineralization*" was introduced by Lowenstam (1981), which regards the biomineral precipitate as a result of interactions between the metabolic processes of the organisms and the surrounding environment. Mann (1983) proposed the other mechanism, "*biologically controlled mineralization*", two years later, which emphasizes the cellular activities that the organism uses to regulate the biomineral formation in terms of nucleation site, phase selection, growth, morphology etc.

Calcium-bearing minerals take up about 50% of all known biomineralization products (Lowenstam & Weiner 1989). This comes as no surprises because calcium is abundant in sea water as well as terrestrial waters, and contributes to many physiological and biochemical activities of the cell (Simkiss & Wilbur 1989). Calcium carbonate minerals are the most abundant biogenic minerals both in quantities and distribution (Weiner & Dove 2003).

1.2 Biological Calcium Carbonate Structural Materials

As one of the most common minerals on the surface of the Earth, there are six calcium carbonate minerals with the same principal chemical composition but different structure: three anhydrous polymorphs, calcite, aragonite, and vaterite; three hydrated forms, monohydrate, hemihydrate and hexahydrate; and the amorphous form, amorphous calcium carbonate (ACC) (Brooks *et al.* 1950; Lippmann 1973; Cartwright *et al.* 2012; Radha & Navrotsky 2013). Calcite and aragonite, the two most thermodynamically stable phases, are by far the most widely produced forms of calcium carbonate biominerals in Nature, such as exoskeletons for molluscs and brachiopods, eye lens for trilobites, eggshells for birds, etc (Lowenstam & Weiner 1989). Magnesium ions are readily incorporated in the calcite lattice, therefore many biological calcites also contain Mg^{2+} ions, which can even up to levels of 30 mol% in some cases (Mann 2001). Vaterite, the last anhydrous polymorph, is rarely found in living organisms (Lowenstam & Abbott 1975; Pokroy *et al.* 2015), however, it is considered to play an important role in CaCO3 precipitation from solution (Grasby 2003) as vaterite will convert to calcite under certain conditions (Subba 1973; Kralj *et al.* 1994; Gómez-Morales *et al.* 1996; Spanos & Koutsoukos 1998). A few bacterium species are able to induce the formation of monohydrocalcite in the laboratory (Rivadeneyra *et al.* 1998; Arias *et al.* 2017; Pan *et al.* 2019), while the hexahydrate form of calcium carbonate, also known by as its geological name ikaite, is not yet known to be formed biologically (Addadi *et al.* 2003).

In addition to the five crystalline phases, amorphous calcium carbonate (ACC) is the only form of calcium carbonate that does not diffract X-ray. Although ACC is described as amorphous, it is believed that ACC actually has a short-ranged order which is, presumably, genetically controlled by organisms (Falini *et al.* 1996; Addadi *et al.* 2003; Marxen *et al.* 2003; Raz *et al.* 2003; Politi *et al.* 2006). The biogenic ACC was first noticed by researchers in the early 20th century as mentioned in the review by Addadi *et al.* (2003), however, the first report of transient ACC was found in the teeth of Cryptochiton stelleri in the late 1960s (Towe & Lowenstam 1967). Up to now, the researchers reported that in biomineralization ACC is considered (a) as a transient precursor phase prior to the formation of biological calcite and aragonite (e.g. molluscs and brachiopods); (b) or as temporary storage for the future availability of calcium carbonate (e.g. earthworms); (c) or as a structural component (e.g. arthropod cuticle, calcitic sponge spicules).

The biogenic carbonates have mainly two unique features that distinguished them from the geologically formed ones: (i) the biogenic minerals often have atypical external morphologies; (ii) the majority of the biominerals are composites, which often consisting of mineral subunits that are separated by organic materials (Weiner & Dove 2003). The term organic matrix is often used to refer to the organic components within the biominerals. Usually it describes a continuous sheet-like structure which subdivides the space where the biomineralization process takes place (Lowenstam & Weiner 1989). In most cases, the organic matrix is a preformed insoluble framework which contains a complex assemblage of macromolecules, for instance collagen in bones (Robinson 1952; Miller *et al.* 1984; Weiner & Wagner 1998), amelogenins in dental enamel (Brookes *et al.* 1995; Fincham & Simmer 2007), silk-like proteins and β-chitin in nacre (Weiner & Traub 1984; Levi-Kalisman *et al.* 2001; Weiss & Schonitzer 2006), etc. Although the organic components are often the minority of the final biomineralization products (i.e. which accounts only for 0.1-5 wt% in molluscan shells, Marin *et al.* 2008), they strongly influence the mechanical properties and material characteristics of the biominerals. The biogenic carbonates specimens involved in present work will be further discussed in the following sections 1.2.1, 1.2.2 and 1.2.3

1.2.1 Coccolithophores

Coccolithophores are unicellular eukaryotic phytoplankton, which assimilates carbon during their photosynthesis process to produce the cell organelles including the calcified exoskeleton, so-called coccoliths (Iglesias-Rodríguez *et al.* 2008). The taxonomic position of coccolithophores is still under discussion. According to the Five Kingdoms Classification (Whittaker 1969), they belong to the kingdom Protista; while in a newer biological taxonomic revision, they are classified in the kingdom Chromista (Ruggiero *et al.* 2015; Cavalier-Smith 2018).

Coccolithophores are one of the most important primary producers (usually contribute about 1 to 10% of primary production) in the marine ecosystem (Poulton *et al.* 2007). Apart from foraminifera, coccolithophores are the most productive calcifiers in the modern ocean (Monteiro *et al.* 2016). The locus of global calcification was shifted from continental shelves towards deep oceans along with the evolution of calcareous nannoplankton, which essentially impacted the global sedimentation patterns and ocean chemistry (Baumann *et al.* 2005). Recently, coccolithophores have gained increased attention as they are likely to give additional feedback to climate change (Westbroek *et al.* 1993).

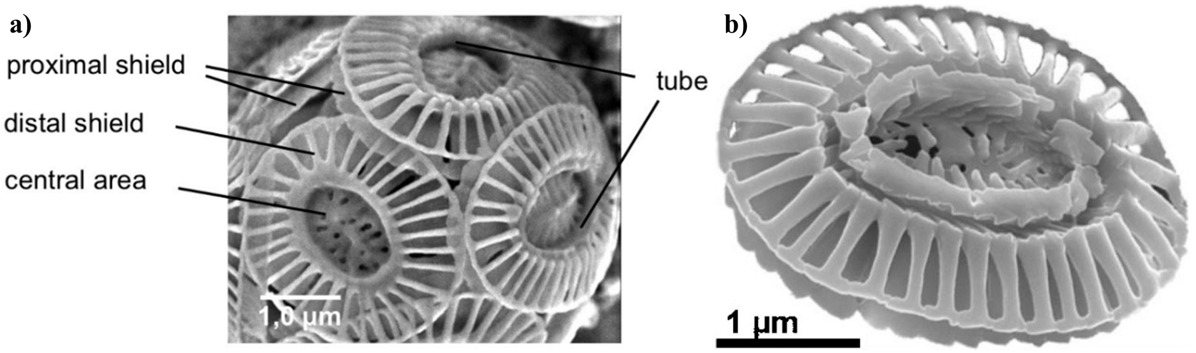

Figure 1.2-1. SEM micrographs showing (a) a complete coccosphere (Yin *et al.* 2018) and (b) a single coccolith (Hoffmann *et al.* 2014a) of the coccolithophore species *E. huxleyi*.

Emiliania huxleyi is the most abundant species of coccolithophore in the modern ocean, as it is capable of adapting extremely different environmental conditions. From subarctic/subantarctic to subtropical habitats (Balch *et al.* 1992), from oligotrophic to eutrophic waters (Hagino & Okada 2006), and from the surface to 200m depth of the ocean (Ahearn *et al.* 2004), *E. huxleyi* is almost ubiquitous. This fascinating species has been the focus of biomineralization studies for a long time, since, it is expected to have a simpler biochemical system and be more amenable to laboratory study than other more complex species as a unicellular organism, and their abundance also makes it an easily accessible study object. Although *E. huxleyi* can be readily cultured, maintained, and investigated in the laboratories, their calcification is a sophisticated intracellular process and their coccoliths are remarkably complex three-dimensionally architectured biominerals (Fig. 1.2-1).

In Nature, an *E. huxleyi* is usually covered with a coccosphere consisting of 15–20 coccoliths. The coccolith production in *E. huxleyi* is a light-dependent process, with an approximate rate of 1 coccolith every 2 hours under optimum conditions (Westbroek *et al.* 1989). The average diameter of an *E. huxleyi* coccolith is about 2.5 μm and its average weight is about 1.8×10^{-12} g (Fagerbakke *et al.* 1994). The shape of the coccoliths is similar to that of a cable reel, which is comprised a central tube that unites the lower proximal shield and the upper distal shield and associates with the central area (Young & Henriksen 2003). With this morphology, the coccoliths of *E. huxleyi* can closely interlock in the coccosphere and form a robust structure (Young & Henriksen 2003). Young *et al.* (1999) proposed that the coccoliths *E. huxleyi* consist of two differently orientated crystallographic units. The radial R-unit builds up with the calcite c-axis parallel to the coccolith plane; while the V-units forms with the crystal c-axis point perpendicular to the coccolith plane (Young & Henriksen 2003).

Despite research over 50 years, for this best-studied coccolithophore species *E. huxleyi*, much remains uncertain: the pathway of calcium and carbonate ion transportation to calcification front, the regulation of coccolith calcite formation, and its coccolith crystallographic organization are not clear enough to fulfil the current general paradigms of biomineralization that appeal to the attachment and assembly of nanoparticles (Weiner & Addadi 2011; De Yoreo *et al.* 2015) as the pathway of biomineral crystallization. To obtain insight into the pathway of biomineralization of *E. huxleyi* coccoliths, the intracrystalline nanostructural features of its coccolith calcite were examined with HR-TEM, in combination with the cell ultrastructural investigation with cryo-prepared SEM and TEM specimens. The details are reported in section 2.1.

1.2.2 Foraminifera

Foraminifera are a large phylum of unicellular calcifying eukaryotes. Most of them produce an elaborate shell-like outer protective layer (called a "test") which can have one or more interconnected chambers. Those tests are often calcareous (or more rarely silica) that can be also agglutinated of sediment particles and organic matters (Loeblich & Tappan 1988). Foraminifera are essentially marine protozoans, nevertheless, freshwater species, even nonaquatic species are proposed to be considered as foraminifera in recent research articles (Holzmann & Pawlowski 2002; Holzmann *et al.* 2003; Lejzerowicz *et al.* 2010). Calcitic foraminifera are estimated to produce approximately 1.4 billion tons of carbonate per year, which presents almost 25% of the global ocean carbonate production (Langer 2008). Foraminifera are widely used for paleoceanographic reconstructions due to their abundance and nearly continuous fossil record (Erez 2003; Gooday 2003).

The calcification in foraminifera is considered to be a biologically controlled process (Lowenstam & Weiner 1989), and mainly two mechanisms have been proposed to explain the calcite formation of different foraminifera. For bilamellar perforate hyaline foraminifera (e.g. Rotaliida), an organic layer that is generally referred to as the “primary organic membrane” is considered to initiate the calcification within confined extracellular space (e.g. Angell 1979; Bé 1982; Hemleben *et al.* 1986; Spero 1988). With the help of ectoplasmic pseudopods, the organism delineates a space that partially isolates itself from the environment as the first step to build a new chamber. In this space, the primary organic membrane forms and may serve as a template for calcite nucleation and the precipitation on both sides. It should be noted that this

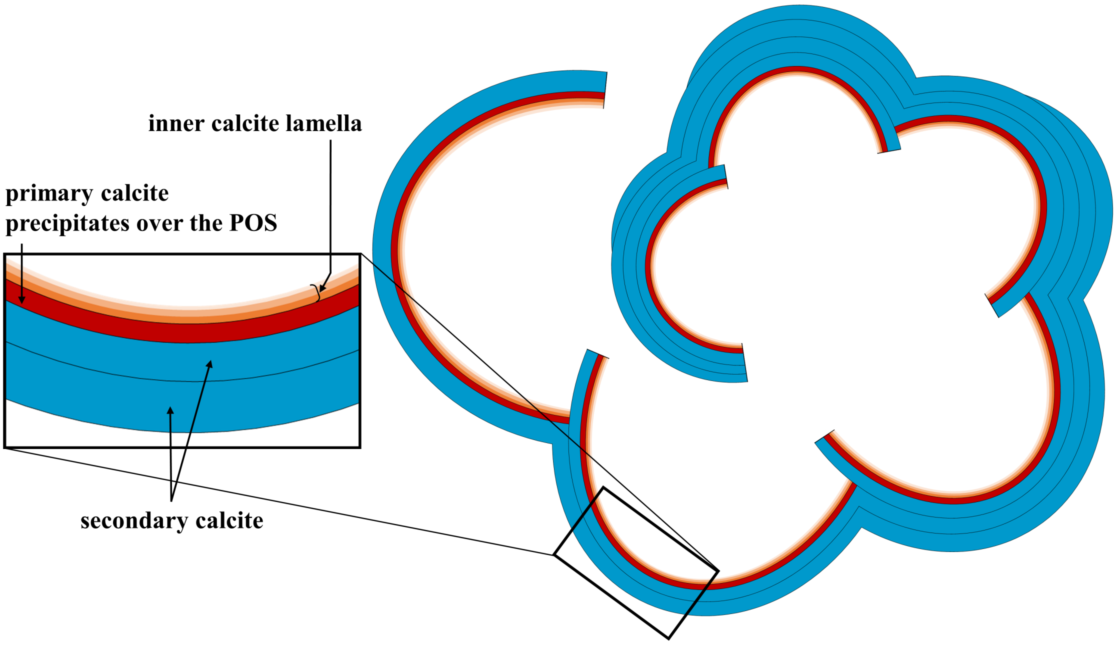

Figure 1.2-2. Schematic drawing showing the lamination in perforate foraminifera, originally from Reiss (1957) and modified after Erez (2003). Every new chamber contains a thin layer of primary calcite (red) that precipitates over the primary organic sheet (POS). The primary calcite is followed by a thick layer of secondary calcite (blue) that covers both the inner lamella and the entire existing shell. An inner calcite layer (orange) may precipitate on the inner chamber walls after the chamber formation, which may also have laminations (Fehrenbacher *et al.* 2017).

thin organic layer is not a cell membrane; researchers also suggested to use the term "primary organic sheet" (POS) to avoid ambiguity (Erez 2003). Lamination (Fig. 1.2-2) is obtained as additional layers of calcite covering the pre-existing chamber calcite during each chamber formation (Reiss 1957, 1960; Bé & Hemleben 1970; Erez 2003). The inner side of each chamber may deposit another thin layer of calcite that may also have a lamella structure as reported in a recent study (Fehrenbacher *et al.* 2017).

The other model applies to the imperforate high-Mg calcite foraminifera (e.g. Miliolida), as those species precipitate their needle-shaped calcite crystals within intracellular vesicles and further deposit the calcite bundles to the sites of chamber formation by exocytosis. The appearances of their tests are often opaque as the calcite crystals are usually randomly orientated during the chamber formation (e.g. Angell 1980; Hemleben *et al.* 1986).

To better understand the microstructures and textures of the foraminiferal test calcite, three benthic foraminifer species *Amphistegina lobifera*, *Amphistegina lessonii* and *Ammonia tepida* (all belong to the Rotaliida order) were microtome polished and investigated with Electron backscatter diffraction. The details are summarized in section 2.2.

1.2.3 Molluscs and Brachiopods

Mollusca, a large and diverse phylum of invertebrate animals, is estimated to contain about 85,000 described species that have a variety of body forms and lifestyles (Chapman 2009). Gastropoda (snails and slugs) and Bivalvia (clams, oysters, cockles and their relatives) are the two largest molluscan classes not only for living species but also in the fossil record (Rosenberg

2014; WoRMS Date accessed: 30.09.2020). Cephalopoda (octopus, squid, nautilus, etc.), another dominant class in the phylum, represents the most intelligent invertebrates that have a well-developed and complex nervous system with a far larger central brain (compare to other molluscs), therefore, are considered to be more closely related to the vertebrates (e.g. fishes) than to other invertebrates (Nixon *et al.* 2003).

Molluscs are grandmaster builders in the natural environment. They form varies biogenic minerals that have different chemical compositions with specialized functionalities, for instance, soft tissue protection (shells), gravity receptors (statoliths), mechanical grinding (teeth), brood chamber (egg cases), reproduction (love darts), etc., which presents a picture of overwhelming diversity all within one phylum (Lowenstam & Weiner 1989). Shell formation is just one perfect paragon of how molluscs utilize the biominerals.

Following the terminology and definition introduced by Mann (1983), the formation of molluscan shells is an archetype of *biologically controlled mineralization*. The molluscan shells are undisputed biogenic structural composites, where the mineral parts are intimately associated with an organic matrix that is consequently sealed within the calcareous exoskeleton during its growth. The matrix is only 0.1–5%wt of the shell that contains proteins, glycoproteins, chitin, and acidic polysaccharides as main components (Marin *et al.* 2008 and the references therein).

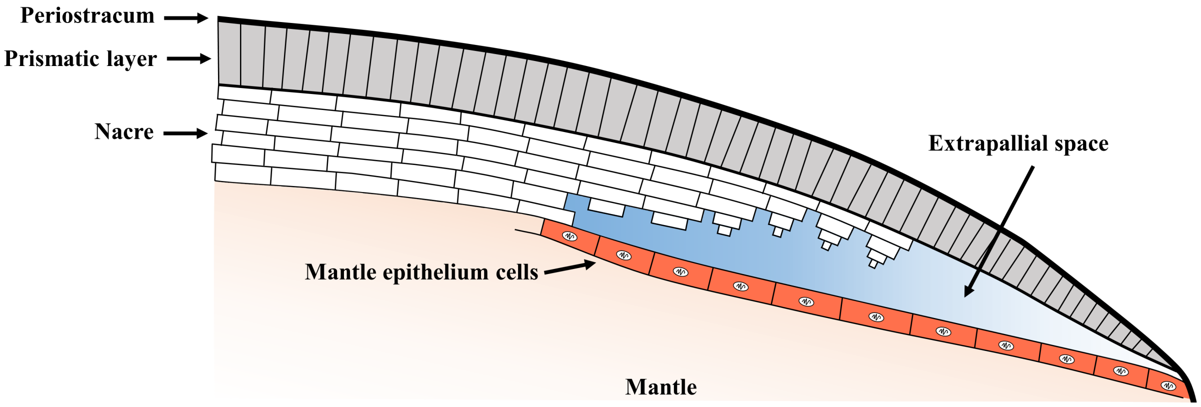

Figure 1.2-3. Schematic of a typical molluscan shell anatomy. It is composed of periostracum, a prismatic layer and nacre. The liquid-filled interlamellar space (extrapallial space) that sealed by the periostracum exists between the mineralized shell parts and the mantle part of the organism, modified after Heinemann *et al.* (2011).

The molluscan shells are calcareous exoskeletons that enclose, support, and protect their soft bodies against predators and external aggression (e.g. from rocks or debris which are displaced by waves). The anatomy of a typical molluscan shell (especially for Bivalvia, Gastropoda, and Cephalopoda) is shown in Figure 1.2-3. A molluscan shell is a characteristically layered structure: the outer layer is the periostracum, which is a primarily proteinaceous layer that the mature shell uses to cover the outside surface of the shell, the middle layer is usually a prismatic layer that is composed of columnar calcite or aragonite, and the inner layer is usually nacre which consists of small flat tightly packed aragonite tablets together with organic cement (Bøggild 1930; Carter 1980; Nakahara 1983; Carter & Clark II 1985). The exterior calcium carbonate layers are often hard and brittle and provide resistance to external impact such as penetration, while the inner nacre layer has striking toughness to resist mechanical deformation like compression, shearing, or bending (Wang *et al.* 2001; Dubey & Tomar 2010; Yourdkhani *et al.* 2011). A small liquid-filled interlamellar space, more often referred to as extrapallial space, is located between the outer mantle epithelium and the growing shell. This space contains the extrapallial fluid, in which the precursor ions for shell mineralization are supposed to concentrate and self-assemble in a precise manner (Misogianes & Chasteen 1979; Moura *et al.* 2000; Marin *et al.* 2008).

The major constituents of the periostracum are quinone-tanned proteins, and chitin is a minor one that is not always present (Brown 1952; Peters 1972; Lowenstam & Weiner 1989). The periostracum is a thin, pliable, fibrous layer that is thought to protect the shell and sever as a substrate upon which the calcium carbonate crystals deposit (Saleuddin & Petit 1983). Another function of periostracum is to completely seal the extrapallial space, for reaching supersaturation conditions that crystallization will happen (Saleuddin & Petit 1983; Simkiss & Wilbur 1989). Prisms are supposed to be an archaic type of shell texture in the outer layer of the molluscan shell. The prims are calcitic or aragonitic needle-shaped calcium carbonate crystals that developed perpendicular to the periostracum. They vary in lengths and diameters depending on the mollusc species.

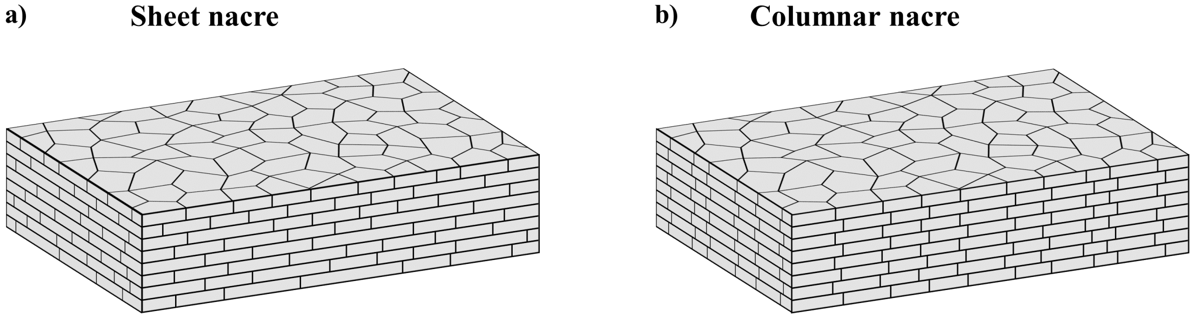

Figure 1.2-4. Schematic illustrations of (a) sheet nacre (pearl oyster, bivalves) and (b) columnar nacre (abalone, gastropods), modified after Sun & Bhushan (2012). Polygonal aragonite tablets are tightly packed into a lamellar structure by thin organic interlayers. In columnar nacre, the inter tablet boundaries are correlated into a tessellated arrangement (Wang *et al.* 2001).

Besides the prisms, nacre, also called mother-of-pearl, is another key model in molluscan shell texture. The tablets of nacre typically are polygonal (e.g. rectangular, hexagonal, or even rounded) which form superimposed layers with uniform thickness (∼300–500nm thick of each layer, Marin & Luquet 2004; Meyers *et al.* 2008; Sun & Bhushan 2012). There are two broad types of nacre, depending on the stacking mode of the tablets as shown in Figure 1.2-4 (Nakahara 1991): “brick wall or sheet” nacre which is classical among bivalves, whereas “columnar” nacre occurs more in gastropods (Currey 1977). In the first type, the bivalves nacre tablets are crystallographically coaligned in three axes, with the c-axis perpendicular to the nacre surface and the b-axis parallel to the local growth direction of the shell margin (Wada 1960, 1962; Weiner & Traub 1984; Weiner & Addadi 1997; Checa *et al.* 2005). In the second type, the gastropods nacre tablets within the same pile/tower have their c-axes co-oriented along the stacking axis. However, from one pile/tower to another, their c-axes are aligned but the a- and b-axes have turbostratic disposition (Lin & Meyers 2005).

Brachiopods (lamp shells), phylum Brachiopoda, a are a group of bivalved marine invertebrates forming calcium carbonate or calcium phosphate shells. Although brachiopods may appear analogous to molluscs at a first superficial glance, their bipartite shell is not symmetrical in contrast to the typical molluscan shells. Instead, a brachiopod generally consists of a dorsal (upper) valve and a ventral (lower) valve, with the ventral valve usually being the larger one of the two valves.

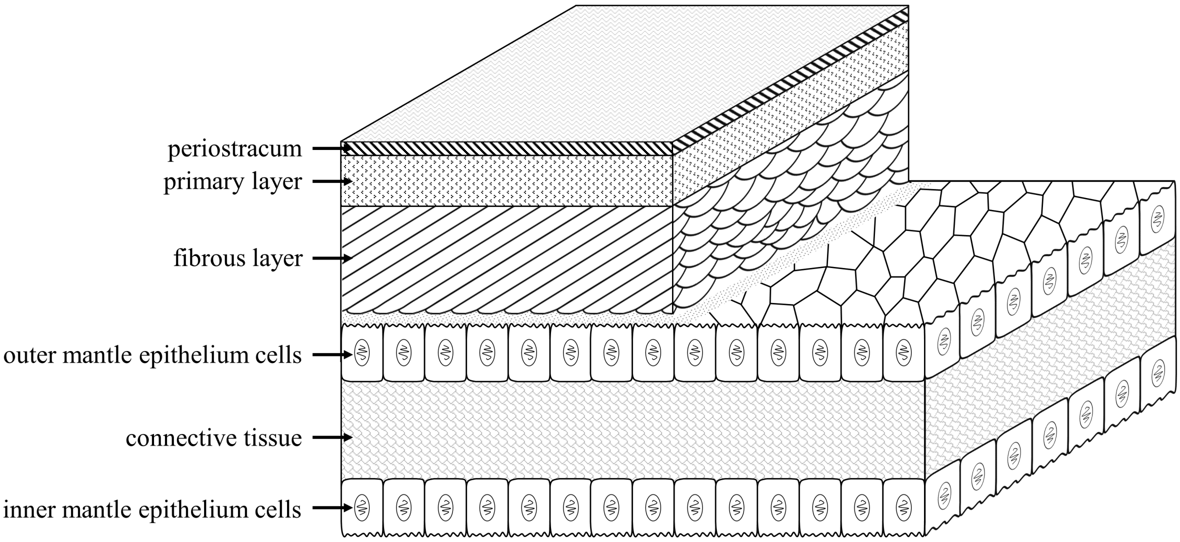

Figure 1.2-5. Schematic reconstruction of a modern terebratulid brachiopod (*Magellania venosa*) shell structure, modified after Simonet Roda *et al.* (2019a).

The construction of the brachiopod shells meets the criteria for "biologically controlled mineralization" in the biomineralization terminology, as the brachiopods, the same as the molluscs, secrete also a mixture proteins and polysaccharides during the mineralization process (Jope 1967b,a; Gaspard *et al.* 2007, 2008). The terebratulid brachiopods also have a trilayered structure: an outer organic periostracum, a primary layer with acicular and granular calcite, and an innermost secondary layer composed of calcite fibres (Williams 1967; Mackinnon & Williams 1974). A schematic reconstruction of a modern terebratulide brachiopod (*Magellania venosa*) shell structure that involved the present work is shown in Figure 1.2-5.

In the present work, eight different molluscan shells (five bivalves, two gastropods, and one cephalopod) and two terebratulide brachiopod shells, prepared by microtome polishing and chemical etching/decalcification, were investigated with FE-SEM imaging. The structures of their organic matrices within the calcium carbonate hard tissues are revealed and compared with the those obtained from the biomimetic experiments. More details could be found in section 2.3.

1.3 Biomimetic Calcium Carbonate Composite Materials

As mentioned in the previous sections, the biogenic calcium carbonates produced by the living organisms are a wide range of composite materials. Most of these materials are generally designed as specific implements to the creatures, in which the structure, shape, size, texture of the constituents are precisely controlled. Biomimetics or bioinspiration is the imitation of nature to solve the critical challenges faced by humanity. The studies of biomineralization are able to provide attractive alternative applications to produce synthetic materials at ambient pressures and temperatures (Aksay *et al.* 1996). The control of crystal nucleation and growth is a key factor of the bottom-up approach synthesis in material science.

1.3.1 Principles of Crystal Nucleation and Growth

Crystals are in general anisotropic solid materials that have periodic atomic arrangements (Sunagawa 2005). Crystallization, or more precisely speaking the pathway to crystallization, is not only an imperative research topic for the biomineralization field but also an essential and critical subject in biomimetic experiments. Classical nucleation theory (CNT) is the most common theoretical model that provides a general framework for predicting the nucleation rates, crystal growth mechanisms, and crystal stability based on thermodynamics. This approximate theory was initiated based on the ideas of Gibbs (1876, 1878) and further developed and improved by Volmer & Weber (1926), Becker & Döring (1935), and Frenkel (1939). CNT first describes the condensation of a vapour to a liquid but can be also extended to other equilibrium systems like vapour-solid and liquid-solid systems to describe crystallization from vapours, melts, and solutions (Mullin 2001).

There are two mechanisms of primary nucleation: homogeneous and heterogeneous nucleation. Homogeneous nucleation is a spontaneous nucleation that occurs in the bulk of supersaturated solutions, whereas heterogeneous nucleation involves the formation of nuclei on a preexisting surface. When the thermodynamic equilibrium system is perturbed (e.g change in temperature), a nucleus of a crystal will be formed and the crystal growth will then begin. As nucleation and crystal growth are processes that result in the formation of a regular solid phase from a disordered and irregular state with a sharp, discontinous interface, it can be regarded as a first-order phase transition. At constant pressure, the driving force of a phase transformation is the change in Gibbs free energy. In the case of homogeneous nucleation, assuming that the formed cluster is a sphere of radius r, the free energy change of the system is given by Equation 1.3-1

$$\Delta G = \frac{-4\pi r^3}{3\nu} kTlnS + 4\pi r^2 \sigma \qquad 1.3\text{-}1$$

where the first term is the volume term, which represents the contribution of the bulk free energy to ΔG. $\frac{4\pi r^3}{3\nu}$ represents the number of molecules in a cluster of radius r, where the volume of a single molecule is ν, and S is the supersaturation ratio. The volume term is negative if the phase to form is thermodynamically more stable than the phase from which it nucleates. The second term is the surface/interface term, where σ is the specific surface energy of the interface between the nucleus and its surroundings (e.g. supersaturated solution and the developing crystalline surface), which is always positive. It is crucial to note that the volume term is proportional to r^3 and the surface energy is proportional to r^2. Thus, there is a radius (r^*) at which the change in Gibbs energy for the formation of the cluster exhibits a maximum (ΔG^*). This aspect is illustrated in Figure 1.3-1. The parameters defining this special point are classically designated as critical parameters. This means that nuclei formed bigger than the critical size will grow without limit and nuclei formed smaller than the critical size will dissolve completely.

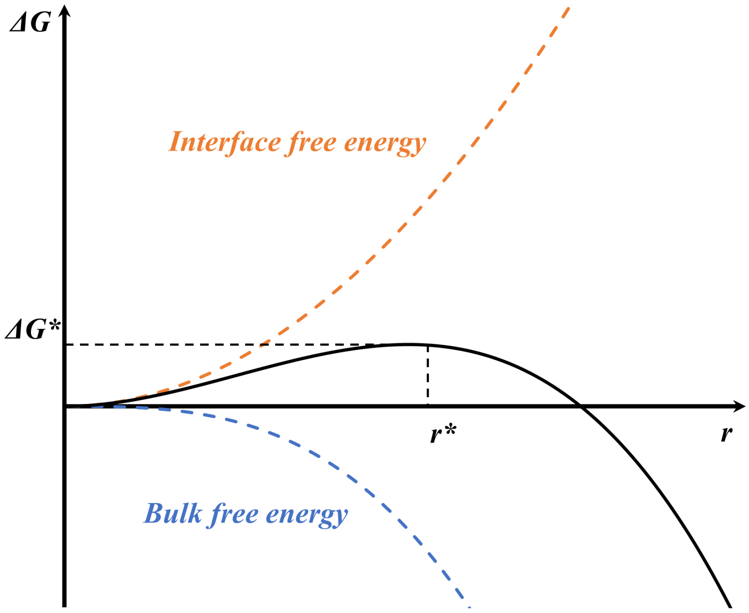

Figure 1.3-1. Schematic plot of Gibbs free energy change due to the formation of a nucleus in a supersaturated medium.

Differentiating Equation 1.3-1 with respect to r, it is found that $r^* = \frac{2\sigma\nu}{kTlnS}$, and the barrier to nucleation is given by Equation 1.3-2

$$\Delta G^* = \frac{16\pi\nu^2\sigma^3}{3(kTlnS)^2} \tag{1.3-2}$$

The nucleation rate J can be expressed in the form of the Arrhenius reaction rate by Equation 1.3-3

$$J = Ae^{-\frac{\Delta G^*}{kT}} \tag{1.3-3}$$

where A is the preexponential factor which is determined by kinetics, k is the Boltzmann constant, and T is the reaction temperature (Volmer & Weber 1926). Substituting the critical nucleation barrier at a given supersaturation in Equation 1.3-3 gives the final expression of nucleation rate J, as

$$J = Ae^{-\frac{16\pi\nu^2\sigma^3}{3k^3T^3(lnS)^2}} \tag{1.3-4}$$

In contrast to "homogeneous nucleation", the other classification of nucleation processes is "heterogeneous nucleation", which considers that the nucleation processes no longer initiate from a supersaturated bulk phase but take place on existing extrinsic interfaces. In solid state nucleation, point, line and planar defects are suitable substrates that facilitate nucleation. In the case of nucleation from solution, nuclei can form on dust particles and vessel walls. The formation of heterogeneous nuclei leads to the generation of interfaces whose energy differs from that of the nucleus-bulk system interface. Equations 1.3-2 shows that both ΔG^* and r^*

depend on the surface energy (σ). Therefore, any process that modifies the surface energy will also affect the nucleation. It has been proven that heterogeneous nucleation is associated with a decrease in σ which results in the reduction of both ΔG^* and r^* at a given supersaturation (Kashchiev & van Rosmalen 2003). The lower activation energy for heterogeneous nucleation is especially relevant at low supersaturation conditions, making it more likely to occur than homogeneous nucleation. Heterogeneous nucleation is further favoured by the existence of structural similarities between the phase that nucleates and the substrate, which allows nuclei to form oriented on the latter, defining an epitaxy. If the substrate and the crystallizing phase have the same nature this type of heterogeneous nucleation is called homoepitactic nucleation, while oriented nucleation that involves nuclei and substrates of different nature is described as heteroepitactic nucleation.

Those particle clusters that exceed the critical size can grow larger and enter the growth stage in its strictest sense (Sunagawa 2005). Crystal growth involves a series of processes through which a pre-existing nucleus develops into a larger crystal as it incorporates growth units (e.g. molecules, ions) (Chernov 1984; De Yoreo & Vekilov 2003). This processes can be summarized into four steps: 1) transport of atoms within the solution; 2) attachment of atoms to the crystal surface; 3) movement of atoms on the crystal surface; 4) attachment of atoms to crystal edges and kinks (Elwell & Scheel 1975). The first step is considered as a transport process, while the other three steps are considered as surface processes. Depending on what step controls crystal growth kinetics, the crystal growth can be described as either transport controlled or surface controlled.

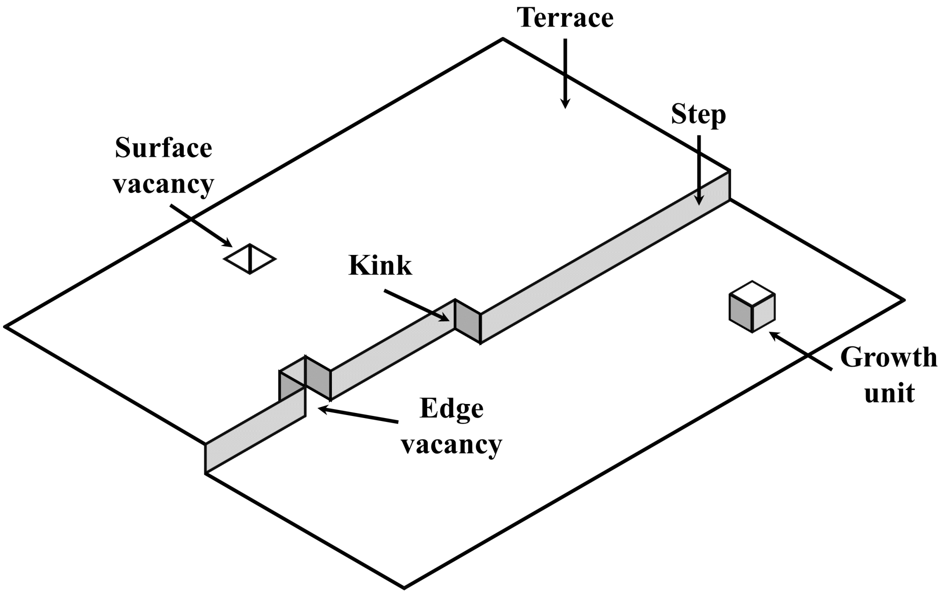

Figure 1.3-2. Schematic diagram of a crystal surface described by the Kossel-Stranski "terrace-step-kink" model.

Crystal growth mechanisms are based on the consideration of crystal surface structure. Kossel (1927) and Stranski (1928) were the first researchers to report studies on this subject. The so-called “Kossel crystal” model idealizes the constituent units of both a crystal and crystal growth units as simple cubes. This model differentiates three different sites on a crystal surface, each characterized by a different attachment/detachment energy: a smooth surface site (terrace), a step, and a kink (Fig. 1.3-2). Kink sites offer the most stable configuration to the attached growth units since it provides three contact sides, whereas steps and terraces only have two and one contact side(s) with the growth unit, respectively. During the growth process, the attachment of a growth unit into a kink site results in the reproduction of the original geometry and does not modify the surface area; the attachment into a step results in the generation of two kink sites. This is even more so for attachment to a terrace. As the addition of surface area increases the energy of the whole surface, the energy of attachment for the growth unit to the crystal decreases in the order of terrace, step, and kink. A growth unit has the highest possibility to be incorporated into the crystal by the attachment to a kink site in steps, the kink will then move along the step until this step reaches the edge of the crystal surface. Then a new step source is required to continue growth. Kossel (1927) and Stranski (1928) assumed two-dimensional nucleation as the mechanism that would provide new kink sites. This crystal growth mechanism is normally referred to as *layer-by-layer growth* or *single nucleation growth*. This growth mechanism varies when the two-dimensional nucleation takes place at such a fast rate that a new two-dimensional layer starts to form before the one that originated previously is still spreading. The 2D nuclei will then form all over the flat terrace and also on top of other nuclei. These nuclei will spread and the spreading layers will coalesce. This growth mechanism is referred to as *multinucleation multilayer growth* or *birth and spread* (Ohara & Reid 1973).

The layer-by-layer growth mechanism formulated by Kossel (1927) and Stranski (1928) requires a relatively high supersaturation condition, since for this mechanism to take place the energy barrier associated with 2D nucleation has to be overcome (e.g. the energy barrier is estimated to be around 25–50% in terms of supersaturation for crystal growth from the vapour phase). However, it was observed in the laboratories that crystals could still grow at much lower supersaturation (e.g. in the case of crystal growth from a vapour phase, crystal growth was observed at as low a supersaturation as 1%) than predicted by the then available crystal growth models (Volmer & Schultze 1931). This large discrepancy between the theoretical model predictions and experimental observations reflected the fact that real crystals are imperfect and contain impurities and dislocations, while the models proposed by Kossel and Stranski idealizes crystals to be perfect (i.e. defect-free).

This predicament was solved by Frank (1949), who proposed that dislocations which are intercepted by crystal surfaces promote crystal growth without the need of 2D nucleation. When a screw dislocation protrudes on a smooth crystal interface, a step is created. Most importantly, the kink site where the dislocation protrudes is perpetuated after the attachment of a growth unit. The growth step starting at the dislocation source advances like a spiral staircase around the dislocation line. This mechanism was further refined by Burton, Cabrera, and Frank (1949; 1951), giving rise to what is known as the BCF theory.

Although the classical nucleation theory has been developed and improved through the past 200 years, modern experiments have shown that in complex materials/systems like proteins, colloids, polymeric solutions, etc. (e.g. ten Wolde & Frenkel 1997; Anderson & Lekkerkerker

2002; Zahn 2004; Gliko *et al.* 2005; Li & Dincă 2015) the CNT may not always be appliable. The non-classical nucleation provides another possible pathway of crystallization (e.g. Wang *et al.* 2005; Niederberger & Cölfen 2006; Cölfen & Antonietti 2008). The review paper of Meldrum & Cölfen (2008) summarized numerous examples in which the CNT can not explain the observed phenomena and discussed a non-classical crystallization framework that mainly focuses on the biomineralization field. A schematic illustration of classical and non-classical crystallization pathways is shown in Figure 1.3-3. More recent researches pointed out that in the biogenic or biomimetic mineralization, precursor phases (i.e. prenucleation clusters, PNCs) and small polymeric molecules are the "protagonists" during the early stages of nucleation (Sommerdijk & Cölfen 2010; Gebauer *et al.* 2014; De Yoreo *et al.* 2015). The validity of classical nucleation in different contexts, including biomineralization, remains controversial (Nielsen *et al.* 2014; Andreassen & Lewis 2017; De Yoreo *et al.* 2017; Smeets *et al.* 2017; Gebauer *et al.* 2018; Henzler *et al.* 2018; Kashchiev 2020).

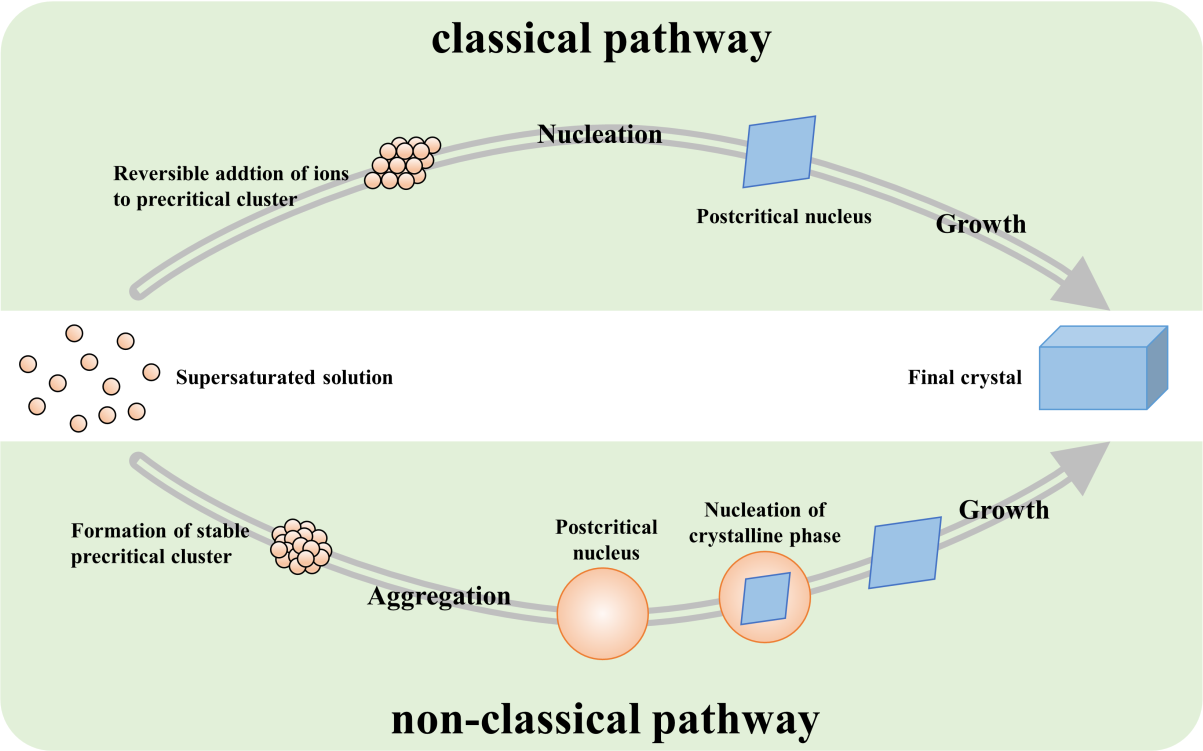

Figure 1.3-3. Schematic illustration of classical and non-classical crystallization pathways modified after Meldrum & Sear (2008)

Regarding the calcium carbonate, which is the central object of this dissertation, the observation of amorphous calcium carbonate (ACC) as solid phase precursor to the formation of crystalline $CaCO_3$ phases has been widely discussed (Gebauer *et al.* 2008; Pouget *et al.* 2009; Demichelis *et al.* 2011; Rodríguez-Navarro *et al.* 2015). The liquid precursors of calcium carbonate can be stabilized by externally supplied additives (e.g. polyaspartate) before the formation of ACC (Bewernitz *et al.* 2012). Based on experimental observations, it has been proposed the existence of pH-dependent prenucleation clusters. which are stable solute species (Gebauer *et al.* 2008). The non-classical nucleation theory postulates that accretion of prenucleation clusters can eventually lead to the formation of crystals through a sequence of intermediate states (Cölfen & Antonietti 2008; Gebauer & Cölfen 2011). The formation of ACC nanoparticles represents one of these intermediate states (Gebauer & Cölfen 2011).

Gebauer *et al.* (2008) claimed the existence of different short-range ordered ACC types, which are correlated with the final crystalline that forms from the solution, and further introduced the notion of proto-calcite ACC (pc-ACC, ACCI) and proto-vaterite ACC (pv-ACC, ACCII) in a later publication (Gebauer *et al.* 2010).

1.3.2 Organic Matrices in Calcium Carbonate Composite Materials

Organic components in biominerals have been proven to hold crucial functions in biomineralization (Cusack & Freer 2008). Biogenic calcium carbonate tends to be associated with mainly two categories of the organic matrix components. Quantitatively, the majority of constituents form a two- or three-dimensional structure onto which or into which the mineral parts can grow (Weiner 1984). These macromolecules are usually highly cross-linked, insoluble, and slightly hydrophobic. Besides providing a volumetric area for mineralization, these "framework macromolecules" may also act as a substrate where other soluble and smaller biopolymers may interact with the mineral phase. The other set of the matrix elements are soluble biomolecules, which could be unbound, adsorbed onto the framework, or even occluded within the mineral parts during the crystal growth process. As Meldrum (2003) summarized in the review paper that these soluble biopolymers could be referred to as "control macromolecules" since they may have more impact on the mineral phase selection, morphology and texture control in comparison to the framework macromolecules, which may only influence the final shape of the biomineralized composite.

Based on the primary structures and pertinent calcium carbonate mineral phase, the "control macromolecules" can roughly be classified into two main groups:

1. proteins and glycoproteins (especially aspartic acid (Asp) / asparagine (Asn), glutamic acid (Glu) / glutamine (Gln), and Serine (Ser) riched ones) (e.g. Weiner & Hood, 1975; Wheeler et al., 1991)
2. Polysaccharide rich macromolecules (e.g. Albeck et al., 1996; Falini et al., 1996)

The first group is usually acidic macromolecules as contain an abundance of carboxylate functional groups within the structure. The high negative charges associated with these proteins and glycoproteins enable them as good candidates to facilitate structured interaction with the crystal faces and also possibly to bind calcium cation at certain sites. The soluble organic matrix components have been shown to exert a remarkable influence on crystal nucleation and morphology even extracted from the whole matrix (Thompson *et al.* 2000; Raz *et al.* 2003). However, during biomineralization studies, it is also indispensable to consider the organic matrix as a whole entity as several research groups have demonstrated the importance of the interactions between the framework macromolecules with acidic proteins and the mineral phases (Albeck *et al.* 1996; Addadi *et al.* 2006; Nudelman *et al.* 2007).

Hydrogels are porous networks which show features strikingly similar to the organic matrices and have been proven to be ideal model systems to understand the process of biomineralization (Nickl & Henisch 1969; Li & Estroff 2007; Li *et al.* 2011b; Asenath-Smith *et al.* 2012; Gal *et al.* 2013). Based on the previous studies on the single hydrogel systems of gelatin and agarose in the research group (Nindiyasari *et al.* 2014a,b, 2015, 2019; Greiner *et al.* 2018), this dissertation aims to understand the biomimetic growth of calcium carbonate in hybrid hydrogel systems as well as simple hydrogels combined with different bacterial extracellular polymeric substances (EPS).

1.3.2.1 Hydrogels

Hydrogels have three critical properties that would be advantageous to mimic the biomineralization process: (i) they can be chemically close to the organic matrices, as is the case for agarose hydrogel, polysaccharide-based, and gelatin hydrogel, a protein-based hydrogel that contains many peptides. (ii) they provide volumetric confinement after gelation, and it is well established that biomineralization processes often take place in confined environments (Levi-Kalisman *et al.* 2001). (iii) hydrogel networks combined with reactants can be easily modified to control the diffusion rates, local concentrations, and supersaturation levels to better mimic the biomineralization process. For all these reasons, hydrogels such as gelatin, agarose, silica, polyacrylamide are popular platforms for biomineralization studies (Dorvee *et al.* 2012, and references therein). In present work, biomimetic crystallization experiments were conducted using agarose and gelatin hydrogel, and the results of these experiments are described and discussed in sections 2.4, 2.5, and 2.6.

Polysaccharides are biopolymers that built up from monosaccharides. They are long-chain polymeric carbohydrates, which are often not pure but associated with polyphenolics, or proteins, either by covalent or by non-covalent bonds. Agarose is a linear polysaccharide consisting of alternating D-galactose and 3,6-anhydro-L- galactose units. Agarose is purified from agar which is generally isolated from certain marine algae (red seaweed) after removing the agaropectin component that is highly sulphated and does not form a gel. Gelatin is a heterogeneous mixture of water-soluble proteins that are present in collagen.

Recent studies on hydrogels biomimetic mineralization showed that lysozyme and calcite crystals incorporate the gel matrix during growth (e.g. Gavira & Garcia-Ruiz 2002; Li & Estroff 2009; Nindiyasari *et al.* 2014a,b, 2015; Greiner *et al.* 2018). Crystal growth rate (which is related to the supersaturation) and gel strength are the two parameters that influence the amount of gel incorporated into the crystal (Li & Estroff 2007, 2009; Asenath-Smith *et al.* 2012). For physical gels such as agarose and gelatin used in the present work, the gel strength is directly related to their solid content (Asenath-Smith *et al.* 2012; Nindiyasari *et al.* 2015; Greiner *et al.* 2018). The growth rate is related to the supersaturation of the solution (Chernov 1984; De Yoreo & Vekilov 2003). According to Estroff's model, fast crystal growth rate and strong gel strength result in the entire gel network to be incorporated within the crystal without any critical damage of the hydrogel network (Asenath-Smith *et al.* 2012; Nindiyasari *et al.* 2015). Low gel strengths and low growth rates facilitate the formation of practically gel-free crystals (Asenath-Smith *et al.*

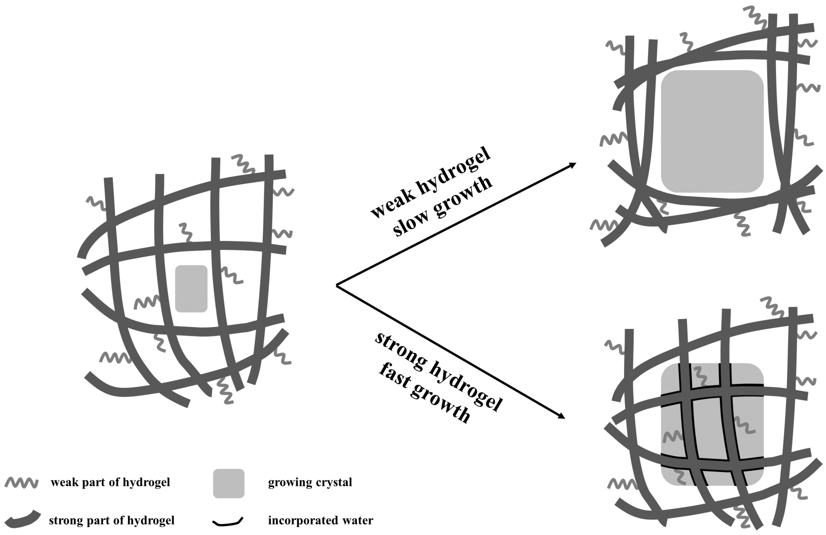

Figure 1.3-4. Schematic illustration for agarose matrix incorporation during calcite crystal growth: a balance between the resistance of the gel fibres to crystallization pressure and the growth rate. Modified after Li & Estroff (2009) and Asenath-Smith *et al.* (2012) .

2012; Greiner *et al.* 2018). A schematic representation described mechanisms related to the balance between gel strength and crystal growth rate in Figure 1.3-4.

1.3.2.2 Bacterial Extracellular Polymeric Substances (EPS)

Bacteria are prokaryotic microorganisms that are found almost everywhere on our planet. They exhibit remarkable genetically and metabolically diversity and are considered to hold a significant role in the deposition and weathering of minerals in the Earth's crust. Most of the bacteria-related biomineralization processes are considered to be biologically induced mineralization processes. This kind of biomineralization is described as the outcome of the bacterial metabolic activity or succeeding chemical reactions involving metabolic by-products, and the minerals primarily nucleate and grow in the extracellular environments (Frankel & Bazylinski 2003). The polymeric substances (exopolymers) exuded by bacteria existing in the form of slimes, sheaths or biofilms, can act as adsorption sites for ions to enable the mineral nucleation and growth (Beveridge 1989; Konhauser 1998; Banfield & Zhang 2001; Bäuerlein 2003).

Chemically, the bacteria-related calcium carbonate precipitation is governed by four key factors: (1) calcium concentration, (2) dissolved inorganic carbon concentration, (3) pH, and (4) nucleation sites availability (Hammes & Verstraete 2002). Three types of hypotheses were suggested to explain the role of bacteria and their activities in carbonate crystallization: (i) first, the mineralization happens as a by-product of the bacterial metabolism (Douglas & Beveridge 1998; Castanier *et al.* 1999; Lian *et al.* 2006); (ii) the nucleation occurs on the bacteria cell wall (Rivadeneyra *et al.* 1998; Castanier *et al.* 2000); (iii) extracellular macromolecules are involved and take roles in the mineralization (Ercole *et al.* 2007; Decho 2010). In present work, the study was based on the last presumption and extracted extracellular polymeric substances (EPS) after the bacteria cultivation was used in the crystallization experiments. Any alive bacteria cells that could remain in the extracted EPS were killed to eliminate any possible influence of bacteria metabolism in the subsequent crystal growth experiment. Similarly, the contribution of the intracellular components (e.g. cell walls) was controlled and minimized in the extraction protocol (Yin *et al.* 2020b).

Extracellular polymeric substances (EPS) is a broad term which includes a large variety of organic polymers secreted by microbial cells. Polysaccharides are the major component of most EPS, in which polypeptides, nucleic acids, phospholipids, and other polymeric compounds are often combined (Decho 1990). As mentioned in the previous two sections, the characteristics of the bacterial EPS are chemically very close to that of the "control macromolecules" whereas the hydrogel may provide a suitable supporting network for crystallization. Therefore, the combination of these two elements could inspire a more appropriate system to mimic the biomineralization process as well as to understand the bacterial mediated calcification process.

1.3.3 Diffusion Systems in Biomineralization

Traditionally, using hydrogels to support crystallization is a technique developed by crystallographers to obtain large crystals (Henisch 1988). Many researchers use double diffusion system to conduct their experiments and various designs of the system have been explored to promote its application field (De Jong *et al.* 1980; Hunter *et al.* 1985; Mandel *et al.* 1990; Boskey *et al.* 1993; Asenath-Smith *et al.* 2012). The system can even interact with external forces, i.e. an electric field (Wada *et al.* 1996; Watanabe & Akashi 2008; Kumar *et al.* 2011). Meanwhile, artificial hydrogels have been proven as excellent model systems for conducting biomimetic experiments, since the majority of biomineralization processes arise in gelatinous environments (García-Ruiz 1991; Grassmann *et al.* 2002; Sugawara *et al.* 2003; Simon *et al.* 2004; Dorvee *et al.* 2012).

Most of the hydrogel-based double diffusion systems, also called counter-diffusion systems, are constructed by a hydrogel and opposing sources (reservoirs) of ions on either side of the gel. The hydrogel becomes the medium through which ions diffuse (creating an ion gradient), and also where crystals growth can occur. Henisch & García-Ruiz (1986a,b) summarized the diffusion relationships, crystallization criteria, and successive precipitation using finite analytical solutions for their description of mass transfer through the gel column. The crystallization criteria were further complemented by the definition of supersaturation rate and threshold supersaturation. In hydrogels, crystallization starts at significantly higher supersaturation levels compared to those in solutions, as there is no volume confinement within the solutions (Prieto *et al.* 1994; Putnis *et al.* 1995; Prieto 2014). The supersaturation threshold depends on the boundary conditions of the system, which mainly correlated to the concentration of reactants and the distance from reactant reservoir to the crystallization front, as they define the supersaturation rate (Prieto *et al.* 1994; Putnis *et al.* 1995). As a time-dependent gradient develops in the gel column when the reactants diffuse towards the reaction front, the evolution of supersaturation with progressive growth is given by the balance between rates of reactant arrival to and reactant consumption by the growing crystal (Prieto *et al.* 1989, 1991; García-Ruiz 1992).

Dorvee *et al.* (2012) classified passive double diffusion systems into two categories: static systems and dynamic systems. For static systems, Fick's 1st Law is utilized. It assumes the flux of ions goes into and comes out of the hydrogel reaches a steady or static state. In one spatial dimension (Eq. 1.3-5), the diffusion flux J depends on the diffusion coefficient D and the change of diffusing spices concentration c, which decreases linearly in the hydrogel along the position x. For more dimensions gradient operator ∇ must be used (Eq. 1.3-6).

$$J = -D\frac{dc}{dx} \tag{1.3-5}$$

$$J = -D\nabla c \tag{1.3-6}$$

While for dynamic systems, the diffusing spices concentration c is a function that depends on both position x and time t, Fick's 2nd Law is then applied to describe the concentration change within the system. It is derived using the law of mass conservation and Fick's first law (Eq. 1.3-7).

$$\frac{\partial c}{\partial t} + \frac{\partial}{\partial x}J = 0 \Rightarrow \frac{\partial c}{\partial t} - \frac{\partial}{\partial x}(D\frac{\partial c}{\partial x}) = 0 \tag{1.3-7}$$

Assuming the diffusion coefficient D to be a constant independent of concentration levels, the spatially one-dimensional formula can be simplified as follows (Eq. 1.3-8). For more dimensions, the Laplacian Δ must be used (Eq. 1.3-9), and D becomes a tensor.

$$\frac{\partial c}{\partial t} = D\frac{\partial^2 c}{\partial x^2} \tag{1.3-8}$$

$$\frac{\partial c}{\partial t} = D\Delta c \tag{1.3-9}$$

In present work, a double diffusion system was used to conduct experiments with mixed hydrogels. The experimental setup is illustrated in Figure 1.3-5. For the experiments containing bacterial EPS, the active gel-based single diffusion system was used. In this system, one of the reactants was mixed with gel, while the other occupied a source reservoir on top of the gel.

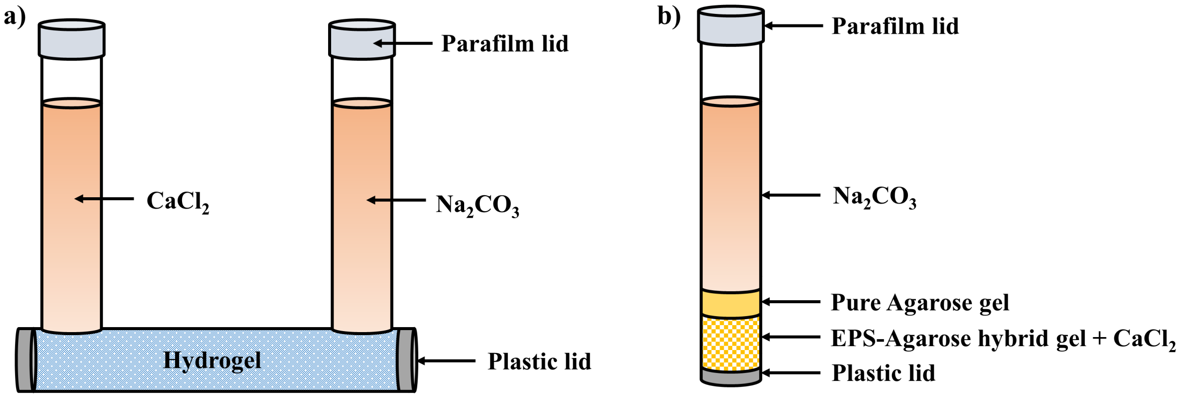

Figure 1.3-5. Schematic illustration of (a) the double diffusion systems (modified after Nindiyasari, 2015) and (b) the single diffusion system (modified after Yin *et al.* 2020a,b).

2 Results and Discussions

The present dissertation focuses on biogenic and biomimetic calcium carbonate composites. Biogenic calcium carbonates often present as biological hard tissues, which are in most cases natural composite materials. These materials are based upon biopolymers and minerals, which produced by living organisms via the process known as biomineralization. The scientific results presented in this dissertation aim to outline the mineral organization pattern and possible biomineralization pathway of a certain marine organism species, coccolithophore *Emiliania huxleyi* (section 2.1); the shell calcite organization in the Formanifera species, *Amphistegina lobifera*, *Amphistegina lessonii* and *Ammonia tepida* (section 2.2), and discuss the resemblance and limitation of the biopolymer structures and characters between the natural biogenic calcium carbonate hard tissue and the biomimetic ones (section 2.3). The mimetic experiments are designed to reproduce the hierarchical composite structure features that the biological hard tissues often have. Crystal growth experiments were performed by using agarose/gelatin hybrid hydrogel to explore the influence of each single hydrogel component of the gel mixtures on calcite aggregate formation. Since magnesium is a common element in exoskeletons of marine organisms, experiments were conducted in parallel with and without Mg dose (section 2.4). Bacterial extracellular polymeric substances were further combined with the agarose hydrogel to investigate the directing influence of native biopolymers on calcium carbonate mineralization. The EPS of *Pseudomonas putida* (section 2.5), *Bacillus subtilis*, *Mycobacterium phley*, and *Mycobacterium smagmatis* (section 2.6) were used in the studies.

Five sections within this chapter are published scientific research journal articles (sections 2.1, 2.2, 2.4, 2.5, and 2.6). The author is the principal author of those four academic publications. The author has made contributions to other six published, one submitted journal articles, and two book chapters as well, and the details can be found in the enclosed publications list.

Section 2.1	Reprinted (adapted) with permission from *J. Phycol.* 2017, 54, 85–104. Copyright ©2017 Phycological Society of America.
Section 2.2	Reprinted (adapted) with permission from *J. Struct. Biol.* 2021, 213 (2), 107707. Copyright ©2021 Elsevier Inc.
Section 2.4	Reprinted (adapted) with permission from *Cryst. Growth Des.* 2019, 19 (10) 5696–5715. Copyright ©2019 American Chemical Society.
Section 2.5	Reprinted (adapted) with permission from *Cryst. Growth Des.* 2020, 20 (3), 1467–1484. Copyright ©2020 American Chemical Society.
Section 2.6	Reprinted (adapted) with permission from *Cryst. Growth Des.* 2020, 20 (7), 4402–4417. Copyright ©2020 American Chemical Society.

2.1 Formation and Mosaicity of Coccolith Segment Calcite of the Marine Algae *Emiliania huxleyi*

Xiaofei Yin[1*], Andreas Ziegler[2], Klemens Kelm[3], Ramona Hoffmann[1], Philipp Watermeyer[3],
Patrick Alexa[1], Clarissa Villinger[2,4], Ulrich Rupp[2], Lothar Schlüter[5], Thorsten B. H. Reusch[5],
Erika Griesshaber[1], Paul Walther[2], Wolfgang W. Schmahl[1]

1. Department of Earth and Environmental Sciences, LMU München, Germany
2. Central Facility for Electron Microscopy, University of Ulm, Germany
3. Institute of Materials Research, German Aerospace Center (DLR), Cologne, Germany
4. Institute of Virology, University Medical Center Ulm, Germany
5. GEOMAR Helmholtz Centre for Ocean Research Kiel, Germany

Journal of Phycology **54**, 85–104 (2018)
https://onlinelibrary.wiley.com/doi/full/10.1111/jpy.12604

Luigi Provasoli Award 2018
for best paper published in the *Journal of Phycology* during 2018

Abstract

Coccolithophores belong to the most abundant calcium carbonate mineralizing organisms. Coccolithophore biomineralization is a complex and highly regulated process, resulting in a product that strongly differs in its intricate morphology from the abiogenically produced mineral equivalent. Moreover, unlike extracellularly formed biological carbonate hard tissues, coccolith calcite is neither a hybrid composite, nor is it distinguished by a hierarchical microstructure. This is remarkable as the key to optimizing crystalline biomaterials for mechanical strength and toughness lies in the composite nature of the biological hard tissue and the utilization of specific microstructures.

To obtain insight into the pathway of biomineralization of *Emiliania huxleyi* coccoliths, we examine intracrystalline nanostructural features of the coccolith calcite in combination with cell ultrastructural observations related to the formation of the calcite in the coccolith vesicle within the cell. With TEM diffraction and annular dark-field imaging, we prove the presence of planar imperfections in the calcite crystals such as planar mosaic block boundaries. As only minor misorientations occur, we attribute them to dislocation networks creating small-angle boundaries. Intracrystalline occluded biopolymers are not observed. Hence, in *E. huxleyi* calcite mosaicity is not caused by occluded biopolymers, as it is the case in extracellularly formed hard tissues of marine invertebrates, but by planar defects and dislocations which are typical for crystals formed by classical ion-by-ion growth mechanisms. Using cryo-preparation techniques for SEM and TEM, we found that the membrane of the coccolith vesicle and the outer membrane of the nuclear envelope are in tight proximity, with a well-controlled constant gap of $\sim$4 nm between them. We describe this conspicuous connection as a not yet described interorganelle junction, the "nuclear envelope junction". The narrow gap of this junction likely facilitates transport of Ca^{2+} ions from the nuclear envelope to the coccolith vesicle. On the basis of our observations, we propose that formation of the coccolith utilizes the nuclear envelope-endoplasmic reticulum Ca^{2+}-store of the cell for the transport of Ca^{2+} ions from the external medium to the coccolith vesicle and that *E. huxleyi* calcite forms by ion-by-ion growth rather than by a nanoparticle accretion mechanism.

Keywords

Emiliania huxleyi; cryo-SEM; electron tomography; cell organelles; cell physiology; diffraction in TEM; microdomains; mosaicity; screw dislocations; small-angle boundaries

2.1.1 Introduction

Coccolithophores are some of the most important calcium carbonate producers in the sea. They are present in large quantities in upper surface ocean waters and are responsible for at least one-third of global marine calcium carbonate precipitates (Milliman 1993). Coccolithophores belong to the class Prymnesiophyceae of the phylum Haptophyta (Edvardsen *et al.* 2000). They are unicellular marine organisms that, in contrast to all other algae, form and cover their cell with elaborately shaped calcium carbonate scales: the coccoliths (Paasche 1968). Their wide occurrence, ecological tolerance, and fast reproductivity render coccolithophores as ideal model systems for studies on biomineralization, cell biology, genetics, evolution and adaptation to new environments (Young *et al.* 1999; Corstjens *et al.* 2001; Paasche 2001; Marsh 2003; Mackinder *et al.* 2010; Lohbeck *et al.* 2012, 2014; Taylor *et al.* 2012; Bach *et al.* 2013; Schlüter *et al.* 2014; Brownlee *et al.* 2015; Monteiro *et al.* 2016; Santomauro *et al.* 2016).

In the geological record, coccolithophores appeared in late Triassic and gained their maximum abundance and diversity in Cretaceous times. Even though at the Cretaceous-Tertiary boundary most coccolithophore species became extinct, from the remaining organisms a few new coccolihtophorid species emerged (Hallam & Perch-Nielsen 1990; Young 1994). *Emiliania huxleyi* differentiated from *Gephyrocapsa* 268,000 years ago, became dominant 73,000 years ago, and is the most abundant coccolithophore species today (Thierstein *et al.* 1977; Paasche 2001).

Wilbur & Watabe (1963); Klaveness (1972); Westbroek *et al.* (1984); van Emburg *et al.* (1986) and, Simkiss & Wilbur (1989) were among the first to perform detailed cytological studies for the description of organelle organization in coccolithophores. Cellular mechanisms that lead to calcite nucleation and coccolith formation were investigated (Nimer & Merrett 1992; Nimer *et al.* 1994; Anning *et al.* 1996; Gussone *et al.* 2006; Taylor *et al.* 2007; Mackinder *et al.* 2010, 2011; Suffrian *et al.* 2011; Bach *et al.* 2013; Holtz *et al.* 2013; Brownlee *et al.* 2015). *Emiliania huxleyi* produces only heterococcoliths that are formed in intracellular compartments, the coccolith vesicles. Calcite growth in these compartments depends upon the coordinated uptake and transport of dissolved inorganic carbon and calcium into and through the cytosol and to the site of calcification (the coccolith vesicle). Transport of Ca^{2+} ions and of HCO_3^- has to be balanced by the removal of protons into and from the cytosol. Westbroek *et al.* (1984) suggested a model in which calcium is first taken up from the seawater by endocytotic vesicles and then transported via Golgi cisternae to the reticular body. Later, based on expression studies, Mackinder *et al.* (2011) proposed uptake of Ca ions through Ca channels and uptake of Ca from the cytosol into peripheral cisternae of the endoplasmic reticulum (ER). With a combination of cryo-soft-X-ray tomography, spectroscopy, and cryo-focused ion beam scanning electron microscopy Sviben *et al.* (2016) visualized a Ca-P-rich compartment within the cell of *E. huxleyi*. These authors regard this as a dynamic reservoir where Ca ions are concentrated and dispatched to the site of calcification, the reticular body-coccolith vesicle system.

When a coccolith is fully developed, it moves with the surrounding vesicle from the nucleus to the periphery of the cell (Taylor *et al.* 2007). Exocytosis of mature coccoliths takes place between the two chloroplasts by fusion of the coccolith vesicle with the plasma membranes. Coccolith exocytosis occurs within a few tens of seconds and is, in contrast to coccolith calcification, independent of light (Taylor *et al.* 2007). When ejected from the cell, the coccolith interlocks with neighboring coccoliths forming the external coccosphere, which can consist of several layers of coccoliths (Hoffmann *et al.* 2015).

Coccolithophore scales have elaborate shapes. Ca-binding acidic polysaccharides are involved in calcite nucleation as well as in the selective growth of coccolith units and subunits (Borman *et al.* 1982; Marsh 1999; Marsh *et al.* 2002; Henriksen *et al.* 2004). For *Emiliania huxleyi*, only one Ca-binding acidic polysaccharide was identified (Borman *et al.* 1982; Henriksen *et al.* 2004), while calcite unit morphology regulation in Pleurochrysis carterae involves at least three acidic polysaccharides (Marsh 1994; Marsh *et al.* 2002). Shape variation occurs by binding the polysaccharide carboxyl groups to Ca ions that are supposed to inhibit or promote the growth of specific crystallographic faces (Henriksen *et al.* 2004). Thus, like hard tissue formation in extracellular matrices, the start of coccolith formation is also a biopolymer templated process as the first set of calcite crystals nucleate onto an organic template, the base plate. However, distinct from extracellular matrices, biopolymers are not occluded into the calcite of the coccolith (Hoffmann *et al.* 2014b; Frølich *et al.* 2015) but are pushed aside during coccolith maturation. When the coccolith is complete, acidic polysaccharides form an organic sheath that covers the calcite and is located next to the coccolith vesicle membrane (Henriksen *et al.* 2004).

Coccolith unit development and morphogenesis was outlined by Didymus *et al.* (1994); Young *et al.* (1992, 1997, 1999), and Marsh (2003). The nucleation of calcite on an organic template (the elliptical base plate) belongs to the very first steps of coccolith formation. It proceeds further with growth in lateral, medial and distal directions and results in the formation of units and subunits with highly specific morphologies and distinct crystallographic orientations (V- and R-units; Young *et al.* 1992, 1997, 1999; Hoffmann *et al.* 2014b). The investigation of the ultrastructure of modern and fossil coccolithophore species disclosed that the basic V/R-unit pattern is conserved (Didymus *et al.* 1994; Saruwatari *et al.* 2011). Didymus *et al.* (1994) extended the V/R model of Young and co-workers and proposed that, as it is opposed to the nuclear envelope, the organic template develops on a curved surface. Hereby the crystallographic alignment of each R-unit is influenced by the curvature of the nuclear envelope and the crystallographic axis of an individual R-unit is neither strictly radial nor vertical to the ring, but inclined to it, depending on the local curvature. However, the crystallographic relations within each R-unit remain consistent over the entire protococcolith ring (Didymus *et al.* 1994; Saruwatari *et al.* 2008).

On the basis of electron diffraction studies in TEM and by observing differences in electron densities Wilbur & Watabe (1963) were the first to suggest that segments of the R-units of *Emiliania huxleyi* are composed of different crystals. The relative orientation of these calcite crystals was fully determined by electron diffraction (Saruwatari *et al.* 2008; Hoffmann *et al.* 2014b), and the microdomains within some coccolith elements of *E. huxleyi* were described (Parker *et al.* 1983; Westbroek *et al.* 1984). The authors reported that the crystallographic lattice structure is not uniform in a coccolith, and it is single crystalline in the basal and the lower coccolith elements, while the upper coccolith elements appear to have an internal mosaic structure.

Even though *Emiliania huxleyi* is, up to now, the best studied coccolithophore species, calcium and carbonate ion transport to the site of calcification, coccolith calcite formation, and its crystallographic organization are not yet fully disclosed enough to test current general paradigms of biomineralization, which invoke assembly of the biomineral by attachment of nanoparticles (Weiner & Addadi 2011; De Yoreo *et al.* 2015) as the pathway of crystallization. For a better understanding of coccolith calcite formation and organization we combine knowledge gained from electron microscopy techniques on coccolith calcite chemistry, crystallography and cytology. We reassess the function of endomembranes (the outer membrane of the nuclear envelope and the membrane of the coccolith vesicle) in calcite nucleation and coccolith unit formation.

Our electron diffraction and EDX results indicate a mosaic block nanostructure of coccolith calcite consistent with features like high and small angle grain boundaries which are common in classical ion-by-ion crystal growth, while indications for a nanoparticulate assembly and intracrystalline organics are lacking completely. Our cytological results suggest the presence of a new interorganelle junction and point to a new pathway of intracellular calcium transport into the coccolith vesicle.

2.1.2 Material and Methods

Material

We investigated cells of cultured *Emiliania huxleyi* clone B62 originally obtained from the bloom in May 2009 in Raunefjorden near Bergen (Lohbeck *et al.* 2012).

Sample preparation

For chemical fixation, seawater from the culture containing *Emiliania huxleyi* was mixed 1:1 with a solution containing 400 mmol·L^{-1} cacodylate buffer (pH 7.6), 5% glutaraldehyde, and 8% paraformaldehyde. Then samples were gently centrifuged and washed three times in 0.1 mmol·L^{-1} cacodylate buffer (pH 7.3), centrifuged again, and postfixed in 1% OsO_4 + 0.8% $K_4Fe(CN)_6$. Then samples were dehydrated in a series of isopropanol and embedded in EPON resin.

For cryo-fixation by high pressure freezing, *Emiliania huxleyi* in the artificial seawater culture medium were concentrated by letting the cells sink to the bottom of a 15 mL Falcon tube. The supernatant was discarded, and the cells collected in 1.5 mL Eppendorf tubes and gently centrifuged down to yield a dense cell suspension. A 50 μm thick gold spacer ring with a diameter of 3.05 mm and a central hole of 2 mm (Plano GmbH, Wetzlar, Germany) was mounted on a 170 nm thick carbon and polylysine-coated sapphire disc (Engineering Office M. Wohlwend GmbH, Sennewald, Switzerland). A small droplet of the cell suspension was placed on the center of the sapphire disk, sandwiched with another uncoated disk and frozen with a Wohlwend HPF Compact 01 high pressure freezer (Engineering Office M. Wohlwend GmbH) within 30 ms at a pressure of 2.3×10^8 Pa (Höhn *et al.* 2011). The sapphire sandwiches were then opened and the samples freeze-substituted overnight in a solution containing 0.2% OsO_4, 0.1% uranyl acetate, and 5% H_2O in acetone from -90 to 0°C (Walther & Ziegler 2002). Then samples were embedded in EPON.

For cryo-SEM imaging, dense cell suspensions of *Emiliania huxleyi* were sandwiched between aluminum planchettes with an outer diameter of 3 mm and a 0.15 μm deep inner cavity 2 mm in diameter. Samples were then high-pressure frozen as described above and cryo-transferred to a BAF 300 freeze-etch device (Balzers, Liechtenstein). The sandwiches were cleaved open, etched at -110°C for 10 s, and subsequently coated with 3 nm of platinum at an angle of 45° and with 20 nm of carbon at an angle of 90°. Etched samples were mounted onto a Gatan cryo-holder 626 (Gatan, Inc., Pleasanton, CA, U.S.A.) and then cryo-transferred for imaging to a Hitachi S5200 FE-SEM.

Calcite orientation measurements and major and minor element chemical mapping were performed on FIB-prepared lamellae. The preparation of some of the FIB sections used is described elsewhere (Hoffmann *et al.* 2014a). Additional FIB sections were obtained with a dual-beam FEI Helios 600i FIB-SEM system equipped with a FEI micromanipulator (FEI, Hillsboro, OR, USA). The individual coccolithospheres collected on filter grids were selected under the electron beam. After electron- and ion-beam coating with platinum, trench cutting with 30 keV Ga^+ ions was followed by lift-out. The lamellae were then mounted on Omniprobe lift-out grids (Omniprobe Inc., Dallas, TX, USA) and thinned with successively reduced ion-beam currents. For a final polishing step, the acceleration voltage was reduced from 30 kV to 5 kV.

Analytical methods

Cryo-SEM imaging was performed on a Hitachi S5200 FE-SEM. The samples were investigated at a temperature of -100°C and an accelerating voltage of 10 kV. Imaging was performed using analysis mode and the backscattered electron signal.

For TEM imaging, ultrathin 20–50 nm thick sections were cut from both chemically fixed and high pressure frozen and freeze-substituted samples, using a Reichert Ultracut S (Leica, Wetzlar, Germany) and an "ultra"-type diamond knife (Diatome, Liechtenstein). Sections were mounted on carbon-coated Formvar films on 1 mm diameter single-hole copper EM grids (Plano GmbH). Sections were stained with lead citrate for 1 min and viewed with a Zeiss 912 TEM (Zeiss, Jena, Germany) using the elastically scattered electrons of the zero-loss peak. Digital micrographs were recorded with a 2k × 2k pixel camera (TRS, Moorenweis, Germany) using TRS software. To screen a large number of cells, we selected thin sections of chemically fixed cells that had a high cell density and were recorded from each of these 100 images at ×6,300 magnification (44 by 44 μm) in 10 × 10 grids. The images were then stitched together into large composite images using the TRS software. Fifty such composite images were used for numerical aspects of the structural analysis.

To determine the distance between nuclear envelope and coccolith vesicle membrane, the open source software program ImageJ (Research Services Branch, National Institute of Mental Health, Bethesda, Maryland, USA) and software Origin Pro 9.0 software (OriginLab, Northampton, MA, USA) were used. With ImageJ a line of 25–70 pixel width was drawn across the boundary layer between the nuclear envelope and coccolith vesicle membrane. Subsequently, along this line a two-dimensional graph of the grey-level intensities of pixels was plotted. To obtain the FWHM (full width at half maximum) between the boundaries, the intensity values were analyzed using the Quick Peaks Gadget of Origin Pro 9.0. After manually choosing the region of interest and creating the baseline as a straight line between two anchor points, the FWHM was calculated. The FWHM was averaged over three measurements per cell.

GraphPad Prism software was used to perform analysis and graphical presentation of statistic data. One-way ANOVA followed by Sidiak's multiple comparisons tests were used to test the statistical significance between selected groups.

For STEM tomography 500–700 nm semithin sections were cut, using a "semi"-type diamond knife (Diatome, Liechtenstein) and a Leica ultra-microtome, and mounted on poly-L-lysine coated copper grids with parallel unidirectional grid bars (Plano GmbH). The sections were again coated with poly-L-lysine to attach 10 nm gold particles on both sides of the sections, serving as fiducial markers for alignment of the images to a tomogram. Tilt series (-60° to +66°, increment 1.5°) were recorded using a Jeol FEM 2100F field emission microscope equipped with a Jeol STEM bright-field detector (Jeol Ltd, Tokyo, Japan) and EM-Menu 4.0 STEM tomography software (TVIPS, Gauting, Germany), at a resolution of 1,024 × 1,024 pixel, an illumination time of 20 s, and an acceleration voltage of 200 kV. The pixel size was either 3 or 1.5 nm depending on magnification. Tomograms were calculated from the tilt series by a weighted backprojection procedure using the standard settings of the IMOD 4.1.2 software (Kremer et al. 1996). Each plane within the tomograms corresponds to a virtual section thickness of 1 pixel (3 or 1.5 nm).

Crystal orientation patterns diffraction measurements were carried out on FIB sections with a Philips Tecnai F30, 300 keV, field emission transmission electron microscope, equipped with a "Super-Twin" objective lens and a STEM unit with bright-field and dark-field detectors (Philips B.V., Eindhoven, the Netherlands). Furthermore, the system was equipped with a high-angle annular dark-field (HAADF) detector (Fischione Instruments, Export, PA, USA) and a bottom mounted CCD-camera (Gatan Inc.). Elemental abundances were determined with an energy dispersive SSD-X-ray spectrometer EDAX Apollo XLTW (EDAX Inc., Mahwah, NJ, USA) attached to the Philips Tecnai F30 TEM system.

To resolve the domain structure, TEM imaging was carried out in HAADF STEM mode on samples tilted so that a low-index zone axis was parallel to the beam. HAADF images were recorded at various camera lengths and, for simplicity, fixed beam convergence. The lattice distortions associated with orientation variations (close to crystal imperfections) lead to well-observable contrast effects depending on beam convergence and dark-field detector acceptance angle (Phillips *et al.* 2011a,b), while an influence from sample bending is negligible (Agudo J. *et al.* 2012). The images showing the most pronounced contrast as a function of camera length were selected for interpretation.

Diffraction mapping in TEM was carried out by scanning the beam in microprobe STEM mode over the area of interest. In each image point, a diffraction pattern was recorded using a CCD camera. The use of microprobe STEM (μP-STEM) allowed collecting diffraction patterns with a small convergence angle. Due to the slow acquisition process, the diffraction mapping had to be limited to small areas with a resolution of 16 × 16 or 32 × 32 pixel and line scans.

EDX mapping in TEM and point analysis was performed in conventional nanoprobe STEM mode.

In this study, we observed several cells that contained coccoliths in two different development phases, usually phase 1 and phase 5. For the assessment of this, we used a systematic sampling method that estimated the possibility of cutting both through the fully developed (phase 5) and through a first-formed, immature (phase 1) coccolith in one 40 nm thick segment (Fig. 2.1-S1 in the Supporting Information). On the basis of TEM images taken on chemically fixed sections, some assumptions had to be made: The cell is spherical, has a diameter of 4 μm, and contained a nucleus. The vesicle of phase 1 coccolith has an average diameter of 900 nm in the X-Y plane and a thickness of 100 nm in Z direction, and the vesicle of phase 5 coccolith has an average diameter of 2.3 μm and a thickness of 500 nm. All sections had to be cut through the nucleus. As both coccolith vesicles have a round shape in the X-Y plane, the X-axis is identical to the Y-axis in this case. Therefore, we can simplify the 3-D cutting model into a 2-D model. We will only discuss sampling in the X-Z plane. Segmentation through the cell is defined using the equation of a straight line: $X + bZ + c = 0$. For a given set of θ (cutting angle) and d (distance between the cutting line and the origin), a line is determined. To sample all possible directions and positions of the line through the cell, we used the following θ and d combinations: The cutting angle θ goes from 1° to 180°, with a step size of 1 degree, and d ranges from -2 to 2 μm, with a step size of 40 nm. In this case, the cutting line can be expressed as $Z = tan\theta \cdot X + d \cdot \sqrt{(1 + (tan\theta)^2}$. With these assumptions, 35,820 combinations are sampled. With this, we would expect that 52.1% of the cells that have a phase 5 coccolith vesicle would also have a phase 1 coccolith vesicle.

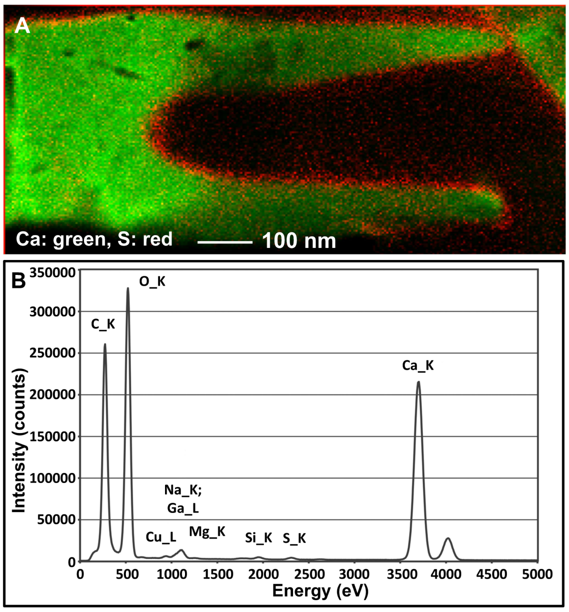

Figure 2.1-1. Major and minor elements in *Emiliania huxleyi* coccolith calcite obtained from EDX measurements in TEM. (A) background-corrected element map (green: Ca, red: S); (B) EDX spectrum. The calcite of *E. huxleyi* is almost devoid of any other major/minor elements, impurities or inclusions. A slight enrichment of sulfur is present along the rim of the coccolith.

2.1.3 Results

Transmission electron microscopic analyses were performed on FIB-prepared thin sections and are presented in Figures 2.1-1 to 2.1-3 and Figures 2.1-S2 to 2.1-S5 in the Supporting Information, respectively. All images represent a cut through a tube with shields, so that the image contains the radial direction of the coccolith (Fig. 2.1-S3).

Coccolithophore calcite: its chemical homogeneity and mosaic structure

EDX analysis (Fig. 2.1-1) shows that the coccolith calcite is rather pure with minor concentrations of S, Na, Mg, and Si. Sulfur is enriched at the rim of the coccolith calcite and is an indication of the organic sheath that envelopes the coccolith. Na tends to appear unevenly also at the rim of the coccolith, however, the Na_K-X-ray signal overlaps with the Ga L-series of signals such that a contamination from FIB preparation cannot be excluded. There is no evident contamination source for the traces of Si, such that they may be real.

High-resolution TEM analysis on coccolith calcite is hampered by the easily occurring beam damage (Hoffmann *et al.* 2014a,b). TEM images recorded in bright-field mode reveal planar internal boundaries (arrows in Fig. 2.1-2A) within the single-crystal-like calcite (Hoffmann *et al.* 2014b). We interpret these boundaries as grain boundaries inclined to the beam direction, due to their characteristic fringe contrast. They define micro-mosaic blocks within the coccolith elements. We assign these boundaries to the overlap of the differently orientated shield (R-crystal unit), tube core (V-crystal unit) and inner tube (R-crystal unit) elements. Microdiffraction point measurements along a profile through the internal boundaries inside the tube of a shield element (Fig. 2.1-S2) document a quite continuous crystal orientation. However, Figure 2.1-3 presents annular dark-field (ADF) images that were taken in STEM mode on the same position in the coccolith depicted in Figure 2.1-2B, in a low-indexed orientation, but with different camera lengths. Contrasts showing planar boundaries, separating mosaic domains within the calcite become visible. The contrast in the ADF images arises due to slight orientation variations due to tilt; thus, small-angle boundaries are the most reasonable explanation. Figure 2.1-3D depicts a HAADF image of the same site performed with the same camera length as Figure 2.1-3C. In the HAADF image these boundaries are absent, which proves that the contrasts are intrinsic to the investigated material and not generated by variations in composition or by thickness variations. Thus, we find small-angle grain boundaries separating micro-mosaic blocks in the calcite, possibly due to dislocations with a notable screw component. As we cannot see any pronounced change in the appearance of the diffraction patterns when scanning the beam over a mosaic block boundary, the misorientation between the blocks has to be smaller than the tilt which leads to a pronounced change in the appearance of these patterns. The qualitative comparison of the measured diffraction patterns with

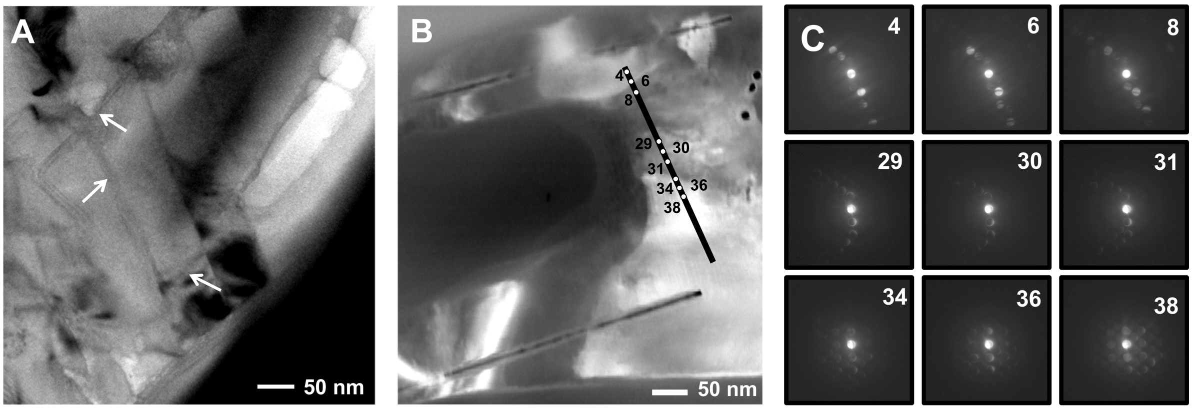

Figure 2.1-2. The internal structure of *Emiliania huxleyi* calcite. (A) TEM micrograph taken in bright-field mode showing bending contours (black shades and grey curved lines) as well as some planar material specific internal boundaries, which we interpret as grain boundaries (arrows) between the R- and V-units at or near the inner tube element of the calcite. (B and C) A profile along which diffractograms were recorded in spot mode on the coccolith calcite. The spot positions along the profile are numbered and the white numbers in the diffractograms in C give the corresponding position. The full set of 64 diffraction images is given in Figure 2.1-S2. Microdiffraction patterns are CBED with a small angle of convergence to produce a more SAED-like appearance without overlapping diffraction discs, obtaining patterns with separated "spots" at a reasonably low beam intensity to avoid beam damage.

calculated patterns with the program EMS (Stadelmann 2012) allows a qualitative estimate of the tilt of ~0.3° between two adjacent mosaic blocks. However, we attribute this tilt mainly to the usual bending of the TEM lamella during preparation, which is indicated by the presence of numerous bending contours (Fig. 2.1-S4). Thus, the real tilt between two different mosaic blocks in the coccolith should be significantly smaller.

Coccolithophore cell ultrastructure: transport of calcium to the calcification site

TEM micrographs from chemically fixed 50 nm thick thin sections confirm the results of Westbroek *et al.* (1989) on the general ultrastructure of *E. huxleyi*. Figure 2.1-4 shows an example of a cell with the major cell organelles such as the chloroplasts, the nucleus, mitochondrion, Golgi body, reticular body, and the coccolith vesicle. Within the coccolith vesicle, calcite crystals (white arrow in Fig. 2.1-4) nucleate on the periphery of an organic template, the base plate (black arrow in Fig. 2.1-5A). Backscatter scanning electron micrographs of high-pressure frozen cells show that the mineral first forms a ring structure (Fig. 2.1-S6 in the Supporting Information). In contrast to previous findings, we observed that cells of the clone used in this study can contain two coccoliths (Fig. 2.1-5B). We examined sections through a total of 1,692 different cells. In 546 cells, the sections traversed through both the nucleus and at least one coccolith vesicle (Table 2.1-1). In 86% of these cells, only a single coccolith vesicle was found intercalated between the reticular body and the nucleus (Figs. 2.1-4 and 2.1-5A, Fig. 2.1-S7 in the Supporting Information). In almost all cells, the membrane of the coccolith vesicle was close to the outer membrane of the nuclear envelope, even for coccoliths that appear almost mature (Fig. 2.1-S7B). Four percent of immature and thus rather small coccolith vesicles had no or only little contact to the nuclear envelope. Interestingly, all of the latter had close contact to a cisterna of the ER instead (Fig. 2.1-S8 in the Supporting Information). In the remaining 10% of the cell sections, a large and likely mature, coccolith vesicle has been found in the periphery of the cells virtually separated from the nuclear envelope and ER cisternae. Only in these, in one-quarter of the cell sections traversing such a large peripheral coccolith vesicle, a second, however, smaller coccolith vesicle occurred in close contact to the nuclear envelope (Fig. 2.1-5B and Fig. 2.1-S9 in the Supporting Information; Table 2.1-

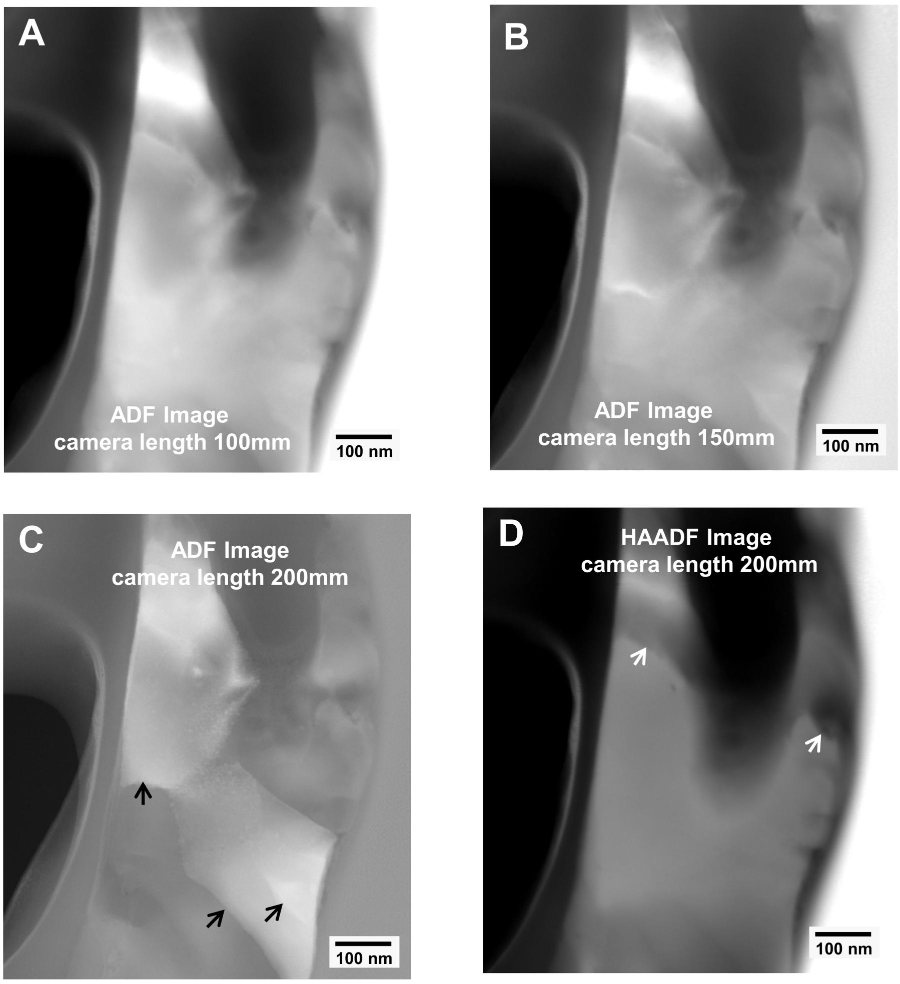

Figure 2.1-3. ADF (A–C) and HAADF (D) images of *Emiliania huxleyi* calcite recorded in STEM mode. The variation in camera length enables visualization of interfaces within the calcite. (C) Clearly internal boundaries (arrows) can be interpreted as small-angle grain boundaries caused by dislocations within the calcite and demonstrate the occurrence of distinct mosaic blocks within coccolith elements. As the HAADF image (D) does not show any internal features (the lines in (D) indicate thickness variations), the sharp grey contours/boundaries in (B) and (C) are not bending contours but internal discontinuities.

1). In cells with two coccoliths, a reticular body was either lacking or consisted of only small cisternae distally of both the mature and the small new coccolith. Although mature coccoliths need to be released from the cell into the surrounding medium after fusion of the coccolith vesicle with the plasma membrane, we have rarely seen such an event in the cells examined (Fig. 2.1-S7, C and D).

To further investigate the relation between coccolith vesicle and reticular body development, we defined five developmental phases for the coccolith vesicle (Fig. 2.1-6). In phases 1–4, the coccolith vesicle is in close contact with the nuclear envelope. Phase 1 coccolith vesicles are small, occur together with a large peripheral one, and have section profiles with either flat or slightly enlarged ends (Fig. 2.1-5B and Fig. 2.1-S9). In phases 2 and 3, the coccolith vesicles are of intermediate size and appear dumbbell- or "bone"-shaped in section, respectively (Figs. 2.1-5A, 2.1-6 and 2.1-7A). In phase 4, the profile is large having distinct forked ends at either side; the fork is formed by the distal and proximal shield elements connected by the tube element (Young *et al.* 1997, 1999; Hoffmann *et al.* 2014b). In phase 5, the profile resembles that of stage 4, however, located in some distance to the nuclear envelope and close to the plasma membrane of the cell. We drew a horizontal and vertical line through the center of the reticular body (Fig. 2.1-S7A) and counted the intersection of the lines with the membranes of the reticular body. We used this as a measure for relative membrane length on micrographs and thus of membrane area (Weibel 1969) of the reticular body. The relative membrane area significantly increased from phase 1 to phase 2 and successively decreased from phase 2 to phase 5 (Fig. 2.1-8).

In most chemically fixed cells the organic matrix of the basal plate, the membrane of the nuclear

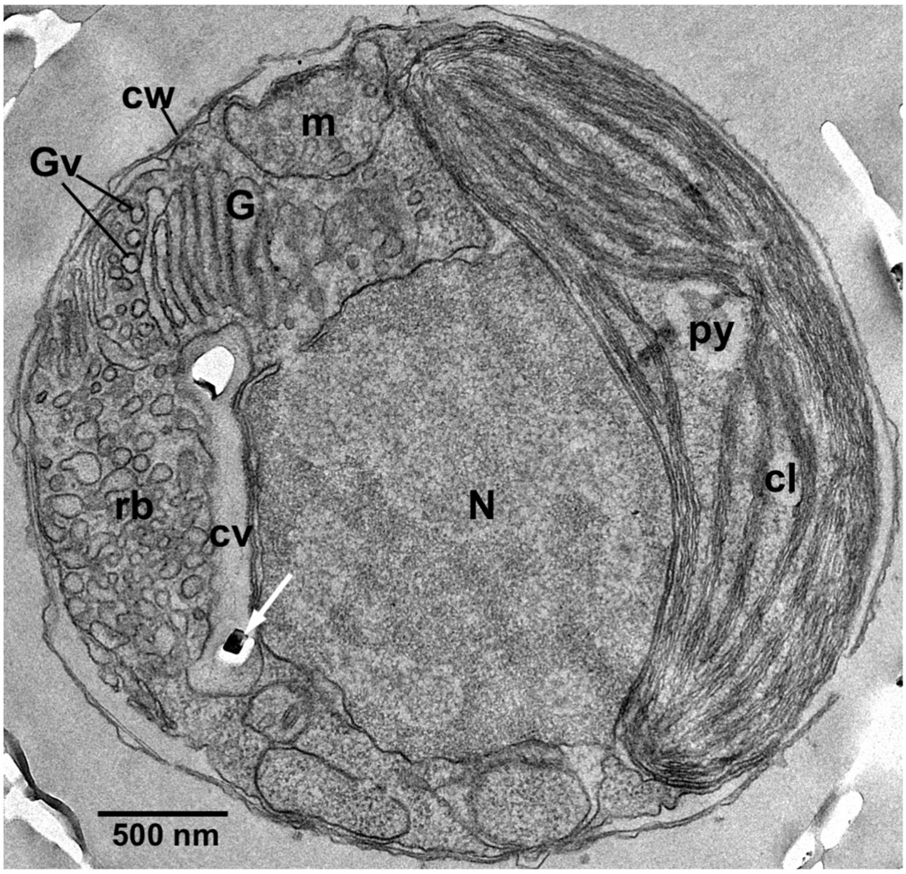

Figure 2.1-4. TEM micrograph of a chemically fixed *Emiliania huxleyi* cell showing a coccolith vesicle (cv) with remains of calcite (arrow). Note that most mineral is dissolved during the procedures for fixation and embedding; cw, cell wall; cl, chloroplast; G: Golgi apparatus; Gv, Golgi vesicles; M, mitochondrion; N, nucleus; py, pyrenoid; rb, reticular body.

envelope and the reticular body appear wrinkled due to sample shrinkage during fixation and dehydration. However, it is of interest that in most cases the two opposite membranes run in parallel over large distances, with the space between them being only a few nanometers wide (Fig. 2.1-5, A and B, Fig. 2.1-S7A). Since in these chemically fixed specimens the spatial arrangement of the proximal membrane of the coccolith vesicle and that of the outer membrane of the nuclear envelope cannot be investigated in its native state, we used high-pressure freezing to circumvent that problem. Thin sections from high-pressure frozen and freeze-substituted *Emiliania huxleyi* reveal a planar rather than wrinkled interface between the two membranes (Fig. 2.1-7, Fig. 2.1-S10, A and B in the Supporting Information) and the matrix of the basal plate appears planar as well. Like in the chemically fixed specimens, the distance between the membranes is very narrow. In chemically fixed cells the gap between the proximal side of the coccolith vesicle and the outer membrane of the nuclear envelope has a spacing of ∼6 nm (Fig. 2.1-9, A–C). In high-pressure frozen samples this gap is ∼4 nm wide over distances of 500 nm and more (Figs. 2.1-7 and 2.1-9, A and C, Fig. 2.1-S10). In phase 2–4 of coccolith formation, the membranes at the attachment of the nuclear envelope with the coccolith vesicle are planar to slightly curved and do not follow the general curvature of the nuclear envelope at the regions which are not in contact with the coccolith vesicle (Figs. 2.1-5, A and B; 2.1-7; and 2.1-10, A and D; Figs. 2.1-S7 and 2.1-S10).

In the high-pressure frozen and freeze-substituted sections of *E. huxleyi*, the cytoplasm appears densely filled with granular material. Often this makes it very difficult to clearly image the membranes of the reticular body at high resolution (Fig. 2.1-S10). We therefore recorded STEM tomograms from 500 to 700 nm thick sections of the freeze-substituted cells, from which images with a thickness of only 1 voxel can be calculated. Membranes in these tomograms often appear in negative contrast, allowing the mem-

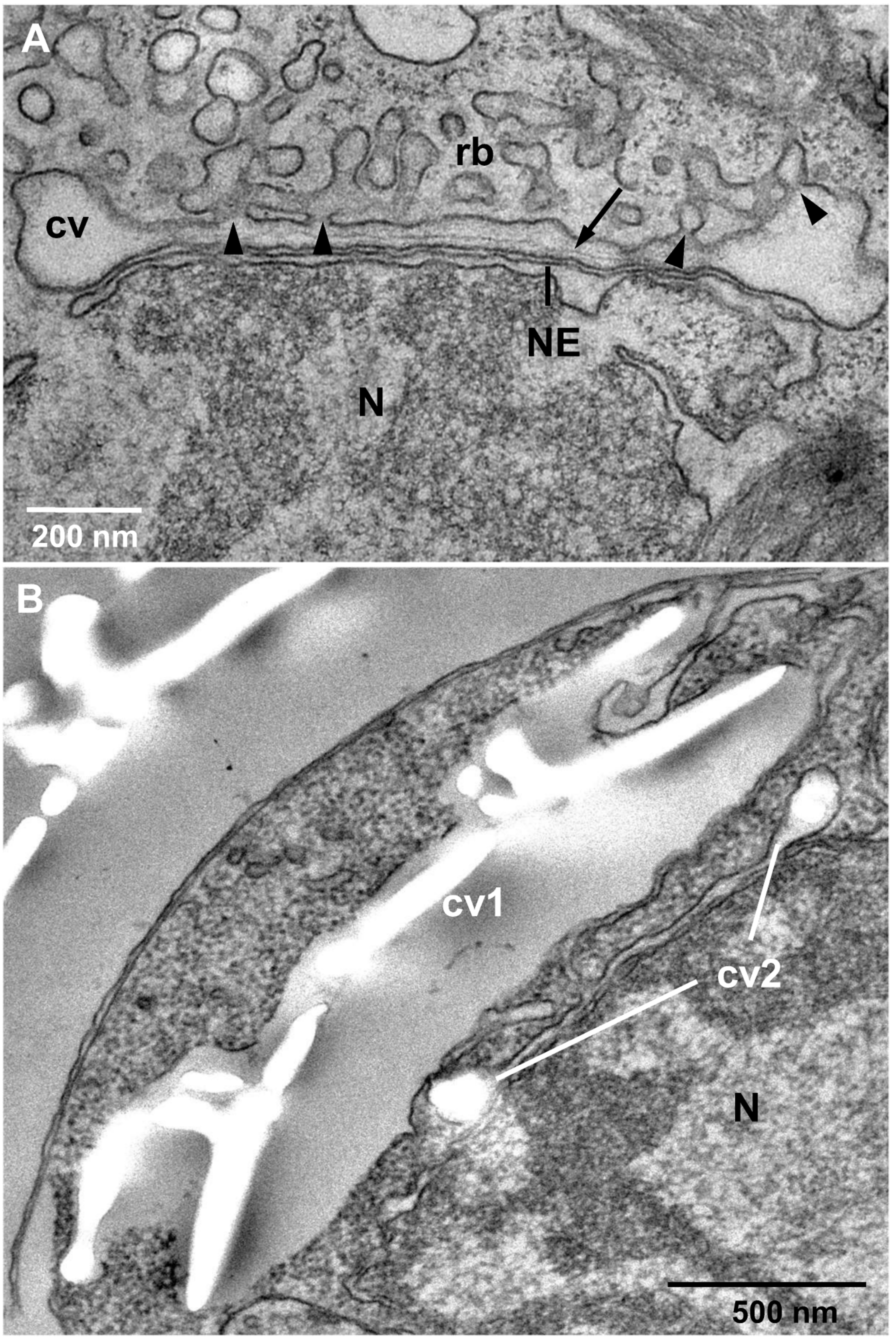

Figure 2.1-5. TEM micrographs of *Emiliania huxleyi* cells containing coccolith vesicles (cv). (A) coccolith in an intermediate stage (phase 3 of Fig. 2.1-6). In its narrow part, the coccolith vesicle contains a thin sheet of organic matrix (black arrow), the base plate, onto which calcite crystals attach to. The lumen of the coccolith vesicle (black arrowheads) is continuous with that of the reticular body (rb). (B) An almost mature coccolith vesicle (cv1) is located close to the plasma membrane of the cell. A second early-stage coccolith vesicle (cv2) is present in close vicinity to the outer nuclear envelope. N, nucleus; NE, nuclear envelope.

branes to be followed throughout the cytoplasm within the limits of the section thickness. In eight tomograms we found dense organelles. The larger of these resemble multivesicular bodies (Table 2.1-2; Video 2.1-V1 in the Supporting Information) or sometimes lipid droplets (Video 2.1-V2 in the Supporting Information). The STEM tomograms show that the cisternae of the reticular body are continuous with one another (Fig. 2.1-11; segmentation of the reticular body shown in Video 2.1-V2). We found no connection of the reticular body to the ER or other organelles except to the coccolith vesicle. In addition, the tomograms reveal dense material lining the luminal side of the reticular body (Fig. 2.1-10, A–E; Video 2.1-V2). The material of the lining consists of nanoparticles that vary in size and can be up to 10 nm thick (Fig. 2.1-10C). In Golgi cisternae at the trans-face and in Golgi vesicles, we find such densely stained nanoparticles in the lumen as well (Fig. 2.1-12, A–D; Video 2.1-V1). In most phase 2 coccolith vesicles, these particles appear to be lacking

Table 2.1-1. Numerical analysis of the spatial relation of the coccolith vesicle to the nucleus.

Number of examined cells	Sections with CV and nucleus	Single CV close to nucleus	CV not at nucleus but at ER cisterna	Phase 5 CV (not at nucleus)	Phase 5 and phase 1 CV present
1,692	546	471	28	47	12

(Fig. 2.1-12, A and B; Table 2.1-2). In most but not all images of more developed (and therefore larger) coccolith vesicles, in which the reticular body is considerably reduced in size (Fig. 2.1-8), the nanoparticles appear at the luminal side of the membrane of the coccolith vesicle as well (Table 2.1-2; Fig. 2.1-12, C and D).

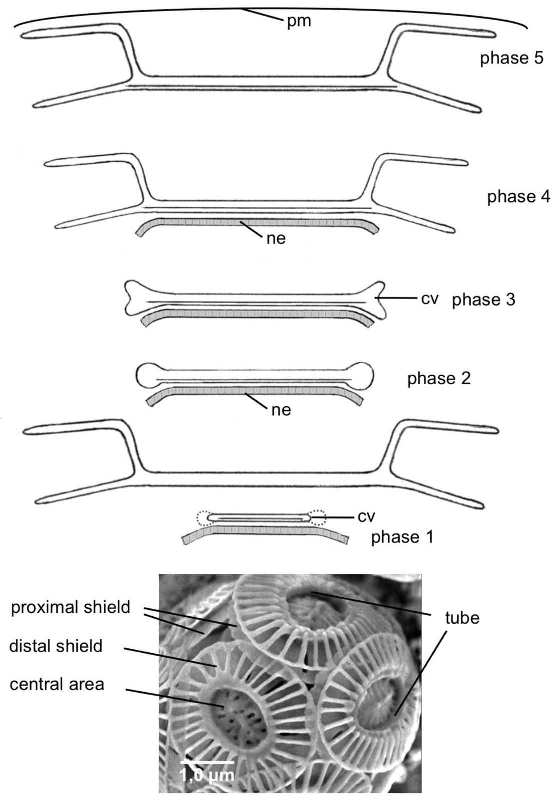

Figure 2.1-6. Five phases of the coccolith vesicle (cv) development. Phase 1, small and flat vesicle with flat or slightly delated rim close to the nuclear envelop, occurring together with a large cv that is detached from the nuclear envelope. An organic template of the base plate is already present. Phase 2, the vesicle is larger and appears dumbbell-shaped in cross-section. Phase 3, the rim has split into proximal and distal shield elements leading to a "bone"-shaped appearance in cross-section. Phase 4, the coccolith has well-developed proximal and distal shield elements and is still close to the nuclear envelope. Phase 5, the mature coccolith has detached from the nuclear envelope and moved tto the periphery of the cell in preparation for exocytosis. The SEM image shows the structure of coccoliths surrounding the cell.

2.1.4 Discussion

Coccolithophores share major architectural features. The cell is surrounded by an external calcitic coccosphere consisting of several coccoliths that are composed of coccolith units containing differently oriented segments. Despite the similarity of these structural principles, a marked variability exists in the size and shape of the cell, the number and arrangement of coccoliths around the cell and the size, shape and architecture of coccolith unit segments (Monteiro *et al.* 2016). Such high diversity in morphology and architecture is an expression of a profound metabolic influence that induces the formation of skeletal calcite with a stringent control over crystal shape, size, and orientation. For a better understanding of coccolith calcite organization, we employed a combined methodological approach. We explored the ultrastructure of the cell with regard to Ca^{2+} transport to the site of calcite nucleation and growth and investigated the pattern of calcite organization.

Coccolith calcite crystallography

Invertebrate carbonate hard tissues are hybrid composites in which extracellular organic matrix and mineral are intricately combined on several scale levels. A popular paradigm of pathways of biomineralization (Weiner & Addadi 2011; De Yoreo *et al.* 2015) invokes the formation of nano-sized vesicles filled with amorphous calcium carbonate (ACC) in the mineralizing cells, followed by the exocytosis of these vesicles and their attachment - as nanoparticles - to the extracellular biopolymer matrix and biomineral, where the ACC is supposed to crystallize. Nanoscale carbonate particles are embedded in a foam-like network of biopolymer fibrils (Rousseau *et al.* 2005, 2009) within the extracellular matrix-defined basic mineral units (Nindiyasari *et al.* 2015; Griesshaber

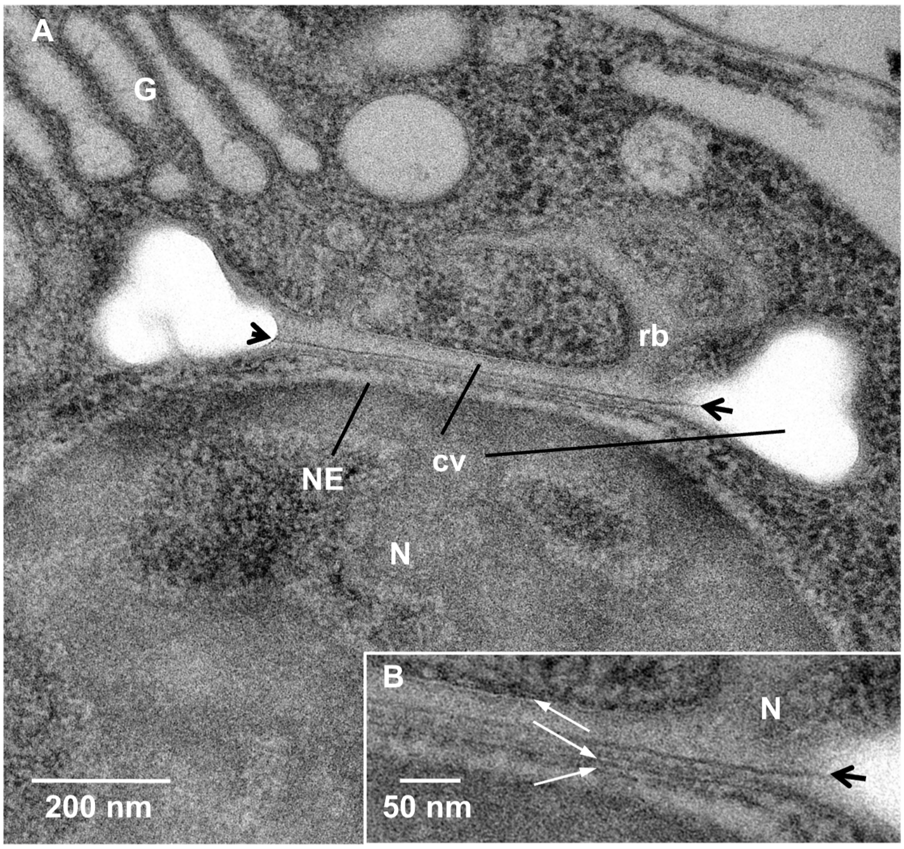

Figure 2.1-7. Micrograph of a thin section from high-pressure frozen and freeze-substituted sample showing the spatial relation between the coccolith vesicle (cv) and the nuclear envelope (NE). (A) Overview. A narrow gap of ∼4 nm between the proximal side of the coccolith vesicle and the outer membrane of the nuclear envelope is maintained over a distance of more than 500 nm. The organic template of the base plate is located at the proximal side of the cv (marked by the black arrow). (B) Details from A depicting the membranes of the cv and NE are marked with white arrows.

et al. 2017). Arrays of basic mineral units form different hard tissue layers, and a combination of the latter comprises the macroscopic shell or the carbonate tooth (Dunlop & Fratzl 2010; Schmahl *et al.* 2012; Goetz *et al.* 2014). Basic mineral units of invertebrate carbonate hard tissues are mesoscopically structured crystals (Cölfen & Antonietti 2008), as they consist of nano-sized subunits, in general, with a coherent crystallographic coorientation and with subunit organization being mediated by interstitial organic fibrils (Vielzeuf *et al.* 2010; Griesshaber *et al.* 2013).

Coccolithophores do not appear to follow the nanoparticulate and hierarchical architecture principle. Even though first nucleation of calcite is guided by biopolymers, the organic base plate, further subunit growth and development of morphology is not mediated by occluded biopolymers. In coccolithophores Ca-binding acidic polysaccharides inhibit or promote the growth of specific crystallographic faces and, thus, generate the intricate shapes of coccolith scales and their subunits (Borman *et al.* 1982; Marsh 1994; Marsh *et al.* 2002). Coccolith units and subunits are not mesostructured crystals, as an organic phase that is occluded into the mineral is absent. However, the diffraction contrast (ADF) imaging in our study shows that coccolith calcite crystal units are charged with planar structural defects, small-angle boundaries induced by arrays of dislocations, between mosaic blocks. Dislocations are generated by any type of stress or strain that might arise during crystal growth (e.g., growth around impurities, or by geometrical lattice mismatch due to misorientation between abutting crystallites). Dislocations interact due to the strain fields surrounding the dislocation line, and they may correlate and form networks. Two-dimensional networks of dislocations correspond to small-angle grain boundaries that are two-dimensional interfaces between blocks in the same crystal that are misoriented relative to each other by a small angle.

This defect microstructure is typical for crystals formed by classical, ion-by-ion growth. Parker *et al.* (1983) and Westbroek *et al.* (1984)

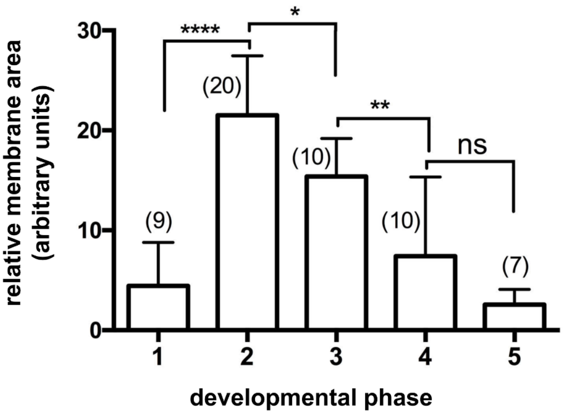

Figure 2.1-8. The relative membrane area of the reticular body in five phases of coccolith development. The relative membrane area was estimated by counting inter-sections of membranes with a horizontal and vertical line through the reticular body. Data are provided as mean values and standard deviation, and numbers in parentheses provide the number of cells analyzed. One-way ANOVA followed by Sidiak´s multiple comparisons tests was used to test the statistical significance of the difference of the mean value between pairs of selected groups. $^{*}P \leqslant 0.05$; $^{**}P \leqslant 0.01$; $^{****}P \leqslant 0.0001$; ns, not significant

reported a mosaic structure within the crystal of the distal coccolith shield elements of *Emiliania huxleyi* employing what was termed “ultrahigh-resolution TEM” at the time. In a recent TEM study, Hoffmann *et al.* (2014a,b) addressed again the question of calcite arrangement in skeletal elements of *E. huxleyi*. Using HRTEM imaging in combination with Kikuchi diffraction tilt angles $\geq 1°$ at a spatial resolution of $\sim$6 to 8 nm were considered to be detectable. A clear shift in Kikuchi lines (and thus a tilt between different parts of a single-crystal-like skeletal element) corresponding to a crystallographic misorientation of $4° \pm 1°$ around the [101] axis was observed between the distal- and the proximal shield elements (Hoffmann *et al.* 2014b).

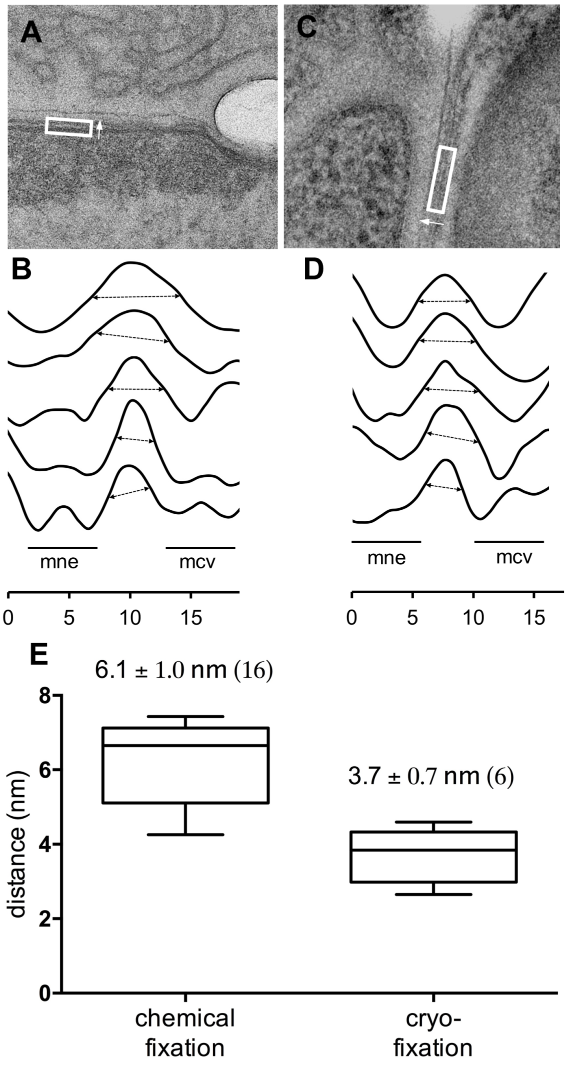

Figure 2.1-9. Distances between the proximal side of the coccolith vesicle and the outer membrane of the nuclear envelope in chemically fixed specimens (A, B) and in high-pressure frozen and freeze substituted specimens (C, D). (A) and (C) provide examples showing how grey-level profiles were plotted. (B) and (D) show such grey-level profiles for five different cells. Full width half maximum (FWHM) were taken as a measure for membrane distances (double arrows). (E) Box-and-whiskers presentation providing 25th to 75th percentiles, maximum and minimum values, respectively, and the median. Mean, standard deviation, and number of cells (in parenthesis) are given on top of the whiskers. For each cell three measurements were averaged.

Our methodological approach, the combination of ADF and HAADF imaging at different camera lengths unequivocally demonstrates the presence of internal boundaries within the calcite crystals of *Emiliania huxleyi*, prove the presence of mosaic blocks within the calcite and define their extent. The only exception appears to be the minute V-unit in *E. huxleyi* that, even with TEM diffraction, appears to be a biologically produced single crystal. Since coccolith calcite is highly electron beam damage sensitive (Fig. 2.1-S5), diffraction patterns cannot be measured with the required quality that allows the direct determination of tilt angles between different mosaic blocks. However, the comparison between measured and diffraction patterns calculated with the simulation program EMS (Stadelmann 2012) allows a qualitative estimation of the tilt of calcite mosaic blocks that is less than 0.3° along the measured line shown in Figure 2.1-2B and Figure 2.1-S2A. As a bending of the FIB-prepared specimen is common, the real tilt between the mosaic blocks in the coccolith crystal element may be notably smaller. Thus, in *E. huxleyi* calcite mosaicity is not caused by occluded biopolymers, as it is the case in extracellularly formed hard tissues of marine invertebrates, but by planar defects and dislocations which are typical for crystals formed by classical ion-by-ion growth mechanisms. This strongly indicates that *E. huxleyi* calcite is not formed by nanoparticle accretion but by ion-by-ion growth.

Cell Ultrastructure

The nanoparticles within the reticular body and Golgi system

STEM tomography has shown for the first time that the cisternae of the reticular body are all interconnected in a reticular manner and contain no membranous cisternae from other organelles or from the plasma membrane. Furthermore, the densely stained material, consisting of particles lining the luminal side of the reticular body in cryo-preserved *Emiliania huxleyi*, has not been described previously. The particles are distinct from the 25 nm thick coccolithosomes that have been found in Golgi cisternae, Golgi vesicles, and the coccolith vesicle in the coccolithophore species *Pleurochrysis carterae* (van der Wal *et al.* 1983; Marsh 1994). Coccolithosomes contain three distinct acidic polysaccharides and are associated with the basal plate during coccolith formation. In vitro, two of them (PS1 and PS2) have been shown to bind calcium (Marsh 1994). Although, an in-situ demonstration of calcium within the coccolithosomes has not yet been proved, they are thought to contribute to coccolith formation (Brownlee & Taylor 2004). A reticular body is absent in *P. carterae* and the coccolith vesicle derives from fusion of Golgi vesicles. The nanoparticles we found in *E. huxleyi* differ from the coccolithosomes in their size and their local preference at the inner side of the organelle membranes. Their presence within Golgi system and the reticular body suggests that the reticular body is formed by fusion of Golgi vesicles. The membrane of the coccolith vesicle in turn appears to derive, at least in part, from the membrane of the reticular body. This is indicated by the absence of the nanoparticles in young coccolith vesicles, the presence of the nanoparticles in more developed ones, and a decrease of the reticular body membrane area concomitant with the size increase of the coccolith vesicle. The nanoparticles are absent from the basal plate in all stages of coccolith development. Thus, their location in the reticular body, which is quite distant from the coccolith, suggests a more indirect role in coccolith formation. Coccolithosomes have not been found in *E. huxleyi*. However, polysaccharides have been localized within the coccolith vesicle, reticular body, and to some extent in Golgi cisternae (van der Wal *et al.* 1983). In addition, the coccoliths of *E. huxleyi* contain a calcium binding acidic polysaccharide, associated with a glutamine/proline/alanine-rich protein (GPA; Corstjens *et al.* 1998), which, however, is down-regulated during coccolith formation (Mackinder *et al.* 2011). The densely stained nanoparticles may consist of acidic polysaccharides as well, and an association with protein may explain their close proximity to organelle membranes.

The close association of the coccolith vesicle with the nuclear envelope

Our results confirm the close association of the coccolith vesicle with the nuclear envelope (Westbroek *et al.* 1989). Using cryo-preserved *E. huxleyi*, we demonstrated for the first time that the narrow gap between the proximal membrane of the coccolith vesicle and the outer membrane of the nuclear envelope has a constant width of only 4 nm. The high precision of the spatial dimensions of this gap over a large area requires specific

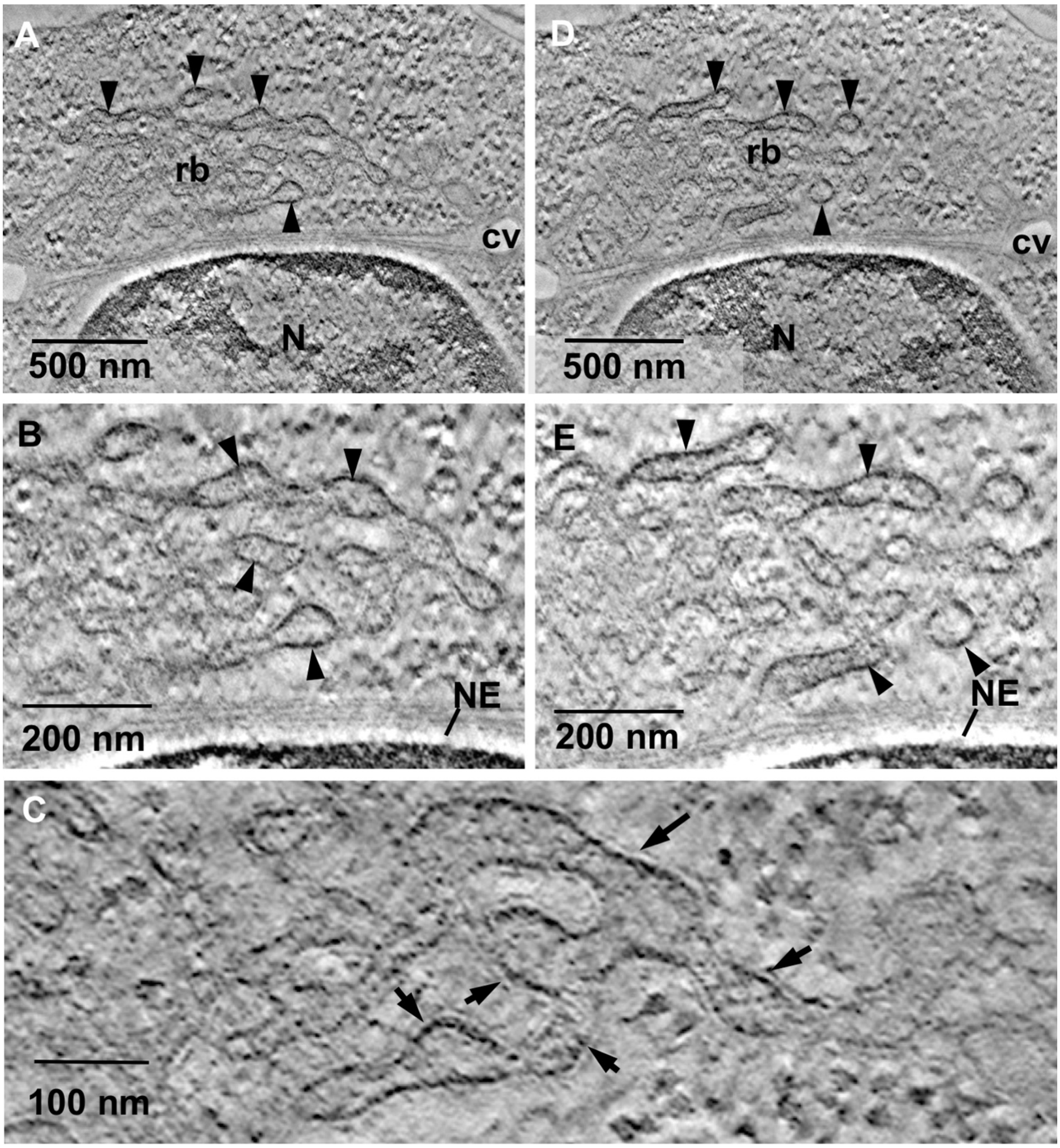

Figure 2.1-10. Overviews (A, D) and details (B, E and C) of sections from a single tomogram through the reticular body (rb) of *Emiliania huxleyi* containing coccolith vesicles (cv) in a young phase. Within the reticular body (rb), densely stained particles (black arrowheads) with diameters of up to 10 nm form seams at the luminal side of the membranes (black arrows in C). N, Nucleus; NE, nuclear envelope. The full tomogram is provided in the Video 2.1-V1.

molecular components capable of maintaining the attachment of the membranes over a significant time of coccolith development. We, therefore, describe this connection between the coccolith vesicle and the nuclear envelope as a new interorganelle junction, in short, the "nuclear envelope junction". The flat shape of the junction in early stages of coccolith formation indicates that the crystallographic alignment of each R-unit is not influenced by the curvature of the nuclear envelope, contrary to the earlier suggestion of Didymus *et al.* (1994). The evolution and high costs to develop such a precise shape of the nuclear envelope junction strongly suggests a significant role in coccolith formation, likely in transport of ions required for calcium carbonate precipitation within the coccolith vesicle. We therefore propose a pathway for calcium to the coccolith vesicle that includes the nuclear envelope for the transport of calcium ions (Fig. 2.1-13). Seawater is the pri-

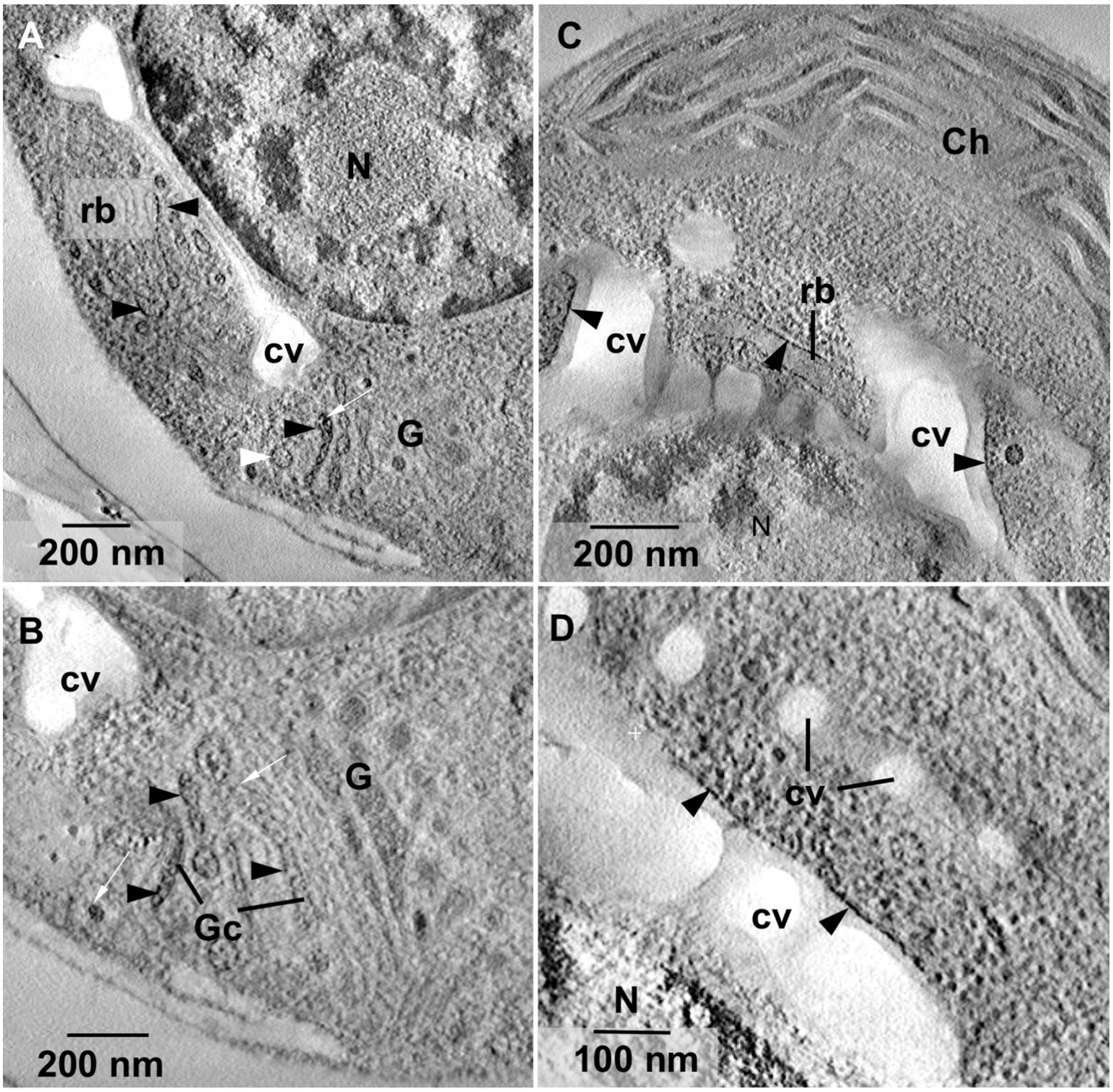

Figure 2.1-11. 3-D reconstruction of the reticular body from a STEM tomogram. (A, B) top and bottom view, respectively and (C, D) view from the side. See Video 2.1-V2 of the supplementary for the full reconstruction.

mary source of the calcium ions and inorganic carbonate (HCO_3^-) required for coccolith formation. As proposed by Brownlee & Taylor (2004), calcium ions rather enter the cells through plasma membrane calcium channels than through endocytotic vesicles. The cytosol has a resting calcium concentration of $\sim 0.1 \times 10^{-6}$ mol·L^{-1}. In order to maintain resting cytosolic concentrations, calcium required for coccolith formation should be taken up near the plasma membrane into peripheral cisternae of the ER, including the chloroplast ER that is continuous with the nuclear envelope, by the activity of a Ca-ATPase of the ER and a $Ca^{2+}/2H^+$ exchange mechanism (Brownlee & Taylor 2004; Mackinder *et al.* 2011). Being part of the vast ER calcium store of eukaryotic cells, the nuclear envelope contains high calcium concentrations of 100–300 μmol·L^{-1} (Petersen *et al.* 1998) and carries the calcium release channels usually involved in the calcium signaling pathway (Gerasimenko *et al.* 1996). We therefore propose a route for calcium uptake into the coccolith vesicle as shown in Figure 2.1-13. Release of calcium from the nuclear envelope at the nuclear envelope junction results in a large local increase in calcium concentration within the well-controlled narrow gap between the membranes of the coccolith vesicle and the nuclear envelope. The narrow distance between

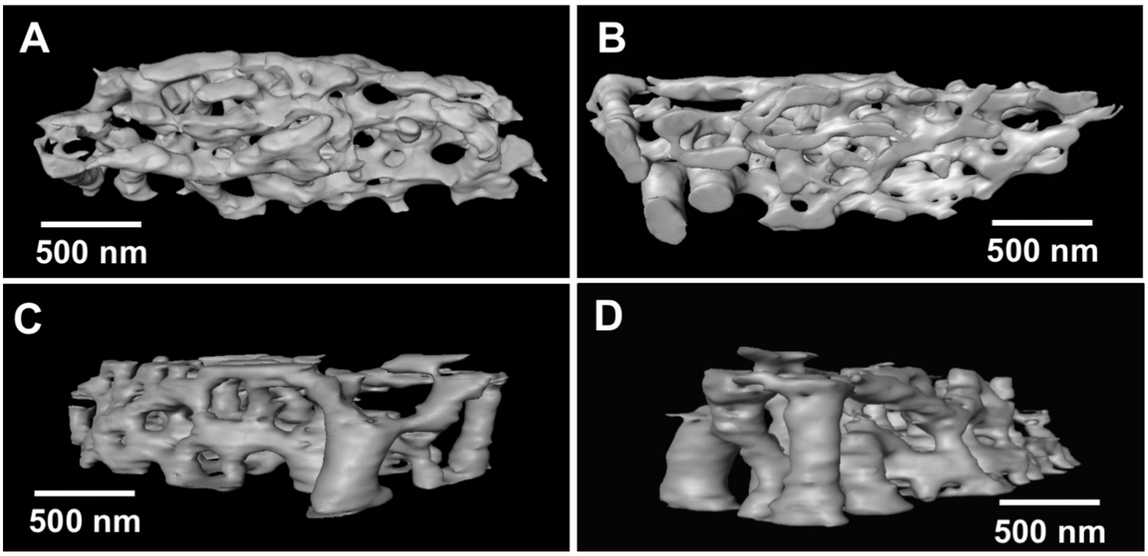

Figure 2.1-12. Overviews (A, C) and details (B, D) of sections from two tomograms through two different cells of *Emiliania huxleyi*. A, B: Images of a cell containing coccolith vesicles (cv) in an intermediate phase. Densely stained particles with diameters of up to 10 nm (black arrowheads) form seams at the inner side of the membranes within the reticular body (rb), within peripheral cisternae (Gc) of the the Golgi body (G), and Golgi vesicles (white arrowhead). In the Golgi cisternae and vesicles dense material occurs within central regions of the organelle as well (white arrows). C, D: Images of a cell containing coccolith vesicles in an advanced phase. Seams of dense particles occur at the inner side of the reticular body and at the coccolith vesicle membranes. Ch, chloroplast, N, nucleus. The full tomogram is provided in the Video 2.1-V2 of the supplementary.

Table 2.1-2. Coccolithophore organelles containing dense particles at the inner side of their membrane; cv, coccolith vesicle; rb, reticular body; v, vesicles, Gc, Golgi cisternae; do, dense organelle. (“+”, present; “-” lacking; “n”, organelle not found).

Tomogram #	cv phase	cv	rb	v	Gc	do
1	2	-	+	n	n	n
2	2	-	+	n	n	n
4	2	-	+	n	n	+
3	2	-	+	+	+	+
5	2	-	+	+	+	n
6	2	+	+	n	n	n
7	3	+	+	+	+	n
8	3	+	+	+	+	n
9	3	+	+	+	+	+
10	3	+	+	+	+	+
11	4	+	+	+	n	n
12	4	+	+	+	n	n
13	4	+	n	n	n	n
14	4	+	n	+	n	n
15	4	-	n	+	n	+
16	4	-	n	+	+	+
17	5	+	n	n	n	n
18	5	-	n	+	+	n

these membranes prevents large losses of calcium, which would occur in a more open system by diffusion into the lateral cytoplasm. Therefore, in the narrow gap of the nuclear envelope junction calcium concentration can raise up to similar values as in the nuclear envelope. To precipitate $CaCO_3$ the solution within the coccolith vesicle needs to be supersaturated. Compared to the electrochemical calcium gradient across the membrane separating this supersaturated space from the cytoplasm, the electrochemical gradient across the membrane of the coccolith vesicle in the nuclear envelope junction can be regulated to a much lower value. Accordingly, uptake of calcium into the coccolith vesicle can occur here at low costs against a low or even along an electrochemical calcium gradient. This uptake may occur by a $Ca^{2+}/2H^{+}$ exchange mechanism, which would maintain the alkaline conditions required for coccolith growth within the coccolith vesicle (Mackinder *et al.* 2011). HCO_3^- may be transported into the coccolith vesicle by an anion/HCO_3^- exchanger (Mackinder *et al.* 2011). Protons released from HCO_3^- during calcium carbonate formation and imported by the V-Type H^+-ATPase are extruded by the $Ca^{2+}/2H^{+}$ exchange mechanism. The last step would lead to

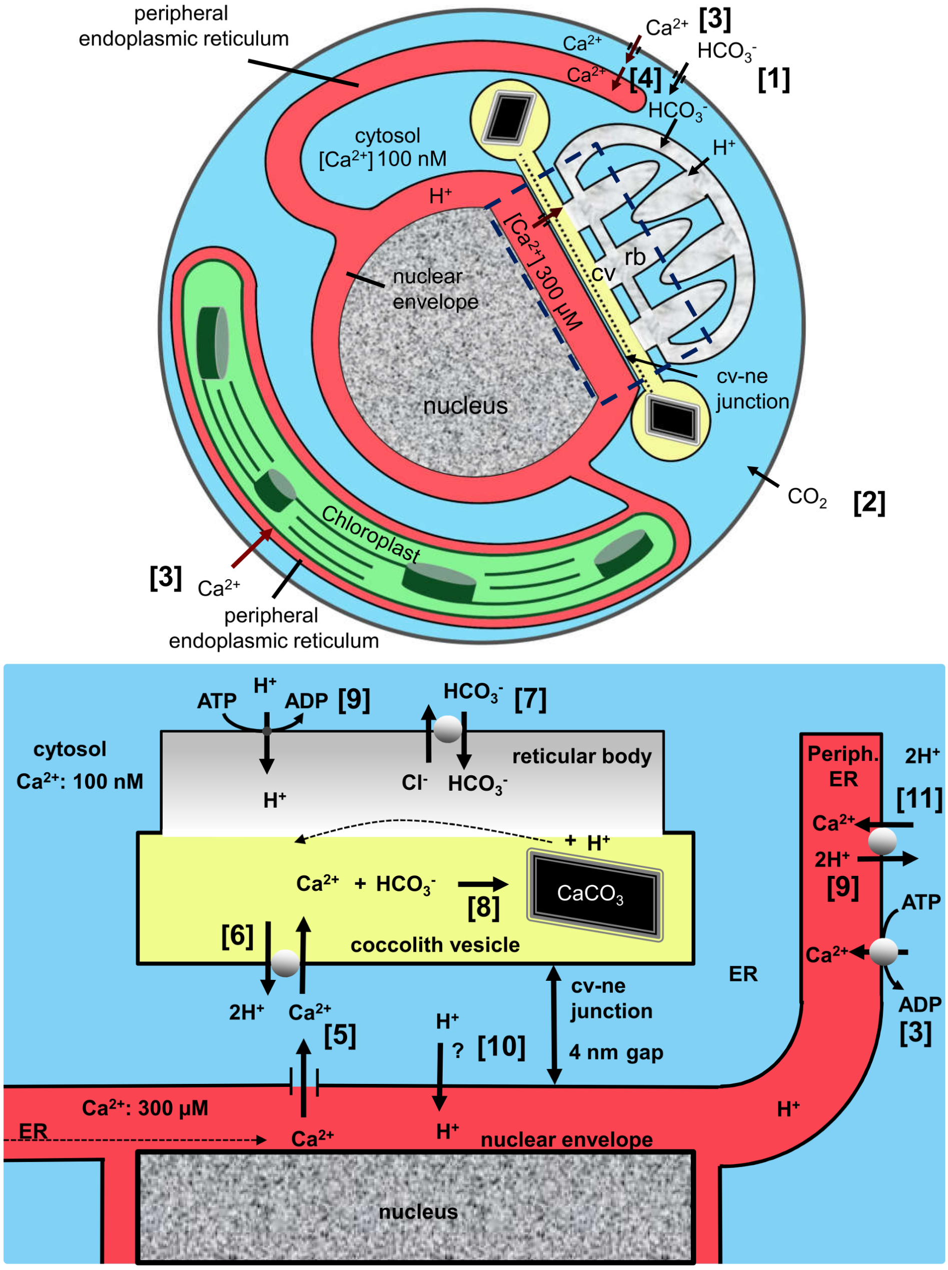

Figure 2.1-13. Hypothetical model of calcium and proton pathways for coccolith formation. The scheme (A) shows an overview of the spatial relation of the coccolith vesicle (cv, yellow), the reticular body (rb, grey), the endoplasmic reticulum (ER)/nuclear envelope (NE) calcium store (red), and the chloroplast (green) within an E. huxleyi cell (the Golgi system is not shown). In addition, the steps for entry of calcium and carbonate from the surrounding medium into the cytoplasm and uptake of calcium into the ER/NE calcium store are depicted [1]–[4]. [1] Hydrogen carbonate from the surrounding water is transported into the cytoplasm by a Cl^-/HCO_3^- exchanger and/or a Na^+/ HCO_3^- symporter. [2] CO_2 can diffuse across the plasma membrane and is converted to HCO_3^- by a carbon-anhydrase. [3] Calcium enters the cell across calcium channels and is taken up into the large ER/NE calcium store by a $Ca^{2+}/2H^+$ exchange mechanism and a Ca^{2+}-ATPase. [4] Within the ER calcium can diffuse into the nuclear envelope. The scheme (B) depicts the pathways for calcium, protons and carbonate at the cv and rb, respectively [5]–[11]. [5] Calcium ions enter the nuclear envelope junction (cv-ne junction) through calcium release channels within the outer membrane of the nuclear envelope. [6] A calcium/proton exchange mechanism transports calcium into the coccolith vesicle in exchange of $2H^+$. [7] HCO_3^- is transported into the cv by an anion exchanger like the Cl^-/HCO_3^- exchanger. [8] Protons are released during precipitation of calcium carbonate. [9] These H^+ and those provided by a V-type H^+-ATPase are transported into the cv-ne junction. [10] Possibly H^+ is sequestered into the nuclear envelope. [11] H^+ diffuses through the ER to peripheral cisternae of the ER to fuel the $Ca^{2+}/2H^+$ exchanger. Note that a possible parallel rout for calcium, by uptake into the Golgi complex and transport by Golgi vesicles to the coccolith vesicle, as proposed by Brownlee *et al.* 2015, are not presented.

a high increase of the H^+ concentration between the membranes of the nuclear envelope junction, opening the possibility that protons are taken up at this junction into the ER. From here the protons could diffuse throughout the ER lumen and possibly fuel the $Ca^{2+}/2H^+$ exchange mechanism in peripheral ER cisternae. We observe that all coccolith vesicles which contain an immature coccolith and are not located at the nuclear envelope, are in close contact with ER cisternae instead. This supports the significant role of the nuclear envelope/ER system for coccolith mineralization. However, our model does not exclude other models for calcium accumulation within the coccolith vesicle that may work in parallel (e.g., possible uptake into the Golgi complex and transport by Golgi vesicles to the coccolith vesicle; Westbroek *et al.* 1984; Brownlee *et al.* 2015), or an involvement of a Ca-P reservoir, from where calcium ions may be dispatched to the reticular body-coccolith vesicle system (Sviben *et al.* 2016).

Pleurochrysis carterae carries multiple but smaller coccolith vesicles in comparison to *Emiliania huxleyi*, likely the reason why a reticular body is lacking in P. carterae. In addition, there is no close association of the coccolith vesicles with the nuclear envelope. Likely these differences indicate that the mechanisms of coccolith formation in *E. huxleyi* and *P. carterae* are distinct from one another (see also the review by Brownlee *et al.* 2015 for a discussion of species specific mechanisms of calcification).

Immunocytochemical and physiological experiments have demonstrated the presence of a V-Type H^+-ATPase in isolated coccolith vesicles of *Pleurochrysis sp.* (Araki & Gonzáles 1998; Corstjens *et al.* 2001). However, the role of the V-type H^+-ATPase is not quite clear. It may provide protons required for the calcium/proton exchange mechanism and/or may be involved in pH regulation in the coccolith vesicle. Protons that are released during calcium carbonate formation need to be transported into the cytosol to maintain alkaline conditions consistent with calcium carbonate precipitation. The V-type H^+-ATPase transports protons into the coccolith lumen which would hinder calcium carbonate precipitation (Sze *et al.* 1999). However, it has been shown that the V-type ATPase can energize numerous proton-coupled transporters (Harvey & Wieczorek 1997; Beyenbach & Wieczorek 2006) that can even lead to an alkalization as required for calcium carbonate precipitation. A recent expression analysis indicates a role of a $Ca^{2+}/2H^+$ exchanger for calcification in *Emiliania huxleyi* (Mackinder *et al.* 2011), which may possibly be involved in such an alkalization.

2.1.5 Conclusions

We investigated the crystallographic defect microstructure of calcite in *Emiliania huxleyi* coccoliths with respect to indications of crystal growth and explored the ultrastructure of the cell with regard to the Ca^{2+} transport to the site of calcite nucleation and growth. The results gained in this study allow us to deduce the following conclusions for *E. huxleyi* coccolith calcite formation and organization:

1. The crystallographic microstructure of *Emiliania huxleyi* R-units shows planar imperfections which separate mosaic blocks. As at these imperfections only minor misorientations (<0.3°) occur, we attribute them to dislocation networks creating small-angle boundaries. Further, there are no occluded intracrystalline biopolymers. The observed defect structure is thus typical for classical ion-by-ion crystal growth. *E. huxleyi* coccolith calcite does not show features of "mesocrystals", and there are no indications of accretion of nanoparticles as the growth mechanism.

2. From cell ultrastructural analysis, we observe over a large distance a narrow, well-controlled gap of 4 nm between the membrane of the coccolith vesicles and the outer membrane of the nuclear envelope. We regard this narrow association between the coccolith vesicle and

the nuclear envelope as a new interorganelle junction, the “nuclear envelope junction”.

3. As the nuclear envelope is confluent with the ER, the newly observed interorganelle junction suggests that calcium ions for the mineralization of the coccolith are transported through the membranes of the junction from the large nuclear envelope-ER calcium store of the cell.
4. This suggests a new pathway for intracellular calcium transport from the ER into the lumen of the coccolith vesicle.
5. Both our microstructure and ultrastructure results argue for calcite formation in *Emiliania huxleyi* coccoliths by a classical ion-by-ion growth mechanism and not by particle accretion.

Acknowledgements

This work was supported by Deutsche Forschungsgemeinschaft (DFG grant No. SCHM 930/15-1). We are indebted to Dr. Fitriana Nindiyasari for her help in the development of the preparation methods used in this work. We sincerely thank Renate Kunz and Chris Hormann of the Central Facility for Electron Microscopy of Ulm University, for technical support and assistance.

2.1.6 Support Information

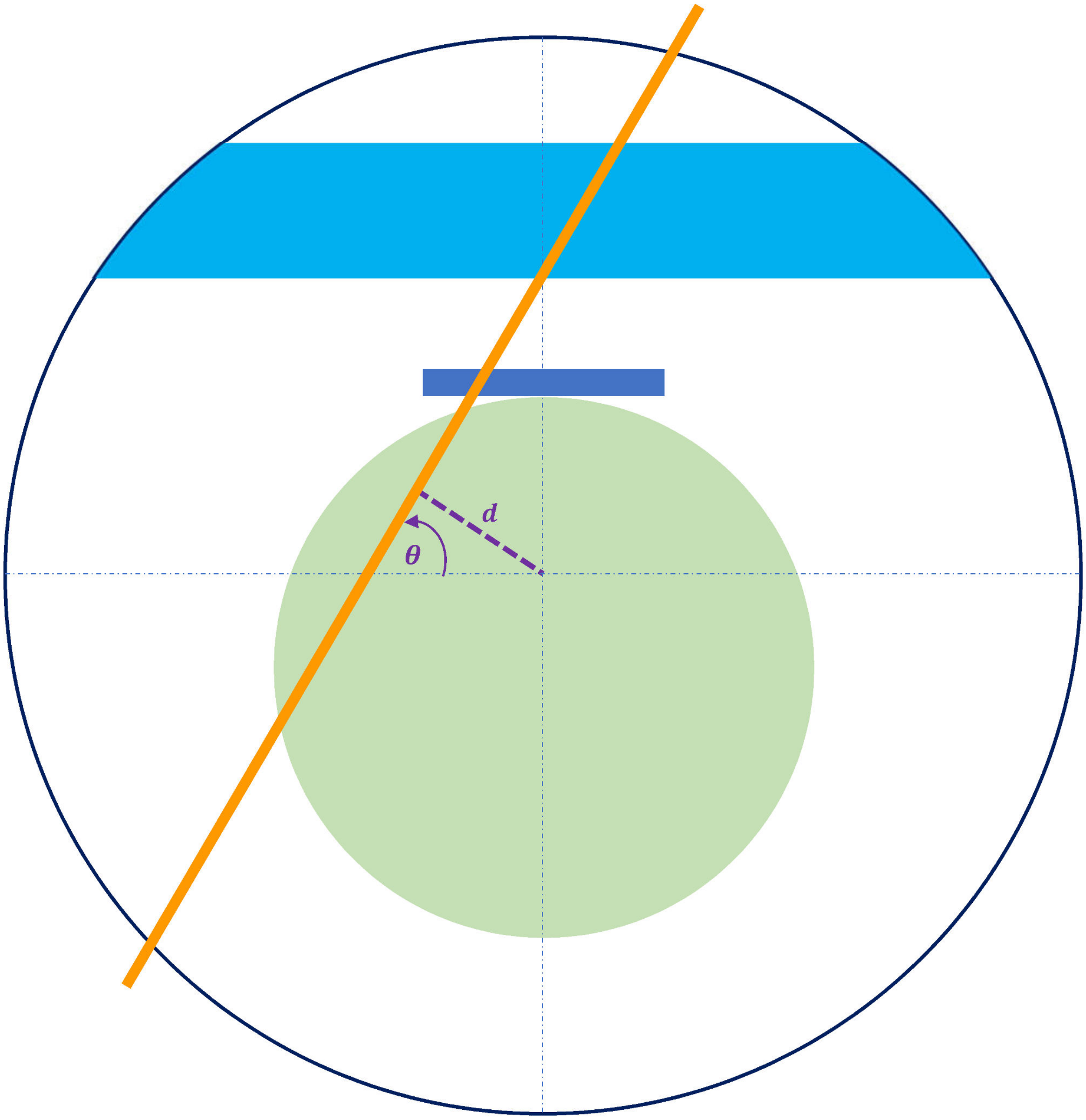

Figure 2.1-S1. Sketch of our systematic sampling model for the assessment of differently aged coccoliths in the same cell. Phase 1 coccolith vesicle is located next to the nucleus, while phase 5 coccolith is close to the plasma membrane of the cell. We assume in this model that the two coccolith vesicles are parallel to each other. Green: nucleus; dark blue: phase 1 coccolith vesicle; light blue: phase 5 coccolith vesicle; orange line: the 40 nm thick cut through the cell.

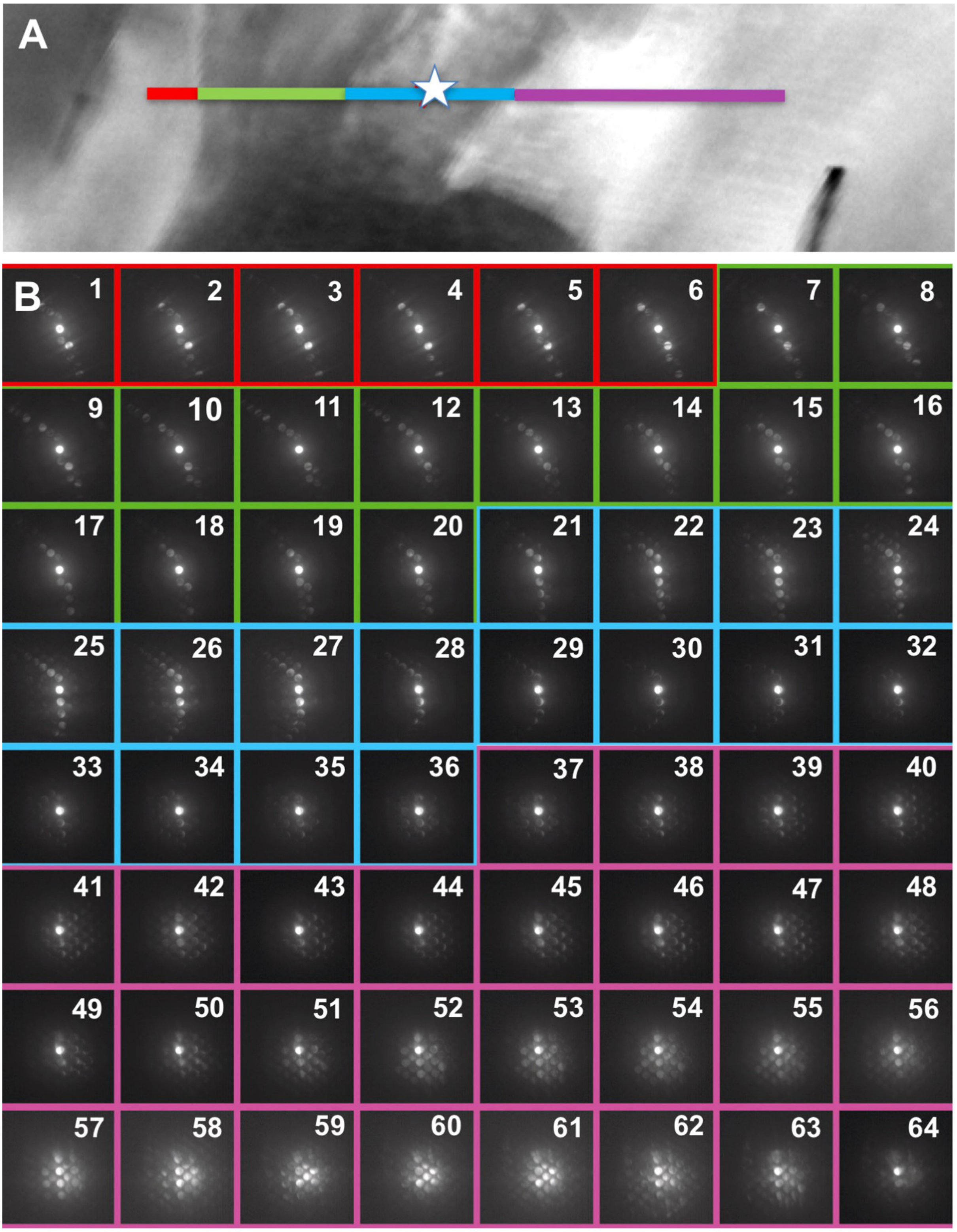

Figure 2.1-S2. The full set (64) of diffraction measurements (B) taken along a profile (A) on the central area element. From the diffraction measurements, we cannot deduce an abrupt change in calcite crystal orientation. Crystal orientation is continuous or differences in orientation are so small that they are not detectable with spot diffraction measurements.

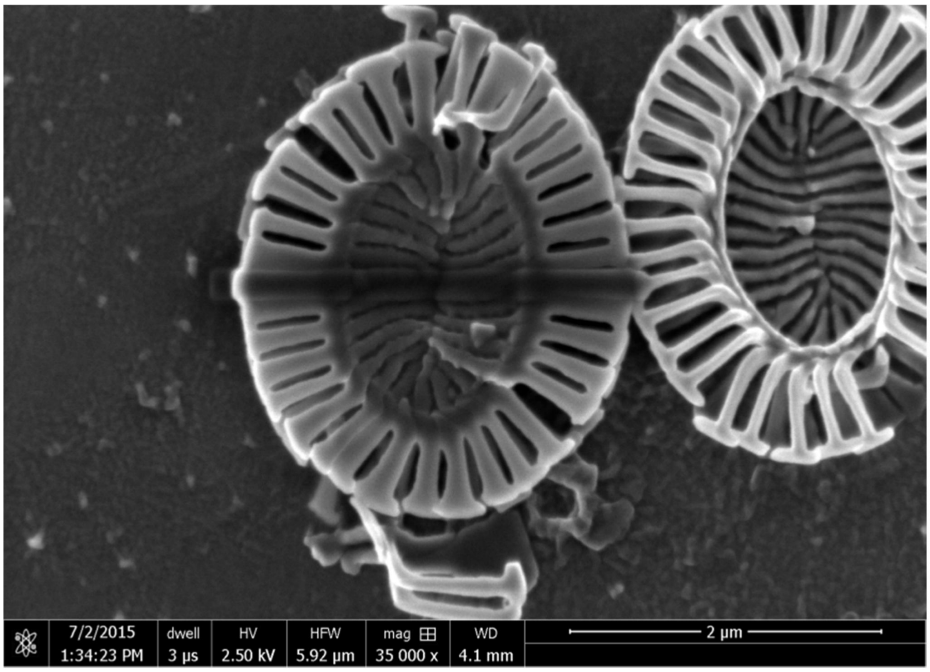

Figure 2.1-S3. SEM image of a coccolith with an applied protective carbon strip as first step for FIB preparation. The central trace of the carbon strip defines the top direction of the prepared FIB lamellae, containing horizontal transverse cut through a whole coccolith segment.

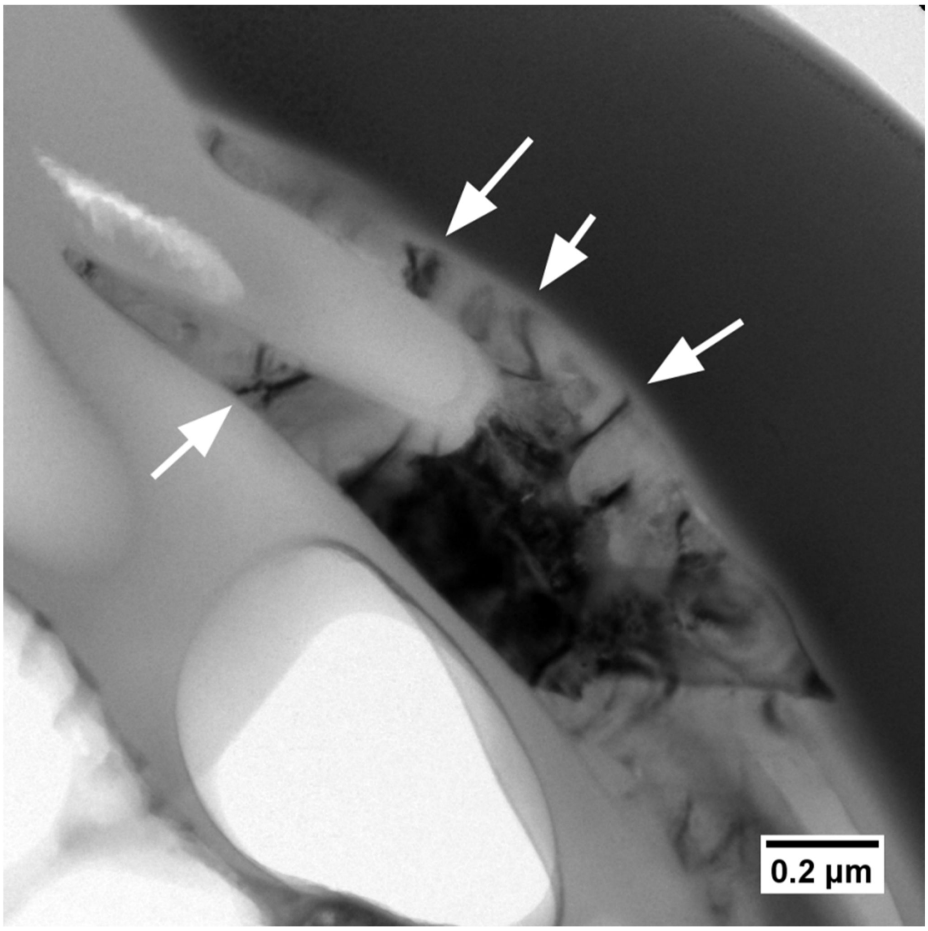

Figure 2.1-S4. TEM bright-field image of the single coccolith shown in Figures 2.1-2B and 2.1-3. White arrows point to bending contours, identified by their characteristic appearance as parallel bands.

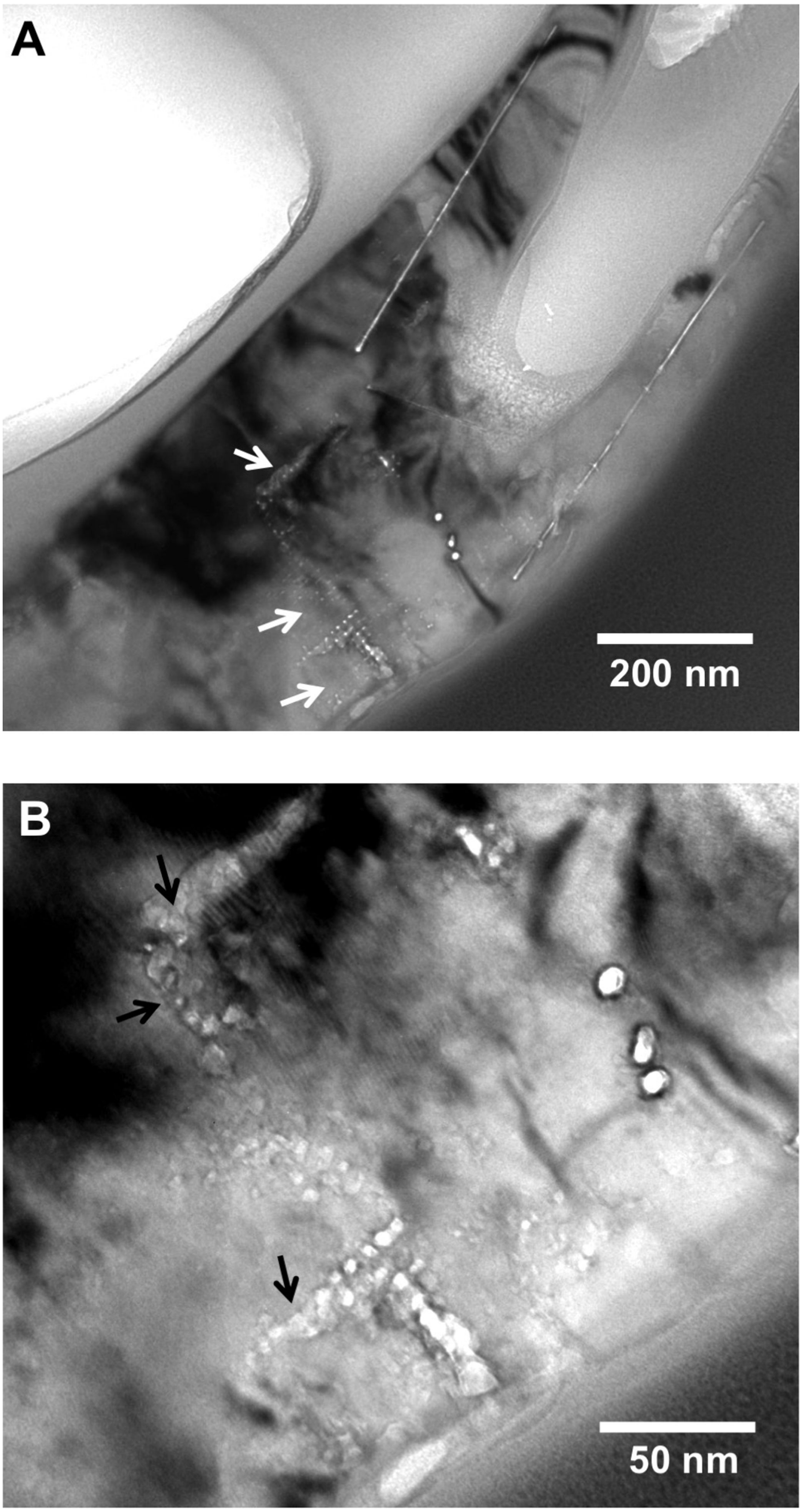

Figure 2.1-S5. Portion of the coccolith on which spot diffraction measurements were carried out. (A) overview, (B) detail. Coccolith calcite is highly delicate, it is destroyed within very few seconds upon illumination with the focused electron beam in diffraction mode (Fig. 2.1-S3B).

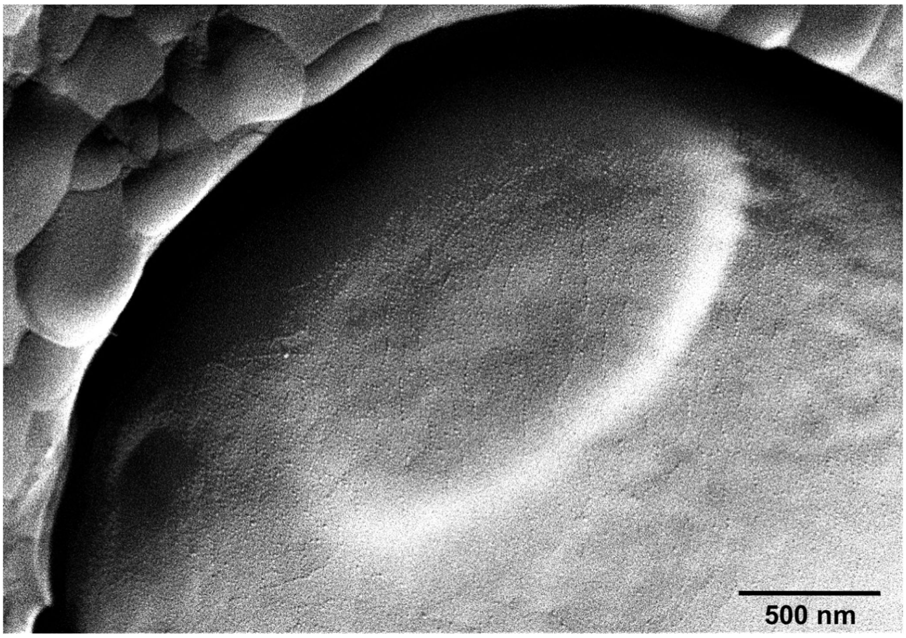

Figure 2.1-S6. Scanning backscatter electron micrographs of a high-pressure frozen cell. A bright signal originating from the interior of the cell shows that the mineral forms a proto-coccolith ring structure in an early phase of coccolith development.

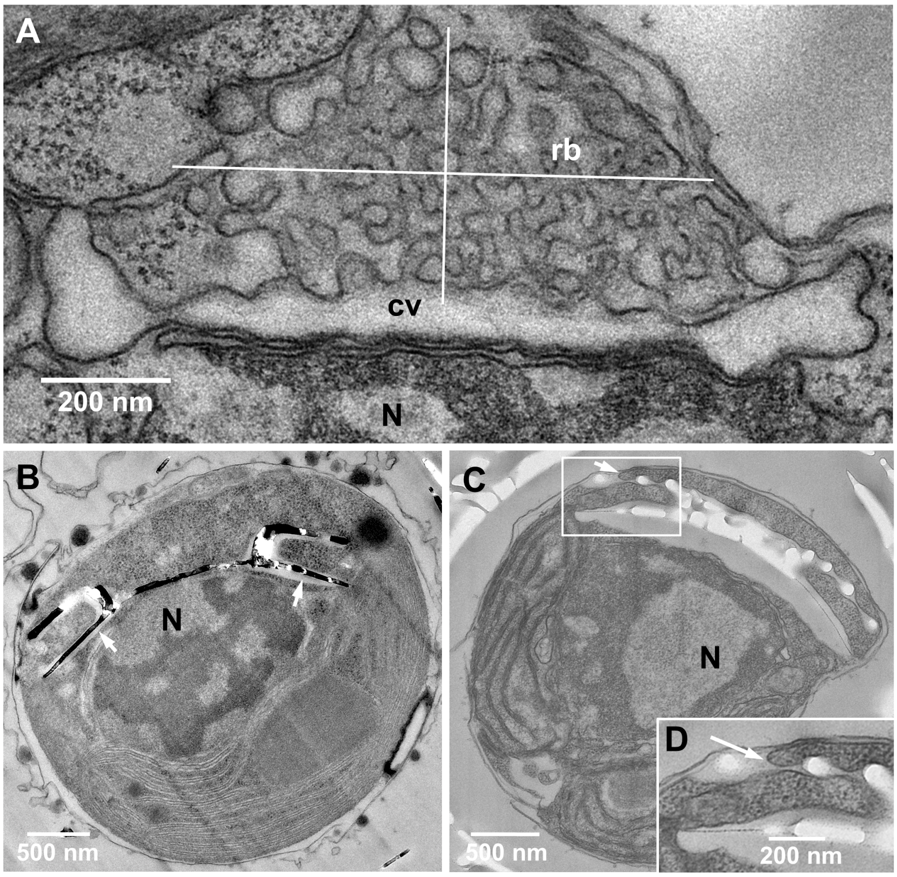

Figure 2.1-S7. TEM micrographs of thin sections from chemically fixed *Emiliania huxleyi* cells. (A) Detail of an intermediate sized coccolith vesicle (cv; phase 3 of Fig. 2.1-6) depicting the connection to the reticular body (rb). The number of intersections between the reticular body and a vertical and a horizontal line through the centre of the reticular body were used as a measure for relative membrane length; N, nucleus. (B, C) Overviews of whole cells containing almost mature coccoliths in phase 4 (B) and phase 5 (C). Note that mineral is preserved within the section shown in B (white arrows). (D) Detail of (C) showing that the coccolith vesicle has fused with the plasma membrane of the cell in preparation for exocytosis.

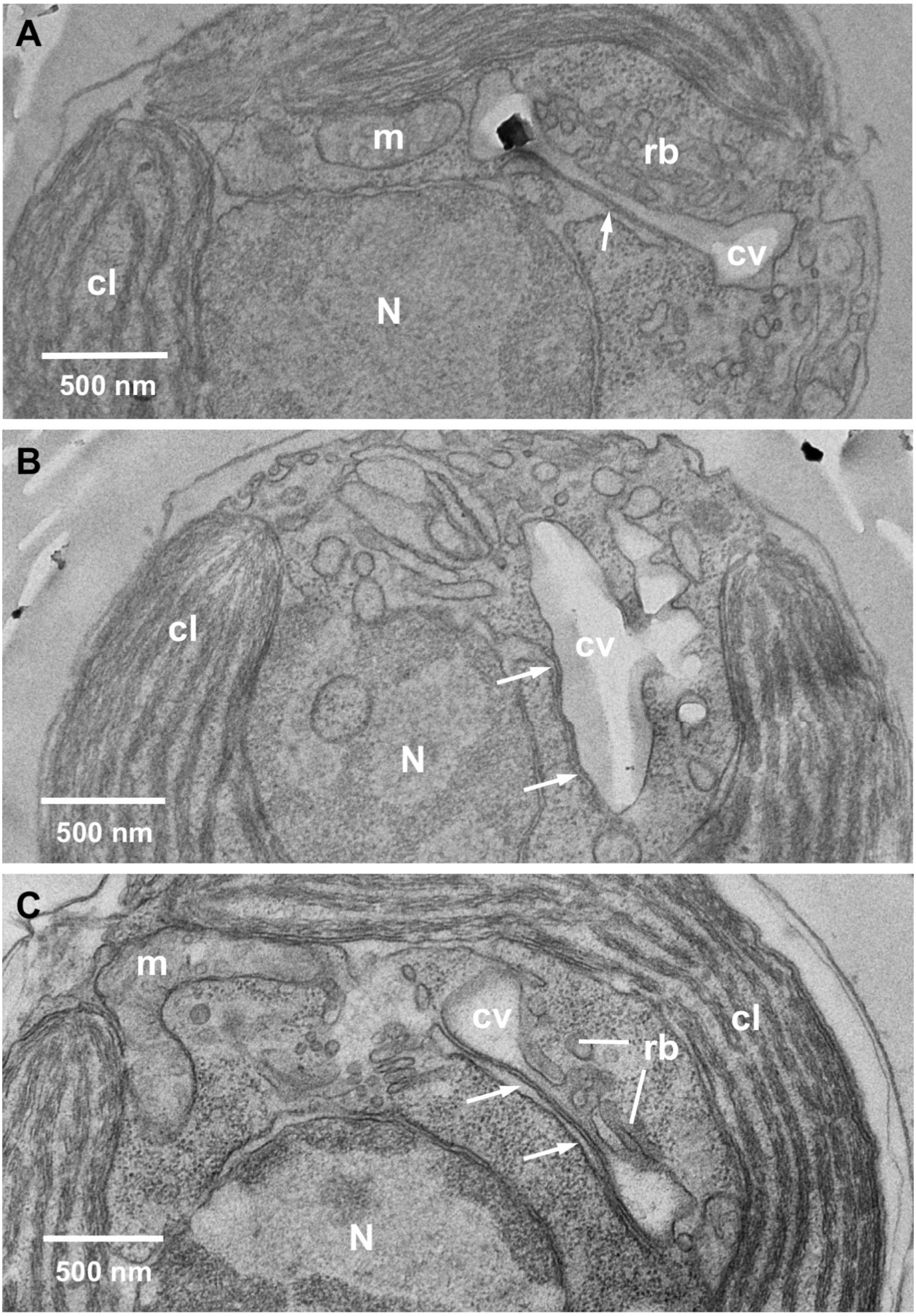

Figure 2.1-S8. Three examples (A–C) of chemically fixed *Emiliania huxleyi* in which the coccolith vesicle is in close contact to a cisterna of the endoplasmic reticulum, rather than the nuclear envelope.

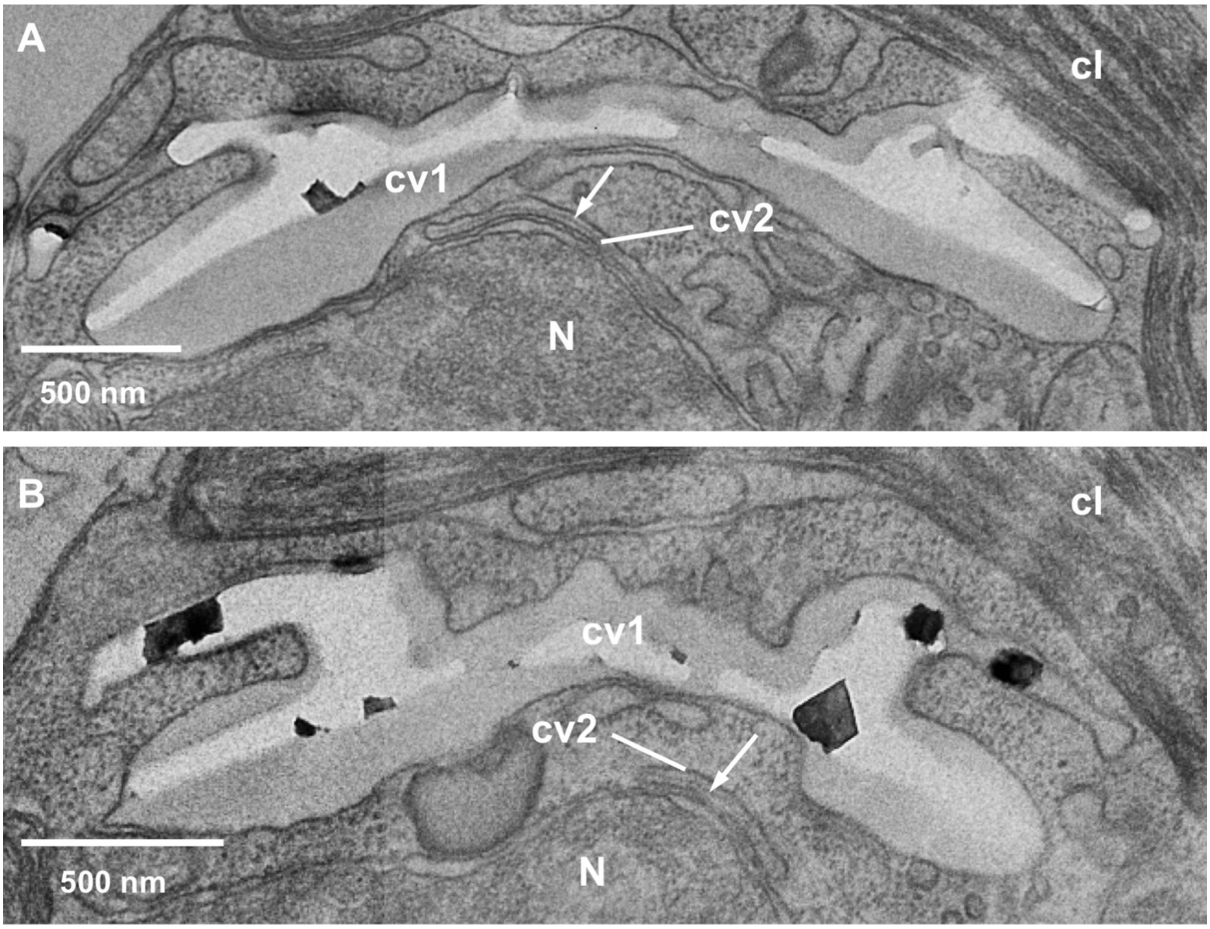

Figure 2.1-S9. Two examples (A) and (B) of chemically fixed *Emiliania huxleyi* that contain a large peripheral coccolith vesicle (cv1), and also a second small one (cv2) in phase1 of coccolith development in close contact to the nuclear envelope. Note that cv1 already contains the organic matrix of the base plate (white arrow); cl, chloroplast; N, nucleus.

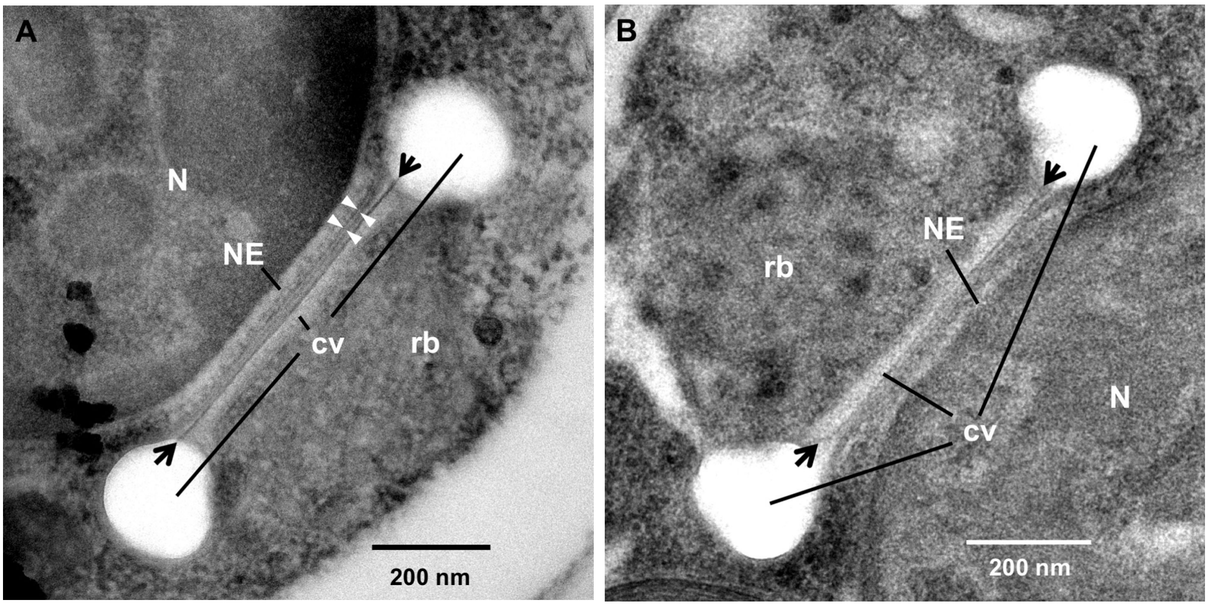

Figure 2.1-S10. Two micrographs (A) and (B) of thin sections through high-pressure frozen and freeze-substituted cells of *Emiliania huxleyi*. The images depict the narrow distances (white arrowheads in A) between the outer membrane of the nuclear envelope (NE) and the membrane of the coccolith vesicle (cv); rb, reticular body.

Video 2.1-V1. Electron tomogram of a ∼400 nm thick section from a high-pressure frozen and freeze-substituted cell of *Emiliania huxleyi*. The movie depicts a coccolith vesicle in a median phase (phase 3) of development. It is in close vicinity to the outer membrane of the nucleus. The reticular body is located between the coccolith vesicle and the plasma membrane of the cell. The various profiles of the coccolith vesicles are continuous with each other and the vesicular body. Densely stained particles occur at the inner side of the membrane of the coccolith vesicle and occur scattered in the lumen of the Golgi apparatus and Golgi vesicles and at the inner side of their membranes. The nucleus, part of the chloroplast, and a densely stained multi-vesicular body is visible.

Video 2.1-V2. Electron tomogram of a ∼400nm thick section from a high-pressure frozen and freeze-substituted cell of *Emiliania huxleyi* and a 3-D reconstruction of the reticular body. It shows the nuclear envelope being continues with an ER cisterna. A large cisterna of ER extents far between the reticular body and the plasma membrane of the cell. The membrane of the coccolith vesicle is close to the nuclear envelope. Mitochondria a part of the chloroplast with the pyrenoid and a large liposome-like structure is visible. The membranes of the reticular body contain dense material at the luminal side of its membrane. The segmentation (blue) shows that the reticular body forms a continuous structure.

2.2 Calcite crystal orientation patterns in the bilayers of laminated tests of benthic rotaliid foraminifera

Xiaofei Yin[1*], Erika Griesshaber[1], Antonio G Checa[2, 3], Fitriana Nindiyasari-Behal[4], Isabel Sánchez-Almazo[5], Andreas Ziegler[6], Wolfgang W. Schmahl[1]

1. Department für Geo- und Umweltwissenschaften, Ludwig-Maximilians-Universität München, Germany
2. Departamento de Estratigrafía y Paleontología, Universidad de Granada, Spain
3. Instituto Andaluz de Ciencias de la Tierra, CSIC-Universidad de Granada, Armilla, Spain
4. Nuclear Research & Consultancy Group (NRG), Petten, the Netherlands
5. Centro de Instrumentación Científica, Universidad de Granada, Spain
6. Zentrale Einrichtung Elektronenmikroskopie, Universität Ulm, Germany

J. Struct. Biol. **213**, 107707 (2021)
https://doi.org/10.1016/j.jsb.2021.107707

Abstract

Shells of calcifying foraminifera play a major role in marine biogeochemical cycles; fossil shells form important archives for paleoenvironment reconstruction. Despite their importance in many Earth science disciplines, there is still little consensus on foraminiferal shell mineralization. Geochemical, biochemical, and physiological studies showed that foraminiferal shell formation might take place through various and diverse mineralization mechanisms.

In this study, we contribute to benthic foraminiferal shell calcification through deciphering crystallite organization within the shells. We base our conclusions on results gained from electron backscattered diffraction (EBSD) measurements and describe microstructure/texture characteristics within the laminated shell walls of the benthic, symbiontic foraminifera: *Ammonia tepida*, *Amphistegina lobifera*, *Amphistegina lessonii*. We highlight crystallite assembly patterns obtained on differently oriented cuts and discuss crystallite sizes, morphologies, interlinkages, orientations, and co-orientation strengths.

We show that: (i) crystals within benthic foraminiferal shells are mesocrystals, (ii) have dendritic-fractal morphologies and (iii) interdigitate strongly. Based on crystal size, we (iv) differentiate between the two layers that comprise the shells and demonstrate that (v) crystals in the septa have different assemblies relative to those in the shell walls. We highlight that (vi) at junctions of different shell elements the axis of crystal orientation jumps abruptly such that their assembly in EBSD maps has a bimodal distribution. We prove (vii) extensive twin-formation within foraminiferal calcite; we demonstrate the presence of two twin modes: 60°/[001] and 77°/ $[6\bar{6}1]$ and visualize their distributions within the shells.

In a broader perspective, we draw conclusions on processes that lead to the observed microstructure/texture patterns.

Keywords

calcite twins; crystal organization in foraminiferal tests; electron backscatter diffrection (EBSD); benthic foraminifera

2.2.1 Introduction

Foraminifera are one of the main carbonate producers in the oceans and form about 25% of the global oceanic carbonate production (Erez 2003; Langer 2008; de Nooijer *et al.* 2014). Foraminifera are among the most abundant shelled organisms in marine environments and can be found in almost all marine habitats: from intertidal zones to deep ocean trenches, from tropic to polar regions (e.g., Goldstein 1999; Debenay *et al.* 2000; Debenay & Guillou 2002; Caulle *et al.* 2014.)

Foraminifera are unicellular eukaryotes that are protected by a shell made of either: (i) organic, (ii) agglutinated or (iii) mineralized, calcareous, material (Lipps 1973; Hemleben *et al.* 1977; Goldstein 1999; Erez 2003; de Nooijer *et al.* 2014). Calcareous shells are in most cases multi-chambered; the latter are interconnected. Accordingly, the cytoplasm might fill more than one chamber (Hemleben *et al.* 1986; Erez 2003). The life span of most foraminifera is short, it lasts from a few weeks to a few months. Accordingly, foraminifera secrete their shells quickly relative to other shelled organisms such as mollusks or brachiopods (Hemleben *et al.* 1989; Lee & Anderson 1991). The absolute majority of calcareous shells consists of calcite, only few species secrete aragonitic shell material (Lipps 1973; Goldstein 1999; Hansen 1999; Gussone *et al.* 2016). Both calcitic and aragonitic shells can be perforate or imperforate; today's oceans are dominated by perforate, calcite-secreting foraminifera.

Since their appearance in the Cambrian (Pawlowski *et al.* 2003) foraminifera developed an extreme diversity of shell morphologies. This characteristic, as well as their distribution in virtually all marine habitats, and their (more or less faithful) recording of changes in seawater chemistry and temperature render these organisms ideal archives for the reconstruction of paleoenvironments and paleoclimates (Erez 2003; Bentov & Erez 2005; Bentov *et al.* 2009; Nehrke *et al.* 2013; de Nooijer *et al.* 2014; Gussone *et al.* 2016; Nagai *et al.* 2018a). However, for the extraction of reliable paleoenvironmental information, it is of major importance to understand shell formation in great detail: shell wall structure as well as shell wall chemical and structural heterogeneities. Previous studies have shown that the major drawback when using foraminifera as an archive is that they form their shells by a complex physiological process (e.g., Nehrke *et al.* 2013; de Nooijer *et al.* 2014; Toyofuku *et al.* 2017; Evans *et al.* 2018. This impacts isotope fractionation and element incorporation, and, with this, the precision of environment information extracted from chemical signals of the shells.

Within the last decades, foraminiferal shell biomineralization was deciphered to some degree. Biochemical, geochemical and physiological studies (Erez 1978, 2003; Bentov & Erez 2005; Bentov *et al.* 2009; de Nooijer *et al.* 2009, 2014; Glas *et al.* 2012; Nehrke *et al.* 2013; Langer *et al.* 2015; Gussone *et al.* 2016; Toyofuku *et al.* 2017; Borrelli *et al.* 2018; Evans *et al.* 2018; Nagai *et al.* 2018a; Levi *et al.* 2019; Tyszka *et al.* 2019; van Dijk *et al.* 2019) concluded that many processes might contribute to foraminiferal shell calcification: e.g., endocytosis of seawater, ion transport through transmembrane transporters, nucleation on ion-specific organic templates, mitochondrial activity together with pH regulation, calcification through an amorphous or metastable phase. It has, furthermore, been shown that foraminifera do not use only one mineralization strategy to produce their shell material, but many. Combinations of these not only vary between the different foraminiferal groups but even within single species (e.g., Nehrke *et al.* 2013; de Nooijer *et al.* 2014; Toyofuku *et al.* 2017; Evans *et al.* 2018; Levi *et al.* 2019).

Many structural studies on foraminiferal shells are available by now. However, most of these are based on light microscopy complemented with some confocal microscopy and little high-resolution electron microscopical imaging. Previous structural characterization of foraminiferal hard tissues concentrated on: (i) descriptions of the gross morphology of the shells, (ii) elucidation of new chamber formation (benthic species: Reiss 1957; Angell 1967, 1979, planktonic species: Hemleben *et al.* 1977; Bé *et al.* 1979; Hemleben *et al.* 1986; Spero 1988; Nagai *et al.* 2018a,b; Tyszka *et al.* 2019; Goleń *et al.* 2020) and illustration of (iii) basic morphological characteristics of shell walls (e.g., Lipps 1973; Hottinger 2006)

In this study, we revisit the structural characterization of foraminiferal shells and disclose in great detail the microstructure and texture of the shells of the three rotaliid foraminifera: *Amphistegina lessonii* (d'Orbigny 1826), *Amphistegina lobifera* (Larsen 1976) and *Ammonia tepida* (Cushman 1926). We base our results and conclusions on patterns of crystal orientation measured with electron backscatter diffraction (EBSD). EBSD measurements yield characteristics of crystal morphologies, sizes, size distributions, crystal orientations, the extent of crystal alignments and modes of crystal interlinkages.

We show:

1. the significant difference of benthic foraminiferal shell microstructure and texture in comparison to that of shelled marine organisms such as mollusks and brachiopods
2. the diversity and irregularity of crystal shapes and sizes within the shells
3. the difference in distribution of twinned and untwinned mesocrystals
4. the widespread occurrence of twinned mesocrystals and the presence of two twin modes of calcite
5. the lamination of chamber walls on the basis of structural aspects of shell calcite

In a broader perspective, we attempt to relate the different modes of calcite organization that we find in the shells to varying structural biomaterial formation processes and strategies. As the EBSD technique is widely established by now, we propose to develop crystal orientation measurements and analyses as a tool to distinguish between the different calcifying foraminiferal groups.

2.2.2 Material and Methods

Materials

Foraminifera of the species *Ammonia tepida*, *Amphistegina lessonii* and *Amphistegina lobifera* were obtained from the Department of Earth and Environmental Sciences, LMU, Munich, Germany, GEOMAR Helmholtz Zentrum, Kiel, Germany, and from the Department of Earth Sciences, Cambridge, UK. We investigated five specimens per foraminifera species.

Methods

All results presented in this contribution are obtained on microtome cut surfaces, not on tomographic slices.

Electron backscattered diffraction (EBSD) measurements were performed on EPON embedded, ultramicrotome cut and polished shells. Foraminiferal shells were oriented within the EPON resin for the required cuts as precisely as possible. Embedding in EPON was necessary and ensured that, when cut and polished, the shells remained more or less fully intact. Cutting and polishing were done with a Leica Ultracut ultramicrotome. After exposing the required surface of the shell from EPON resin with a trimming knife (Diatome), shells were polished subsequently with a dry diamond knife (Diatome). Polishing of the cut surfaces involved the stepwise removal of material in a series of sections with successively decreasing thicknesses (90 nm, 70 nm, 40 nm, 20 nm, 10 nm), whereby each step was repeated 15 times.

Shells were dissected in two directions (Cut 1, Cut 2, Fig. 2.2-1). With Cut 1 we sectioned the shells axially (as axially as possible), with Cut

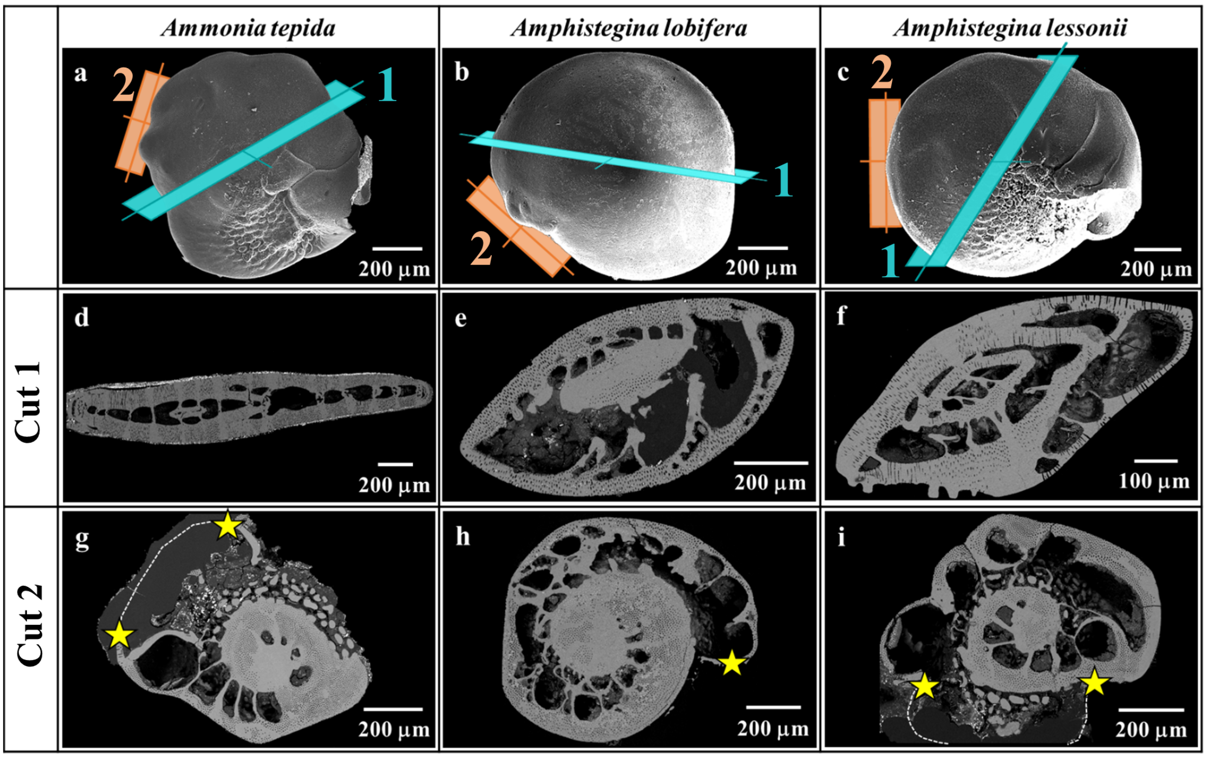

Figure 2.2-1. Investigated foraminifera species and mode of sectioning the shells; FE-SE (a–c) and FE-BSE (d–i) images. Foraminifera were dissected in two directions (a–c): Cut 1 is a near axial cut, Cut 2 is a near equatorial cut. Images shown in (d–i) are images of those surfaces that were scanned with EBSD. Well visible is the irregularity in dense and perforated shell regions, different chamber generations, the dense calcite in the central part of the shells, and the thin walls of the youngest chambers in the cuts (yellow star in g–i). Dashed white lines in (g) and (i) indicate the position of the youngest chamber wall. The latter broke at microtome preparation.

2 equatorially (as equatorially as possible, Fig. 2.2-1a-c). For EBSD measurements and SEM imaging, samples were coated with 4–6 nm of carbon and 6–8 nm of Pt/Pd, respectively. EBSD measurements and SE, BSE imaging were carried out with a Hitachi SU5000 FE-SEM, equipped with a Nordlys II EBSD detector. EBSD measurements were done with a step size of 200 to 350 nm. Data acquisition and evaluation were achieved with the Oxford Instruments AZTec and CHANNEL 5 HKL software, respectively. We scanned each cut surface with at least 10 EBSD measurements. Figure 2.2-13 depicts an EBSD panorama image. We visualize the distribution patterns of large and small crystals, strongly mineralized shell regions (Fig. 2.2-13a,b), the distribution of 77° misorientation boundaries (Fig. 2.2-13c) and the distribution pattern of 60° misorientation boundaries (Fig. 2.2-13d). The EBSD panorama image consists of 24 individual EBSD maps, all measured with a step size of 200 to 300 nm. Accordingly, we base the results shown in this contribution on 82 EBSD measurements, at least 20 measurements per species.

We present *microstructures* with color-coded as well as grey-scaled EBSD band contrast measurement maps and color-coded EBSD orientation maps. The coloring code is indicated either in the figure or is stated in the relevant figure caption. In crystal orientation maps, similar colors indicate similar orientations, while distinct colors highlight different crystallite orientations. Band contrast images depict the signal strength in each measurement point. High signal strength (strong mineralization) corresponds to light colors and indicates strong diffraction at the crystal lattice. Faint or dark colors are indicative of non-diffracting substances, e.g., polymers, or an overlap of minute crystallites that could not be indexed with the EBSD software.

The *texture*, crystallographic preferred orientation, is presented with pole figures. The latter give orientation data or density distributions of these. For the orientational density distributions, we use the lowest possible setting for half width and cluster size in the CHANNEL 5 software: a half width of five and a cluster size of three degrees. The half width controls the extent of the spread of the poles over the surface of the projection sphere, a cluster comprises data with the same orientation. *Calcite co-orientation* strength (given with MUD values) is derived from density distributions of the measured EBSD data. The MUD (multiple of uniform (random) distribution) value is calculated with the Oxford Instruments CHANNEL 5 EBSD software. High MUD values indicate high crystal co-orientation, low MUD values reflect a low strength of crystallite or/and mineral unit co-orientation. A MUD of 1 indicates random distribution and no preferred orientation, a MUD higher than 700 documents almost perfect co-orientation, single crystallinity (Greiner *et al.* 2018; Yin *et al.* 2019).

An *axial texture* is given when the c-axes show co-orientation (clustering in the pole figure around a single direction), while the corresponding a*-axes vary in orientation on a great circle perpendicular to the texture axis direction.

We use in this study the term *mesocrystal* to describe a crystalline entity over space, which consists of numerous smaller subunits on the submicrometer to $\sim$1 μm scale which are mutually slightly misoriented and which thus are separated by small-angle boundaries.

We use terms for crystal morphology such as *dendritic-fractal* and describe their interlinkage as *interdigitated.* A dendritic crystal has a multibranching morphology, e.g., the morphology of a snowflake. Dendritic crystallization induces the formation of fractal patterns. Dendritic crystals have convex/concave morphologies, recesses and protrusions. When forming dense mineralized skeletal parts neighboring and abutting dendritic biocrystals interweave and interlink in three dimensions and interdigitate (Goetz *et al.* 2011).

In this study, we describe the phenomenon of *twinning in foraminiferal calcite* and demonstrate the presence of a rational twin orientation relationship with a 60° rotation around [001], abbreviated in the following as 60°/[001] twins (twin 1) and a recurring irrational orientation relationship with a 77° rotation around approximately $[6\bar{6}1]$, abbreviated in the following as 77°/$\sim[6\bar{6}1]$ (twin 2). We show (i) 60° and 77° misorientation boundaries (ii) characteristic peaks in the relative frequency - misorientation angle distribution diagram, and (iii) {001}, {104}, {108}, {018}, {012} pole figures representing the twin relationships of calcite. So far five twin relationships have been described for calcite (Richards 1999; Pokroy *et al.* 2007): (i) twinning on a plane parallel to {001} (growth twin), (ii) twinning on the faces {018}, {104} or {012} (stress-induced shear deformation) and (v) twinning on the plane {108}. As the orientation relationship of twinned individuals has to be related through a mirror operation on a plane or a rotation around an axis, calcite c- and a-axes orientations for two twin individuals have to be similar and will fall on the same spot in c- and a*-axes pole figures. The above-described characteristics (points i, ii, iii) can be obtained from electron backscatter diffraction measurements and have to be fulfilled for the definite proof of a particular twin relationship.

2.2.3 Results

The overall pattern of calcite orientation within the shells

SE and BSE images shown in Figure 2.2-1 depict a shell for each investigated foraminifera species (Fig. 2.2-1a–c) and highlight the two modes of sectioning performed in this study (Fig. 2.2-1d–i). The shells were cut in two directions: axially (Cut 1) and equatorially (Cut 2). Well visible are some internal features: different chamber generations, arrangement of septa, pattern of perforated and dense calcite distribution within

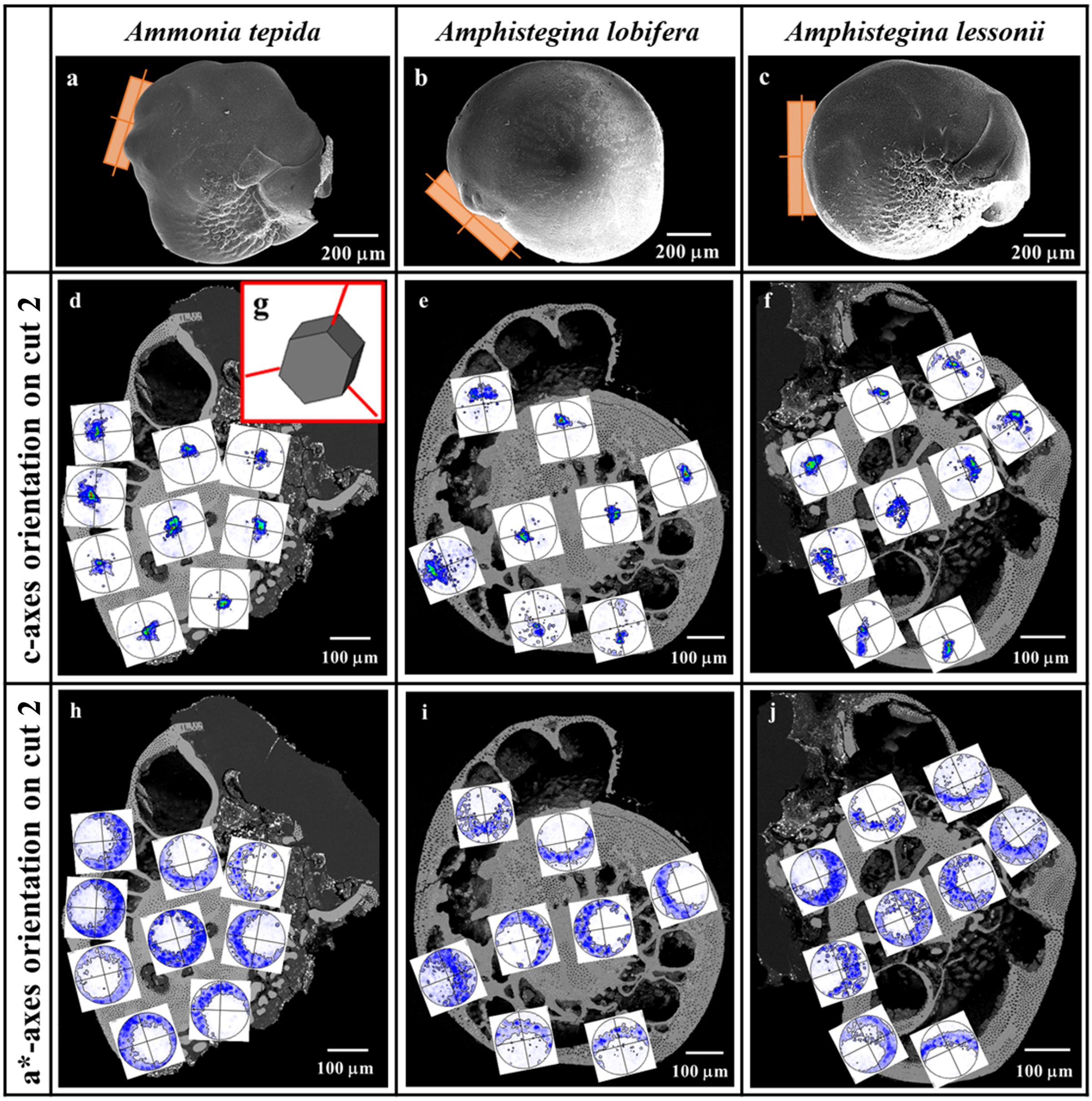

Figure 2.2-2. Patterns of calcite c-, and a* axes orientation on an equatorial cut (Cut 2) through the shells. Pole figures derive from EBSD scans. As shown in Appendix Figure 2.2-A1 for an individual chamber, calcite c-axes are perpendicular to the outer surface of the shell wall and rotate with its curvature. The a*-axes are on great circles around the c-axes. This pattern persists for all chamber generations. As the cut is never precisely central through the equator of the shell and the scanned surface corresponds to calcite formed also in earlier stages of development, in this "equatorial" mode of sectioning, calcite c-axes point out of the plane of view, shown exemplarily in the insert (g).

chamber walls, dense calcite in the center of tests, perforated calcite often in the walls of younger chambers, decrease in chamber wall thickness towards the youngest chamber (Fig. 2.2-1d–i).

Overall orientation patterns of calcite crystallites are given in Figures 2.2-2 to 2.2-4, 2.2-A1, 2.2-A2. For all measurements, we find an axial texture as in the pole figures a one-dimensional co-orientational order of the c-axes is evident, while the corresponding a*-axes vary randomly in orientation on a great circle perpendicular to the texture axis. Calcite crystal co-orientation strength is often low (Figs. 2.2-2, 2.2-3a,b), the investigated shells have MUD values that scatter between 20 and 50. On a near equatorial cut through the shells calcite c-axes point out of the plane of view (Fig. 2.2-2g), while when sectioned axially, calcite c-axes are approximately within the plane of view (Fig. 2.2-3d) as they are perpendicular to outer

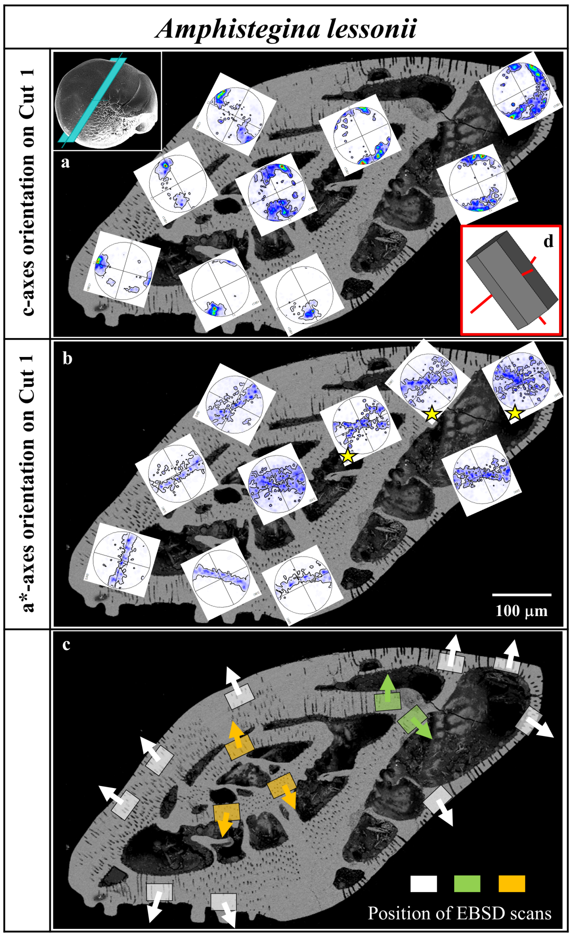

Figure 2.2-3. Patterns of calcite orientation (a,b) obtained from an axially sectioned shell (Cut 1) of *A. lessonii*. {001} pole figures are shown in (a), {100} pole figures are given in (b), related EBSD scanned areas are shown in (c). In the present, axial mode of sectioning, calcite c-axes are within the plane of view, as shown exemplarily in (d). Deviations from this rule arise when the radius of curvature of the corresponding shell element is not exactly in the plane of the cut. Colored rectangles in (c) give the position of EBSD maps, arrows indicate calcite c-axis orientations deduced from the measurements. As many pole figures (a,b) demonstrate, calcite co-orientation strength is low in many parts of the shells, even though calcite c-axes orientation follows the curvature of the shell (c).

shell surfaces. The c-axes rotate with the curvature of the shell (Figs. 2.2-3c, 2.2-A1). For all three species and all chamber generations, we find in EBSD maps measured at peripheral shell margins (at the keel) a bimodal distribution of calcite orientation (Fig. 2.2-4, yellow stars in and Figs. 2.2-3b, 2.2-A1). These areas are junctions of differently oriented shell walls. The bimodal distribution reflects the two different monomodal axial textures of the two abutting shell walls. Bimodality in calcite orientation occurs not only at the keel, but at other junctions as well, e.g., when a septum attaches to the shell wall (shown in Fig. 2.2-11e).

The septa are formed of a multitude of minute to small crystallites (Fig. 2.2-A2). These show a wide range of misorientation angles that spans almost 100° (Fig. 2.2-A2c). In contrast to chamber walls, the septa are devoid of perforations. If based on calcite orientation only, the continuation of the septa into, predominantly, inner chamber wall portions is very smooth (Fig. 2.2-A2b). However, as it is observable in the pole figures (Fig. 2.2-A2b,c), the axial texture of the septa is perpendicular to the septum wall such that at junctions of septa and shell walls there is a switch of the texture axis of the calcite that forms the different elements of the shell.

The crystals that comprise the shells

The shells of *A. tepida*, *A. lessonii* and *A. lobifera* are formed of a multitude of distinctly shaped and sized crystals (Figs. 2.2-5 to 2.2-11 and appendix figures 2.2-A3, 2.2-A4, 2.2-A6 to 2.2-A9). Irrespective of their size and orientation, the main characteristics of all crystals that form the shells is their dendritic-fractal morphology and their strong interdigitation with neighboring crystals (Figs. 2.2-5, 2.2-6, 2.2-A3, 2.2-A4).

We find two main types of crystals: large units, a few tens of micrometers in size (white stars in Fig. 2.2-5a,b) and small units, very few micrometers in size or even in the sub-micrometer size range (Fig. 2.2-5c, yellow star in Fig. 2.2-5a). In general, the large units form outer shell wall sections (white stars in Fig. 2.2-5a,b), the small units comprise innermost shell layers (yellow star in Fig. 2.2-5a, yellow arrows in Fig. 2.2-5b) or/and accumulate around pores and perforations (Fig. 2.2-5c).

Large parts of the central portion of equatorially sectioned shells consist of dense calcite (Figs.

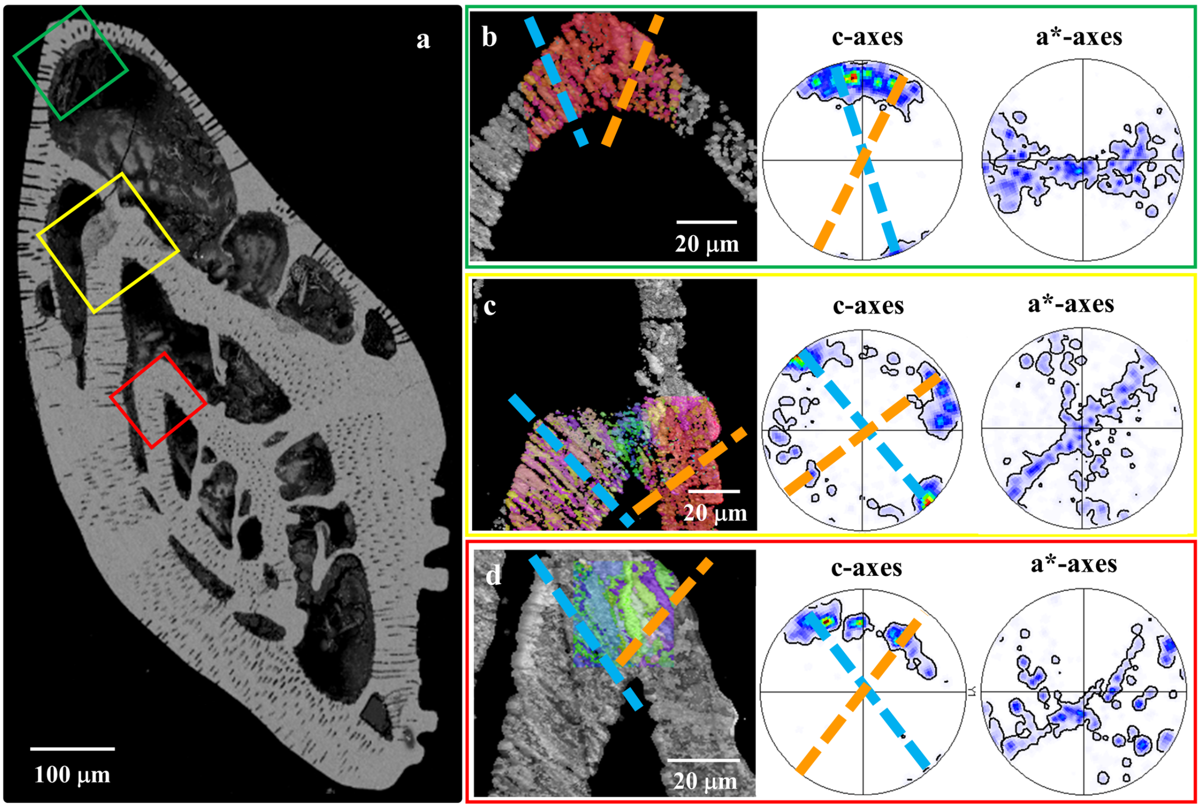

Figure 2.2-4. Distribution pattern of calcite orientation in maps taken at peripheral shell margins, the keel, for three chamber generations. (a) BSE image, shell sections shown in grey in (b–d) are band contrast measurement images gained from EBSD scans. Pole figures in (b–d) present orientation density distributions for those shell regions which are displayed in color in the adjacent maps. The keel corresponds to junctions of abutting but differently oriented shell walls. In each shell wall the axial texture is monomodal; the bimodal distribution in the pole figure results from the representation of two walls in one EBSD map and in the same pole figures. Blue and yellow dashed lines in the maps indicate the orientation of c-axes in the different elements of the shell in the pole figure and the EBSD map. The wall shown in (b) belongs to the youngest chamber that we find in our cut (Fig. 2.2-1a); see also Figure 2.2-11.

2.2-6b–d, 2.2-A4), formed of large, interdigitating crystals. For these shell regions, we find an accumulation of 60° grain boundaries (Fig. 2.2-6e) and a prominent peak at 60° misorientation in the relative frequency - misorientation angle diagram (Fig. 2.2-6f). The 60° misorientations correspond to {001} twinning, i.e. rotation by 60° around the c-axis, the twinning axis (60°/[001] (twin 1)).

The distribution pattern of 60° misorientation grain boundaries is structured in the shells (Figs. 2.2-6e, 2.2-A4a), such that in shell sections consisting of dense calcite and large crystals there is a high frequency of 60° grain boundaries, while shell sections that contain mainly the small crystallites, e.g., in the case of crystal assemblies around the small pores, 60° grain boundaries occur significantly less frequently (Figs. 2.2-6e, 2.2-A4a). Misorientation vs. distance profiles (e.g., profile 1 in Fig. 2.2-6i) show the systematic variation in misorientation between sub-crystals of a twinned calcite individual. We find that very many of the large crystals (Fig. 2.2-6g,h) are twinned, while the small crystals that, e.g., seam the pores (Fig., 2.2-6j,k), are not twinned. For comparison, Figure 2.2-A5 gives relative frequency misorientation angle diagrams of an untwinned biological calcite reference.

From our EBSD data evaluation, we can deduce that all crystals that comprise the shells, small as well as large, are mesocrystals (Fig. 2.2-7); definition of the term mesocrystal is given in the methods section). This finding is based on the following: (i) What we detect as cross-sections of crystals in the map are continuous arrays of pixels with similar calcite orientation, which are connected by paths in which the misorientation

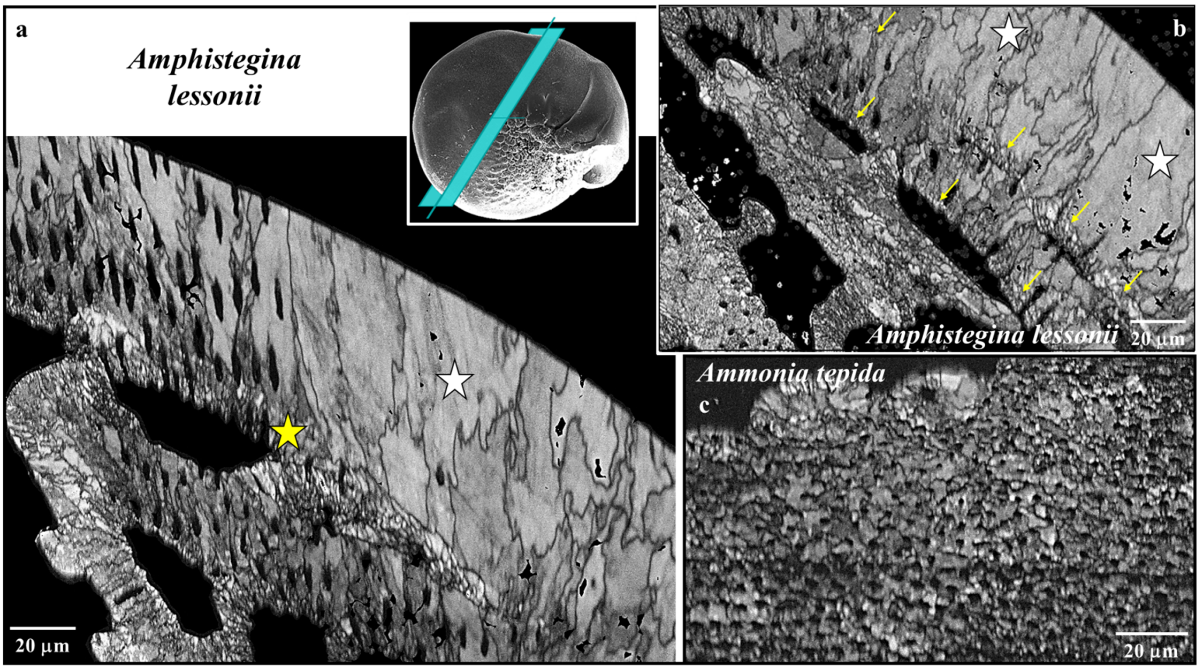

Figure 2.2-5. The two types of crystals that we find in benthic rotaliid foraminifera shell walls. EBSD band contrast measurement images of shell walls of *Amphistegina lessonii* (a,b) and *Ammonia tepida* (c), respectively. The shells were sectioned axially, Cut 1. See appendix Figure 2.2-A3 where we give corresponding crystal orientation patterns. Well observable are the two major types of biomineral crystals that comprise the shells: (i) large, strongly interlinked crystals at outer (white stars in a,b) and small crystallites at inner wall sections, respectively (yellow star in a, yellow arrows in b). Perforations are generally seamed by micrometer- to submicrometer sized, irregularly shaped small crystallites (c)

between neighboring pixels does not exceed a given threshold, in this study a misorientation of 2°. All these crystals have the same color in the color-colored EBSD map (see the similarity in colors for individual crystals, Fig. 2.2-7a,e) and show a high calcite co-orientation strength (see high MUD values, especially for the small crystals, Fig. 2.2-7a). However, we detect structured internal misorientation of mosaic blocks within the crystals (see the different colors in the internal misorientation maps shown in Fig. 2.2-7b,c,d,f,g). In small crystals (10 micrometer size range) internal misorientation is about 3 degrees (see legend in Fig. 2.2-7b–d), while in the larger (10–50 micrometer size range) and twinned crystals the range in misorientation extends to 6° (see legend in Fig. 2.2-7f,g). In the small crystals, the size of internally misoriented sub-domains scatters around 5 micrometers and is in the size range of primary fragments that form the primary walls of benthic foraminifera observed by Bentov and Erez (Fig. 5c in Bentov & Erez 2005). However, even though very many of the large mesocrystals are twinned (Fig. 2.2-8a), we observe occasional occurrences of large, but untwinned, mesocrystals (Fig. 2.2-8b). This is shown in the misorientation vs distance diagram in Figure 2.2-8b, where the profile traverses an untwinned and a twinned large mesocrystal.

In axial sections it is well visible for all chamber walls, except for the wall of the youngest chamber sectioned in the cut, that the large, very often, twinned crystals occur predominantly at outer wall layers (Figs. 2.2-9, 2.2-10, 2.2-A6). At the innermost chamber wall layers, the small and mainly untwinned crystallites predominate. Figures 2.2-9b–d, 2.2-10b,c show band contrast measurement images; Figures 2.2-9b, 2.2-10b,c are band contrast given color-coded images; Figure 2.2-9c,d are band contrast images given in grey. The band contrast is obtained from EBSD measurements and gives the Kikuchi pattern strength in each measurement point. Thus, when a diffracting material, a mineral, is scanned, there is a strong backscattered signal, while, when an un-

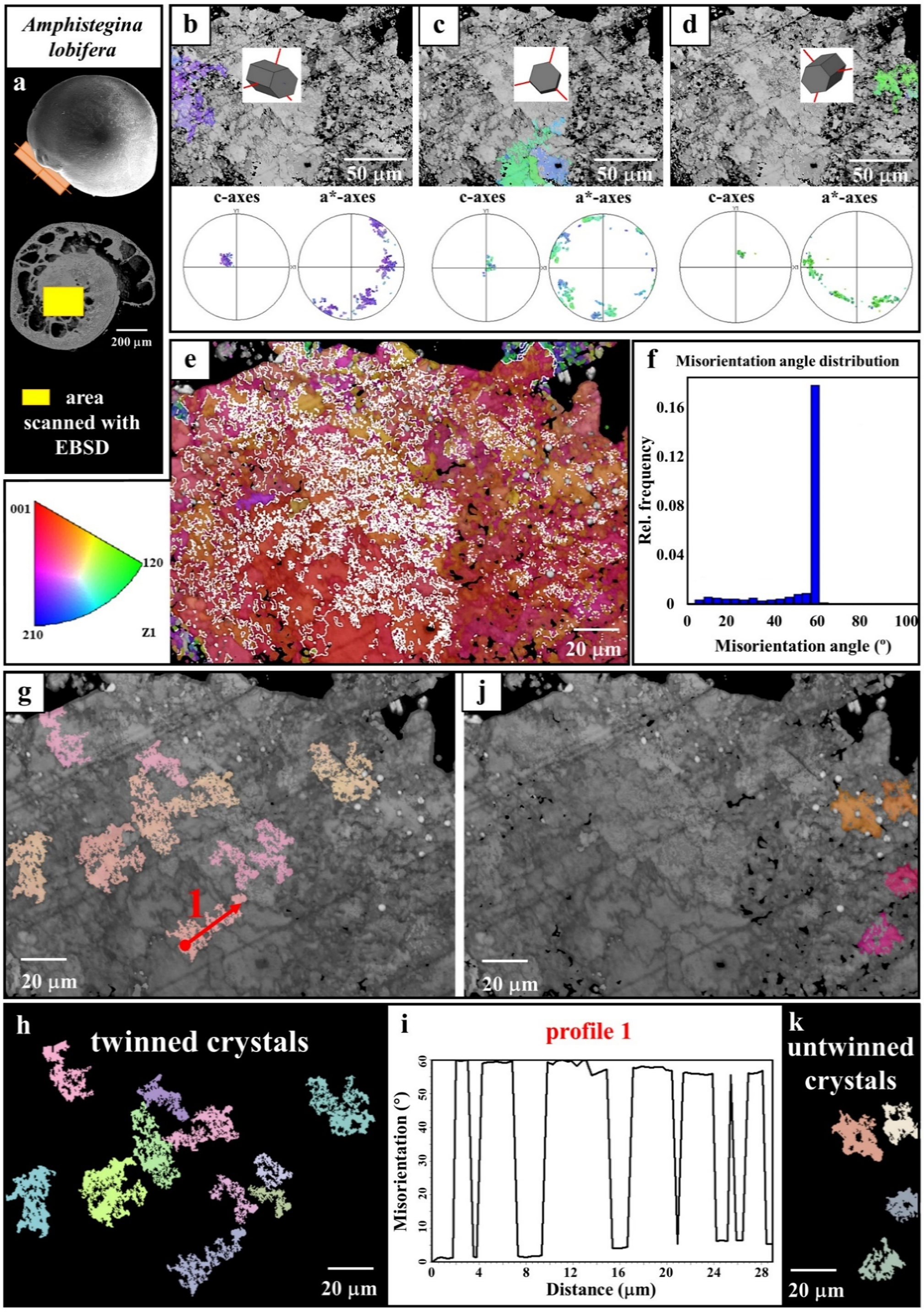

Figure 2.2-6. Calcite within the central, oldest, part of the shell of Amphistegina lobifera. The sample was sectioned equatorially, Cut 2. (a) SE image indicating the mode of sectioning, and BSE image depicting the cut through the shell, the yellow rectangle highlights the shell region that was scanned with EBSD. (b–d): EBSD band contrast measurement images. Well visible in (b–d) are: (i) the unstructured distribution of perforated and dense shell regions, (ii) the diversity and irregularity of crystal shapes and sizes, (iii) the dendritic-fractal crystal morphology and interdigitation of all (small and large) crystals. Despite the morphological irregularity, there is some regularity in overall calcite orientation as calcite c-axes are co-aligned (b–d). The corresponding orientation map is presented in Figure A4b. (e) depicts the distribution pattern of 60° grain boundaries (white lines in c) that are superimposed onto crystal orientation; for better visualization, an enlargement of the map is presented in Figure 2.2-A4a. (f) gives the misorientation angle distribution diagram for the shown EBSD map. A large peak at 60° misorientation is visible, accompanied by a range in misorientation angle that scatters from 5° to 60° (f). Two types of crystals comprise the shells: (1) large (g, h) and very often twinned crystals (e.g., misorientation profile 1 in panel (i)); these form densely mineralized regions. (2) Small crystals (j,k) not or rarely twinned (see distribution pattern of 60° grain boundaries in panel e) that seam the perforations.

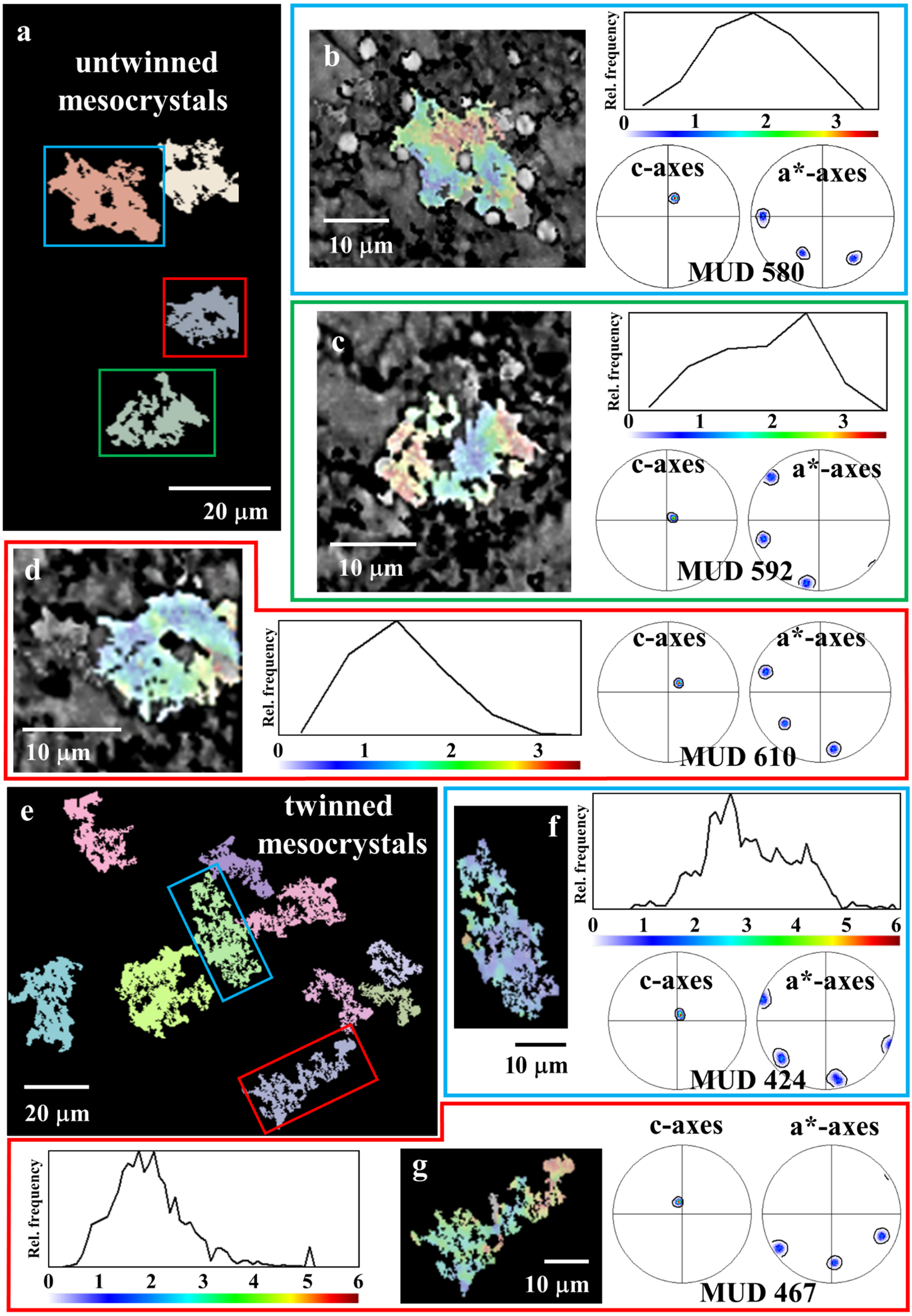

Figure 2.2-7. Small and mainly untwinned (a) and large and mainly twinned (e) mesocrystals. We regard the crystals within the shells as mesocrystals as the individual crystals show co-oriented lattice with moderately high MUD values, but consist of small, slightly misoriented units (b–d,f,g). Internal misorientation within individual crystals is shown color-coded in (b,c,d,f,g). The small, untwinned crystals seaming perforations have an internal misorientation spread of 3° to 4° (relative frequency versus misorientation graphs in b,c,d); the large, twinned, crystals show a misorientation spread of about 6° (relative frequency versus misorientation graphs in f,g). MUD values are higher for the untwinned than for the twinned crystals.

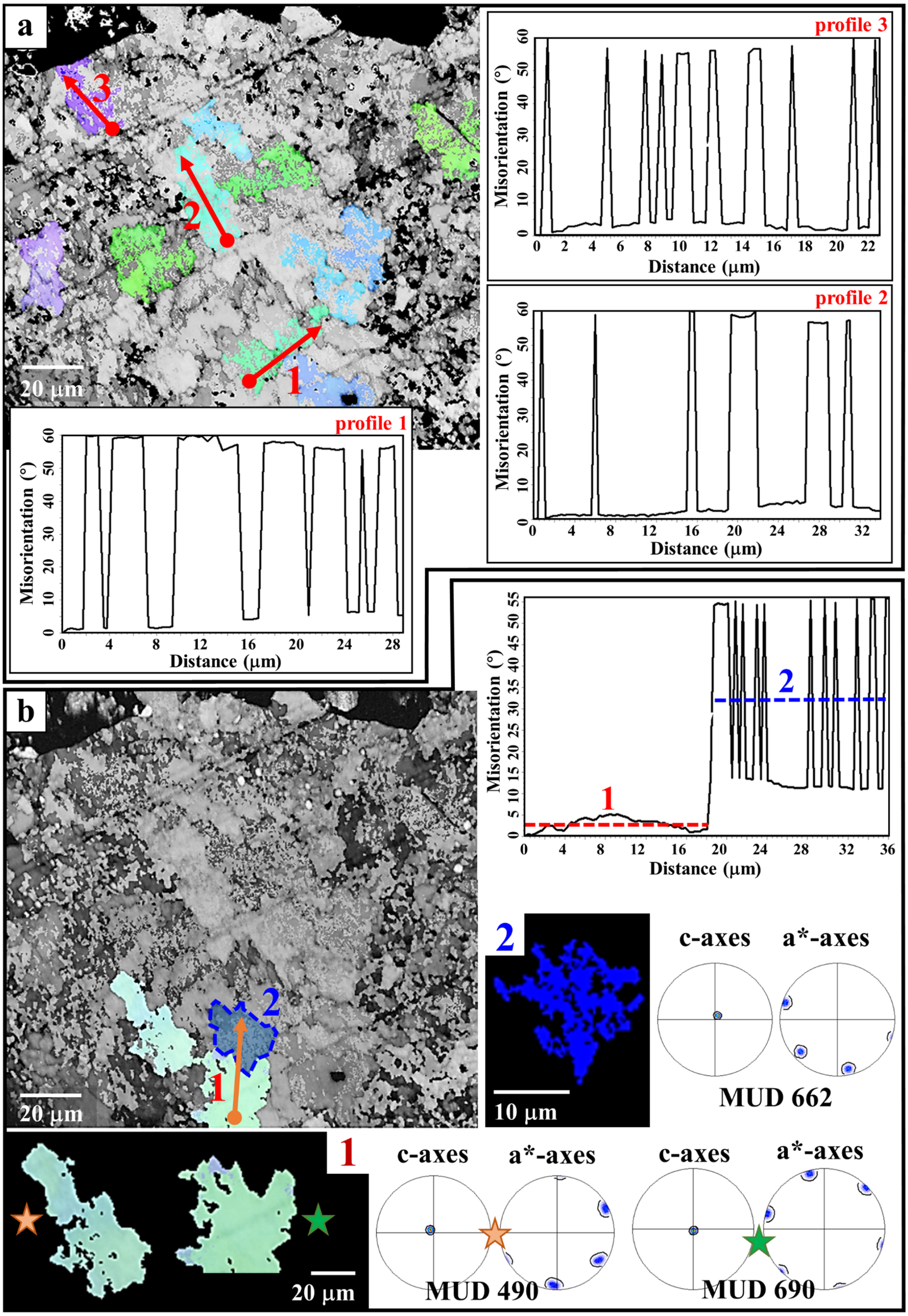

Figure 2.2-8. Large mesocrystals that form compact calcite regions. In most cases, these crystals are twinned (panel (a) and misorientation versus distance profiles 1, 2, 3). However, untwinned, large mesocrystals are occasionally present in the shells as well (b). Calcite in these mesocrystals is highly co-oriented, see the high MUD value of 690 in (b). The misorientation versus distance profile shown in (b) traverses (1) an untwinned (red dashed line in b) and adjacent (2) a twinned crystal (blue dashed line in b).

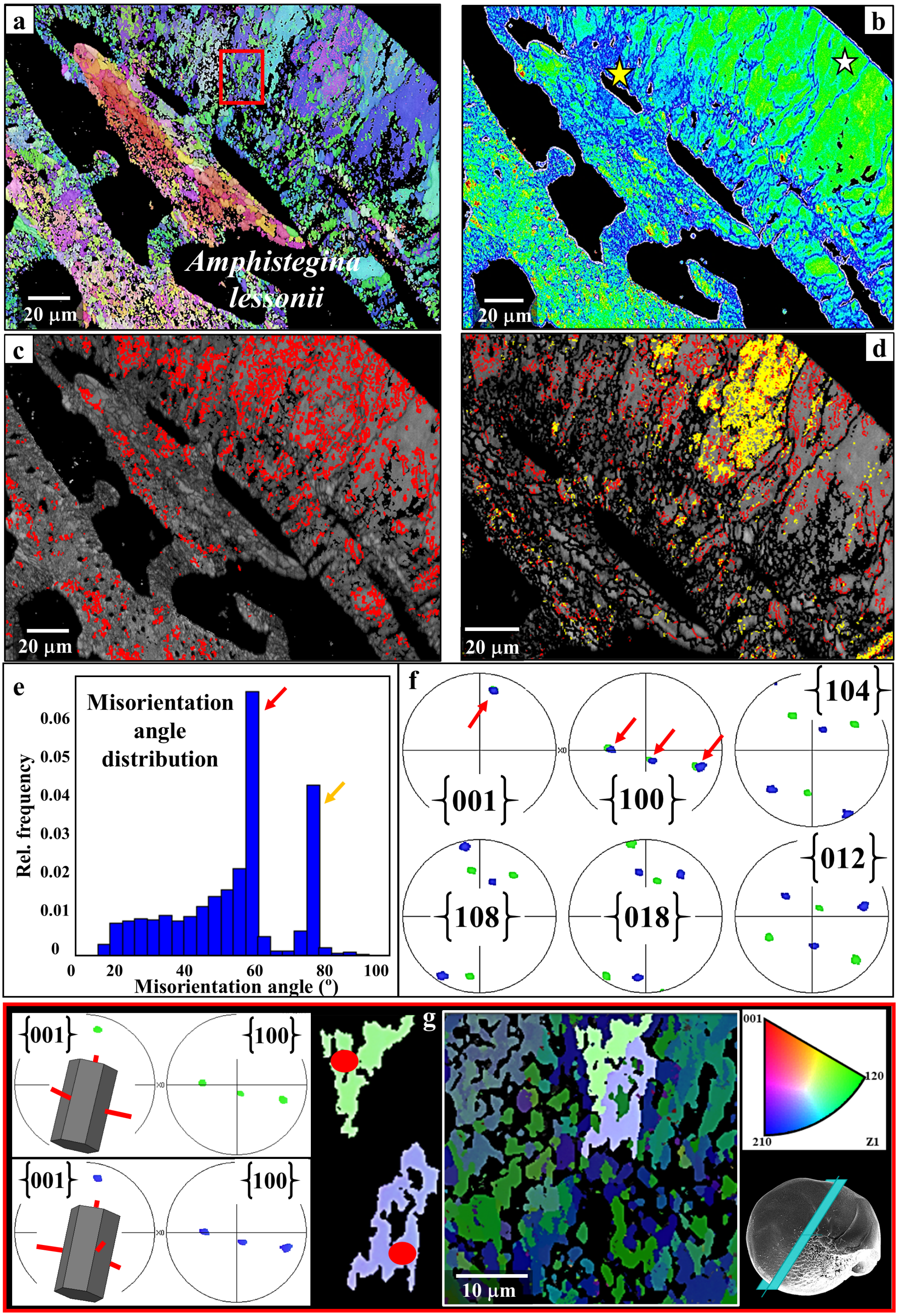
a
Amphistegina lessonii
20 µm
b
20 µm
c
20 µm
d
20 µm
e
Misorientation angle distribution
Rel. frequency
0.06
0.05
0.04
0.03
0.02
0.01
0
0
20
40
60
80
100
Misorientation angle (°)
f
{001}
{100}
{104}
{108}
{018}
{012}
g
{001}
{100}
{001}
{100}
10 µm
001
120
210
Z1

Figure 2.2-9. Distribution pattern of large, very often twinned, crystals within the shell wall of *Amphistegina lesonii* and the two misorientation relationships that we observe in the shell. The sample was sectioned axially, Cut 1. (a): color-coded orientation image, (b–d): EBSD band contrast images shown in color (b) and in grey (c,d) with the distribution pattern of 60° grain boundaries (shown in red) superimposed on the band contrast (c), and the distribution of 77° boundaries superimposed on band contrast (d). The misorientation angle distribution (e) shows two maxima: (i) misorientation at 60° (red arrow in e) and (ii) misorientation at 77° (yellow arrow in e). This regularly occurring misorientation at 77° points to a twin relationship, even though it does not correspond to any of the known twin laws for calcite (Richards 1999; Pokroy *et al.* 2007). It is well visible that large crystals occur at outer chamber wall regions (white star in b), small crystals are predominantly present at inner chamber wall sections (yellow star in b). Many large crystals are internally twinned. Twinning follows the {001} twin relationship as visualized with the distribution pattern of 60° grain boundaries (given in red, (c)), the large misorientation peak at 60° in the misorientation angle distribution diagram (e) and, as shown for one twinned individual (g), with the {001} and {100} pole figures (f), where the c- and a*-orientations of the two sub-units is similar (red arrows in f), similarity in orientation of the two sub-units of the twin is reached through rotation at the twin axis (see pole figure in g). The red rectangle in (a) indicates the position of the twinned individual shown in (g). Five twin laws are identified for calcite. As the pole figures in (f) show the mode of twinning for the individual given in (g) is the {001} twinning and none of the others, as for all the other twinning laws {104}, {108}, {018}, {012} orientations for the sub-units of the twinned crystal (g) differ from each other (f). The 60° rotation of the poles in these pole figures between the two crystals is indicative also of the {001} twin.

or little diffracting phase is hit, EBSD signal strength is low or absent. Accordingly, the band contrast visualizes well strong mineral accumulations (white star in Fig. 2.2-9b, Fig. 2.2-10b). Figures 2.2-9c and 2.2-10c show the distribution pattern of 60° grain boundaries superimposed on the band contrast. The comparison between Figures 2.2-9b,c and 2.2-10b,c demonstrate that 60° grain boundaries occur within and between the large mesocrystals. Correspondingly, many of the large mesocrystals at outer shell wall sections are twinned. Twinning is present in both within as well as between (Figs. 2.2-A7, 2.2-A8) the large dendritic-fractal crystals.

Even though twinned calcite forms major parts of shell walls of many chamber generations, in the wall of the youngest (Fig. 2.2-11b,c,d) and the penultimate chamber generation (Fig. 2.2-A9) twinned calcite, as well as the large crystals, are almost absent. The walls of the youngest and penultimate chambers are formed of an assembly of many untwinned, small crystallites, variably misoriented to each other (Fig. 2.2-11d: see the large variation of misorientation angles and an increased relative frequency in the misorientation angle - relative frequency diagram). The penultimate chamber has a few interdigitating larger crystals, however, almost none of these are twinned (Figs. 2.2-11b,c, 2.2-A9). Calcite in the wall of the youngest chamber has an axial texture and a high preferred orientation (Fig. 2.2-11e), calcite co-orientation strength is increased (MUD values scatter between 55 and 126, Fig. 2.2-11e).

Even though the twinned calcite of the walls of older chambers consists mainly of 60°/[001] twins (twin 1), we observe a further systematic orientation relationship documented by a marked peak at 76°–79° in the misorientation angle distribution diagram (twin 2, Figs. 2.2-9e, 2.2-14d, 2.2-15c–e). This orientation relation of neighboring crystals accumulates strongly locally and is mainly connected to the large crystals (Fig. 2.2-13b,c) at outer test wall layers, predominantly in central wall regions (Fig. 2.2-13c,d). The 76°–79° orientation relationship does not correspond to any of the twin laws of calcite know up to now (Richards 1999; Pokroy *et al.* 2007). We performed an in-depth investigation of the crystallography of this relationship for a few twin contacts. The exact value of the rotation angle and the direction of the rotation axis change within a few degrees in different locations. Given the mosaic spread of biocalcite crystals, this is not surprising. In a representative example with a 77.0°(±0.5) misorientation, the rotational axis deviates by 0.2° from the $[6\bar{6}1]$hex axis. The EBSD measurement error of our system is estimated to ±0.2° (Yin *et al.* 2019). The relationship is equivalent to a 180.0°±0.5° rotation around an axis within 2.5° of $[451]_{\text{hex}}$ (Fig. 2.2-A12).

In summary: With the exception of the wall

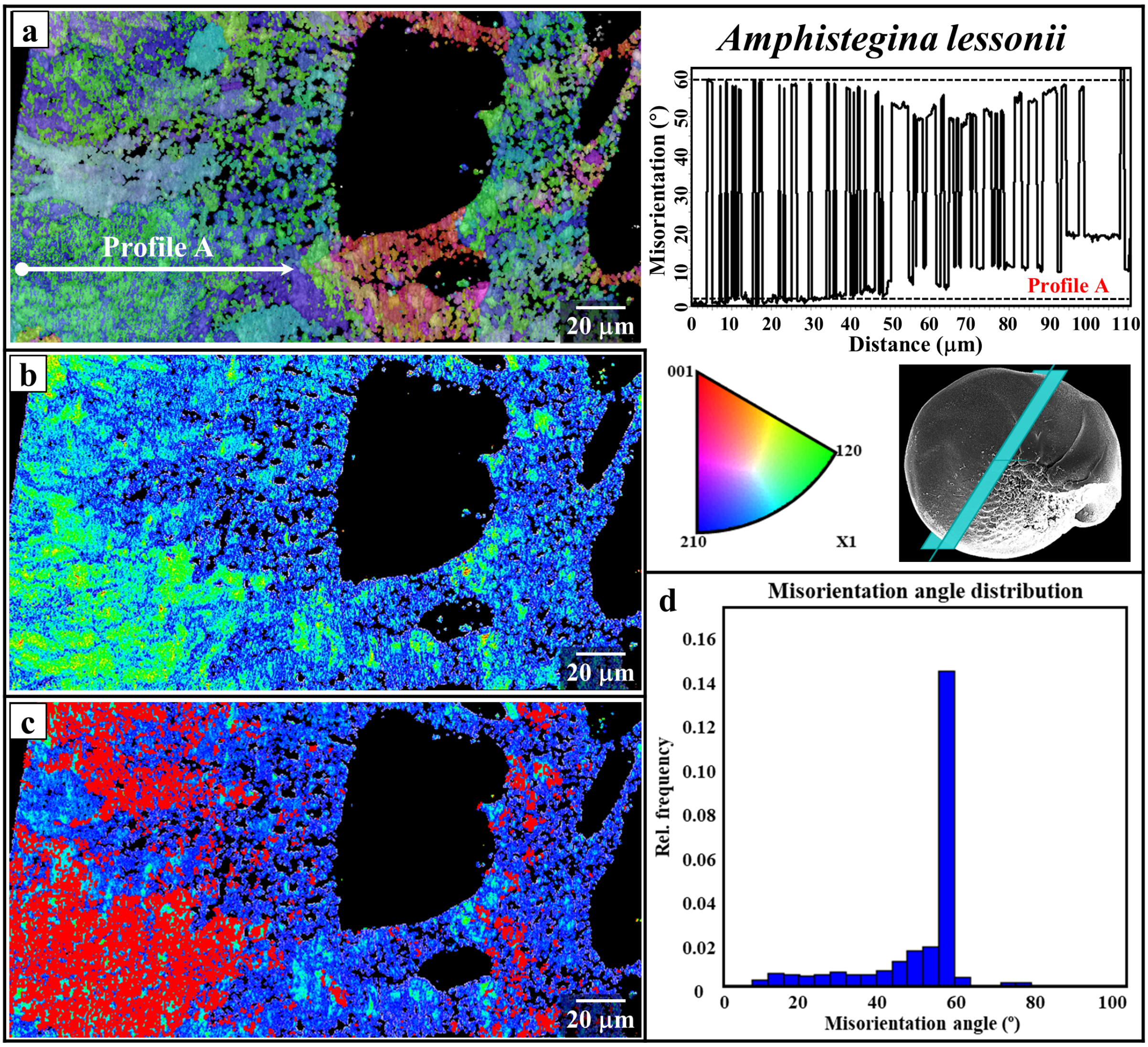

Figure 2.2-10. Distribution of large twinned and small untwinned mesocrystals within the wall of an older chamber generation. The sample, *Amphistegina lessonii*, was sectioned equatorially, Cut 2. (a) depicts color-coded crystal orientation. (b,c) are color-coded band contrast measurement images. Well visible is the distribution pattern of larger crystals (in green in b) and the striking correspondence of 60° misorientation grain boundaries (shown in red in c) with the distribution pattern of large crystals in outer shell wall portions. {001} twinning of the large crystals is demonstrated with the misorientation versus distance graph along profile A given in (a) and the marked peak at 60° in the misorientation angle distribution diagram (d). Note that the misorientation angle in the misorientation vs. distance graph (profile A) in (a) is sometimes smaller than 60°; it shows well the cyclic variation in the degree of misorientation. This is related to the small-angle grain boundary misorientations which are present in these mesocrystals.

of the youngest chamber, walls of all older chambers show a thick, outer layer consisting of large dendritic-fractal and twinned mesocrystals and a thinner, inner layer comprising small, mainly untwinned, mesocrystals. We regard these two types of crystals as corresponding to (i) the calcite layer mineralized outward of the primary organic sheet (POS) and (ii) the layer secreted inward from the POS

2.2.4 Discussion

The overall pattern of calcite organization in rotaliid shells – what is the difference to crystal assemblies in invertebrate shells?

XRD and EBSD measurements of carbonate biological hard tissues of the last decades revealed two major structural material characteristics: (i) diversity in biocrystal morphologies and sizes, with the biocrystals being intercalated into organic matrices with a structured fabric and (ii) diversity of microstructural organization and texture patterns that range from almost unaligned to highly coaligned biocrystal assemblies (e.g., Chateigner *et al.* 2000; Schmahl *et al.* 2004, 2012; Rodríguez-Navarro *et al.* 2012; Huber *et al.* 2015; Almagro *et al.* 2016; Griesshaber *et al.* 2017; Checa *et al.* 2018; Seidl *et al.* 2018; Crippa *et al.* 2020a,b). To achieve composite hard tissues with the above-mentioned characteristics invertebrates developed a variety of hard/soft tissue formation strategies that range from crystal growth processes, self-organization to direct cellular activity (Checa *et al.* 2018; Simonet Roda *et al.* 2019a,b).

Despite the large variety of biocarbonate microstructures and textures, we can extract some general organization principles for carbonate biological hard tissues:

1. For all shelled organisms (mollusks, brachiopods, coccolithophores, echinoderm shells) the carbonate material shows a crystallographic preferred orientation, where usually, but not always, the carbonate c-axes are more or less perpendicular to the outer surface of the skeleton and rotate with the curvature of the skeletal element. All these hard tissues consist of a well-organized extracellular biopolymer matrix that is mineralized with carbonate mineral.
2. The crystallographic preferred orientation varies from a 3-dimensional, almost single-crystal-like co-orientation (e.g., in sea urchin calcite), via less stringent 3-dimensional co-orientation (found in some mollusks and brachiopods), to the most frequently encountered one-dimensional (axial) crystallographic texture (e.g., in mollusks and brachiopods).
3. Mollusk and brachiopod shells are, in general, constructed from crystals with regular morphologies and sizes such as tablets, fibers, lamellae, columns. However, these are rarely regular in the sense of defined crystallographic faces.

Calcite organization in the shells of the benthic foraminifera *Ammonia tepida*, *Amphistegina lessonii*, *Amphistegina lobifera* diverges significantly from the crystal assembly patterns that we usually observe e.g., for mollusk and brachiopod shells. We see for the shells of the investigated foraminifera the following main texture/microstructure characteristics:

1. In one and the same shell different texture patterns prevail. Accordingly, even within the same specimen, calcite crystallographic co-orientation ranges from poorly ordered, over axial to seemingly multimodal patterns.
2. Foraminiferal calcite shows a comparatively low co-orientation strength.
3. Even though, it is most remarkable that despite the poorly ordered texture, calcite c-axes are oriented perpendicular to outer shell surfaces and rotate with the curvature of the shell. The latter appears to be a prevalent characteristic for very many carbonate biological hard tissues, it is also observed for mollusks, brachiopods, barnacle shells (Schmahl *et al.* 2004; Griesshaber *et al.* 2007, 2017; Checa *et al.* 2020).
4. At all keeled margins and skeletal junctions, the pattern of calcite organization is bimodal due to a superposition of axial textures in the abutting skeletal elements. Bimodality is rarely observed in hard tissues of shelled organisms. It is occasionally developed in modern terebratulide brachiopod shells (Griesshaber *et al.* 2017), but has not yet been observed for mollusks.
5. All crystals in the shells of the investigated foraminifera species are mesocrystals with dendritic-fractal morphologies. These vary significantly in (i) size, (ii) morphology, (iii) interlinkage, (iv) twinning pattern.
6. When based on size and development of twins, we find two main types of crystals in the investigated rotaliid shells: (i)

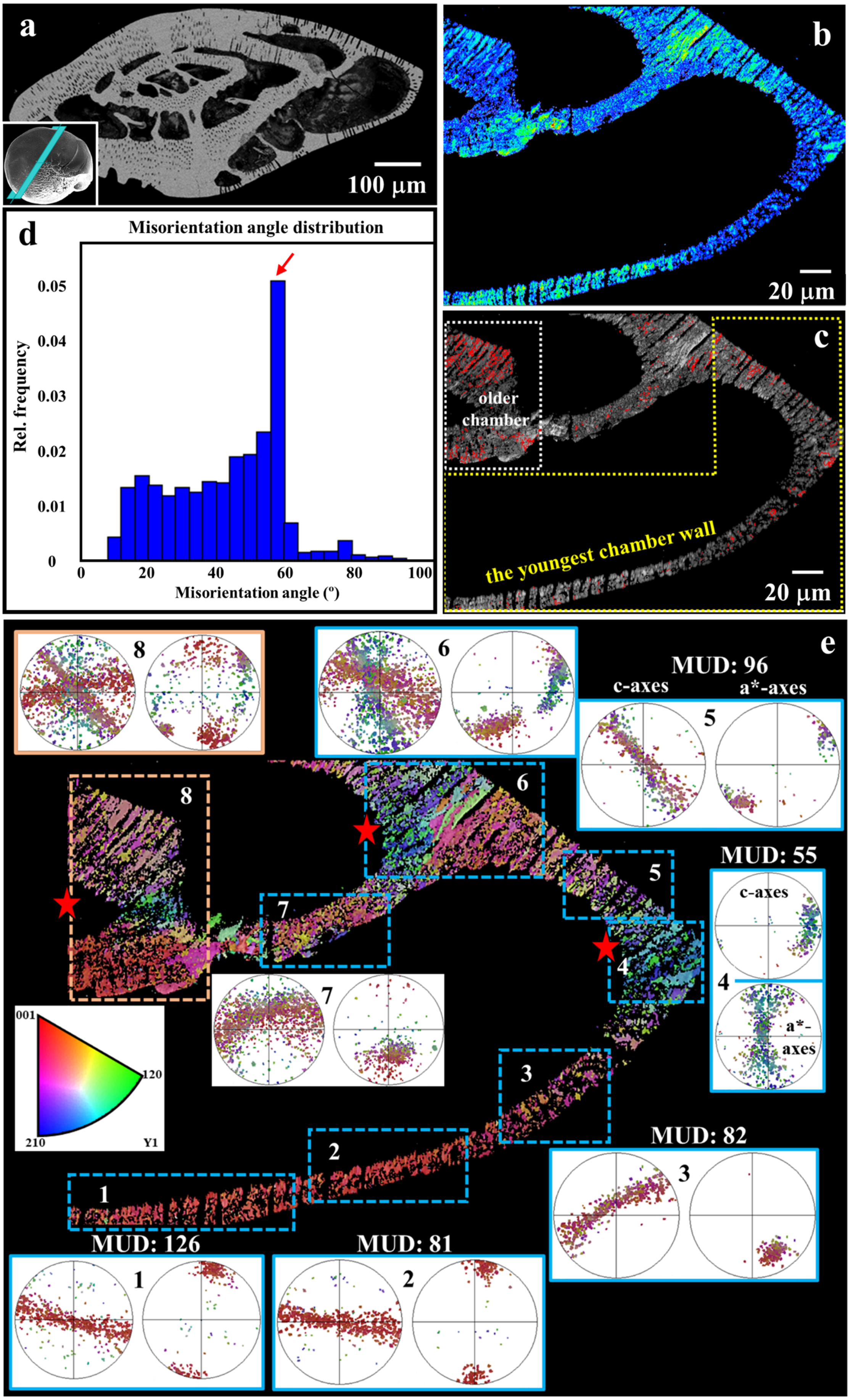
a
100 µm
b
20 µm
d
Misorientation angle distribution
Rel. frequency
0.05
0.04
0.03
0.02
0.01
0
0
20
40
60
80
100
Misorientation angle (°)
c
older chamber
the youngest chamber wall
20 µm
e
8
6
MUD: 96
c-axes
a*-axes
5
7
4
MUD: 55
c-axes
a*-axes
001
120
210
Y1
3
MUD: 82
2
1
MUD: 126
MUD: 81

Figure 2.2-11. Size and type of crystals and mode of calcite orientation in the chamber wall of the youngest chamber generation encountered in the shown cut. The shell of *Amphistegina lesonii* is depicted which was sectioned axially, Cut 1 (a). (b,c) are EBSD band contrast images (b in color, c in grey). In (c) EBSD band contrast is overlaid with the distribution of 60° misorientation grain boundaries, the latter given in red. It is well visible that the wall of the youngest chamber (outlined with a dashed yellow line in c) is almost fully devoid of large and twinned crystals; the latter are present in the chamber wall of the penultimate generation (b,c). The wall of the penultimate chamber (outlined with a dashed white line in c) is significantly more twinned. The misorientation angle distribution diagram (d) depicts for the data set shown in (e): (i) a wide range in misorientation angle up to about 90°, (ii) a high relative frequency for misorientations at 60° and (iii) a marked peak at 60° misorientation. (e) gives for the youngest and the penultimate chamber calcite orientation in an EBSD map and corresponding pole figures. Eight subsets were taken; these are given with dashed rectangles. Well visible is the bimodality at shell element junctions (red stars in e) and the rotation of crystal orientation with the curvature of the shell.

small, few micrometers-sized, mainly untwinned mesocrystals, and (ii) several tens of micrometers large, generally twinned mesocrystals. These two groups of crystals appear to be restricted to certain chamber wall regions: twinned, large crystals form outer chamber wall layers (secondary calcite), untwinned, small crystals form inner chamber walls (primary calcite), the septa and segregate around pores.

7. With the exception of red coral sclerites (Floquet & Vielzeuf 2011) twinned calcite has not yet been observed in mollusks and brachiopods. It is, however, a prominent feature of the investigated foraminiferal shells. The largest part of the shell wall consists of calcite twinned according to 60°/[001] and 77°/∼[$6\bar{6}1$] twin laws.

The structure of the bilayers forming laminated rotaliid foraminifera shells

Shell formation of bilamellid, rotaliid foraminifera is a multi-stage process (e.g., Lipps 1973; Angell 1979; Hemleben *et al.* 1986; Spero 1988; Nagai *et al.* 2018a,b; Tyszka *et al.* 2019, Fig. 2.2-A10a,b,d). First mineral deposition is templated by an organic sheet (the primary organic sheet, POS, e.g., Nagai *et al.* 2018a; Tyszka *et al.* 2019) with mineral deposition occurring on both sides of the organic template. The shape of the new chamber is formed by a rhizopodium that determines the shape of an organic inner and outer organic layer; these belong to a single lamellipodium. The rhizopodium and two laminopodia (according to Tyszka *et al.* 2019) form a structure called globopodium. The latter outlines and defines the shape of each newly formed chamber. At formation of each chamber generation, the mode of mineral deposition changes with ongoing carbonate secretion, such that at late stages of chamber wall formation calcite deposition occurs predominantly between the POS and the outer lamellipodium (e.g.,Hemleben *et al.* 1986; Spero 1988; Nagai *et al.* 2018a; Tyszka *et al.* 2019). This generates the thickening of the walls and determines their layered nature (e.g., Lipps 1973; Angell 1979; Hemleben *et al.* 1986; Spero 1988; Nagai *et al.* 2018a; Tyszka *et al.* 2019). As our study shows, the result of this specific, multi-stage secretion process is the formation of a laminated composite material (Fig. 2.2-A10c,e,f), formed of calcite crystals with different sizes (Figs. 2.2-5, 2.2-A10c,e) internal misorientations and degree of twinning.

The pseudopodia

A major difference between foraminifera and other exoskeletal invertebrates is that on certain occasions the pseudopodia of the foraminiferal organism extend beyond the exoskeleton (e.g., Goldstein 1999; Hansen 1999; Nagai *et al.* 2018a,b; Tyszka *et al.* 2019; Goleń *et al.* 2020). When foraminifera secrete their shell this happens regularly, each time at new chamber formation. Foraminiferal carbonate is not secreted into an extracellular biopolymer matrix that has a pre-formed and well-structured fabric such as biopolymer matrices in the hard tissues of shelled organisms. Benthic foraminiferal calcite is secreted onto pseudopodial strands (e.g., Hemleben

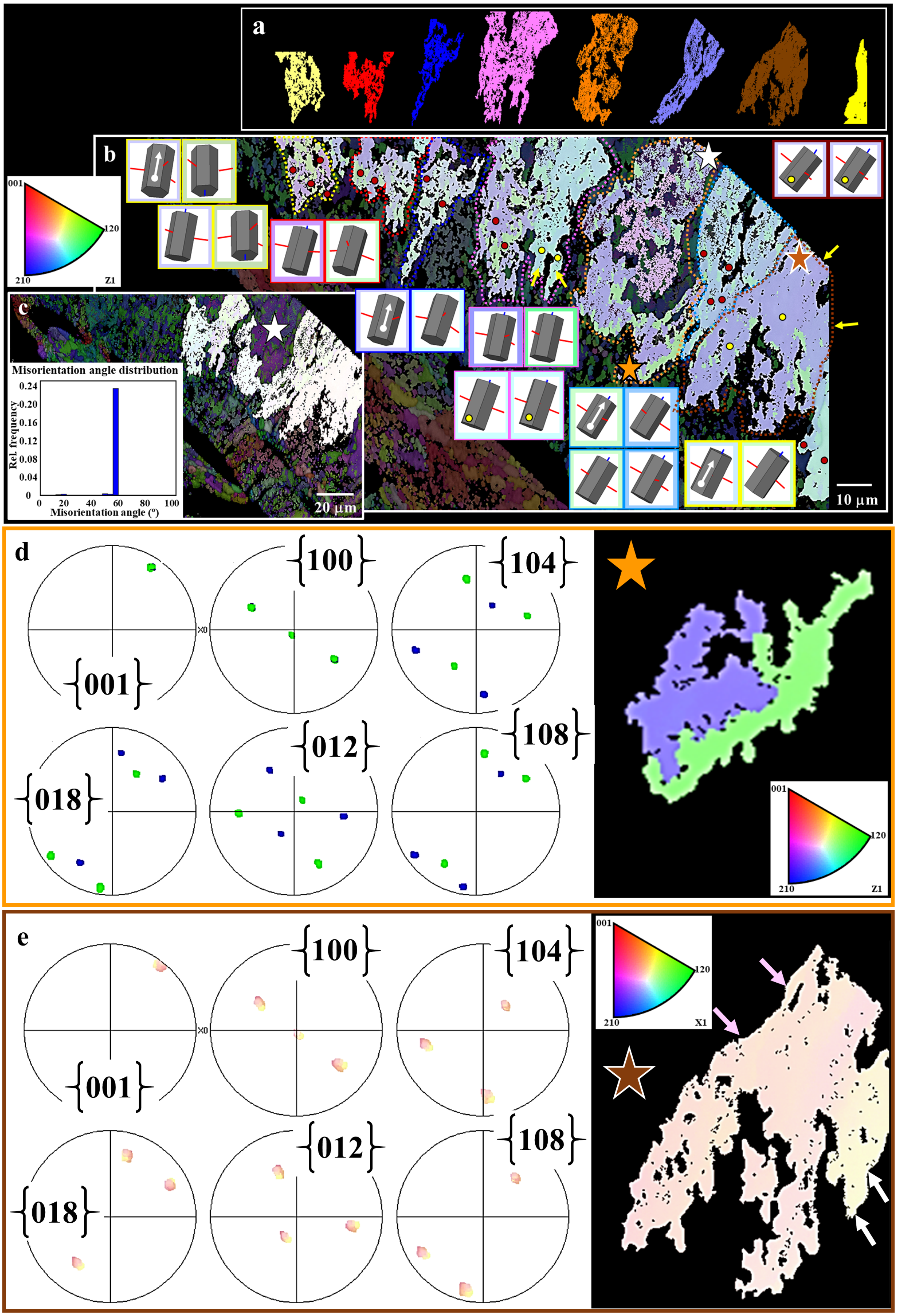
a
b
001
120
210
Z1
c
Misorientation angle distribution
Rel. frequency
0.24
0.20
0.16
0.12
0.08
0.04
0
0
20
40
60
80
100
Misorientation angle (°)
20 µm
10 µm
d
{001}
{100}
{104}
X0
{018}
{012}
{108}
001
120
210
Z1
e
{001}
{100}
{104}
X0
{018}
{012}
{108}
001
120
210
X1

Figure 2.2-12. Array of twinned mesocrystals (a,b) in outer chamber wall portions in the shell of *Amphistegina lesonii*. The shell was sectioned axially, Cut 1. (a): crystals shown in random color; well visible is their dendritic-fractal morphology. Colors in (b) code for calcite orientation. Sketched crystal cartoons (b) visualize their mode of orientation and twinned character; red and yellow dots within the dendritic-fractal crystals (b) indicate the positions that correspond to the sketched crystals showing c- and a*-axes orientation at this particular spot. Red dots in (b): twinned mesocrystals; yellow dots in (b): untwinned mesocrystals. Twinning follows the {001} twin relationship, see {001} and {100} pole figures for the two individuals shown in (d), the sketched crystals, and the huge and almost only peak at 60° in the misorientation angle distribution diagram (c). Yellow arrows in (b) point to two large crystals that form an exception as these are not twinned; in the corresponding sketched crystals there is no change in orientation or rotation. This crystal (e) is a mesocrystal as the gradual change in orientation and color from light red to yellow in the EBSD map and corresponding pole figures indicates. White arrows within the sketched crystals indicate the change of c-axes orientation that follows the curvature of the shell. The crystal marked with a white star in (b,c) exhibits the 77° misorientation and is described in more detail in Figure 2.2-14.

---

et al. 1986; Spero 1988; Erez 2003; Nagai *et al.* 2018a,b; Tyszka *et al.* 2019) possibly comparable to a network of hydrogel fibers (Nindiyasari *et al.* 2015).

Even though, biopolymers are occluded within foraminiferal carbonate, however, not as a structured matrix delineating/encasing individual biocrystals, as it is the case in mollusk and brachiopod shells, but as intercalated sheets. Up to now, we know of three sheets: (i) the POS, the polysaccharide template for first crystal nucleation (Hemleben *et al.* 1986; Spero 1988; Erez 2003; Nagai *et al.* 2018a,b; Tyszka *et al.* 2019), and the (ii) outer and (iii) inner organic layers, consisting of lamellipodia (Fig. 6d in Spero 1988) that line outer and inner shell wall surfaces (Nagai *et al.* 2018a,b; Tyszka *et al.* 2019). Indeed, the very smooth outer and inner chamber wall surfaces, especially their smooth curvature (Fig. 2.2-11b), and the rotation of crystal orientation with the curvature of the shell (Fig. 2.2-11e) might be taken as an expression of lamellipodia closely framing the calcite at secretion and, with progressive skeletal growth, withdrawing successively away from the POS.

In rotaliid foraminifera organic sheets are not equidistant to each other, as it is the case for extracellular organic matrix membranes in the shells of mollusks and brachiopods (Nakahara 1991; Checa *et al.* 2019; Simonet Roda *et al.* 2019a,b). The organic sheets that develop at foraminiferal chamber formation evolve from an interwoven network of pseudopodia (granulopodia, lamellipodia); multifunctional cellular extensions that originate from the cytoplasm (Nagai *et al.* 2018a,b; Tyszka *et al.* 2019). The latter two authors have shown that at new chamber formation at least two types of pseudopodia are active: (i) first mineralization is controlled by a radiating spray of thin and densely arranged filamentous pseudopodia; (ii) at later stages of mineral secretion, when the thickening of the chamber wall is carried out, fewer, thicker and wider-spaced lamellar pseudopodia develop and guide the mineralization process (Nagai *et al.* 2018a,b). Nagai *et al.* (2018a) observed many more pore openings in the inner organic layer (inner lamellipodum according to Tyszka *et al.* 2019) which lines the first-formed calcite from the inside, than the outer organic layer (outer lamellipodium according to Tyszka *et al.* 2019). Within the inner organic layer (the inner lamellipodium) pore openings occur every 2–5 μm (Fig. 5 of Nagai *et al.* 2018a). This mesh of pores can be related to the smaller size of calcite crystals growing between the inner organic layer and the POS.

The ragged, dendritic morphologies and fractal-like arrangement of all crystals within the investigated foraminiferal shells are a consequence of the mineralization process by (i) pseudopodia, the cellular extensions, and (ii) the utilization of different types of pseudopodia. The findings of Nagai *et al.* (2018a,b) and Tyszka *et al.* (2019) are reflected by our observation of the two main types of crystals that we find developed in the shells. At innermost chamber wall surfaces and around perforations we find a multitude of small, often untwinned, crystals, while outer chamber walls consist of the large and very

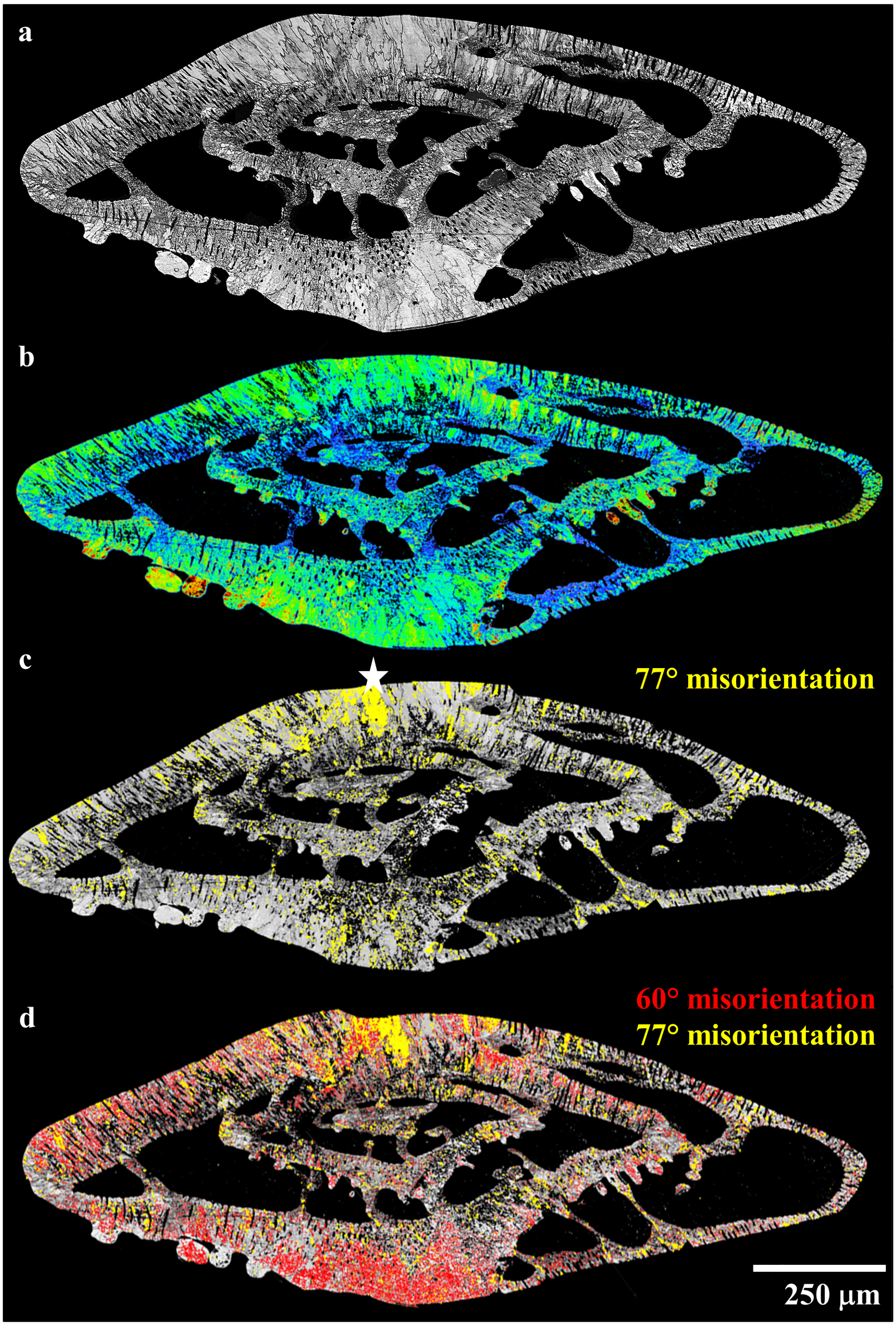

Figure 2.2-13. Panorama image compiled of 24 individual EBSD scans covering the entire surface cut through the shell of Amphistegina lesonii. The shell was sectioned axially, Cut 1. We visualize the distribution patterns of: (i) large and small crystals with EBSD band contrast measurement images (a,b), (ii) the pattern of distribution of 77° misorientation (c) and (iii) the pattern of distribution of 77° and 60° misorientations (d). It is well visible that both misorientations, identified as two twining modes are not singular events but widespread characteristics of all chamber generations and cut through the shell. (a) band contrast given in grey, (b) band contrast given color-coded; for both figures, a and b, light colors indicate strong mineralization, dark colors weak mineralization. The crystal marked with a white star in (c) is discussed in great detail in Figure 2.2-14.

often twinned crystals. Goetz *et al.* (2011) report for the primary shell layer of modern terebratulid brachiopods a microstructure and texture that consists also of dendritic-fractal, highly interwoven, calcite crystals. Simonet Roda *et al.* (2019b) investigated brachiopod primary and fibrous shell layer calcite secretion for modern terebratulid brachiopods. The authors observe that the periostracum and the primary shell layer are secreted only by extensions of outer mantle epithelium cells. These cells are devoid of cell bodies containing a nucleus (Fig. 1b in Simonet Roda *et al.* 2019b) and secrete dendritic-fractal calcite crystals. The adjacent fibrous shell layer of terebratulid brachiopods consists of calcite fibers with regular morphologies encased by a structured organic matrix. The fibrous shell layer is secreted by outer mantle epithelium cells with cell bodies having a nucleus (Simonet Roda *et al.* 2019a). Accordingly, we might find for both single as well as multi-cellular organisms two different calcification scenarios: (i) secretion by cellular extensions and (ii) secretion by cells containing a nucleus.

The calcite

The shells of rotaliid foraminifera show five major structural characteristics (this study but also partly described by Reiss 1957; Lipps 1973; Angell 1979; Erez 2003):

(i) lamination of the shell initiated by the two-staged mineral secretion process
(ii) secretion of two types of mesocrystals
(iii) a highly dendritic-fractal morphology and interdigitation of all crystals
(iv) extensive formation of calcite twins
(v) development of two types of calcite twins

This study demonstrates that twinned calcite forms the largest part of older shell walls (Figs. 2.2-10, 2.2-13, 2.2-15), however, it is very little represented in the walls of the youngest and penultimate chambers (Figs. 2.2-11, 2.2-A9). We show that the chamber walls consist of two sublayers, a thin inner and a thick outer sub-layer (Figs. 2.2-5a, 2.2-15a). Based on microstructure and texture observations we can differentiate between these two sub-layers: the thin, inner, sub-layer is formed predominantly of small crystals that segregate around the many perforations, the latter very most probably, the former sites of the filamentous pseudopodia network. The thick, outer sub-layer comprises the large dendritic and twinned crystals that develop when the thicker pseudopodia, the lamellipodia, secrete the calcite for thickening and stabilizing the shell wall.

Dendritic-fractal morphologies of crystals in carbonate biological hard tissues are not rare and are observed for structural materials of other invertebrate taxa as well (Fig. 2.2-A11 this study, Goetz *et al.* 2011; Checa *et al.* 2016; Harper & Checa 2017; Seidl *et al.* 2018). However, what is unique for benthic foraminiferal calcite is the connection of dendritic crystal morphologies and twinned crystals.

The observed dendritic-fractal morphology of the crystals and their mesocrystalline mosaic pattern of crystal orientation requires three mechanisms to be operative: (i) obstacles in crystal growth inhibiting the lateral movement of crystal growth ledges over - atomistically - large distances, (ii) introduction of small angle misorientations, and (iii) interruption of crystal growth and homoepitactical recommencement in twin orientation. We exclude oriented attachment of crystalline nanoparticles, as (i) they have not been reported in foraminifera, and (ii) as there are no conceivable forces to rotate all those particles into the “right” positions when they “attach to the substrate” in a viscous medium. Fractal-dendritic growth occurs when the crystal forms under conditions of (i) high supersaturation and (ii) limited diffusional transport along the interface of the crystal and the surrounding medium (e.g., Levi & Kotrla 1997). Requirement (i) provides a high rate of homoeptitactic nucleation of new monoatomic growth layers onto the substrate, while requirement (ii) prevents their spreading over large distances so that there is no volume-

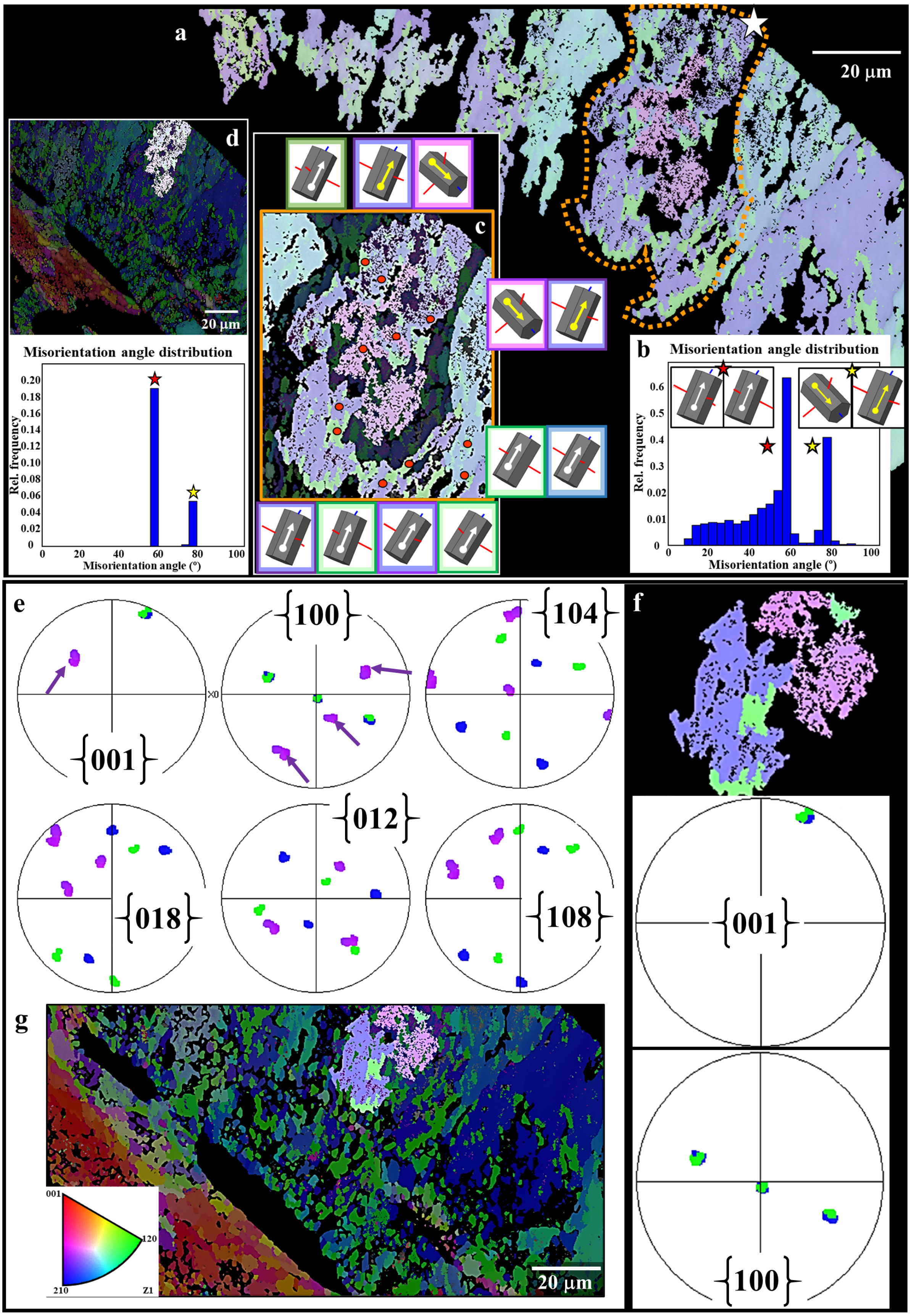
a
20 µm
d
20 µm
c
Misorientation angle distribution
Rel. frequency
0.20
0.18
0.16
0.14
0.12
0.10
0.08
0.06
0.04
0.02
0
0
20
40
60
80
100
Misorientation angle (°)
b
Misorientation angle distribution
Rel. frequency
0.6
0.5
0.4
0.3
0.02
0.01
0
0
20
40
60
80
100
Misorientation angle (°)
e
{001}
{100}
{104}
x0
{018}
{012}
{108}
f
{001}
{100}
g
001
120
210
Z1
20 µm

Figure 2.2-14. Twinned and misoriented calcite mesocrystals (a) in outer chamber wall portions of *Amphistegina lesonii*; attention focusses on the crystal that is outlined with a brown dashed line/marked with a white star in (a). The position of this crystal is also marked with a white star in Figure 2.2-13c. This crystal has individuals marked with blue, green and magenta colors (f,g). The shell was sectioned axially, Cut 1. (b) gives misorientation angle distribution for all crystals shown in (a), while (d) gives misorientation angle distribution only for the crystal shown in (c) (marked with a white star in a). In this specific mesocrystal we detect two systematic misorientations: (a) 60° misorientation (red star in b,d) indicative of 60°/[001] twinning; see pole figures in (f) for the blue and green individuals and the corresponding {001} and {100} poles that demonstrate the similarity of orientation of the twin individuals and (b) misorientation at 77° (yellow star in b,d) indicative of 77°/$[6\bar{6}1]$ twinning. Sketched crystals in (b,c) visualize the 60° and 77° misorientation characteristics for the marked crystal in (a); red dots in (c) point to the position that was chosen for the orientation of the corresponding sketched crystals. White and yellow arrows superimposed on the sketched crystals in b and c indicate c-axis orientations. Pole figures in (e) show the following: (i) {001} and {100} poles demonstrating the 60°/[001] twin relation of the blue and green individuals of the crystal depicted in f and g. (ii) Alternating positions of the poles for {104}, {018}, {012}, {108} orientations demonstrates that these twins do not apply for the blue and green individuals of the crystal depicted in f and g. (iii) The orientation of the magenta individual relative to that of the blue and green individuals that shows the 77° misorientation.

filling growth mechanism (as this usually forms regular growth faces and predominantly convex morphologies). For dendritic snowflake crystals, for example, condition (i) is due to low temperatures. In the case of foraminiferal shell formation condition (i) may be attributed to organic molecules bound to/adsorbed on the growing calcite (Figs. 1 and 2 in Nindiyasari *et al.* 2014a). The small angle misorientations (condition (ii) for the observed foraminiferal mesocrystals) are likely to arise when at crystallization and growth adsorbed molecules or macromolecular entities such as organic fibres or membranes are pushed to the side (e.g., Li & Estroff 2009; Asenath-Smith *et al.* 2012; Fig. 4 in Nindiyasari *et al.* 2014a; Figs. 4 and 5 in Nindiyasari *et al.* 2015). Minute stresses are sufficient to introduce dislocations and misalignments during growth.

The possible presence of amorphous calcium carbonate (ACC) as a precursor to calcite has been suggested by Jacob *et al.* 2017 on the basis of their observation of 3–4.5 weight % vaterite in *Orbulina universa* and *Neogloboquadrina dutertrei*. Furthermore, Mor Khalifa *et al.* 2018 infer from cryo-EDS spectra of Mg-calcite particles in *Amphistegina lobifera* and *Amphistegina lessonii* that ACC cannot be ruled out as a possible precursor. It may, thus, be speculated that the nanoparticulate-mesocrystalline appearance of the investigated foraminiferal calcite may be due to an attachment process of pre-formed particles of metastable ACC or vaterite. The ACC or vaterite particles would need to attach to the substrate of an already formed chamber, crystallize to the stable phase calcite and adopt the crystallographic orientation of the substrate by a homoepitaxial mechanism (Gal *et al.* 2014; Addadi & Weiner 2014; Addadi *et al.* 2016; Albéric *et al.* 2019). One group of particles described by Mor Khalifa *et al.* 2018 fits the $\sim 1\mu$m size-range which may support this mineral growth scenario. However, this scenario requires ordered growth of the calcite lattice through a vast number of precursor particles to produce the observed foraminiferal calcite and needs as well the above described conditions (i), (ii), and (iii) to explain the dendritic-fractal morphology of the crystals and their internal misorientations. As the dendritic-fractal nature and short-range orientational mosaic-spread is extreme in the investigated foraminifera compared to that of other marine carbonate-forming life forms, we conclude that the organic matrix in foraminifera contains components that bind much more strongly to calcite surfaces than it is the case in the other marine life forms.

In essence: Foraminiferal microstructure and texture is highly distinct to what was observed so far for carbonate biological hard tissues of invertebrate marine organisms (with the exception of the primary shell layer of modern terebratulid brachiopod shells) and is an expression of a specific mode of mineralization of carbonate hard tissue. Many observations indicate that, at least, two, not only time-delayed but also mechanistically different, secretion processes are active at rotaliid shell calcification (i) the structured distribution of some chemical elements within the shells (Bentov & Erez 2005, 2006; van Dijk *et al.* 2019), (ii) the utilization of different types of pseudopodia when secreting the shell (Spero 1988; Nagai *et al.* 2018a,b; Tyszka *et al.* 2019; Goleń *et al.* 2020) and (iii) the distinctness in microstructure, texture,

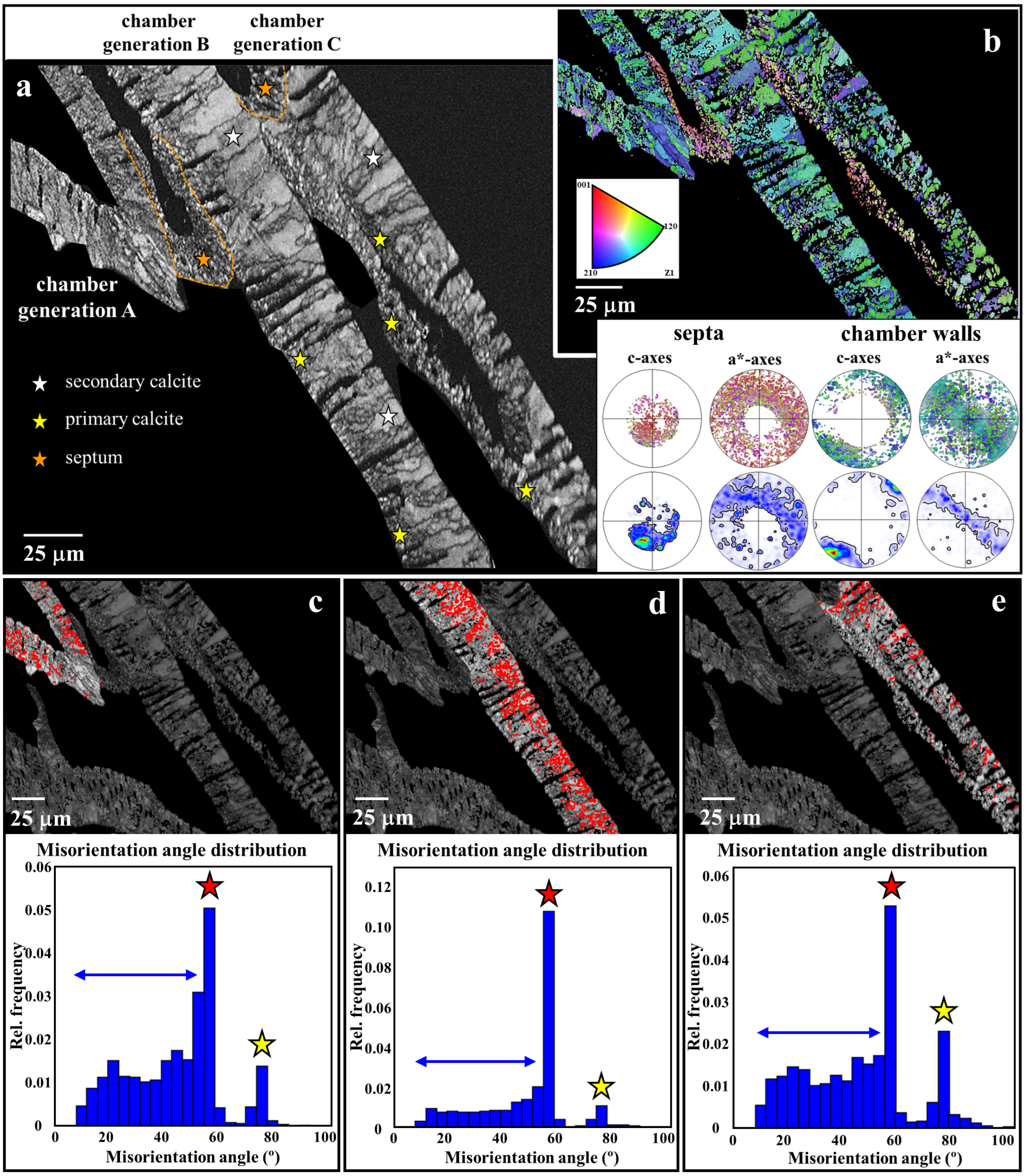

Figure 2.2-15. Section through the chamber wall of three adjacent chamber generations (A, B, C). (a) EBSD band contrast measurement image (in grey) visualizing characteristics of inner (yellow star) and outer (white star) calcite layers, respectively, and of calcite of the two connecting septa (orange star). (b) Pattern of calcite orientation in shell walls and the two connecting septa given with the color-coded EBSD map and corresponding pole figures. Note the difference in calcite orientation between the septa and the chamber walls. (c–e) depict the distribution of 60° and 77° grain boundaries and their accumulation at outer chamber wall sections. Misorientation angle distribution diagrams in c, d, e highlight the grain misorientation statistics for the three chamber generations, with the prominent peaks at 60° and 77° for the two detected twin relationships: 60°/[001] and 77°/$[6\bar{6}1]$.

twin formation of innermost and outer chamber wall portions (this study).

Why twinning in benthic rotaliid foraminifera?

When compared to bivalve, gastropod, and brachiopod shells it is striking that the shells of the investigated benthic foraminifera are moderately to poorly textured and do not show any clear-cut crystal morphologies, such as fibers and columns (in e.g., brachiopod shells), tablets (in e.g., columnar and sheeted nacre in gastropods and bivalves), spherulites (in e.g., scleractinian corals), lamellae and folia (in e.g., crossed-lamellar and crossed-foliated microstructures of bivalves and gastropods). Even though, foraminifera are among the most abundant shelled organisms in marine environments and are extant in almost all marine habitats. Hence, foraminiferal cytoplasm is well protected by the shells and in very many environments.

Research of the last decades has shown that twinning in *non-biological materials* occurs often and frequently as a material property-enhancing mechanism (Barber & Wenk 1979; Burkhard 1993; Rybacki *et al.* 2003; Ferrill *et al.* 2004). The phenomenon of twinning is a regular intergrowth of two crystals of the same phase in different orientations. The orientation relationship is not random, it is usually related to either a mirror operation on a crystallographic lattice-plane (the twinning plane) or a rotation around a crystallographic axis (the twinning axis). These usually have small integer crystallographic indices. Twinning can be the result of (i) a symmetry-breaking phase transition process, (ii) shear deformation mechanisms by dislocation glide, or (iii) an interruption of the crystal growth process with subsequent continuation with the new crystal nucleating homoepitactically on the pre-existing one, but with a different orientation (e.g., Burkhard 1993; Richards 1999; Schedl 2006; Kelly & Knowles 2012).

Twinned carbonate occurs in biological hard tissues as well. It has widely been observed for biological aragonites (bivalves, gastropods, one otolith, one coral; Suzuki *et al.* 2012; Kogure *et al.* 2014), mainly for three microstructures: for columnar (Mutvei 1978; Suzuki *et al.* 2012) and sheeted (Suzuki *et al.* 2012; Griesshaber *et al.* 2013; Kogure *et al.* 2014) nacre and for crossed-lamellar aragonite (Kobayashi & Akai 1994; Suzuki *et al.* 2012; Kogure *et al.* 2014; Almagro *et al.* 2016; Crippa *et al.* 2020a,b) . For biological calcite proof for the existence of intrinsically twinned calcite is given so far only for red coral sclerites (Floquet & Vielzeuf 2011). A possible twin relationship between foliated and chalky calcite is described for the shell of the oyster Magallana gigas (Checa *et al.* 2018), where most probably the crystallographic order of the chalk is inherited from that of the foliated calcite due to transfer of crystallographic orientation by a {018} twin relationship (Checa *et al.* 2018). Li & Ortiz (2014) described the development of nanoscale twins in the calcitic shell of the bivalve Placuna placenta. Nanotwins are observed to develop around an indenter tip when deformation to the shell is induced through nanoindentation. Pokroy *et al.* (2007) report the formation of {108} type twins in biomimetic calcite composites containing the protein Caspartin extracted from Pinna nobilis shells.

Our study shows that twinning is a main structural characteristic of the calcite of the investigated foraminifera species and that it is strongly concentrated at outer shell wall regions (Figs. 2.2-6, 2.2-8–2.2-10, 2.2-12–2.2-15). The main twin is defined by a misorientationof 60° around [001] and occurs together with a further systematically recurring misorientation of 77° around $\sim[6\bar{6}1]$. The 77°/ $[6\bar{6}1] = 180°/\sim[451]$ orientation relationship observed here (Figs. 2.2-9d–f, 2.2-13c,d, 2.2-14, 2.2-15 and calculated pole figures in Figure 2.2-A12) requires some further remarks. Unlike 60°/[001] it is obviously not a simple rational relationship leading to a dense mesh of overlapping lattice points of the two abutting twin individuals.

However, we do not think that the 77° misorientation is an artifact, as we did not observe a similar phenomenon in many hundreds of EBSD scans on samples of other geologic or biogenic calcite microstructures. Further, as Figure 2.2-13c visualizes for *A. lessonii*, the 77° misorientation is not a singular event that occurs in one grain only. The 77° misorientation is present in the wall of all chamber generations and in many wall regions (Fig. 2.2-13c).

We address the 77° orientation relationship in benthic foraminiferal calcite as an irrational twin. It occurs systematically, albeit it does not appear to be related to a simple and rational-crystallographic geometric relationship between the abutting twin individuals. The hexagonal setting used for calcite leads to cumbersome crystallographic indices for simple directions with the strongest ionic bonds in the system. To achieve a more vivid description, the calcite structure can be derived from the face-centered cubic NaCl structure, where the planar geometry of the $[CO_3]^{2-}$ groups replacing the essentially spherical Cl^- leads to a rhombohedral distortion of the cube. The faces of this rhombohedron are the natural $\{104\}_{hex}$ cleavage faces of calcite. Crystal growth processes and mechanical twin planes of calcite can be described with simpler crystallographic indices if indexed with this face-centered unit cell setting related to the pseudocubic (pc) rhombohedral unit cell (see Bueble & Schmahl 1999, for the transformation matrix and further details). The $[6\bar{6}1]_{hex}$ becomes $[5\bar{4}5]_{pc}$. This in turn is close to the pseudocubic space diagonal $[1\bar{1}1]_{pc}$, which deviates by 4.4° from the observed rotation axis. These are simple rational indices, however, a 77° rotation angle is not an obvious attribute to be associated with this lattice direction which is related to a triad (120°) pseudosymmetry. The symmetry-equivalent rotation of approximately 180° around an axis close to [451]hex = $[85\bar{1}]_{pc}$ (within 2.5°) does not indicate a simple rational relationship either. The closest simple rational $[210]_{pc}$ direction is already 12° away from the observed rotation axis. Therefore, none of these data reveals a simple rational twin law for the 77° misorientation at the present time. In addition, so far we did not observe a regular planar interface between related twin individuals. A regular planar interface is not a precondition for a twin relationship, but it usually helps to identify the twin law.

In summary: The 77°/∼$[6\bar{6}1]$ orientation is a repeatedly and systematically occurring orientation relationship between neighboring crystallites and fulfills the definition of twinning. However, it does not correspond to any obvious twin operation, be it rotation or rotoinversion (the latter was also tested) around a low-indexed crystallographic direction or a plane normal and which would lead to a dense mesh of overlapping lattice points (site coincidence lattice) of the abutting twin individuals. The observed statistical variation of rotation angle and axis may be the simple consequence of the crystallographic mosaic spread, i.e. the abundance of small-angle grain boundaries in biogenic and biomimetic carbonate crystals. Small angle grain boundaries are crystallographically non-rational and are associated with arrays of recurring dislocations in the boundary (e.g., (Griesshaber *et al.* 2007, 2017; Maier *et al.* 2014; Nindiyasari *et al.* 2014a, 2015; Greiner *et al.* 2018; Yin *et al.* 2019)). Similarly, the small-angle deviation from a crystallographically rational twin interface orientation could be associated with such a systematic array of dislocations in the twin interface. For the time being, although we have observational evidence of this twin relationship, we still lack a less speculative explanation. A statistical evaluation of a multitude of the observed twin contacts is currently carried out and will be published in a subsequent paper.

All studies that investigated twinning mechanisms in biological carbonate materials conclude that the formation of twins is utilized as an additional and very effective means of improving biomaterial mechanical properties: (i) energy-dissipation and (ii) damage localization at crack formation and crack propagation (Bruno *et al.* 2010; Kunitake *et al.* 2013; Li & Ortiz 2014; Côté *et al.* 2015; Shin *et al.* 2016). Wolf *et al.* (2005) and Zhu & Gao (2012) have shown that twin boundaries increase hardness in the same way as grain boundaries. Côté *et al.* (2015) demonstrated that occlusion of impurities results in a higher density of twin boundaries; this affects dislocation motion and crack propagation and increases the hardness of the material. Accordingly, when extensive twinning is utilized, the hardening mechanism is based on hindered dislocation motion and not on crack deflection (Kim *et al.* 2010; Kunitake *et al.* 2013; Li & Ortiz 2014; Côté *et al.* 2015). Foraminiferal calcite is not deposited in an extracellular matrix similar in fabric to that in shells. It does also not exhibit such an extensive hierarchical organization of the mineral component as observed for shells, e.g., as it is the case for crossed-lamellar microstructures (Crippa *et al.* 2020a,b). Thus, hardening of foraminiferal calcite will not occur through crack deflection, e.g., at organic membranes that delineate neighboring crystals on many hierarchical levels (crossed-lamellar microstructures). Nonetheless, foraminifera are ecologically very successful organisms, are, however, short-lived and, thus have to calcify quickly. Accordingly, they have to produce in a short time an efficient, adaptive and protective hard tissue. In the investigated species the sub-layer with the twinned crystals is always the thicker layer and is predominantly at outer chamber wall portions. It serves as a protective cap to divert impact from the outside and to strengthen the wall of the chamber.

At each new chamber formation, a layer of laminated calcite covers the pre-existing shell and older chamber walls consisting of a sequence of alternating untwinned and twinned crystal sub-layers. Thus, (i) the twinning characteristic per se, (ii) the sequence of alternating laminae consisting of sub-layers of twinned and untwinned crystals, (iii) the dendritic-fractal crystals and (iv) their interlinkage are the main mechanisms that strengthen foraminiferal calcite and affect the resistance that foraminiferal shells have to sustain. Indeed, there are roughly 4,000 extant foraminifera species; the absolute majority of these is benthic and very few are planktonic (Lipps 1973; Hemleben *et al.* 1977; Erez 2003). Benthic foraminifera survive perfectly well in very diverse marine environments. Microstructure and texture research of the last decades identified major carbonate biological material formation principles/strategies (e.g., Checa *et al.* 2018 and references therein). With this study, we document an additional, a very specific and effective one.

2.2.5 Conclusions

Foraminifera are an important group of protozoa for evolutionary, biostratigraphic and paleoecologic studies. Calcifying foraminifera possess a skeleton, which forms the basis for species description, classification of the phylum, geographical provenance, and distribution of the species in time. Even though the gross morphology and some internal structures of the shells was assessed in previous studies, shell microstructure is little and texture is not characterized.

In this study we attempt this and draw from crystal orientation measurements the following conclusions for the shells of the benthic foraminifera *A. tepida*, *A. lessonii*, *A. lobifera*:

1. Skeletal elements of the investigated shells are formed of mesocrystals. These are characterized by a mosaic of subcrystallites which are in the 4–5 μm size range and are misoriented relative to each other by several degrees. These mesocrystals and their subcrystallites have highly irregular dendritic-fractal morphologies and interdigitate strongly.
2. The mesocrystals can be grouped into two types: (i) large mesocrystals having dimensions of several tens of micrometers and an internal mosaic-misorientation between

5-6 degrees and (ii) small mesocrystals having dimensions below 10° with an internal mosaic-misorientation spread of up to 3 degrees.

3. The large dendritic mesocrystals are frequently twinned. Twinning follows the relationships of 60° rotation around [001] and a 77° rotation around $[6\bar{6}1]$.
4. The individual twin-units have no regular morphologies and are likewise dendritic-fractal in nature and highly interdigitating.
5. The small mesocrystals are in general untwinned.
6. The large and twinned mesocrystals form outer shell wall portions, while the small, mainly untwinned mesocrystals occur at innermost shell margins and seam the perforations of the shell.
7. We identify the small untwinned mesocrystals with the inner calcitic shell part, forming between the inner organic lamellipodial lining and the primary organic sheet, and the large and usually twinned dendritic mesocrystals with the outer calcitic layer, between the primary organic sheet and the outer organic lamellipodial lining.
8. The crystallographic preferred orientation, the texture, of the calcite assembly of the chamber walls is axial with the crystallographic c-axis forming the texture axis. The c-axis is always perpendicular to outer shell surfaces and rotates with the curvature of the shell.
9. At keeled margins and junctions between septa and chamber walls, there is an abrupt change of the radial vector of the wall; thus the orientation of the texture axis switches abruptly. In the calcite maps across these junctions, the texture axes show a seemingly bimodal or multimodal orientational distribution, which is due to the superposition of the different monomodal textures of the abutting units.
10. The conjunction of extremely pronounced dendritic-fractal, mesocrystalline patchwork and the twinning of the crystals is a unique feature of benthic foraminiferal calcite. Dendritic morphologies of biocalcite crystals were already observed, e.g., the "primary" shell layer of modern terebratulid brachiopods (Goetz *et al.* 2011), the calcite and aragonite of *Chama arcana* (Harper & Checa 2017), the calcite of belemnoid rostra and calcite enclosed within cavities of pterioid bivalve shells (Checa *et al.* 2016), cephalopod and isopod calcite (Fig. 2.2-A11, this study). Fractal morphologies are observed in conjunction with long extensions of mineralizing cells (Nagai *et al.* 2018b; Tyszka *et al.* 2019; Simonet Roda *et al.* 2019b).
11. The formation of the dendritic-fractal mesocrystals must be related to calcite crystal growth in the presence of obstacles such as organic matrix molecules binding more strongly to the calcite than in other carbonate-shell forming organisms.

Acknowledgments

We thank Prof. A. Altenbach, Department of Earth and Environmental Sciences, LMU Munich, Germany and Prof. S. Redfern, Department of Earth Sciences University of Cambridge, UK for providing the foraminifera samples. We thank the staff of Central Facility for Electron Microscopy at Ulm University for their technical support at sample preparation for EBSD. This project was partly funded by the European Union's Horizon 2020 research and innovation program under grant agreement No. 643084 and supported by Deutsche Forschungsgemeinschaft, DFG Grant GR-1235/9-1. A.C. and I. S.-A. were funded by Project CGL2017-85118-P, Spanish Ministry of Education and Science.

2.2.6 Appendix

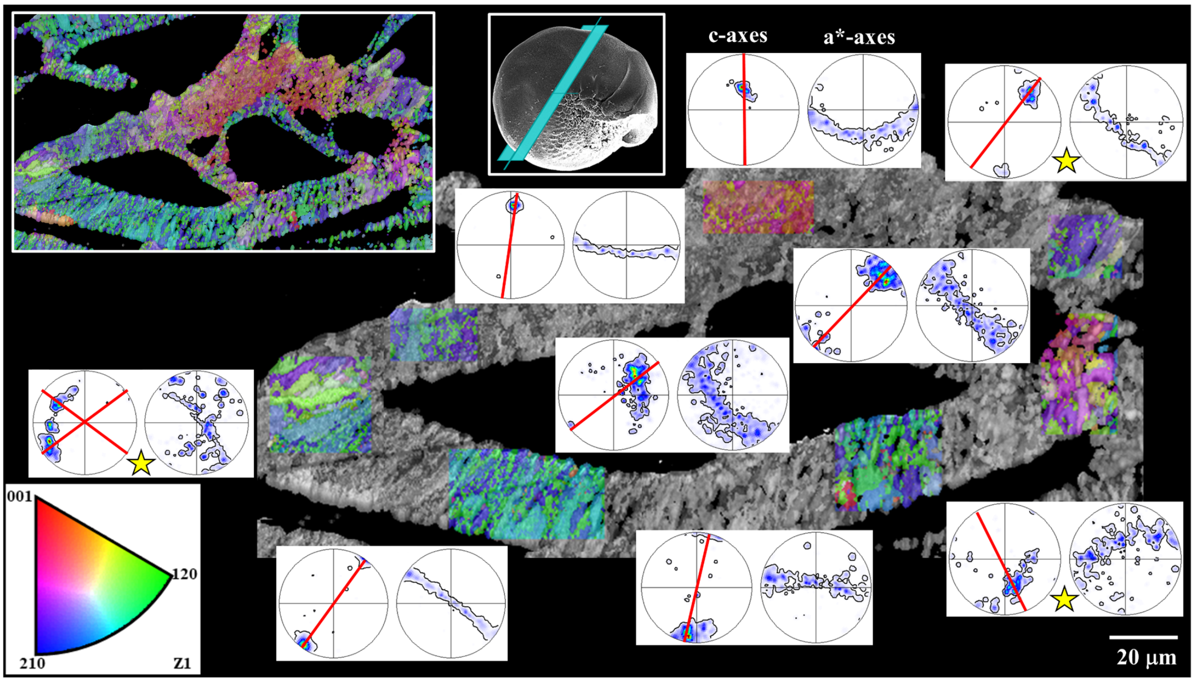

Figure 2.2-A1. EBSD band contrast measurement image (given in grey) depicting one of the first chambers in the shell of *Amphistegina lessonii*. The sample was sectioned axially, Cut 1. The portions shown in color are subsets of the EBSD scan that is given in the insert. Red lines in the pole figures indicate the change of calcite orientation that follows the curvature of the shell; yellow stars in the figure point to the bimodal behavior of crystal orientation at keeled margins, which results from the junction of the monomodal axial textures of the wall on both sides of the keel. Calcite orientation of the septa is perpendicular to the septum wall.

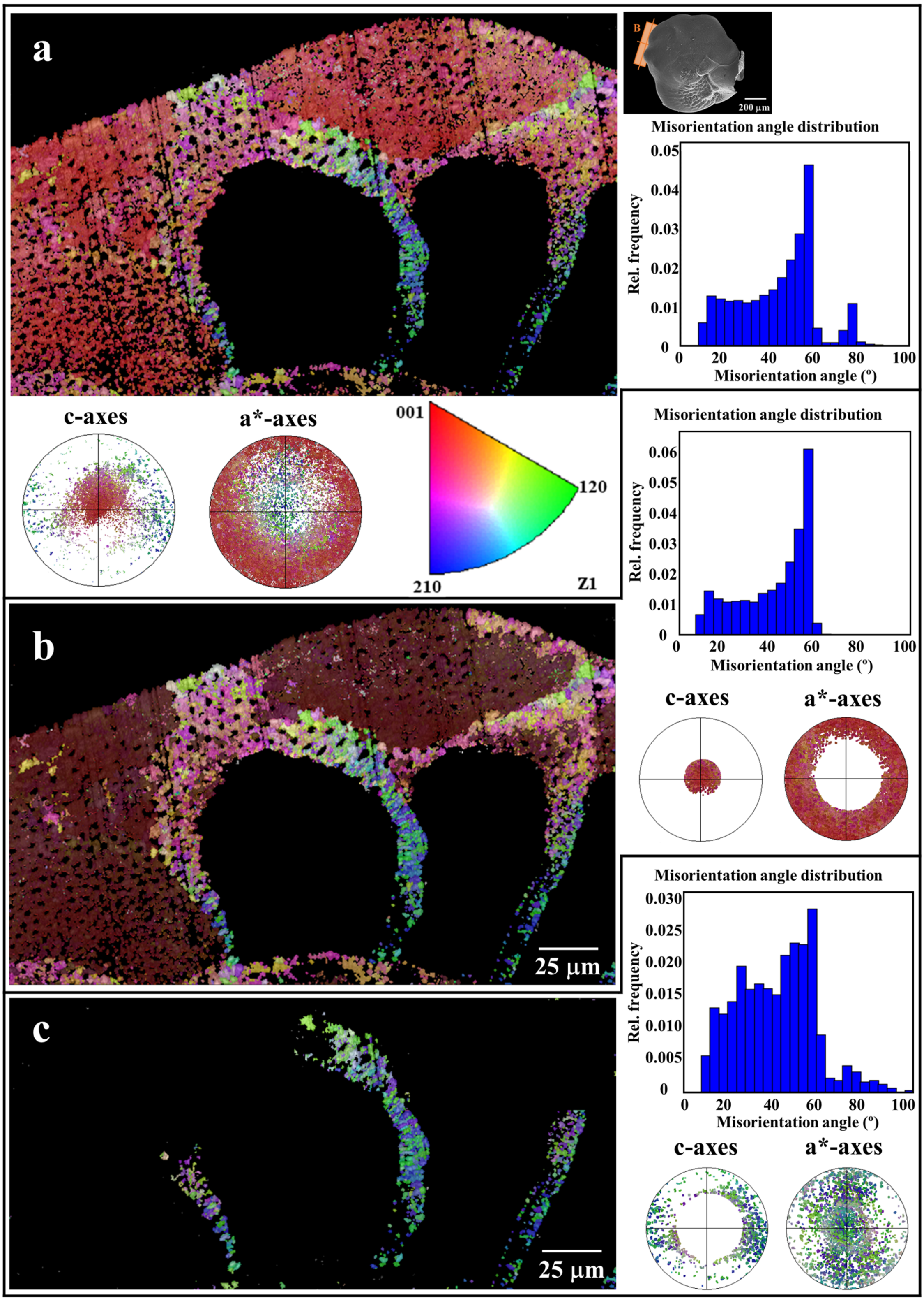

Figure 2.2-A2. Calcite orientation of septa and their rootage within test walls. The test of the shown species, *Ammonia tepida*, was sectioned equatorially, cut 2. (a) Overall orientation within septa and test wall. There is a 90° change of calcite c-axes orientation between septa and test walls (compare pole figures in b and c), such that (in this cut) calcite c-axes of the septa are mainly perpendicular to the septum and thus within the plane of view, while calcite orientation of the test wall points out of the plane of view. The septa are formed by a multitude of small crystals (see the high relative frequency of misorientation angles), with these being variably misoriented relative to each other (see the large range of detected misorientation angles).

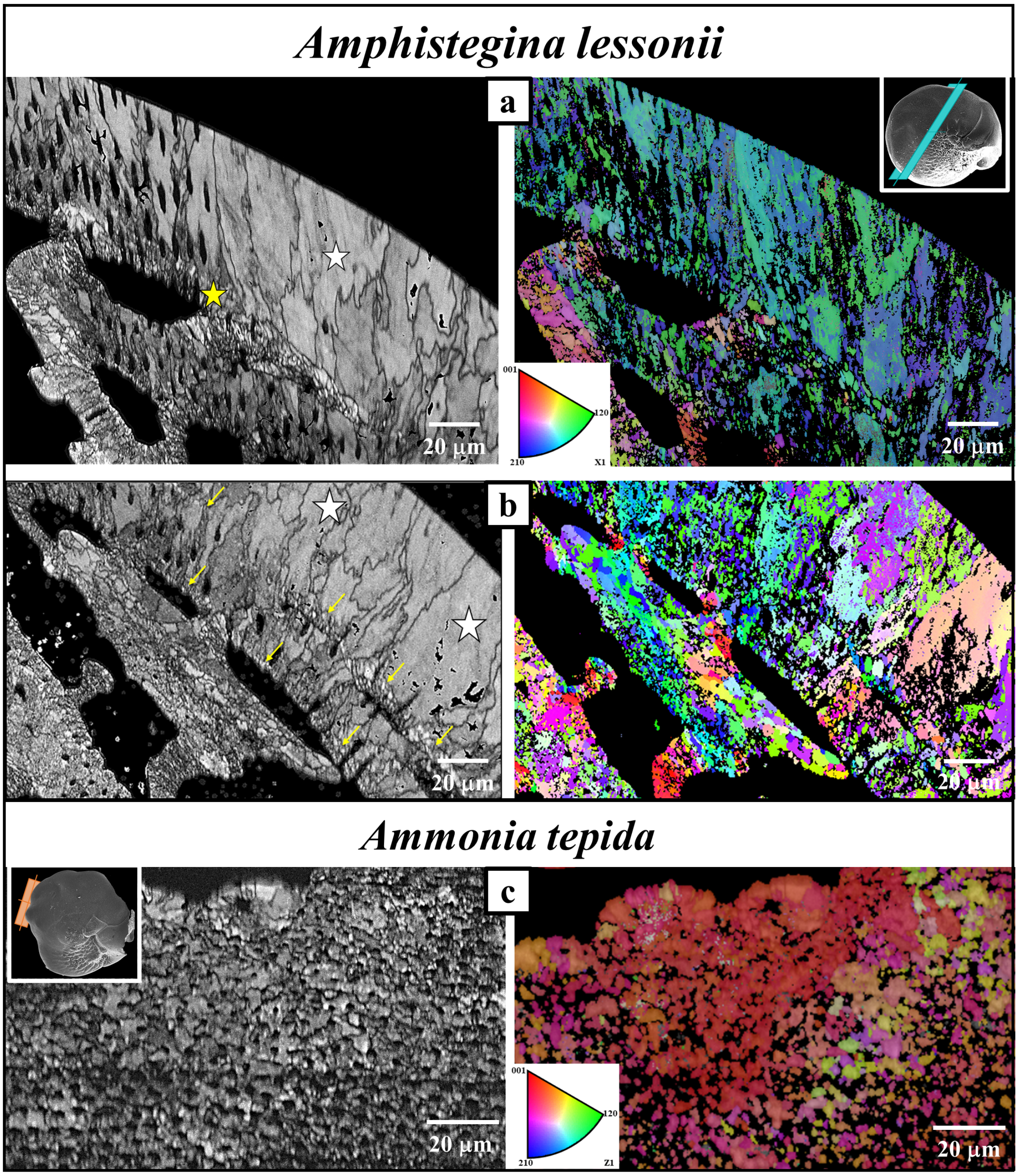

Figure 2.2-A3. Microstructure of the different types of crystals that we find in the tests shown with EBSD band contrast (in grey) and pattern of crystal orientation (color-coded). (a, b) *Amphistegina lesonii*, (c) *Ammonia tepida*. The mode of sectioning the shell is given in the inserts.

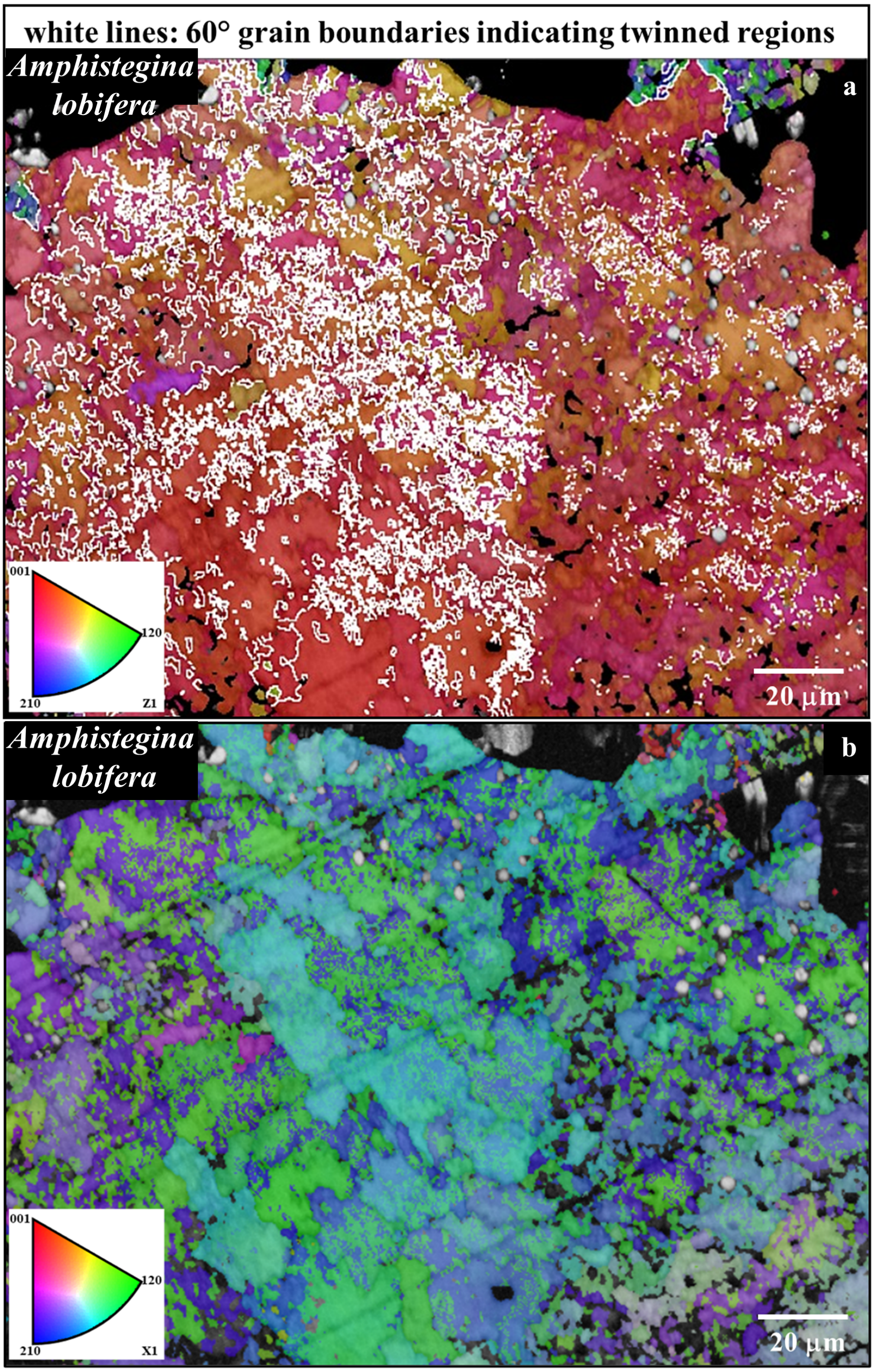

Figure 2.2-A4. Compact calcite and perforated calcite in the central shell portion of *Amphistegina lobifera*. The sample was sectioned equatorially, Cut 2. Insets in both images are color codes for calcite orientation. Well visible is the fractal-dendritic interlinkage of the variously sized and shaped crystals (b) and the inhomogeneous distribution pattern of 60° grain boundaries (a). Test regions containing perforations tend to have smaller crystals and fewer 60° misorientation grain boundaries, while test sections characterized by large crystals are more or less devoid of perforations and show a high accumulation of 60° grain boundaries.

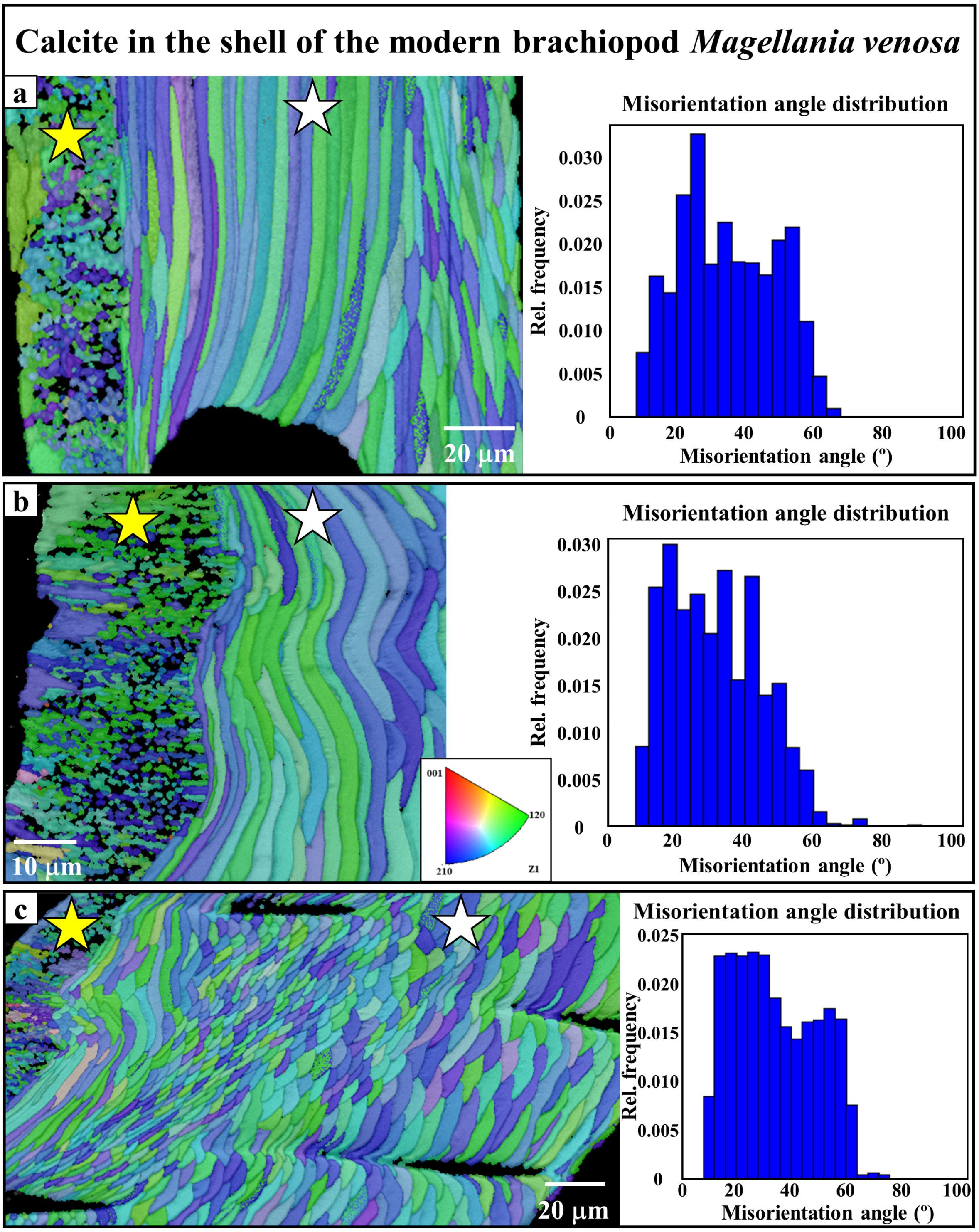

Figure 2.2-A5. Example of untwinned biological calcite. EBSD color-coded orientation map taken on cross-sections through the shell of the modern terebratulid brachiopod *Magellania venosa* and corresponding misorientation angle distribution diagrams. Well visible in all three EBSD maps is the outer "primary" shell layer (yellow star in a, b, c) and the adjacent, inward fibrous shell layer (white star in a, b, c). The misorientation angle distribution diagrams clearly show that the calcite of the brachiopod shell does not follow any particular twin relationship.

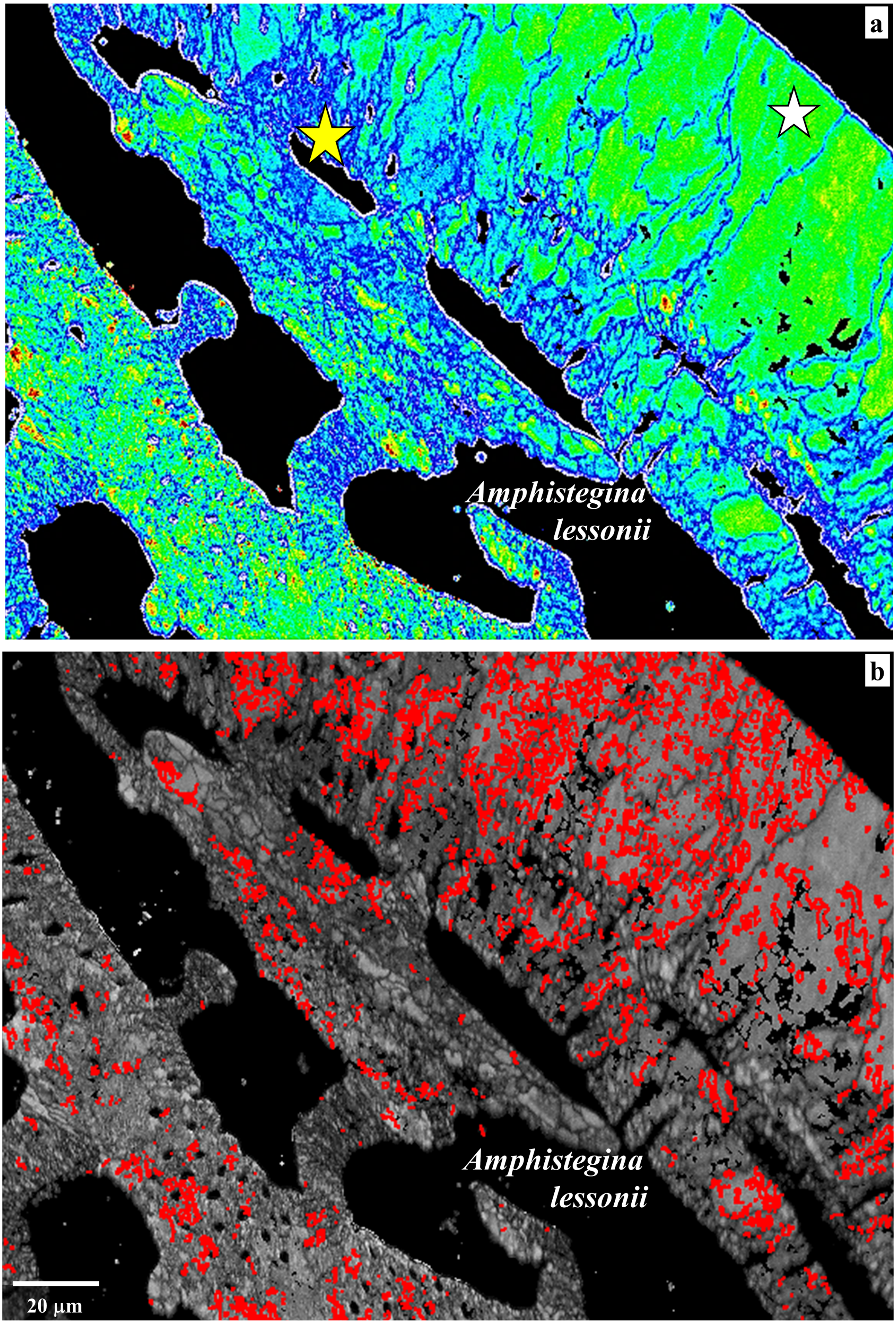

Figure 2.2-A6. EBSD band contrast shown in color (a) and in grey (b) for the test wall of Amphistegina lesonii. The sample was sectioned axially, Cut 1. The shown figures are enlargements of Figure 9b and 9c. Large crystals form often outer test wall portions (white star in a), while small crystals seam inner test wall sections (yellow star in a). The distribution pattern of 60° misorientation boundaries (in red in b) indicates 60°/[001] twinning.

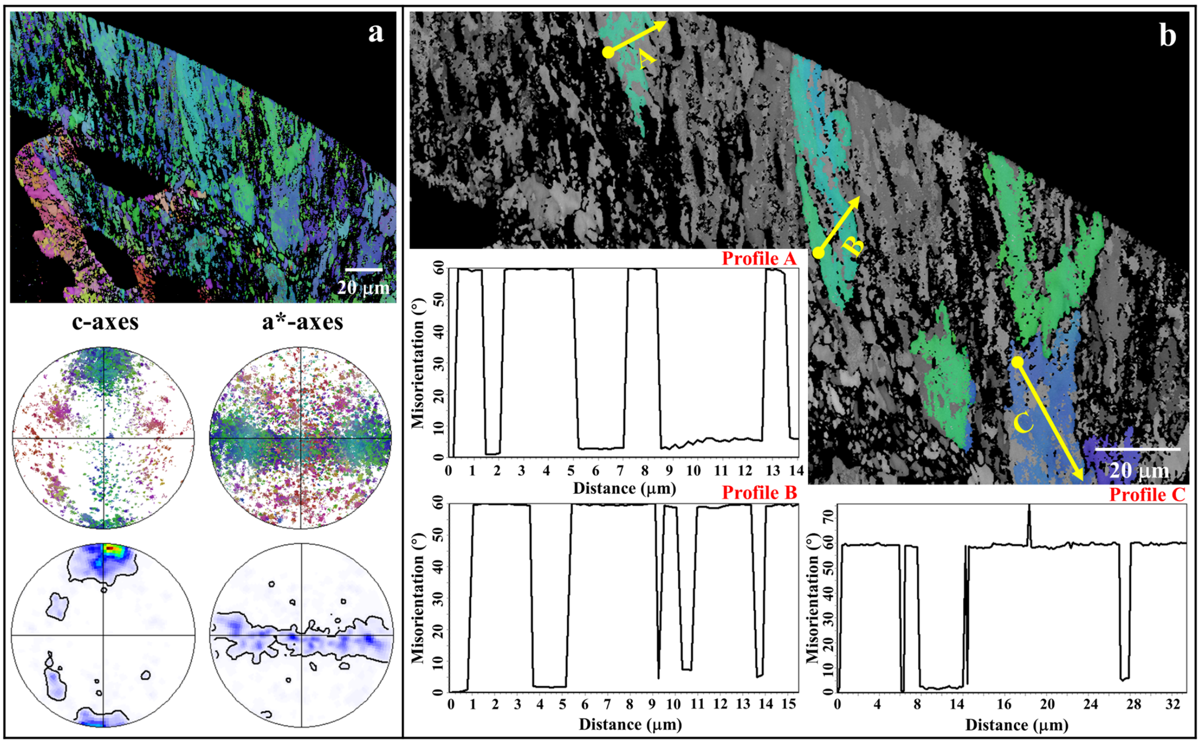

Figure 2.2-A7. Figure A7. Calcite twinning within and between large crystals at outer chamber wall sections. The sample, *Amphistegina lessonii*, was sectioned axially (Cut 1). (a) The entire EBSD scan with corresponding pole figures showing calcite orientation in two chamber generations. (b) misorientation versus distance diagrams along profiles within (profile C) and between (profiles A, B) crystals highlight their twinning pattern.

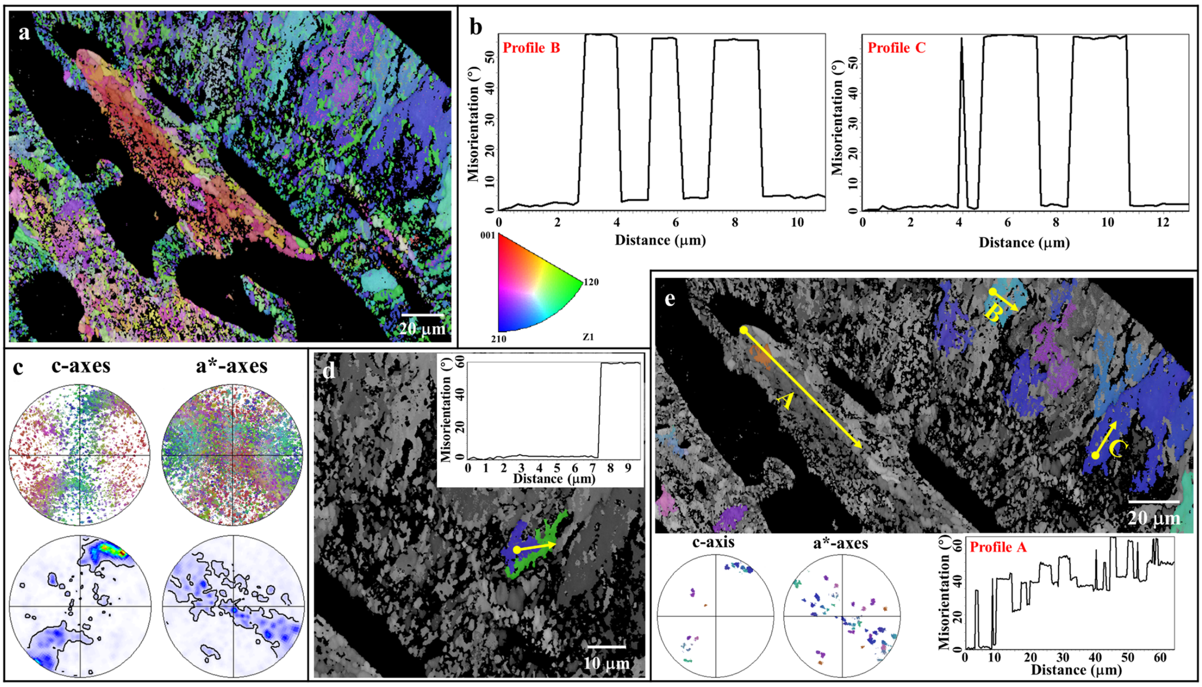

Figure 2.2-A8. Distribution pattern of twinned and untwinned calcite crystals in the chamber walls of *Amphistegina lessonii*. The sample was sectioned axially (Cut 1). Polysynthetic twinning occurs within (profiles B, C in b) as well as between crystals (d). However, not all crystals are twinned (profile A in e). (a, c) give the entire measurement and the corresponding pole figures.

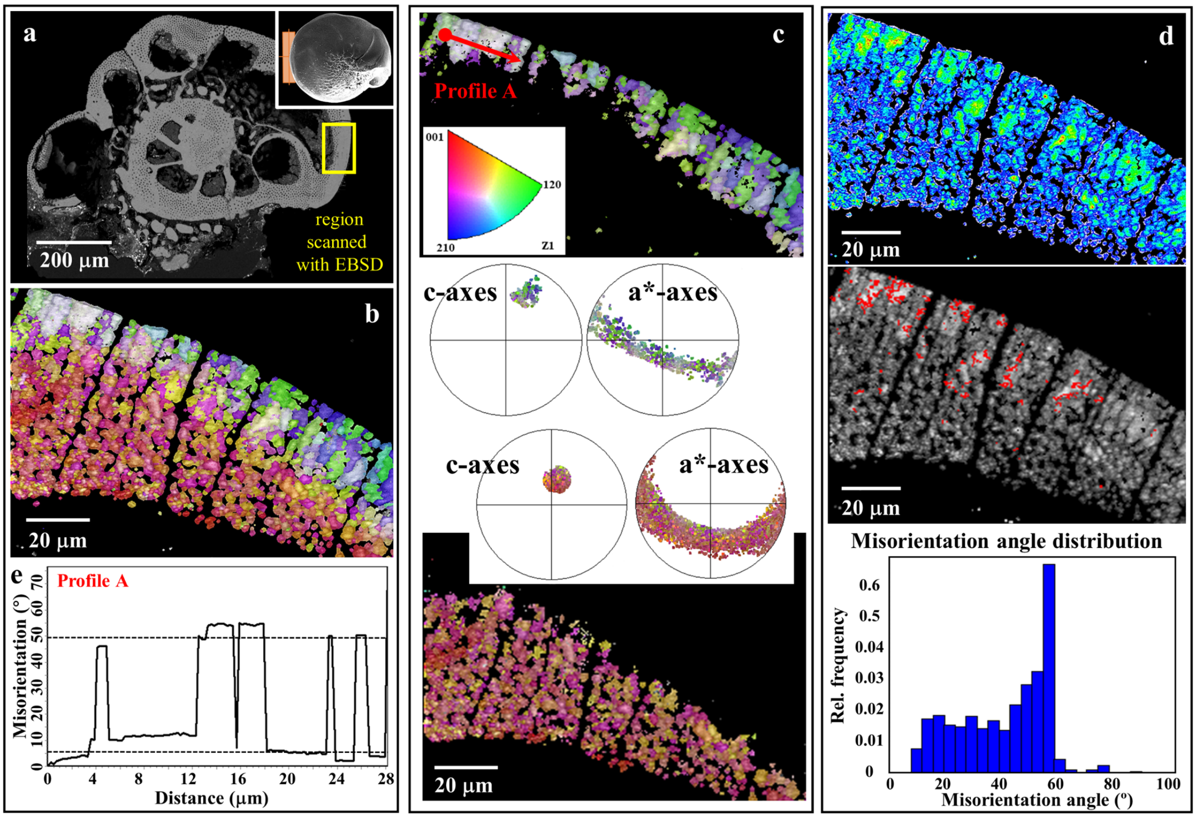

Figure 2.2-A9. Structural characteristics of the wall of the penultimate chamber of *A. lesonii*. The sample was sectioned equatorially, Cut 2 (a). Figure (b, c) show in color calcite orientation in an EBSD map and corresponding pole figures; (d) gives band contrast images in color and in grey, respectively. The grey-scaled band contrast image is overlain with the distribution pattern of 60° misorientation boundaries, the latter depicted in red. Even though larger crystals occur at outer wall portions (d), many of these are not twinned (profile A in c, misorientation vs distance diagram in e, 60° grain boundary distribution shown in red in d). The wall of the penultimate chamber is formed of small, mainly untwinned crystals (band contrast image in d) delineating the perforations; these crystals are variously misoriented relative to each other (blue arrow in the misorientation angle distribution diagram in d). Pole figures in (c) show the very slight difference in orientation between the larger and smaller crystals in this region of the test wall, between outer and inner wall portions.

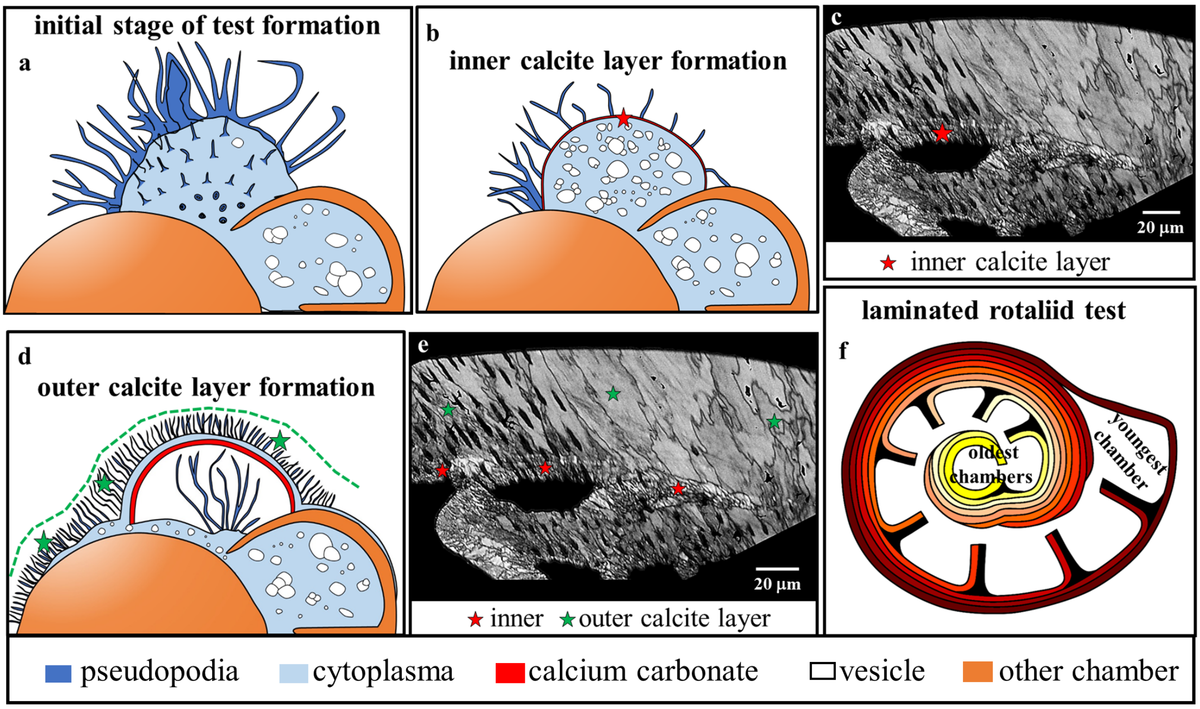

Figure 2.2-A10. Scheme and working hypothesis used in this study visualizing major stages of chamber wall formation in perforate rotaliid foraminifera (a, b, d) in relation to some structural findings of this study (c, e). Sketches in (a, b, d) are modified after Nagai *et al.* 2018a,b. (c, e) are band contrast measurement images of a cross-section through a chamber wall segment of Amphistegina lesonii. Green stars point to wall portions that represent the outer calcitic layer, red stars indicate chamber wall regions that comprise the inner calcitic layer (e, c). (f) visualizes the lamination scheme of shells of perforate rotaliid foraminifera, scheme modified after Reiss 1957. Chamber formation starts with the secretion of an organic template consisting of a network of thin pseudopodia, the globopodia Nagai *et al.* 2018a; Tyszka *et al.* 2019. These aggregate to a sheet (the POS) which serves as a substrate for calcite nucleation and first deposition on both of its sides. As this first-formed calcite is deposited within a network of and around pseudopodial strands, an aggregation of small crystallites seams the numerous perforations in the shells (c). The POS and the first formed calcite outline the extent of the new chamber. This calcite layer is thin, it is in cross-section very few micrometers Spero 1988; Nagai *et al.* 2018a,b and consists of the small mesocrystals (this study). With ongoing chamber wall formation thicker pseudopodia, lamellipodia, become active Nagai *et al.* 2018a; Tyszka *et al.* 2019. This stage of shell formation is characterized by extensive deposition of calcite, the formation of the large, very often twinned crystals with dendritic morphologies, interdigitating strongly in 3D (e).

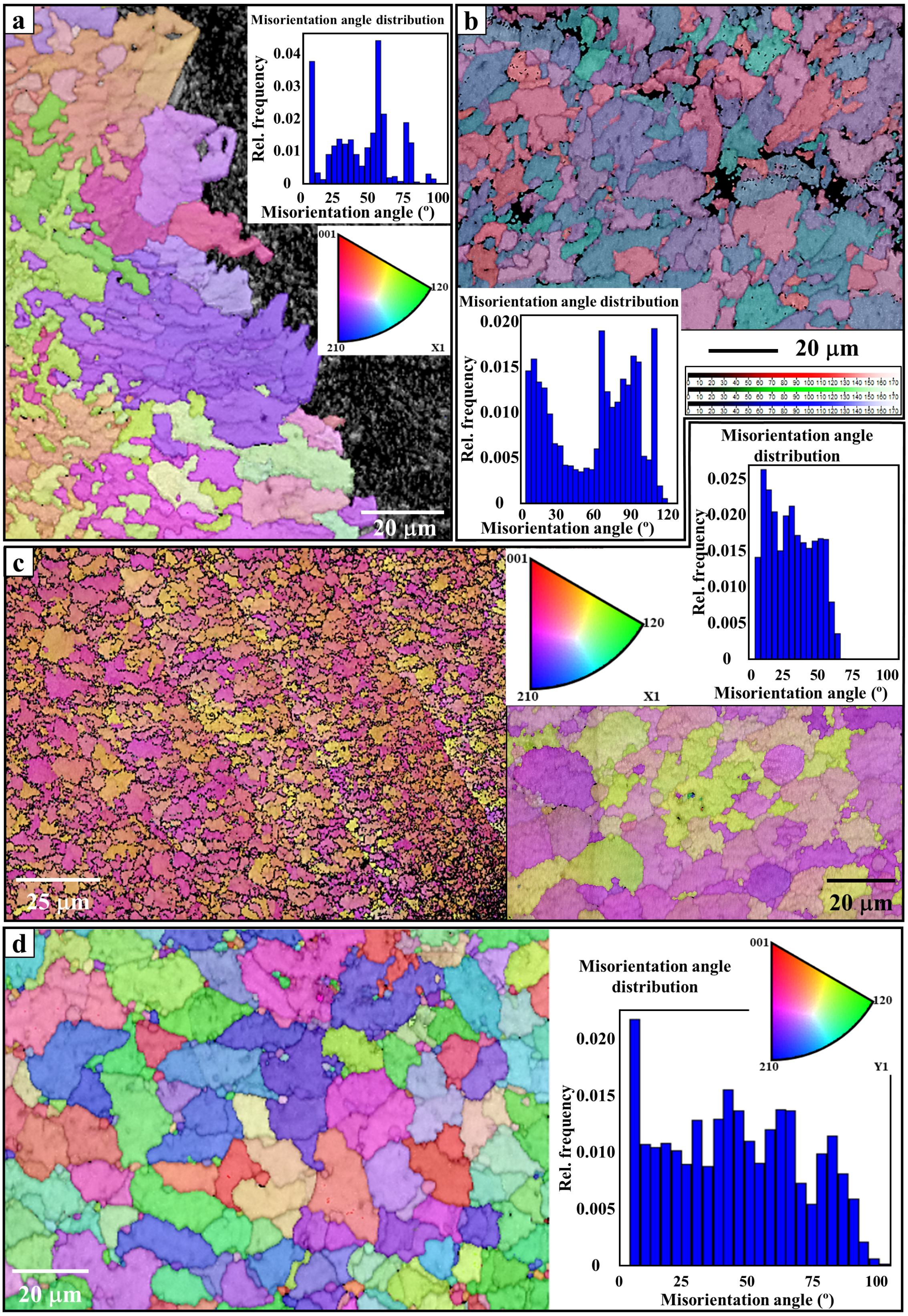

Figure 2.2-A11. Dendritic-fractal morphologies of carbonate crystals in bivalve (a, b), cephalopod (c) and isopod (d) structural materials shown with color-coded EBSD measurement images. (a) *Chama arcana* calcite, (b) *Chama arcana* aragonite, (c) *Argonauto argo* calcite, (d) *Helleria brevicornis* calcite. The corresponding misorientation angle distributions diagrams show a vast range in misorientation angles that scatter between 5 and 110 degrees. Marked peaks at specific degrees of misorientations that would indicate twin relationships are absent.

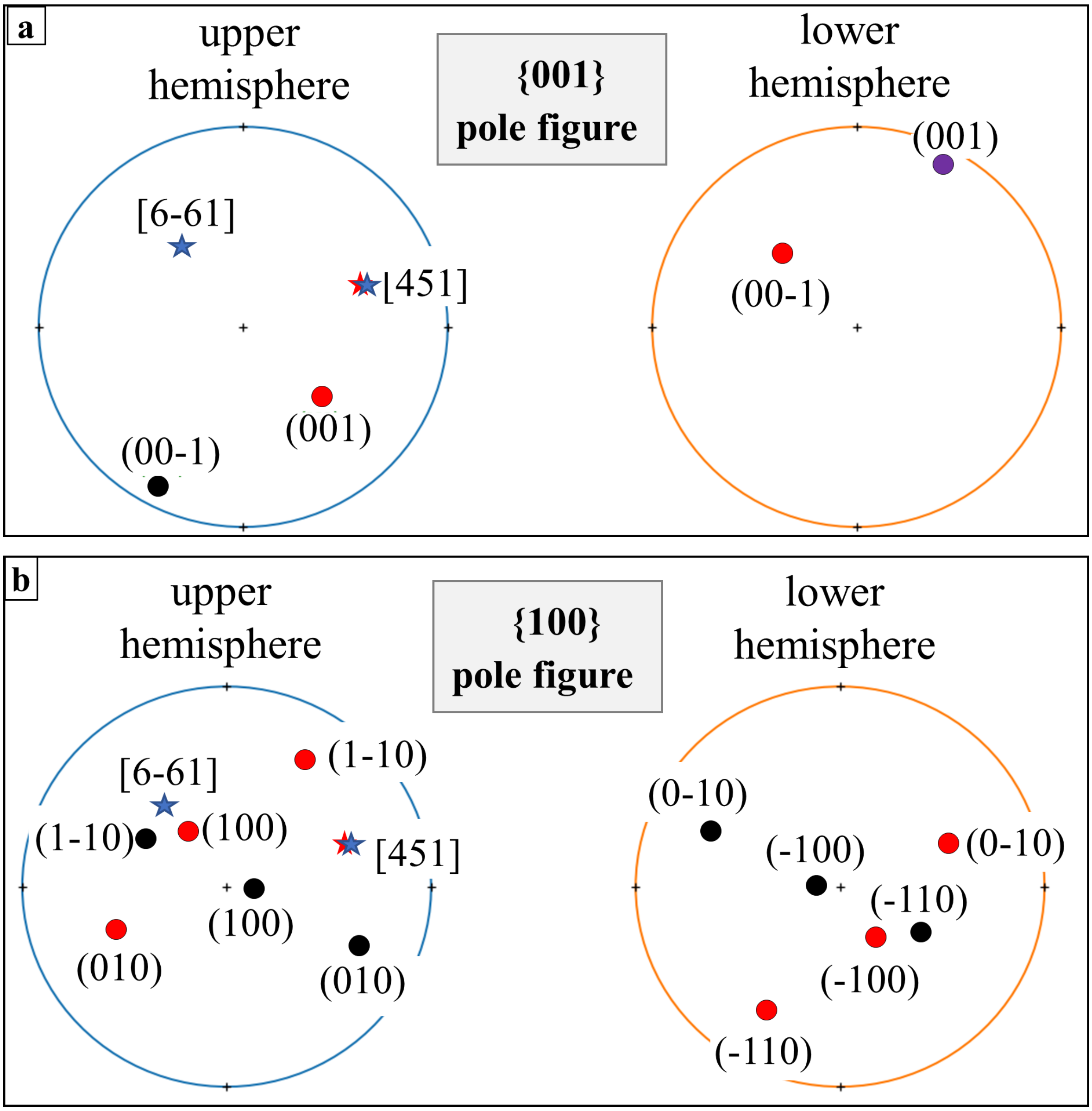

Figure 2.2-A12. Pole figures indicating the 77°/ $[6\bar{6}1]$ ≈ 180°/ [451] twin relationship.
Top: 100 pole figure, bottom 100 pole figure.Poles of crystal 1: black, poles of crystal 2: red. The rotation axes for the twin relationship are marked by asterisks: $[6\bar{6}1]$ for the 77° rotation and [451] for the symmetry-equivalent 180° rotation, direction indices are with respect to crystal 1. The integer direction indices match the actual observed rotation axes only approximately: within 0.2° for $[6\bar{6}1]$ and 2.5° for [451]. The actual rotation axis for the 180°/ [451] case is marked by a red asterisk. The orientation of the pole figures corresponds to that of the EBSD maps and their pole figures.

2.3 Structures and Characters of the Biopolymers in Biomineralized Materials and Biomimetic Composites

Most natural materials are composites that comprise both hard but brittle mineral parts and soft and flexible organic parts. Despite the limitation of biopolymers that biology is able to use (mainly protein and sugar-based polymers), the delicate hierarchical architecture of the biological composites facilitates incredible variability of material properties (Dunlop & Fratzl 2010; Vincent 2012). As mentioned in section 1.3.2, the biologically mineralized calcium carbonates associate with mainly two kinds of organic matrix components. The majority are typical highly cross-linked, insoluble, and slightly hydrophobic macromolecules that are often referred to as the "framework macromolecules". Those framework macromolecules form a two- or three-dimensional structure, onto/into which the mineralization can occur (Weiner 1984). The other criteria are soluble and smaller biopolymers which have more impact during the mineral phase formation compared to the framework macromolecules (Meldrum 2003).

This section features the structure (on micrometre scale level) of the biopolymers matrix within both biomineralized and biomimetic calcium carbonates as visualized with chemical etching and/or decalcification. Here, the organization patterns of organic networks/matrices within several representative biominerals (e.g. the shells of molluscs, bivalves, and brachiopods) are illustrated, discussed and compared with those obtained from the diffusion crystal growth experiments carried out with hydrogels.

2.3.1 Methods

Biogenic specimens were fixed onto aluminium rods using super glue. Desired cross-sections were polished with an ultramicrotome. The surfaces were then etched in a stirred solution containing fixative at pH 6.5. Decalcification was conducted with a solution containing EDTA and fixative at pH 7.8. Crystal aggregates obtained in biomimetic experiments were first embedded in EPON if their size is smaller than 500 μm. Otherwise, they were prepared using the same procedure as the biogenic specimens. For bacterial extracellular polymeric substances (EPS), 5×5 mm square blocks were dissected from the growth area and then transferred into a buffer solution containing fixative at pH 7.3. The chemically etched or decalcified specimens were further critical point dried, coated, and imaged with an SEM. The detailed experimental protocols can be found in Appendix C.1 and C.2 .

2.3.2 Results and Discussion

2.3.2.1 Organization patterns of the organic components in biological calcium carbonate materials

Mollusc and brachiopod shells are two calcareous exoskeleton examples that fulfill the criteria of *biologically controlled mineralization* (Mann 1983). As mentioned in section 1.3.2, both of them have a layered structure. Despite an outermost organic layer (periostracum), some mollusc shells have a fibrous calcitic layer and an innermost nacreous layer composed of aragonite platelets, whereas some modern terebratulid brachiopod shells are composed of a primary layer that consists of an array of interdigitating, irregularly shaped micrometre sized calcite units (Goetz *et al.* 2011), a calcitic fibrous layer (Williams 1967; Cartwright *et al.* 2009), and an innermost columnar layer (Ye *et al.* 2018a,b).

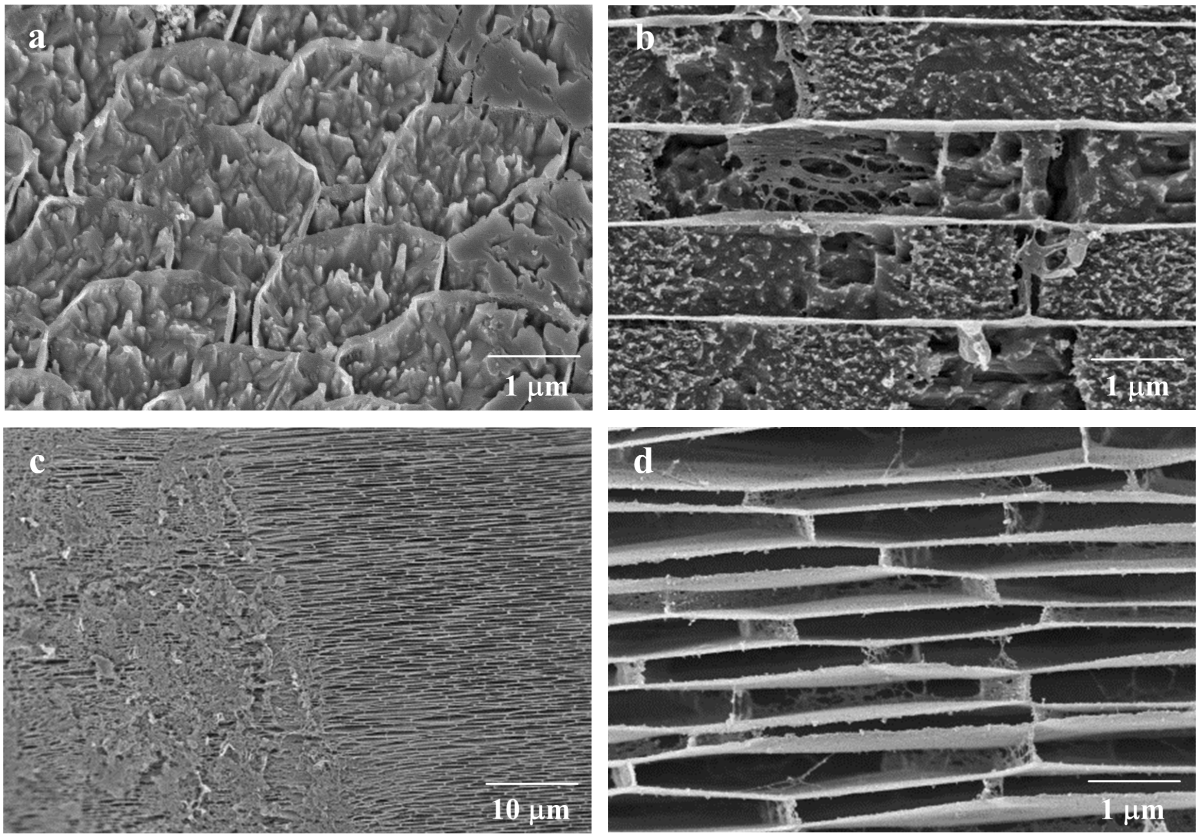

Figure 2.3-1. FE-SEM micrographs visualizing the extracellular matrices in two bivalves: (a) the fibrous layer of *Mytilus edulis*; (b) the nacre layer of *Mytilus edulis*; (c) both prismatic layer and nacre layer of *Cristaria plicata*; (d) a zoom-in of the nacre layer in *Cristaria plicata*.

In the bivalve species *Mytilus edulis*, both the calcitic fibres in the fibrous layer and the aragonitic tablets in the nacreous layer are surrounded by a membranous organic matrix which structures the mineral of the shell in a characteristic grid arrangement as shown in the chemically etched specimens (Fig. 2.3-1a,b). The organic components in the decalcified specimens of the other two bivalves *Cristaria plicata* and *Elliptio crassidens* present analogous organization patterns (Figs. 2.3-1c,d and 2.3-2a,b). It is also noticeable that besides the relatively thick surrounding membranes, there are also thin fibrous or network like biopolymers embedded within the nacre tablets (Fig. 2.3-1b,d). Levi-Kalisman *et al.* (2001) demonstrated in a cryo-TEM observation that the membrane sheets between the nacre platelets are composites that have several components: β-chitin, a highly ordered polymer, is sandwiched between the layers of a hydrophobic framework of insoluble macromolecules (the silk fibroin-like proteins); the silk fibroin-like proteins are secreted as a disordered gel, which is pushed aside during the lateral growth of mineral tablets; the gel comprises also clusters of acidic macromolecules which are occluded into the mineral parts during crystal nucleation and growth (Nakahara 1983; Addadi *et al.* 1991). This model was further integrated into a dynamic perspective that proposed the formation of nacre occurs in four stages: first, the organic matrix is assembled (first chitin, then silk gel); then, the ACC is formed; subsequently, the aragonitic tablets are shaped via polyanionic polymers; and finally grow into the tablets, first in thickness then laterally (Addadi *et al.* 2006). Cartwright & Checa (2007) further demon1strated that the growth of nacre is a hierarchical self-assembly process that organized around a liquid-crystal core of chitin crystallites. The spiral and target patterns that have long been noted in bivalve nacre can be achieved through the liquid-crystal layer growth model as Cartwright *et al.* (2009) reported in an article two years later.

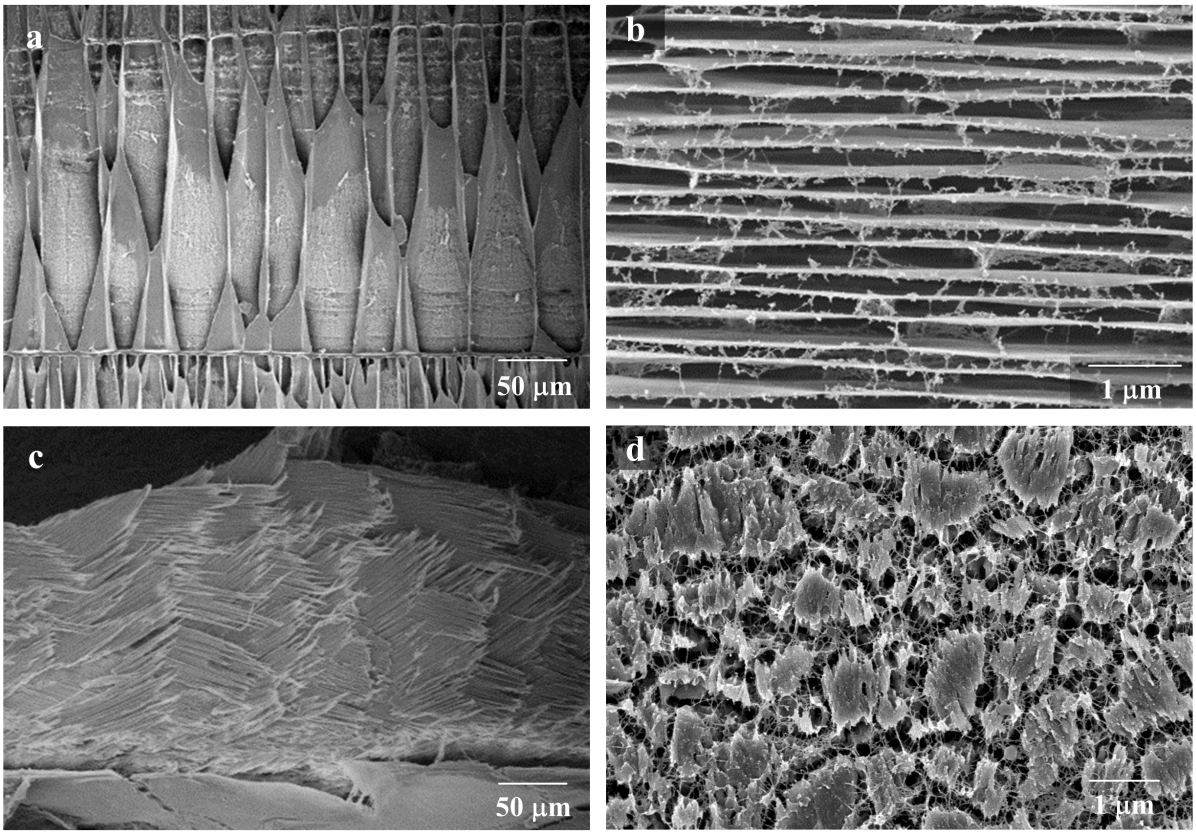

Figure 2.3-2. FE-SEM micrographs visualizing the extracellular matrices in three bivalve specimens: *Elliptio crassidens* (a, b), *Propeamussium jeffreysii* (c), and *Arctica islandica* (d).

However, despite the fibrous and nacreous microstructure as described above, bivalves have also other microstructures in their shells, such as columnar prismatic, granular prismatic, foliated, chalk and crossed-foliated for calcitic microstructures, and columnar prismatic, fibrous prismatic, lamellar, and crossed-lamellar for aragonitic microstructures (e.g. Bøggild 1930; Kennedy *et al.* 1969; Taylor & Layman 1972; Carter *et al.* 2012; Checa 2018). The etched image (Fig. 2.3-2c) implies that the organic components within the internal ribs of *Propeamussiu jeffreysii* have an organization similar to a parquet floor, in which the lath-like organic fibres formed a herringbone pattern. Figure 2.3-2d is the chemically etched FE-SEM micrograph of the inner aragonitic shell layer of another bivalve species *Arctica islandica*. The inner shell layer has a homogenous microstructure that consists of irregularly sized and shaped mineral units, which are connected and infiltrated by a network of organic fibrils.

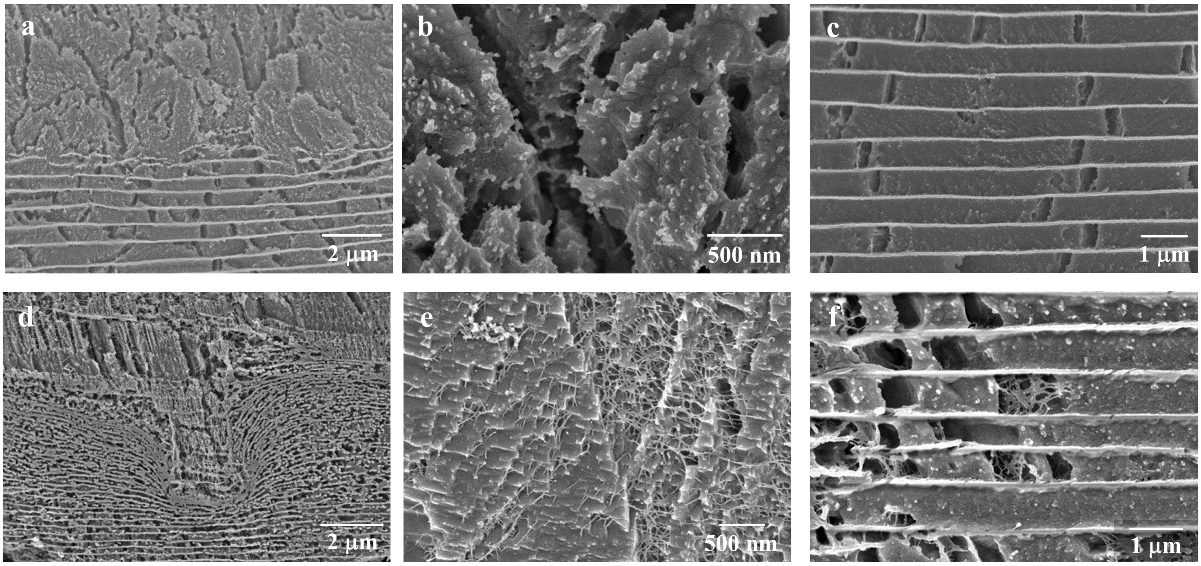

Figure 2.3-3. FE-SEM micrographs visualizing the extracellular matrices in two gastropods: *Haliotis asinina* (a-c) and *Haliotis laevigata* (e-d). (a) the interface between prismatic layer and nacre layer of *H. asinina*; (b) a zoom-in of the organic fibres occluded within the prismatic part of *H. asinina*; (c) a zoom-in of the columnar nacre layer of H. asinina. (d) the interface between the prismatic layer and nacre layer of *H. laevigata*; (e) a zoom-in of the organic network occluded within the prismatic part of *H. laevigata*; (f) a zoom-in of the columnar nacre layer of *H. laevigata*.

Figure 2.3-3 shows the chemically etched specimens of two gastropods, *Haliotis asinina* and *Haliotis laevigata*, respectively. As discussed in section 1.3.2, the shell organization of gastropods is similar to some bivalves. However, the stacking mode of nacre tablets often

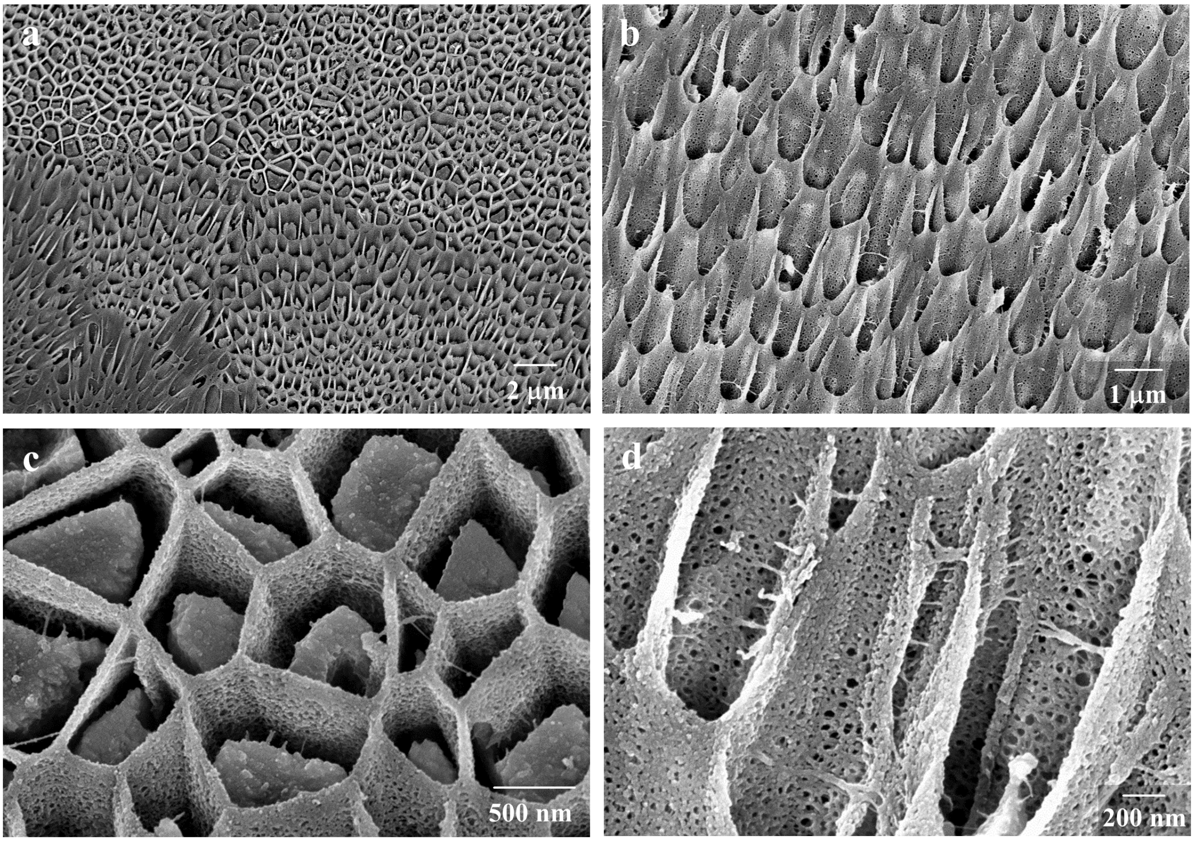

Figure 2.3-4. FE-SEM micrographs of the extracellular matrix organizations and networks of biopolymer fibrils in a modern octopus *Argonauta argo*.

occurs as “columnar nacre” in gastropods rather than “sheet nacre” in bivalves. Figures 2.3-3c and 2.3-3d show the features of columnar nacre. The nacre tablets are surrounded by scaffold membranes, where thinner organic fibrils are occluded within the mineral platelets during their growth.

Figure 2.3-4 reveals the organic matrix within the shell of a modern cephalopod Argonauta argo. The overall image (Fig. 2.3-4a) indicates the two different organization patterns of the organic component within this species, as the right-upper part of the image shows a dense honeycomb-like structure with irregular polygons, while the left-bottom part of the image exposes a branched foliated feature. The zoom-in images (Fig. 2.3-4b-d) show the mineral parts within the “honeycomb” structure are separated by denser and thicker membrane walls, however, the foliated parts are composed of more porous fibrous networks.

Regarding the terebratulid brachiopod shells, an organic membrane that separates each calcite fibre in the fibrous layer is well visible in both species (*Magellania venosa* and *Gryphus vitreus*) as shown in Figure 2.3-5. Simonet Roda *et al.* (2019a) showed that this organic layer is secreted by the outer mantle epithelium cells after the calcite fibres grow to their full width, and the organic layer will finally close at the basal convex part of the fibre after the growth of the fibre is terminated. Organic networks that are embedded within the primary layer are also revealed by the chemical etching preparation.

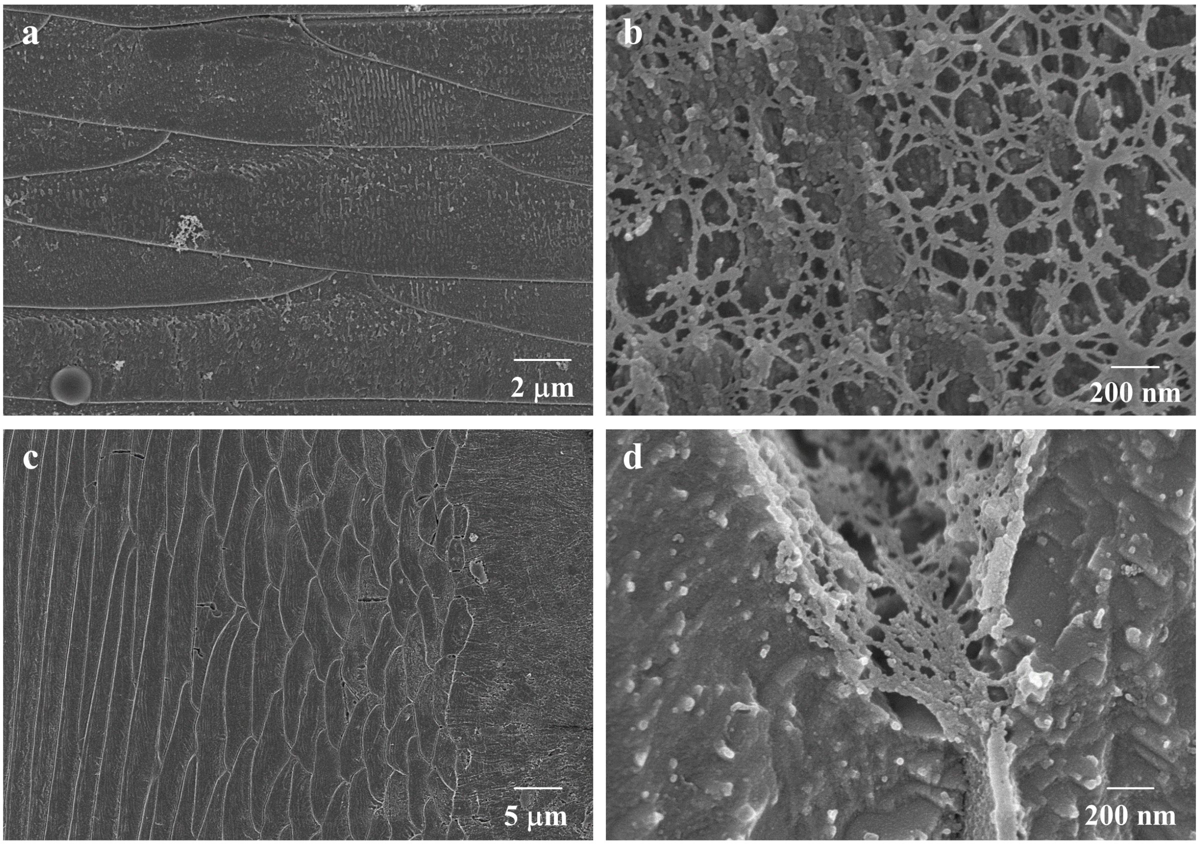

Figure 2.3-5. FE-SEM micrographs visualizing the extracellular matrices in two modern brachiopods: *Magellania venosa* (a, b) and *Gryphus vitreus* (c, d).

2.3.2.2 Organization patterns of the biopolymers in biomimetic composite materials based on hydrogels

As mentioned in section 1.3.2, hydrogels have three advantages for mimicking the biomineralization process: chemically close to the organic matrices within the biological composites, providing volumetric confinement after gelation, and can be easily tuned in laboratories to fulfill different research foci. Figure 2.3-6 presents two pristine hydrogel networks prepared by cryo-fixation. Both agarose and gelatin hydrogels have a porous gel network after gelation. The 1 wt % agarose gel produces much thicker fibres compared to those of the 10 wt % gelatin gel. However, the gelatin hydrogel developed a more sheet- or membrane-like structure than the agarose gel.

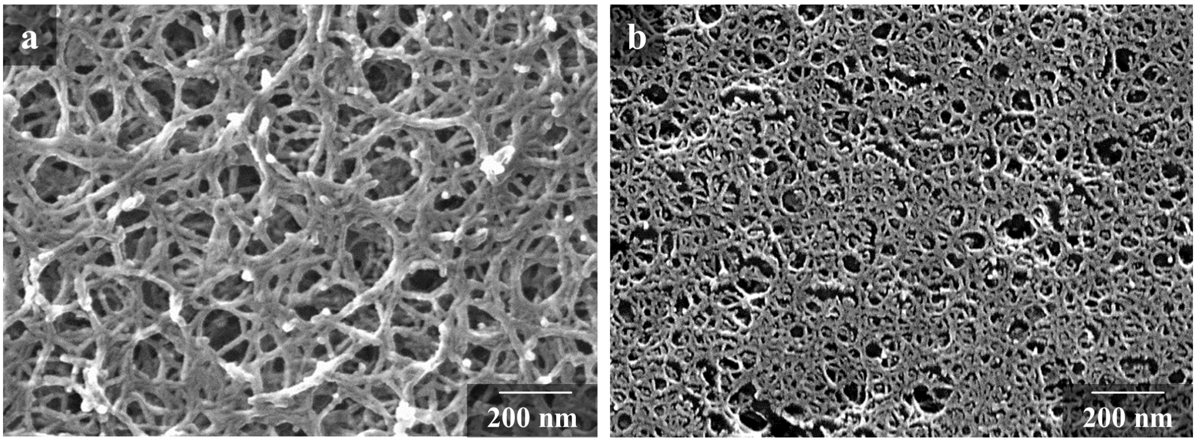

Figure 2.3-6. Cryo-FE-SEM images of high-pressure frozen pristine hydrogels, a) 1 wt % agarose and b) 10 wt % gelatin, respectively.

Extracted extracellular polymeric substances (EPS) of bacteria were also used for biomimetic experiments due to native attributes which are lost by the commercially available hydrogels

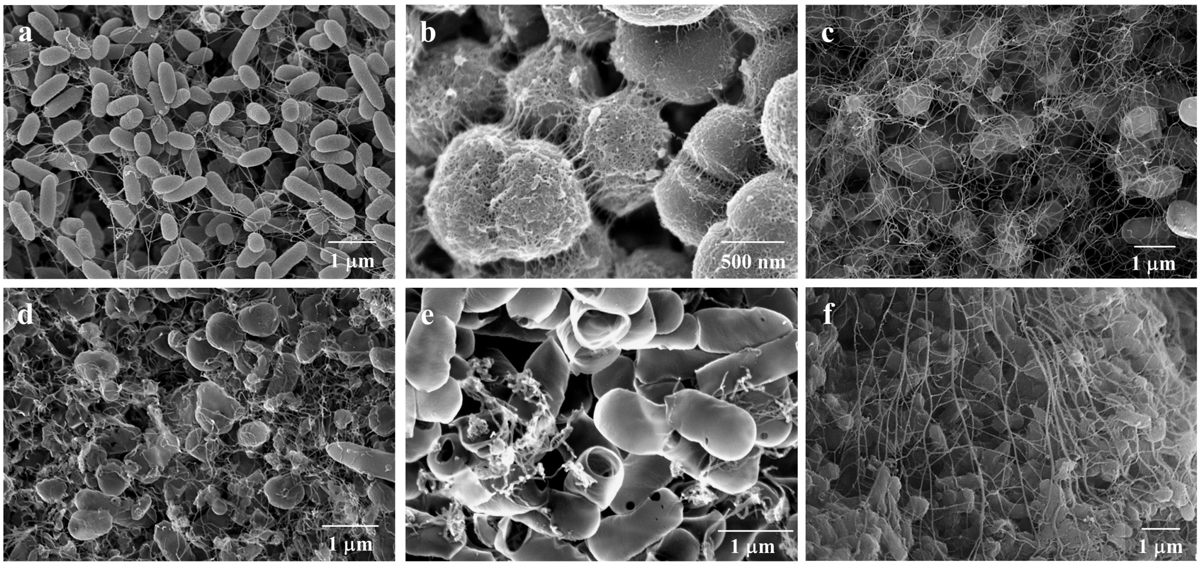

Figure 2.3-7. FE-SEM micrographs of chemically fixed cells and extracellular polymeric substances of six different species of bacteria. (a) *Brevundimonas sp.*, (b) *Micrococcus sp.*, (c) *Bacillus subtilis*, (d) *Pseudomonas putida*, (e) *Mycobacterium phley*, f) *Mycobacterium smagmatis*.

during their manufactory process. Polysaccharides are the major components of almost all EPS, in which polypeptides, nucleic acids, phospholipids, and other polymeric compounds are often combined.

Figure 2.3-7 gives six examples of the chemically fixed bacterial EPS with their corresponding bacterial cells. It shows that there is a significant difference in the productivity of EPS between the different species of bacteria. *Bacillus subtilis* and *Mycobacterium smagmatis* produced a remarkable amount of EPS during the incubation period, as their EPS network covers the majority of the cells in the SEM micrograph. However, *Mycobacterium phley* and *Micrococcus sp.* ended up with only a small amount of EPS, which can be barely seen in the SEM images and only near the surface of the bacterial cells. It should be noted that the bacteria are killed and the significant occurrence of cell rupture could be excluded for the protocol used in this study (Yin *et al.* 2020a,b). The research question how the intracellular components or the metabolism of the bacteria can influence calcite crystallization are beyond the scope of this work. Therefore, the impact of these two aspects was attempted to be minimized with the current protocol and experimental setup.

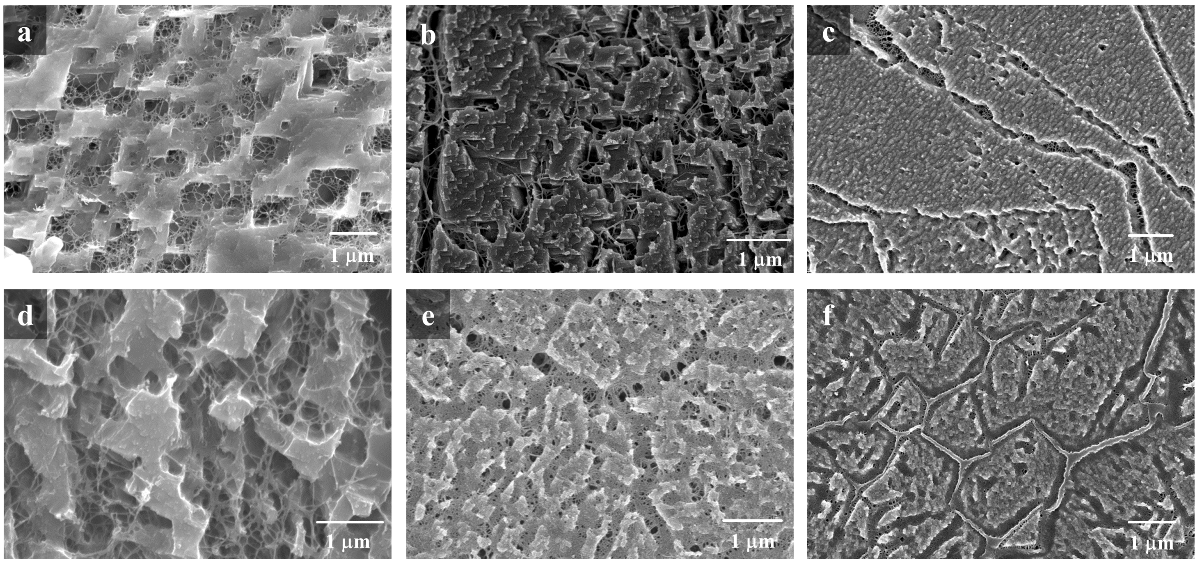

Figure 2.3-8. FE-SEM images of microtome cut, polished, etched, and critical point dried surfaces of calcite aggregates that grew in different biomimetic crystal growth experiments. (a) an aggregate grew in 0.5 wt % pure agarose hydrogel, (b) an aggregate grew in 1 wt % pure agarose hydrogel with 0.01M Mg, (c) an aggregate grew in 2.5 wt % gelatin with 0.01 M Mg, (d) an aggregate grew in 0.5 wt % agarose-bacterial EPS hybrid hydrogel, (e) an aggregate grew in gelatin-agarose gel mixture with 0.01 M Mg, (f) an aggregate grew in 10 wt % gelatin with 0.01 M Mg in the gel

Figure 2.3-8 demonstrates several biomimetic calcite crystals and hydrogel membranes or networks occluded within the aggregates during the crystal growth. Figure 2.3-8a is an aggregate grew in 0.5 wt % pure agarose gel, in which the etched surface reveals the conventional rhombohedron morphologies of the calcite and the gel networks are homogeneously distributed within the aggregate. Figure 2.3-8b is an aggregate that grew in 1 wt % agarose gel with 0.01M Mg. The rhombohedral shapes of the etch pits are lost in this specimen and an inhomogeneous gel network distribution is observed. Figure 2.3-8c is an aggregate that formed in 2.5 wt % pure gelatin hydrogel with 0.01M Mg. The gel network separates the mineral parts into irregularly shaped subunits and was embedded into the mineral during the crystal growth process. Figure 2.3-7d is an aggregate that crystallized in a hybrid hydrogel containing 0.5 wt % and agarose and Mycobacterium smagmatis EPS. The gel network distribution pattern is similar to those obtained in the same weight percentage pure agarose gel as shown in Figure 2.3-7a, however, the etched surface contains randomly shaped etch pits. Figure 2.3-8e is an aggregate mineralized in a synthetic hydrogel mixture having 2 wt % gelatin and 1 wt % as the component. The occluded gel network seems to be much denser than that of the 0.5 wt % pure agarose gel or that of the 2.5 wt % gelatin. Figure 2.3-8f is an aggregate grew in 10 wt % gelatin gel containing 0.01 M Mg. The hydrogels embedded within the crystals have developed thick membrane-like scaffold organization.

2.3.3 Conclusions

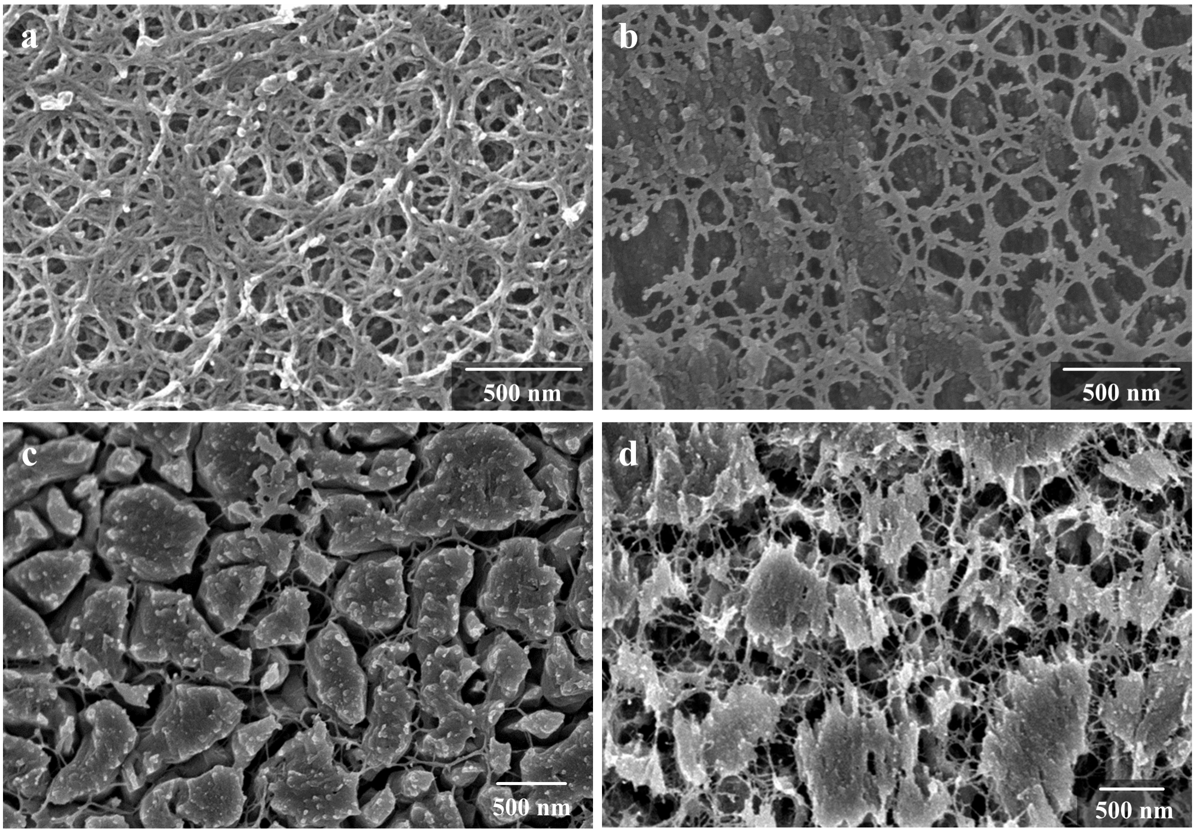

Figure 2.3-9. Comparision of the biopolymers between the biological ones formed in some marine invertebrates and biomimetic ones within the hydrogel crystal growth experiments. (a) Hydrogel fibres of cryo-fixed 1 wt % pure agarose gel; (b) organic fibres within calcitic part of a brachiopod shell (*Magellania venosa*); (c) hydrogel networks within a calcite aggregate that grew in Mg bearing (0.1M) agarose hydrogel; (d) organic fibres within aragonite part of a bivalve shell (*Arctica islandica*).

Comparing the chemically etched images of the biogenic calcium carbonates samples to the biomimetic ones as mentioned above, the results show that the hydrogel network organization within the biomimetic (magnesium) calcite specimens only partially reproduces the features of biologically mineralized calcium carbonates. The pristine hydrogel network may have a similar organization to the occluded organic macromolecules within the biomineralized calcite (Fig.

2.3-9a,b), and those sheet-like hydrogel networks could be well preserved within the calcite aggregates (Fig. 2.3-9c,d) which imitate the biopolymer networks that are involved in some natural samples.

However, the membrane-like gel accumulations found in the crystal aggregates are randomly distributed as the hydrogel networks are indiscriminately pushed away by the mineral during crystal growth, which is very different from those membranes in the biological hard tissues, for instance, the β-chitin layers that constrain the growing space of a mollusc nacre tablets, or the organic lining finishes and maintains the shape of a calcite fibre in a brachiopod shell. The hydrogel systems are useful tools to understand the crystallization process in biomineralization, however, they do not actively control the mineralization process such as the organisms usually do. Further mechanisms should be designed and integrated into the current system, e.g. to introduce a self-assembly feature after the crystals are grown. The mimetic experiments up to now are able to reproduce some basic unit as compared to natural composite materials. To fully achieve and reproduce the hierarchical structure of biological hard tissues, more aspects need to be considered in further research projects.

2.4 Influence of Gelatin-Agarose Composites and Mg on Hydrogel-Carbonate Aggregate Formation and Architecture

Xiaofei Yin[1], Erika Griesshaber[1], Lurdes Fernández-Díaz[2, 3], Andreas Ziegler[4],
F. Javier García-García[5], Wolfgang W. Schmahl[1]

1. Department für Geo- und Umweltwissenschaften, Ludwig-Maximilians-Universität, Germany
2. Departamento de Cristalografía y Mineralogía, Universidad Complutense de Madrid, Spain
3. Instituto de Geociencias (UCM, CSIC). C/ José Antonio Novais 2, Spain
4. Central Facility for Electron Microscopy, University of Ulm, Germany
5. ICTS-CNME, Universidad Complutense de Madrid, Madrid, Spain

Crystal Growth & Design **19**, 5696–5715 (2019)
http://dx.doi.org/10.1021/acs.cgd.9b00679

Abstract

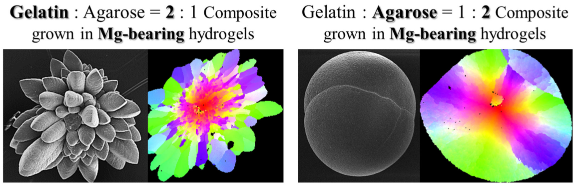

Hydrogels are adequate systems for investigating biological structural material formation as they mimic a wide range of biomineralization conditions. Previous studies focused on the influence of *single component gel systems* in the growth of calcite aggregates and their microstructure characteristics. In this work, we investigate the effects of *hydrogel mixtures* (gelatin/agarose), in the presence and absence of Mg in the growth medium, on calcite aggregate formation, hydrogel incorporation in the calcite, mode of crystallite assembly, and hierarchical mineral organization. We find marked differences between aggregates developed in gel mixtures with increased content of either gelatin or agarose. The presence of Mg, in addition to the gel incorporation, strongly influences the local lattice deformation within the aggregates. The mode of local deformation (homogeneous or localized) is closely related to the size, distribution, and crystallographic co-orientation of subunits within the aggregate. An increase in agarose induces homogeneous distribution of local deformation within the aggregates and formation of a graded mineral arrangement (archetypical spherulites), while an increase in gelatin leads to differentiation of the center and rim portions within the same aggregate. On a higher hierarchical level, when all subunits of an aggregate are considered, both agarose and gelatin evoke the formation of polycrystals.

Keywords

calcite; gel occlusion; EBSD; crystal growth; microstructure

2.4.1 Introduction

Structural materials secreted by multicellular organisms are hierarchically organized composites that are lightweight and have unique combinations of strength and toughness (Fratzl & Weinkamer 2007; Bar-On & Wagner 2013; Dunlop & Fratzl 2013). These materials consist of two material classes, with each retaining its individual chemical, physical, and mechanical properties (Mann 2001; Schmahl *et al.* 2012). The two material classes behave as a matrix and as a reinforcement: the matrix consists of biopolymers and the reinforcement is minerals. Matrices in biological structural materials meet structural as well as functional tasks. Biopolymers form either membranes that constitute the scaffold of the composite hard tissue or a foam-like network of fibrils that becomes occluded within the biocrystals and regulates crystallite attachment and orientation within the space that is defined by the matrix membranes (Checa *et al.* 2005, 2011). Scaffold membranes in biological hard tissues are also composites. Osuna-Mascaró (2015) and his co-workers demonstrated that, in the nacreous shell portion of the bivalve Pteria hirundo, the matrix membranes consist of hierarchically arranged β-chitin and proteins, with each chitin fiber being encased by a protein sheath. These fibers form networks, which, in turn, are embedded into a proteinaceous ground mass. The entire hierarchical biopolymer composite constitutes the extracellular matrix membrane of the biological structural material.

Crystallization in hydrogels is often used to study the process of mineralization in biological environments (Asenath-Smith *et al.* 2012; Dorvee *et al.* 2012; Nindiyasari *et al.* 2014a,b; Schenk & Kim 2015; Di Profio *et al.* 2016). Indeed, mineral formation in hydrogel-like medium was identified for barnacles and mollusks and was recently suggested to be a widespread biological hard tissue formation strategy (Levi-Kalisman *et al.* 2001; Addadi *et al.* 2006; Nudelman *et al.* 2007; Mor Khalifa *et al.* 2011). Hydrogels are porous networks that are filled with an aqueous solution whose composition can easily be varied (Sanchez-Pastor *et al.* 2011). During the aggregate formation, the mineral fills the porous network of the gel, which is similar to biopolymer matrices within the biocrystals, as the gel matrix becomes intercalated into the growing inorganic crystal (Nickl & Henisch 1969; Li & Estroff 2007, 2009; Li *et al.* 2011a; Asenath-Smith *et al.* 2012; Nindiyasari *et al.* 2015). These characteristics render crystallization experiments with hydrogels as ideal systems to explore parameters that might be involved in the incorporation of organic matrices into biocrystals and help to understand how characteristics of this incorporation influence the structuring and hierarchical organization of the inorganic component. Investigations conducted by Estroff´s group on calcite-agarose gel composites show that the amount of gel polymeric matrix that incorporates within calcite results from the balance between growth rate and gel strength. Calcite crystals with the highest amounts of the gel occlusion formed when both the growth rate and gel strength were high (Asenath-Smith *et al.* 2012).

In previous studies, we investigated the effect of the different gels on composite aggregates formation in single gel systems (inorganic silica, and the organic agarose and gelatin gels, respectively). We demonstrated that gel occlusion induces the internal structuring of the calcite in a unique way and that it relates to the specific mechanical response of each gel to crystallization pressure (Nindiyasari *et al.* 2015). This influence can be further modulated by the presence of Mg in the crystallization medium and, at least in the case of calcite-gelatin composites, by the solid content of the hydrogel (Nindiyasari *et al.* 2014a). Compared to the silica gel network, the fabrics of gelatin and agarose matrices resemble the characteristics of organic fibers in carbonate biological hard tissues (Nindiyasari *et al.* 2015). More recently, by studying calcite-agar gel composites, we could show that changes in growth rate and gel strength influence characteristics of gel occlusion such that high growth rates result in calcite aggregates with homogeneous distributions of occluded gel, while calcite-hydrogel aggregates formed under low growth rate regimes show local membrane-like gel accumulations (Greiner *et al.* 2018).

Gelatin is collagen that is denaturalized by partial hydrolysis and depending on the preparation procedure, it can be richer either in acidic or in basic amino acids. Because of its high content in polypeptide bonds, gelatin is regarded to be a chemically active gel. In contrast, agarose is a polysaccharide and, due to its neutral character, has a limited chemical influence on composite aggregate growth. The organic matrix occluded in most biominerals contains covalent interconnections between proteins, oligo- and polysaccharides. This means that, even though commercial gelatin contains 0.5–1.0 wt% covalently bound saccharides, hydrogels exclusively formed of either gelatin or of agarose mimic only partially the chemical complexity of organic matrices in biological hard tissues (Koide & Nagata 2005; Simon *et al.* 2011). A closer resemblance to biopolymer matrices in biological hard tissues is achieved by mixing different gels. Indeed, it was demonstrated that calcite aggregates that contained mixtures of hydrogels reproduced morphological characteristics of human otoconia more closely than calcite aggregates that formed in pure gelatin gels (Huang *et al.* 2008; Simon *et al.* 2011). For a better understanding of the influence of biopolymer matrices on the mineral organization in biological hard tissues, we conducted crystal growth experiments with hydrogel mixtures in Mg-free and Mg-bearing environments. We present morphological and microstructural results of composite aggregates grown in hydrogels with three different gelatin to agarose wt% ratios. We explore the influence of each hydrogel component in the gel mixture on the mode and pattern of gel occlusion, subunit formation, subunit size distribution within the aggregate as well as hierarchical mineral assembly, and crystal co-orientation strength. We conclude our discussion with a contrasting juxtaposition between characteristics of carbonate-hydrogel-composites obtained in gel mixtures and in single gel systems, as well as their characteristics of composite structural biomaterials.

2.4.2 Experimental Procedures

Crystal growth experiments

Table 2.4-1. Summary of crystallization experiments

Experiment	Gelatin wt%	Agarose wt%	[Mg^{2+}] (M)	[$CaCl_2$] (M)	[Na_2CO_3] (M)
A	1	1		0.5	0.5
B	1	2		0.5	0.5
C	2	1		0.5	0.5
D	1	1	0.01	0.5	0.5
E	1	2	0.01	0.5	0.5
F	2	1	0.01	0.5	0.5

Crystallization experiments (Table 2.4-1) were carried out using a double diffusion setup consisting of a hydrogel column (70 mm long and 9 mm in diameter) that separates two vertical reservoirs. The reservoirs were filled with 5 mL of a 0.5 M $CaCl_2$ (Sigma-Aldrich) aqueous solution and 5 mL of a 0.5 M Na_2CO_3 (Sigma-Aldrich) aqueous solution, respectively. The counter-diffusion of the reagents through the porous structure of the hydrogel eventually leads to the formation of a $CaCO_3$ precipitate. Hydrogels were prepared by dissolving different amounts of porcine gelatin (Sigma-Aldrich; Type A, Bioreagent) and agarose (Sigma-Aldrich; Purified; Plant Cell Culture) in hot water. Three gelatin to agarose concentration ratios were used: 1 to 1 wt% (G/A 1:1), 2 to 1 wt% (G/A 2:1), and 1 to 2 wt% (G/A 1:2). The mixture was stirred at 100 rpm for 1 h. The gelation was carried out at 4°C for 1 h. Afterward, the mixed hydrogels were stabilized at 15 °C for 24 h. Finally, the reagents were poured into the vertical reservoirs. All solutions were prepared using high-purity deionized (Milli-Q) water (18.2 MΩ). Experiments were conducted at 15°C.

Crystals were collected two months after the crystallization of $CaCO_3$ occurred. The slice of hydrogel with crystals grown inside was dissolved in hot water (80 °C), then filtered through a 1-μm pore size membrane and washed 3 times with hot Milli-Q water. Afterward, the precipitate was dried at room temperature. The whole extraction procedure took between 15 and 30 min.

Morphological characterization of crystal aggregates

Crystal aggregates grown in the three intermixed hydrogels were selected under a binocular stereomicroscope and picked using a fine paintbrush. The samples were mounted on holders, coated with carbon, and studied using scanning electron microscopy (JEOL JSM6400; JEOL JSM 7600F, at 2 and 4 kV). To avoid charging, some samples required a double coating, first with carbon and then with gold.

Preparation for SEM imaging of decalcified crystal-hydrogel surfaces

The obtained crystals grown in the hydrogel were glued on Al rods (diameter 3 mm). First, the samples were cut using an Ultracut ultramicrotome (Leica) and diamond knives (Drukker, Diatome) to obtain plane surfaces within the material. As a second step, these surfaces were polished with a diamond knife (Diatome) by stepwise removal of material in a series of sections with successively decreasing thicknesses (90 nm, 70 nm, 50 nm, 30 nm; each step was repeated 15 times) (Fabritius *et al.* 2005). The polished crystals were decalcified for at least an hour using 0.25 M HEPES and 0.05 M EDTA (pH=7.8) containing 2.5% glutaraldehyde and 2% paraformaldehyde as a fixation solution. The decalcification procedure was followed by washing three times with bidest for 10 min each, and then dehydrating with an isopropanol series from 30%, 50%, 70%, and 90% up to 100% isopropanol (5 min for each step). Afterward, the specimens were critical point dried in a BAL-TEC CPD 030 (Liechtenstein). The dried samples were rotary coated with 3 nm platinum before being imaged using a Hitachi S5200 FE-SEM at 4 kV.

Preparation of the crystals for electron backscatter diffraction (EBSD) analysis

Electron backscattered diffraction (EBSD) measurements were performed on microtome cut and polished surfaces coated with 4–6 nm of carbon. Measurements were carried out with a field emission FE-SEM (Hitachi SU5000) equipped with a Nordlys II EBSD detector, AZtec and CHANNEL 5 HKL software. Diffraction data gained from EBSD measurements were processed for visualization of the following:

1. Crystal orientation patterns are shown with color-coded orientation maps and corresponding pole figures. Contoured versions of the pole figures, indicate the strength of the clustering of the poles. In this study, we use the lowest possible setting for half width and cluster size for data evaluation in this study. A half width of five and a cluster size of three degrees are chosen. The half width controls the extent of the spread of the poles over the surface of the project sphere, while the cluster comprises data with the same orientation. Co-orientation strength of the crystallographic axes is derived from density distributions of pole figures. It is quantified with a MUD multiple of uniform (random) distribution (MUD) value, which is calculated with the Oxford Instruments CHANNEL 5 EBSD software. High MUD values indicate high crystal co-orientation, while low MUD values reflect a low to random co-orientation.

2. The microstructure of an aggregate is visualized by greyscale EBSD band contrast images. EBSD band contrast represents the pattern quality of the EBSD-Kikuchi diffraction pattern in each measurement point. Thus, a strong EBSD signal yields a bright image point if a well-crystallized site is detected. A weak or absent signal results in a dark point, which indicates, for example, overlapping crystal boundaries, pores, organic material, or amorphous calcium carbonate in the specimen.

3. Local kernel misorientation maps, which show the deviation in orientation between neighboring measurement points, are calculated with 3 × 3 pixel clusters. This deviation corresponds to local internal strain. We attribute this strain

to gel occlusion within the composite and in addition to the Mg incorporation generating small-angle boundaries, as these features are not observable on pure calcite single crystals grown from solution.

4. Point-to-origin misorientation profiles, which depict the angle of misorientation with respect to a chosen reference orientation for all measurement points along the trajectory of a line through the map. We use the orientation of the starting point of the line as the reference orientation. The misorientation (in degrees) is plotted as a function of distance (in μm) from the reference point.

2.4.3 Results

Aggregate morphology and surface constitution

Figures 2.4-1 and 2.4-2 depict composite aggregate morphologies and their surfaces obtained in hydrogel mixtures with three different gelatin to agarose ratios in both Mg-free and Mg-containing growth environments. Composites that formed in Mg-free gelatin-agarose gel mixtures (Fig. 2.4-1a–c) are developed as blocky, slightly elongated rhombohedra, which are bounded by poorly developed (104) surfaces, rough and strongly terraced vicinal surfaces, and a combination of straight and curved edges (Fig. 2.4-1a–c). Although dendritic developments can be observed, in aggregates that formed in an environment devoid of Mg, dendritic growth is most pronounced in composites that grew in the G/A 1:2 gel mixture (Fig. 2.4-1c). Hence, dendritic arrangements appear when the agarose content is increased in the gel mixture (Fig. 2.4-1c).

The mean size of the obtained composites varies between 250 and 600 μm for those that formed in the G/A 1:1 gel mixture. For those that formed in the G/A 1:2 gel mixture, aggregate sizes scatter between 300 and 550 μm, while the sizes are between 150 and 400 μm for aggregates that grew in the G/A 2:1 gel mixture. Hence, in a growth medium devoid of Mg, an increase in gelatin induces the formation of slightly smaller aggregates, while an increase in agarose does not seem to have a major effect on aggregate size.

Calcite-gel composites that grew in Mg-bearing growth environments (Fig. 2.4-1d–i) have a wide range of morphologies that includes sheaf-, flower-, cauliflower-like (Fig. 2.4-1d–f) but also spherical (Fig. 2.4-1g–i) structures. The mean size of aggregates that developed in the presence of Mg varies between 200 and 600 μm for those that formed in the G/A 1:1 gel mixture; it scatters between 90 and 400 μm for those that formed in the G/A 1:2 gel mixture, while it is between 150 and 500 μm for those that grew in the G/A 2:1 gel mixture. Accordingly, the largest sized aggregates formed in the G/A 1:1 gel mixture, irrespective of the presence or absence of Mg in the growth medium. When Mg is added, an increase in either gelatin or agarose in the gel mixture induces the formation of slightly smaller sized aggregates.

The smoothness of calcite surfaces (Fig. 2.4-2) varies according to the experimental conditions. Compared to the composites that grew in the presence of Mg, aggregates that formed in growth environments devoid of Mg have smoother surfaces, especially the surface of those that formed in the G/A 1:2 gel mixture. When gelatin is increased in the gel mixture, aggregate surfaces become rougher and are covered with growth steps parallel to the rhombohedral edges. The addition of Mg to the growth environment changes the surfaces of the aggregates (Fig. 2.4-2), such that all aggregate surfaces have a nanoparticulate appearance, however keeping the rhombohedral edges of calcite (yellow stars in Fig. 2.4-2a,b).

Hydrogel distribution, subunit formation, Mg-content variation

Figures 2.4-3, and 2.4-S2 to 2.4-S7, show local kernel misorientation maps for aggregates obtained in the different gelatin to agarose gel mixtures, in the absence and presence of Mg in

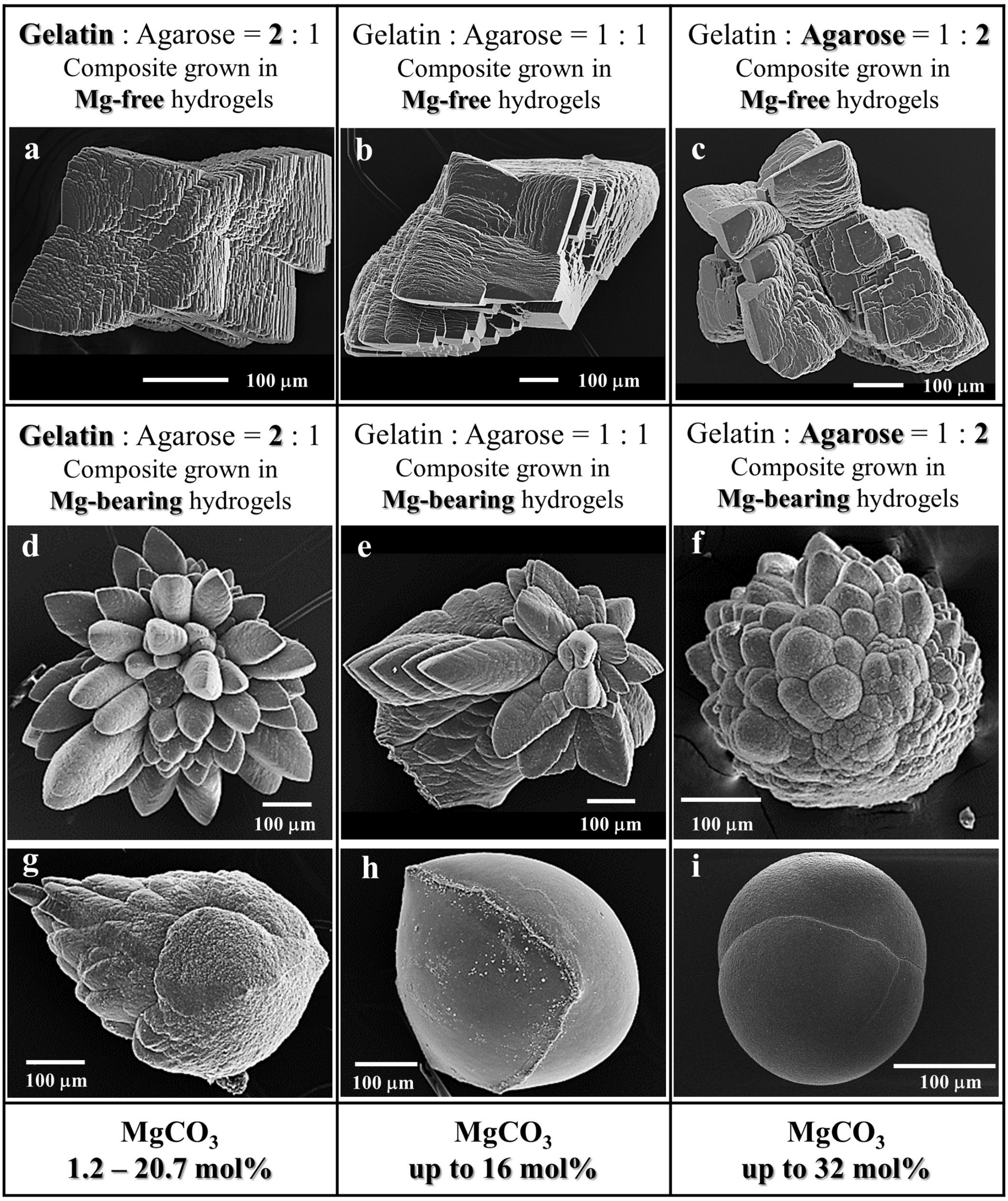

Figure 2.4-1. FE-SEM micrographs of composite aggregate morphologies obtained in three different gel mixtures, grown in a Mg-free (a–c) and Mg-bearing (d–i) growth environment. Panels a, d, g show composites that grew in the gel G/A 2:1; panels b, e, h depict aggregates that grew in the hydrogel G/A 1:1, and panels c, f, and i highlight aggregate morphologies that we obtained in the gel G/A 2:1. Note the blocky, slightly dendritic morphology of aggregates obtained in Mg-free growth media, in contrast to the rounded and spherulitic appearance of aggregates that developed when Mg was added to the growth environment (panels d–i).

the growth medium. Local kernel misorientation is derived from EBSD measurements and shows the color-coded deviation in orientation between neighboring measurement points. In this study, local kernel misorientation is calculated for 3 × 3 pixel clusters. Local kernel misorientation visualizes the pattern of distribution of the local deformation within the aggregates, which results from the internal strain that is due to gel occlusion and from small-angle boundaries induced by

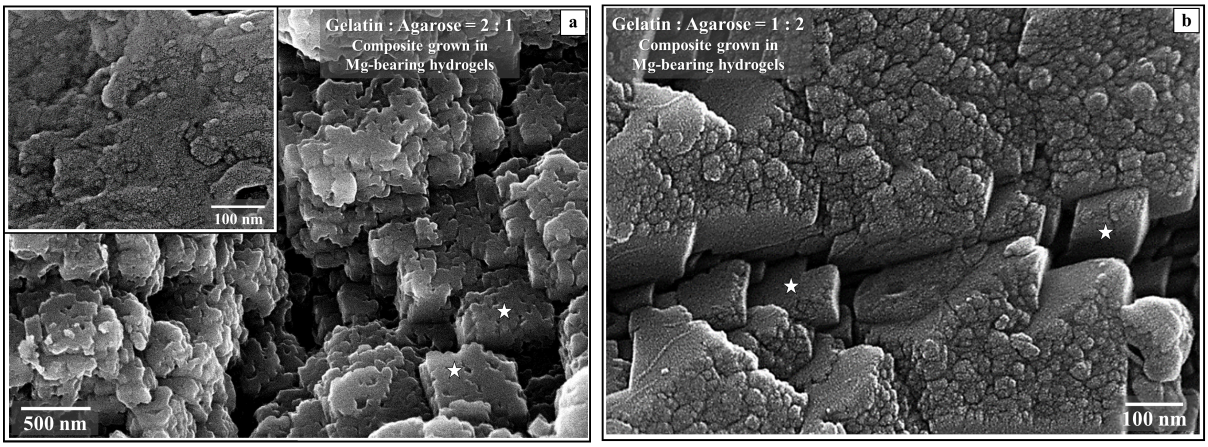

Figure 2.4-2. High-resolution FE-SEM images of fracture surfaces of aggregates grown in the presence of Mg in the growth medium in gel mixtures with increased gelatin (a) and an increased agarose (b) content, respectively. Note the nanoparticulate appearance of calcite on crystal surfaces, especially for aggregates that grew in gel mixtures where agarose was increased; however, the rhombohedral edges of calcite persevere (yellow stars).

Mg within the mineral. On the reference crystal (a calcite single crystal grown from solution, Fig. 2.4-S1a–c), this feature is not observable as the crystal is pure calcite and does not contain any gel or Mg. Corresponding to each local kernel misorientation map we give diagrams showing the relative frequency of local kernel misorientations (Fig. 2.4-3). These highlight the extent of misorientation between neighboring mosaic blocks or crystallites. A low degree of local kernel misorientation indicates a low amount of occluded gel and few Mg-induced small-angle grain boundaries within the crystal (visualized with blue colors in Fig. 2.4-3; see also local kernel misorientation of the reference crystal, Fig. 2.4-S1b,c). When the gel and/or Mg incorporation is high, misorientation between crystallites is increased (visualized with green colors in Fig. 2.4-3). All local kernel misorientation maps that are given in Figure 2.4-3 are shown enlarged in Figures 2.4-S2 to 2.4-S8.

Irrespective of the presence or absence of Mg in the growth medium, we find that all composites contain occluded gel (Figs. 2.4-S9 to 2.4-S11). However, aggregates formed in gel mixtures containing Mg show a significantly higher local deformation compared to aggregates that grew in Mg-free gels (compare Fig. 2.4-3a–c to Fig. 2.4-3d–f). The mode of local deformation within the aggregate is also influenced by the gelatin to agarose ratio in the mixture; the feature is best visible for aggregates that grew without Mg (Fig. 2.4-3a–c). The highest degree of local kernel misorientation, irrespective of the presence or absence of Mg in the growth medium, was observed in the aggregates that grew in the G/A 1:1 gel mixture (see arrows in frequency versus misorientation diagrams in Fig. 2.4-3b,e). An increased amount of either gelatin or agarose in the gel mixture, decreases the degree of local kernel misorientation (see arrows in Fig. 2.4-3a–f). In the aggregates that grew without Mg in the growth medium, when gelatin is increased in the gel mixture, we find that the accumulation of gel at grain boundaries increases (Figs. 2.4-3a, and 2.4-S3a), and gel membranes develop and delineate subunits. When agarose is increased in the gel mixture, gel accumulations at grain boundaries are also present, however, and in addition, the gel is also markedly dispersed within the aggregate (Figs. 2.4-3c, and 2.4-S4a).

The pattern of local deformation within the aggregate is mirrored by the size and the arrangement of subunits. Subunit formation, subunit size generation, and subunit size distribution are triggered by the local deformation (Figs. 2.4-4, and 2.4-S2 to 2.4-S8). In Mg-free growth environments, the aggregate grown in the G/A 1:1 gel mixture consists of mainly one large crystal (Fig. 2.4-4b). When agarose is increased, additional

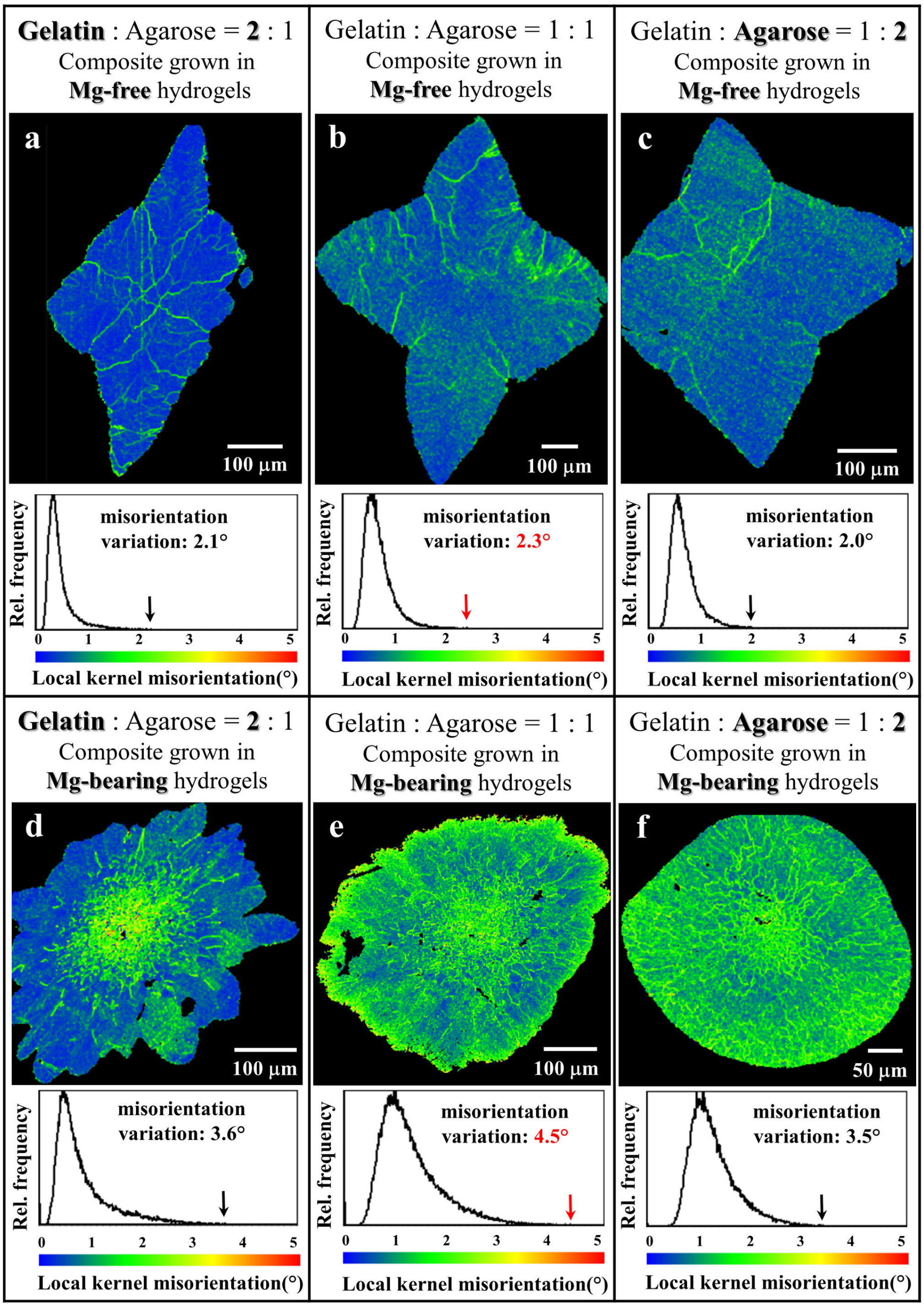

Figure 2.4-3. Local kernel misorientation evaluation (calculated for 3 *times* 3 pixel clusters) for different aggregates obtained in this study, in Mg-free (a–c) and Mg-containing (d–f) growth medium, respectively. Local kernel misorientation is given color-coded and depicts increased local strain induced by gel occlusion and/or Mg incorporation. Relative frequency of local kernel misorientation diagrams are given below the misorientation maps. Arrows point to maximal misorientation values. The increased strain is shown with yellow to green colors, and the absent or small strain is depicted with blue colors. See also local kernel misorientation evaluation for a reference crystal, single-crystalline calcite grown from solution (Fig. 2.4-S1 and Figs. 2.4-S2 to 2.4-S7), where we show enlargements for better visualization of the pattern of strain distribution within the aggregate. The gel mixture and/or Mg are inhomogeneously distributed not only within an individual aggregate but also vary between the aggregates obtained at different experimental conditions. For aggregates that grew without Mg and with an increase of gelatin (a), we see the formation of gel membranes delimiting subunits from each other. An increasing amount of agarose (c) in the gel mixture affects a more homogeneous pattern of gel distribution within the aggregate, even though some membrane formation is visible. The addition of Mg (d–f) in the growth medium induces a higher local kernel misorientation inside the aggregates, which is affected by both the amount of gel occlusion and small-angle boundaries generated by Mg incorporation.

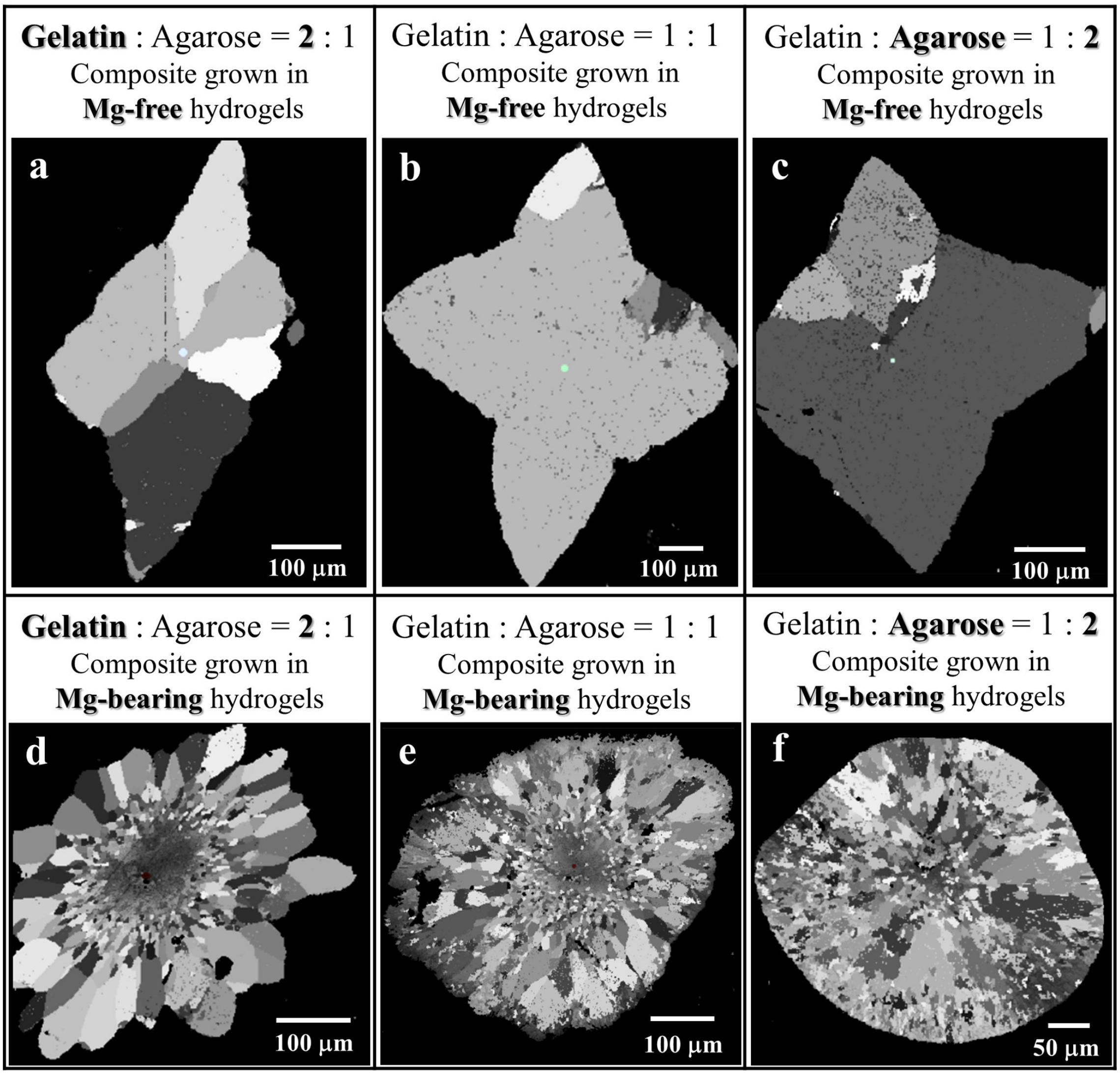

Figure 2.4-4. Patterns of subunit distribution derived from EBSD measurements in composite aggregates obtained with different gel mixtures in Mg-free (a–c) and Mg-containing (d–f) growth environments. Formation of subunits occurs when gelatin is increased (a), and especially when Mg is present (d–f) in the growth medium. Numerous subunits form when Mg is present in the growth environment. Two things are observable: (i) the concentration of minute subunits is the highest in aggregates that formed with an increased amount of gelatin (d) and is lowest when the agarose content is raised (f) in the gel mixture; (ii) subunits size developed a distribution pattern as they increase in size from the center toward the rim of the aggregate when gelatin is increased in the gel mixture, while subunit size distribution is random when the agarose content is raised in the gel mixture.

(but very few) large subunits developed (Fig. 2.4-4c), and the main crystal that constitutes the aggregate is slightly smaller relative to the aggregate formed in G/A 1:1 gel mixture. When gelatin is increased, the aggregate is a mosaic crystal composed of a few (six in Fig. 2.4-4a) radially arranged and fairly similarly sized subunits. When Mg is added to the growth medium, a multitude of subunits formed in all investigated aggregates (Figs. 2.4-4d–f, and 2.4-S5 to 2.4-S7). Their size distribution within the aggregate is structured for aggregates that grew in G/A 1:1 and G/A 2:1 gel mixtures (Fig. 2.4-4e,d), while it is random in aggregates that grew in the G/A 1:2 gel mixture (Fig. 2.4-4f). Hence, in the presence of Mg in the growth medium, an increase in gelatin induces a stringent subunit size structuring (minute in the center and increasing in size towards the aggregate rim, Fig. 2.4-4d), while when agarose is the dominant component in the gel mixture, the microstruc-

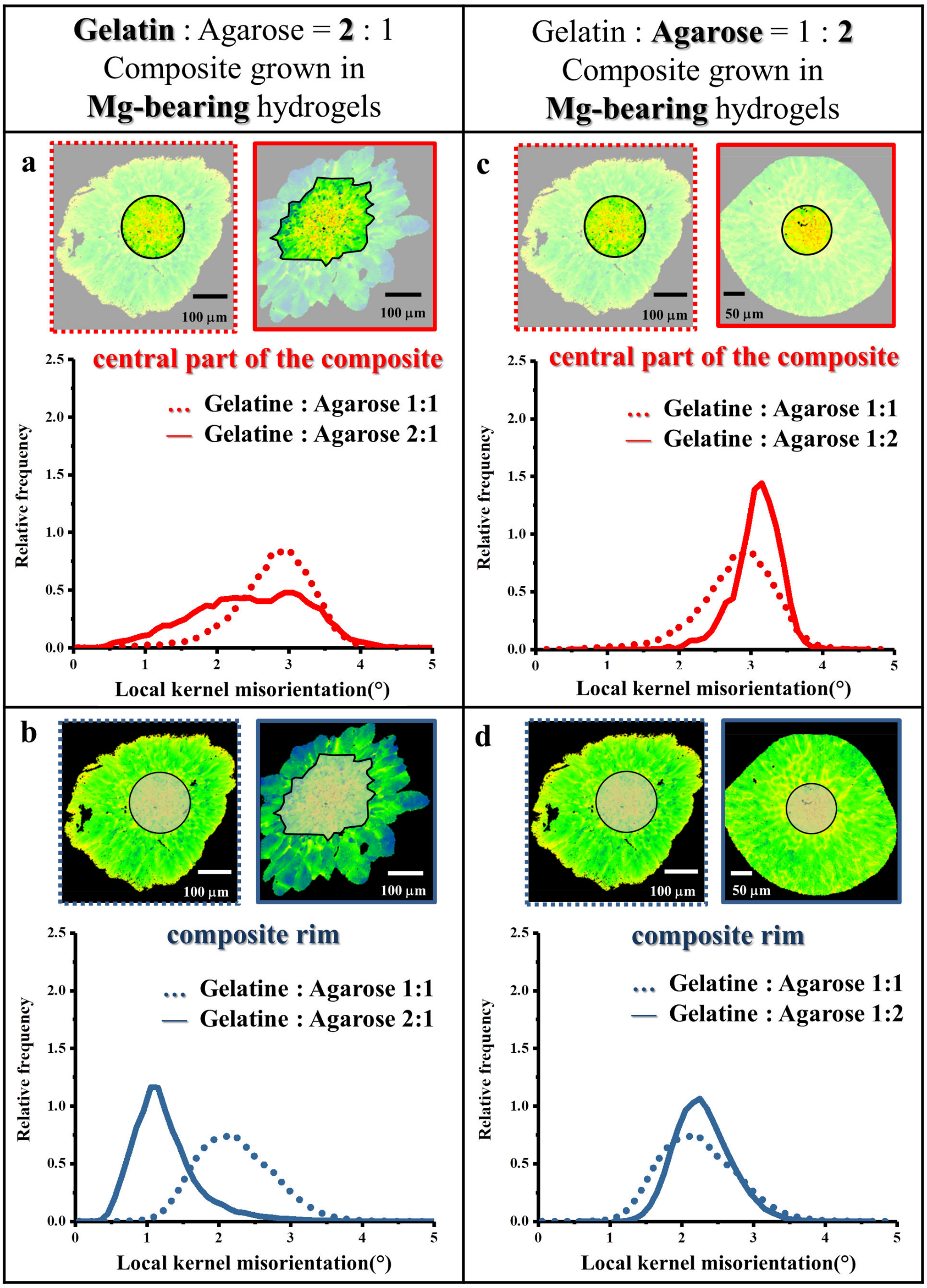

Figure 2.4-5. Relative frequency diagrams of local kernel misorientation visualize small orientation changes of the central and marginal portions of aggregates that formed in gel mixtures with an increased gelatin (a, b) or an increased agarose (c, d) content, respectively, compared to that of an aggregate that grew in the G/A 1:1 gel mixture (shown with a dotted line in panels a–d). When gelatin is increased in the gel mixture, local kernel misorientation in the center is nonuniform and spreads over several degrees. Hence, the local deformation distribution within the center of the aggregate is inhomogeneous. Along its rim, the peak of the local kernel misorientation curve is at 1° with a narrower misorientation spread. Thus, along its rim, a lower degree of local deformation exists and distributes relatively homogeneously to the center of the aggregate. When agarose is increased in the gel mixture, a significantly different pattern of local deformation distribution within the aggregate emerges. The peak of the local kernel misorientation curve in the center part of the aggregate is at about 3° with a more concentrated distribution than that of the G/A 2:1 aggregate. Along the rim of this aggregate, local deformation distribution is quite uniform however slightly more scattered than that in the center.

ture becomes archetypically spherulitic with subunits so small and only slightly misoriented relative to their neighbors that they can hardly be resolved as individuals by EBSD (Fig. 2.4-4f).

Figure 2.4-5 summarizes the difference in local kernel misorientation in the different parts of the aggregate (center and rim) when (i) agarose is increased and (ii) gelatin is increased in the gel mixture. We show these differences relative to our reference aggregate (shown with a dotted red or blue line in Fig. 2.4-5), the composite that grew in the G/A 1:1 gel mixture with Mg in the growth medium (see also Fig. 2.4-S8).

When gelatin is increased in the gel mixture (Fig. 2.4-5a,b), we see very different patterns of local deformation (i) between the center (Fig. 2.4-5a) and the rim (Fig. 2.4-5b) part of same aggregate; (ii) to the aggregate that grew in the gel mixture where agarose was increased (Fig. 2.4-5c,d). Local kernel misorientation in the center is nonuniform and spans several degrees, although the peak position of the curve does not shift much compared to the reference. Accordingly, local deformation is inhomogeneous in this part. Along the rim of the aggregate (Fig. 2.4-5b), the degree of local kernel misorientation is lower than that of the reference crystal, with the peak position of the curve at a misorientation of about 1°. Thus, the degree of local deformation is fairly homogeneously distributed in the rim of the aggregate.

When agarose is increased in the gel mixture (Fig. 2.4-5c,d), local kernel misorientation in the center of the aggregate is shifted to slightly higher values relative to that of the reference (composite grew in the G/A 1:1 gel mixture) as we see the peak is at a misorientation of 3°, and the spread of local kernel misorientation also becomes slightly narrower. Hence, in the center of the aggregate, most crystals have a local kernel misorientation of 3°; local deformation distribution is rather homogeneous. Along the rim of this aggregate (Fig. 2.4-5d), we see comparable characteristics: relative to the reference aggregate, misorientation is also slightly shifted to higher values, and the spread of local kernel misorientation is slightly more concentrated. This translates to a slightly more homogeneous pattern of local deformation along the rim of the aggregate.

FE-SEM images of Figures 2.4-S9 to 2.4-S11 depict morphological characteristics of the three gel mixtures including the porosity of the gel mixture network after the crystallization experiments. We see clear differences in the fabric of the three different gel mixtures, however, no major difference in gel network structure between a specific gel used in Mg-free and Mg-containing experiments. Irrespective of the presence of Mg in the growth medium, gel mixtures with an increased agarose content (G/A 1:2, Fig. 2.4-S9) have a fibrous appearance and display highly varying pore sizes. This is especially obvious for the gel mixture that was used in experiments that were devoid of Mg (Fig. 2.4-S9a), we find two different porosities: very small pores that are surrounded by large and thick pores. Less difference in pore size is present in the Mg-bearing gel mixture (Fig. 2.4-9b). When the gelatin content is increased (Fig. 2.4-S10), the gel mixture shows a denser fabric. Domains with a granular appearance are present and are separated from each other by short-ranged gel accumulations, indicating the formation of membranes (yellow stars in Fig. 2.4-S10a). The addition of Mg to the G/A 2:1 gel does not alter significantly the overall fabric of the gel mixture (Fig. 2.4-S10b). The main difference is in the absence of gel accumulations and the existence of slighter larger pores surrounding dense gel regions (Fig. 2.4-S10b). Figure 2.4-S11 presents SEM images of the G/A 1:1 gel mixture. This gel fabric is the least homogeneous, containing regions where the fabric is dense like a sheet (red stars in Fig. 2.4-S11a,b), portions with thick fibers (yellow stars in Fig. 2.4-S11a,b), and regions where very large pores formed due to rupture of the walls of smaller pores. We do not find a significant difference in the structure between the G/A 1:1 gel mixture used for aggregate growth in Mg-free and

Mg-containing media. We can only observe that broken pore walls and, consequently, very large pores are less abundant in the Mg-bearing gel.

EDS analyses were carried out on aggregate surfaces (Fig. 2.4-1) as well as on planes cut through the composites (Fig. 2.4-S12). Mg contents on aggregate surfaces are highly variable. For composites that formed in the G/A 1:1 gel, detected Mg content was up to 16 mol% $MgCO_3$. The highest Mg content detected on aggregate surfaces that formed in the presence of increased gelatin content was 20 mol% $MgCO_3$, while aggregates that grew in gels where agarose was increased showed up to 32 mol% $MgCO_3$.

The Mg content that we find on aggregate surfaces appears to vary with the morphological complexity of the aggregates. Regardless of the gelatin to agarose wt% ratio in the gel mixture, analyses on the surface of sheaf- and flower-like composites yield Mg contents that range from 1 to 3.5 mol% $MgCO_3$. On surfaces of spherical and morphologically complex aggregates, we find much higher Mg concentrations, up to 32 mol% $MgCO_3$. This might indicate that morphologically complex composites are compositionally inhomogeneous, with differences above 15 mol% $MgCO_3$ in the Mg content.

EDS analyses carried out on planes cut through the composites (Fig. 2.4-S12) point to a structured pattern of Mg distribution within the aggregates. The EBSD measurements that we report in this study were also carried out on these planes where we performed the EDX analyses. The lowest Mg content was measured for the aggregate that was obtained in the gel mixture with an increased gelatin content (Fig. 2.4-S12d), while we find a slightly higher Mg content on planes through aggregates that grew in G/A 1:1 and G/A 1:2 gel mixtures (Fig. 2.4-S12e,f). For all aggregates, we find differences in Mg content between the central and the peripheral part of the composite (Fig. 2.4-S12d–f). For the aggregate that grew in the G/A 2:1 gel mixture (Fig. 2.4-S12d) Mg concentration decreases from the center toward its rim, while for aggregates that grew in the G/A 1:1 and G/A 1:2 gel mixture the Mg concentration increases from the aggregate center toward its rim (Fig. 2.4-S12e,f). An Mg-rich rim (Fig. 2.4-S12e) seams the aggregate that formed in G/A 1:1 gel. Furthermore, a significant enrichment in Mg is observable in some marginal regions of the aggregate that grew in a gel mixture with an increasing amount of agarose content (Fig. 2.4-S12f).

Calcite organization

Figures 2.4-6, 2.4-7, 2.4-8, and 2.4-S13 to 2.4-S15 highlight the mode of calcite organization in the composites that formed in Mg-free (Fig. 2.4-6a–c) and Mg-containing (Figs. 2.4-6d-f, 2.4-7, 2.4-8, 2.4-S13 to 2.4-S15) growth environments. Calcite orientation is presented with color-coded EBSD maps and corresponding pole figures showing both c- and a*-axes data sets as well as density distributions. The strength of crystal co-orientation is expressed as multiples of uniform (random) distribution (MUD) values, derived from c- and a*-axes pole density distributions. The MUD value is high when crystallites are well co-oriented, and it is low when crystallites are poorly co-oriented (e.g. in the case of polycrystals). As the uniformity of colors shows, calcite co-orientation is high for all aggregates that grew in gel mixtures devoid of Mg (Fig. 2.4-6a–c). Crystal co-orientation strength is the highest when agarose is increased in the gel mixture (MUD value of 405, Fig. 2.4-6c), while an increase of gelatin lowers the strength of calcite co-orientation (MUD value of 337, Fig. 2.4-6a). We measured crystallite co-orientation strength on a calcite single crystal grown from solution (Fig. 2.4-S1a), and obtain a MUD value of 673; calcite co-orientation strength in this crystal is very high, all measured 100,500 orientation data points are superimposed onto each other (see pole figures in Fig. 2.4-S1a).

When Mg is added to the growth medium, a multitude of subunits develops (Fig. 2.4-6d–f)

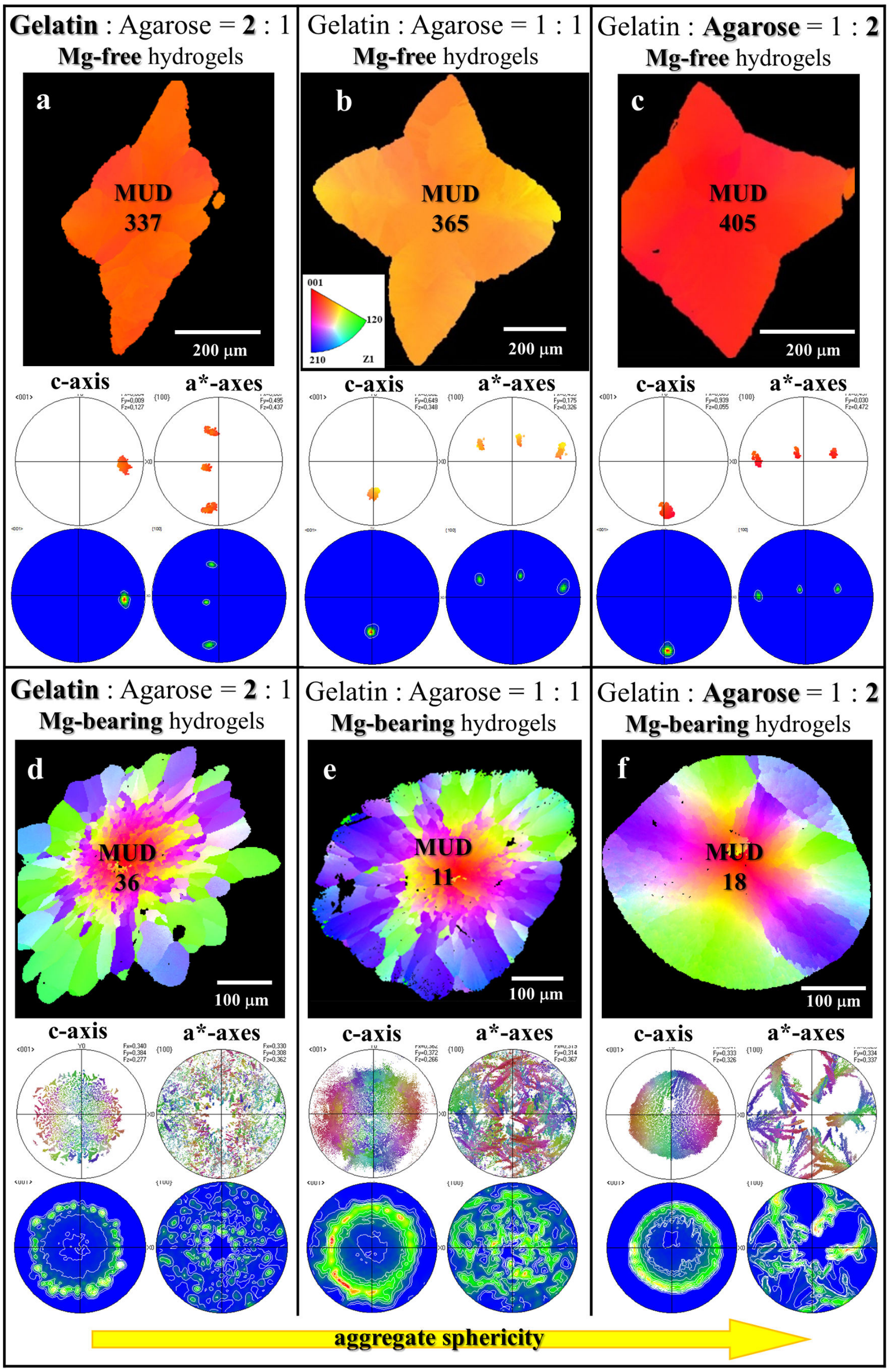

Figure 2.4-6. Color-coded EBSD maps and corresponding c- and a*-axes pole figures giving the (i) orientation data points and (ii) pole density distributions depicting patterns of calcite orientation in aggregates obtained in the three gel mixtures in Mg-free (a–c), and Mg-bearing (d–f) growth medium. Crystal co-orientation strengths, expressed with MUD values, are given for each aggregate (EBSD map). The calcite present in the aggregates grown in Mg-free environments is highly co-oriented (a–c), while the calcite comprised of aggregates obtained in Mg-bearing growth solutions is significantly more misoriented (d–f) and spherulitic. For aggregates formed without Mg, calcite co-orientation strength increases when the content of agarose is increased (c), while it decreases when the content of gelatin is increased (a). When Mg is added to the growth medium, we find an increase in MUD for both, an increased content of agarose (f) as well as an increased content of gelatin (d) relative to the MUD value that we calculate for the aggregate that we obtain in the G/A 1:1 gel mixture (e). The color code in panel (b) is valid for all the panels in this figure.

and calcite co-orientation strength decreases significantly: MUD values are 36, 11, and 18 for aggregates that grew in the G/A 2:1, G/A 1:1, and G/A 1:2 gel mixtures, respectively. The highest MUD value was obtained for the aggregate that grew in a gel mixture where the gelatin content was increased, a feature that corresponds to our observation that this aggregate has the least amount of local deformation (Fig. 2.4-3d). This aggregate shows also the highest consistency in subunit size distribution so that there is a steady increase in subunit size from the center to the rim of the aggregate (Fig. 2.4-6d). The least calcite co-orientation strength is present in the composite that grew in the G/A 1:1 gel mixture (Fig. 2.4-6e). For the composite that grew in a gel mixture with increased agarose content, we observe only a slight increase in calcite co-orientation strength (Fig. 2.4-6f) relative to the reference crystal that grew in the G/A 1:1 gel mixture. As the pole figures in Figure 2.4-6d–f show, for all three aggregates calcite c-axes are tilted between 40 and 90 deg out of the plane of view (Fig. 2.4-6d–f), while a*-axes are randomly oriented for the aggregate that grew in a gel mixture where the gelatin content was increased (Fig. 2.4-6d) and increases when the agarose content is increased in the gel (Fig. 2.4-6f).

For aggregates that grew in Mg-containing growth environments, we investigated the mode of calcite organization in more detail (Figs. 2.4-7, 2.4-8, and 2.4-S13 to 2.4-S15). Irrespective of the used gel mixture calcite crystal orientation, in the very center of all composites that grew in an Mg-bearing environment, the calcite c-axes are pointing 90° out of the plane of view with the crystals having a high co-orientation strength (Figs. 2.4-7a,d, and 2.4-8b). MUD values are 55 (Fig. 2.4-7a) for the aggregate that grew in G/A 1:1 gel mixture, 104 (Fig. 2.4-8b) for the aggregate that grew in the G/A 1:2 gel mixture and 99 (Fig. 2.4-7d) for the composite that grew in G/A 2:1 gel mixture, respectively. This central region of high crystal co-orientation is flanked by an aggregate portion with larger subunits (Fig. 2.4-7b,e). Here MUD values are significantly lower, 11 (Fig. 2.4-7b) for the aggregate that grew in the G/A 1:1 gel mixture and 15 (Fig. 2.4-7e) for the composite that formed in the G/A 2:1 gel. The rim of aggregates shown in Figure 2.4-7 is formed by an assembly of large subunits (Fig. 2.4-7c,f). MUD values increase slightly. MUD is 16 for the composite that formed in the G/A 1:1 gel (Fig. 2.4-7c) and 58 for the aggregate that grew in the G/A 2:1 gel mixture (Fig. 2.4-7f), respectively. The increased MUD value for the aggregate that grew in a gel mixture with an increased gelatin content is in concert with the observation that the subunits along the rim of this aggregate contain little local deformation (see Fig. 2.4-3d).

The aggregate that grew in the gel mixture with an increased agarose content forms a special case. Even though this aggregate consists of three different subunits (Fig. 2.4-8c–e) that are highly misoriented to each other (80° misorientation between subunit 1 and subunit 2; Fig. 2.4-8a, misorientation versus distance diagram D), the overwhelming part of the aggregate is formed solely by one entity, or subunit, entity no. 2 (Fig. 2.4-8d). Calcite crystallites within the subunits are highly co-oriented and are arranged in a perfectly graded spherulitic fashion, (misorientation versus distance curves A, B, C, and E in Fig. 2.4-8, and Fig. 2.4-S15). The misorientation versus distance profiles A, B, C prove the degree of gradation is highest (almost perfect) in the center of the aggregate (Profile C, Fig. 2.4-8a), while it becomes slightly disturbed along its rim (Profile A, Fig. 2.4-8a). This is in contrast to the calcite arrangement in composites that grew in the G/A 1:1 and G/A 2:1 gel mixtures. In the latter two aggregates, a graded arrangement of calcite is only present in the central part of the aggregates and not along their rim; in the latter misorientation between subunits scatters in the range of a few tens of degrees. It should be noted that even though there is a perfect gradation in calcite organization for the composite that formed in the gel mixture

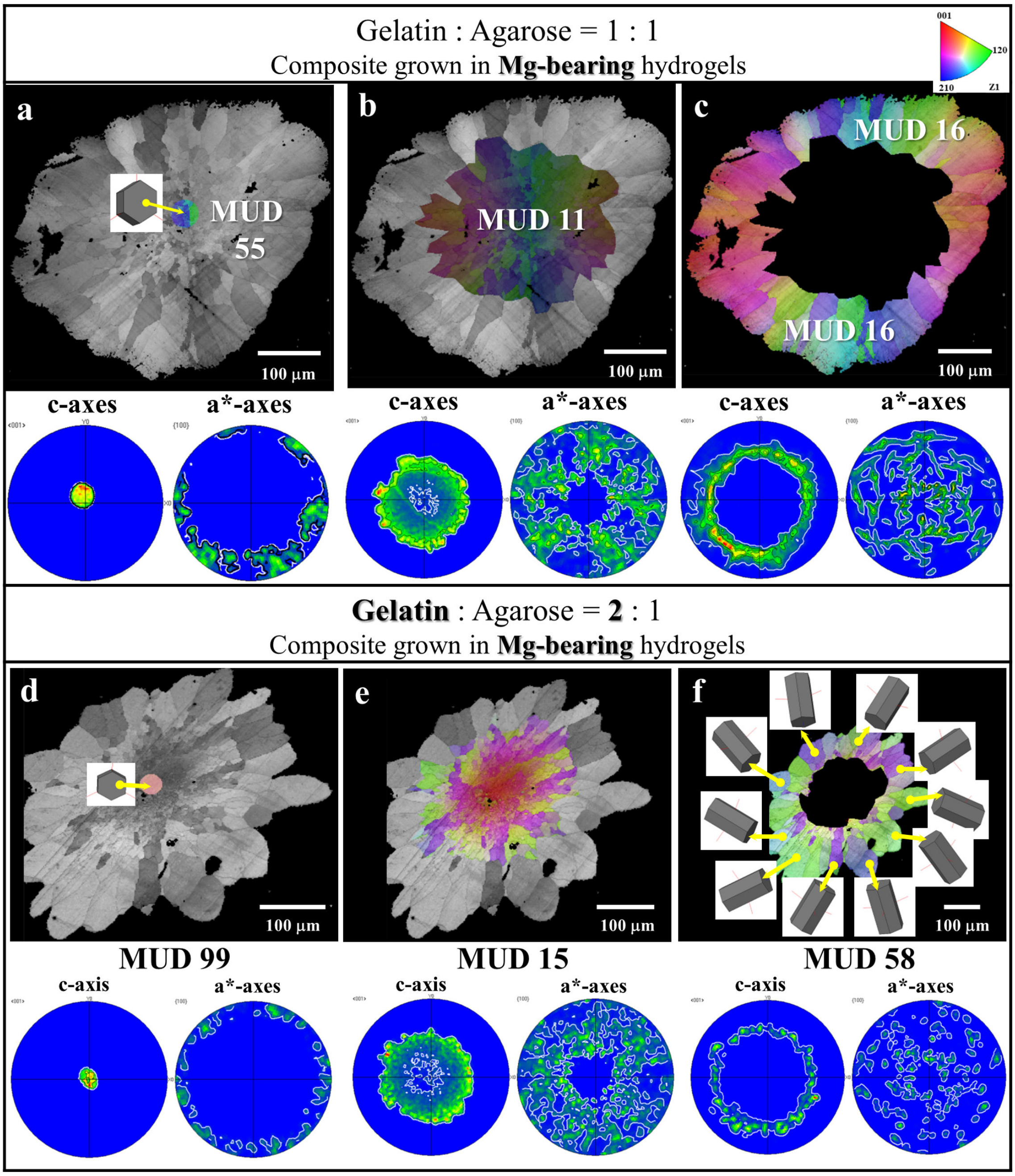

Figure 2.4-7. Color-coded EBSD and gray-scaled band contrast maps with corresponding pole figures show patterns of calcite organization in Mg-bearing hydrogel-calcite composites grew in the G/A 1:1 gel (a–c), and G/A 2:1 gel (d–f). Three regions can be distinguished within the composites: (a, d) an innermost portion with calcite crystallites in high co-orientation (MUD values of 55 and 99) of minute crystallite size, and the c-axis of calcite crystals oriented pointing out of the plane. This central region is surrounded by an aggregate portion that is formed by an assembly of slightly larger crystallites (b, e), which has a lower degree of co-orientation strength (MUD values are 11 and 15). The rim of the aggregate is seamed by an assembly of large subunits, and calcite c-axes are now within the plane of view (c, f). Calcite crystal co-orientation strength increases; MUD values are 16 and 58. The color code (top right) is valid for all the panels in this figure.

with an increased amount of agarose (Figs. 2.4-8, and 2.4-S15), entity/subunit size distribution within this aggregate is random (Fig. 2.4-8c–e). This characteristic is in contrast to subunit size distribution patterns in aggregates that formed in the G/A 1:1 and G/A 2:1 gel mixtures. In the two latter aggregates, subunit size gradation is well observable and is more regular (especially for the aggregate that grew in a gel mixture with increased content of gelatin, e.g., Fig. 2.4-4d,e,

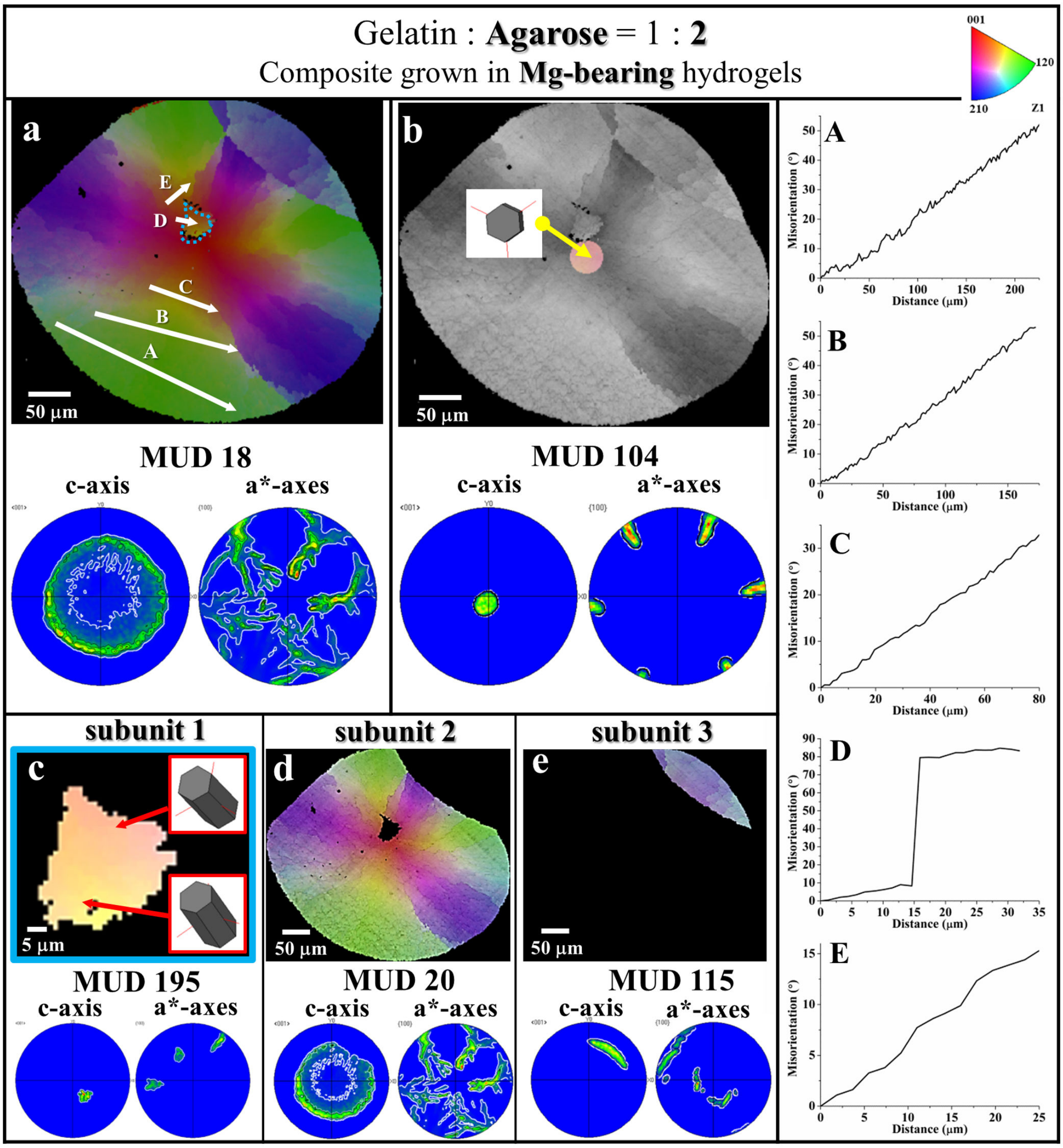

Figure 2.4-8. Color-coded EBSD and gray-scaled band contrast maps, corresponding pole figures, and misorientation versus distance diagrams show patterns of calcite organization in a spherulitic hydrogel-calcite composite that grew in the gel G/A 1:2 with Mg in the growth medium. The aggregate comprises three subunits: a central subunit 1 (c); subunit 2 (d), an archetypical spherulitic object with an almost continuously graded change in crystallographic orientation of the constituting crystallites, which located around the center; subunit 3 (e), which is placed at the rim of the aggregate. Subunit 2 forms the largest part of the aggregate, at its center (b) calcite c-axis is pointing out, while along with its rim calcite c-axis orientation is more within the plane of view. Misorientation versus distance diagrams A–E (location of profiles is shown in (a) visualize differences in calcite assembly within different parts of the aggregate. While calcite alignment within individual subunits is highly graded (profiles A, B, C, E), misorientation between neighboring subunits is very high (e.g., 80° between subunit 1 and subunit 2; profile D). The strength of calcite co-orientation within the large subunit is low (d, MUD value: 20); it increases significantly in the two small subunits (MUD values: c, 195; e, 115). The color code (top right) is valid for all the panels in this figure.

and Figs. 2.4-S13 and 2.4-S14).

Hierarchical organization of the mineral

The three different gel mixtures in combination with Mg in the growth medium induce different modes of calcite organization, not only within individual subunits but also in the as sembly of subunits within a particular aggregate. We find a hierarchical organization of calcite within the aggregates; hierarchy is different for the three investigated composites.

Figure 2.4-9a–c shows, for each aggregate, c- and a*-axes orientations for one individual subunit. Calcite co-orientation strength within an individual subunit is lowest for the composite that formed in the G/A 1:1 gel mixture (black arrows in Fi. 2.4-9b), while it is highest for the composite that formed in G/A 2:1 gel mixture, thus, for a subunit that grew in a gel with an increased gelatin content (green arrows in Fig. 2.4-9a). The orientation spread in c- and a*-axes is minimal for subunits in the G/A 2:1-calcite composite, while it is highest for the subunits of the G/A 1:1-calcite composites.

Calcite organization in subunits of the G/A 1:2 aggregate (red arrows in Fig. 2.4-9c) is intermediate between that of the G/A 1:1 and that of the G/A 2:1 aggregates. On the one hand, the limited spread in c- and a*-axes distribution resembles the pattern that we find for subunits of the aggregate that formed in the gel mixture where gelatin was increased. However, the smooth change in color in the pole figure for both crystallographic axes (Fig. 2.4-9c, as well as in the EBSD map) visualizes well the stringently graded mode of calcite c- and a-axes orientation variation. Some gradedness in calcite orientation is also present in subunits that grew in the G/A 1:1 gel mixture, but it is not as pronounced as it is the case when agarose is increased in the gel mixture.

On the next hierarchical level, when the interlinkage of all subunits is considered (thus, the entire aggregate), the composite that grew in a gel mixture with an increased gelatin content shows the lowest degree of subunit coalignment, especially as the calcite a*-axes are concerned (see pole figures in Fig. 2.4-9a,d). In contrast, an increase in agarose in the gel mixture induces a marked coalignment between subunits, for both the c- and the a*-axes (see pole figures in Fig. 2.4-9c,e). If we only considered the coalignment of the a*-axes of the entire aggregate, it is increased when the agarose content is increased in the gel mixture (Fig. 2.4-9c,e), while it decreases when gelatin is increased in the gel mixture (Fig. 2.4-9a,d).

2.4.4 Discussion

Figure 2.4-10 summarizes structural characteristics of aggregates that formed in the different hydrogel mixtures; Figure 2.4-10a shows difference in local deformation due to gel occlusion and/or Mg incorporation with in the aggregates, Figure 2.4-10b–g shows the aggregate morphology, development of subunits, subunit size distribution, and Figure 2.4-10h–m shows the aggregate texture.

Consequences of hydrogel occlusion

The absence or presence of Mg in the growth medium induces a significant difference in aggregate morphology (Figs. 2.4-6, and 2.4-10a). Without Mg in the growth medium, the aggregates are elongated rhombohedra, while when Mg is added, they are spherical (Figs. 2.4-6, and 2.4-10b–g) aggregates. The obtained morphologies that developed in mixed gels are similar to those that formed in either pure gelatin or pure agarose gels (Nindiyasari *et al.* 2014a,b). In all cases, aggregate morphology is dominated by F faces (104), which are terraced with growth steps that run parallel to periodic bond chain directions (Heijnen 1985).

Our previous studies (Nindiyasari *et al.* 2014b, 2015; Greiner *et al.* 2018) demonstrated that in the absence of Mg in the growth medium a direct relationship exists between the amount of occluded gel and the microstructural organization of the composite. Low amounts of gel occlusion result in the formation of calcite aggregates that show high crystal coalignments. MUD values of these are high and are close to those found for calcite single crystals grown from solution (Kim *et al.* 2014). In contrast, incorporation of a high amount of gel into the aggregates leads to the formation of composites with low

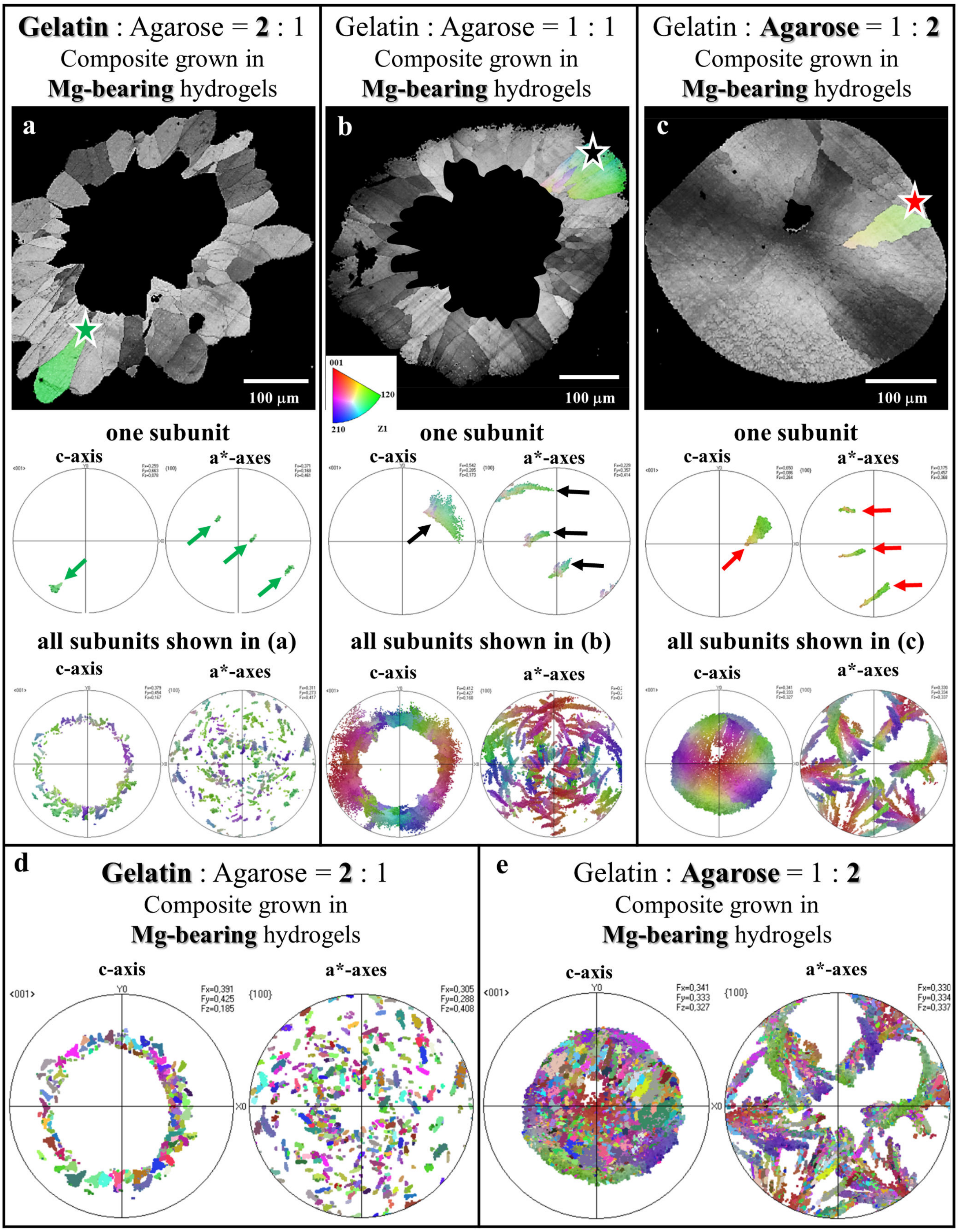

Figure 2.4-9. Differences in calcite organization in individual, as well as in assemblages of subunits between aggregates that formed in G/A 2:1 (a), G/A 1:1 (b), and G/A 1:2 (c) gel mixtures with Mg in the growth medium. Panels a, b, c show patterns of individual calcite subunit orientation color-coded, while panels d and e highlight all calcite subunits in subunit/aggregate organization in random color. Calcite is best co-oriented in the individual subunit of the aggregate that formed in the G/A 2:1 gel mixture and is least co-oriented in subunits of an aggregate that developed in the G/A 1:1 gel mixture. The calcite that assembles the subunits of an aggregate that grew in the gel mixture with increased agarose content is stringently graded by a high density of small angle misorientations. When calcite organization is assessed on a higher hierarchical level, the least co-orientation is observed for aggregates that form in a hydrogel with an increased gelatin content (d) in comparison to aggregates that develop in a gel mixture with an increased agarose content (e). The color code in (b) is valid for panels a–c in this figure.

MUD values and significant differences in crystallite orientation pattern (Nindiyasari *et al.* 2014b, 2015; Greiner *et al.* 2018). The formation of subunits that constitute the aggregates depends on the pattern of distribution of the occluded gel (Nindiyasari *et al.* 2015; Greiner *et al.* 2018). When the distribution is homogeneous, few subunits develop (Nindiyasari *et al.* 2015; Greiner *et al.* 2018). Inhomogeneities in the amount of incorporated gel result in local gel accumulations and lead to the formation of membrane-like gel walls. All these lead to the formation of polycrystalline aggregates that comprise many subunits that are misoriented to each other.

Estroff and her co-workers demonstrated that the amount of occluded gel by the growing crystal is controlled by the balance between two parameters: gel strength and growth rate (Asenath-Smith *et al.* 2012). Gel strength is an intrinsic property of the hydrogel, which in physical gels (e.g. gelatin and agarose) is directly correlated with their solid content (Asenath-Smith *et al.* 2012; Nindiyasari *et al.* 2015; Greiner *et al.* 2018). Gel strength determines the response of the hydrogel to crystallization pressure, the pressure that the growing crystal exerts against the gel fabric (Asenath-Smith *et al.* 2012; Nindiyasari *et al.* 2015; Greiner *et al.* 2018). Moreover, there is a direct correlation between crystallization pressure and growth rate and, consequently, supersaturation. Hence growth rate relates directly to supersaturation (De Yoreo & Vekilov 2003). According to Estroff's model, the highest amount of gel occlusion is reached when a crystal grows at fast rates in a strong gel; in this case, all the gel would become incorporated into the mineral (Li & Estroff 2007, 2009; Li *et al.* 2011a; Asenath-Smith *et al.* 2012). On the other hand, a slowly growing crystal in a weak gel would form virtually gel-free (Asenath-Smith *et al.* 2012). Different combinations of gel strength and growth rates would result in intermediate amounts of gel becoming incorporated into the growing crystal (Li & Estroff 2007, 2009; Li *et al.* 2011a; Asenath-Smith *et al.* 2012; Greiner *et al.* 2018).

Although Estroff's model explains the main characteristics of gel occlusion by a growing crystal, it fails to account for all the complexity of the gel occlusion process. It does not take into account that the growth process can modify the fabric of the gel as well (Greiner *et al.* 2018). It is generally acknowledged that the characteristics of a growing crystal are altered by the occlusion of a polymer matrix, as this matrix introduces strain into the crystal lattice (Pokroy *et al.* 2015). However, it has rarely been taken into account that the structure of the matrix can also be altered, by the crystal that forms. For example, fibers of a light gel, whose gel strength is too weak to resist crystallization pressure, will be pushed ahead by the growing crystal. These fibers will approach other fibers, and gel density will increase locally. As a direct correlation exists between gel strength and gel density, and as more fibers are pushed ahead and approach each other, the gel fabric around the growing crystal becomes stronger (Greiner *et al.* 2018). This effect will make it likely that the gel at this particular site will be occluded into the mineral, provided that the growth rate does not decrease.

Furthermore, there is a relationship between gel density and features of the gel porosity network. Changes in the latter can modify diffusivity properties of the gel network, thereby hindering mass transfer to the growth front (Nindiyasari *et al.* 2014b; Greiner *et al.* 2018). The consequence is a decrease in growth rate at these particular sites. Hence, the distribution pattern of occluded gel within the mineral is governed by the complex dynamic interplay between changes in gel strength resulting from a crystal-growth-induced alteration of the gel structure and changes in growth rate as a consequence of mass-transfer-alteration associated with rearrangements of the gel matrix.

Modification of matrix features due to the influence of the growing crystal was identified for

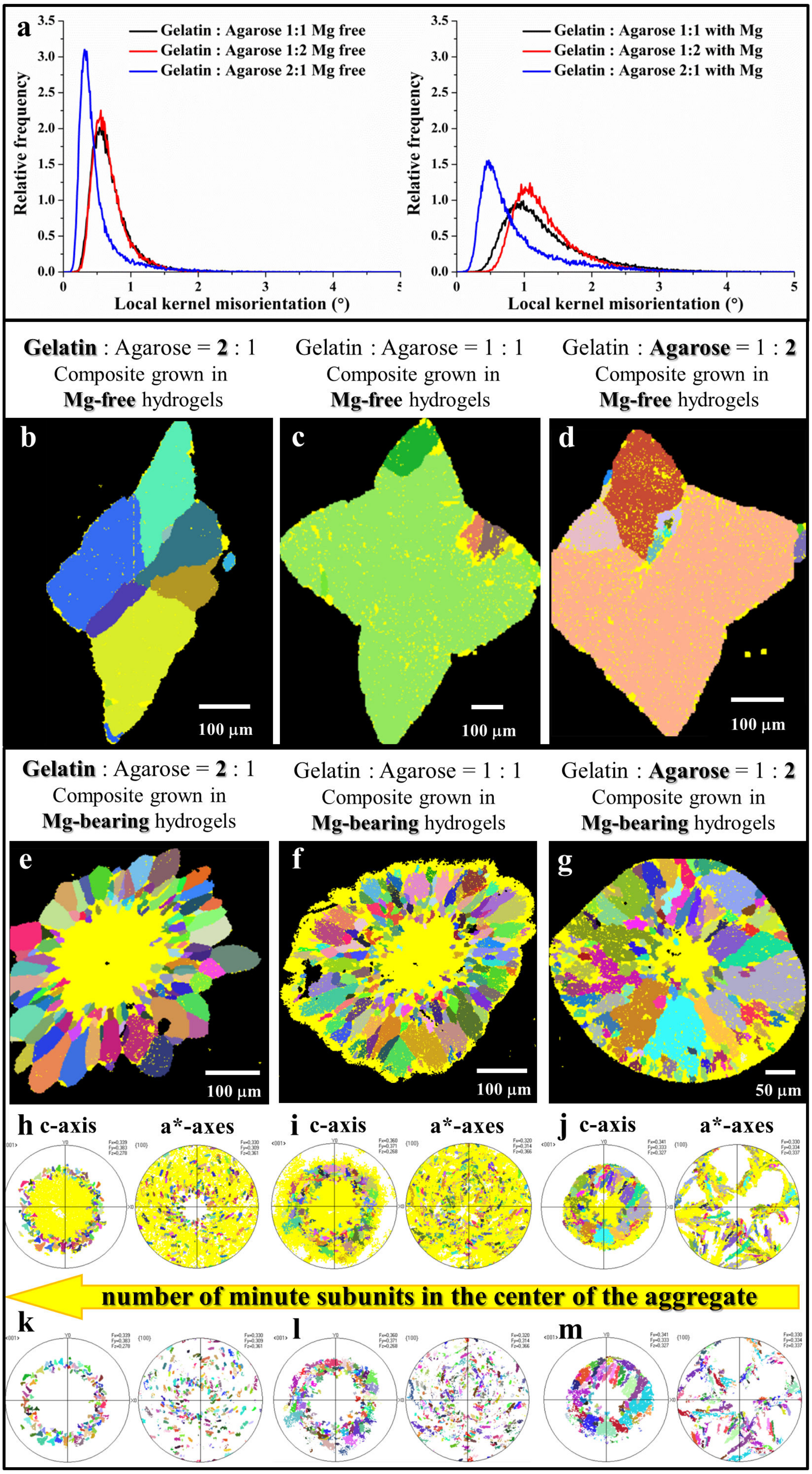
a
Gelatin : Agarose 1:1 Mg free
Gelatin : Agarose 1:2 Mg free
Gelatin : Agarose 2:1 Mg free
Relative frequency
Local kernel misorientation (°)
0.0
0.5
1.0
1.5
2.0
2.5
3.0
3.5
0
1
2
3
4
5
Gelatin : Agarose 1:1 with Mg
Gelatin : Agarose 1:2 with Mg
Gelatin : Agarose 2:1 with Mg
Relative frequency
Local kernel misorientation (°)
Gelatin : Agarose = 2 : 1 Composite grown in Mg-free hydrogels
Gelatin : Agarose = 1 : 1 Composite grown in Mg-free hydrogels
Gelatin : Agarose = 1 : 2 Composite grown in Mg-free hydrogels
b
c
d
100 µm
100 µm
100 µm
Gelatin : Agarose = 2 : 1 Composite grown in Mg-bearing hydrogels
Gelatin : Agarose = 1 : 1 Composite grown in Mg-bearing hydrogels
Gelatin : Agarose = 1 : 2 Composite grown in Mg-bearing hydrogels
e
f
g
100 µm
100 µm
50 µm
h c-axis
a*-axes
i c-axis
a*-axes
j c-axis
a*-axes
number of minute subunits in the center of the aggregate
k
l
m

Figure 2.4-10. Summary, derived from EBSD measurements, of the cooperative influence of Mg and gelatin-agarose composites on local deformation within the mineral (a), subunit formation and subunit size distribution within the aggregate (b–g), and mode of calcite organization in aggregates that grew in the different gel mixtures with Mg in the growth medium (h–m). For better visualization of mineral organization within the aggregate, we distinguish between the minute and very small subunits (shown in yellow) and larger and large-sized subunits (shown in random color) in (e–j). Pole figures (k–m) visualize only the texture of the larger/large subunits. Colors in EBSD maps and corresponding pole figures are random colors and do not code for orientation. Diagrams of relative frequency of local kernel misorientation (a) visualize differences in local deformation and, thus, the degree of small orientation changes between aggregates that formed in Mg-free and in Mg-containing growth environments. Aggregates that formed without Mg in the growth medium comprise very few subunits (b–d), in contrast to aggregates that grew in Mg-containing growth media (e–g). An increase in gelatin affects the formation of a multitude of small subunits, all of them being located in the center of the aggregate and being seamed by large subunits with calcite in these being highly co-oriented (see pole figures in h and k). An increase in agarose induces the formation of distinctly sized subunits, which are distributed all over the aggregate and exhibiting a highly graded pattern of calcite orientation (see pole figures in j and m).

gelatin, agar, and agarose hydrogels (Nindiyasari *et al.* 2015; Greiner *et al.* 2018). These involve changes in (i) hydrogel pores and (ii) gel fiber structure. Changes of hydrogel pores relate to the distribution of pore sizes and the presence or absence of broken pore walls. Changes regarding gel fibers refer to the degree of bundling of the gel fibers when these are pushed together by the growing crystal. This can result in the formation of fiber assemblies, the formation of membrane-like structures, but also to the dispersion of gel. The consequence is the development of inhomogeneities in the distribution of the occluded gel that, in turn, leads to the formation of aggregates with an increased number of subunits. Misalignments between these subunits relate to the amount of occluded gel and the homogeneity of its distribution over the volume of the subunit.

Agarose hydrogels are stronger than gelatin hydrogels even with similar solid contents (product specification sheets, Sigma-Aldrich (Normand *et al.* 2000; Boran *et al.* 2010). Consequently, among the three gel mixtures investigated in this work, the strongest gel is the G/A 1:2 gel mixture and it can be expected that the fabric of this gel mixture will be the least altered when it becomes occluded within the growing crystal. This is the case if we regard features depicted in Figure 2.4-S9a: Fiber thickness and pore size distribution are remarkably homogeneous compared to those shown in Figure 2.4-S10a (G/A 2:1) and Figure 2.4-S11a (G/A 1:1), where membrane-like gel accumulations and strikingly high differences in pore size and gel fiber thickness can be observed. It is worthwhile to note that the highly homogeneous fabric of the occluded G/A 1:2 mixture correlates with the smaller number of subunits and the highest MUD value (405) observed for the three types of aggregates (Fig. 2.4-6a–c). The higher inhomogeneity of the occluded matrix fabric (Mg-free G/A 2:1 and Mg-free G/A 1:1 gel mixtures) correlates well with their lower MUD values (337 and 365, Fig. 2.4-6a,b) and, as the aggregate that formed in the Mg-free G/A 2:1 gel mixture is concerned, with the formation of a higher number of subunits (Figs. 2.4-3a, and 2.4-4a). This latter feature can be explained because, even though the gel strength of this gel mixture is higher than that of the G/A 1:1 gel mixture, it is not high enough to prevent gel fibers from being pushed ahead by the growing crystal. Because of the higher density of fibers in this gel mixture compared to the G/A 1:1 gel, a higher number of fibers will be pushed together by the growing crystal; hence, more membrane-like gel accumulations will develop (yellow stars in Fig. 2.4-S10a), separating regions within the aggregate that are misoriented to each other and thereby explaining the lower MUD value of entire aggregate (Fig. 2.4-6a).

Influence of magnesium

Our study shows that one of the major microstructural and morphological differences between composite aggregates obtained in a Mg-free and Mg-containing growth media is that those aggregates that grew in Mg-containing growth environment consist of numerous and differently sized subunits (Figs. 2.4-1d–f, 2.4-4, 2.4-6, and 2.4-10b–g). These subunits are arranged according to patterns that are characteristic for each gel mixture. We also find some common features: (i) very low MUD values compared to their Mg-free counterparts, (ii) graded calcite alignments within the subunits, and (iii) high misorientations between neighboring units. We found similar features in composite aggregates grown in Mg-containing pure gelatin and pure agarose gels (Nindiyasari *et al.* 2014a) and relate these to effects derived from Mg incorporation into the calcite structure substituting Ca (Nindiyasari *et al.* 2019). This substitution provokes the tilting of the planar carbonate groups and, as a consequence, induces structural disorder (Bischoff *et al.* 1985; Urmos *et al.* 1991). In addition, aggregates are not homogeneous regarding their Mg content (Fig. 2.4-S12) but show specific patterns of Mg content distribution. Mg content inhomogeneity induces lattice mismatch between regions with different Mg concentrations. It has been demonstrated with AFM and molecular dynamics modeling that accommodation of lattice strain induced by Mg-related lattice mismatch between Ca-calcite and Mg-calcite occurs through segmentation into microcrystals and involves the formation of dislocations (Astilleros *et al.* 2010; Sethmann *et al.* 2010). The progressive accumulation of dislocations at low angle boundaries could lead to the observed graded alignment of calcite crystals and the formation of the very many subunits.

It can also be argued that the correlation between higher Mg contents and higher amounts of occluded gel within the composite indicates that Mg enters the aggregate adsorbed onto the gel rather than substituting Ca in the calcite structure. We do not deny that a small amount of Mg incorporated into the aggregates is connected to the occluded gel through active groups of gelatin or/and agarose. However, Raman spectra of calcite aggregates grown in Mg-containing gelatin gel showed a marked broadening of bands as well as a shift toward higher frequencies corresponding to the CO_3^{2-} symmetric stretching mode ($\nu 1$) and the CO_3^{2-} in-plane bending mode ($\nu 4$) (Bischoff *et al.* 1985; Urmos *et al.* 1991; Nindiyasari *et al.* 2014a). Band broadening and band shifting are typical features for Mg-calcite. This feature together with the observation of a correlation of a bandwidth increase with the Mg content of calcite aggregates supports the interpretation that most of the Mg incorporate into the calcite structure and substitutes Ca (Nindiyasari *et al.* 2014a). It has been argued (Elhadj *et al.* 2006; Nindiyasari *et al.* 2014a) that this incorporation could be facilitated by active functional groups like amino acids, peptides, and other moieties present in gelatin and agarose fibers. These moieties would promote Mg desolvation, thereby counterbalancing the inhibitory effect of Mg on calcite growth (Elhadj *et al.* 2006; Nindiyasari *et al.* 2014a). It is important to note that as soon as experiments start reagent counter-diffusion through the hydrogel leads to the development of space-temporal reagent concentration, pH, and supersaturation gradients in the system. Since the activity of functional groups strongly depends on pH, the existence of space-temporal pH gradients can determine that calcite crystal aggregates growing near each other show small differences in their Mg content, as well as differences in the amount and distribution of gel occluded within them. Similarly, some degree of inhomogeneity regarding these features can be expected within given calcite aggregates due to pH and Mg concentration changes along time. Furthermore, since reagent diffusivity through the porosity network of a hydrogel depends on features of the latter like chemical composition and gel solid content, the space-temporal evolution of pH will differ for hydrogels with different gelatin and agarose solid content, which in turn may contribute to modulate gel-calcite composite features. Validating this interpretation of a possible role of pH evolution within hydrogel systems in defining some of characteristics calcite aggregates is beyond the scope of this work and will have to be addressed in future research. On the other hand, the characteristics of the occluded gel fabric in aggregates grown in Mg-containing environments, as visualized after decalcification, are a clear indication that Mg interacts with the gel fibers and affects their mechanical response to crystallization pressure (Nindiyasari *et al.* 2019). Indeed, the fabric of occluded gel in aggregates grown in Mg-free and Mg-containing environments show some differences that refer to gel pore size distribution, gel fiber thickness, and the presence of gel accumulations. In general, pore sizes are more homogeneous, and fibers are thinner in gels that contain Mg. Hence, membrane-like accumulations are absent in composite aggregates grown in a Mg-containing environment. The smaller difference in characteristics of the occluded gel matrix in Mg-containing composites supports the interpretation that the increased number of subunits and the high misalignment between the subunits are features that relate mainly to the effect of Mg incorporation into the calcite structure. Furthermore, it is likely that gel occlusion contributes to a modulation of the influence of Mg. In this context, it is significant to note that the aggregate that grew in a gel mixture with an increased agarose content consists of only three subunits/entities, an overwhelmingly large one, and two smaller ones, with calcite in all subunits being highly co-oriented and being arranged in a graded fashion. The gel mixture fabric of this aggregate has the most homogeneous features.

Is there a similarity between the occluded hydrogel mixture and biopolymer matrices in invertebrate shell materials?

Skeleton biominerals of marine invertebrates such as mollusks and brachiopods are formed in a thin nanoscale extracellular layer (Checa *et al.* 2014, 2016; Simonet Roda *et al.* 2019b,a) and they contain occluded biopolymers (Nakahara 1983, 1991). It is assumed that this extracellular space is filled with an extracellular polymeric substance (EPS) that is probably gel-like. In this EPS, the crystallization of the mineral takes place, leading to the observed association of the mineral with intracrystalline and intercrystalline organic matrix in invertebrate shells (Nakahara 1983, 1991; Nudelman *et al.* 2006; Checa *et al.* 2009; Nindiyasari *et al.* 2015; Griesshaber *et al.* 2017). This further leads to a pronounced mosaic-spread or misorientation within the mineral crystals (Griesshaber *et al.* 2013; Goetz *et al.* 2014; Maier *et al.* 2014). In contrast, biomineral crystallization in intracellular vesicles as observed in coccolithophores does not lead to occluded intracrystalline biopolymers (Yin *et al.* 2018). The EPS substance is rich in polysaccharides, and it also contains proteins. At present, there are very few studies that examined the true composition of the organic matrices and the structural interconnection of polysaccharides and proteins (Falini *et al.* 2003). This is mainly due to a lack of appropriate methods, such that the structural organization is still subject to hypotheses (Levi-Kalisman *et al.* 2001). With our experiments in a simplified system, we were able to show the trends in the modes of gel incorporation and crystal mosaicity in gels where either protein or polysaccharide is dominant.

Donald and Windle (1992) demonstrated that many polymers have structural characteristics of liquid crystals; materials that can self-assemble into larger units without requiring any confinement. Liquid crystals found in nature are lyotropic: their organization is determined by changes in concentration. Because of the combination of order and mobility, liquid crystals possess the basic requirements for self-organization and play, hence, an important role in nature. The liquid crystal structure that is ubiquitously present in living material, and whose chirality is a highly important characteristic, is a cholesteric structure (Rey 2010; Rey *et al.* 2014; Mitov 2017). Cholesteric liquid crystals form elementary entities such as molecules, macromolecules, and microfibrils of many biological materials, e.g. chitin, collagen, and cellulose (Rey 2010).

Agarose is a polysaccharide and is extracted from marine red algae. The polymer chains form single and double helices that bundle together to a three-dimensional fibrous network when being in gel form. Gelatin is a polypeptide derived from natural collagen and is obtained through hydrolytic degradation. This breaks the triple-helix structure of collagen into single-strand molecules. Experiments of Neville and Luke (1971) have shown that generation of gelatin from collagen causes the denaturation of the original secondary structure and involves the formation of another configuration, a new secondary, however, more structure. Accordingly, important attributes of the original pristine material are lost. Hence, even though the hydrogel systems used in our experiments combine two different molecules in different proportions and have some structural and mechanical properties (fibrous fabric, porosity, viscoelastic behavior), they do not mirror the biochemical complexity of natural systems and lack their capacity for ordering and self-organization.

Extracellularly formed biological structural materials are hybrid mesocrystals, which are morphologically well-defined in three dimensions, contain intercalated biopolymer matrices (membranes, networks of fibrils) and, where organic membranes define morphology, occur in a higher-order superstructure. Cartwright and Checa (2007; 2015) transferred the concept of liquid crystal self-assembly from polymers to biopolymers in structural biological materials. They suggested that scaffold membranes in mollusk nacre form via liquid-crystallization, thus, a self-assembly process. In extrapallial space, chitin/protein fibers form through self-organization first a network of fibrils that with time develops into the membranes of the scaffold matrix. At mineral secretion, the space between the membranes becomes infiltrated through pores in the membranes with aragonite mineral (Cartwright & Checa 2007).

Hence, when characteristics of biopolymer matrices in biological hard tissues and matrices of the studied hydrogels are juxtaposed, we find that some structural features are comparable. However, gelatin and agarose hydrogels do not have the ordering and self-organization capability. Membranes of hydrogels do not form through self-organization but through the bundling of gel fibers that are pushed together by the growing crystals. So formed gel membranes lack any structuring and hierarchy, in contrast to membranes in biological hard tissues. Consequently, large differences can be found between the characteristics of calcite-gel composites and biological hard tissues. However, the study of the effects that the occlusion of hydrogel fibril network within calcite crystals can contribute to understanding the origin of specific features of the mineral component of biominerals, such as its higher lattice strain and lower MUD values, when compared to its geological counterpart (Kim *et al.* 2016; Seknazi & Pokroy 2018). On the other hand, it is well established that biological hard tissues show increased hardness compared to their geological counterpart (Wählisch *et al.* 2014). The enhanced mechanical properties of these biogenic materials are mainly defined by higher thresholds for plastic deformation as well as crack propagation. Plastic deformation relates to glide of dislocations under applied stress, while crack propagation in carbonates is mainly related to crystallographic cleavage. The presence of occluded biopolymers in biological hard tissues on the nanoscale inhibits dislocation glide over large distances. Furthermore, it provides biological hard tissues with tensile strength, a property absent in geological calcium carbonate phases, which can prevent material fracture by inhibiting the opening of cleavage cracks. Understanding the parameters that control gel occlusion and how this phenomenon modulates microstructural arrangements in synthetic organic/inorganic hybrid nanocomposite may be inspirational to develop novel routes for producing materials with enhanced mechanical properties. Blending hydrogels with different chemical moieties as well as

Table 2.4-2. Influence of Mg and agarose-gelatin composites on hydrogel-carbonate aggregate structural and chemical characteristics

		Composite grown in Mg-free hydrogels			Composite grown in Mg-bearing hydrogels		
		G/A 2:1	G/A 1:1	G/A 1:2	G/A 2:1	G/A 1:1	G/A 1:2
Aggregate Formation	morphology	blocky elongated	blocky elongated	blocky elongated spherulitic	spherical with ragged rim	spherical	almost perfect sphere
	aggregate size (μm)	150–400	250–600	300–550	150–500	200–600	90–400
	number of subunits	6	mainly 1	1–3	many	many	3
	subunit distribution pattern	radially arranged		tendency to radial distribution	strict size distribution	little size distribution	no size distribution
Mg incorporation (Distribution)	EDX surface (mol %)				up to 21	up to 16	up to 32
	EDX cutting plane Centre (wt %)				1.36	1.43	1.58
	EDX cutting plane Rim (wt %)				0.8	2.81	2.19
Calcite Orientation	overall co-orientation (MUD)	337	365	405	36	11	18
	co-orientation in the center (MUD)				99	55	104
	co-orientation at the rim (MUD)				58	16	18
Mineral Assembly	texture and microstructure	mosaic crystal	mosaic crystal	almost single crystal	radial polycrystal	radial polycrystal	finely graded spherulite

water diffusivities and Young's and shear modules provides a wealth of possibilities to tune mechanical and microstructural properties of these hybrid materials (Lopez-Berganza *et al.* 2017, 2019; Caccavo *et al.* 2018).

2.4.5 Conclusions

Attachment, morphology, phase, and organization of crystals in biological carbonate structural materials are regulated by a complex set of macromolecules. These form matrices, are occluded within the skeleton, and organize biocrystallites spatially to biomaterials with intricate microstructures and specific textures. Hydrogels mimic to some extent chemical and physical characteristics of biological matrices, as these consist of a three-dimensional network of fibers/particles and, thus, have local crystallization microenvironments that are different from those present in solution. For understanding the directing influence of biopolymer matrices on the mineral organization in biological structural materials, we investigated the combined effect of Mg and gelatin-agarose mixtures on composite aggregate formation, gel and/or Mg incorporation and distribution in the mineral, and on the mineral organization. From our study, we deduce the following conclusions (Table 2.4-2, Fig. 2.4-10).

Composite aggregate morphology and size

Aggregates that formed in Mg-free growth environments are blocky, elongated rhombohedra. With an increase in agarose in the gel mixture, there is a tendency for the development of dendrites. An increase in agarose does not impact the aggregate size much, while an increase in gelatin induces the formation of small-sized aggregates. The addition of Mg to the growth medium initiates for all investigated gel mixtures the growth of spherulitic aggregates. Sphericity increases significantly with an increase in agarose in the gel. Aggregate sizes are reduced in both cases, an increase in gelatin as well as in agarose in the gel mixture.

Hydrogel distribution within the mineral and subunit generation

In aggregates that form in growth environments devoid of Mg, the pattern of gel occlusion becomes more homogeneous when agarose is increased, while it is more localized and leads to the formation of membranes when the gelatin content is raised in the gel mixture. Accordingly, an increase in gelatin leads to the formation of gel membranes and results in the development of subunits, while an increase in agarose leads to a more uniformly distributed intercalation of gel into the mineral, and hence, does not generate the formation of many subunits. The aggregate consists mainly of one large mineral unit. The addition of Mg to the growth medium induces the formation of numerous and very differently sized subunits. When gelatin is increased in the growth medium, there is a structured distribution of subunit size, as the subunit sizes increase steadily toward the rim of the composite. An increase in agarose results in a random distribution of subunit sizes.

Aggregate texture and microstructure

Without Mg in the growth medium, the increase in gelatin results in the aggregate becoming a radial mosaic crystal, while the increase of agarose makes the aggregate a much better co-oriented “almost single crystal” as it mainly consists of one large unit. Crystallite co-orientation strength increases with an increase in agarose and decreases with an increase in gelatin in the gel mixture, respectively. With the addition of Mg, when gelatin is increased in the gel mixture, the aggregate that forms is still a radial polycrystal, however, now developed with a multitude of subunits with the latter being in a strictly ordered size arrangement. An increase of agarose results in the development of a spherical aggregate with a highly graded, archetypically spherulitic pattern of mineral organization. In the presence of Mg in the growth environment, crystallite co-orientation strength is similar, irrespective of an increase in agarose or gelatin in the gel mixture.

In summary

The presence Mg in the growth medium, in addition to the gel incorporation, strongly influences the local deformation within the aggregates. The mode of local deformation distribution within the mineral (homogeneous or localized) determines subunit formation, subunit size generation, and subunit size distribution. The latter three factors regulate the microstructure and texture of the aggregate. The mode of Mg incorporation combined with the development of membranes or fine dissemination of the gel matrix affects crystal co-orientation strength.

Acknowledgments

This research was partially supported by the MINECO (Spain) under Projects CGL2016-77138-C2-1-P. We are grateful to Dr. Fitriana Nindiyasari and Martina Greiner for their experience on the crystallization experiments. We would like to thank the staff from the National Microscopy Centre (ICTS) and the X-ray Diffraction Central Service of the Complutense University (UCM) and the group of Central Facility for Electron Microscopy in Ulm University for their kind technical support.

2.4.6 Support Information

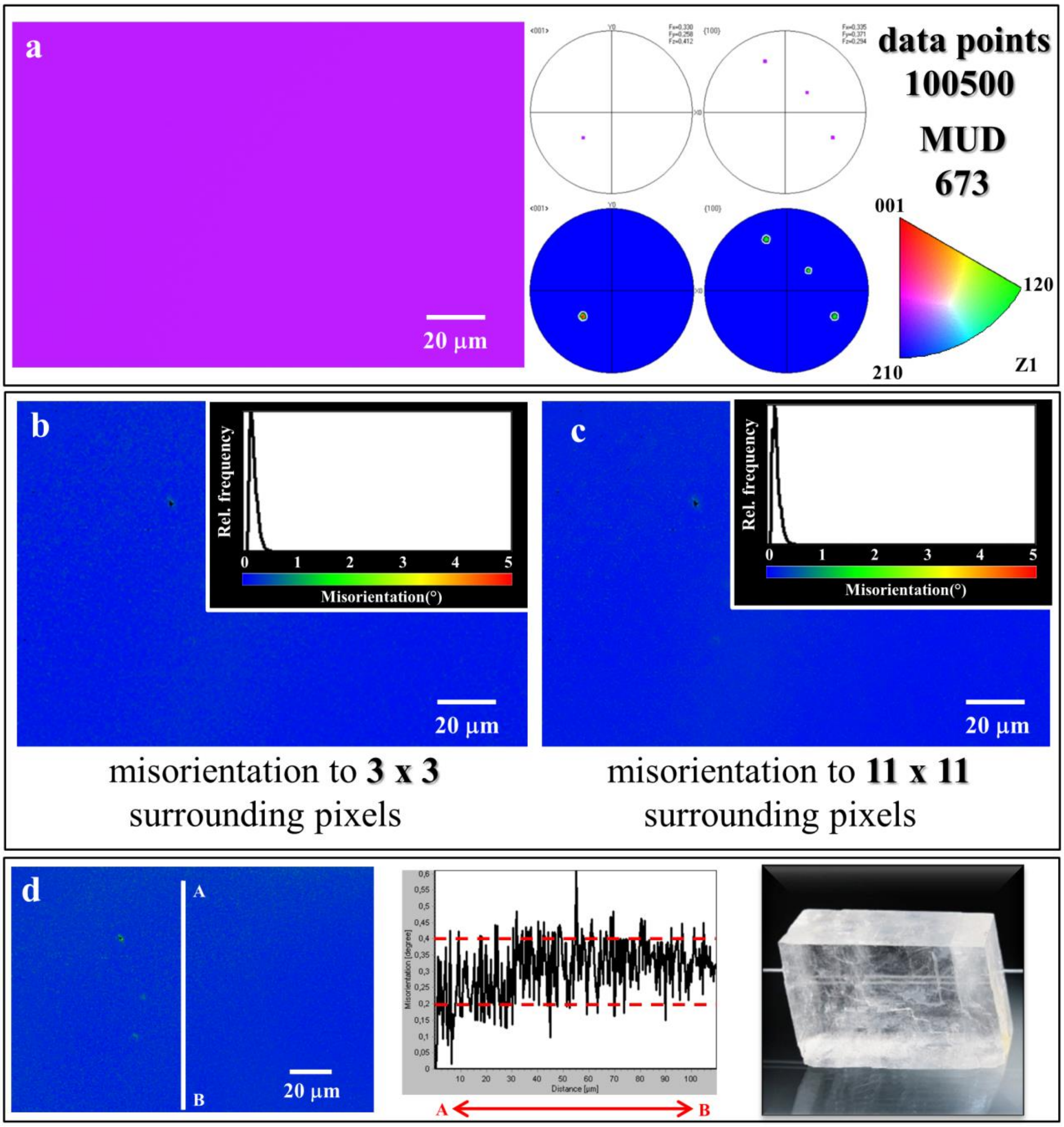

Figure 2.4-S1. EBSD reference measurement on a calcite single crystal grew from solution (measured with a raster step size of 280 nm). (a) Color-coded orientation map, corresponding pole figures, and strength of calcite co-orientation expressed with MUD value 673 (b) Local kernel misorientation evaluation with a 3 x 3 and (c) 11 x 11 filter (d) Misorientation versus distance diagram.

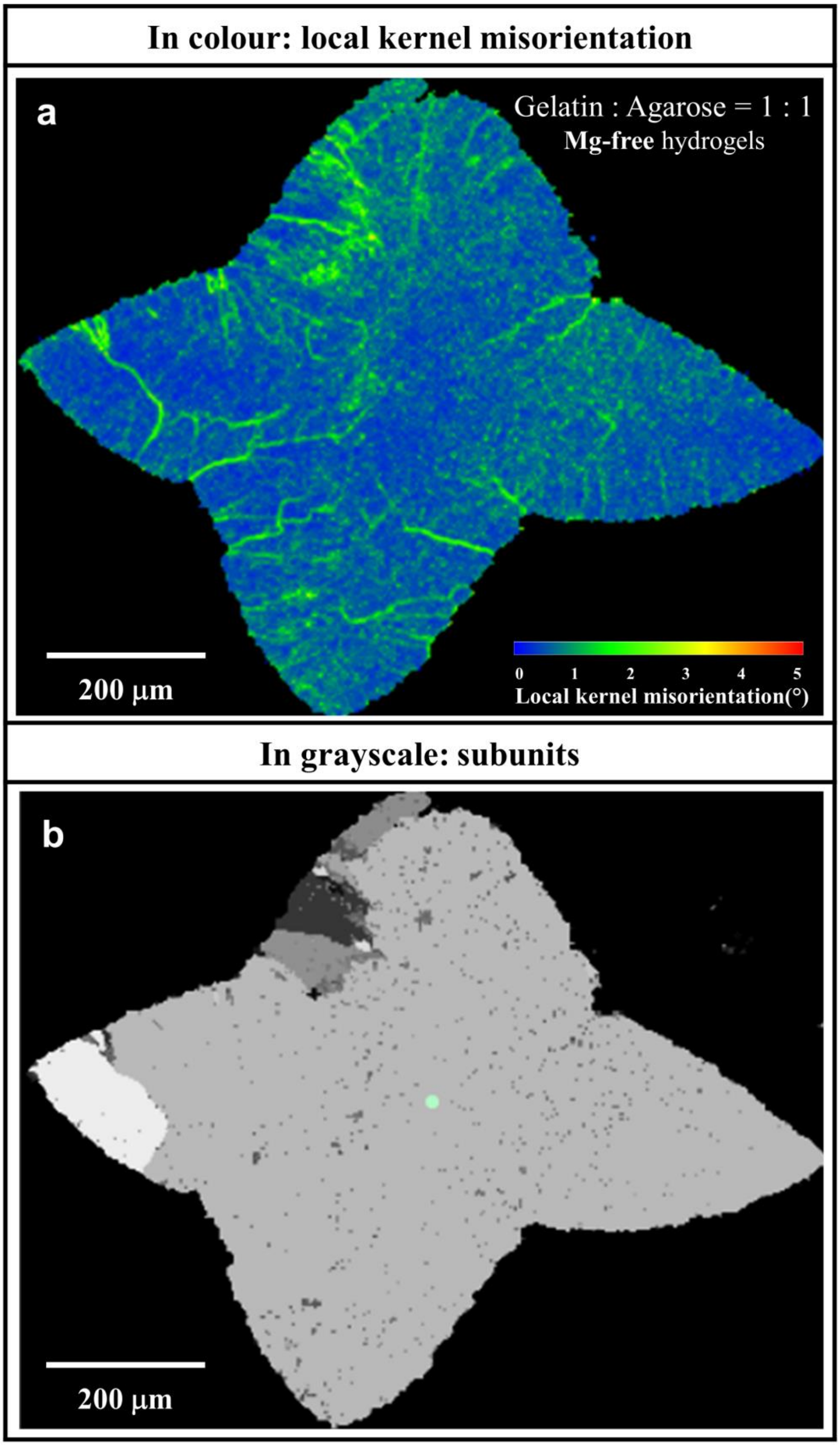

Figure 2.4-S2. EBSD data showing local kernel misorientation evaluation (calculated for 3x3 pixel clusters) and subunit formation for a composite grew in the G/A 1:1 gel mixture in Mg-free growth environment. Local kernel misorientation is given color-coded and depicts increased local strain induced by gel occlusion.

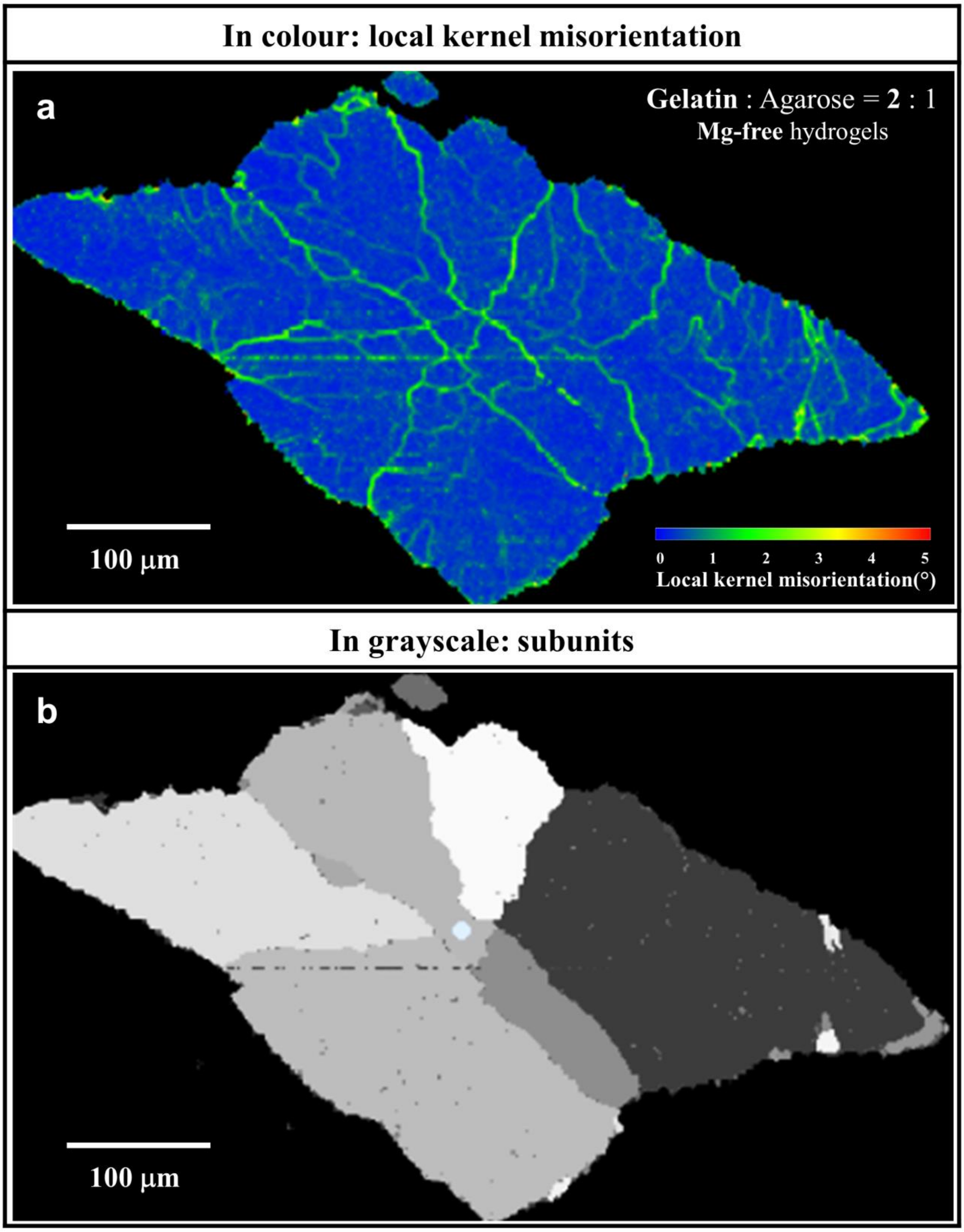

Figure 2.4-S3. EBSD data showing local kernel misorientation evaluation (calculated for 3x3 pixel clusters) and subunit formation for a composite grew in the G/A 2:1 gel mixture in Mg-free growth environment. Local kernel misorientation is given color-coded and depicts increased local strain induced by gel occlusion.

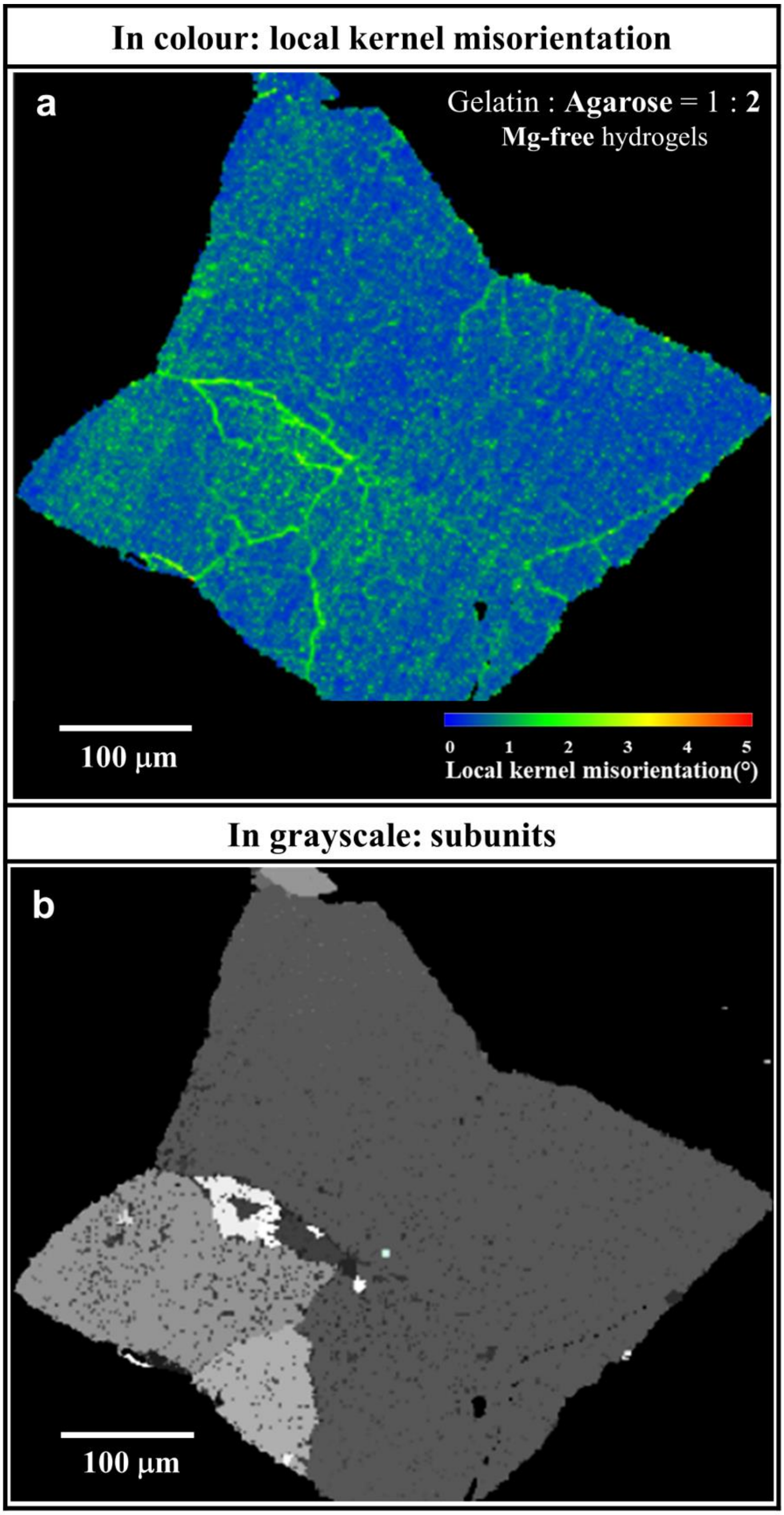

Figure 2.4-S4. EBSD data showing local kernel misorientation evaluation (calculated for 3x3 pixel clusters) and subunit formation for a composite grew in the G/A 1:2 gel mixture in Mg-free growth environment. Local kernel misorientation is given color-coded and depicts increased local strain induced by gel occlusion.

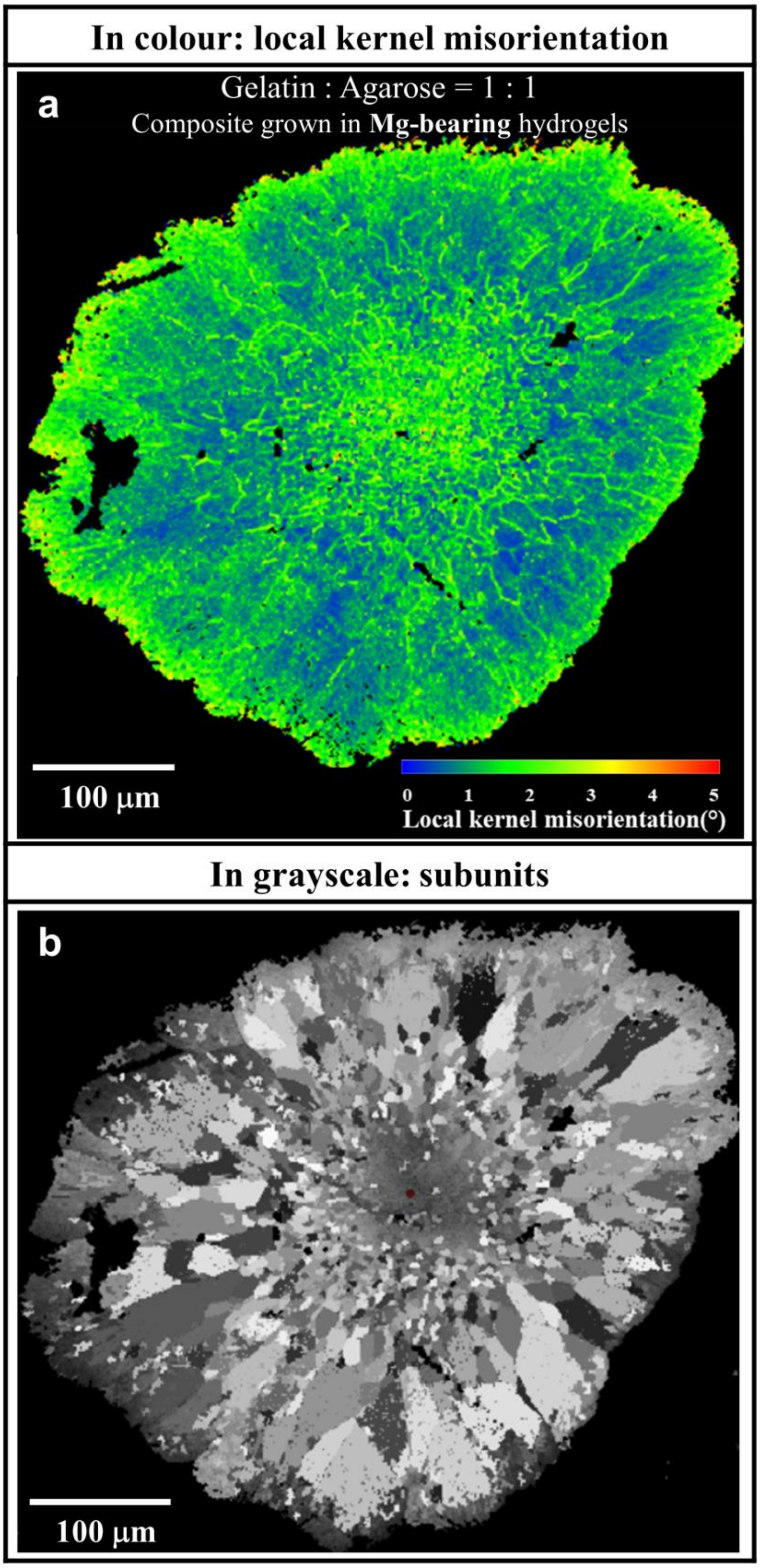

Figure 2.4-S5. EBSD data showing local kernel misorientation evaluation (calculated for 3x3 pixel clusters) and subunit formation for a composite grew in the G/A 1:1 gel mixture in the Mg-containing growth environment. Local kernel misorientation is given color-coded and depicts increased local strain induced by gel occlusion and Mg incorporation.

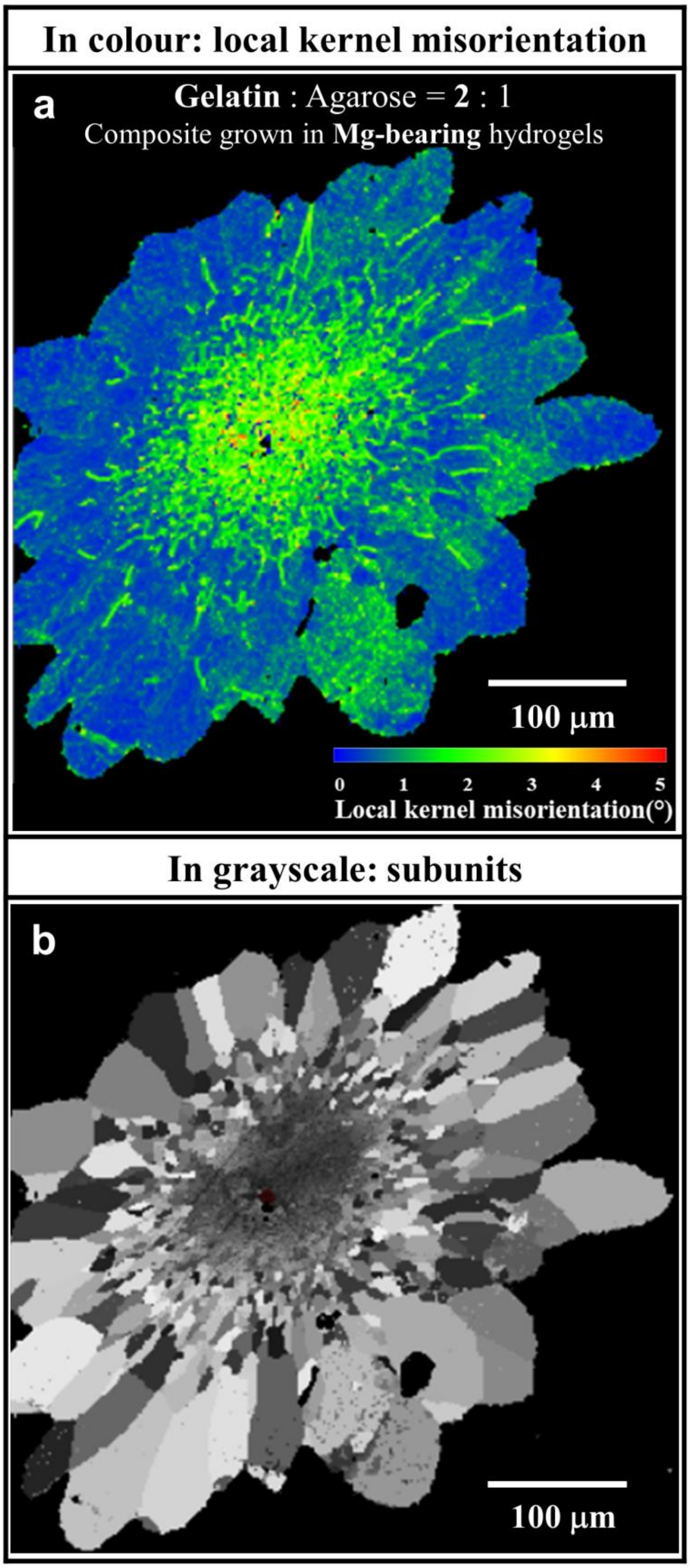

Figure 2.4-S6. EBSD data showing local kernel misorientation evaluation (calculated for 3x3 pixel clusters) and subunit formation for a composite grew in the G/A 2:1 gel mixture in the Mg-containing growth environment. Local kernel misorientation is given color-coded and depicts increased local strain induced by gel occlusion and Mg incorporation.

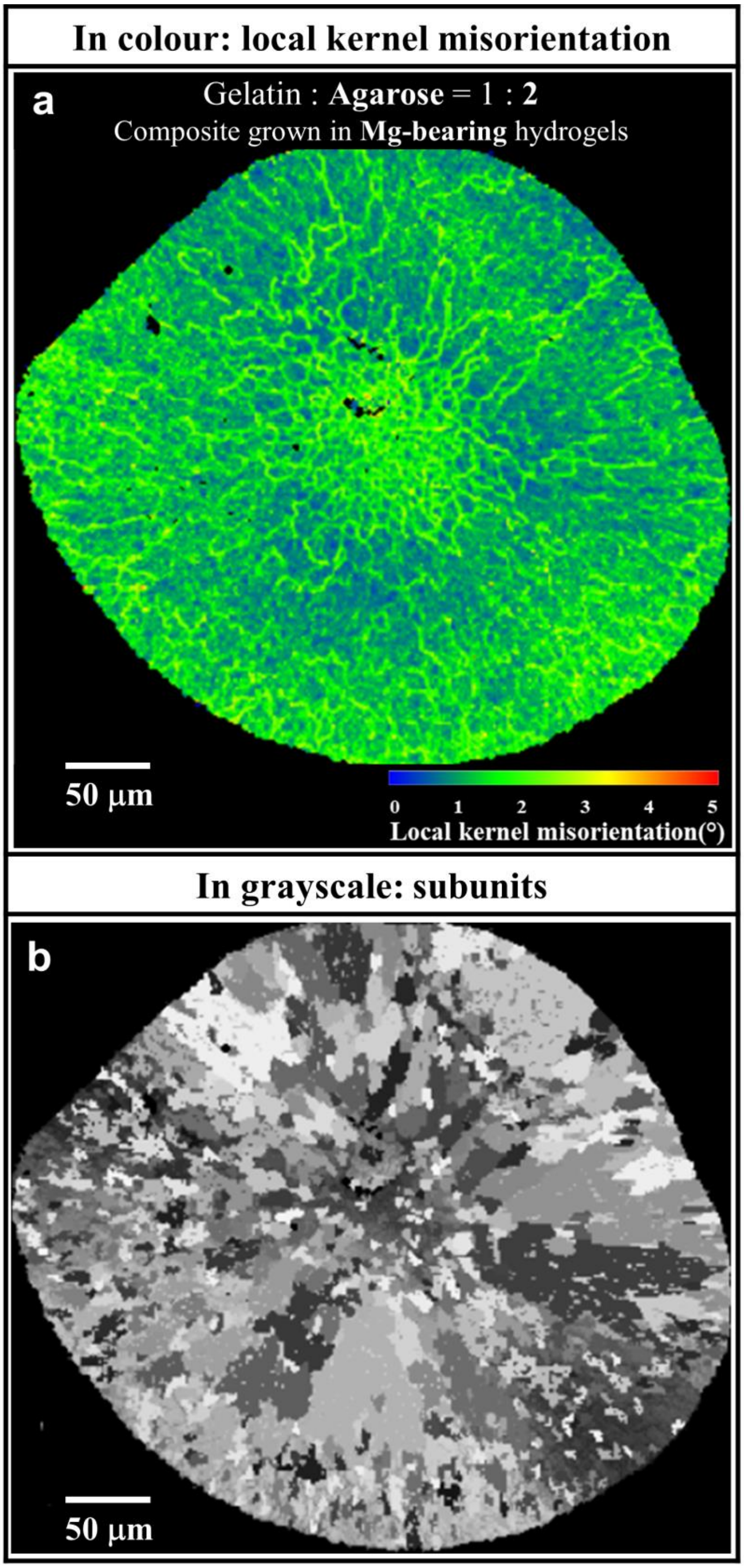

Figure 2.4-S7. EBSD data showing local kernel misorientation evaluation (calculated for 3x3 pixel clusters) and subunit formation for a composite grew in the G/A 1:2 gel mixture in the Mg-containing growth environment. Local kernel misorientation is given color-coded and depicts increased local strain induced by gel occlusion and Mg incorporation.

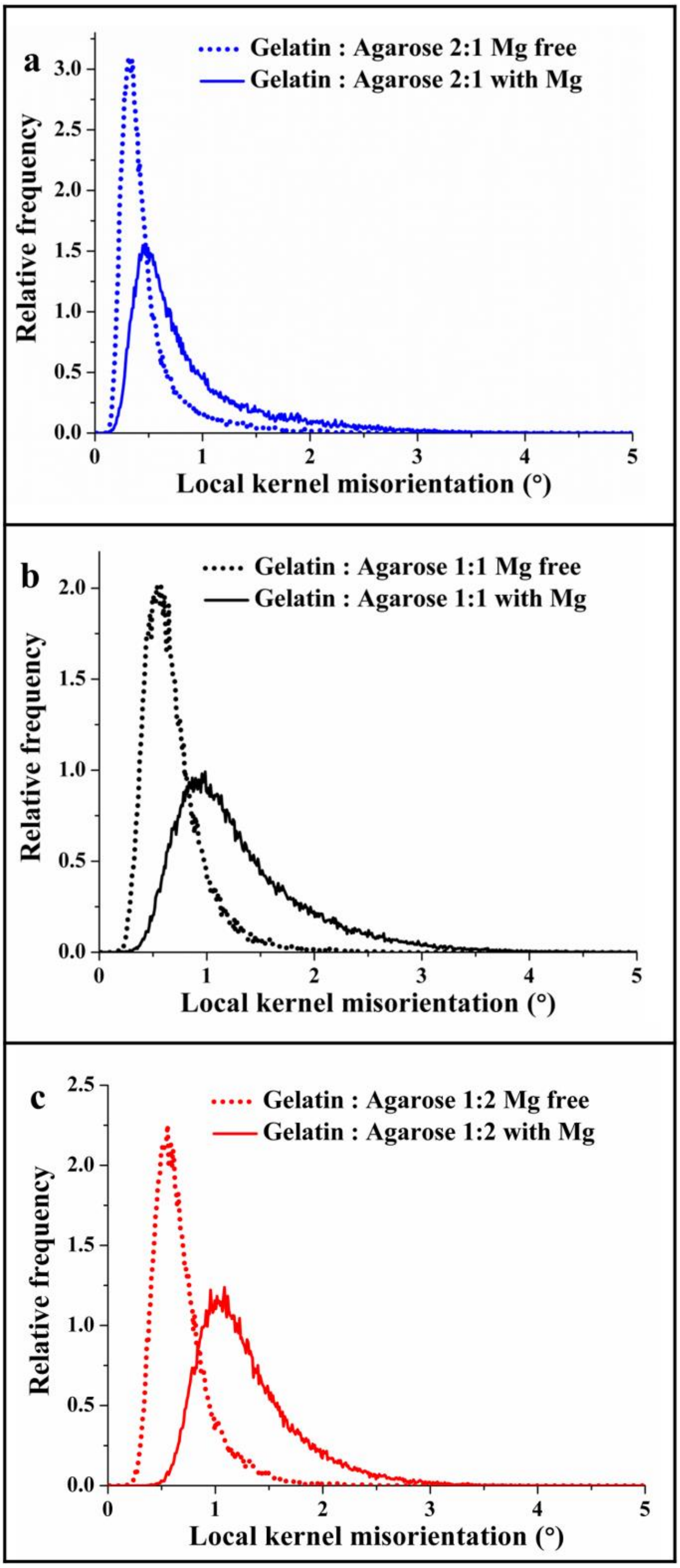

Figure 2.4-S8. The difference in the degree of misorientation between calcite crystals induced by gel occlusion with (solid lines) and without (dotted lines) Mg in the growth medium. (a) Aggregate grew in G/A 2:1 gel mixture. (b) Aggregate grew in G/A 1:1 gel mixture. (c) Aggregate grew in G/A 1:2 gel mixture. Irrespective of the relative gel contents, the degree of local kernel misorientation between calcite crystallites increases significantly when Mg is present in the growth medium.

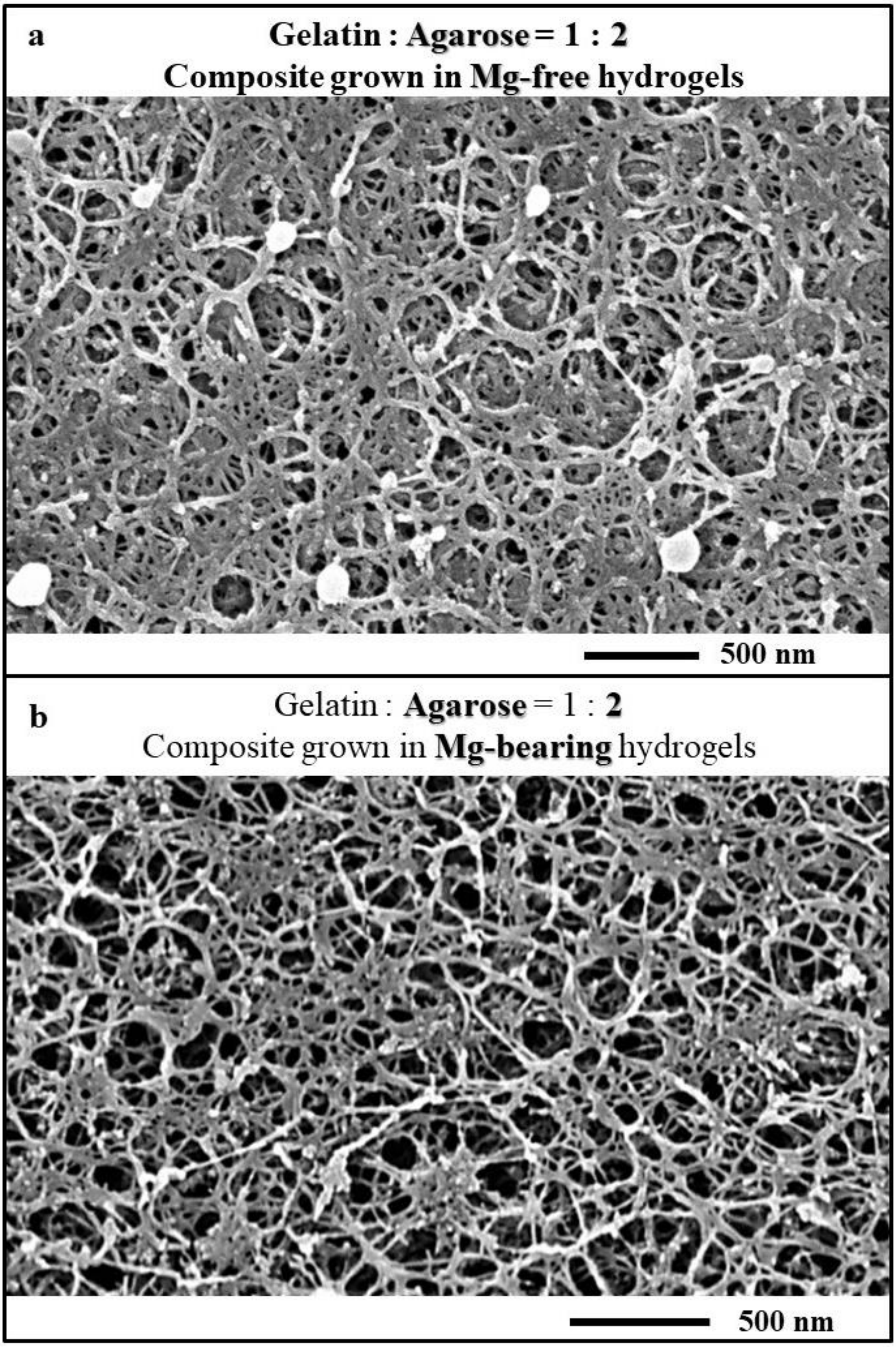

Figure 2.4-S9. G/A 1:2 gel fabric present in aggregates that grew in Mg-free (a) and in Mg-bearing (b) environment. Note the fibrous nature of the gel when agarose is increased in the gel mixture.

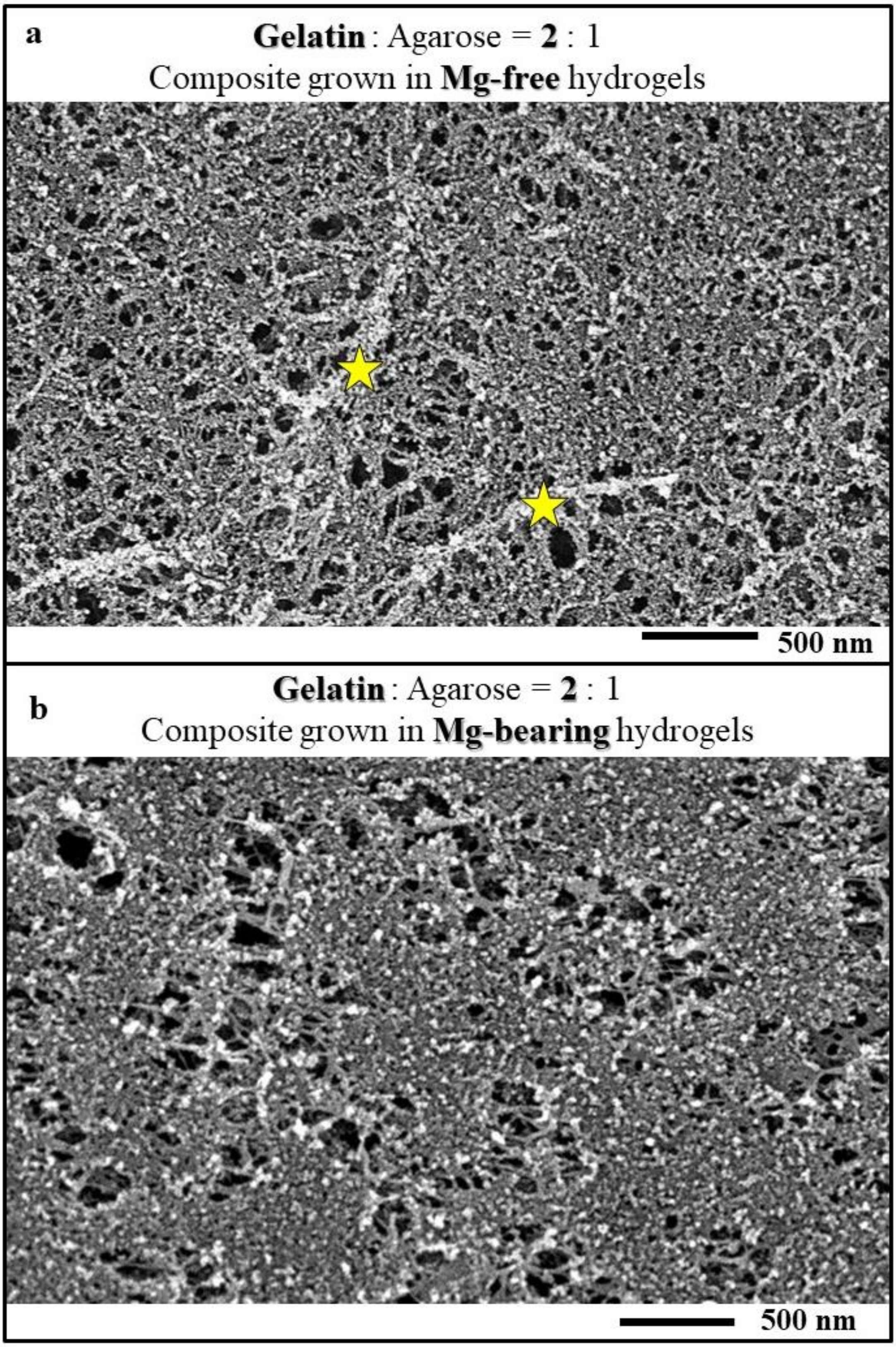

Figure 2.4-S10. G/A 2:1 gel fabric present in aggregates that grew in Mg-free (a) and in Mg-bearing (b) environment. Domains with a granular appearance are present and are separated from each other by short-ranged gel accumulations, indicating the formation of membranes (yellow stars in a). At an increase in gelatin, the gel mixture becomes compact, nonetheless, containing fibrous gel portions with arrays of large pores (b) and short-ranged elongated gel accumulations resembling membranes (b).

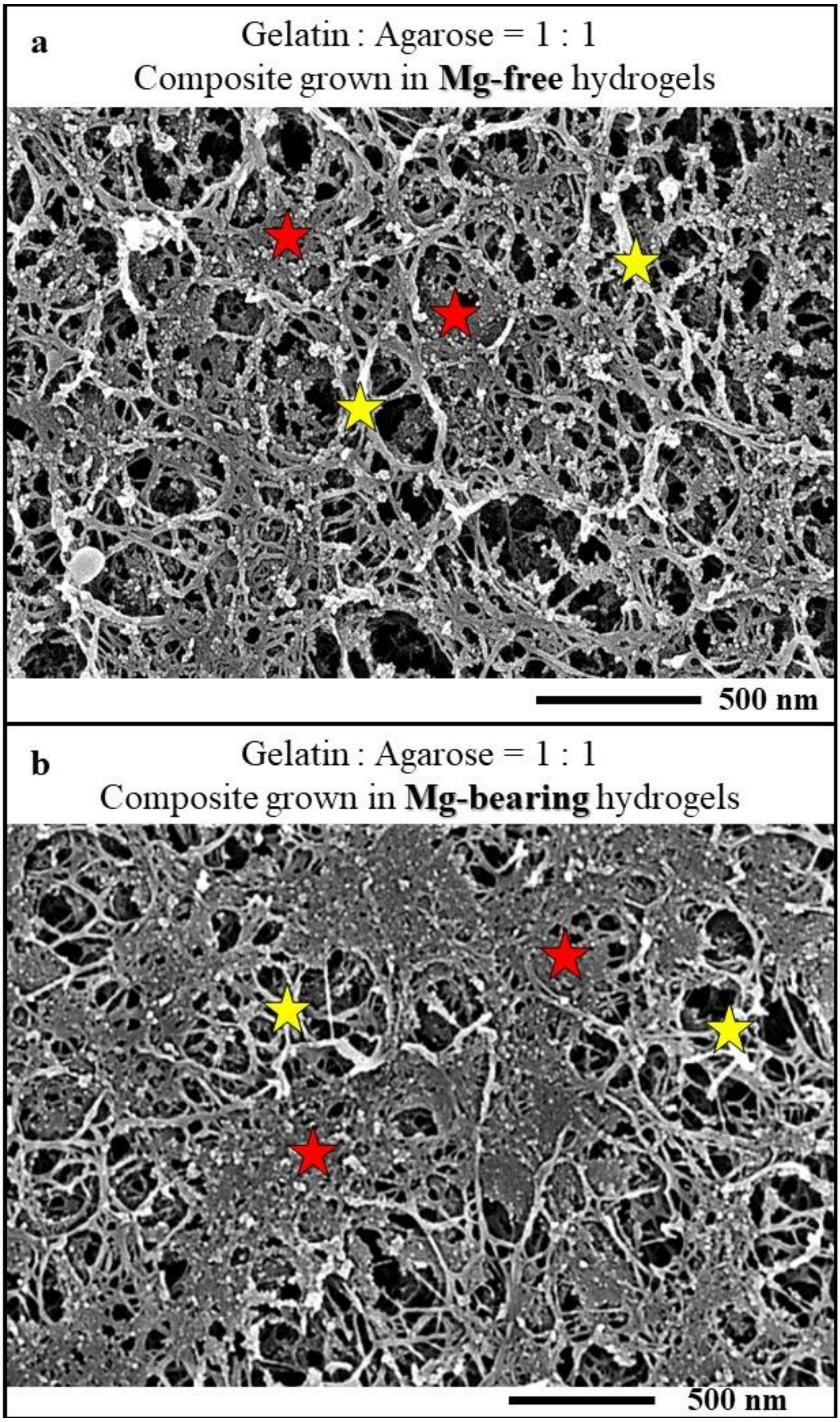

Figure 2.4-S11. G/A 1:1 gel fabric present in aggregates that grew in Mg-free (a) and in Mg-bearing (b) environment. In both, Mg-free and Mg-bearing growth environments we find the fabrics of gels containing regions where the fabric is dense like a sheet (red stars), portions with thick fibers (yellow stars), and regions where very large pores formed due to rupture of the walls of smaller pores.

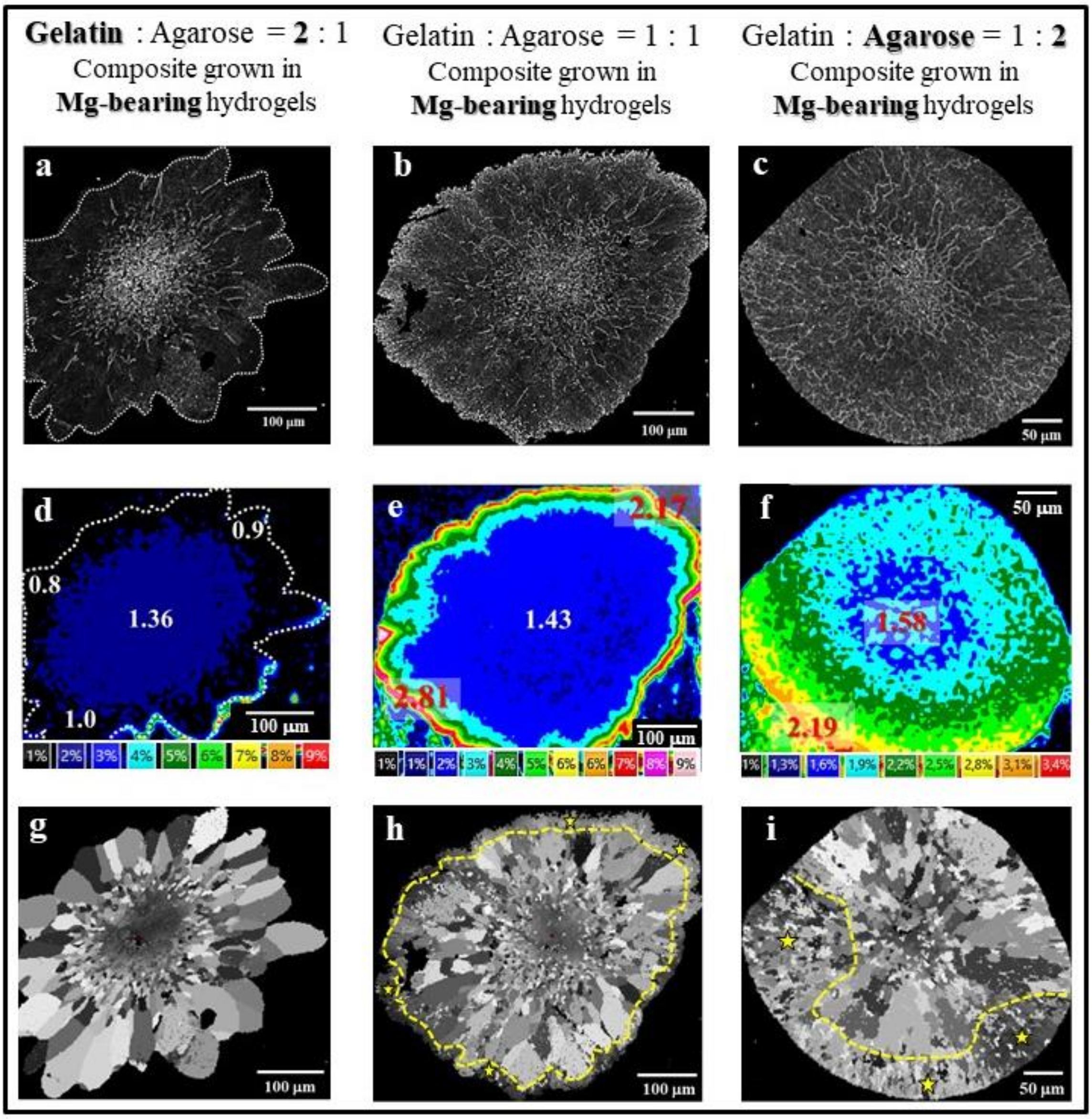

Figure 2.4-S12. EDS measurements depicting the distribution pattern of Mg on planes cut through aggregates grown in Mg-bearing growth media (d–f). These surfaces were also scanned with EBSD. (a–c) the pattern of hydrogel accumulation and distribution within the aggregates are visualized with grey-scaled kernel misorientation maps. (g–i) the pattern of subunit size variation and distribution within the aggregates is shown in greyscale. Areas contain numerous small size subunits are mark with yellow dot lines and stars.

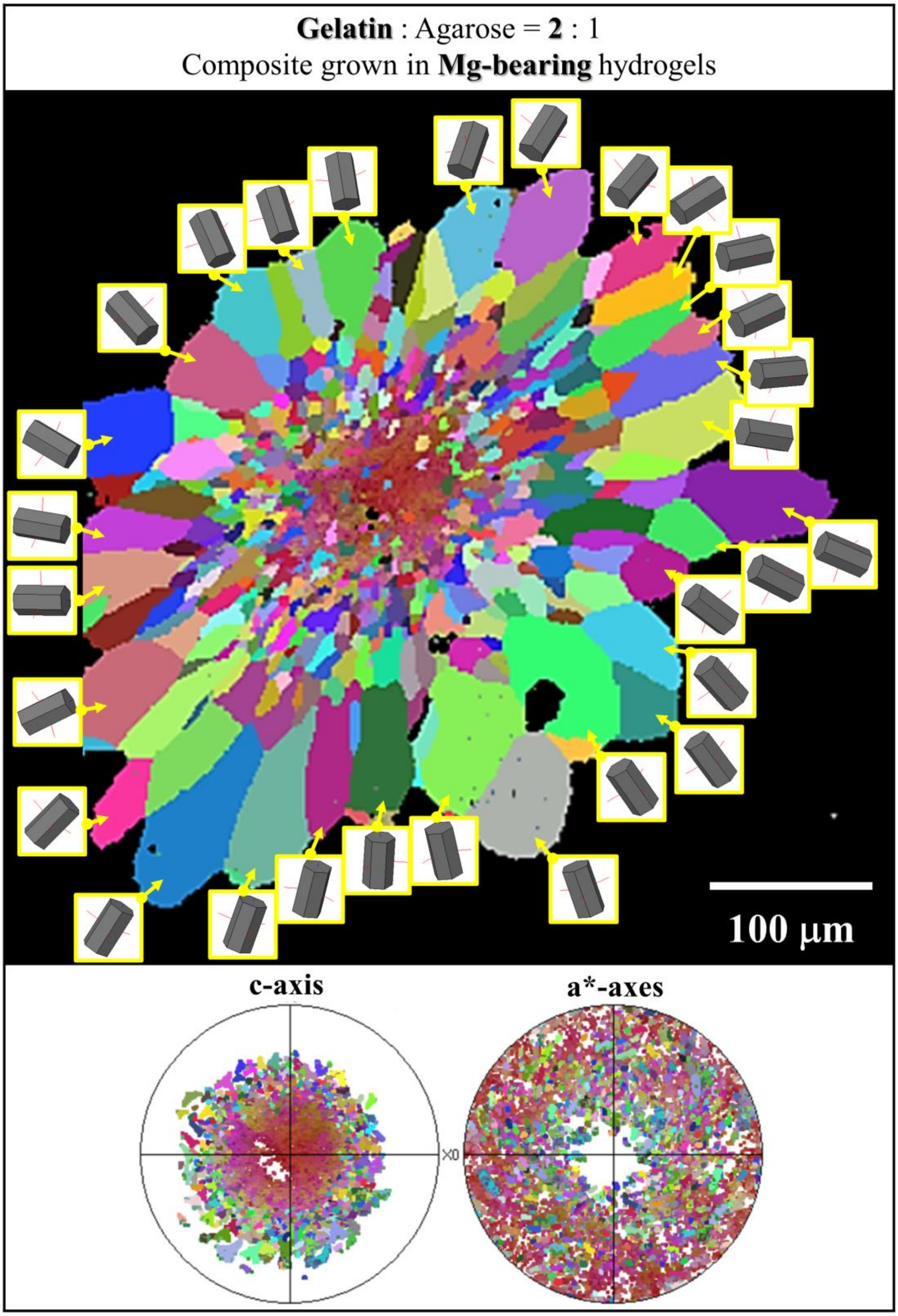

Figure 2.4-S13. The pattern of grain/subunit size distribution together with subunit organization in an aggregate that grew in the presence of Mg in the G/A 2:1 gel mixture. Grains are shown in random color.

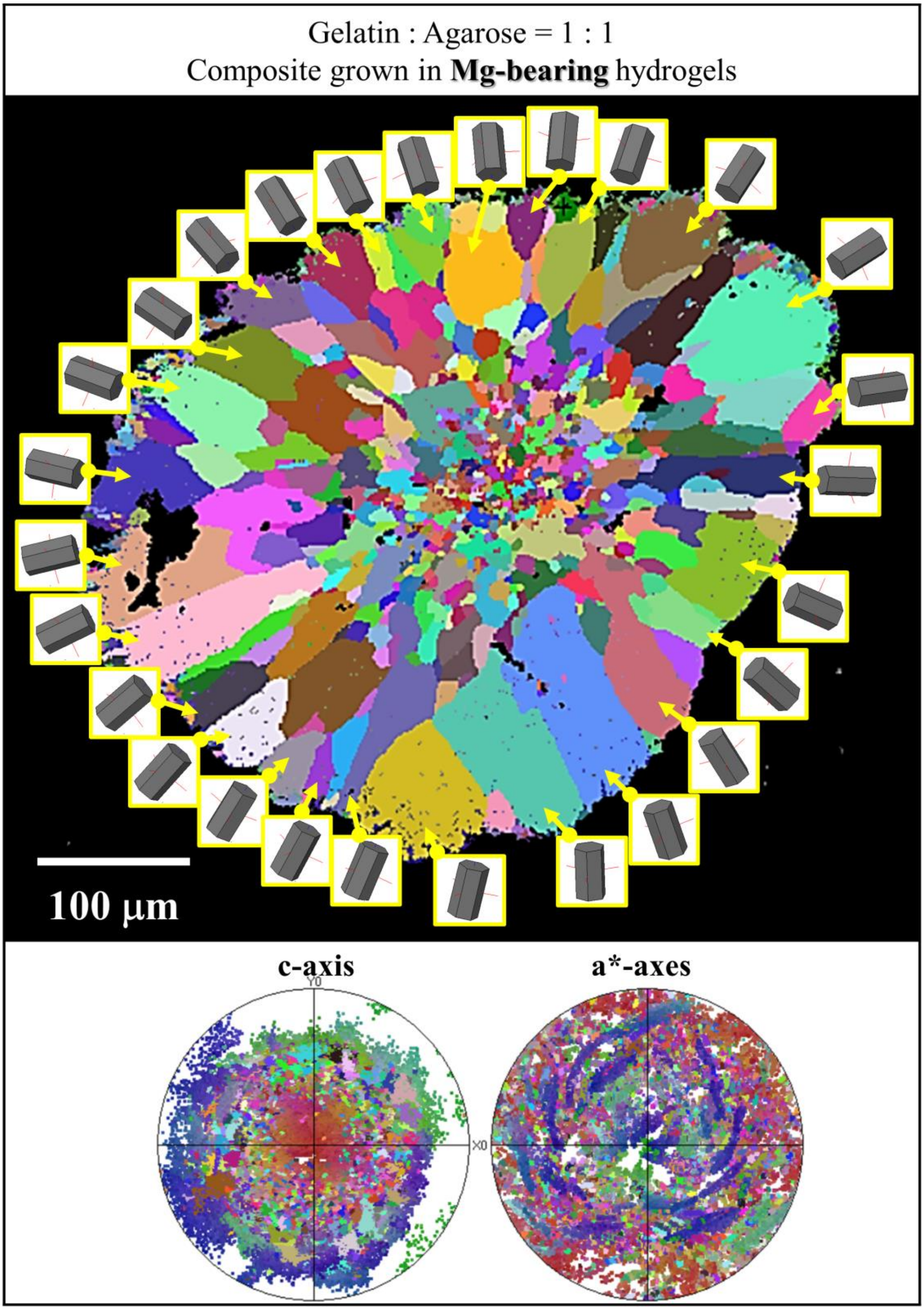

Figure 2.4-S14. The pattern of subunit size distribution, subunit organization in an aggregate that grew in the presence of Mg in the G/A 1:1 gel mixture. The color in the map and in the corresponding pole figures does not give calcite orientation; grains are shown in random color.

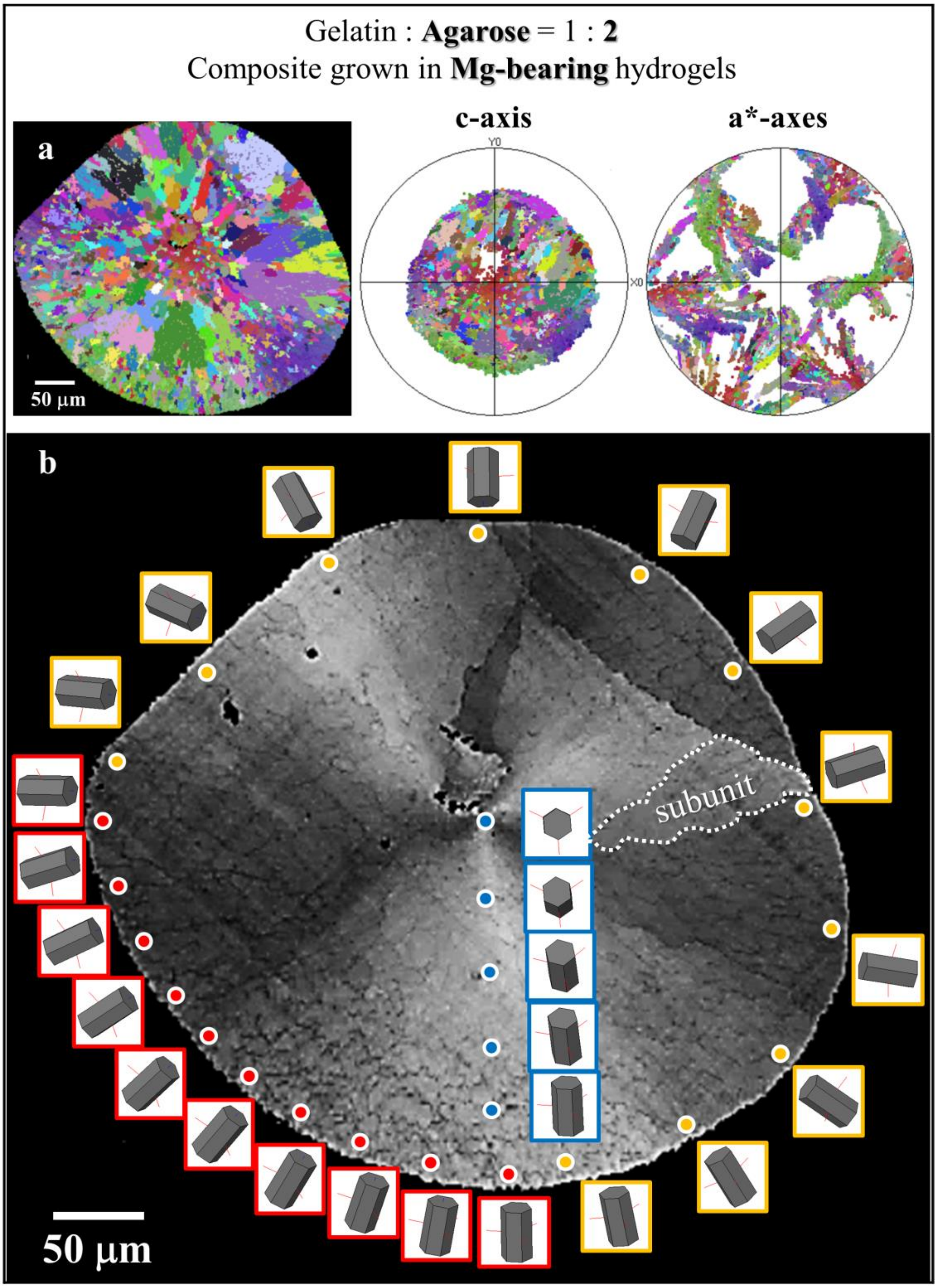

Figure 2.4-S15. Grains are shown in random color visualize patterns of the grain size distribution (a) in an aggregate that grew in the presence of Mg in the G/A 1:2 gel mixture. Even though there is a high variation in grain size and an inhomogeneous pattern of grain size distribution, calcite crystallites are oriented to each other in a perfectly graded.

2.5 Directing Effect of Bacterial Extracellular Polymeric Substances (EPS) on Calcite Organization and EPS-Carbonate Composite Aggregate Formation

Xiaofei Yin[1], Florian Weitzel[1], Concepcion Jimenez-Lopez[2], Erika Griesshaber[1], Lurdes Fernández-Díaz[3, 4], Alejandro B. Rodriguez-Navarro[5], Andreas Ziegler[6], Wolfgang W. Schmahl[1]

1. Department für Geo- und Umweltwissenschaften, Ludwig-Maximilians-Universität, Germany
2. Departamento de Microbiología, Universidad de Granada, Spain
3. Departamento de Cristalografía y Mineralogía, Universidad Complutense de Madrid, Spain
4. Instituto de Geociencias (UCM, CSIC). C/ José Antonio Novais 2, Spain
5. Departamento de Mineralogía y Petrología, Universidad de Granada, Granada, Spain
6. Central Facility for Electron Microscopy, University of Ulm, Germany

Crystal Growth & Design **20**, 1467–1484 (2020)
http://dx.doi.org/10.1021/acs.cgd.9b01113

Abstract

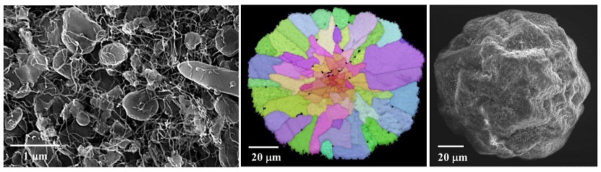

Mineralized structures generated under biological control are hierarchical composites that consist of biopolymer matrices and minerals. The biopolymer matrix in biological material is developed as membranes or as a network of fibrils, which has structural as well as functional roles for the composite hard tissue. Microorganisms are surrounded by microbial extracellular polymeric substances (EPS), which consist of self-organized macromolecules and have a fibrous fabric. The EPS enables the survival of microorganisms with their modes of organization in different physicochemical states. To understand the influence of biopolymer matrices on the composite material formation we conducted growth experiments with the EPS of the bacteria *Pseudomonas putida*. We synthesized EPS-agarose-calcite aggregates, characterized aggregate morphologies, EPS-hydrogel distribution, and mineral organization. We find that *P. putida* EPS exerts a tremendous influence on morphology, polymer distribution, and crystal assembly. Aggregates containing *P. putida* EPS are spherical polycrystalline entities without texture, while aggregates without EPS are branched dendrites. Polymer distribution in aggregates where EPS is intercalated is inhomogeneous. It is mainly present as membranes, which induces the formation of irregular-shaped, different-sized, highly misoriented subunits. *P. putida* EPS changes the microstructure of the mineral in a specific manner. This can be used as a tool for the identification of bacterially mediated calcification.

Keywords

Pseudomonas putida EPS; biopolymers; agarose hydrogel; mineral organization; EBSD; biomarker

2.5.1 Introduction

Microorganisms are the most ubiquitous life forms on Earth and live in highly diverse environments (Atlas *et al.* 1998). The vast majority of microorganisms live attached to surfaces, in soils, sediments, and aquatic systems (McLean *et al.* 1989; Braissant *et al.* 2002; Rodríguez-Navarro *et al.* 2007). The adhesion of microorganisms (i.e. bacteria) to surfaces takes place via biofilms, which is a self-produced matrix consisting of biopolymer macromolecules (the extracellular polymeric substances (EPS) matrix) that constitute the immediate environment of these cells (Flemming & Wingender 2010; Flemming *et al.* 2016b; Neu & Lawrence 2016). Biofilms have various physical and chemical properties and many biological roles: they afford microbial cells a significant potential of resilience to external physical stress, protect microbial cells, enhance and structure their physiological activities, and enable nutrient dynamics (e.g., Dupraz *et al.* 2009; Flemming & Wingender 2010; Tourney & Ngwenya 2014; Flemming *et al.* 2016a). Biofilms consist of high molecular-weight polysaccharides that include proteins, peptides, lipids, sulfates, and phosphates (Flemming *et al.* 2004; Dupraz & Visscher 2005; Aguilar *et al.* 2007; Marvasi *et al.* 2010). Biofilms are often highly hydrated and exist in a continuum of physical states that range from a cohesive gel to a highly viscous sol (Wingender *et al.* 1999; Decho 2000; Sutherland 2001). Hence, for survival, microbial life relies on the mode of organization of the entire biofilm, the EPS matrix in general and its chemical and physical structure and states (e.g., Flemming *et al.* 2016b).

Carbonate biological hard tissues are composites of biopolymer matrices that are reinforced by minerals (e.g., Checa *et al.* 2015; Simonet Roda *et al.* 2019b,a). Hydrogels can be regarded to some extent as model systems for the biopolymer matrices in biologic structural materials as they yield information on the influence of biopolymers on crystal nucleation and growth, mineral orientation and composite hard tissue organization (e.g., Nindiyasari *et al.* 2014a,b, 2015, 2019) For instance, similar to the extracellular matrices in biological hard tissues, the fibrous fabric of agarose and gelatin gels forms compartments where specific diffusion rates, as well as local concentrations and supersaturation of solutes, prevail. Nonetheless, even though an environment is generated in an artificial system (hydrogels) that is comparable to that at sites of mineralization in biological hard tissues, major differences still remain between the hydrogel/mineral systems and the composite biological hard materials.

Research in the past decade has shown that microbial biofilms are able to mediate mineral dissolution, precipitation, and phase formation (Douglas & Beveridge 1998; Lian *et al.* 2006; Sánchez-Román *et al.* 2007; Ercole *et al.* 2012). Accordingly, the extrapolymer substance secreted by bacteria is closer to chemical and physical properties of biopolymer matrices of biological hard tissues than artificial hydrogels, as those are the denaturalized products of natural substances. Hence, when using hydrogels as model systems, some original attributes are lost. Biofilms are a community of microbial cells that are immersed within a matrix of EPS. A growing number of research articles on composition and reactivity of EPS matrix materials indicate that EPS substance exerts a significant influence on crystal nucleation and mineral growth: some functional groups of the EPS matrix serve as initial nucleation sites, while other moieties control the extent and the type of mineral precipitation (e.g., Douglas & Beveridge 1998; Dupraz *et al.* 2009; Decho 2010; Gallagher *et al.* 2010). EPS matrices are mediators of mineral precipitation/dissolution and, if it is necessary for the biofilm community, are able to inhibit, alter, or even enhance precipitation of minerals, in both natural environments as well as in the laboratory.

To better understand the directing influence of biopolymers on the mineral organization in biological structural materials, we investigate the influence of bacterial EPS on polymer-mineral composite formation. We synthesized *Pseudomonas putida* EPS-agarose hydrogel-calcite aggregates and discussed the effect of the EPS matrix on calcite organization, aggregate formation, and aggregate growth. We used the EPS of the Gram-negative, rod-shaped, saprotrophic soil bacterium *P. putida* that is well known for EPS production in nature and the laboratory. *Pseudomonas* species have the ability to induce calcium precipitation, which is mainly carbonate or phosphate (Hammes *et al.* 2003; Connolly *et al.* 2013; Daskalakis *et al.* 2013; Fishman *et al.* 2018). The bioinduced mineralization is driven by the organism's metabolism. The EPS is the organic matrix for this mineralization. This matrix may not just be a passive carrier medium, as it cannot be excluded a priori that the EPS is a factor exerting some morphological control on the crystallization of the mineral.

In the present contribution we describe, relative to reference aggregates grown without EPS, the pattern of EPS distribution within the aggregate and explore how *P. putida* EPS influences aggregate morphology, surface constitution, mineral organization, and aggregate growth. We find that *P. putida* EPS exerts a significant and characteristic impact on mineral assembly and composite aggregate architecture. A specific microstructure and texture forms when *P. putida* EPS is present in the growth environment, a feature that could be used as a signature for the recognition of a biogenic origin of carbonates.

2.5.2 Materials and Methods

Bacteria cultures

Pseudomonas putida 324 (CECT) was used to produce extracellular polymeric substances (EPS). Pure cultures of this bacterium were grown in 1 L of LB culture medium enriched with 0.5% KH_2PO_4 (w/v), 0.5% NaCl (w/v), 1% glucose (w/v) and 0.5% yeast extract (w/v), pH 7. Cells were grown at 28°C, under 180 rpm stirring for 2 days.

Cells were concentrated by centrifugation at 11000 rpm at 4°C for 40 min and the pellets were harvested and suspended in 30 mL 0.9% NaCl (w/v) in an ultrasonic bath for 5 min. Subsequently, cells were again concentrated by centrifugation (11000 rpm at 4°C for 40 min), treated with ethanol to reduce cell viability, suspended again in 0.9% NaCl (w/v) and stored at 4°C for 12 h.

EPS extraction

The extraction process has been projected to extract three different types of EPS, namely "soluble EPS", "loosely bound EPS" and "tightly bound EPS". The protocol is based on the work of Eboigbodin & Biggs (2008) and Pellicer-Nàcher *et al.* (2013) with some modifications to kill the cells, so they do not contribute to the formation of the carbonate crystals.

Soluble EPS

Samples were centrifuged at 5000 rpm at 4°C for 20 min to separate the "soluble EPS" from the "loosely bound EPS" and "tightly bound EPS". After centrifugation, the supernatant (containing the "soluble EPS") was separated from the pellet (here referred as initial pellets, containing the "loosely bound EPS" and "tightly bound EPS") and the "soluble EPS" was precipitated by adding 96% ethanol (1:3 v/v) to the supernatant and kept overnight at 4°C.

Loosely bound EPS

The initial pellets containing "loosely bound EPS" and "tightly bound EPS" were suspended in a 1:1 (v/v) mixture of 0.9% NaCl (w/v) and 2% EDTA (w/v) solution for 60 min. The mixture was centrifuged at 5000 rpm at 4°C for 60 min. After centrifugation, the supernatant containing the "loosely bound EPS" was separated and filtered through a 0.45 μm nitrocellulose-acetate filter to get rid of cell residuals. The loosely bound EPS contained in the filtrate was precipitated with ethanol (1:3 v/v) overnight at 4°C.

Tightly bound EPS

The pellet containing the "tightly bound EPS" was re-suspended in a 1:1 volume of 0.9% NaCl (w/v) and 2% EDTA (w/v), vortexed and left for 1–2 h before proceeding. The mixture was sonicated by repeating three times a cycle of 5 min sonication plus 5 min of rest. The samples were centrifuged at 5000 rpm at 4°C for 60 min. The supernatant containing the “tightly bound EPS” was separated and filtered through a 0.45 μm nitrocellulose-acetate filter. The tightly bound EPS contained in the filtrate was precipitated with ethanol (1:3 v/v) overnight at 4°C.

Once the three types of EPS were extracted, they were all mixed to obtain a final sample, here referred to as “total EPS”. The total EPS sample was then resuspended in Milli-Q water to a total volume of 3 mL for further analyses.

IR analyses of EPS samples

The chemical composition of EPS from bacteria was characterized by infrared spectroscopy. EPS samples were analyzed by reflection using an ATR diamond crystal window (MIRacle Single Reflection ATR, PIKE Technologies) on an FTIR spectrometer (model 6200, JASCO Analytical Instruments Japan). Infrared spectra were recorded at a 2 cm^{-1} resolution within the 400–4000 cm^{-1} range, over 100 scans. The presence and relative abundance of polysaccharides, proteins, and carbonate were determined from the absorption peaks associated with the characteristic molecular groups of each component: C–H: polysaccharides (2700–3000 cm^{-1}); amide I: proteins (1590–1640 cm^{-1}); ν2, ν3 CO_3: carbonates (1400, 870 cm^{-1}); COC and COH: polysaccharides (900–1200 cm^{-1}) (Grube *et al.* 2002; Wiercigroch *et al.* 2017).

Crystal growth experiments

Crystallization experiments were carried out at 13°C using a single-diffusion system which consisted of a 100 mm in length and 9 mm in diameter Pyrex glass tube, closed on one side by a polystyrene cap (Fig. 2.5-S1). The tube was filled with a 1.5 mL slide of a hybrid EPS-agarose gel and a 0.5 mL slide of pure agarose gel on top of it. Finally, 5 mL of 0.1 M Na_2CO_3 was poured on top constituted the carbonate reservoir. The pure agarose gel was prepared by dissolving agarose powder (0.5 wt%, Type I-A, low EEO; Sigma-Aldrich) in Milli-Q water at 90°C, while the hybrid gel was prepared by dissolving agarose powder (0.5 wt%) in a solution of 0.1M $CaCl_2$ heated to 90°C. Prior to gelation, the so-prepared $CaCl_2$-bearing agarose sol was mixed under continuous stirring (1400 rpm) with the extracted EPS (2:1 v/v) in a water bath at 45°C. This mixture was poured into the experimental glass tube. After gelation, the pure 0.5 wt% agarose sol was poured on the top of the $CaCl_2$-bearing gel. The open end of the tube was then sealed with Parafilm, and the tube was set in a refrigerated chamber at 13°C and left to settle overnight. Afterward, the Parafilm seal was removed and the 0.1 M Na_2CO_3 solution was poured on top of the gel. The tube was then resealed with Parafilm and set in a refrigerated chamber at 15°C. The crystallization experiments were stopped after 6 weeks. The hybrid EPS-agarose gel slide was extracted and dissolved in hot water. The aggregates were then picked using a fine painting brush under a binocular stereomicroscope, washed three times with hot (60°C) water, and air-dried at room temperature for 24 h. All chemicals used were reagent quality and purchased from Sigma-Aldrich. For all procedures, high-purity deionized (Milli-Q) water (18.2 MΩ) was used. Meanwhile, a reference set experiment prepared without any EPS in the growth media was conducted. The EPS part was substituted by Milli-Q water in the reference experiment.

All aggregates that were investigated in this study are composites, which consist of polymers and carbonate mineral. Aggregates that formed without *P. putida* EPS in the growth medium are the reference aggregates; these are composites of carbonate mineral and pure agarose gel. The main focus of the investigation was placed on composite aggregates that grew in the presence of *P. putida* EPS in the growth medium. These aggregates consist of carbonate mineral and a mixture of *P. putida* EPS and agarose hydrogel.

Morphological and phase characterization of crystal aggregates

Crystal aggregates grown in both hydrogels were selected under a binocular stereomicroscope and picked using a fine painting brush. The samples were mounted on holders, coated with 15 nm carbon and studied using a Hitachi SU5000 FE-SEM at 20 kV.

Powder X-ray diffractograms were recorded on a Debye-Scherrer geometry STOE diffractometer equipped with a curved Ge (111) primary monochromator to produce Mo-Kα_1 radiation (λ = 0.07093 nm) at 50 kV and 30 mA. The aggregates were sealed in ∅0.3 mm glass capillaries and kept in rotation during the measurement for obtaining texture-free powder diffraction data. Data were collected in the range of 7–60 deg with a step size of 0.1 deg and a step time of 15 s, using a position-sensitive detector with an angular resolution of 0.01 deg. The diffractograms are normalized and arbitrarily shifted along the intensity axis.

Chemical fixation for SEM imaging of bacterial EPS

P. putida was grown in a 5 mL test tube containing LB medium overnight at 28°C, under 180 rpm. Then, 10 μL bacterial suspension drops were deposited on Petri dishes containing 20 mL of LB culture medium containing 2% agar-agar (w/v), and enriched with 0.5% KH_2PO_4 (w/v), 0.5% NaCl (w/v), 1% glucose (w/v) and 0.5% yeast extract (w/v), pH 7. The dishes were incubated at 28°C for 4 days.

A surface of 5 × 5 mm square block was dissected from the growth area and transferred into 0.1 M sodium cacodylate (Sigma-Aldrich) buffer solution containing 2.5% glutaraldehyde (v/v) as fixative at pH 7.3 for 1 h. The specimens were washed in 0.1 M sodium cacodylate buffer solution 3 times for 10 min each and dehydrated in a series of isopropanol (30 vol%, 50 vol%, 70 vol%, 90 vol%, 100 vol%) for 5 min each. After washing three times in 100% isopropanol for 10 min each, the specimens were critical point dried in a BAL-TEC CPD 030 (Liechtenstein). The dried samples were rotary coated with 3–4 nm of platinum (BAF 100, Balzers) at a tilt angle of 45 and investigated with a Hitachi SU5000 FE-SEM at an acceleration voltage of 20 kV.

Selective etching preparation for SEM imaging of aggregates surfaces

The obtained aggregates grown in the hybrid EPS-agarose hydrogels were embedded in EPON resin. The samples were first cut using an Ultracut ultramicrotome (Leica) and diamond knives (Drukker, Diatome) to obtain plane surfaces within the material. These surfaces were then polished with a diamond knife (Diatome) by stepwise removal of material in a series of sections with successively decreasing thicknesses (90 nm, 70 nm, 50 nm; each step was repeated 15 times Fabritius *et al.* 2005). The polished crystals were etched for 90 s using 0.1M HEPES (pH = 6.5) containing 2.5% glutaraldehyde (v/v) as a fixative. The etching procedure was stopped with 100% isopropanol and then washed in 100% isopropanol three times for 10 min each. Afterward, the specimens were critical point dried in a BAL-TEC CPD 030 (Liechtenstein). The dried samples were rotary coated with 3 nm platinum and imaged using a Hitachi SU5000 FE-SEM at 20 kV.

Preparation of the crystals for electron backscatter diffraction (EBSD) analysis

Electron backscattered diffraction (EBSD) measurements were carried out on microtome cut and polished aggregate surfaces coated with 4–6 nm of carbon. For measurements, a Hitachi SU5000 FE-SEM equipped with a Nordlys II EBSD detector was used. Data acquisition and evaluation were done with the Oxford Instruments AZtec and CHANNEL 5 HKL software, respectively. Crystal orientation patterns are presented as color-coded EBSD maps and corresponding pole figures. In addition to pole figures showing individual data points, c- and a*-axes pole density distributions of calcite is also given. At data evaluation, the lowest possible setting for half width and cluster size: a half width of five and a cluster size of three deg was used. The half width controls the extent of the spread of the poles over the surface of the project sphere; a cluster comprises data with the same orientation. The co-orientation strength of the crystallographic axes is derived from density distributions of pole figures. It is quantified with the MUD (multiple of uniform (random) distribution) value, which is calculated with the Oxford Instruments CHANNEL 5 EBSD software. High MUD values indicate high crystal co-orientation, while low MUD values reflect a low to random co-orientation (see also Nindiyasari *et al.* 2015; Greiner *et al.* 2018).

EPS-hydrogel occlusion induces misorientation between crystallites and, thus local strain. This can be visualized with local kernel misorientation maps and relative frequency versus local kernel misorientation diagrams. In this study, local kernel misorientation is calculated with 3 × 3 pixel clusters.

EPS-hydrogel occlusion within the composite aggregate can be highlighted with point-to-origin misorientation profiles. The latter depicts the angle of misorientation with respect to a chosen reference orientation for all measurement points along the trajectory of a line through the EBSD map. The orientation of the starting point of the line was used as the reference. Misorientation (in deg) is plotted as a function of distance (in μm) from the reference point.

2.5.3 Results

EPS composition

Figure 2.5-1 shows a representative FTIR spectrum of the total EPS of *P. putida*. On the basis of the strongest absorption bands, three different spectral zones can be identified: zone 1 covers the spectral region between 3000–2800 cm^{-1}, zone 2 is located at the spectral region between 1750–1500 cm^{-1} and zone 3 is in the spectral range between 1200–900 cm^{-1} (Parker 1983). As the absorption peaks between 3000–2800 cm^{-1} are due to stretching vibrations of methyl and methylene groups (νCH, νCH$_2$), it could be deduced that polysaccharides contribute the strongest peaks in zone 1. In addition, polysaccharides contribute in zone 3 the strong absorbance peaks at 1034, 1043, and 1078 cm^{-1}, and these are due to the presence of C–O, C–OH, and C–C groups (Wiercigroch *et al.* 2017). In zone 3, absorbance peaks at 929 and 1034 cm^{-1} are characteristic for xylose, which indicates that *P. putida* EPS has also a high content of monosaccharides (Sardari *et al.* 2017). Absorption bands at 1730, 1457 and 1400 cm^{-1} are derived from the presence of carboxylic groups in polysaccharides (Marxen *et al.* 1998). The broad peaks in zone 2, located at an absorbance of about 1620 and 1550 cm^{-1}, can be attributed to amide groups in proteins. In summary, our FTIR measurements indicate that *P. putida* EPS consists of polysaccharides and proteins.

EPS chemistry depends on the extraction method (Comte *et al.* 2006; Klock *et al.* 2007; Redmile-Gordon *et al.* 2014). The extraction method followed in this study (triplicate extraction with NaCl, triplicate centrifugation and alcohol precipitation) has been proposed before as a suitable procedure to extract EPS (Klock *et al.* 2007). The influence of intracellular components in the chemistry of the EPS needs to be taken also into account. Previous work has shown that when the ratio of protein/polysaccharides in the EPS was low (< 2) a significant occurrence of cell rupture cold be excluded (Comte *et al.* 2006). In our case, this ratio is ∼1, and therefore, the intracellular components do not have a significant occurrence in the EPS composition.

Characteristics of the composites

Figures 2.5-2 to 2.5-4, 2.5-S2 to 2.5-S4, and 2.5-S7 depict the fabric of agarose hydrogel and that of *P. putida* EPS, characteristic morphologies of the investigated aggregates, their surface constitution, and mode of EPS-agarose hydrogel occlusion and distribution within the aggregate.

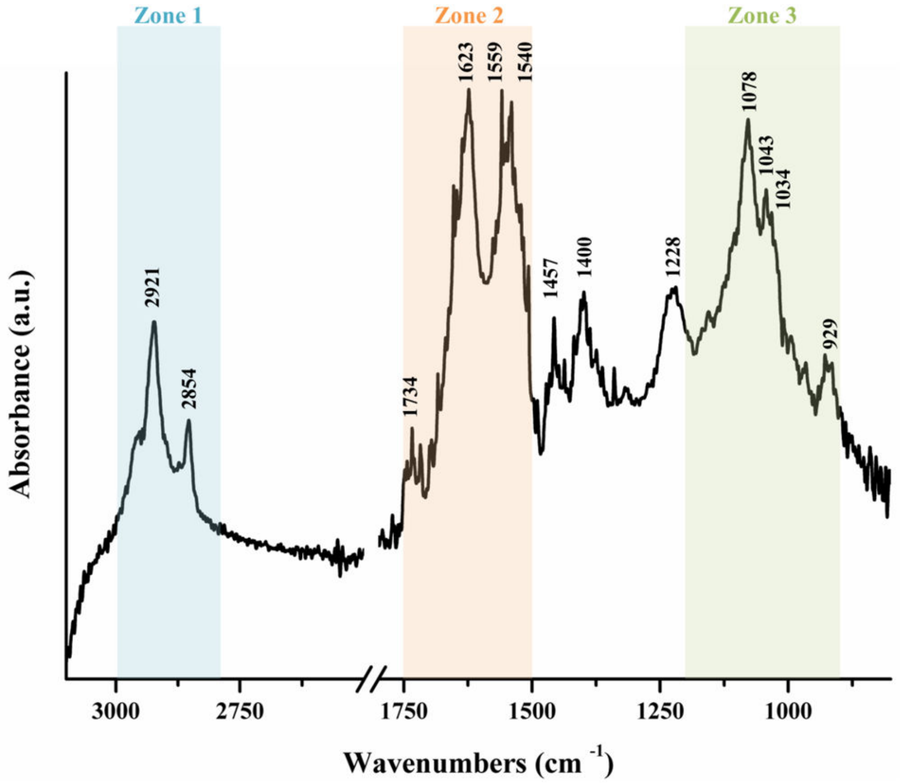

Figure 2.5-1. FTIR spectra of *P. putida* total EPS. The wavenumbers of the main absorption bands are indicated. The three marked zones define regions of functional groups, which can be associa-ted with proteins (zone 2) and polysaccharides (zones 1 and 3).

Figures 2.5-2c,d,g, 2.5-3a–c, 2.5-4a, 2.5-S4a, and 2.5-S7b,c show aggregates that grew in an environment devoid of EPS, while Figures 2.5-2e,f,h, 2.5-3d–g, 2.5-4b, 2.5-S4b, and 2.5-S7a depict composite aggregates that formed in growth media containing *P. putida* EPS. For all aggregates, the carbonate phase is calcite (Fig. 2.5-S5). Reference aggregates that grow in pure agarose gel have mean sizes of 250 ± 50 μm and consist of six dendritic branches (Fig. 2.5-2c). These branches are organized in two sets of three branches each arranged such that they reproduce the $\bar{3}$ axis of the calcite symmetry. The branches are oriented parallel to <4$\bar{4}$1> directions. A detailed inspection of the branches reveals that these comprise many highly stepped {104} rhombohedron and nonsingular, curved surfaces, respectively (Fig. 2.5-2d). Even though most steps that bound these surfaces are straight and parallel to [4$\bar{4}$1] and [48$\bar{1}$] directions, some rough steps that are parallel to <010> are found.

The morphology of aggregates that grow in a polymer mixture consisting of *P. putida* EPS and agarose gel is radial (Fig. 2.5-2e). Aggregate mean sizes scatter around 120 ± 20 μm. These aggregates consist of small, blocky rhombohedron-like subunits bounded by extremely rough {104} surfaces and poorly defined edges and corners (Fig. 2.5-2f). The close observation of these rough surfaces is evidence that they are comprised of numerous triangle-like sub-blocks, which appear to be highly co-oriented locally.

EPS and/or agarose gel occlusion and the pattern of distribution within the aggregate are visualized with local kernel misorientation maps (Figs. 2.5-2g–i, 2.5-3, and 2.5-S7). Occluded gel and/or EPS induces misorientation and strain between crystallites. Misorientation between neighboring crystallites is increased (visualized with green to yellow colors) where polymer occlusion is extensive, while aggregate portions that contain little gel or/and EPS show a low degree of misorientation between crystallites (indicated with bluish colors; see also Greiner *et al.* 2018; Yin *et al.* 2019). In calcite single crystals grown from pure hydrous solution, misorientation is well below 0.2 deg as these do not contain any occluded gel (Fig. 2.5-S6a,b).

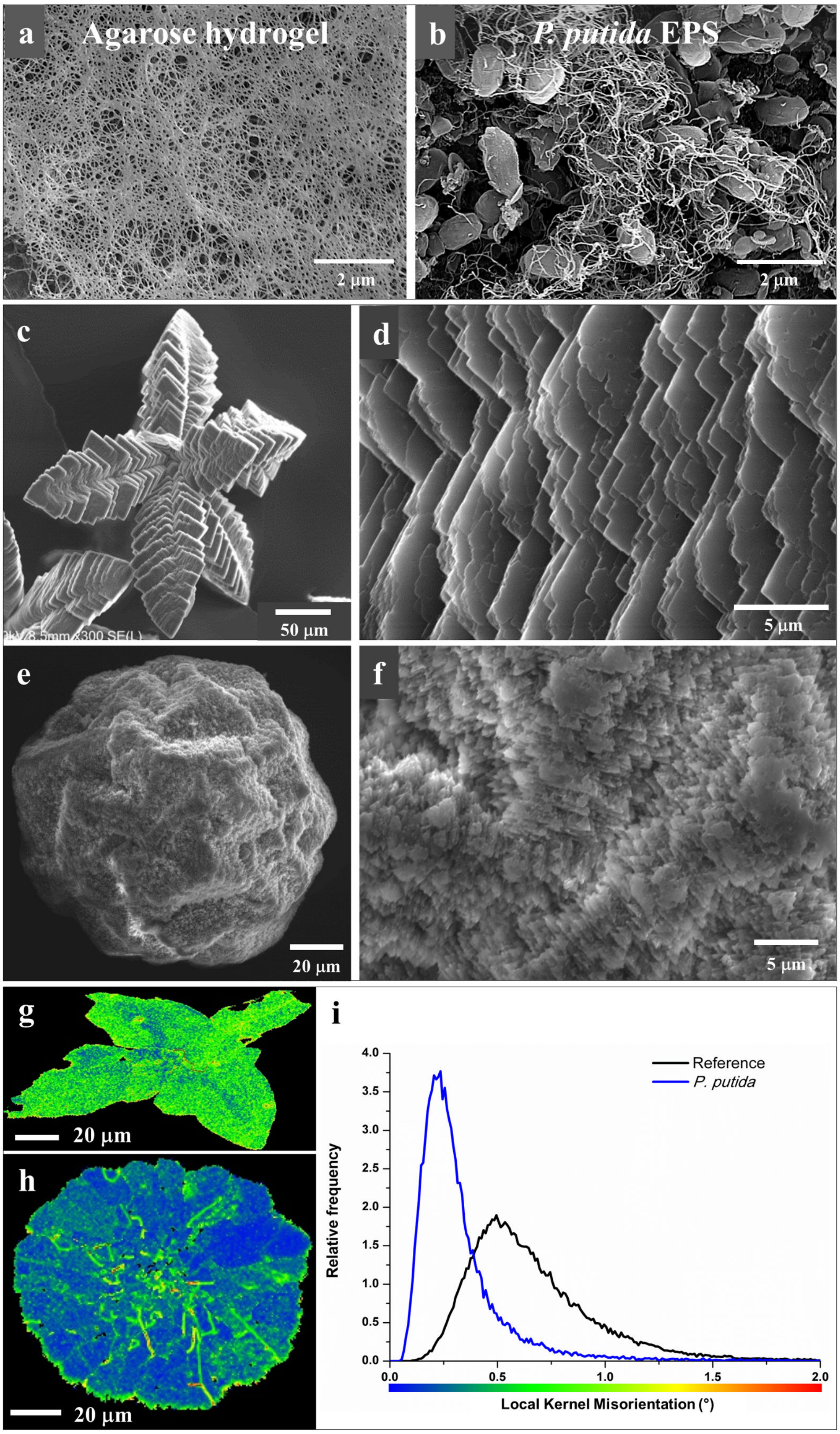

Figure 2.5-2. FE-SEM images of (a) pure agarose hydrogel fabrics and (b) *P. putida* EPS fabrics; morphology and surface constitution of composite aggregates that formed in (c, d) pure agarose gel and in (e, f) EPS agarose gel mixtures, respectively. The local kernel misorientation map, which visualizes the distribution pattern of the local strain within the aggregates that mainly results from the gel occlusion in our study (g) a reference aggregate formed in pure agarose hydrogel and (h) an aggregate grown in an EPS containing medium. (i) The diagrams showing that of the corresponding relative frequency vs local kernel misorientation.

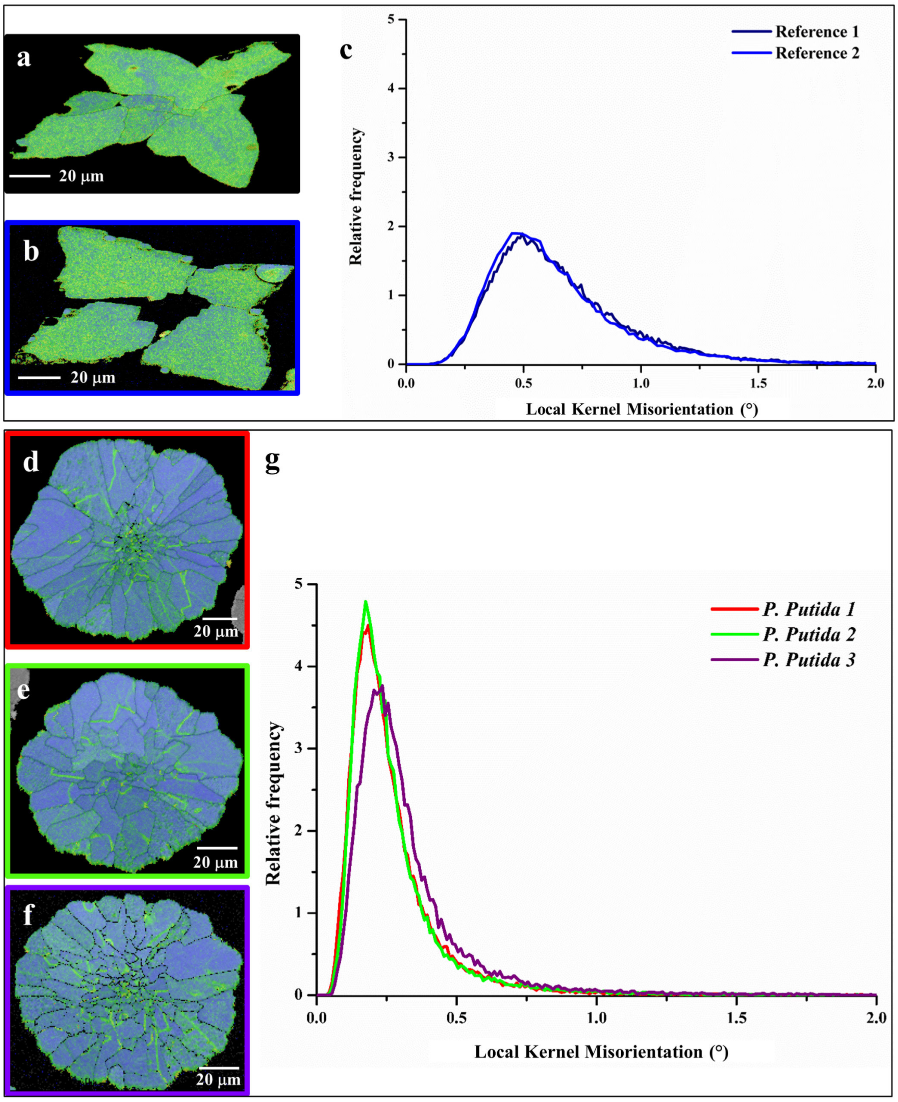

Figure 2.5-3. Local kernel misorientation maps and corresponding relative frequency versus misorientation diagrams for aggregates that grew in pure agarose hydrogel (a–c), and aggregates obtained in an EPS agarose gel mixture (d–g). The addition of *P. putida* EPS to the growth environment influences the amount and pattern of distribution of gel and/or EPS within the aggregate.

We observe significant differences in the patterns of EPS-hydrogel occlusion and distribution (Figs. 2.5-2g–i, 2.5-3, and 2.5-S7) between aggregates that grew in EPS-free and EPS-containing environments. In the EPS-free reference aggregate, gel occlusion is increased, relative to aggregates that contain *P. putida* EPS, and the gel is pervasively distributed within the aggregate (Figs. 2.5-3a–c and 2.5-S7b,c).

Aggregates that formed in an environment containing EPS are comprised of many subunits (Figs. 2.5-3d–g and 2.5-S7a). Gel occlusion in these subunits is either very low or even almost nonexistent. EPS-hydrogel accumulations are present as membranes. These are observable: (i) as minor amounts of polymers at boundaries delineating subunits (Fig. 2.5-S7a) and (ii) as high amounts of polymers defining membranes that often cross-cut the subunits (Figs. 2.5-3d–g and 2.5-S7a). The lateral extent of the membrane as visible in the cross-sections is in the order of 10–100 μm.

The development of subunits is a major difference between aggregates that formed in growth media with and without EPS. They are rare in reference aggregates, while they are highly developed in aggregates that contain EPS. Furthermore, in the latter, there is a large variation of subunit sizes and no structured distribution of the differently sized subunits within the aggregates. As shown by misorientation profiles across the subunits, they are tilted relative to each other by 10 to 20 deg (Fig. 2.5-4b). The tilt between subunits of the reference aggregate is in most cases below 10

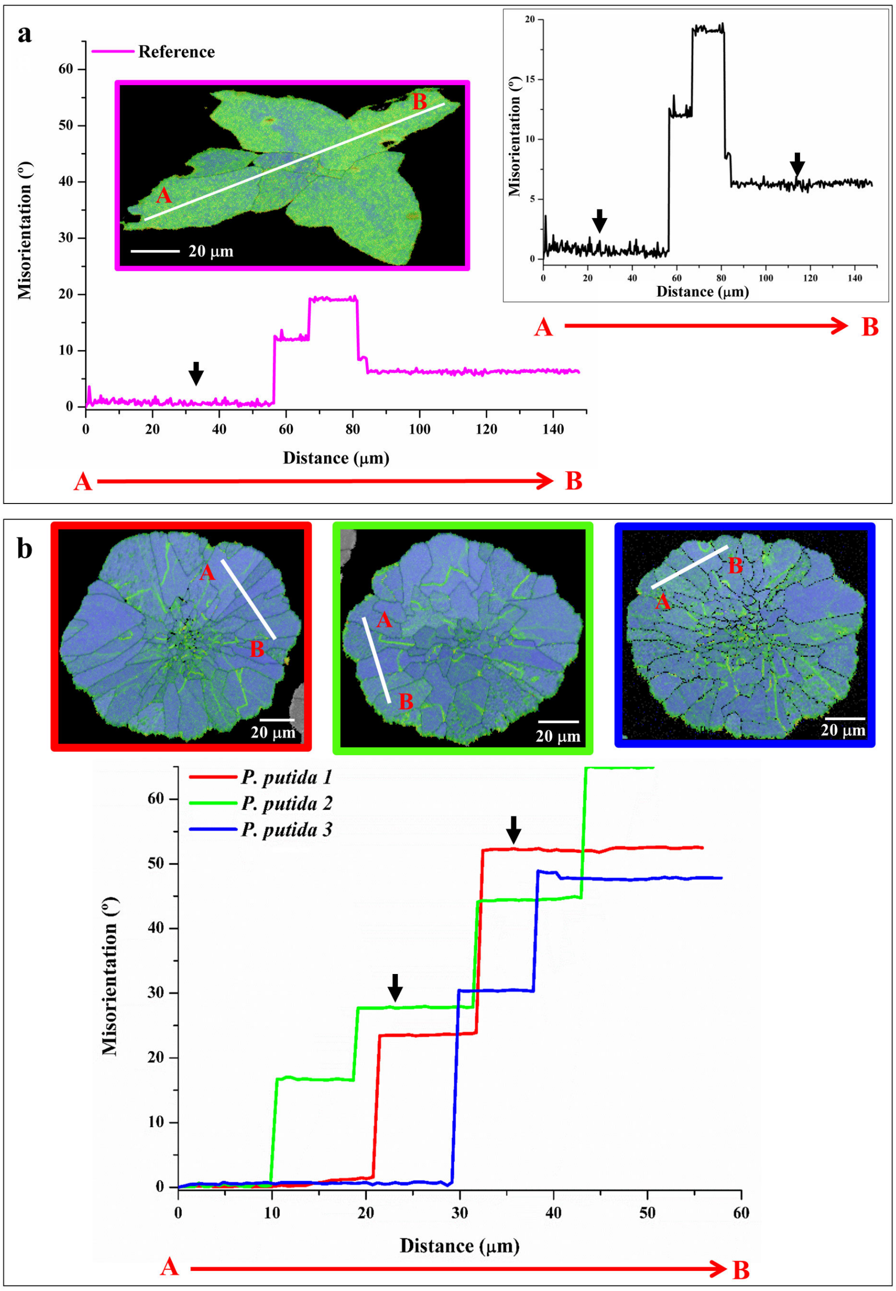

Figure 2.5-4. Plots of the misorientation versus distance diagrams along with the profile from A to B for (a) an aggregate obtained in pure agarose hydrogel (the insert in the panel is an enlargement of the same plot), and (b) for aggregates formed in EPS-agarose hydrogel mixtures (b), respectively. Irrespective of the presence or absence of EPS in the growth environment, all aggregates we obtained in this study are mosaic crystals with the tilt between two neighboring subunits varying between 10 and 30 deg. The wiggle in the misorientation vs distance profiles of the composite aggregates formed without EPS is very visible (black arrows in a, seen better in the inset in the figure). This indicates the pervasive occlusion of gel within the calcite of the reference, which is in contrast to the point-to-origin misorientation profiles of the aggregates grown with EPS (black arrows in b). A wiggle in the plot of panel b is almost absent and indicating very little EPS-agarose is intercalated in the subunits.

deg (Fig. 2.5-4a). In contrast to the misorientation versus distance curves of aggregates that formed in the presence of EPS, the curves we obtain from reference crystals have a marked scatter (wiggle) in misorientation along the given profiles (see the black arrows in Fig. 2.5-4). The scatter is on the order of a few deg and points to the presence of an occluded gel (Fig. 2.5-4a and the inset in 2.5-4a). Experimental scatter of a misorientation curve of a single crystal, a crystal without any occluded polymer, is in the range of 0.2 to 0.4 deg (Fig. 2.5-S6d). It is interesting to see that in aggregates that grew in growth media containing bacterial EPS, the scatter in misorientation is almost absent (Fig. 2.5-4b). This feature is a clear indication that very little (or no) EPS-hydrogel is occluded within the subunits. The pervasive occlusion of gel in the reference aggregate is apparent with its highly stepped {104} rhombohedron surfaces (Fig. 2.5-S9a). This is not the case for aggregates that grew in an EPS-agarose hydrogel mixture. Local kernel misorientation analysis shows most of the polymer that is occluded within the aggregate is present as membranes, delineating the subunits.

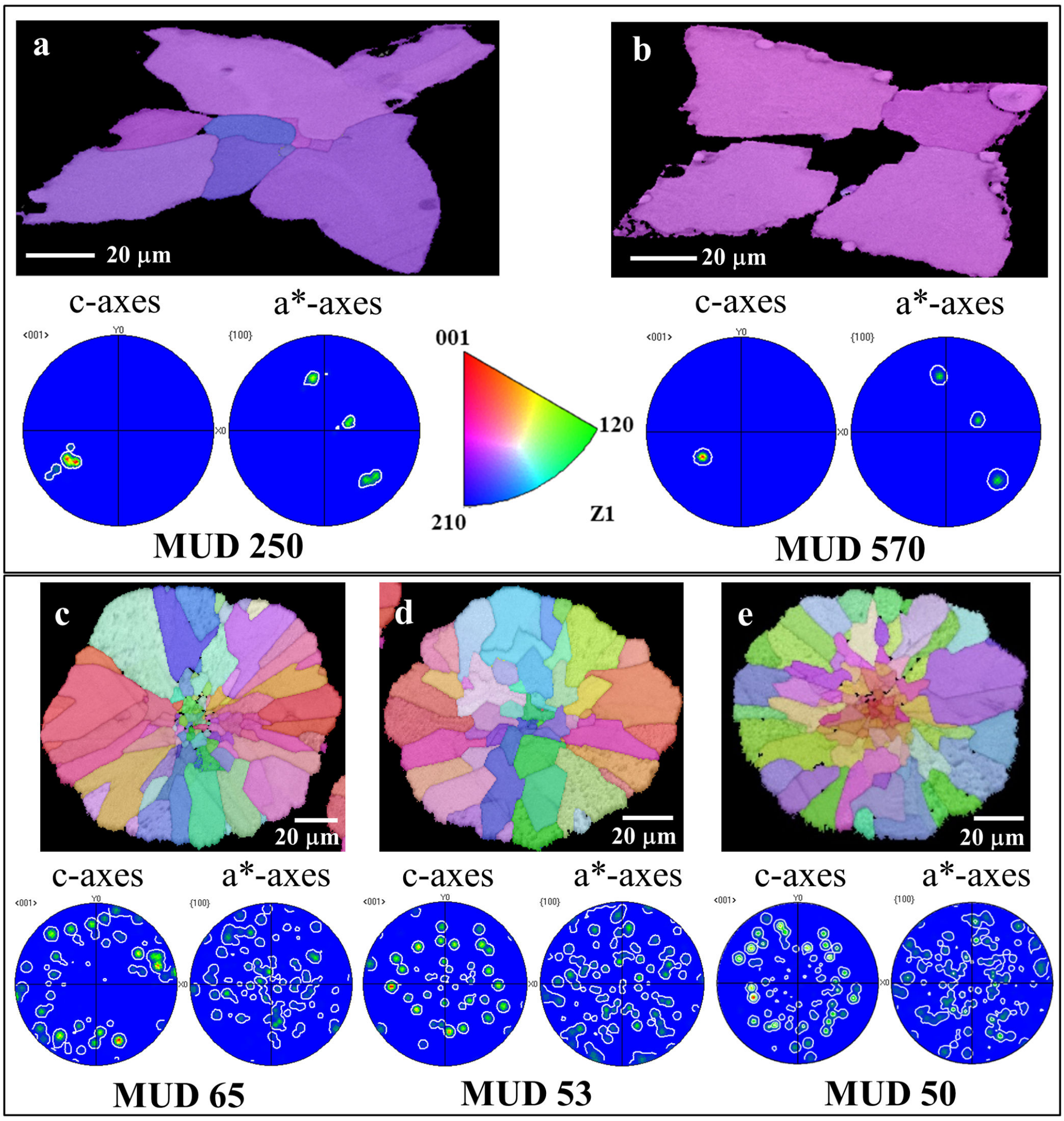

Figure 2.5-5. Crystal orientation patterns are shown with color-coded EBSD maps and corresponding pole figures: (a, b) calcite composites formed in pure agarose hydrogel; (c–e) calcite aggregates obtained in *P. putida* EPS-agarose gel mixtures. The pole figures give the density distributions of calcite c-axis and a*-axes. The color in the maps codes for calcite orientation. The color code in the center is valid for all EBSD maps in this figure. In contrast to the reference crystals (a, b) where coalignment of calcite is high (MUD values of 250 and 570), the strength of overall calcite co-orientation is low in aggregates that formed in the presence of *P. putida* EPS (MUD values, 50, 53, and 65).

Calcite organization in the composite aggregates and their subunits

The mode of crystal organization and co-orientation strength within all aggregates was determined with electron backscattered diffraction (EBSD). Orientation information, texture (Figs. 2.5-5, 2.5-6, and 2.5-S8), is presented with color-coded orientation maps and corresponding pole figures, the latter showing either the individual data or pole density distributions for calcite c-axes ({001}-poles) and a*-axes ({100}-poles). The strength of crystal co-orientation is expressed with the MUD value. This value is high when crystal co-orientation is high (e.g., in the case of single crystals) and is low when crystal co-orientation is low (e.g., in the case of randomly oriented polycrystals). For calcite single crystals grown from solution, the MUD value scatters around 700 (Nindiyasari *et al.* 2014a). Microstructural characteristics of the investigated aggregates and their constituting subunits are visualized with EBSD

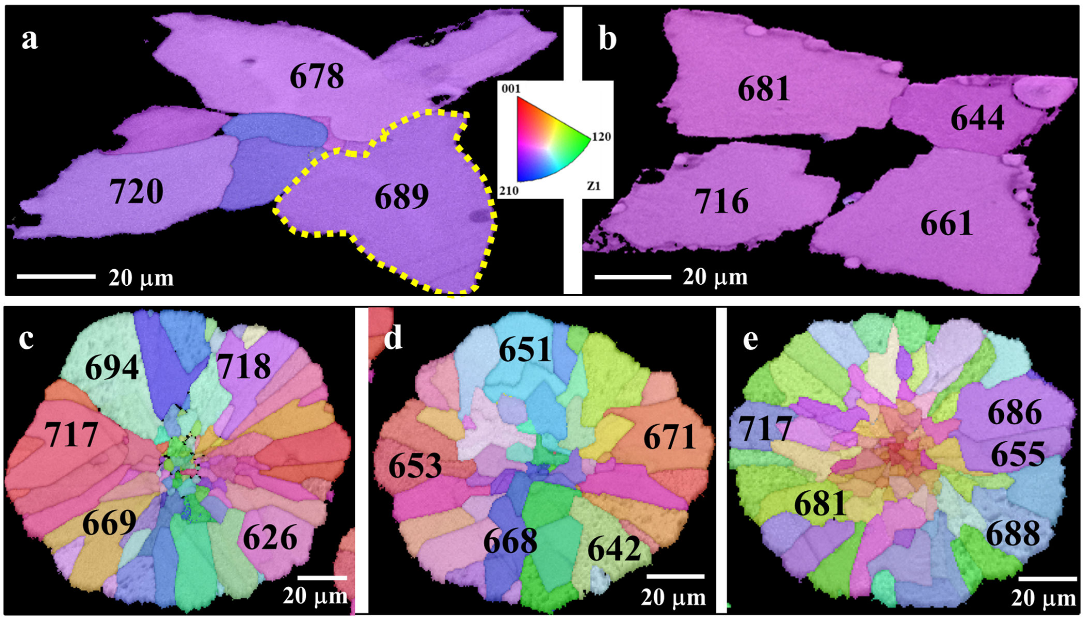

Figure 2.5-6. MUD values for subunits given on color-coded EBSD maps of aggregates that formed in (a, b) pure agarose gel and (c–e) aggregates obtained in a *P. putida* EPS-agarose gel mixtures. MUD values indicate the strength of calcite co-orientation. It is high within individual subunits and similar for all aggregates, irrespective of the presence or absence of EPS in the growth medium. The color code in the center is valid for all EBSD maps in this figure.

band contrast images (Figs. 2.5-S7 and 2.5-S8). EBSD band contrast gives the signal strength of the EBSD-Kikuchi diffraction pattern in each measurement point. This signal is high when a mineral is detected, while it is weak or absent when a polymer or an amorphous phase is scanned.

There is a striking difference in calcite organization between aggregates that grew in the absence (Figs. 2.5-5a,b and 2.5-S8a,b) and presence (Figs. 2.5-5c–e and 2.5-S8c–e) of EPS in the growth medium. *P. putida* EPS in the growth environment led to spherically-shaped aggregates that consist of dozens of subunits, which have no, or very little, systematic orientation relationship to each other. The calcite that constitutes aggregates that grew in pure agarose gel is highly co-oriented (MUD values of 250 and 570, Figures 2.5-5a,b and 2.5-S8a,b), while the calcite in aggregates that formed in a growth environment that contained EPS shows almost no co-orientation of crystallites (MUD values scatter between 50 and 65, Figures 2.5-5c–e and 2.5-S8c–e). However, investigating calcite co-orientation strength on a different hierarchical level, at the level of individual subunits (Fig. 2.5-6), does not show a major difference in calcite co-orientation strength between aggregates that formed without (Fig. 2.5-6a,b) or with EPS (Fig. 2.5-6c–e) in the growth medium, respectively. For all subunits of all aggregates, their MUD values are high and very close to that of calcite single crystals grown from pure hydrous solution. Thus, EPS in the growth medium influences the number of subunits that developed and their mode of assembly within the aggregate. In the aggregate that contains EPS, the polymer (EPS and hydrogel) is mainly occluded as membranes, and a strong coalignment of subunits is prevented. A homogeneously occluded network of fibrils is present to a lesser degree than that in the reference. In summary, all aggregates that occlude bacterial EPS investigated in this study can be addressed as spherical polycrystalline aggregates without or very little texture. Although the aggregates are spherical, they do not show the typical spherulitic microstructure with c-axes pointing outward and small misorientation between neighboring crystallites (e.g., Yin *et al.* 2019).

Fabric of occluded EPS-hydrogel matrices

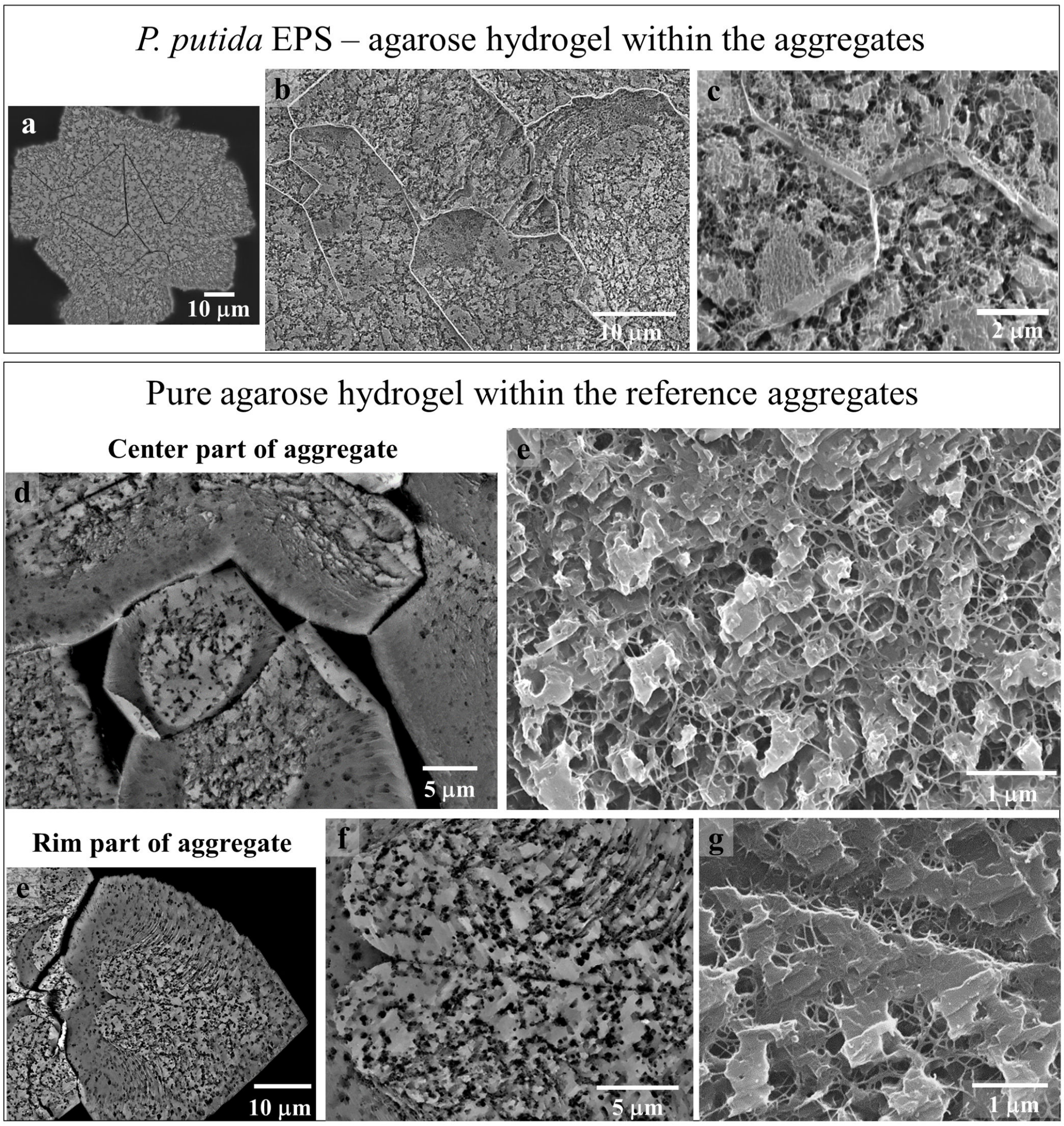

Figure 2.5-7. Mode gel of occlusion within (a, b) *P.putida* EPS-agarose hydrogel calcite composite, and (c–g) pure agarose-calcite aggregates. (a, b) Aggregates that grew in an agarose-EPS gel mixture. (c, d) Center part and (e–g) rim part of an aggregate that formed solely in agarose hydrogel. When EPS is absent in the growth medium, the gel network is pervasively distributed within the aggregate. Slight differences in the amount of occluded gel are observable between the center and the rim portions of the reference aggregate. However, the addition of EPS to the growth medium causes the formation of polygonal membranes that cross-cut the aggregate. Therefore, the occluded biopolymer is concentrated at the sites of these membranes, while very little gel/EPS is present within the subunits.

Figure 2.5-7 depicts the fabric of the occluded polymers. Figure 2.5-7a,b depict EPS-agarose hydrogel polygonal membranes cross-cutting the aggregate. Figure 2.5-7c–g visualize the presence of the pervasively occluded gel network within the reference aggregate, the aggregate that formed without EPS in the growth medium. In the latter case, a pattern arises from slight differences in the amount of the occluded hydrogel network between the center part and the rim part of the same aggregate.

2.5.4 Discussion

The chemical influence of bacterial EPS matrices: mineral nucleation

Microbial biofilms are characterized by the production of an, often extensive, hydrated network of exopolysaccharides. The EPS matrix consists of high molecular-weight polysaccharides that may include proteins, peptides, acidic moieties, phosphates, sulfates, even extracellular DNA (Neu & Lawrence 2016). Accordingly, the EPS matrix is chemically complex and reactive (Decho 1990, 2000; Dupraz & Visscher 2005; Flemming *et al.* 2007, 2016a; Dupraz *et al.* 2009; Gallagher *et al.* 2010; Pellicer-Nàcher *et al.* 2013) Depending on its chemical characteristics, the EPS matrix can influence, as outlined below, carbonate mineral formation in different ways:

1. Acting as a template and with this favoring nucleation. EPS surfaces are rich in negatively charged carboxylic groups. Around these groups, the concentration of positively charged ions will increase. This may reduce the nucleation barrier and can serve as a template that directs nucleation. The templating effect of EPS polymers may lead to preferred orientation if there is a structural matching between the organic molecules of the EPS matrix and specific (hkl) planes of the mineral (Rivadeneyra *et al.* 1996; Dupraz & Visscher 2005; Pan *et al.* 2019).

2. Promoting the formation of metastable polymorphs and inhibiting their transformation into the thermodynamically stable polymorph calcite: e.g EPS matrix promotes the formation of aragonite needles in modern stromatolites, xanthan-rich EPS induce the preferential formation of vaterite in soils, halophilic bacteria EPS promotes de the formation of monohydrocalcite (Braissant *et al.* 2003; Dupraz & Visscher 2005; Tourney & Ngwenya 2009). It has also been demonstrated that cyanobacteria EPS matrices can also promote the formation of amorphous calcium carbonate (ACC) nanoparticles (Benzerara *et al.* 2003; Hammes *et al.* 2003; Benzerara *et al.* 2006; Obst *et al.* 2009; Jones & Peng 2012; Diaz *et al.* 2017). *P. putida* EPS does not seem to stabilize any metastable calcium carbonate polymorph. Since all aggregates obtained in this work exclusively consist of calcite, had any other phase formed in EPS-agarose gels, it would have been short-lived.

3. Chelating ions through functional groups, and with this, affecting the local supersaturation of the solution. The chelating property of the EPS matrix is called forth through the presence of polysaccharide functional groups that can reduce the activity of some ions in the solution in the pore space. In systems such as hydrogels, where mobility is reduced as convection and advection are restricted, and mass transfer exclusively takes place through diffusion, chelating is particularly important. It reduces or delays the buildup of supersaturation in the hydrogel during the diffusion experiment (Henisch 1988; Prieto *et al.* 1989, 1994). The smaller size of calcite aggregates formed in hybrid *P. putida* EPS-agarose hydrogels compared to that of those formed in pure agarose gel hints at *P. putida* EPS influencing the formation of carbonate mineral by chelating ions.

Physical influence of bacterial EPS matrices: aggregate morphology and growth

The main morphological feature of calcite aggregates that grow in pure agarose gel, without EPS in the growth medium, is the formation of dendritic branches that reflect the characteristic $\bar{3}$ symmetry of calcite (Fig. 2.5-2c). All flat surfaces in these branches correspond to the $\{104\}$ form (Fig. 2.5-2d). These surfaces are the one with the lowest attachment energy and, consequently, the most stable surface in the calcite structure (Hartman & Perdok 1955a,b,c; Heijnen 1985; Staudt *et al.* 1994; Paquette & Reeder 1995). They contain four periodic bond chains (PBCs): two straight PBCs parallel to $[4\bar{4}1]$ and $[48\bar{1}]$ directions and two undulated PBCs that run along $[42\bar{1}]$ and $[010]$. The former of these two PBCs is rougher and, therefore, less stable than the latter. In calcite aggregates that grew in pure agarose gel, $\{104\}$ faces are highly stepped which gives rise to nonsingular vicinal surfaces. All steps observed in both flat and vicinal surfaces are parallel to the three most stable PBCs in {104}. Furthermore, consistent with the nanoscopic character of these PBCs, those steps that are parallel to $[4\bar{4}1]$ and $[48\bar{1}]$ appear to be straight, while those that are parallel to [010] are undulated (Fig. 2.5-2d). Both, the dendritic structures and the existence of nonsingular surfaces indicate that the growth of these aggregates (aggregates that form in pure hydrogel) takes place under supersaturation conditions that are close to the threshold value that marks the transition from a surface-controlled to a diffusion-controlled crystal growth regime (Sunagawa 1987).

Calcite that formed in hybrid *P. putida* EPS-agarose hydrogels is polycrystalline and consists of numerous radially arranged interlocking individual crystals in the size range of micrometers to tens of micrometers (Fig. 2.5-2e,f). These crystals have no preferred crystallographic orientation with respect to their neighbors and the overall spheroidal shape of the aggregate (Fig. 2.5-2e). The crystals are bound by rough surfaces parallel to the stable {104} surface and consist of nanometric triangular-shaped sub-blocks that are locally highly coaligned (Fig. 2.5-2f). Similar sub-block arrangements have been identified in biominerals such as calcareous sponge spicules (Sethmann *et al.* 2006) and sea-urchin skeletal elements.70 The formation of nanometric triangular sub-blocks was visualized in situ by Sethmann *et al.* (2005). during the growth of a calcite {104} substrate that was in contact with a highly supersaturated aqueous solution containing polyaspartate (pAsp). Polyaspartate is a polyanionic chain molecule that is considered to be a simple model substance for mimicking proteins that are associated with carbonate biominerals. In AFM experiments (Sethmann *et al.* 2005), the formation of triangular sub-blocks was preceded by coagulation and precipitation of a gelatinous film on the calcite substrate. The authors interpreted this sequence of events as reflecting the stabilization of colloidal amorphous calcium carbonate through binding to pAsp molecules that are attached to steps on the calcite surface.

The inhibition of regular calcite growth (through Kossel-Stranski step advancement Kossel 1927; Stranski 1928; Chernov 1984; De Yoreo & Vekilov 2003), resulting from biomolecule adsorption would trigger an alternative growth mechanism that involves synchronous homoepitactic nucleation at numerous locations on the substrate. In that case, calcite growth would progress by a continuum of nucleation events resulting in the formation of nanometric sub-blocks that grow on top of each other. This growth mechanism allows for the preservation of crystallographic orientation as well as for its transmission from one nanometric sub-block to the other. However, locally the transmission of crystallographic orientation might be disrupted, e.g., at those sites where biomolecules accumulate to a denser film or membrane. The triangular shape of the individual nanometric sub-blocks can be regarded to be the consequence of preferential adsorption of biomolecules onto specific planes in the calcite structure.

Calcite growth through deposition of a liquid or colloidal mineral precursor followed by separation of liquid droplets, the well-known polymer-induced liquid precursor (PILP) process has been used to explain the formation of some biominerals (Politi *et al.* 2004; Sethmann *et al.* 2005, 2006). This growth mechanism was confirmed experimentally in systems where calcite growth takes place in the presence of a variety of polypeptides (Gower & Odom 2000; Raz *et al.* 2003; Politi *et al.* 2004; Sethmann *et al.* 2005; Cheng & Gower 2006; Sethmann *et al.* 2006; Rodríguez-Navarro *et al.* 2016). *P. putida* EPS comprises a complex mixture of polysaccharides and proteins, the former having many active functional groups. A bimodal functionality of the polymers is easily conceivable, having chelating functions as well as inhibiting mineral growth. The accumulation of biomolecules at the growth front, as discussed above, could lead to a surface-directed formation of PILP-like layers and particulate precursors, that form side-by-side to sequences of homoepitactic nucleation events. This alternative growth mechanism would explain many of the observed features of aggregates occluding *P. putida* EPS-agarose hydrogel polymers, e.g., the numerous locally highly co-oriented nanometric sub-blocks. Furthermore, molecular recognition between specific *P. putida* EPS components and planes in the calcite structure could account for the unusual triangular shape of the constituting nanometric sub-blocks (Mann *et al.* 1990; Aizenberg *et al.* 1997; Teng & Dove 1997; Metzler *et al.* 2010). However, it should be borne in mind that on the micrometer scale the aggregate is polycrystalline as it consists of dozens densely interlocking crystals that have no or little mutual co-orientation. Between those crystals membranes of accumulated polymer are frequent.

Physical influence of bacterial EPS matrices: EPS and agarose gel occlusion

All aggregates investigated in this study are polymer-mineral composites that contain *P. putida* EPS and/or agarose hydrogel intercalated within the mineral. We find distinct differences between aggregates that formed in pure agarose gel and aggregates that grew in the presence of EPS-agarose gel hybrids, regarding both (i) the content of occluded gel and (ii) the pattern of gel distribution within the mineral. The occluded hydrogel content is higher, and its distribution is more homogeneous in that calcite that formed in pure agarose gel (Figs. 2.5-2g and 2.5-3a,b). In contrast, in aggregates that grew within hybrid EPS-agarose gels the polymer (EPS-hydrogel) is mainly concentrated at sites of membranes. These membranes delineate the many, irregularly sized, shaped and distributed subunits (Figs. 2.5-2h and 2.5-3d–f). Individual subunits contain only a very small amount of occluded EPS-hydrogel.

Gel occlusion during crystal growth is controlled by two main parameters: (i) gel strength and (ii) growth rate (Li & Estroff 2007, 2009; Asenath-Smith *et al.* 2012). High values of both parameters facilitate the occlusion of the entire gel network within the growing crystal without any significant disruption of gel pore shapes and size (Asenath-Smith *et al.* 2012; Nindiyasari *et al.* 2015). Low gel strengths and/or low growth rates promote the formation of crystals that are virtually gel-free (Asenath-Smith *et al.* 2012; Greiner *et al.* 2018). The gel strength of physical gels, as it is the case for agarose hydrogel, relates directly to its solid content (Asenath-Smith *et al.* 2012; Greiner *et al.* 2018). As we used the same agarose concentration in all our experiments (with and without EPS), it must be expected that both (i) pure agarose gel as well as (ii) the hybrid EPS-agarose gel have similar gel strengths, even though, we cannot discard entirely that EPS in the used polymer mixture affected the rheological properties of agarose gel; increasing or decreasing its gel strength. The evaluation of such an effect is beyond the scope of this work, however, we regard it very unlikely that the mechanical response of agarose and EPS-agarose gels to crystallization pressure was significantly different in our crystal growth experiments. It can be safely assumed that the distinct characteristics of gel occlusion that we observe for aggregates that formed without and with EPS in the growth medium reflect the growth of aggregates under different crystal growth regimes. The latter involves different growth mechanisms and, consequently, different growth rates.

The data presented here suggest that in the presence of *P. putida* EPS calcite growth takes place through an alternative mechanism that results from both, physical as well as chemical interaction of polymers with the calcite structure and involves a suite of many nanoscale nucleation events. It stands to reason that the growth processes that involve a high number of growth steps will yield slower growth rates, as the aggregates that formed in an EPS-containing hydrogel are smaller than those that formed in pure agarose hydrogels. This could explain that the subunits of aggregates that contain *P. putida* EPS comprise much less gel in comparison to those that grew in an agarose gel matrix devoid of EPS (Figs. 2.5-3 and 2.5-7).

Hydrogel fibers that are not occluded within the growing crystal are displaced and become squeezed together, hence, the gel solid content concentrates ahead of the crystal growth front (Nindiyasari *et al.* 2014b, 2015; Greiner *et al.* 2018). The rearrangement of gel fibers accounts for the formation of the numerous membrane-like gel accumulations. These we find in aggregates that grow in hybrid EPS-agarose hydrogel, as membranes separating their almost gel-free subunits (Fig. 2.5-7a,b).

In the case of a fast growth rate, a scenario that is given when pure agarose gel is used in the growth experiments, hence, in the absence of potential chelates, the calcite aggregates that formed are characterized by a pervasive and mostly homogeneous entrapment of gel (Fig. 2.5-7c–g). The assumption of a fast growth rate for these, the reference crystals is in good agreement with the morphological features that we observe: dendrite-like branches (Fig. 2.5-2c) that indicate that their formation is taking place at relatively high supersaturation conditions and comparably reduced mobility of Ca^{2+}/CO_3^{2-} building units along the crystal surface (Sunagawa 2005).

The physical influence of bacterial EPS matrices: Subunit formation and hierarchical calcite organization

The pervasive occlusion of gel observed in calcite grown in pure agarose gel causes local strain within the aggregate and induces misorientation. Accordingly, the MUD values of the subunits that constitute this aggregate are below 700 (Fig. 2.5-6a, b), indicating a weaker co-orientation than found in calcite single crystals grown from solution (MUD = 725) (Nindiyasari *et al.* 2014a). Even though the distribution of occluded gel throughout the reference aggregate is mostly homogeneous, slight variations in the amount of entrapped gel can be seen between inner parts of the aggregate and regions close to the tip of the constituting dendritic branches (Fig. 2.5-7c,e).

The tip of the dendrites occludes more gel than the central regions of the reference aggregate (Fig. 2.5-7c,e). The gel-poorer rim can be explained by a decrease in the growth rate at later stages of the crystal growth process. The concentration and rearrangement of gel fibers ahead of the growth front at these later stages could lead to the formation of gel membranes that would necessarily by few in number and very short-ranged. The lack of thick laterally extended gel membranes explains that aggregates that formed in pure agarose gel comprise very few and highly co-oriented subunits, separated by small-angle boundaries of 6 to 10 deg (Fig. 2.5-4a). The microstructure and texture that result when these small-angle boundaries are developed explain the observed low MUD value (250) for the overall reference aggregate (Fig. 2.5-5a,b).

In contrast, the largely inhomogeneous entrapment of the gel network during the growth of aggregates in EPS-agarose hybrid gels and the concomitant formation of numerous and laterally much more extended membrane-like gel accumulations within these aggregates determines that they consist of many strongly misoriented subunits (Fig. 2.5-7a,b). Misorientation-angles across grain boundaries vary between 5 deg and close to 40 deg (Fig. 2.5-4b) and are thus significantly larger than the small-angle boundaries that we find for the dendritic reference crystal that formed without EPS in the growth medium.

The calcite grown in EPS-agarose forms spheroid-like shaped polycrystalline aggregates of dozens of densely interlocking but mutually non-co-oriented crystals in the size range of one to some tens of micrometers. Individually these crystals show good internal co-orientation (Fig. 2.5-6c–e) and rhombohedral {104}-type surfaces,

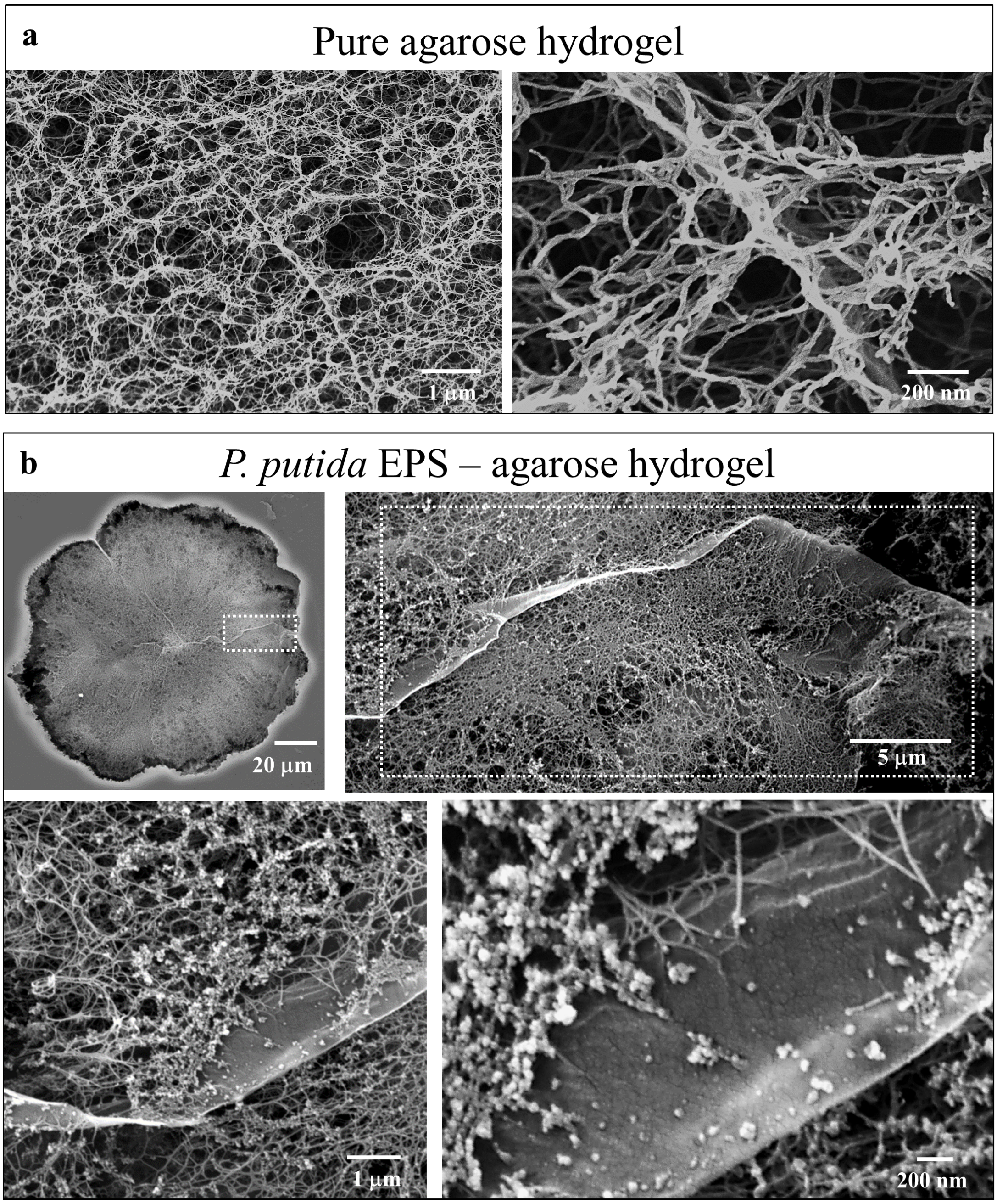

Figure 2.5-8. Fabric of (a) pure agarose hydrogel and (b) *P. putida* EPS-agarose mixture after composite aggregate crystallization. The mineral of the composite is dissolved by decalcification, and the biopolymer is fixed simultaneously with fixatives. (a) In pure agarose hydrogel, the fibrils of the agarose are occasionally pushed together by the growing calcite during the composite formation. (b) When EPS is included in the growth medium, dense solid membranes were developed.

---

which may hint to episodic homoepitactic growth on the nanoscale. The membranes of accumulated gel separate the microscale crystal units (Fig. 2.5-7a,b). The membranes clearly form as the growing crystal pushes the organic gel network ahead of the growth front. Gel/EPS accumulation is most pronounced at the contact of two growing and abutting crystals. As long as the EPS-gel accumulation at the growth front is small and contains pores, crystal growth can proceed homoepitaxially into unoccupied space. However, when gel accumulation leads to a dense surface film, which significantly blocks the access of further ions from the solution, crystal growth under the film will stop. At the same time, in the type of experiment performed here, the diffusion from the reservoirs will continuously feed ions into the system and built up supersaturation. At a certain threshold, heterogeneous nucleation will occur on the outside of the accumulated gel film, such that a new crystal with a random crystallographic orientation with respect to the underlying crystal will start to grow. This scenario will act in an episodic fashion (a temporary depletion of the solution surrounding the growing crystal may also lead to intermittent cessation of crystal growth) and the spheroidal portions of interlocking, mutually misoriented microcrystals can develop.

Both calcite aggregates that grow in pure and EPS-bearing agarose hydrogels consist of subunits that contain occluded gel and are internally highly co-oriented calcite crystals. Following the definition proposed by Greiner *et al.* (2018). and according to their microstructural characteristics, these aggregates and their constituting subunits fall into one of three categories:

1. The subunits, which in both types of aggregates have MUD values that are indicative of a high internal co-orientation (although weaker than that of calcite single crystals formed from aqueous solution, MUD = 725) can be classified as *mosaic crystals*.
2. The aggregates grown in pure agarose hydrogel consist of a few highly co-oriented subunits which are arranged with large angle boundaries between them and can be described as *well co-oriented polycrystal composites*.
3. The aggregates obtained from EPS-agarose hybrid hydrogel are constituted by numerous internally highly co-oriented subunits that are structured leaving large angle boundaries between them in almost randomly co-oriented arrangements. These aggregates can be referred to as *poorly co-oriented polycrystal composites*.

The resulting objects are mineral-polymer composites that resemble gel-grown calcite crystals having hierarchical mesocrystalline microstructures (e.g., Cölfen 2001; Sugawara *et al.* 2003; Kulak *et al.* 2007; Nindiyasari *et al.* 2014a). Nindiyasari *et al.* (2014a,b, 2015) have shown that the morphology, mosaicity, and degree of coalignment in gel-grown calcite aggregates relates directly to the type of gel, where the aggregates form, the unique rheological properties of the gel and its chemical characteristics such as type and amount of functional groups present on the walls of the gel pores. The gel polymeric matrix of the hydrogel becomes occluded within the mineral during growth, strongly influencing its microstructural organization. This influence is higher when the gel is stronger and can be significantly enhanced by the presence of certain foreign ions, such as Mg or organic macromolecules in the growth medium (Nindiyasari *et al.* 2019).

Polymer accumulation and membrane formation

Research of the last few decades has shown that organic matrices incorporated within the biological hard tissue significantly influence crystal nucleation, mineral organization, and material properties of the structural biomaterial (Nudelman *et al.* 2007; Checa *et al.* 2016). Biopolymer matrices are occluded within the hard tissues with organism-specific characteristic mesoscale grid structures (matrices of membranes and networks of fibrils). The organic scaffold controls the architecture of basic mineral units (e.g., nacre tablets, calcite fibers) as well as their assembly to a functional structural material (Checa *et al.* 2009). Hence, the assembly pattern of the biomineral is adjusted according to the fabric of the preformed organic matrix, the scaffold membranes, and the network of fibrils (Simonet Roda *et al.* 2019a). Accordingly, in order to understand patterns of mineral organization in carbonate biological hard tissues, it is of specific interest to understand the incorporation of the biopolymer network into the biomineral, particularly, patterns of local accumulations up to the formation of membranes. An appropriate approach is to juxtapose and compare characteristics of the effect of polymer matrices within biomimetic composite aggregates with biopolymer matrices present in carbonate biological hard tissues.

In the EPS-free synthetic agarose system, we only find the incorporation of a gel network, and as a consequence of aggregate formation at higher growth rates, the gel is pervasively and homogeneously distributed/occluded within the calcite of the aggregate. In aggregates that formed in the growth medium containing EPS, the occluded polymer is inhomogeneously distributed as both networks and membranes. Our results show that membrane formation occurs extensively in aggregates that form in the presence of the used EPS. On rare occasions, when membrane-like accumulations develop in reference aggregates, these appear as loosely connected fibrils that are pushed together (Fig. 2.5-8a). In contrast, membranes within aggregates containing EPS are thick, solid walls and are without any pores or perforations (Fig. 2.5-8b). This is of major importance and contrasts with the features of scaffold membranes in biological hard tissues (Fig. 2.5-9). Even though membrane thickness in aggregates containing EPS is quite similar to that present in biocarbonate structural materials, membranes within the latter materials are always porous. Extracellular matrix membrane porosity in biological hard tissues is an intrinsic requirement, as at hard tissue formation, the mineral, its phase, and crystallographic information on biocrystallites have to be transmitted from one compartment to the other (Checa *et al.* 2011, 2013; Griesshaber *et al.* 2013; Macías-Sánchez *et al.* 2015; Osuna-Mascaró *et al.* 2015). The lack of porosity of biopolymer membranes would impede the transmission of this information, and thus, the biological structural material could not be fabricated. Furthermore, the arrangement of membranes and fibrils of extracellular matrices in biological structural materials is highly structured (Fig. 2.5-9, see also Osuna-Mascaró *et al.* 2015). This characteristic as well contrasts significantly with the irregular pattern of membrane distribution that we observe in aggregates that formed in the presence of bacterial EPS within the growth medium.

2.5.5 Conclusions

Bacterial communities are embedded in a self-produced matrix, a three-dimensional network of extracellular polymeric substance (EPS). This matrix enables microbial cells social and physical interaction as well as cooperation, resource capture, and survival (Flemming *et al.* 2016a). The achievement of these fundamental properties relies on the structural and functional characteristics of the EPS matrix. Moreover, the exquisitely structured Ca-carbonate in the shells of marine invertebrates is likely to form in an extracellular polymeric matrix formed by the outer mantle epithelial cells. For understanding the directing influence of a natural biopolymer matrix such as bacterial EPS on biomineral organization, we synthesized polymer-carbonate composite aggregates with and without EPS of the Gram-negative bacteria *Pseudomonas putida* in the growth medium. We deduce the following conclusions from our results:

1. The addition of a small amount of *P. putida* EPS to the growth medium exerts a tremendous influence on composite aggregate size, morphology, surface constitution, and mesoscale mineral organization. Bioinduced mineralization by bacteria is thus accompanied by some control of the microorganism and the surrounding polymer (EPS) matrix.

2. With the addition of *P. putida* EPS composite aggregate size is reduced and aggregate morphology changed from dendritic to radial forms.

3. *P. putida* EPS significantly changes the micrometer-scale mineral organization. It induces the formation of numerous irregularly shaped but densely interlocking subunits in

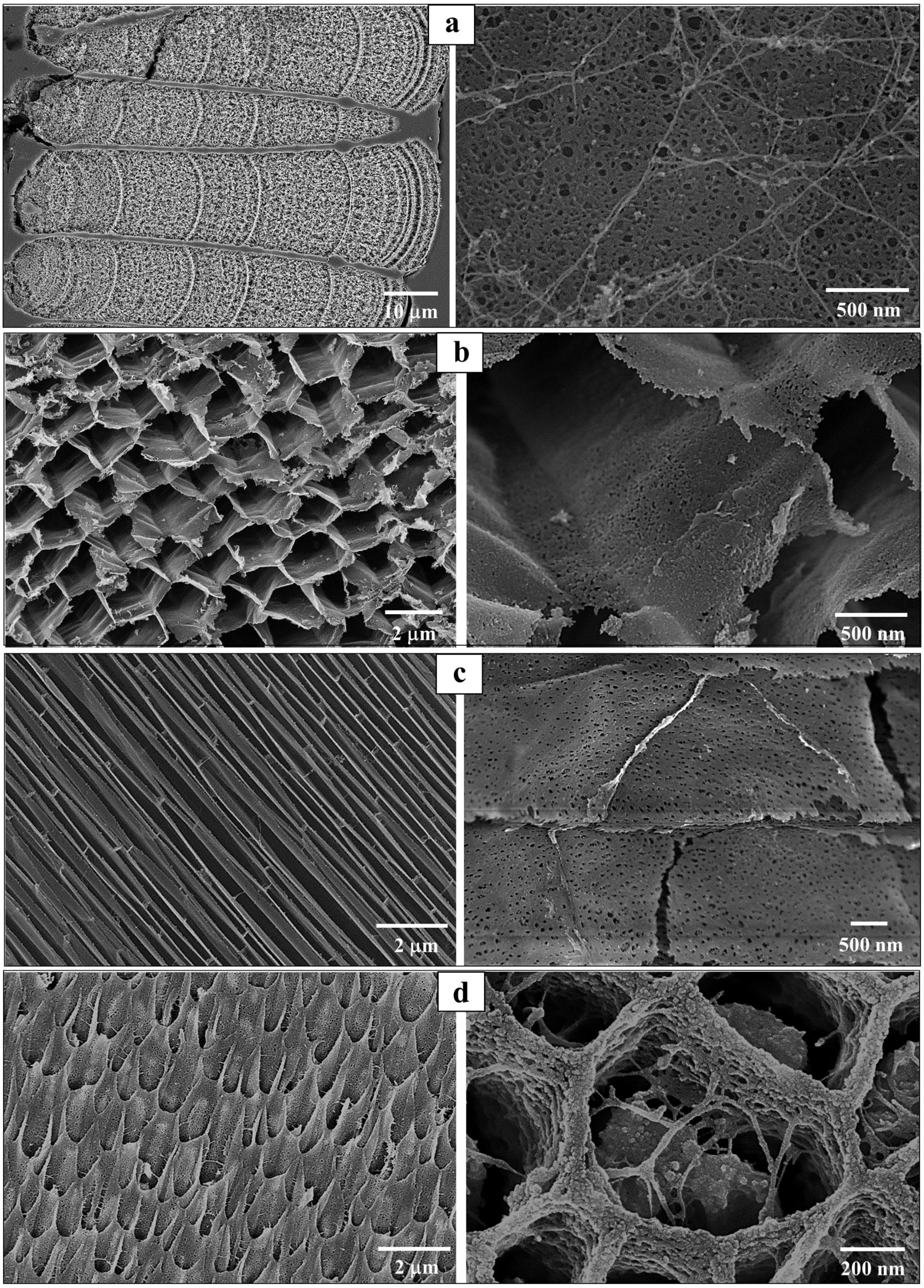

Figure 2.5-9. FE-SEM micrographs depict characteristics of extracellular matrices in carbonate biological hard tissues: (a) the prismatic shell layer of the bivalve *Cristaria plicatus*; (b) the biopolymer sheath around the calcite fibers in the shell of the bivalve *Mytilus edulis*; (c) the extracellular matrix within the nacreous shell portion of the bivalve *Mytilus edulis*; (d) the biopolymer matrix within the calcitic shell of the cephalopod *Argonauta argo*. Images on the left-hand side of the figure give overviews, and those on the right-hand side are zoom-ins. The porous nature of extracellular matrix membranes, as well as the irregular arrangement of the pores, are very visible, which is an intrinsic characteristic of carbonate biological hard tissues. To visualize the membranes, shell samples were microtome-cut, microtome-polished, decalcified, and critical point dried. Decalcification (for 1–2 days) was applied to remove the carbonate mineral(s) in order to visualize the spatial distribution of (glutaraldehyde-stabilized) biopolymers within the shell.

the size range of micrometers to tens of micrometers. These subunits are highly relative misoriented to each other and separated by membranes of gel accumulated during crystal growth. This is in contrast to the EPS-free reference crystal, where the calcite is highly co-oriented throughout, from the nano- to the microscale. We infer that the spheroidal polycrystalline aggregate induced by *P. putida* EPS in the experiment forms as crystal growth is episodically stopped by gel accumulation, while the diffusion from the reservoirs continuously builds up supersaturation until heterogeneous nucleation of a randomly oriented crystal occurs on the outside of the gel membrane.

4. On the nanometer scale, the pattern and strength of calcite crystal co-orientation are similar for all aggregates, irrespective of whether these grew in the presence or absence of EPS in the growth medium.

5. *P. putida* EPS influences the mode of polymer occlusion into the mineral. In aggregates that grew without EPS in the growth medium, the polymer, agarose gel, is pervasively distributed within the aggregate. The prevailing polymer fabric is a network of fibrils. In contrast, polymer (*P. putida* EPS-agarose hydrogel) occlusion into aggregates that formed in growth media containing EPS is highly inhomogeneous. Only a minor amount of EPS-agarose hydrogel is occluded within the subunits. The majority of the occluded EPS-hydrogel mixture forms membranes that separate but also crosscut neighboring subunits.

6. *P. putida* EPS influences composite aggregate formation through physical and chemical interaction with both the hydrogel and the calcite structure and promotes an alternative growth mechanism that involves a sequence of successive events of homoepitactic nucleation on the nanoscale. The result is a changed amount of occluded polymer, the pattern of polymer distribution and polymer fabric. This, in turn, influences the mesoscale mineral organization and morphological features of both the aggregate constituting subunits and sub-blocks.

7. The strong influence of *P. putida* EPS in the calcite growth mechanism results in a specific mode of calcite organization, a microstructural fingerprint that is characteristic for a specific microorganism. This microstructural signal can be used for constraining the mode of carbonate precipitation, e.g., to distinguish between microbial and chemical precipitation of the carbonate mineral.

Acknowledgments

F.W. was financially supported by Deutsche Forschungsgemeinschaft, DFG Grant GR-1235/9-1. L.F.-D. would like to acknowledge the Spanish Ministry of Science, Innovation, and Universities for financial support through project CGL2016-77138-C2-1-P. We would like to thank the staff of Central Facility for Electron Microscopy at Ulm University for their technical support.

2.5.6 Support Information

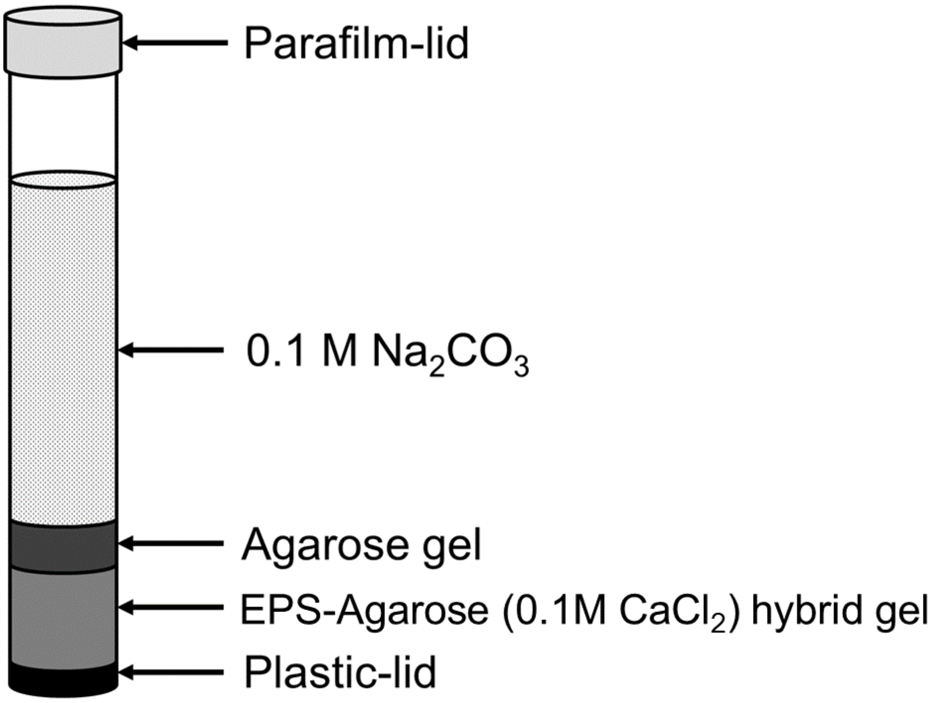

Figure 2.5-S1. Schematic visualizing of the used crystal growth experimental setup (single-diffusion system) for the investigated composite aggregates.

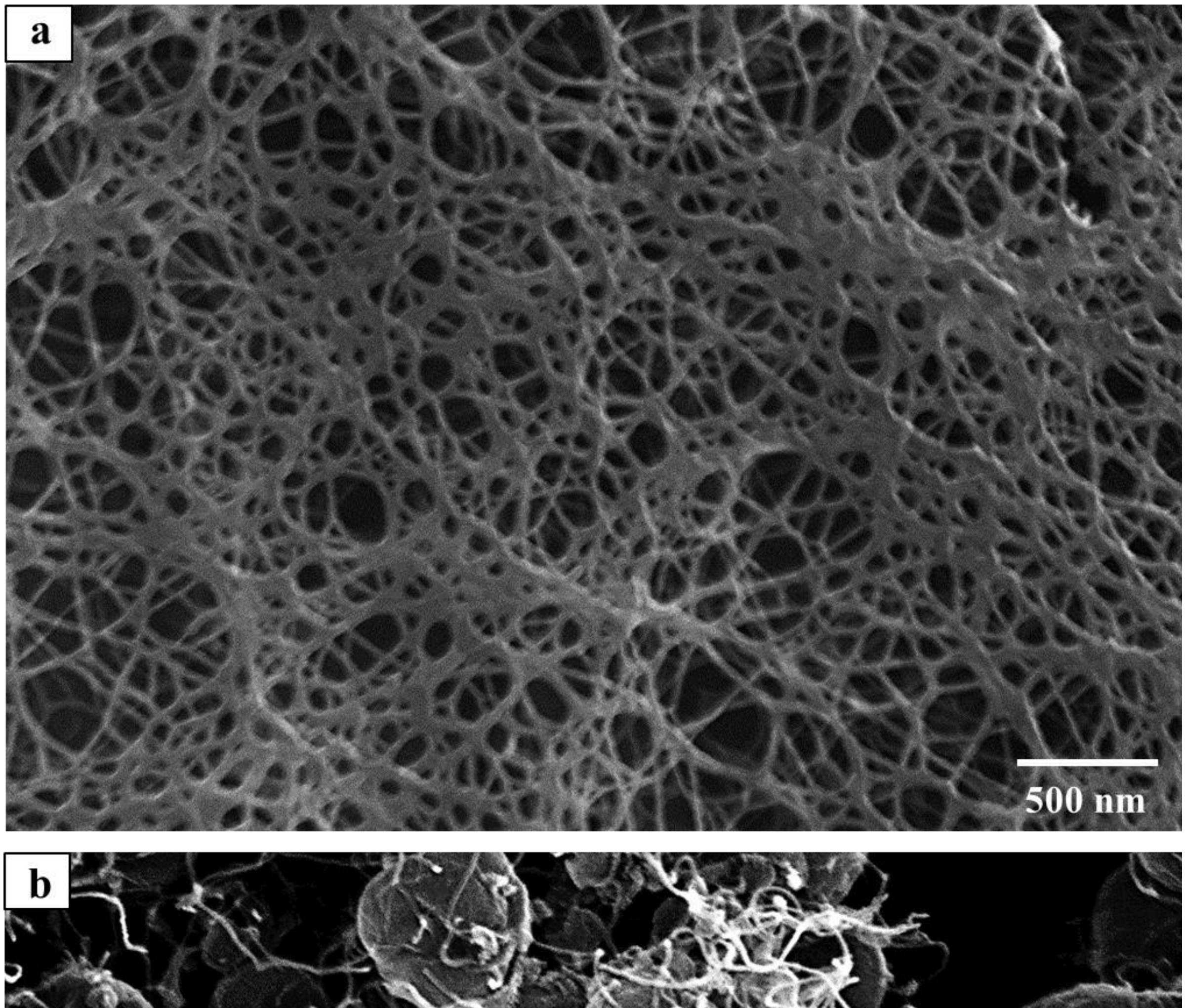

Figure 2.5-S2. The fabrics of (a) pure agarose hydrogel and (b) *P. putida* EPS.

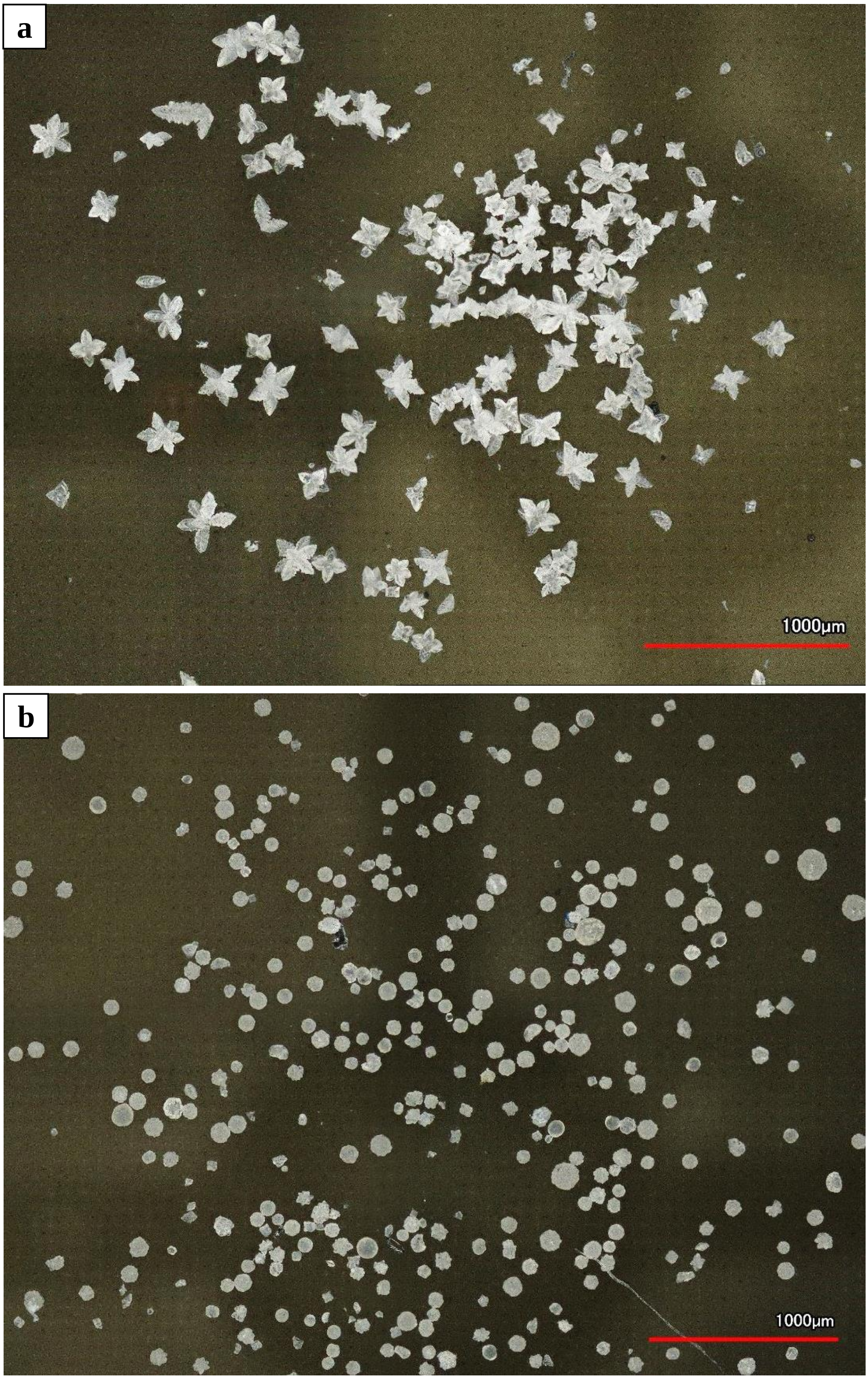

Figure 2.5-S3. Optical microscopy images show the difference in composite aggregate morphology. (a) Aggregates formed in pure agarose gel. (b) Aggregates grew in a mixture of *P. putida* EPS and agarose hydrogel.

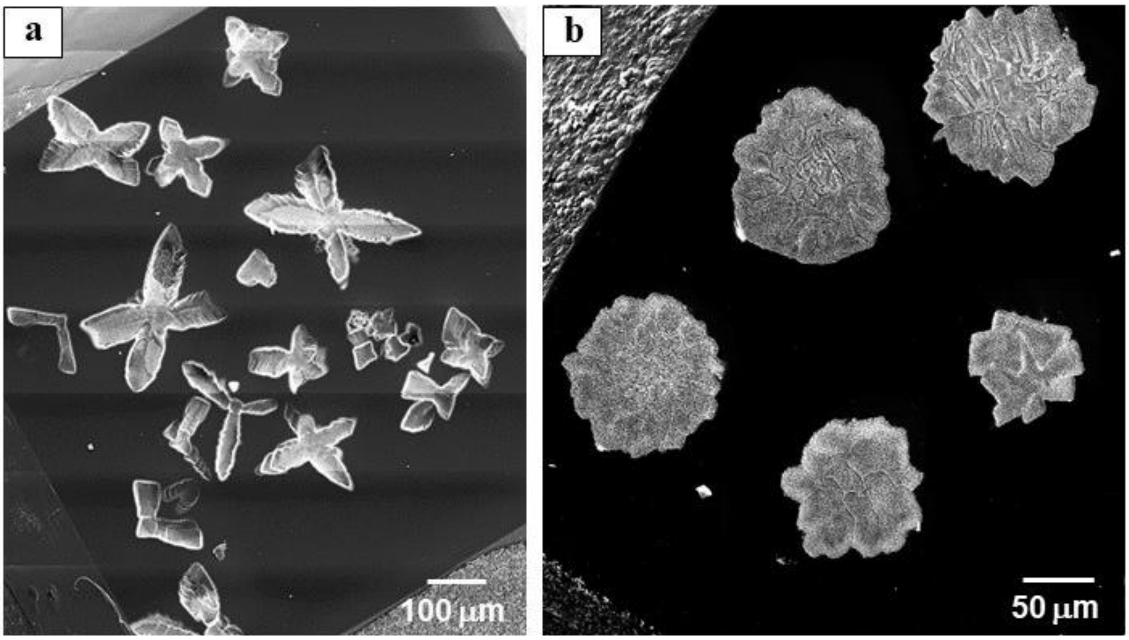

Figure 2.5-S4. The difference in composite aggregate morphology. (a) Aggregates formed in pure agarose gel. (b) Aggregates grew in a mixture of *P. putida* EPS and agarose hydrogel.

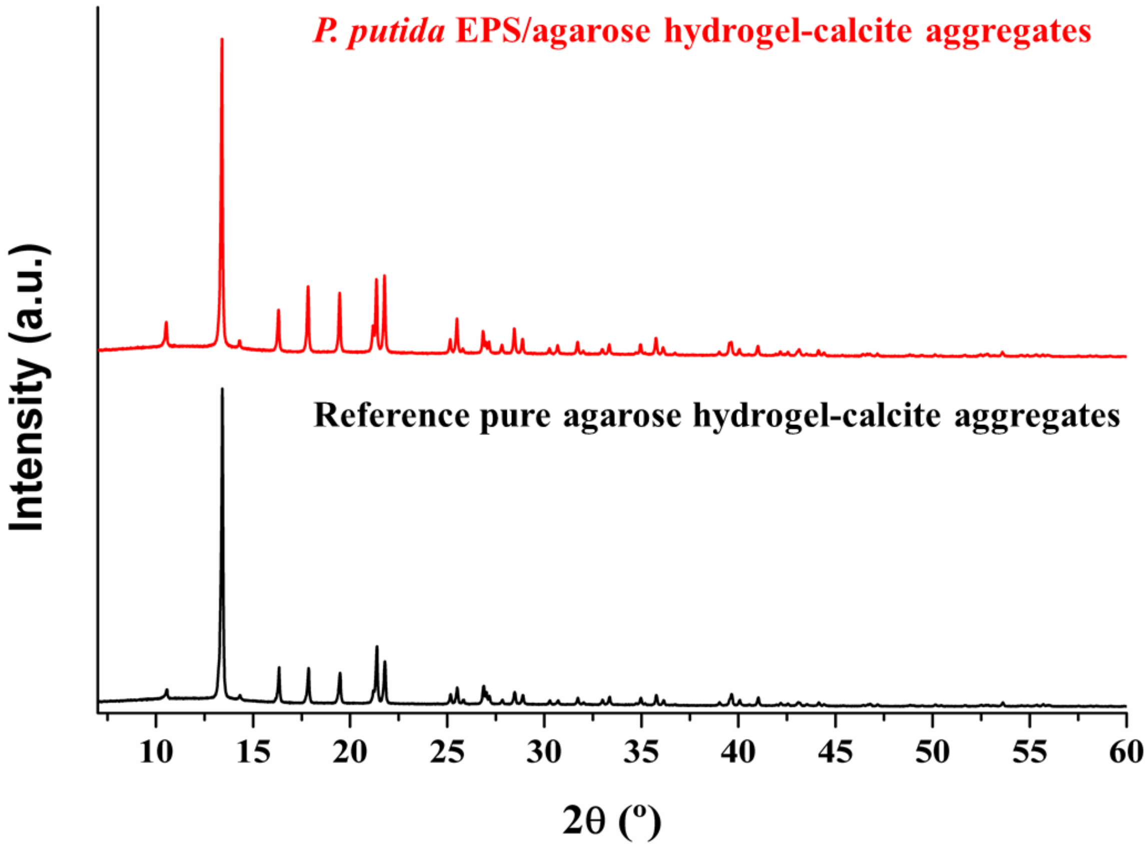

Figure 2.5-S5. Powder x-ray diffractograms of aggregates obtained from pure agarose (reference shown in black) and from a *P. putida* EPS-agarose hydrogel mixture (shown in red). Diffractograms were recorded on a Debye-Scherrer geometry STOE diffractometer equipped with a curved Ge (111) primary monochromator to produce Mo-Kα_1 radiation ($\lambda = 0.07093nm$) at 50 kV and 30 mA. Aggregates were sealed in ⌀0.3mm glass capillaries and were kept in rotation during the measurement. To allow a common representation, the diffractograms are normalized and arbitrarily shifted along the intensity axis. Only calcite was detected in both samples.

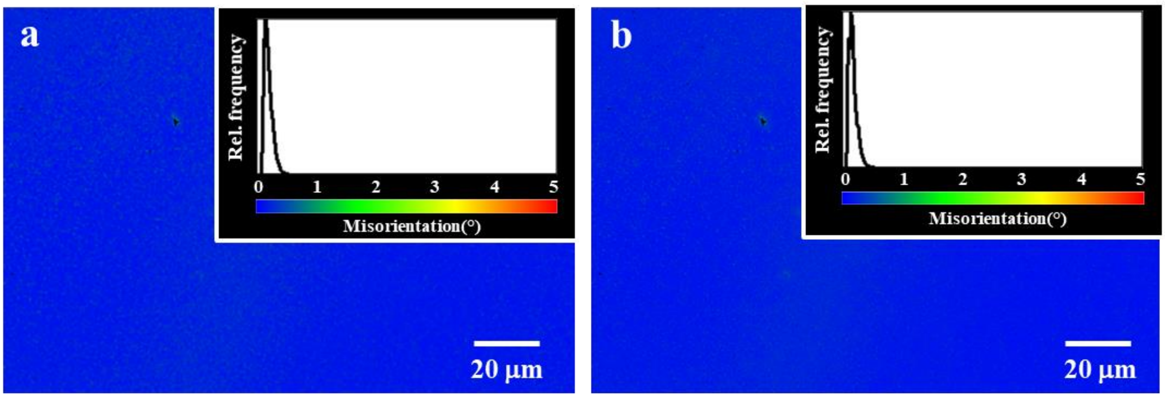

misorientation to **3 x 3** surrounding pixels

misorientation to **11 x 11** surrounding pixels

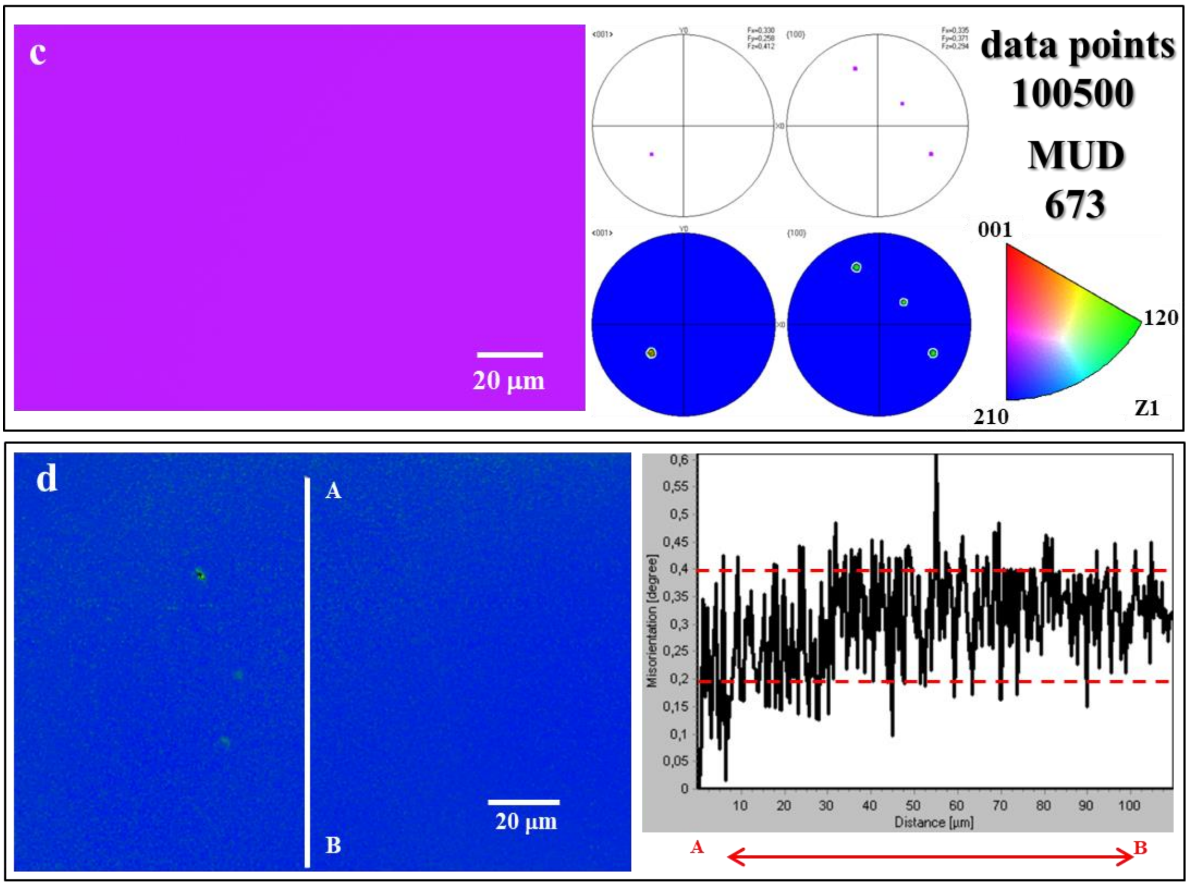

Figure 2.5-S6. EBSD reference measurement on a calcite single crystal grew from solution (measured with a raster step size of 280 nm). (a) Local kernel misorientation with a 3 × 3 and (b) 11 × 11 filter. (c) Color-coded orientation map, corresponding pole figures, and strength of calcite co-orientation expressed with MUD value 673. (d) Point-to-point misorientation along with a profile from A to B in a map given as a misorientation versus distance diagram.

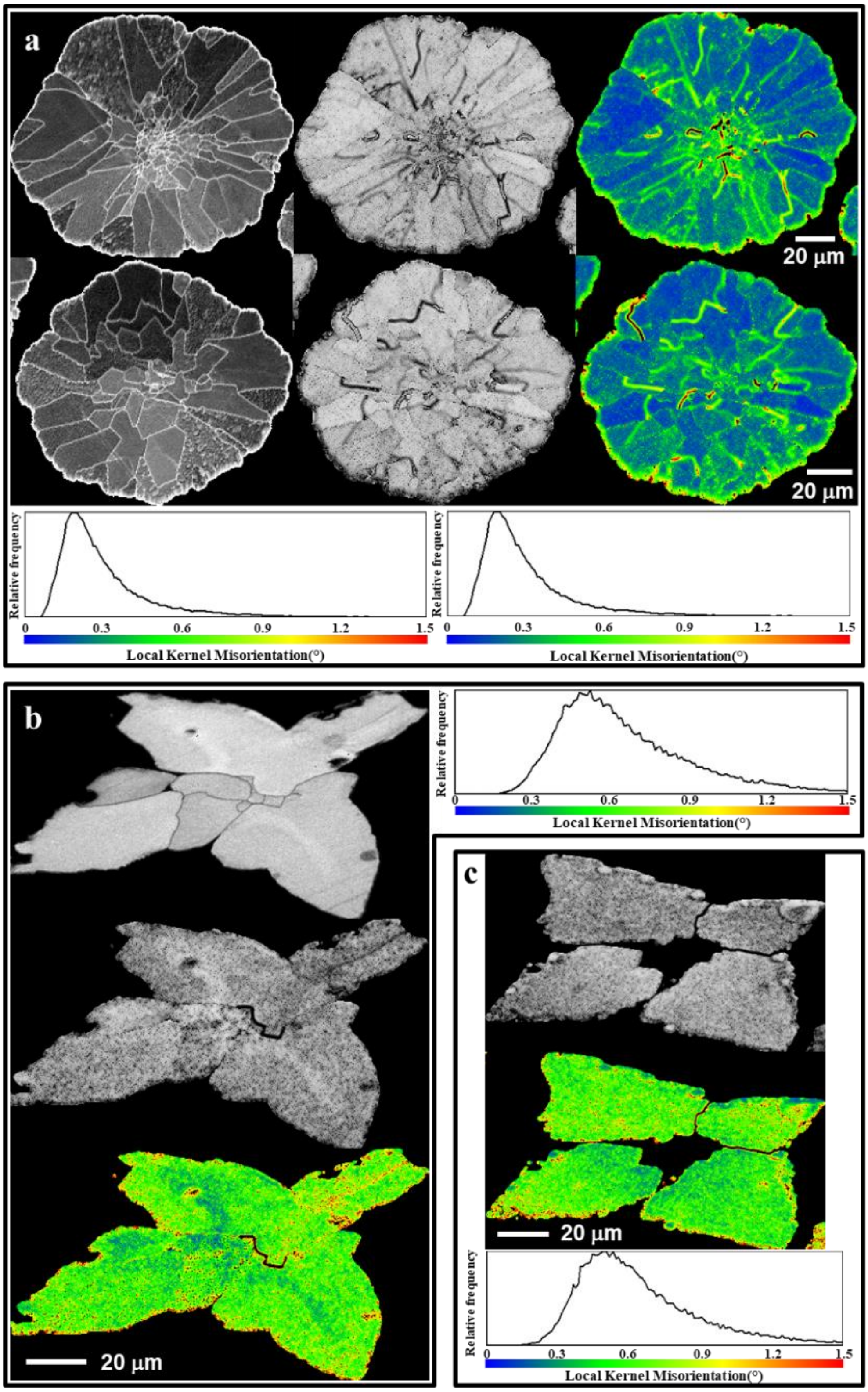

Figure 2.5-S7. Band contrast and local kernel misorientation maps derived from EBSD data of composite aggregates that formed without *P. putida* EPS (a, b) and with *P. putida* EPS in the growth medium (c). With band contrast images (left column images in (a), and top image in (b)) we visualize the morphology, subunits size and distribution within the aggregates. Local kernel misorientation, calculated with a 3 × 3 filter, is given in greyscale (central column images in (a), the middle image in (b), and top image in (c)) and in a colored version. Greyscale kernel misorientation images particularly well highlight the distribution of membranes within the aggregates. The color-coded visualization of kernel misorientation depicts the pattern of EPS/agarose distribution within the subunits and within the entire aggregate.

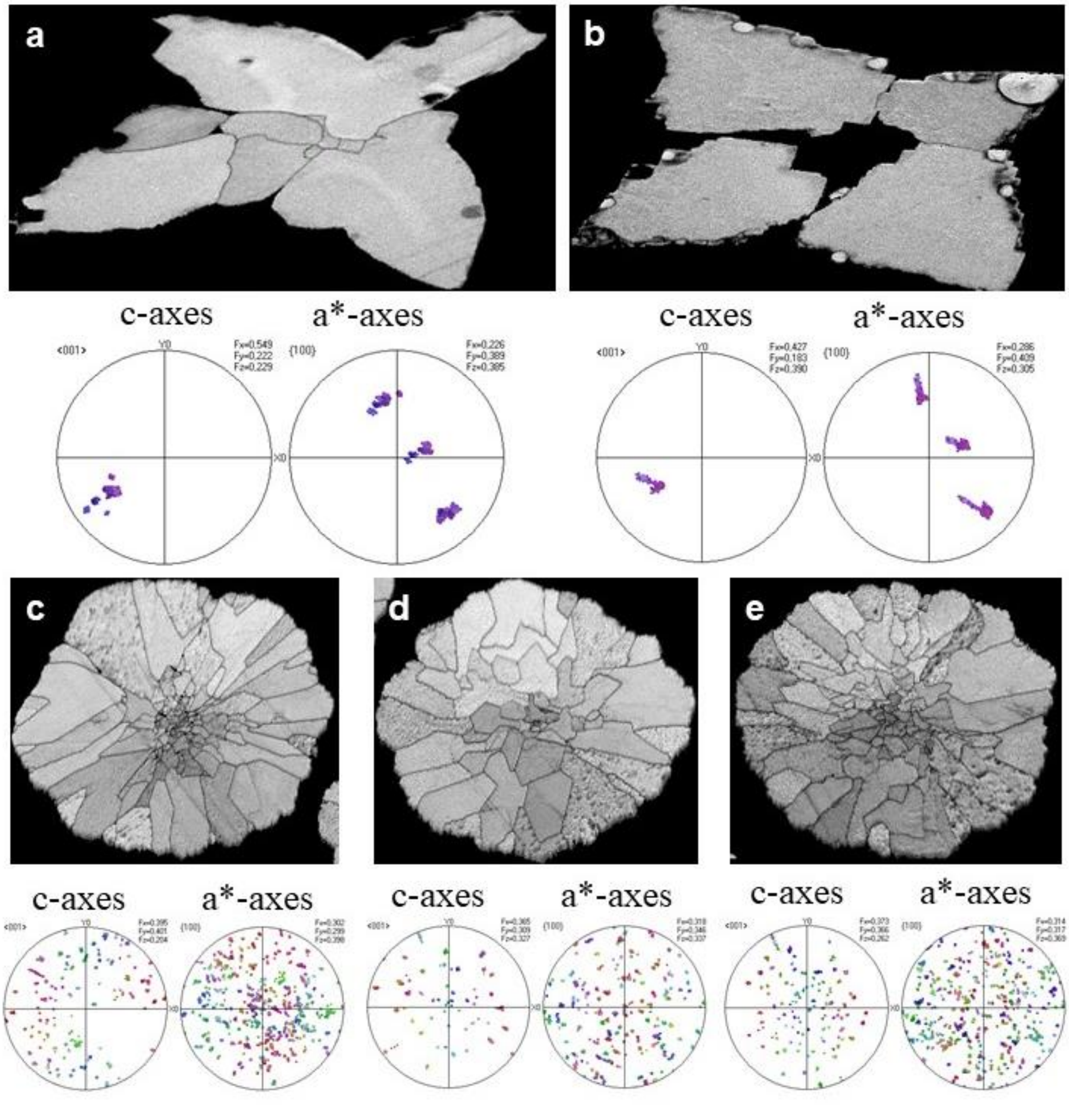

Figure 2.5-S8. EBSD measurements of band contrast images and color-coded pole figures show the difference in calcite organization between aggregates formed without *P. putida* EPS (a, b) and with *P. putida* EPS (c–e) in the growth medium. The corresponding color-coded EBSD maps are given in Figure 5.

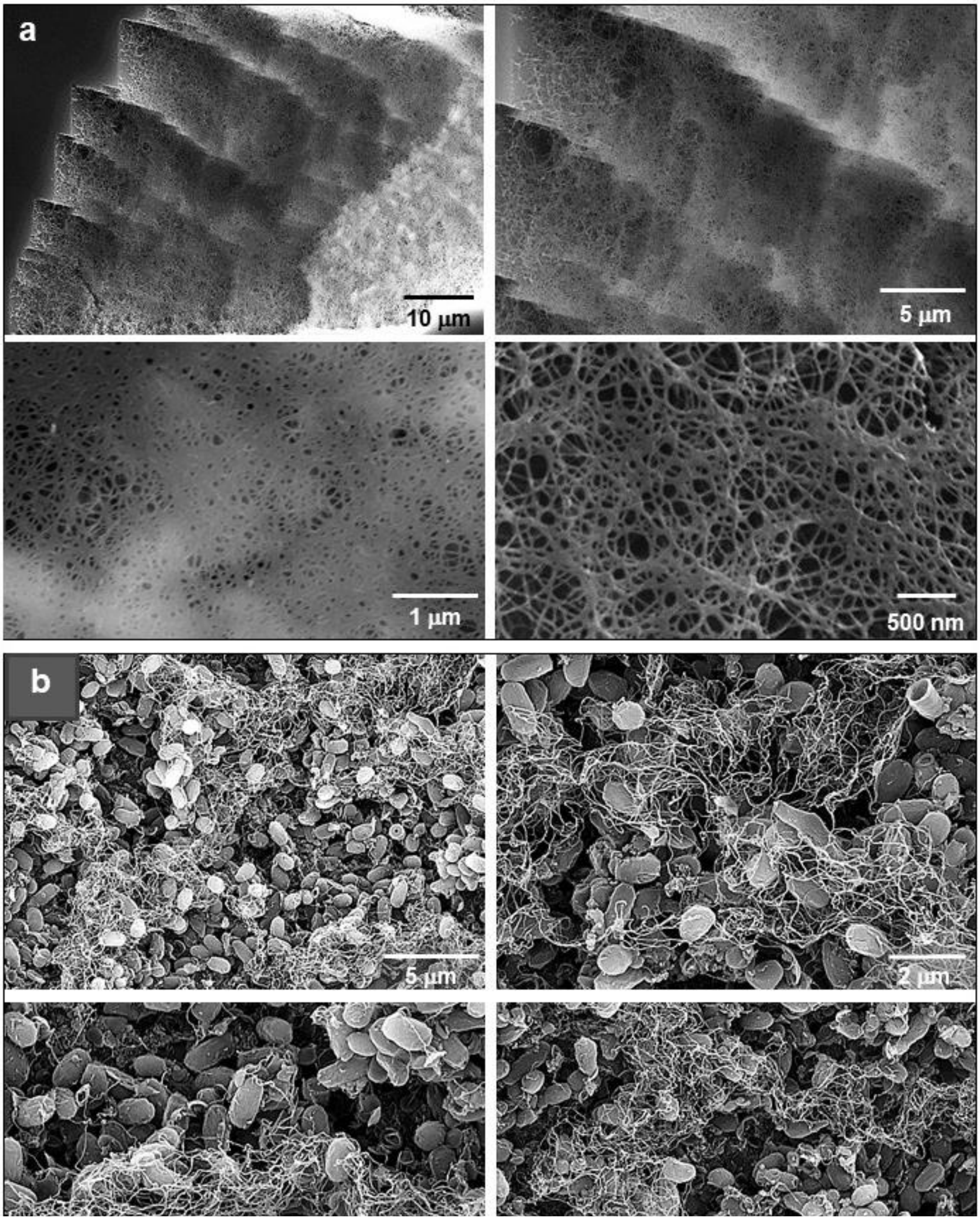

Figure 2.5-S9. FE-SEM images depicting of (a) pure agarose gel, and (b) *P. putida* EPS fabrics.

2.6 Bacterial EPS in Agarose Hydrogels Directs Mineral Organization in Calcite Precipitates: Species-Specific Biosignatures of *Bacillus subtilis*, *Mycobacterium phley*, *Mycobacterium smagmatis*, and *Pseudomonas putida* EPS

Xiaofei Yin[1], Florian Weitzel[1], Erika Griesshaber[1], Lurdes Fernández-Díaz[2, 3], Concepcion Jimenez-Lopez[4], Andreas Ziegler[5], Alejandro B. Rodriguez-Navarro[6], Wolfgang W. Schmahl[1]

1. Department für Geo- und Umweltwissenschaften, Ludwig-Maximilians-Universität, Germany
2. Departamento de Cristalografía y Mineralogía, Universidad Complutense de Madrid, Spain
3. Instituto de Geociencias (UCM, CSIC). C/ José Antonio Novais 2, Spain
4. Departamento de Microbiología, Universidad de Granada, Spain
5. Central Facility for Electron Microscopy, University of Ulm, Germany
6. Departamento de Mineralogía y Petrología, Universidad de Granada, Granada, Spain

Crystal Growth & Design **20**, 4402–4417 (2020)
http://dx.doi.org/10.1021/acs.cgd.0c00231

Abstract

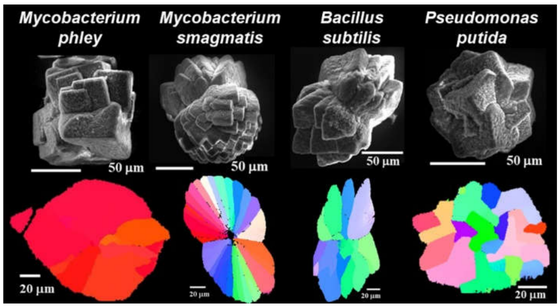

Hydrogels present model systems for biopolymer matrices in biological-structural-materials, as their fabric and physico-chemical properties can be tailored to mimic characteristics of polymer matrices in biological hard tissues. However, hydrogels comprise synthetic compounds and lack attributes of native biopolymers, in contrast to extracellular-polymeric-substance (EPS) actively secreted by microbes for protection and enhancement of physiological activities. For testing the directing influence of native biopolymers on mineralization, we precipitated calcite/gel composite aggregates from agarose gels containing EPS of *Bacillus subtilis*, *Mycobacterium phley*, *Mycobacterium smagmatis*, or *Pseudomonas putida*, respectively. We characterized the aggregates with Fourier transform infrared spectroscopy, field-emission scanning electron microscopy imaging, and electron backscatter diffraction. Relative to reference aggregates devoid of EPS, aggregates containing EPS are reduced in size and show distinctive morphologies directed by the EPS of a specific bacterium. In *P. putida* and *M. phley* composites, occluded polymers are present as membranes, for *M. smagmatis* and *B. subtilis* occluded polymers are mainly developed as networks of fibrils. Precipitate crystal subunit formation in EPS-containing composites is extensive compared to the reference crystal; subunits vary in shape, size, and organization: for *M. smagmatis* and *B. subtilis*, subunit organization is radial to spherulitic, for *P. putida* it is random; for *M. phley* it is coaligned in all three dimensions (single-crystal-like). Bacterial EPS changes mineral-microstructure/texture in a species-specific manner, a characteristic that, when developed further, might be used as an identification tool for bacterial-calcification in present/past environments.

Keywords

bacterial EPS-calcite composites; biomineral organization; microstructure; texture related biological marker

2.6.1 Introduction

Bacteria inhabit almost every environment on Earth's surface, in the oceans, and within the upper parts of the Earth's crust. When associated with surfaces, most bacteria secrete a mucilaginous matrix and form a biofilm (e.g., Decho 2000 and refs therein, Flemming & Wingender 2010; Flemming *et al.* 2016a). Biofilms are communities of bacterial cells including the surrounding extracellular polymeric matrix (EPS). In natural environments, they also comprise nonbiological substances as well, such as rock and mineral particles.

EPS is a pliant matrix that structures, stabilizes, and protects biofilm communities (Whitfield 1988; Decho 1990; Czaczyk & Myszka 2007; Mishra & Jha 2013; Nwodo *et al.* 2012). EPS is highly versatile and occurs in many physical states that range from a tight cohesive gel to dissolved and colloidal conformations. The gel state is present when the EPS forms a capsule around the cell membrane and encases the bacterial cell. Dissolved and colloidal states prevail in outer and more hydrated layers of the EPS matrix, which delineates biofilm communities from the surrounding environment. Additional diversity of EPS substances arises from the large variety of components that constitute EPS matrices: carbohydrates, proteins, nucleic acids, glycoproteins, phospholipids, humic substances, and many more (Whitfield 1988; Decho 1990; Czaczyk & Myszka 2007; Di Martino 2018). The EPS substance has significant sorptive as well as adsorptive capacities. Sorptive capabilities result from the three-dimensional organization of polymer fibrils, their high surface area, and the various chemical states of EPS matrices (Decho 2000). EPS matrices are also highly adsorptive, as the net anionic charge of the EPS allows the polymer to sequester efficiently positively charged ions. Accordingly, EPS matrices act as binding ligands for dissolved components. At interaction, hydroxyl groups of polysaccharides form weak associations, and carboxyl groups have significantly stronger binding capacities (Decho 1990, 2000; Loaëc *et al.* 1997; Vijayaraghavan & Yun 2008; Gupta & Diwan 2017; Costa *et al.* 2018), while amine groups are the most effective in binding positively charged ions. Amine groups not only chelate ions but also adsorb these through electrostatic interaction or hydrogen bonding (Decho 1990, 2000; Vijayaraghavan & Yun 2008). Moreover, it has been demonstrated for in vitro model systems that amine functional groups (primary amines, in particular) have a very strong effect on calcium carbonate precipitation (Cantaert *et al.* 2012; Schenk *et al.* 2014).

Bacterial communities are often associated with mineral precipitation. The microorganisms induce and influence mineral nucleation, while the surrounding environments generate the necessary geochemical conditions to guide the ongoing deposition of minerals (Dupraz & Visscher 2005; Obst *et al.* 2009; Decho 2010; Tourney & Ngwenya 2014). Mineral precipitation in biofilms is a combination of adsorption, precipitation, and dissolution and is influenced by both (i) the microbial community (bacteria and EPS) and (ii) environmental factors (Flemming *et al.* 2016a). The above-given summary illustrates that microbial communities (bacteria and the associated EPS) are capable to mediate, coordinate, and regulate biopolymer matrix formation as well as mineral precipitation.

Biofilm communities are snapshots of bacterial adaptations to specific living conditions and bacterial life stages (Decho 2000; Costerton *et al.* 1995; HobleyHobley *et al.* 2015). It has been shown that, for accomplishing different circumstances, microbial communities not only change levels of supersaturation within the biofilm but also react to the induced changes. They alter kinetic pathways of crystal nucleation and mineral growth and, with this, generate microorganism-specific signals: indicators of biogenic, environmental, and geochemical processes (Arp *et al.*

1999; Visscher & Stolz 2005; Simoneit 2002, 2004; Durak *et al.* 2019). As the latter is of immense importance in many Earth science disciplines, the central objective of our study is to identify and characterize further microorganism-specific signatures.

Following the surprising discovery of the very specific morphological control on calcite precipitation in agarose gels by adding *P. putida* EPS in our pilot study (Yin *et al.* 2020b), we extended this work to other bacteria. In this study, we highlight and discuss microorganism-specific signals for the four different bacteria *Bacillus subtilis*, *Mycobacterium smagmatis*, *Mycobacterium phley*, and *Pseudomonas putida*. We synthesized in single-diffusion crystallization experiments bacterial EPS-hydrogel-calcite composite aggregates with the EPS of the Gram-positive bacteria *B. subtilis*, Gram-negative bacterium *P. putida*, and two bacteria belonging to the *Mycobacterium* genus, *M. smagmatis*, and *M. phley*. We investigated the mode of biopolymer (EPS/hydrogel) incorporation into the mineral, the pattern of crystal organization within the aggregate, as well as aggregate morphology and size. We report results relative to hydrogel-mineral composites devoid of bacterial EPS. Chemical characteristics of the EPS matrix were determined with Fourier transform infrared (FTIR) spectroscopy; EPS incorporation and distribution into the calcite was visualized with high-resolution scanning electron microscopy (SEM) imaging of etched and decalcified aggregate surfaces; the carbonate mineral phase and crystal organization were measured with electron backscatter diffraction (EBSD). We find that the mode of EPS occlusion/distribution is characteristic for the EPS of a specific microorganism. This generates the differences that we observe in mineral organization, mineral co-orientation strength, and aggregate morphology. Accordingly, our study demonstrates that the EPS of the four investigated bacteria induces specific mineral microstructures and textures. These are characteristics that could be developed as biosignatures for an identification of microorganisms in microbial communities.

2.6.2 Materials and Methods

Pure cultures of the bacteria *Bacillus subtilis*, *Mycobacterium smagmatis*, *Mycobacterium phley*, and *Pseudomonas putida* were grown in 1 L of LB medium at 28°C with 180 rpm stirring for 2 d. The culture medium was enriched with 0.5%KH_2PO_4, 0.5% NaCl, 1% glucose, and 0.5% yeast extract, and the pH was adjusted to 7. Cells were concentrated by centrifugation and 0.9% NaCl (w/v) solution. Ethanol was added to reduce cell viability; the cells were suspended in 0.9% NaCl (w/v) solution and stored for 12 h at 4°C.

The used EPS extraction protocol is detailed in Yin *et al.* (2020b) and modified from protocols presented in Eboigbodin & Biggs (2008) and Pellicer-Nàcher *et al.* (2013) to reduce the viability of the cells and to avoid metabolism contribution to carbonate precipitation. A volume of 3 mL of total EPS suspension of each bacterium was obtained by triplicate extraction with 0.9% NaCl (w/v), centrifugation, and alcohol precipitation. Considering the influence of intracellular components in the chemistry of the EPS, the research of Comte *et al.* (2006) shows that, if the ratio of protein to polysaccharides in the EPS was lower than 2, a significant occurrence of cell rupture could be excluded. In our case, this ratio is $\sim$1, and therefore, the intracellular components do not have a significant occurrence in the EPS composition.

Crystallization experiments were performed by using a single-diffusion hydrogel system (Fig. 2.6-S1). In the experiments with EPS, a hybrid gel prepared by mixing 0.5 wt% agarose gel (Sigma-Aldrich) and the extracted bacterial EPS (2:1 v/v) in 0.1 M $CaCl_2$ (Sigma-Aldrich) aqueous solution was used. In the reference experiment, Milli-Q (18.2 MΩ) water substituted the bacterial EPS in the hybrid mixture. After the gelation of 1.5 mL of hybrid gel in a Pyrex glass tube, 0.5 mL of 0.5 wt% pure agarose sol was poured on top. Finally, after gelation of the latter, the tube was filled with 5 mL of 0.1 M Na_2CO_3 (Sigma-Aldrich) aqueous solution as the reactant. The crystallization was performed in a refrigerated chamber at 13°C for six weeks. The aggregates were extracted by dissolving the gels in hot water (60 °C), washed three times, and air-dried at room temperature for 24 h.

The extracted total EPS was analyzed by reflection mode on an FTIR spectrometer (model 6200, JASCO Analytical Instruments) to understand the chemical composition. Aggregate morphologies were investigated with a Hitachi SU5000 FE-SEM at 20 kV. Powder X-ray diffraction was performed on a Debye–Scherrer geometry STOE diffractometer (Mo-Kα_1 radiation λ = 0.07093 nm) using capillaries to identify the mineral phases of the aggregates. Selective etching was made on the EPON embedded and ultramicrotome polished aggregate cross sections by using 0.1M 4-(2-hydroxyethyl)-1-piperazineethanesulfonic acid (HEPES) (pH = 6.5) containing 2.5% glutaraldehyde as a fixation solution. Electron backscattered diffraction measurements were performed also on microtome polished aggregate crosscuts (coated with 4–6 nm of carbon) by using a Hitachi SU5000 FE-SEM equipped with a Nordlys II EBSD detector. Color-coded crystal orientation maps, corresponding pole figures and pole density distributions, band contrast maps, local kernel misorientation maps, relative frequency versus local kernel misorientation diagrams, and misorientation versus distance diagrams were obtained from the data evaluation. A more detailed description of the methodology is presented in Yin *et al.* (2020b).

2.6.3 Results

Bacterial EPS – agarose gel – calcite aggregates

Figure 2.6-1a shows the morphology of the reference composite, the aggregate that formed without bacterial EPS in the growth medium. Figure 2.6-1c,e,g,i depicts composite morphologies that were obtained with bacterial EPS in the growth medium (further images with different magnifications are shown in Figs. 2.6-S2 to 2.6-S4). Figure 2.6-1b,d,f,h,j shows surfaces of cross-sections through the aggregates; these were the surfaces that we used for EBSD measurements. All investigated aggregates are radial aggregates and consist of calcite (Fig. 2.6-S5). The calcite occluded variable amounts of agarose gel (the reference sample, Fig. 2.6-1a,b) or a mixture of bacterial EPS and agarose gel (Fig. 2.6-1c–j) during growth. For the five investigated aggregates we find three major morphologies (Fig. 2.6-1): (i) starlike, Figure 2.6-1a, (ii) blocky, Figure 2.6-1c,i, and (iii) sheaflike, Figure 2.6-1e,g.

The reference aggregate has a starlike morphology (Fig. 2.6-1a,b). The composite has six dendritic branches, which are related to each other by the threefold symmetry operator characteristic for calcite crystals. The branches are elongated parallel to the <$4\bar{4}1$> directions and are bounded by highly stepped {104} rhombohedron faces and curved, nonsingular surfaces as well as straight and curved edges. Straight steps on the {104} surfaces are oriented along the [$4\bar{4}1$] and [$48\bar{1}$] directions. Of the five investigated aggregates the reference aggregate has the largest size of 250 ± 50 μm.

The four aggregates that grew with EPS in the growth medium are smaller than the reference aggregate. The composite that formed in agarose hydrogel and *M. phley* EPS (Fig. 2.6-1c,d) has a blocky morphology and consists of a small number of slightly misoriented, rhombohedron shaped subunits. The morphology of the subunits is dominated by flat {104} as well as rough, slightly curved, {012} "steep" rhombohedron surfaces. The steep surfaces are highly stepped, with the steps oriented approximately parallel to the <010> directions, and are bounded by poorly defined edges. In contrast, the flat surfaces are bounded by straight [$4\bar{4}1$] and [$48\bar{1}$] edges that meet at the c-axis and by curved edges that are oriented

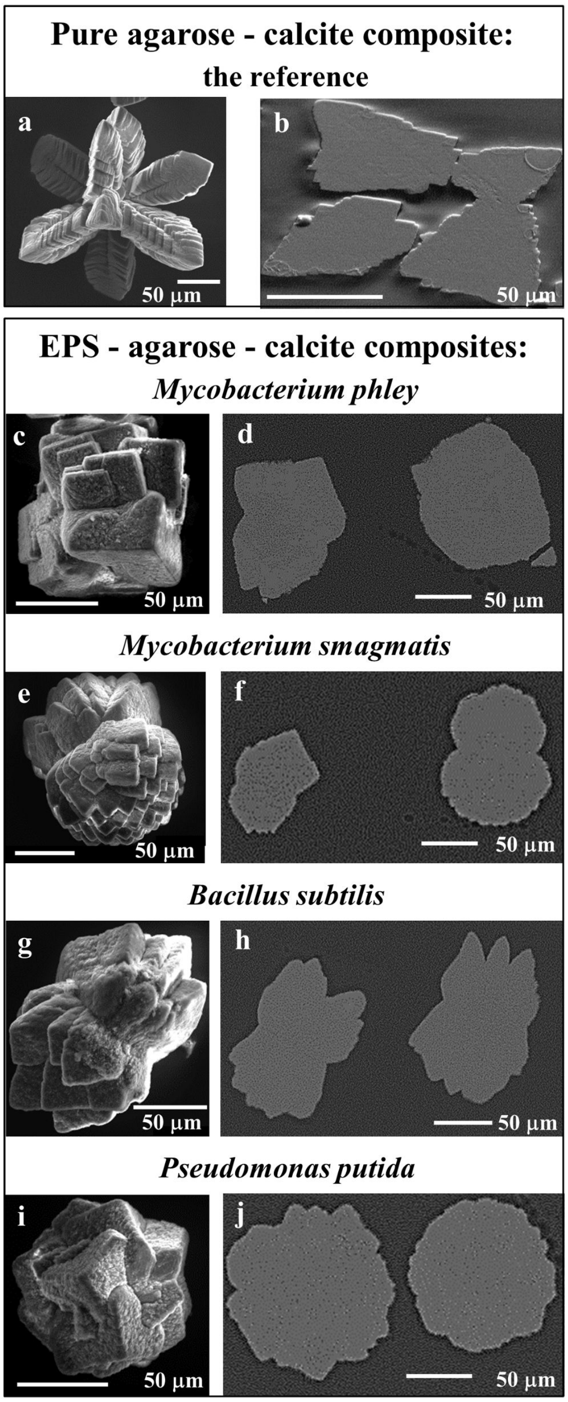

Figure 2.6-1. FESEM-SE (a, c, e, g, i) and FESEM-BSE (b, d, f, h, j) images depicting morphologies of the composite aggregates (a, c, e, g, i) and surfaces sectioned through them (b, d, f, h, j). The reference aggregate that formed in a growth medium without bacterial EPS is shown in (a, b). Composites that occlude bacterial EPS are depicted in (c–j). Well visible is the dendritic morphology of the reference aggregate that contrasts with the radial, blocky rhombohedral morphology of aggregates that grew in a bacterial EPS-agarose hydrogel mixture.

roughly parallel to <010>. Both types of surfaces have a granulated appearance. The mean size of the aggregate is in the range of 100 ± 20 μm.

Composites that formed in agarose gel and *M. smagmatis* or *B. subtilis* EPS (Fig. 2.6-1e,f, and Fig. 2.6-1g,h) have sheaflike morphologies and their mean sizes are $\sim$100 ± 20 and 150 ± 20 μm, respectively. These aggregates consist of two sub-blocks with each of these having subunits with an orientational spread of the c-axis. This results in reentrant surfaces around the equatorial region of the aggregate and defines here a cleft. Aggregates that formed with the EPS of *Mycobacterium smagmatis* (Fig. 2.6-1e) show a deeper cleft and comprise more subunits than those grown with the EPS of *Bacillus subtilis* (Fig. 2.6-1g). Subunits in both aggregates are bounded by flat but rough rhombohedra as well as nonsingular surfaces. The latter surfaces are more curved in aggregates that grew with *Mycobacterium smagmatis* EPS in the growth medium.

Composite aggregates that were obtained with *P. putida* EPS (Fig. 2.6-1i,j) are blocky and consist of numerous rhombohedron-like subunits that are organized in a radial arrangement; the subunits are bounded by very rough rhombohedron {104} surfaces. The mean size of these aggregates is 120 ± 20 μm.

In conclusion, when bacterial EPS was present in the growth medium, we obtained two cases of blocky and two cases of sheaflike aggregates. In the case of the blocky aggregates, the one that formed with *P. putida* EPS is more rounded (Fig. 2.6-1i,j) than the (also blocky) aggregate that grew with *M. phley* EPS (Fig. 2.6-1c,d). In the case of sheaflike aggregates, the composite that occluded *M. smagmatis* EPS (Fig. 2.6-1e,f) consists of many subunits, while the composite that contains *B. subtilis* EPS (Fig. 2.6-1g,h) has fewer, but larger, subunits. Contrasted with the composites that formed with bacterial EPS, the reference aggregate (Fig. 2.6-1a,b) has a strikingly different morphology (starlike) as well as different subunit shapes and arrangements.

Bacterial EPS composition, fabric and mode of incorporation into the mineral

Figure 2.6-S6 shows representative FTIR spectra of the total EPS of the investigated bacteria. On the basis of the strongest absorption bands between 800 and 3100 cm^{-1}, we can identify three different special regions: zone 1 covers the spectral range between 3000 and 2800 cm^{-1}, zone 2 is located between 1800 and 1500 cm^{-1} and zone 3 ranges from 1200 to 1000 cm^{-1}. In general, our FTIR results indicate for all four bacterial EPS the presence of lipids (zone 1), proteins (zone 2), and polysaccharides and nucleic acids (zone 3). For the EPS of all bacteria, proteins form the strongest FTIR signal, followed by polysaccharides and nucleic acids.

The FTIR results show that the spectral region of zone 2 is very similar for the EPS of all four investigated bacteria, while zones 1 and 3 differ slightly for the EPS of the different bacteria species. In addition, the FTIR spectra of zone 1 are similar for the EPS of *P. putida* and *M. phley* as well as for the EPS of *M. smagmatis* and *B. subtilis*. The FTIR peaks of zone 3 show slight differences for the EPS of the four investigated bacteria and indicate either slightly different polysaccharide and nucleic acid components or amounts in the EPS of the investigated microorganisms. In conclusion, on the basis of the FTIR results, we find no marked difference in the EPS composition of the four investigated bacteria.

All investigated calcite aggregates incorporated polymers during the growth process. EPS and hydrogel occlusion induce misorientation between crystallites. Misorientation of a subunit/grain to neighboring subunits/grains can be visualized with local kernel misorientation maps (Figs. 2.6-2, 2.6-S7, and 2.6-S8) and corresponding relative frequency versus local kernel misorientation diagrams (Fig. 2.6-2). Both of them are derived from EBSD data. We present local kernel misorientation as color-coded maps; a low degree of misorientation between crystallites due to EPS/polymer occlusion is presented with dark blue colors (e.g., Fig. 2.6-2a,b), while misorientation due to widespread occlusion of EPS/ hydrogel is visualized with light green to yellow colors (e.g., Fig. 2.6-2e).

Local kernel misorientation analysis indicates that polymer occlusion within the reference composite is pervasive and very homogeneous (Figs. 2.6-2e and 2.6-S7b). Accordingly, the degree of local kernel misorientation between calcite crystallites is relatively high for the entire aggregate (Fig. 2.6-2e). However, occlusion of agarose gel does not disturb the overall texture of the aggregate. As the pole figures for the reference composite show (Fig. 2.6-2e), calcite (001) (c-axis) and (100) (a*-axes) co-orientation are high. The aggregate has the highest co-orientation among all investigated composites (compare the pole figures that are given in Fig. 2.6-2). Hence, the mode of hydrogel occlusion and the related assembly of calcite crystals are highly regular within the reference composite. For the reference, we did not observe the presence of membranes.

The pattern of local kernel misorientation for aggregates that occlude bacterial EPS is significantly different from that of the reference composite. For aggregates that contain *M. smagmatis* and *B. subtilis* EPS, we see a highly patchy mode of EPS/hydrogel incorporation (Figs. 2.6-2c,d, and 2.6-S8a,b), while aggregates that incorporate *P. putida* and *M. phley* EPS appear to occlude little polymer within their subunits (expressed with blue colors in Figs. 2.6-2a,b, and 2.6-S7c,d). In the latter aggregates, the EPS/hydrogel mixture is mainly concentrated at the sites of membranes (white arrows in Fig. 2.6-S7c,d). These membranes occasionally, but not necessarily, delineate the subunits of the aggregate. When *P. putida* EPS is present in the growth environment, the subunits are little cooriented (see the corresponding pole figure in Fig. 2.6-2a); however, when the composite forms with *M. phley* EPS in the polymer mixture, the subunits are well cooriented (see the

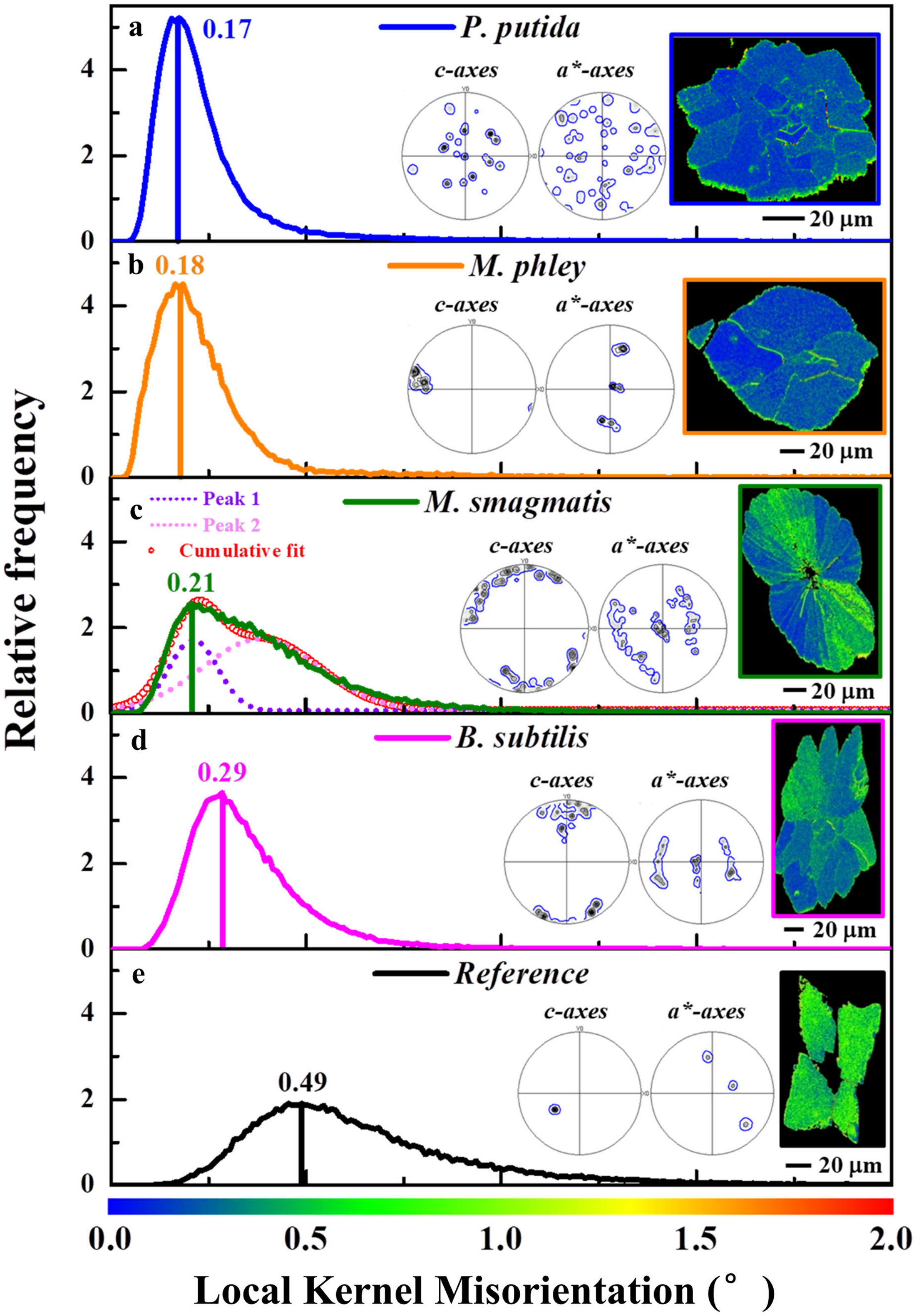

Figure 2.6-2. Hydrogel and bacterial EPS incorporation and distribution within the mineral of the composites visualized with color-coded (blue to green) local kernel misorientation maps and corresponding relative frequency vs misorientation diagrams. (a–d) Aggregates that grew in an EPS-agarose gel mixture. (e) The reference aggregate that formed in pure agarose gel. The inserted pole figures highlight characteristics of calcite orientation (cf. Figs. 2.6-3–2.6-6): high mineral coalignment for the reference aggregate, almost random mineral orientation for the aggregate that intercalates *P. putida* EPS, an increased mineral coorientation for the aggregate that occludes *M. phley* EPS, and spherulitic patterns of mineral assembly for the aggregates that occlude *M. smagmatis* and *B. subtilis* EPS, respectively.

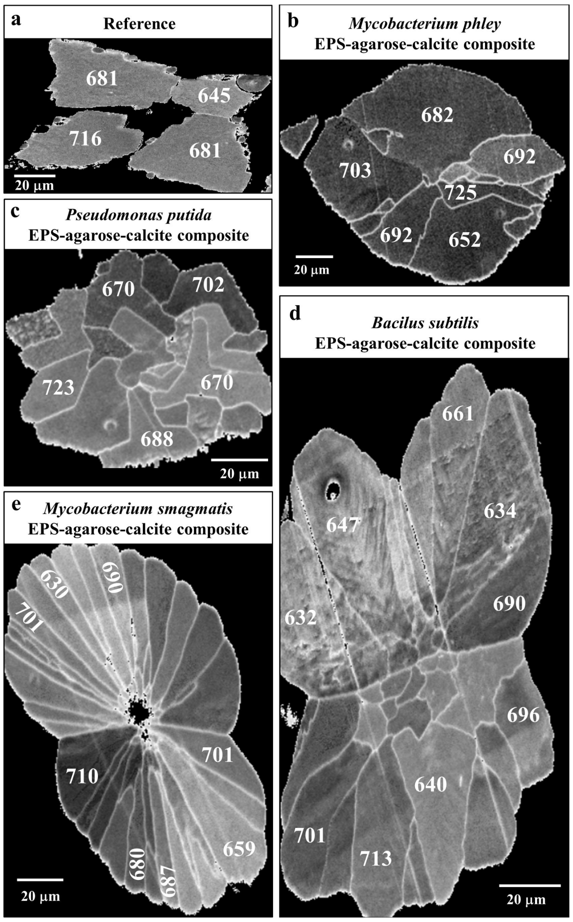

Figure 2.6-3. Calcite crystallite co-orientation strength, expressed with MUD values, of representative subunits of the reference aggregate (a) and aggregates that incorporate bacterial EPS (b–e). The calcite is highly co-oriented in the subunits of the reference as well as within the composites grown with EPS in the gel growth medium. (a–e) Grey-scaled EBSD band contrast images.

corresponding pole figure in Fig. 2.6-2b).

Local kernel misorientation highlights that EPS/polymer distribution within the composite containing *M. smagmatis* EPS is structured (Figs. 2.6-2c and 2.6-S8a), such that in two quadrants of the composite the EPS/hydrogel distribution is pervasive within the calcite, while within the other two quadrants it cannot be visualized with local kernel misorientation analysis. This characteristic is mirrored by graphs displaying the relative frequency of the local kernel misorientation for composites obtained with the *M. smagmatis* EPS compared to the others. The curve can be deconvoluted into two parts (Figs. 2.6-2c and 2.6-S9): one indicating low misorientation and little gel occlusion within the calcite, while the other depicts increased misorientation due to a more substantial occlusion of EPS and hydrogel into the mineral. The corresponding pole figure of the aggregate shows that calcite assembly follows a spherulitic pattern for both the c- and the a*-axes (pole figures in Fig. 2.6-2c). The mode of EPS/hydrogel incorporation into the composite that formed with *B. subtilis* EPS is like that of the aggregate that incorporated *M. smagmatis* EPS (Figs. 2.6-2d and 2.6-S8b). Nonetheless, EPS/hydrogel distribution in the latter aggregate is rather patchy and not as structured as it is for the *M. smagmatis* EPS occluding composite.

In conclusion, as a consequence of bacterial EPS/agarose gel occlusion into the calcite, we find for the investigated aggregates four distinct patterns of mineral organization at the aggregate ($\sim$50 μm) scale level: (1) almost no co-orientation at the aggregate level (Fig. 2.6-2a); highly co-oriented at the aggregate level (Fig. 2.6-2b), spherulitic at the aggregate level (Fig. 2.6-2c,d), highly co-oriented–almost single crystalline (reference crystal, Fig. 2.6-2e). On the sub-micrometer- to nanometer-scale level within the subunits, we find only two patterns: (i) almost perfect crystalline co-orientation within the resolution of the EBSD measurement (represented by blue colors in the maps of Fig. 2.6-2), and (ii) disturbed co-orientation in specific subunits, but not in all subunits of the spherulitic aggregates (green colors in Fig. 2.6-2c,d) and in the reference crystal (Fig.e 2.6-2e).

The fabric of agarose and bacterial EPS network is depicted in Figures 2.6-S10, 2.6-S13, 2.6-S15, 2.6-S17, and 2.6-S19; polymer-calcite interlinkage is shown in Figures 2.6-S11, 2.6-S12, 2.6-S14, 2.6-S16, 2.6-S18, and 2.6-S20. We find a dense network of polymers for the 0.5 wt% agarose gel (Fig. 2.6-S10) and for the EPS of *M. smagmatis* (Fig. 2.6-S19). The network of *B. subtilis* EPS (Fig. 2.6-S17) is significantly less dense but still well-developed. In contrast, the network of *P. putida* (Fig. 2.6-S13) and that of *M. phley* EPS, respectively, is little developed and scarce, especially that of *M. phley* (Fig. 2.6-S15).

For the reference aggregate, we see a tight interlinkage between the hydrogel network and the calcite in both portions of the aggregate, the rim, as well as the center (e.g., Fig. 2.6-S12). From local kernel misorientation we know that polymer distribution is pervasive within the reference aggregate; hence, this close interlinkage between the calcite and the agarose hydrogel network must be present throughout the entire reference composite. This feature was not observed for aggregates that contain bacterial EPS. Many subunits of the latter aggregates occlude little EPS and, if at all, a significantly less dense EPS/agarose network (compare Fig. 2.6-S11c,d with Figs. 2.6-S14g, 2.6-S16d, 2.6-S18f, and 2.6-S20f,g).

Individual subunits of aggregates that formed with bacterial EPS in the growth medium are well-developed and clear-cut; however, in most cases they are not separated from each other by membranes (e.g., Figs. 2.6-S14b, 2.6-S18b,c, and 2.6-S20b). Membranes can be present within the composites that contain bacterial EPS (e.g., Fig. 2.6-S14a,g), occasionally outlining the subunits (e.g., Fig. 2.6-S18e). However, in most cases, polymer membranes appear to be incorporated randomly (e.g., Figs. 2.6-S14d,f, 2.6-S18c,d,g, and 2.6-S20d,e). For the composite that formed with *P. putida* EPS in the growth environment, we find a higher abundance of membranes within the aggregate (Fig. 2.6-S14) in comparison to all other composites that occluded bacterial EPS.

In conclusion, for the reference aggregate, we see a close interlinkage between calcite and the polymer network and this characteristic is ubiquitous throughout the composite. For the aggregates that occlude bacterial EPS, we observe the formation of polymer networks and membranes; however, the interlinkage between the polymer and the mineral components appears to be arbitrary. Formation of membranes takes place in aggregates that occlude bacterial EPS, however, these do not necessarily delimit individual subunits.

Subunits and their organization within the composite aggregates

Band contrast images in Figure 2.6-3 depict subunit size, morphology, and the mode of their assembly for all investigated aggregates. The degree of calcite co-orientation strength within a subunit is expressed with multiples of uniform distribution (MUD) values; these are given in Figure 2.6-3 for selected subunits. High MUD indicates high, and low MUD indicates low to almost random crystal co-orientation strength. Calcite single crystals grown from solution, crystals entirely devoid of polymers, have MUD values above 700 (e.g., Fig. 2.6-S21 Yin *et al.* 2020b, Nindiyasari *et al.* 2015; note that MUD values depend on the settings for computation of the orientational density in the Channel 5 software Yin *et al.* 2020b). MUD values of subunits of all investigated aggregates are well above 600 (Fig. 2.6-3), most values are close to a MUD of 700 or even higher. Accordingly, calcite co-orientation strength is high for individual subunits, irrespective if these grew with or without bacterial EPS in the growth medium and irrespective of the EPS of a specific bacterium species (Fig. 2.6-3).

Figures 2.6-4 and 2.6-5 depict misorientation profiles for the investigated composites. The least misorientation/tilt between neighboring subunits we find for the reference aggregate (Fig. 2.6-4a, misorientation between 4 and 5°). Misorientation between subunits for aggregates that occlude bacterial EPS is always increased, relative to that in the reference composite. The highest misorientation between subunits (up to 40°) we find for the composite that incorporated *P. putida* EPS (Fig. 2.6-4c). For aggregates that formed with *M. phley* or *M. smagmatis* EPS misorientation between subunits scatters between 2 and 10° (Figs. 2.6-4b and 2.6-5b), while for the composite containing *B. subtilis* EPS misorientation varies between 10 and 20° (Fig. 2.6-5a). Within a subunit, mis-

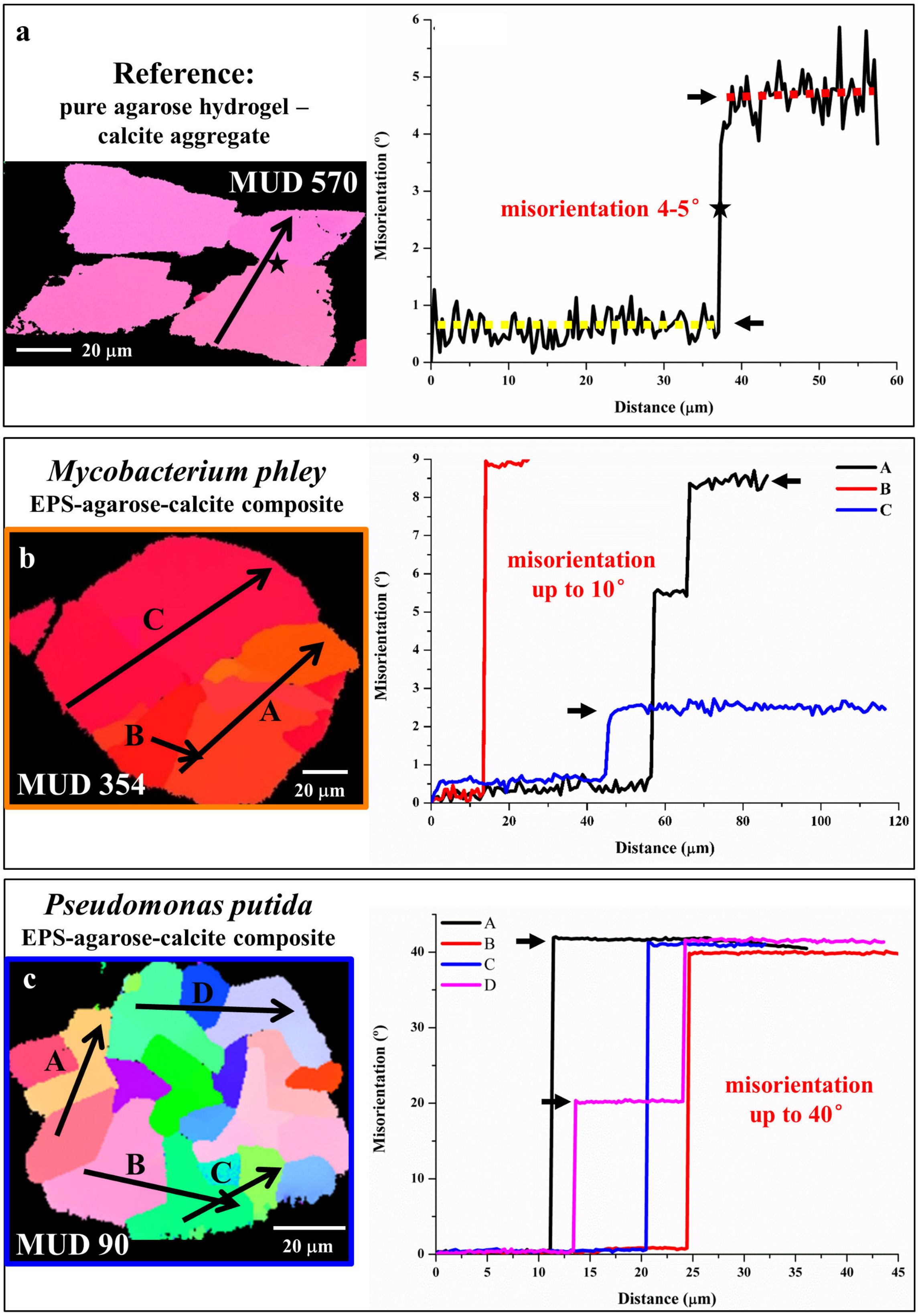

Figure 2.6-4. Misorientation vs distance graphs along profiles A, B, C, D for the reference (a) and composites that occlude bacterial EPS (b, c). Well visible is the scatter in the misorientation-distance graphs (black arrows in (a, b)) of the reference (a) and the *M. phley* EPS (b) aggregates, respectively. This scatter is absent for the aggregate that contains *P. putida* EPS (black arrow in (c)). The oscillation in the graphs indicates a pervasive occlusion of polymer (hydrogel or/and bacterial EPS) and contrasts to the smoother misorientation vs distance graphs obtained for the composite that occludes *P. putida* EPS (c). In color (a–c) we show calcite orientation maps derived from EBSD measurements.

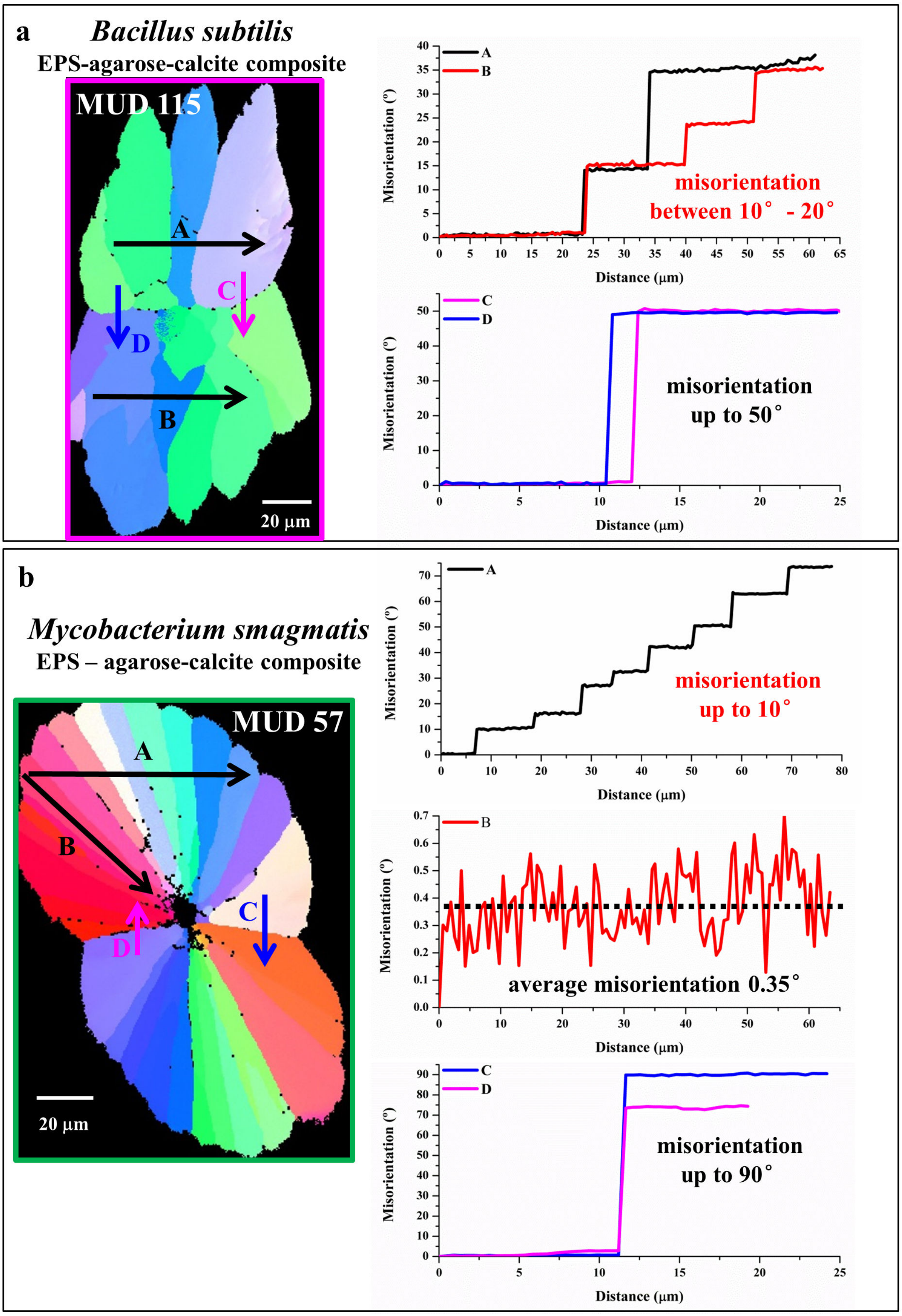

Figure 2.6-5. Misorientation vs distance graphs along trajectories A, B, C, D for composite aggregates that occlude *B. subtilis* (a) and *M. smagmatis* (b) EPS. Misorientation between abutting spherulitic subunits of the *B. subtilis* EPS-containing aggregate scatters between 10 and 20°, while misorientation between the upper and the lower half of the aggregate is ~50°. Misorientation between abutting subunits of the aggregate that contains *M. smagmatis* EPS varies between 8 and 10°; the stepped misorientation vs distance curve for trajectory A (b) visualizes the spherulitic arrangement of the subunits. Within individual subunits, the calcite is highly co-oriented (profile B in b), and misorientation scatters between 0.2 and 0.4°. Misorientation between the upper and lower half of the aggregate shown in (b) is very high, it is ~80 to 90°. The colors shown in (a, b) code for crystal orientation.

orientation between crystallites is between 0.3 and 0.4° (Fig. 2.6-5b). It is interesting to note that, even though the degree of misorientation between subunits is comparable for the composite that occludes *M. phley* and *M. smagmatis* EPS, respectively (up to 10°), the mode of assembly of the subunits within the aggregate is significantly different: for the composite with *M. phley* the subunits are highly co-oriented, while for the composite that contains *M. smagmatis* EPS subunits are arranged in a spherulitic fashion (compare Figs. 2.6-4b and 2.6-5b). Misorientation between the two halves of the sheaflike aggregates (Fig. 2.6-5) is 50° for the *B. subtilis* containing EPS and even 90° for the *M. smagmatis* containing EPS.

Figures 2.6-6 and 2.6-S22 give a compilation of the microstructure, texture, and calcite co-orientation strength for aggregates that occlude bacterial EPS. For the reference aggregate, these characteristics are given in Figure 2.6-4a. For the bacterial EPS containing aggregates, we find highly diverse microstructure and texture patterns. In contrast to the reference, aggregates that incorporate bacterial EPS are radial aggregates (see band contrast images in Fig. 2.6-6). In addition, when the EPS of *B. subtilis* (Fig. 2.6-6b) or that of *M. smagmatis* (Fig. 2.6-6c) is present in the growth medium, spherulitic orientational patterns form. The aggregates in Figure 2.6-6b,c are both composed of two spherulites that each occupies approximately half of the space of the aggregate ("half-spherulites"). The spherulitic arrangement of subunits is best developed for the composite that contains *M. smagmatis* EPS, which consists of two almost perfect half-spherulites. The corresponding pole figures (Fig. 2.6-6b,c) indicate that the c-axis and a*-axes are each distributed on a different great-circle. Calcite and subunit co-orientation strength are increased within each half of the half spherulites (Fig. 2.6-S22). However, when the entire sheaflike aggregate is considered, the MUD value is low (Fig. 2.6-6b,c), as there is, for both spherulitic aggregates, a high misorientation between the two half-spherulites at the membrane that is present at the equatorial cleft. When *M. phley* EPS is present in the growth environment, calcite crystallites and the subunits within the aggregate are highly co-oriented (MUD: 354). In contrast, with *P. putida* in the growth medium, the calcite within the subunits is still highly co-oriented; however, the subunits are highly misoriented relative to each other (MUD: 90). The highest subunit co-orientation strength (MUD: 570) is the reference aggregate.

In summary, bacterial EPS has a profound influence on the microstructure and texture of the composite aggregate (Fig. 2.6-6). The aggregate that occluded *M. phley* EPS is a radial polycrystal with highly co-oriented subunits, the one that incorporates *P. putida* EPS is a polycrystal with little co-oriented subunits, and the aggregates that occlude *B. subtilis* and *M. smagmatis* EPS are spherulites. Within the subunits calcite crystallites are always highly co-oriented; however, the mode and co-orientation strength of the subunit assemblage differs significantly and depends on the EPS of a given bacterium.

Bacterial EPS highly influences subunit morphology, size, and shape (Figs. 2.6-7 and 2.6-8). Most distinct are these for the aggregates containing *M. phley* and *P. putida* EPS (Fig. 2.6-7), even though, as local kernel misorientation shows, the occluded amount of EPS is low for both aggregates. Spherulitic assemblies of subunits are obviously less influenced by the amount of occluded polymer (bacterial EPS or agarose hydrogel). We find well-developed half spherulites despite large differences in the amount of occluded EPS/agarose polymers (Fig. 2.6-9).

2.6.4 Discussion

Bacterial EPS – agarose hydrogel incorporation and distribution

In our previous study on *P. putida* alone (Yin *et al.* 2020b), we showed for the first time that even a very small amount of bacterial EPS in the growth environment of biomimetic aggregates exerts a major influence on the composite aggregate formation: incorporation of polymers, mode of polymer distribution within the aggregate, development of polymer fabric within the aggregate, the pattern of crystallite and subunit co- and misorientation, composite aggregate morphology and size (Figs. 2.6-1 to 2.6-9). Our present results show that calcite microstructure and texture are characteristic for the EPS of different bacteria in the EPS-agarose mixture.

Two main factors control the amount of hydrogel that becomes occluded within a growing crystal: (i) gel strength and (ii) growth rate. The higher these parameters are the more gel becomes occluded and the more evenly it is distributed within the mineral (Nindiyasari *et al.* 2014a, 2015, 2019; Asenath-Smith *et al.* 2012; Greiner *et al.* 2018). At a given temperature, the strength of agarose gels depends on the concentration of the agarose solid content. In all experiments that we conducted for this study, the used gel was prepared with the same concentration of agarose: 0.5 wt%. Nonetheless, we have to keep in mind that the addition of EPS to the agarose sol might have changed the strength of the resulting EPS-agarose polymer mixture. We regard this as very unlikely; however, if this was the case, then, this fact could contribute to explain the differences in the distribution pattern of occluded polymers (i) between the reference aggregate and aggregates containing EPS as well as (ii) the distinctness in polymer distribution pattern between the different EPS-containing aggregates investigated in this study.

In an ideal system, the growth rate of each specific calcite surface would directly depend on the supersaturation of the system with respect to the relevant phase (Fernández-Díaz *et al.* 2006). As in hydrogel media advection and convection mechanisms are suppressed (Henisch 1988), mass transport through a gel occurs through diffusion. In hydrogels, crystallization starts at significantly higher supersaturation levels relative to those in solutions, as within the latter there is no confinement (Prieto *et al.* 1994; Prieto 2014; Putnis *et al.* 1995). The supersaturation threshold also depends on the boundary conditions of the system, mainly on the concentration of reactants and the distance from the reactant reservoir to the crystallization front (Prieto *et al.* 1994; Putnis *et al.* 1995). As time-dependent gradients develop in a gel when reactants diffuse toward the reaction front, the evolution of supersaturation with progressive growth is given by the balance between rates of reactant arrival to and reactant consumption by the growing crystal (Prieto *et al.* 1989, 1991; García-Ruiz 1992). The morphology of our reference aggregate indicates that this balance resulted in sustained high supersaturation throughout the entire growth process. Supersaturation values were around that threshold value that marks the transition from a surface- to a diffusion-controlled crystal growth regime. High supersaturation gradients facilitated the development of distinct morphological features that we observe for our reference aggregate: (i) dendritic branches (Fig. 2.6-1a) that result from faster growth at corners and edges of the polyhedral crystal compared to its faces (Sunagawa 1981; García-Ruiz & Otálora 1993), (ii) a dense fabric of occluded polymers (Fig. 2.6-9f), (iii) a tight interlinkage of the polymer with the mineral (Fig. 2.6-S12), and (iv) a pervasive and homogeneous distribution of polymers over the aggregate volume (Fig. 2.6-2e) (Nindiyasari *et al.* 2014a, 2015, 2019; Greiner *et al.* 2018). Obviously, this type of polymer occlusion does not affect the microstructure and texture of the calcite significantly. The reference aggregate consists of very few highly co-oriented subunits; the entire aggregate has a high MUD value (570) that qualifies it as being almost a single crystal (Figs. 2.6-2e, 2.6-3a, and 2.6-4a).

Relative to the reference aggregate, all aggregates that grew in hybrid EPS-agarose gels occluded polymers with each showing a different mode of distribution. In these aggregates, the polymer appears to be less dense, and its interlinkage with the mineral is less tight than that observed

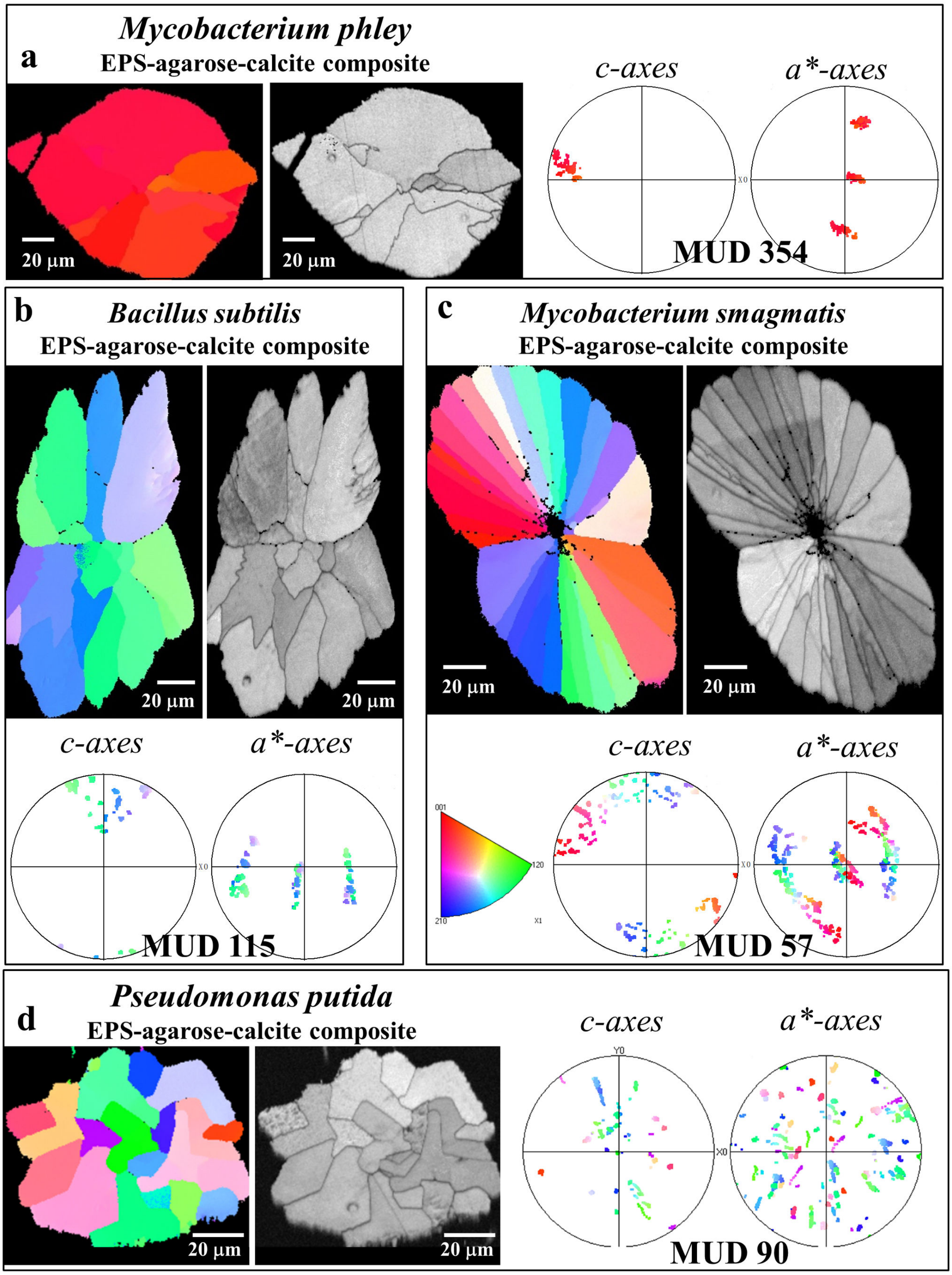

Figure 2.6-6. Microstructure (gray-scaled band contrast images) and texture (color-coded EBSD maps and corresponding pole figures) of composite aggregates that grew in a bacterial EPS–agarose hydrogel polymer mixture. Crystal orientation strength is given with MUD values, the latter are plotted at each pole figure. We find a high calcite co-orientation strength for the aggregate that occludes *M. phley* EPS (MUD 354) and a significantly lower crystallite co-orientation for composites that formed in a polymer mixture that contained *B. subtilis*, *M. smagmatis*, and *P. putida* (MUD 115, 57, 90) EPS, respectively.

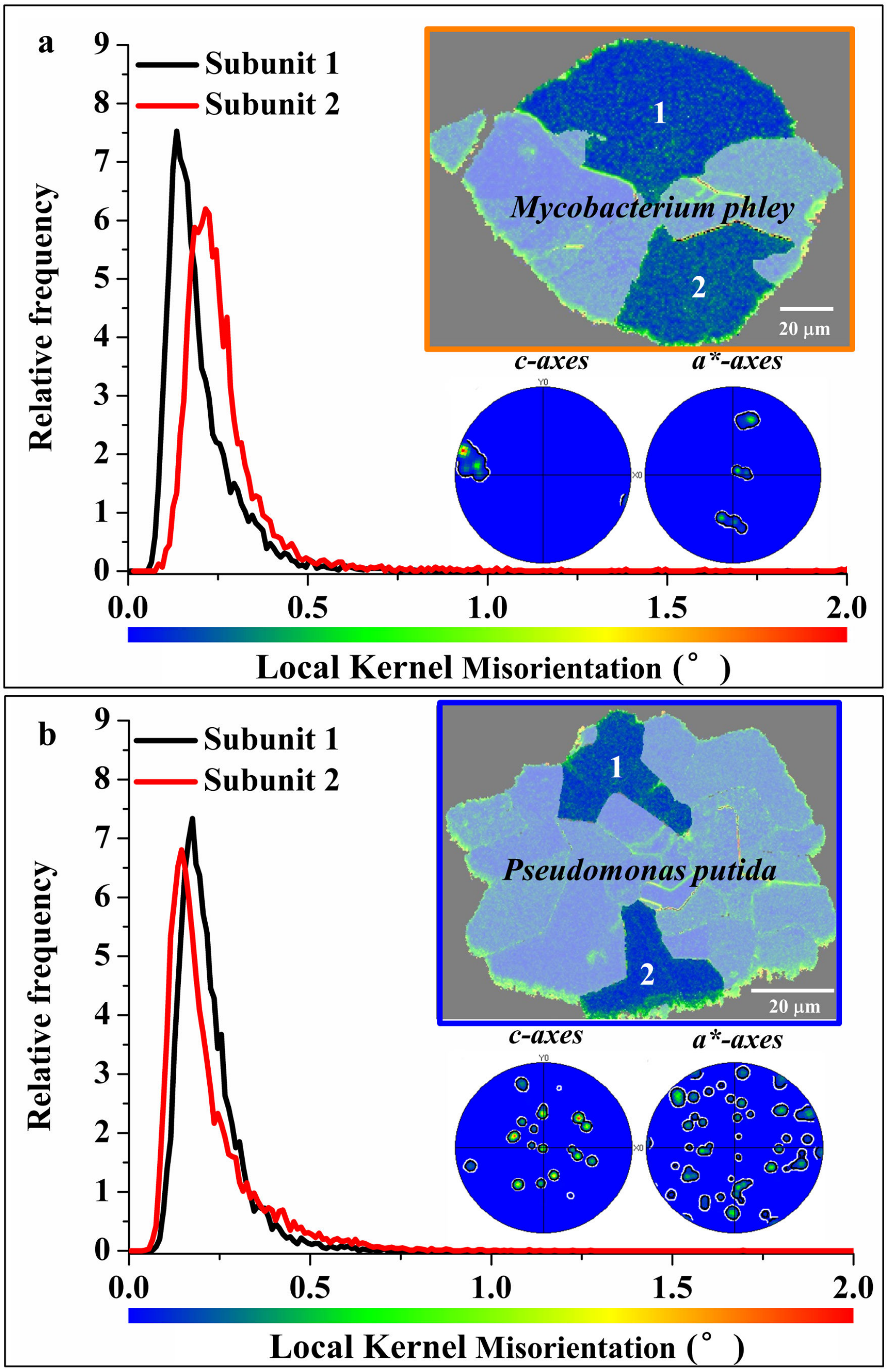

Figure 2.6-7. Local kernel misorientation analysis for subunits of aggregates containing *M. phley* (a) and *P. putida EPS* (b). Even though we find similar patterns of EPS and agarose gel occlusion within the aggregates, subunit sizes, morphologies, and assemblies differ significantly; compare pole figures shown in (a, b).

for the reference aggregate. The scarce occlusion of gel explains that, except for the aggregate that occluded *M. smagmatis* EPS, all other aggregates have lower local kernel misorientation with a narrower distribution, relative to that of the reference (Fig. 2.6-2). A wider distribution of local kernel misorientation is found for the aggregate that intercalated *M. smagmatis* EPS and reflects a specific gel occlusion behavior for this aggregate: (i) pervasive in two quadrants with a larger spread in local kernel misorientation, and (ii) scarce in the other two quadrants, with local kernel misorientation for these having a significantly smaller spread (Fig. 2.6-2c). Accordingly, the distribution pattern of occluded gel in aggregates that formed in hybrid EPS-agarose gels points to their growth taking place at slower growth rates in comparison to that of the reference. It is indeed demonstrated by now that calcite crystals that grow at slower rates occlude less gel (Asenath-Smith *et al.*

2012; Greiner *et al.* 2018); those gel fibers that do not become incorporated into the mineral are pushed ahead by the growing crystal. Gel density and gel strength increase locally and cause the patchy/inhomogeneous distribution of the gel within the mineral. We observe this for aggregates that formed in hybrid polymers containing EPS of either *M. smagmatis* or *B. subtilis* (Figs. 2.6-2, 2.6-9, and 2.6-S8). Where gel fibers are pushed together by abutting crystals, membranes are formed. Inhomogeneous gel distribution and development of gel membranes are associated with aggregates that consist of many, usually mutually misorientated, subunits (Nindiyasari *et al.* 2014a, 2015, 2019; Greiner *et al.* 2018; Yin *et al.* 2020b). All aggregates that occluded EPS have more subunits than the reference aggregate that is devoid of bacterial EPS as well as of gel membranes (Figs. 2.6-9, 2.6-S7, and 2.6-S8). The presence of gel membranes within aggregates is associated with a large misorientation between the subunits that can reach values above 50° (Figs. 2.6-4 and 2.6-5). This results in much lower MUD values for the entire aggregate compared to that of the reference (MUD between 57 and 354 for aggregates grown in hybrid gels against 570 for the reference, Figs. 2.6-4, 2.6-5, 2.6-6, and 2.6-S22)

Lower growth rates for calcite can, however, be related entirely to the effect of bacterial EPS:

A (i) To the chelating influence of the EPS through the negatively charged carboxylic groups in the polysaccharide components. The binding of Ca^{2+} to these functional groups alters Ca^{2+} diffusion through the gel, modifies Ca^{2+} concentration gradients around the growing crystals, and reduces supersaturation at aggregate growth. (ii) To the inhibition of calcite growth by the numerous functional groups of the polysaccharide and protein components of the EPS. These two above-mentioned effects are not exclusive and can operate simultaneously. Slight differences in the percentage of different functional groups of EPS components secreted by different bacteria can impact an individual contribution that modulates variably calcite growth and results in specific modes of gel occlusion, which leads to distinct calcite textures and microstructures.

B A further variation of calcite growth characteristics arises from molecular recognition between EPS components and specific directions and planes in the calcite structure. Stabilization of directions and planes due to molecular recognition might affect gel occlusion, promote branching, and induce the development of a variety of bacterial EPS-characteristic microstructural and morphological features of the composite aggregates. For example, although further evidence would be needed to support this hypothesis, molecular recognition could be underlying the highly structured occlusion of the polymer matrix within the different quadrants observed in aggregates grown with *M. smagmatis* EPS (Figs. 2.6-9 and 2.6-S8).

Accordingly, bacterial EPS substance not only exerts a major influence on crystal nucleation and mineral growth; there is also diversity in its influence on composite aggregate formation, as we see differences when we use the EPS produced by the different bacteria (e.g., Figs. 2.6-2 and 2.6-9). However, our FTIR results (Fig. 2.6-S6) do not depict large variations in chemical composition between the investigated EPSs: both the proteins as well as the lipids seem to be very similar for the four investigated EPSs. Polysaccharides differ slightly from each other. This might indicate that slightly different functional groups played a role in nucleation, mineral growth, and composite aggregate formation. However, one should keep in mind that shapes of FTIR curves are also influenced by the amounts of the different components.

Metazoan versus microbial controlled / influenced biomineralization

Biological mineralization is the process by which organisms convert ions in solution into solid minerals (Simkiss & Wilbur 1989). The

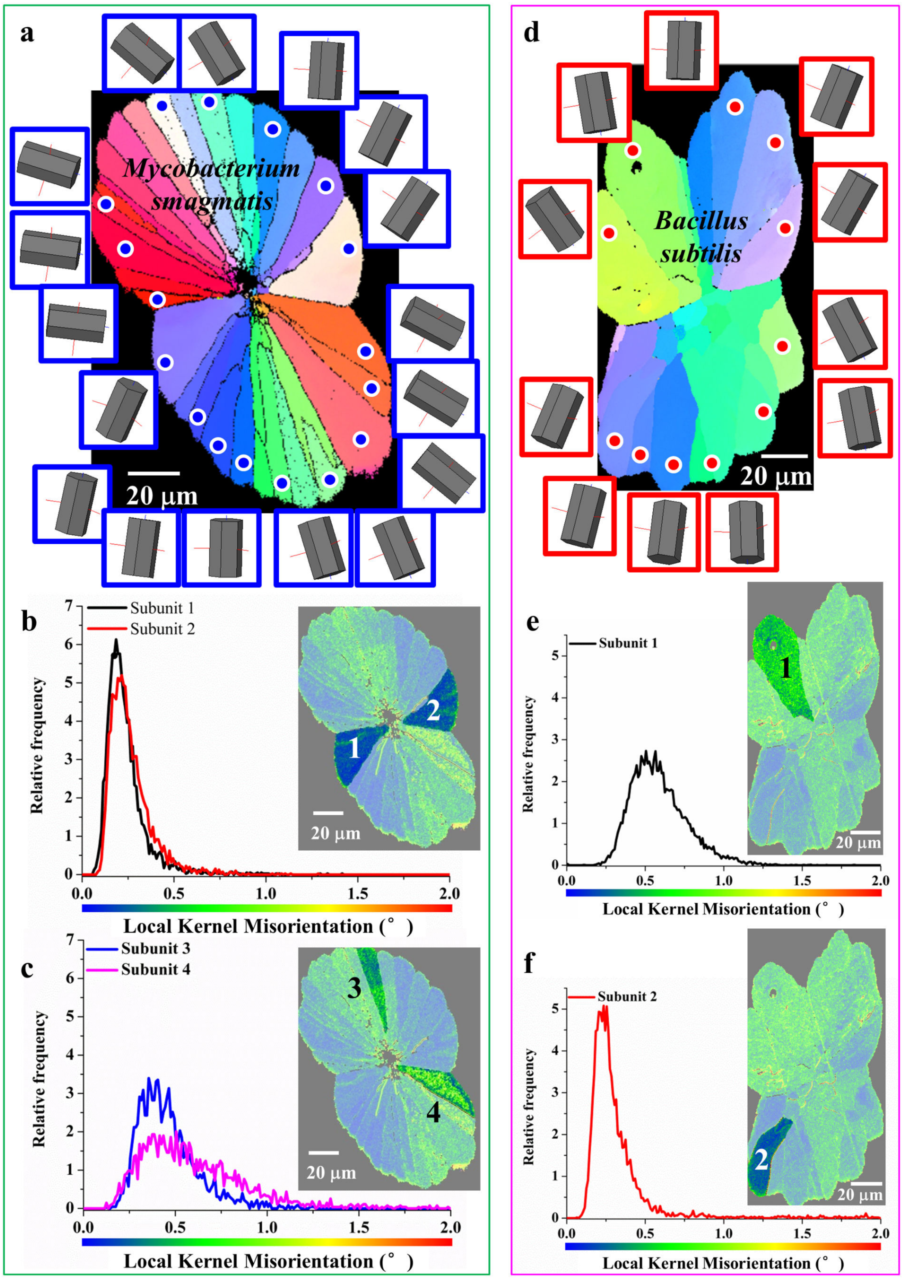

Figure 2.6-8. Spherulitic nature of aggregates that occlude *M. smagmatis* (a) and *B. subtilis* (b) EPS. For both aggregates we see an inhomogeneous pattern of EPS and agarose hydrogel occlusion: some subunits contain a higher content of occluded polymers (yellow to light green colors in (b, c, e, f)), while other subunits are almost EPS-agarose hydrogel free (blue colors in (b, c, e, f).

conversion is the consequence of cellular activity: the cells create the necessary physicochemical changes that have to take place when biologically secreted/precipitated minerals nucleate and grow (Simkiss & Wilbur 1989). Research within the last decades revealed that several degrees of biological control are possible (Lowenstam 1981; Lowenstam & Weiner 1989; Simkiss & Wilbur 1989; Mann 2001),47-50 an insight that led to the definition of the two main concepts of biological mineral formation: (i) biologically controlled and (ii) biologically induced/influenced mineral generation and deposition (Lowenstam 1981; Lowenstam & Weiner 1989; Simkiss & Wilbur 1989; Addadi *et al.* 2006; Dupraz *et al.* 2009; González-Muñoz *et al.* 2010; Decho 2010; Gallagher *et al.* 2010).

The process of biologically controlled mineralization is based on genetic determination. It is a highly regulated process steered by the metabolic requirements of an organism (Simkiss & Wilbur 1989). Mineralization is templated by a polymer matrix (in single-celled coccolithophores as well, e.g., Yin *et al.* 2018) that consists mainly of proteins, glycoproteins, and lipids. As the proteins are folded, they shield their functional groups from the surrounding environment. The deposition of biominerals within and outside cells occurs in a confined space (e.g., Yin *et al.* 2018 and Simonet Roda *et al.* 2019b,a), in which the organism has complete control of the chemical conditions. Morphologic control is determined simply by the available space for mineral deposition, which is confined by the polymer network/membrane fabric. During mineralization and formation of the structural biological material, matrix polymers become occluded within the biomineral. The result is a hierarchical, highly functional, and environment-adapted biological structural material with a well-defined composition, array of components, mode of component organization, and overall ultrastructure (e.g., Dunlop & Fratzl 2010 and refs therein).

In biologically induced/influenced mineralization, biominerals are formed by precipitation that arises from the interaction of microbial metabolic processes with the surrounding environment (Mann 2001; Dupraz *et al.* 2009; Decho 2010). Like in biologically controlled mineralization, mineral precipitation occurs onto organic templates; however, these are predominantly polysaccharides and only to a lesser degree proteins. Polysaccharides are long-chained linear and/or branched carbohydrates and possess a wide variety of carboxyl and hydroxyl functional groups. The microorganism-led mineral deposition takes place in two stages (Fortin *et al.* 1997; Dupraz & Visscher 2005; Braissant *et al.* 2007) and occurs on cell walls and within EPS matrices. First, a modification of physicochemical conditions such as pH, Eh, P_{CO_2}, and ion concentration takes place either within or in the direct surroundings of the bacterial cell. Subsequently, supersaturation is increased, which leads to the precipitation of the biomineral. Because of the precipitative process, size, shape, structure, composition, and organization of microbially formed crystallites appear only moderately regulated (e.g., Konhauser 2007 and refs therein) . Mineral formation is induced when microbial activities generate biochemical conditions that facilitate precipitation, while it is influenced when passive interactions of extracellular polymers with the geochemical environment are the driving forces of the precipitation (Dupraz *et al.* 2009; Decho 2010). It was suggested that controlled biomineralization is the biomineral formation process in metazoan and unicellular eukaryotes, the process of induced/influenced biomineralization is the process that is utilized by bacteria for secreting minerals (Dupraz *et al.* 2009; Decho 2010; Flemming & Wingender 2010; Flemming *et al.* 2016a). However, the formation of magnetosomes in bacteria is highly controlled with an obvious functional aim.

Microbially induced/influenced extracellular biomineralization is not just passive precipitation. Research of the last years disclosed the influence that bacteria, bacterial cell walls, and bacterial EPS have on several aspects of biomineral formation.

(i) Braissant *et al.* (2003); Lian *et al.* (2006); Sánchez-Román *et al.* (2007); Obst *et al.* (2009); Tourney & Ngwenya (2009) and Shirakawa *et al.* (2011) demonstrated the influence of bacterial EPS on polymorphism, carbonate phase selectivity, carbonate nucleation (Obst *et al.* 2009), and the inhibition or promotion of the entire carbonate growth process (Lian *et al.* 2006).

(ii) The work of Sánchez-Román *et al.* (2007); Tourney & Ngwenya (2009); Ercole *et al.* (2012) and Wei *et al.* (2015) described the role of bacterial EPS in carbonate mineral morphology formation.

(iii) Oppenheimer-Shaanan *et al.* (2016) demonstrated the formation of three-dimensional mineral scaffolds within the EPS matrix. These surround bacterial cells and serve functional purposes, as they hold the extracellular matrix and bacterial cells together for cell protection.

(iv) Our study demonstrates the substantial influence of bacterial EPS on crystallite organization, mineral microstructure, and texture in biomimetic EPS-carbonate composites (Fig. 2.6-6). Influence on the mineral organization is exerted through the mode of EPS incorporation into the mineral (Fig. 2.6-9). The latter is linked to the EPS fabric (Figs. 2.6-9b–e, 2.6-S13, 2.6-S15, 2.6-S17, and 2.6-S19), EPS composition (Fig. 2.6-S6), type (a network of fibrils and membranes), and pervasiveness of polymer distribution/occlusion within the mineral (Fig. 2.6-9g–j). We observe large differences in mineral organization not only between aggregates that formed with the EPS of the different bacteria but also between the reference aggregate that formed in an environment devoid of EPS (Fig. 2.6-9k,f) and aggregates that grew in media containing bacterial EPS (Fig. 2.6-9b–e, 9g–j).

All this is not surprising, however, as even artificial "simple and clean" soluble polymers with anionic or cationic functional groups strongly influence morphologies of precipitated calcite (Cantaert *et al.* 2012 and Schenk *et al.* 2014, and the literature cited therein).

The above summarized studies document the significant influence of microorganisms and associated EPS on biomineralization, an influence that may be as vital and consequential as the influence of metazoan cells on biomineralization of functional elements of their body. In metazoa, the formation of biominerals and biopolymer matrices draws deeply on the energy reserves of an organism (Palmer 1992). Biomineralization processes are rooted in transcellular transport and cellular storage possibilities. The biomineralized products that are formed by metazoan organisms are of considerable importance also for the functioning of cells, for example, calcium transport out of the cells for avoiding cell poisoning. In the case of microorganism induced extracellular biomineralization, the mineralization process takes place in two steps (Konhauser 2007). First, the many functional groups of polysaccharides bind cations to anionic ligands on bacterial cell surfaces. These, in a further step, may serve as nucleation sites for mineral deposition/precipitation (Konhauser 2007). The growth process may be inorganically driven dependent on the available ions within the surroundings of a microorganism, which in turn is highly determined by the chemical characteristics of the environment the microorganism lives in (Konhauser 2007). So, in contrast to the precisely controllable chemistry and fluxes of the nanoenvironment employed in biocontrolled mineralization (Simonet Roda *et al.* 2019b,a; Yin *et al.* 2020b), extracellular microbial-induced biomineralization takes place in a more open system, for which the EPS adds at least some degree of control by reducing advection and diffusion in the immediate extracellular environment, and–with the functional groups and chelating abilities of the EPS–by providing some storage of ions.

We were able to show that a specific microstructure/texture signal can be related to the EPS of a specific microorganism (at least for the four used EPS samples of the four bacteria in this study). It must be said that Chekroun *et al.* 2004 and González-Muñoz *et al.* 2010 were led to an opposite conclusion from their investigation of one organism (in living and killed forms, respectively) and their classical SEM investigation of the external and surface morphology of the precipitates, as they observed morphological phenomena that are also observed in inorganic contexts. The microstructure/texture signal that we get from the EBSD investigation is significantly more prominent and unambiguous than just morphological SEM images or the information that we gain from the relevant FTIR measurements of the EPS. This insight can be projected into the hypothesis that morphology of bioinduced extracellular precipitates can indeed potentially be used as a biomarker for the identification of activity of certain bacterial species. However, for a reliable identification, we need to interlink signals derived from already well-established biomarkers for microbes (Arp *et al.* 1999; Simoneit 2002, 2004; Frankel

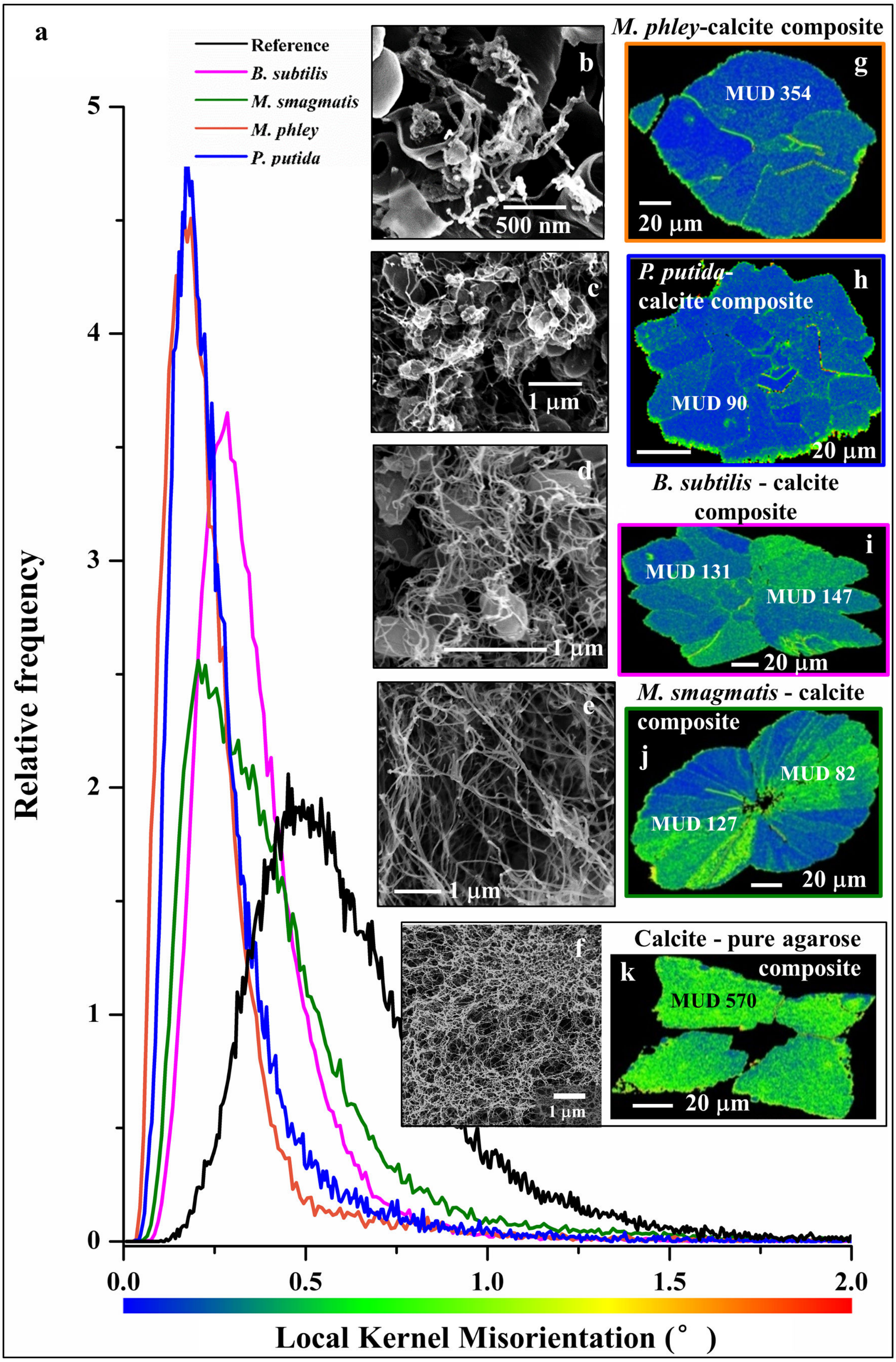

Figure 2.6-9. Summary of the influence of bacterial EPS/hydrogel polymers on polymer distribution, subunit organization, mineral co-orientation strength, and aggregate morphology. (a) Degree of local kernel misorientation of calcite crystallites due to polymer occlusion; bacterial EPS (b–e) and agarose hydrogel (f) network; (g–k) maps of local kernel misorientation displaying the pattern of polymer distribution and composite aggregate morphology.

& Bazylinski 2003; Visscher & Stolz 2005; Tourney & Ngwenya 2009) with the morphological, microstructural, and texture signatures.

2.6.5 Conclusions

Biofilms consist of a community of microbial cells and the associated matrix of extracellular polymeric substance, EPS, that in nature is interspersed with rock and mineral particles. Growing information on the composition and reactivity of EPS matrix materials indicates that the EPS substance exerts a significant influence on crystal nucleation and mineral growth. While some functional groups of the EPS matrix serve as initial nucleation sites, other moieties control the extent and the type of mineral precipitation. Accordingly, EPS matrices are able to inhibit, alter as well as to enhance precipitation of calcium carbonate. The focus of this study is to investigate whether EPS matrices influence microstructure and texture characteristics of precipitated calcite, and if so, how and to what degree. From our work we deduce the following conclusions (Fig. 2.6-9):

1. The EPS of microorganisms has a profound influence on EPS-hydrogel-calcite composite aggregate formation: (a) aggregate morphology and size, (b) mode of polymer occlusion, (c) subunit formation and subunit assemblage, (d) calcite co-orientation strength on sub-micrometer- and micrometer-scale levels, and (e) calcite microstructure and texture.
2. The influence of the EPS on aggregate formation and structural organization is unique for a specific microorganism and differs from each other for the investigated bacteria species.
3. Our results strongly indicate that the role of microorganisms is not as passive as it has been regarded; microorganisms can influence and mediate biomineralization through their EPS.
4. The observed microstructure and texture characteristics are well-observable individual biosignatures that can potentially be developed to an identification tool for the recognition of bacterially mediated calcification.
5. In a broader perspective, our study documents that the influence of bacterial EPS on mineralization and mineral organization is not at all as small as generally thought. In both, biologically controlled and biologically induced/influenced mineralization, the influence of the organism on the mineral formation can be substantial. Evolutionary advantage may be seen as the opportunity of an organism to increase the efficiency in the use of the environmental resources in energy and matter to grow its population. We do not hesitate to call a biomineralization process “biocontrolled” if this advantage is apparent to our intelligence, and obviously this controlled process is part of the organism’s metabolism, which clearly depends on the environment that the organism lives in. It is also commonly thought, in mechanistic philosophies, that evolutionary advantage arises by chance rather than by something like intelligence. Speaking of bacteria or bacterial colonies, it is likely and, to our opinion, quite obvious that bacteria or bacterial colonies gain some biologic/evolutionary advantage by the “induced” extracellular precipitation. Taking this together with the observation of a control mechanism for bacteria to shape this precipitate makes it impossible to draw a clear dividing line between “biocontrolled” and “bioinduced” mineralization.

Acknowledgments

F.W. was financially supported by Deutsche Forschungsgemeinschaft, DFG Grant GR-1235/9-1. L. F-D would like to acknowledge the Spanish Ministry of Science, Innovation, and Universities for financial support through project CGL2016-77138-C2-1-P. We would like to thank the staff of Central Facility for Electron Microscopy at Ulm University for their technical support.

2.6.6 Support Information

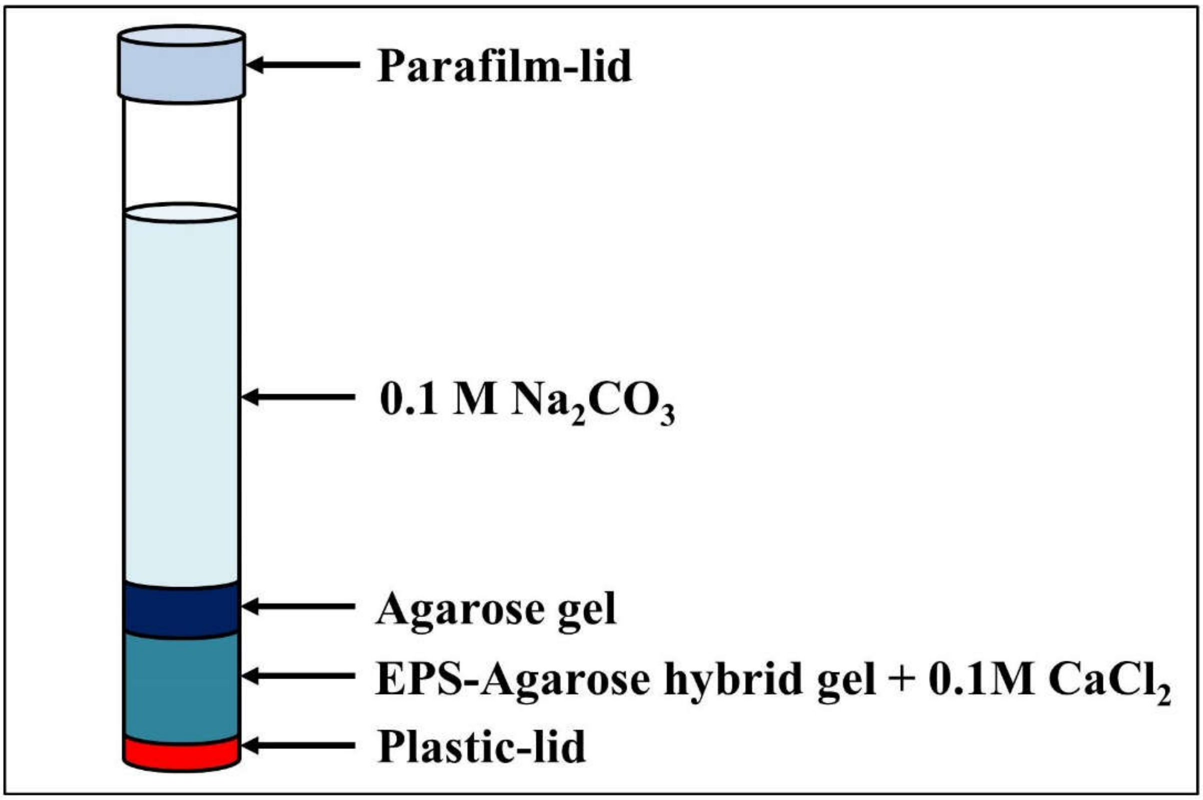

Figure 2.6-S1. The used single-diffusion system setup for the growth of the investigated bacterial EPS-agarose hydrogel-calcite aggregates.

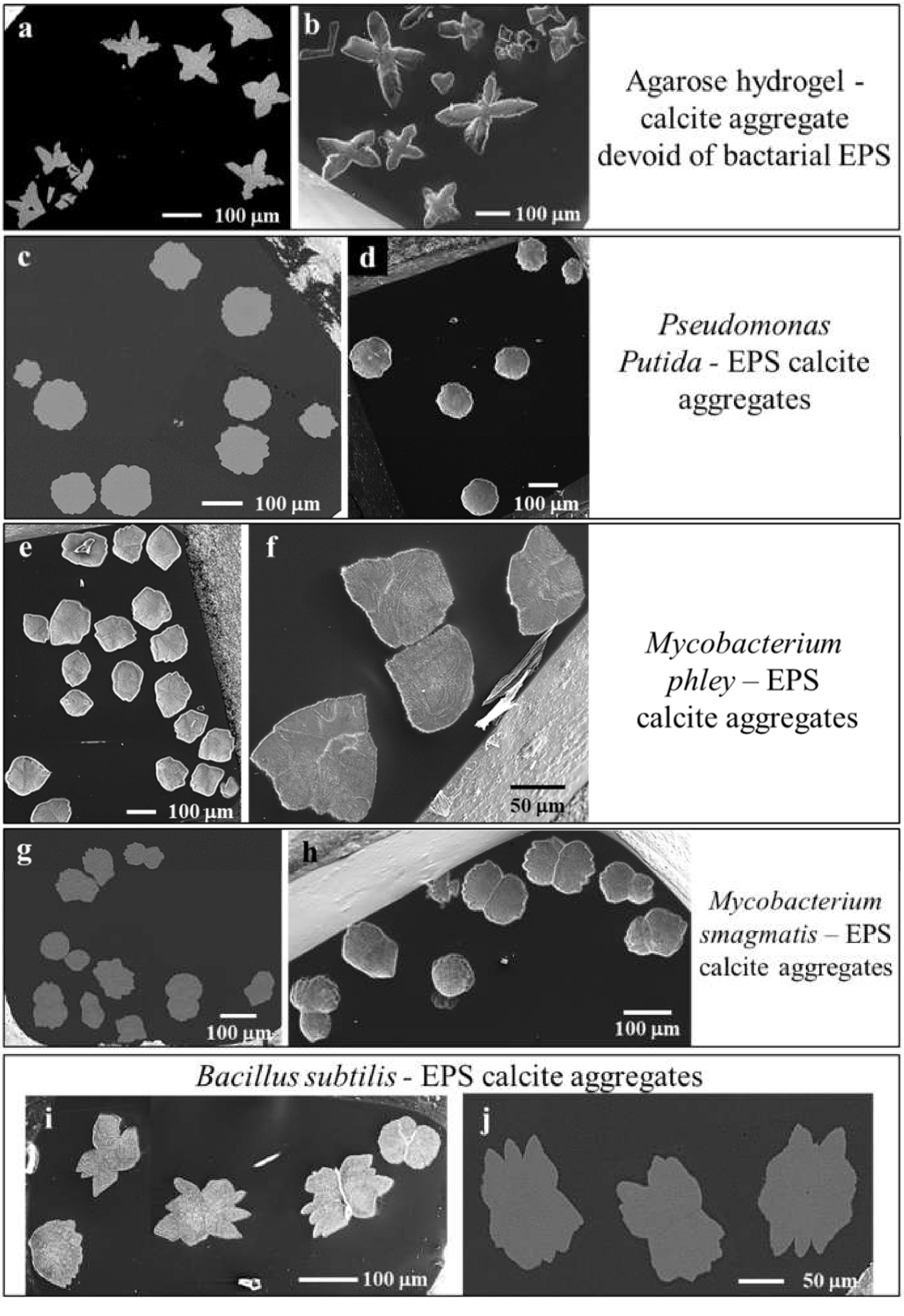

Figure 2.6-S2. BSE images showing the difference in morphology between (i) the reference aggregate and the aggregates that formed in the presence of bacterial EPS and (ii) the diversity of composite morphologies that we obtained when the EPS of a specific microorganism was used for the growth of the composite aggregate. BSE images of etched (a) and decalcified (b) surfaces of the reference aggregate. BSE images of microtome polished (c) and decalcified (d) surfaces of composite aggregates containing *P. putida* EPS. BSE images of etched (e) and decalcified (f) surfaces of aggregates that formed in the presence of *M. phley* EPS in the growth medium. BSE images of microtome polished (g) and decalcified (h) surfaces of composite aggregates occluding *M. smagmatis* EPS. BSE images of etched (i) and microtome polished (j) surfaces of aggregates containing *B. subtilis* EPS.

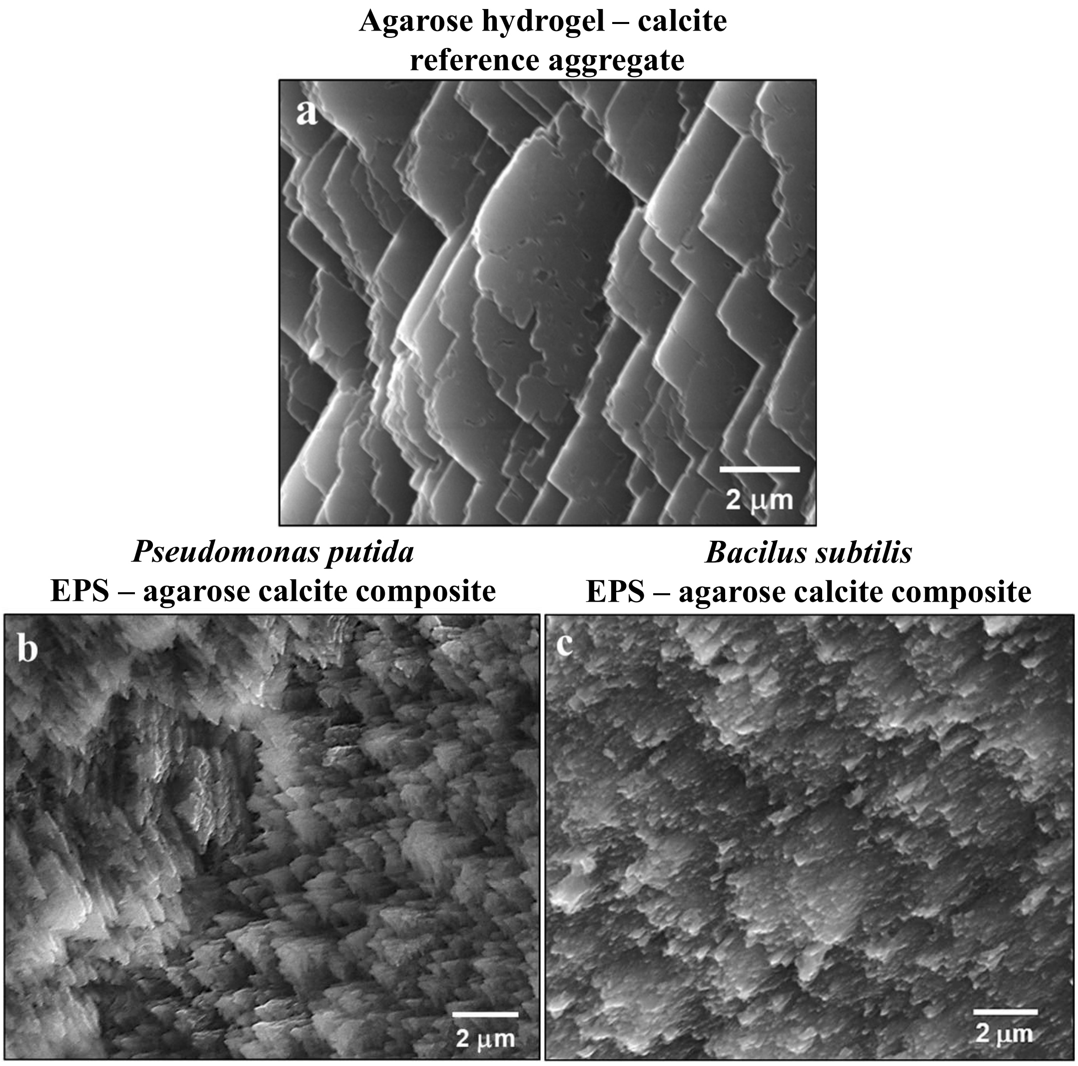

Agarose hydrogel – calcite reference aggregate

***Pseudomonas putida* EPS – agarose calcite composite**

***Bacilus subtilis* EPS – agarose calcite composite**

Figure 2.6-S3. High magnification images of the surface for the reference aggregate (a) and the two aggregates formed in the presence *P. putida* (b) and *B. subtilis* (c) bacterial EPS in the growth medium, respectively.

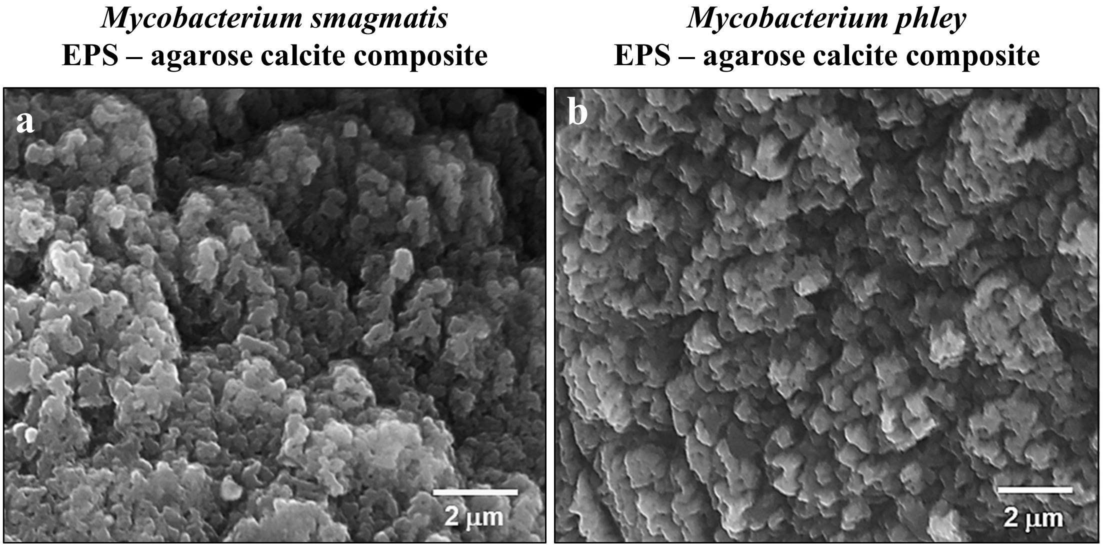

***Mycobacterium smagmatis* EPS – agarose calcite composite**

***Mycobacterium phley* EPS – agarose calcite composite**

Figure 2.6-S4. High magnification images of the surface for the aggregates that formed in the presence of *M. smegmatis* (a) and *M. phley* (b) bacterial EPS, respectively.

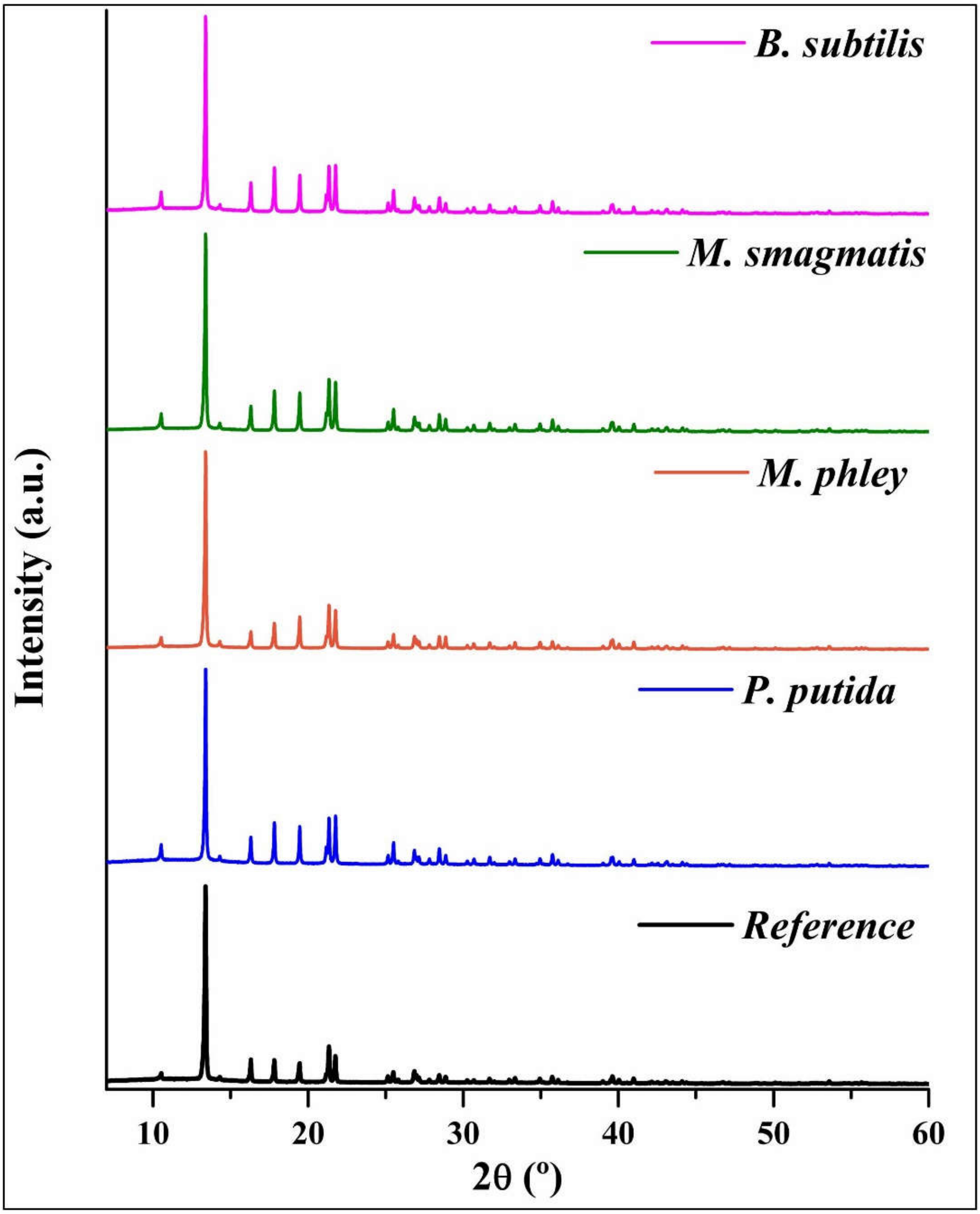

Figure 2.6-S5. Powder x-ray diffractograms of aggregates obtained from pure agarose (the reference, shown in black) and *Bacillus subtilis*, *Mycobacterium phley*, *Mycobacterium smagmatis*, *Pseudomonas putida* EPS-agarose hydrogel mixtures. Diffractograms were recorded on a Debye-Scherrer geometry STOE diffractometer equipped with a curved Ge (111) primary monochromator to produce Mo-Kα_1 radiation (λ = 0.07093 nm) at 50 kV and 30 mA. Aggregates were sealed in ∅0.3mm glass capillaries and were kept in rotation during the measurement. To allow a common representation, the diffractograms are normalized and arbitrarily shifted along the intensity axis. Only calcite was detected in all samples.

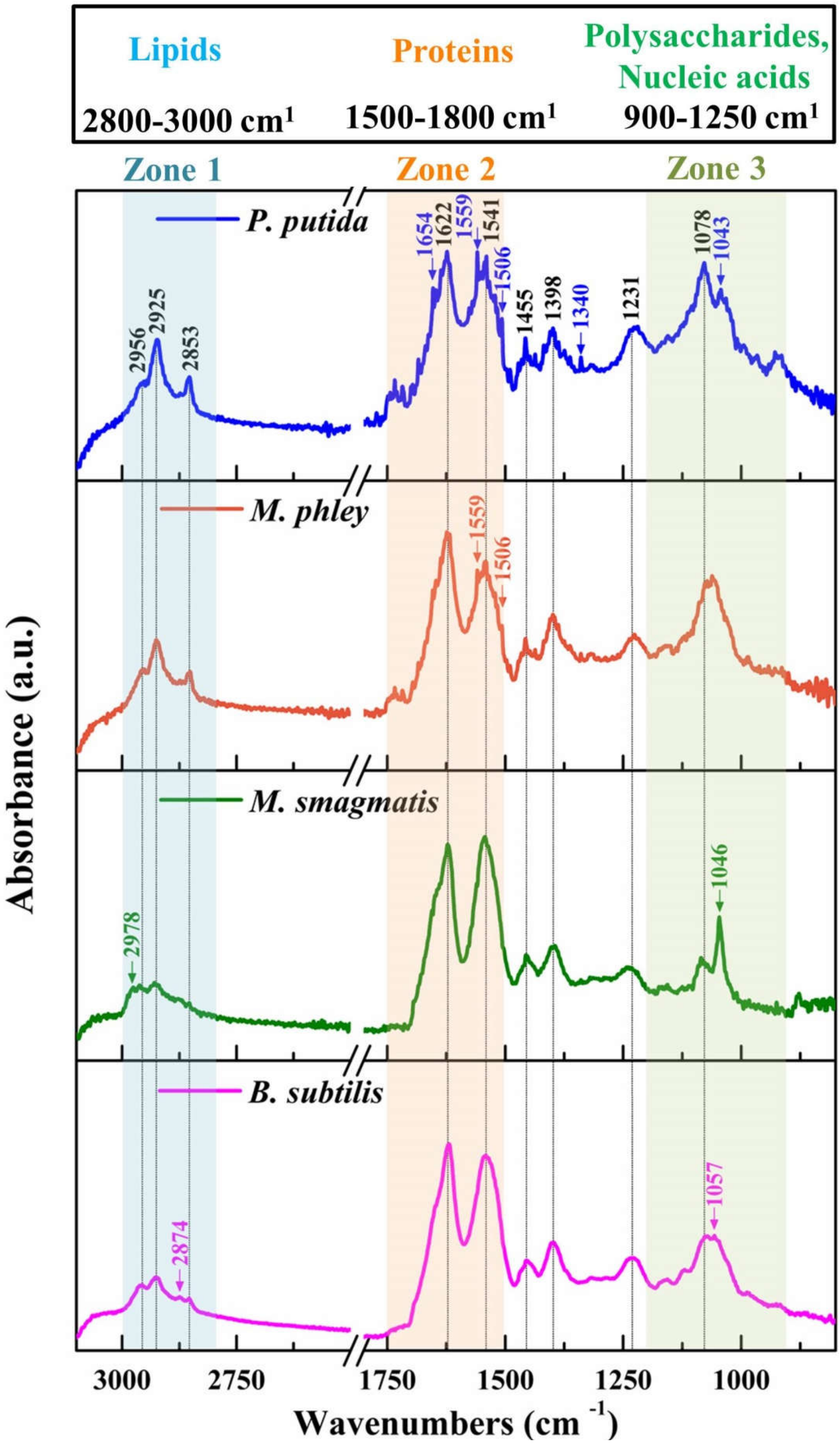

Figure 2.6-S6. FTIR spectra of *Bacillus subtilis*, *Mycobacterium phley*, *Mycobacterium smagmatis*, *Pseudomonas putida* total EPS. The three marked zones define regions of functional groups, which can be associated with lipids (zone 1), proteins (zone 2), and polysaccharides (zones 3).

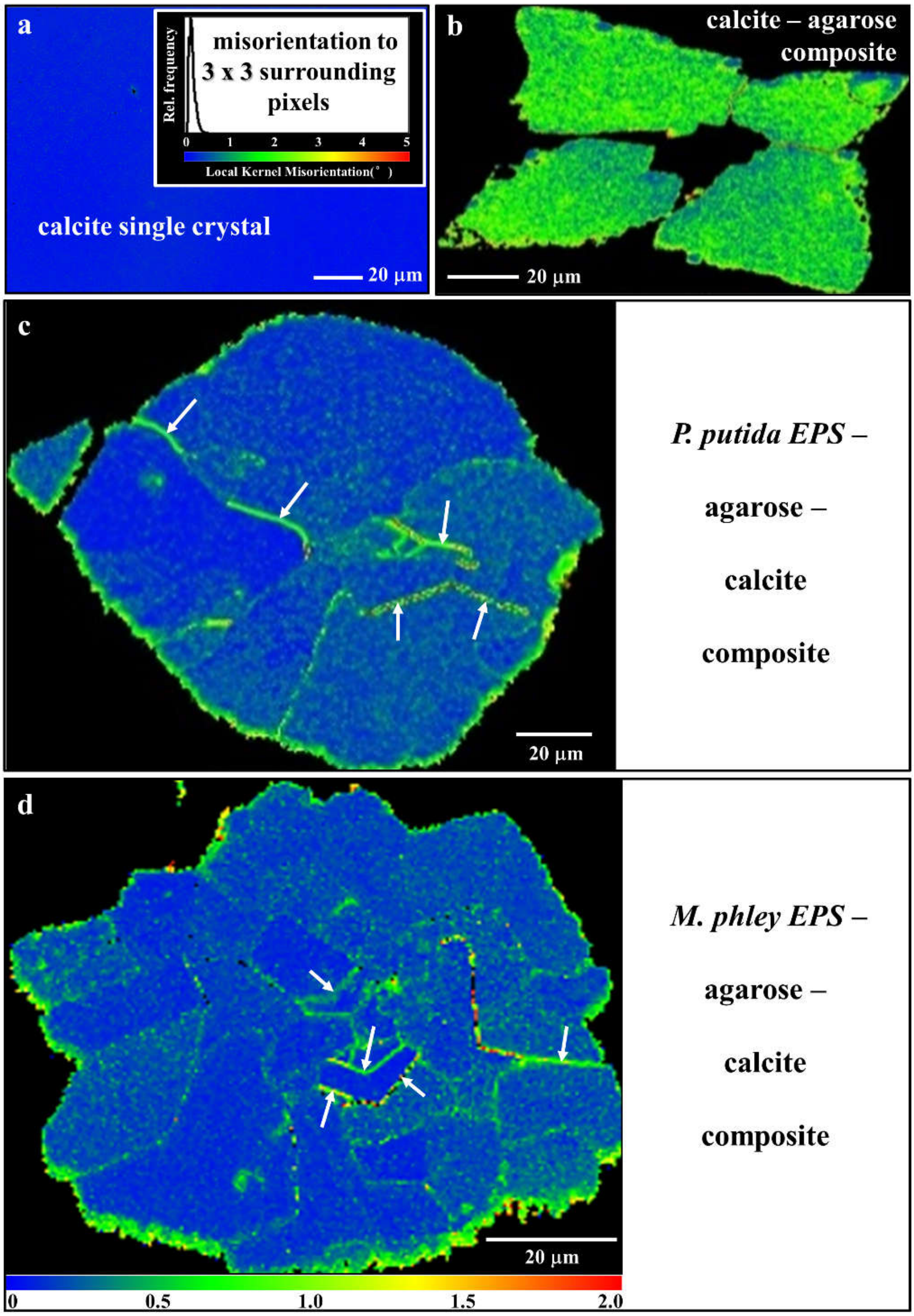

Figure 2.6-S7. Local kernel misorientation maps derived from EBSD data of composite aggregates that formed with and without bacterial EPS. Local kernel misorientation map evaluated with a 3 $times$ 3 filter (a) for a calcite single crystal devoid of EPS and hydrogel, (b) a reference aggregate consisting only of calcite and agarose gel and (c, d) the aggregates that comprise bacterial EPS, agarose gel and calcite. The used color legend is given in (d). The inhomogeneous and patchy distribution of EPS and hydrogel polymers in aggregates that formed with bacterial EPS in the growth medium is well visible, which are more or less randomly formed as membranes (white arrows in c and d). The dark blue colors that we obtain for aggregates shown in (c) and (d) indicate little misorientation between calcite crystallites that points to low amounts of trapped gel within the calcite.

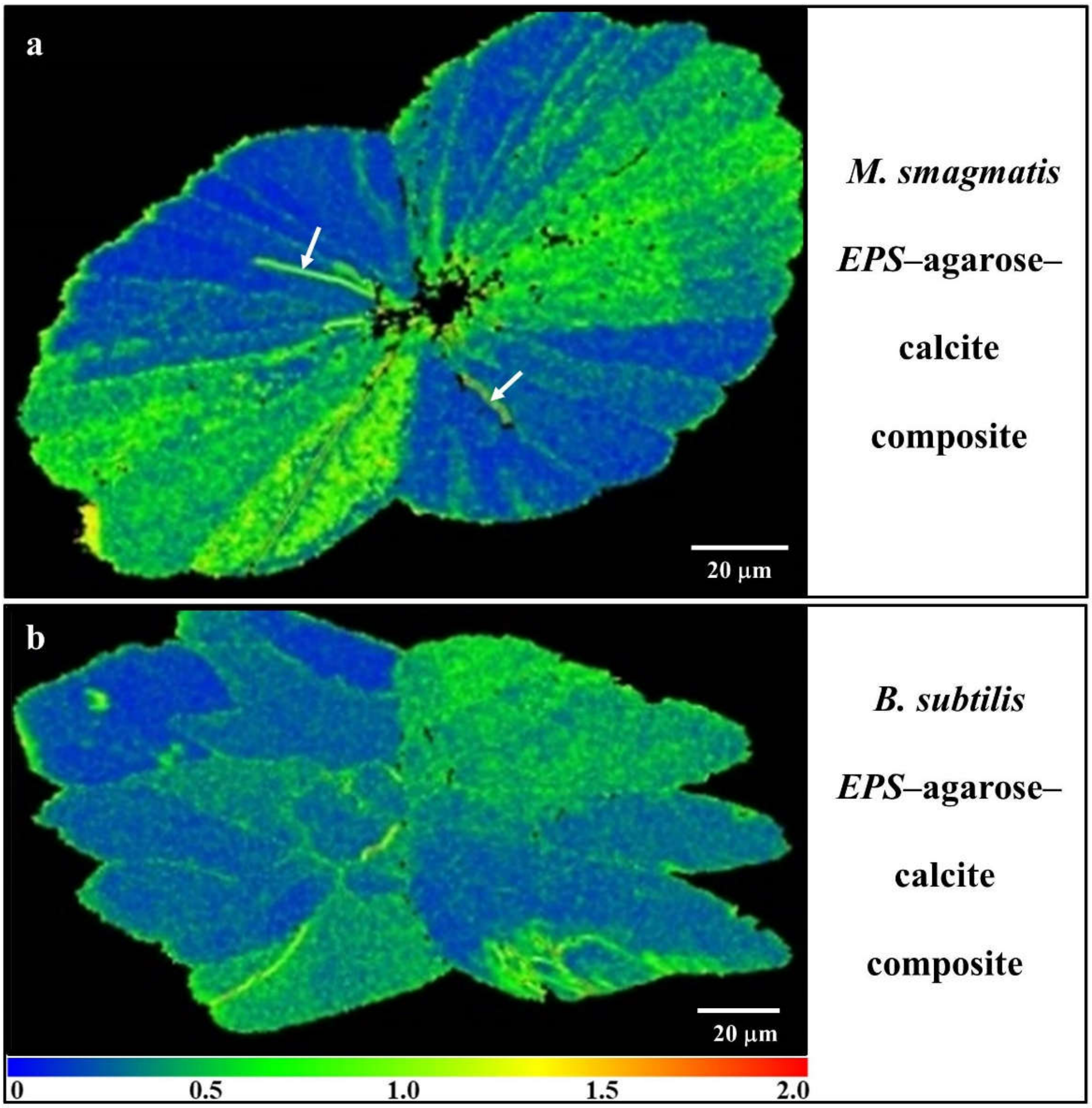

Figure 2.6-S8. Local kernel misorientation maps derived from EBSD data of composite aggregates that formed with (a) *M. smagmatis* and (b) *B. subtilis* EPS in the growth medium. The used color legend is given in (b). Polymer occlusion within the calcite is structured in composite aggregates that incorporate *M. smagmatis* EPS (a) and is inhomogeneous in composites that occlude *B. subtilis* EPS (b). The polymer is only little accumulated to membranes, when it is incorporated within the calcite.

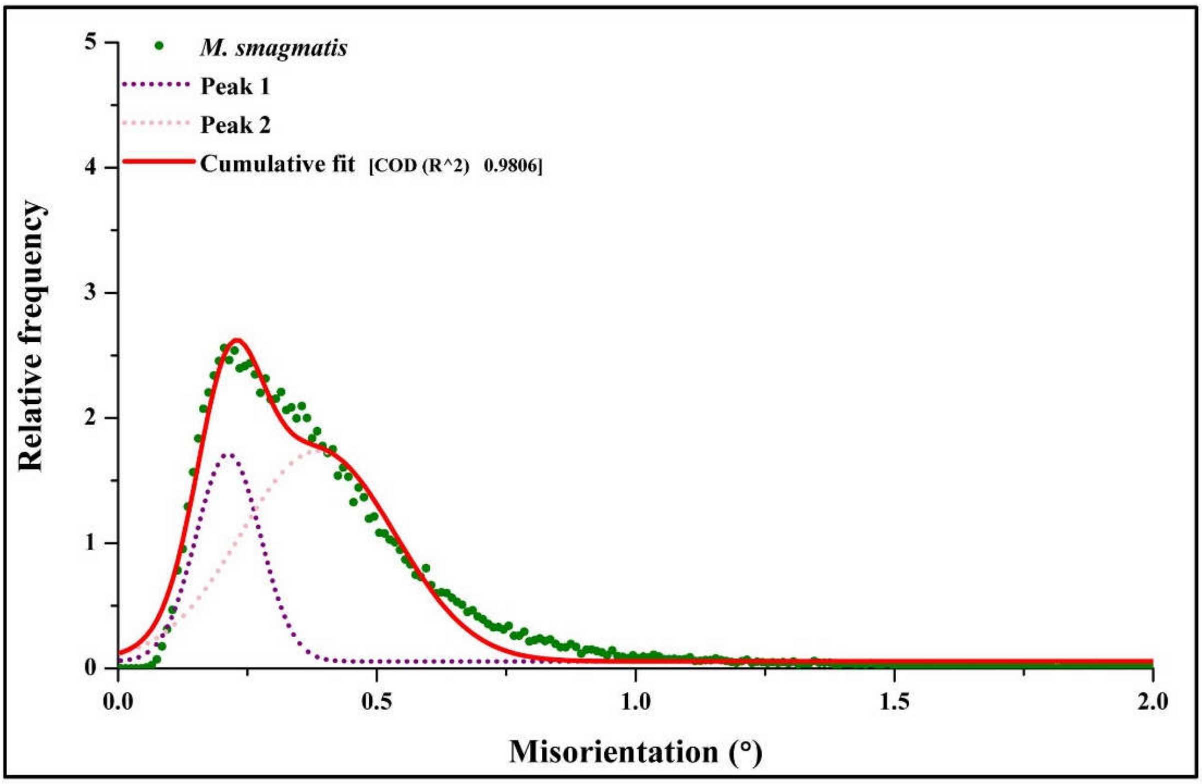

Figure 2.6-S9. Zoom-in into the deconvoluted relative frequency versus local kernel misorientation curve shown in 2.6-2c.

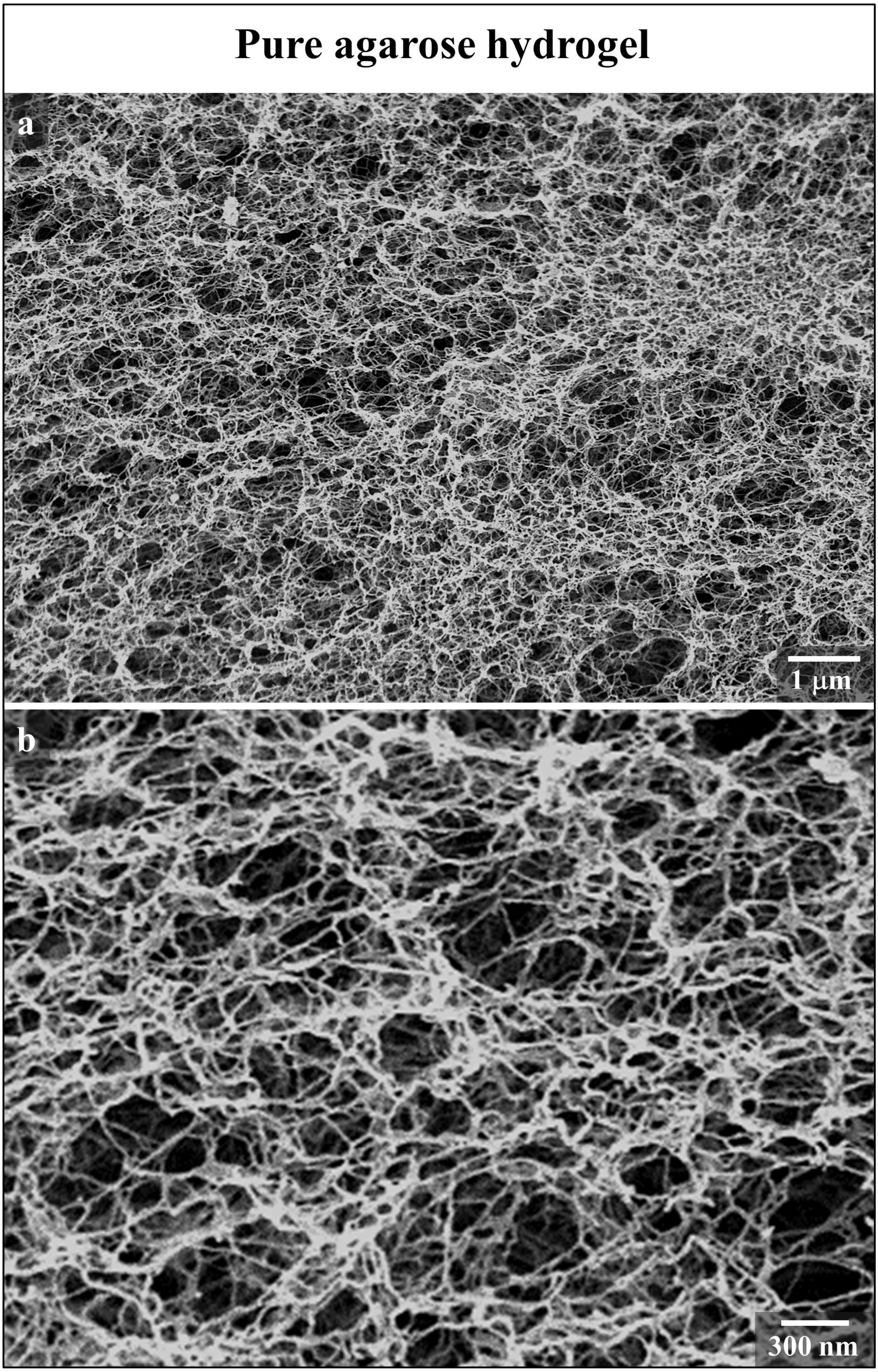

Figure 2.6-S10. FE-SEM images depicting the fabric of pure agarose gel.

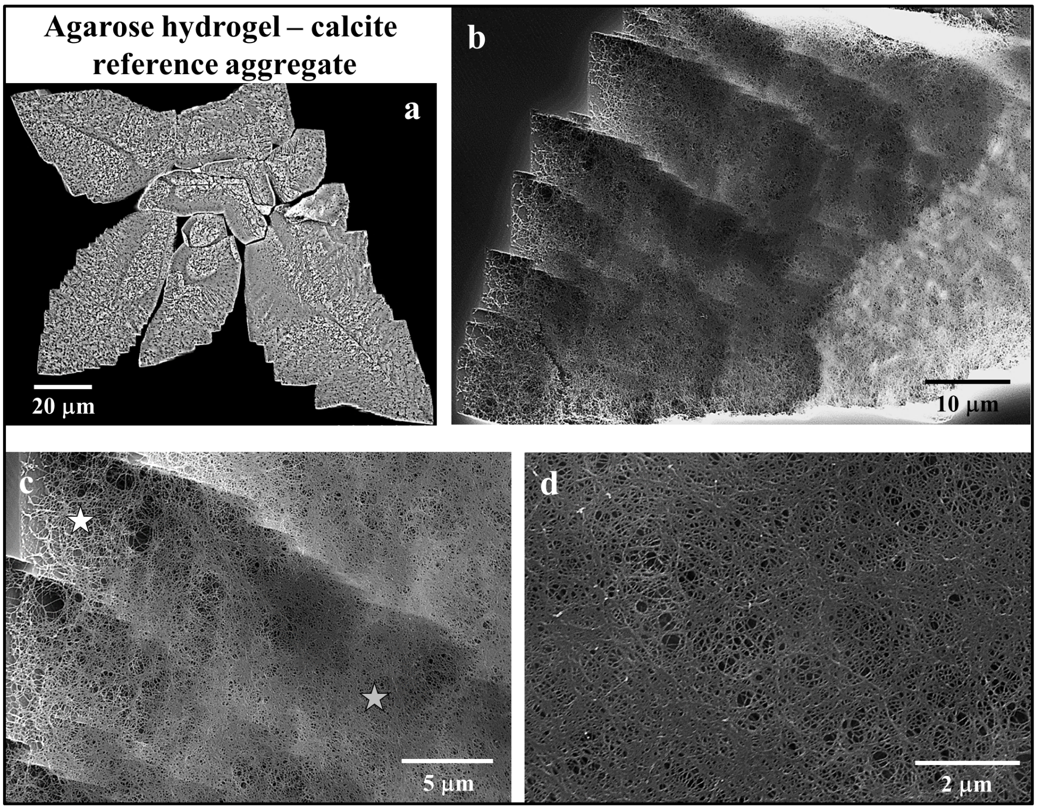

Figure 2.6-S11. FE-SEM images depicting the fabric and network thickness of agarose hydrogel occluded within the calcite-agarose reference crystal. The white star in (c) points to the rim, and the grey star in (c) to the center of the subunit.

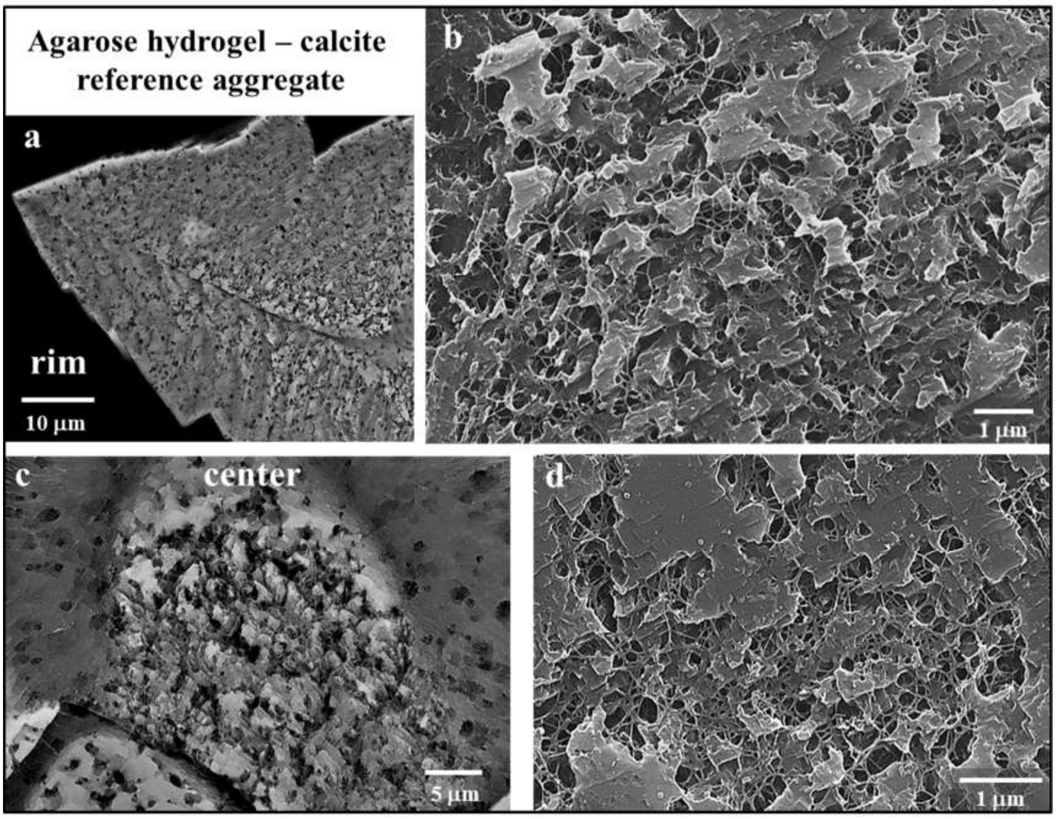

Figure 2.6-S12. FE-SEM images depicting the interlinkage of calcite and the agarose network in the rim (a, b) and within the center (c, d) of the calcite-agarose reference crystal (see 2.6-S11a).

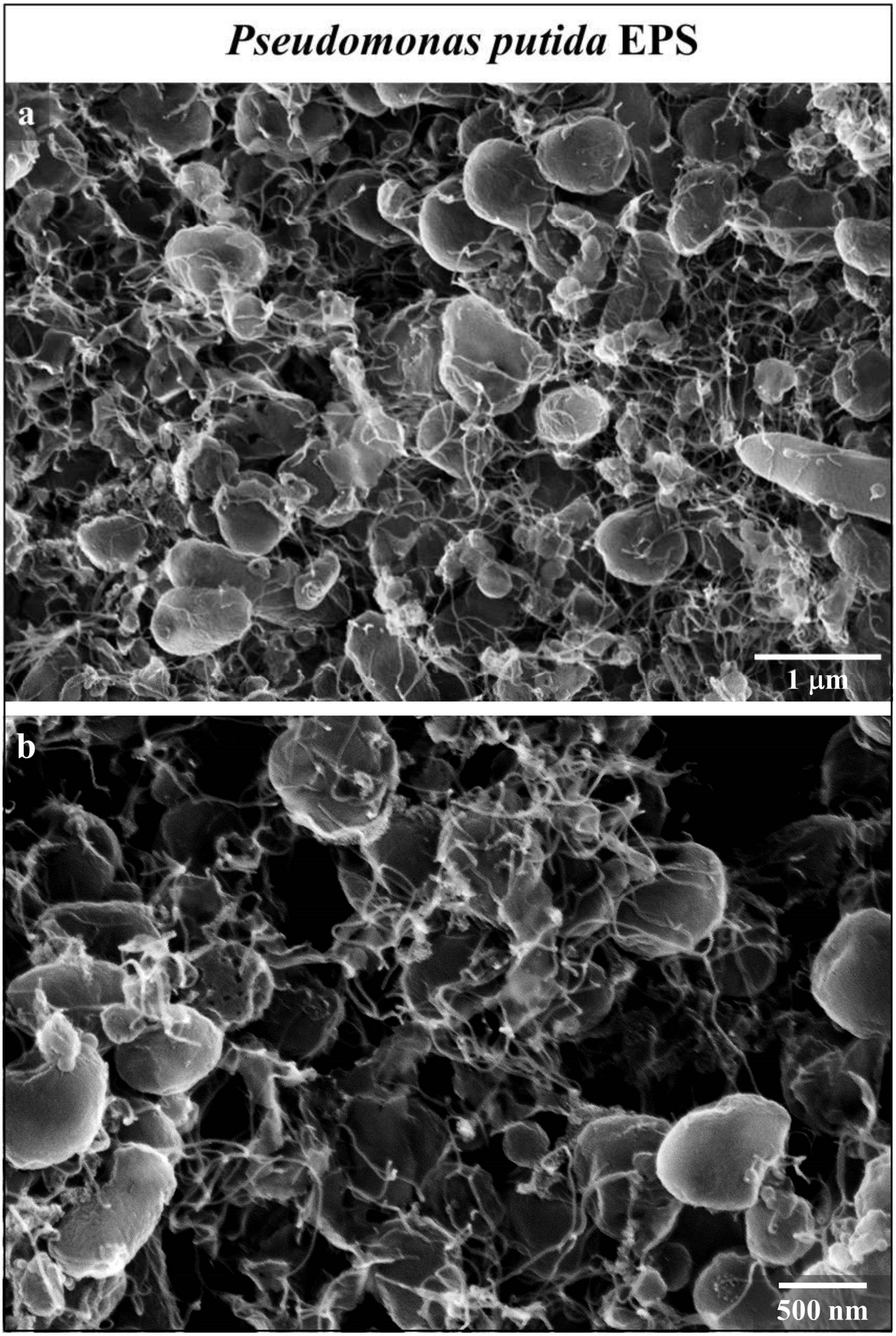

Figure 2.6-S13. FE-SEM images depicting *P. putida* EPS fabrics and bacterial cell walls.

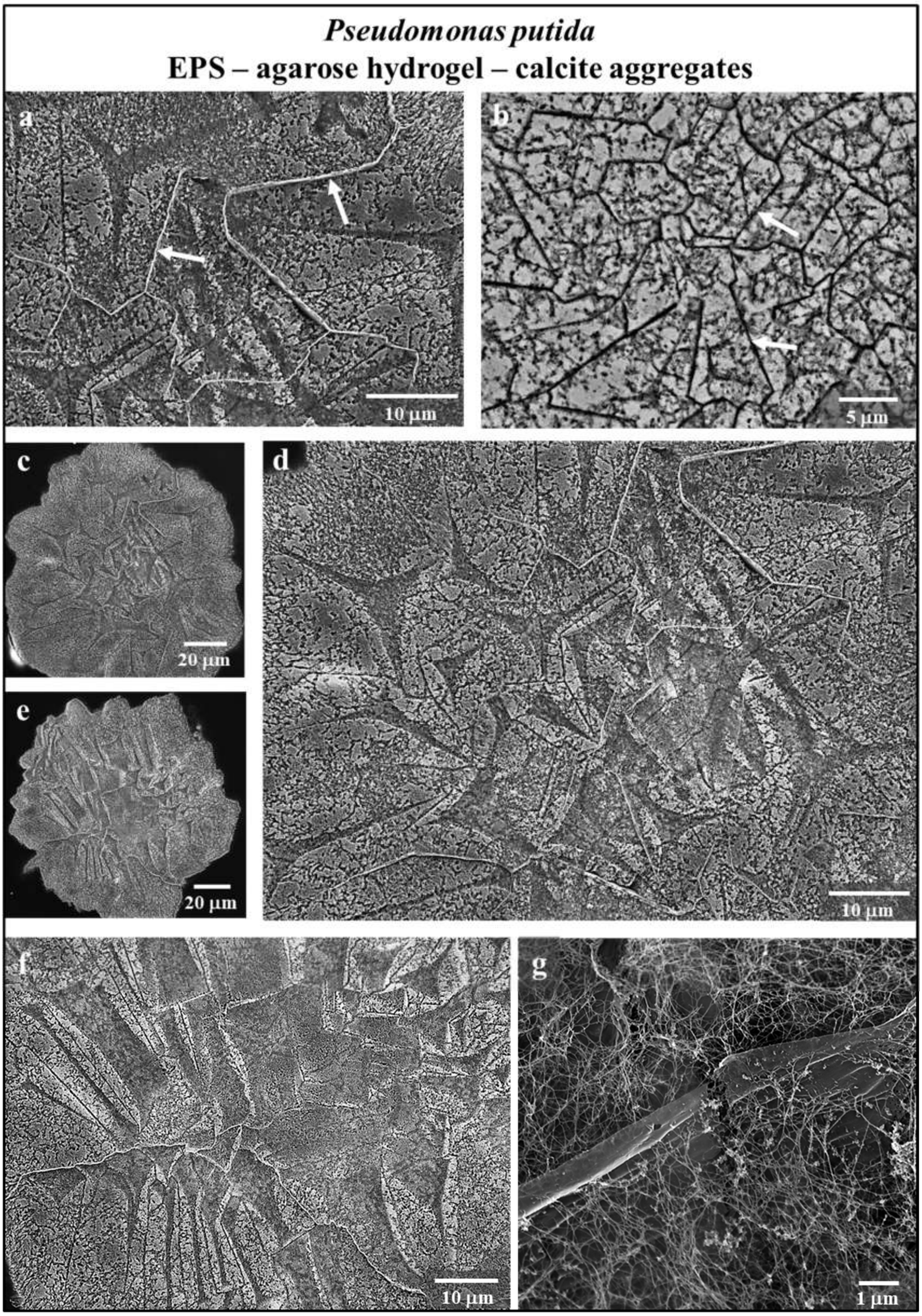

Figure 2.6-S14. FE-SEM images depicting aggregate morphology, the formation of subunits, and the interlinkage of calcite and the agarose network in the rim and within the center of *P. putida* EPS – agarose gel – calcite aggregates. The presence of membranes within the composites (white arrows in panel a and b) are well visible, which are developed as thick solid walls in (f) and (g).

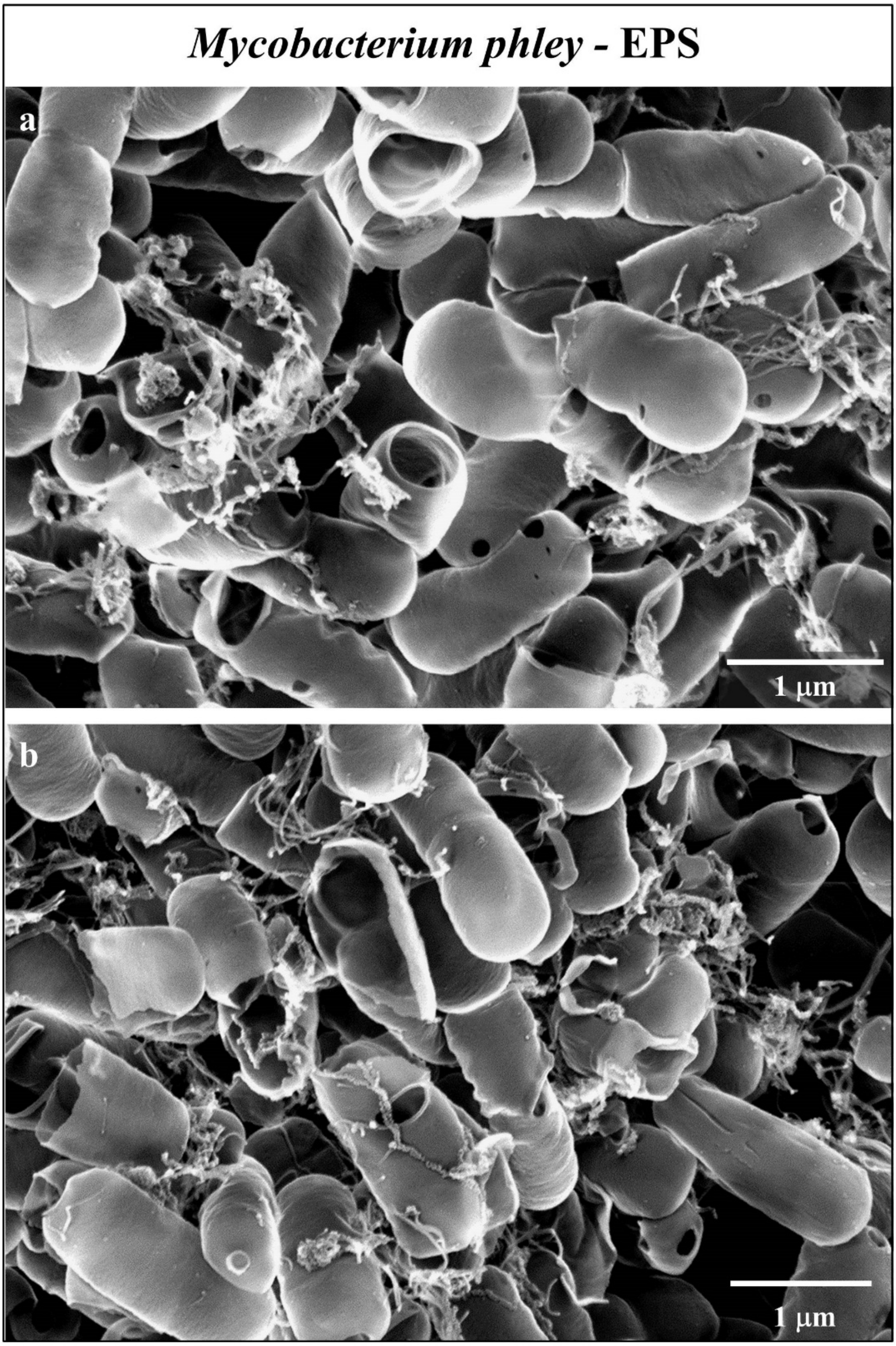

Figure 2.6-S15. FE-SEM images depicting *M. phley* EPS fabrics and bacterial cell walls.

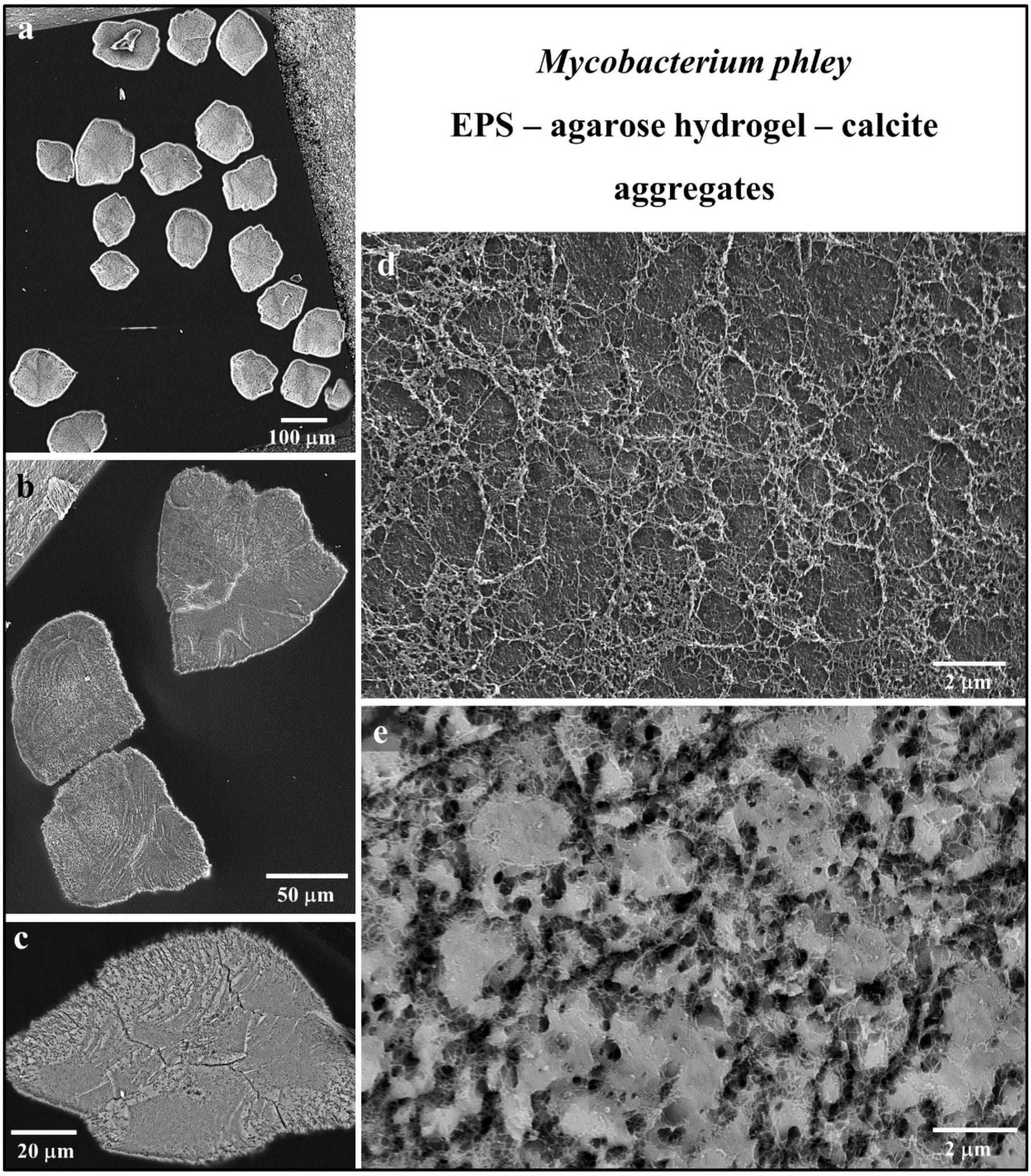

Figure 2.6-S16. FE-SEM images depicting aggregate morphology, the distribution pattern of subunits and interlinkage of calcite, and the EPS - agarose network within the composite aggregate containing *M. phley* EPS.

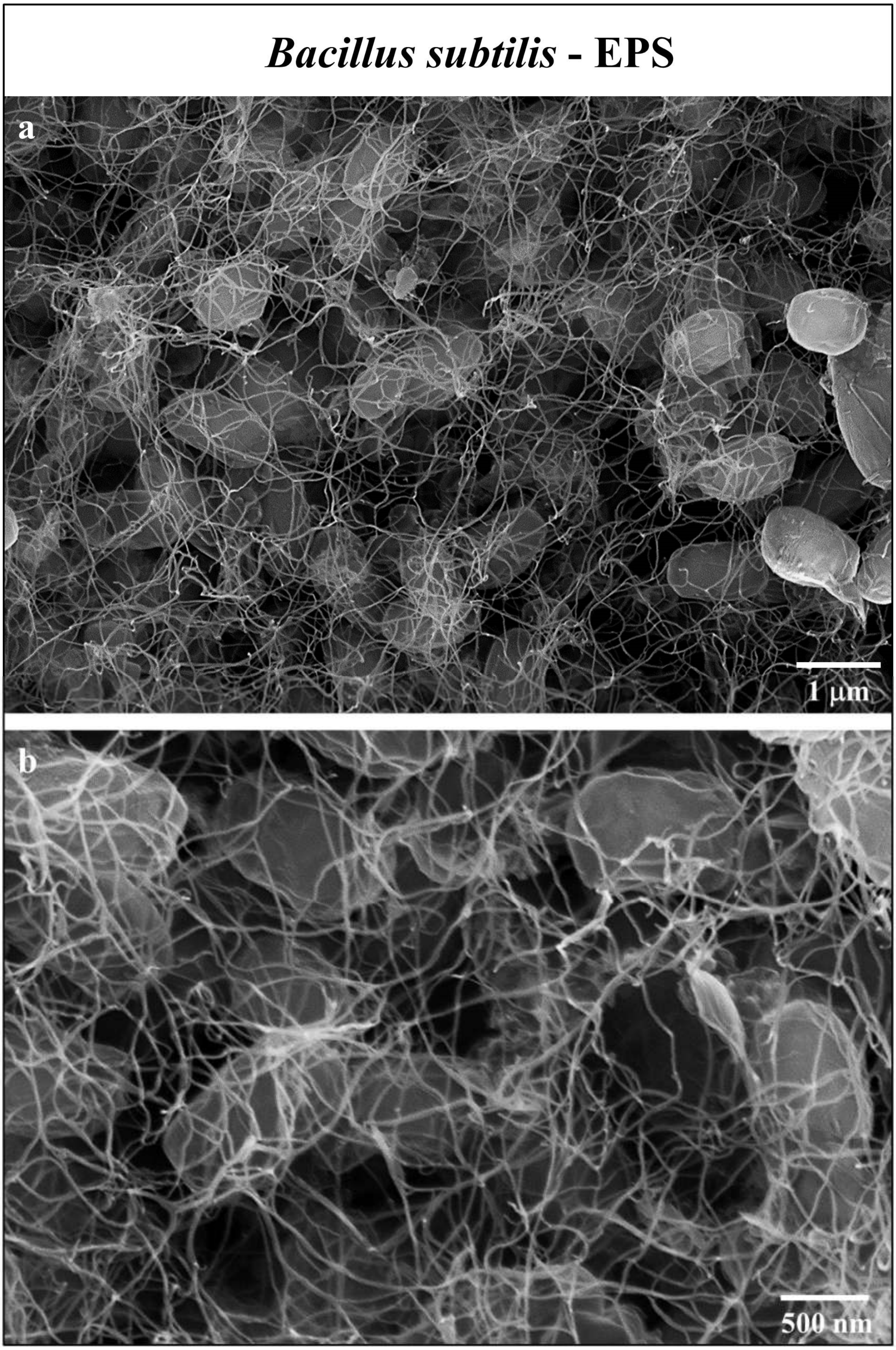

Figure 2.6-S17. FE-SEM images depicting *B. subtilis* EPS fabrics and bacterial cell walls.

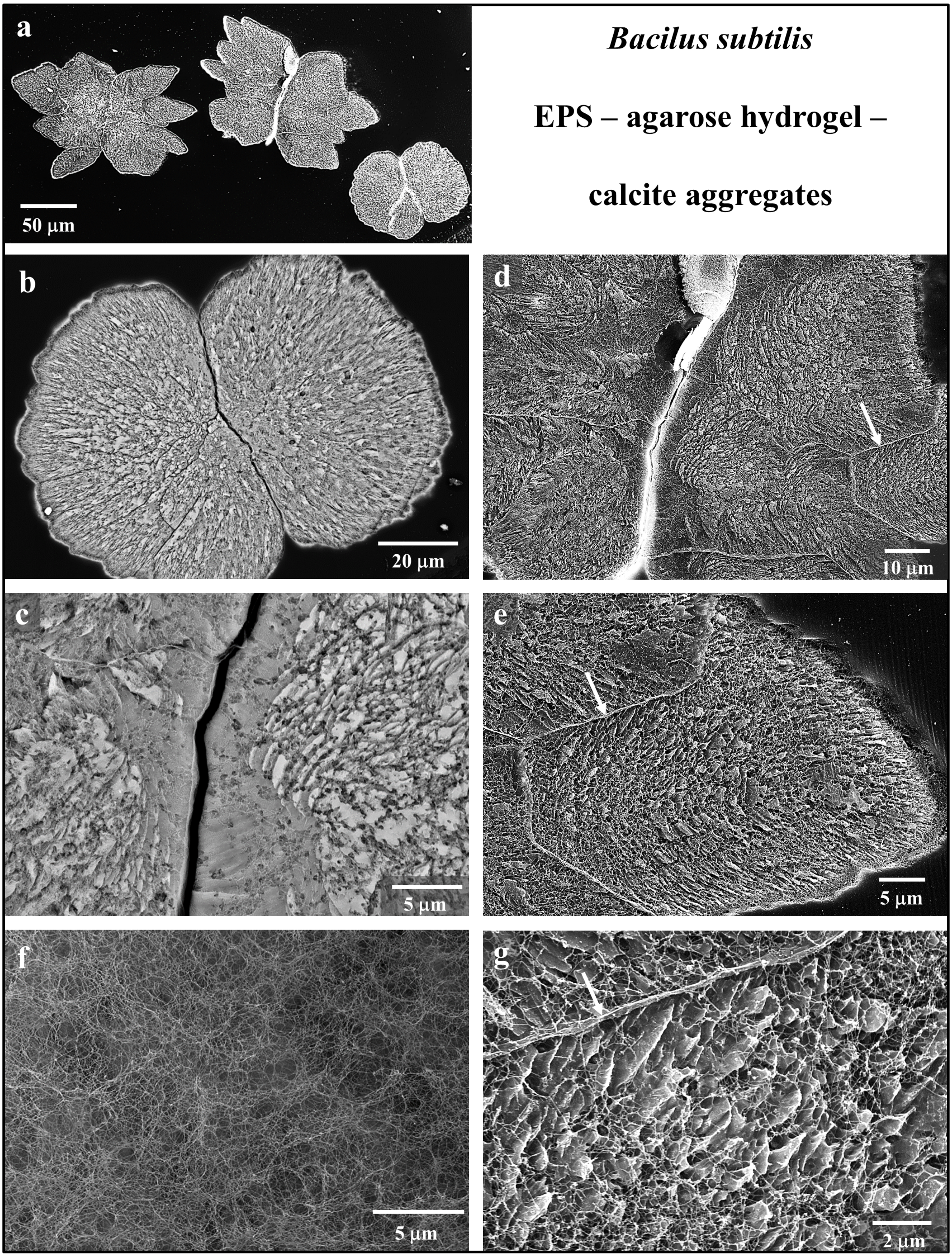

Figure 2.6-S18. FE-SEM images depicting aggregate morphology, the distribution pattern of occluded EPS-agarose polymers and interlinkage of calcite, and the EPS - agarose network within the composite aggregate containing *B. subtilis* EPS. White arrows point to the presence of membranes within the composites.

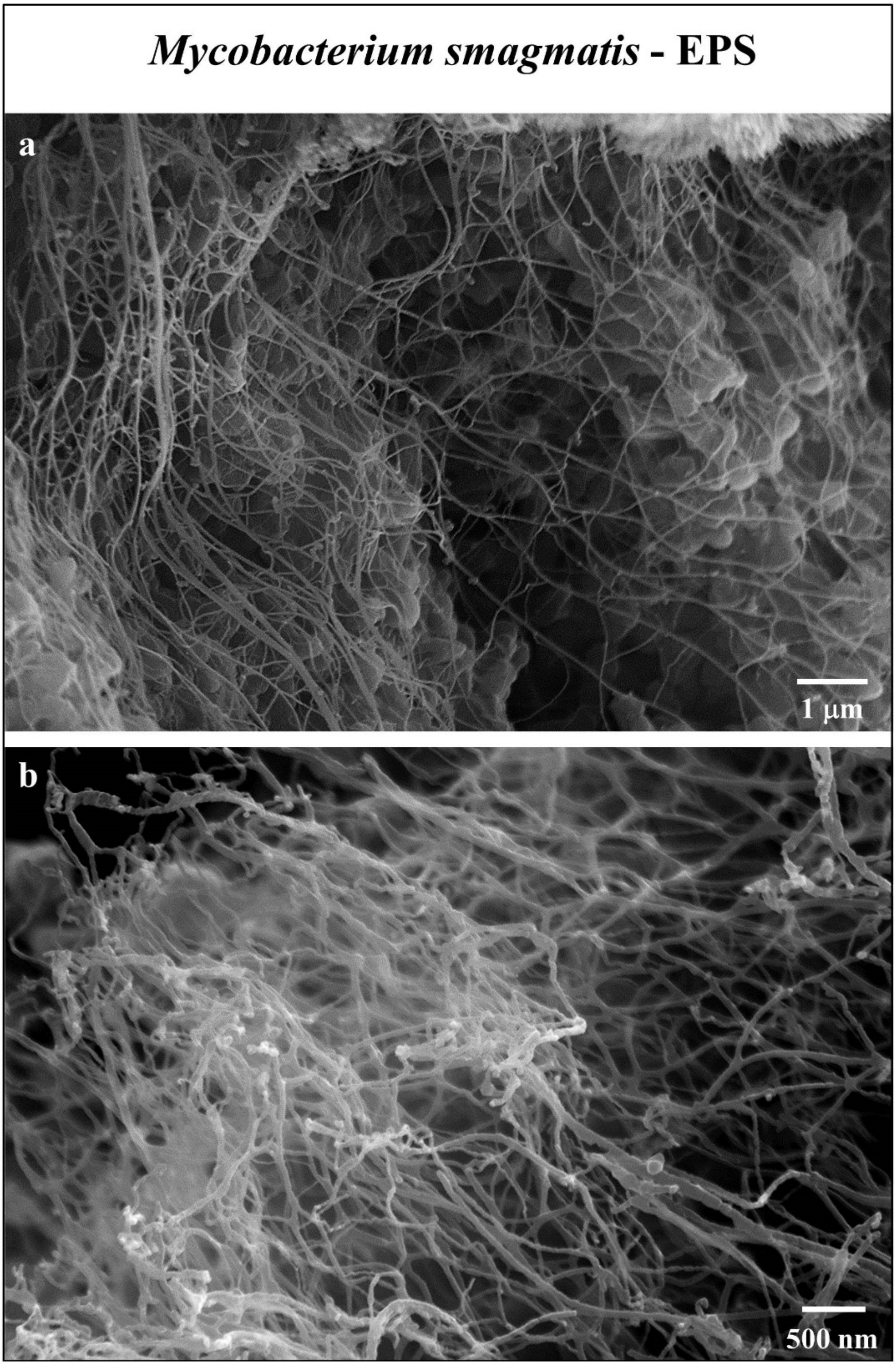

Figure 2.6-S19. FE-SEM images depicting *M. smagmatis* EPS fabrics.

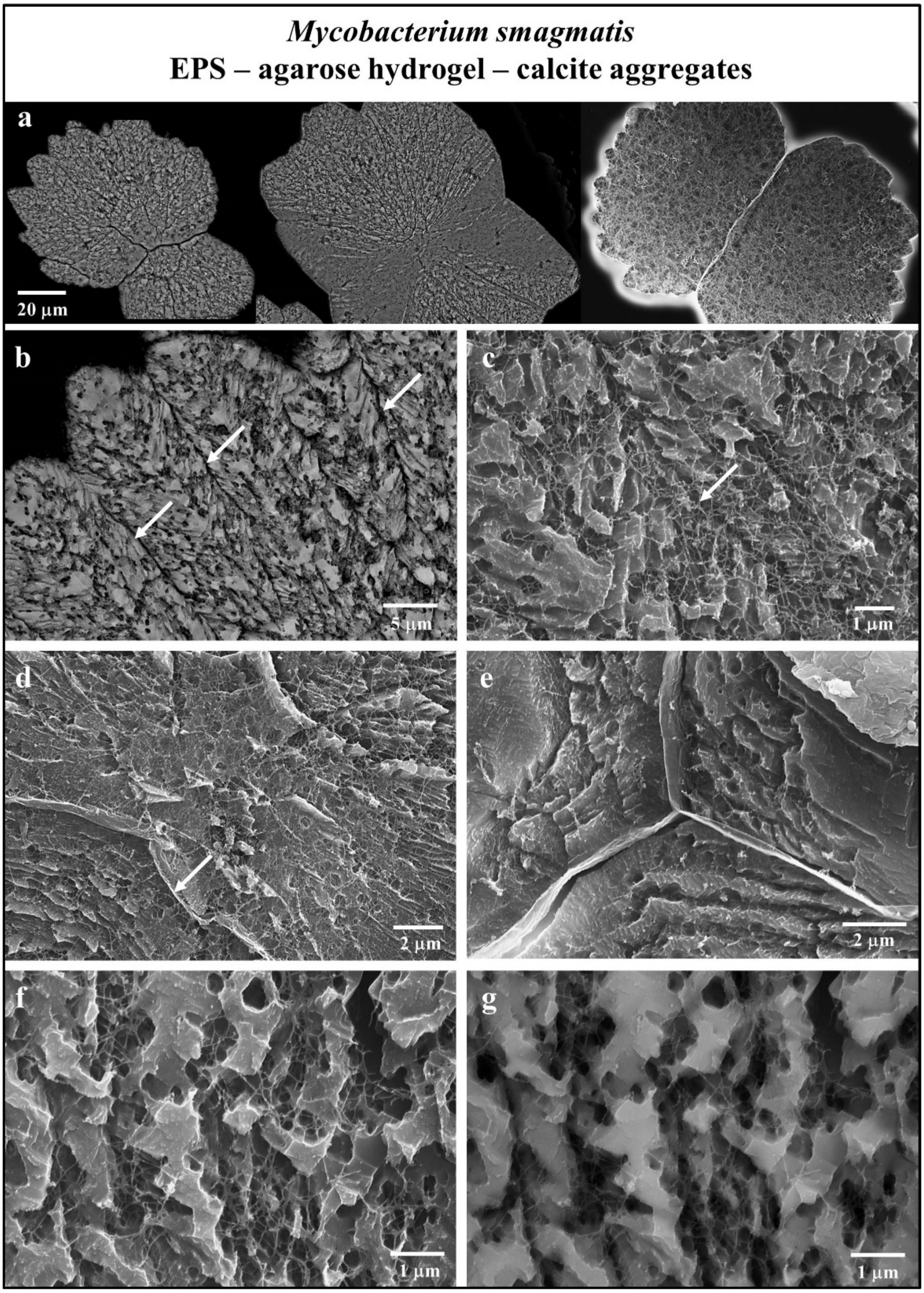

Figure 2.6-S20. FE-SEM images depicting aggregate morphology, the distribution pattern of occluded EPS-agarose polymers and interlinkage of calcite, and the EPS - agarose network within the composite aggregate containing *M. smagmatis* EPS. White arrows in (d) and (e) point to the presence of membranes, however, these are rarely developed and short-ranged in these composites. For the majority of the composite, we did not find membranes between the subunits (white arrows in panel b and c).

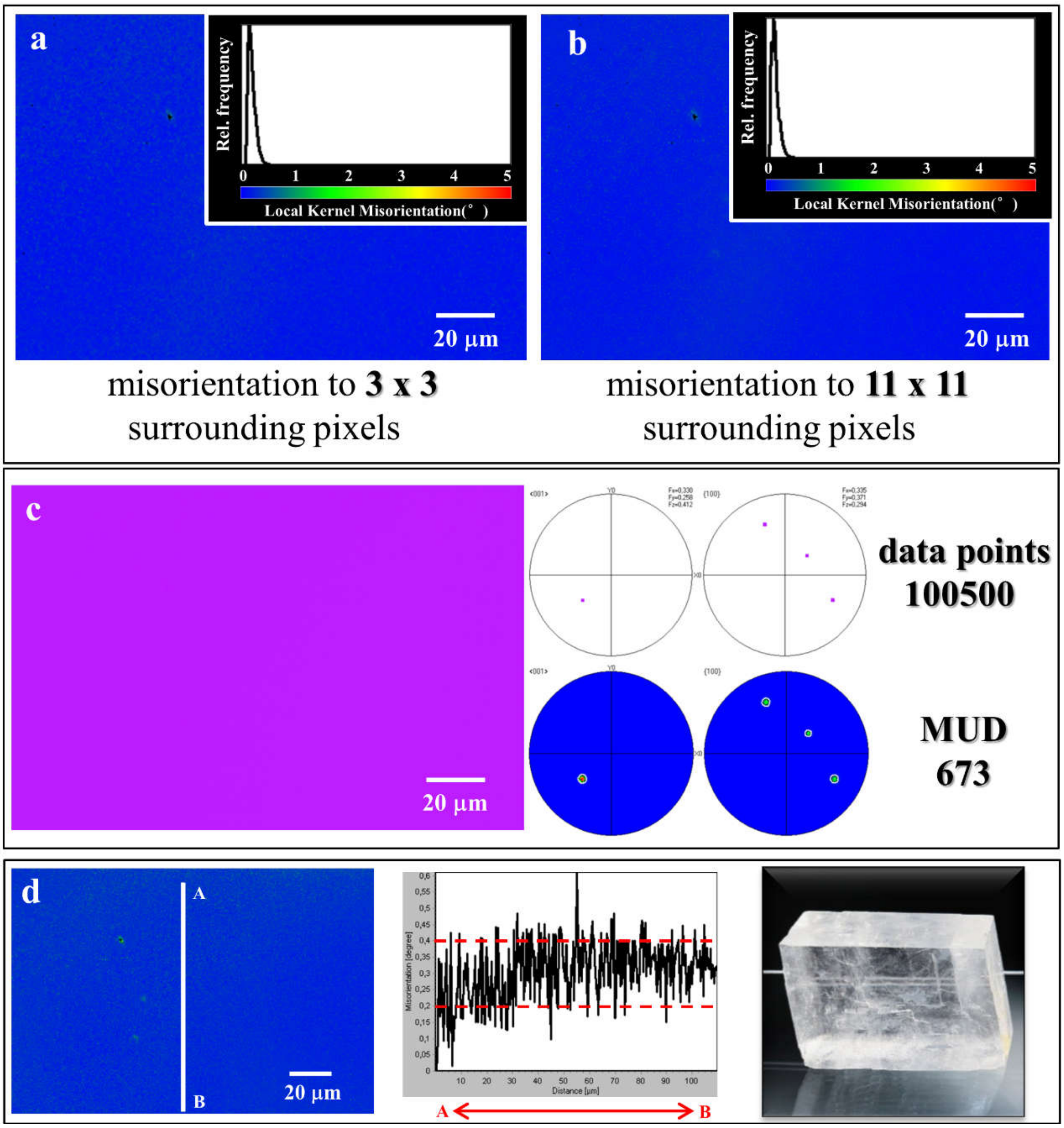

Figure 2.6-S21. EBSD data of a calcite single crystal obtained from solution and devoid of agarose hydrogel as well as bacterial EPS (see also reference 28 and 32). (a, b) EBSD measurements expressed as local kernel misorientation with 3 *times* 3 and 11 *times* 11 filters. (c) Diffraction measurements depicted color-coded in an orientation map and corresponding pole figures given as individual data points as well as density distributions. The MUD value, derived from the density distribution of orientation data is an indication for the strength of crystallite co-orientation. (d) Point to origin misorientation along a profile A to B in the EBSD map and the corresponding misorientation versus distance diagram. The reference calcite single crystal is shown in the left panel.

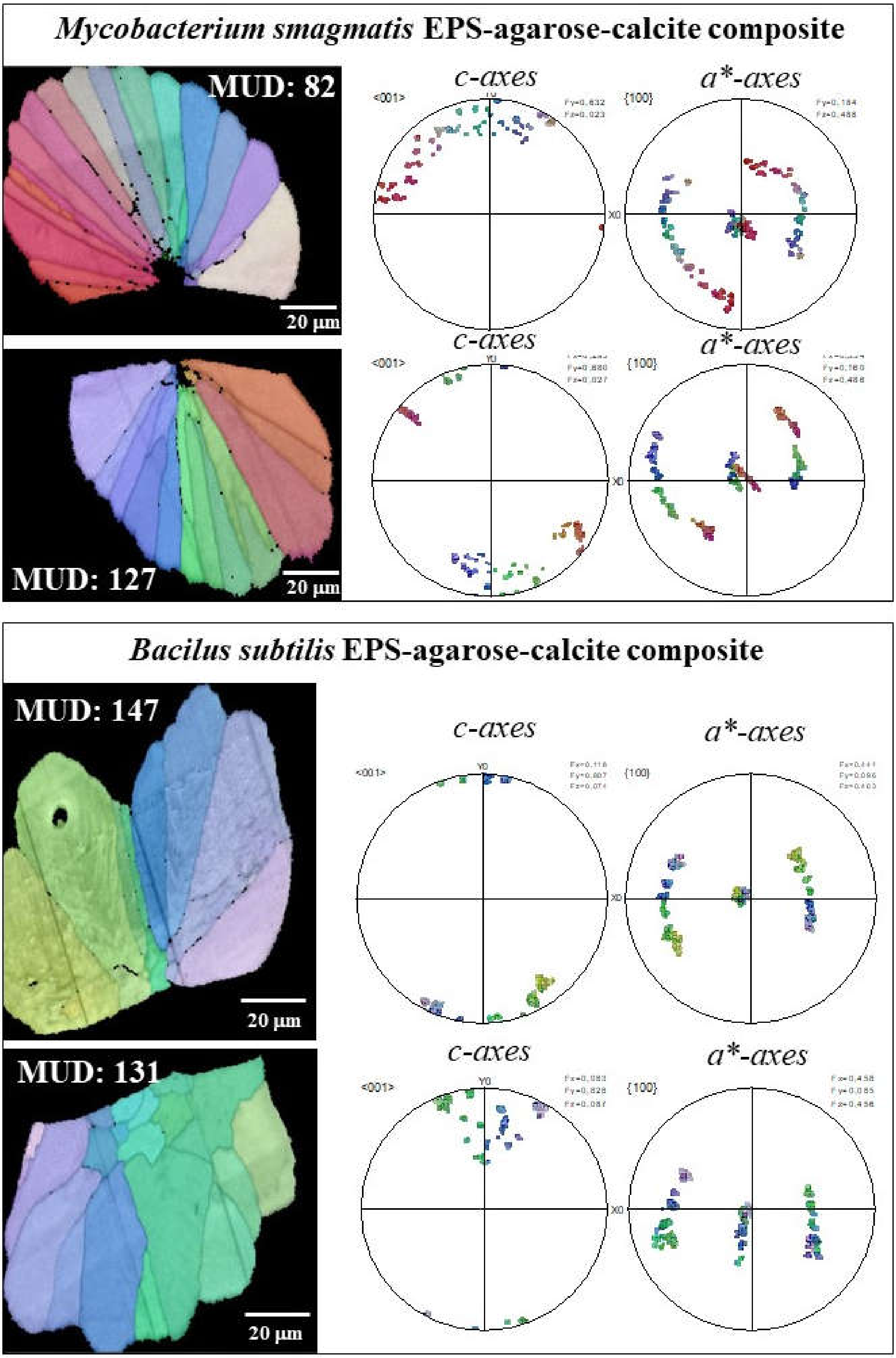

Figure 2.6-S22. EBSD maps carried out on *M. smagmatis* and *B. subtilis* composite aggregates, visualizing calcite arrangement in (a) the two halves of the aggregates and within their subunits.

3 Conclusion and Perspectives

3.1 Concluding Summary

Biomineralization products are hybrid (inorganic/organic) composites. They based on only very few minerals, but they show a huge biodiversity of mineral morphologies and microstructures, which are quite different from their inorganic counterpart, for which morphological variations are very limited. The limited assortment of the inorganic mineral is given by the diversity of variations of the physicochemical conditions under which crystal growth or dissolution processes occur without the action of life forms.

The morphological biodiversity of the biomineral, however, derives from the variety of organisms and how they control the biomineral formation process. This control process is reflected not only in external morphology – which is generally controlled by biological membranes such as cell walls or extracellular matrix structures, but also by organic matter embedded inside the biomineral. For the actual growth mechanism, a process of nanoparticle accretion is strongly advocated by some authors (e.g., Rousseau *et al.* 2005; Sethmann *et al.* 2005, 2006; Cölfen & Antonietti 2008; Gebauer *et al.* 2008; Goetz *et al.* 2011; Weiner & Addadi 2011; Gal *et al.* 2013; De Yoreo *et al.* 2015; Rodríguez-Navarro *et al.* 2016) and echoed by the community.

The present dissertation seeks to get insight into processes of calcite biomineralization by structural studies of two examples of biological calcite and examples of experimentally produced "biomimetic" calcite crystals grown in organic hydrogels. The main part of the thesis is the study of the ultrastructural relation between the formed calcite crystal and the cell organelles that are in contact with the intracellular vesicle in which the calcite forms. The biomimetic experiments employed hydrogels and hydrogels doped with bacterial EPS as an organic matrix for mimicking the organic environment of the biological crystal growth to some extent.

Section 2.1 summarizes the investigation of an exemplary biomineralization product, which is intracellularly formed by the coccolithophore species *Emiliania huxleyi*. The crystallographic microstructure of *E. huxleyi* coccolith R-units has dislocation-induced minor planar imperfections. The mosaic blocks are separated by small-angle boundaries where only minor misorientations (< 0.3°) occur. The EDS analysis confirmed that there are no occluded intracrystalline biopolymers. Further cell ultrastructural analysis reveals a narrow, well-controlled 4 nm narrow gap that extends laterally over a large distance between the membrane of the coccolith vesicle and the outer membrane of the nuclear envelope. This narrow association is considered to be a new inter-organelle junction, the "nuclear envelope junction". The observation of the new inter-organelle junction proposed a new pathway for intracellular calcium transport from the large nuclear envelope- endoplasmic reticulum (ER) calcium store of the cell, further through the membranes of the junction, finally into the lumen of the coccolith vesicle, as the nuclear envelope is confluent with the ER. The microstructure data, as well as the cytological results, indicate that the calcite formation in *E. huxleyi* coccoliths follows a classical ion-by-ion growth mechanism rather than by nanoparticle accretion as the current general paradigms of biomineralization advocate.

Section 2.2 explores another biomineralization example, foraminifera. In the three examined benthic rotaliid foraminifera species (*Amphistegina lobifera*, *Amphistegina lessonii* and *Ammonia tepida*), our EBSD results show that the skeletal elements of the foraminiferal tests are formed of mesocrystals, which have highly irregular dendritic-fractal morphologies and interdigitate strongly. Those mesocrystals are characterized by a mosaic of subcrystallites that have a size of 4–5 μm and are misoriented relative to each other by several degrees. Those mesocrystals can be grouped into two types: large (several tens μm) and frequently twinned crystals (internal mosaic-misorientation spread around 5–6°) and small ($\sim$10–20 μm) usually untwinned crystals (internal mosaic-misorientation spread up to 3°). The twinning of large mesocrystals mainly follows the $\{001\}$ twinning pattern, and results in a marked peak at 60° in the grain boundary and misorientation angle statistics for this specific microstructure. However, a further unknown twin type is also observed which has systematic misorientation of 78°. The twinned large mesocrystals occur at the outer test wall portions, however, the untwinned small mesocrystals are deposited at innermost test margins and seam the perforations of the test. Therefore, we identify the small untwinned mesocrystals with the inner calcitic layer, forming between the inner organic lamellipodial lining and the primary organic sheet, and the large and usually twinned dendritic mesocrystals with the outer calcitic layer that forming between the primary organic sheet and the outer organic lamellipodial lining. Dendritic morphologies of biocalcite crystals were already observed, for instance in modern terebratulid brachiopods or pterioid bivalve shells (Goetz *et al.* 2011; Checa *et al.* 2016; Harper & Checa 2017). However, the conjunction of twinning and development of dendritic calcite crystal morphologies is so far only observed for benthic foraminiferal calcite. The formation of the dendritic-fractal mesocrystals must be related to calcite crystal growth in the presence of obstacles such as organic matrix molecules of the lamellipodial all structures binding more strongly to the calcite than in other carbonate-shell forming organisms.

Hydrogels have emerged as a popular biomimetic platform for modelling and understanding the process of biomineralization, as their three-dimensional fibrous, porous, and hydrated gel networks are analogous to organic matrices of the biologically formed minerals. These matrices provide both the structural framework upon which minerals can grow and the chemical functionalities to control/induce phase selection, morphology and texture of the minerals. Nindiyasari *et al.* (2014a,b, 2015, 2019) studied the impact of different hydrogel (gelatin, agarose or silica) systems on calcium carbonate crystal growth. Greiner *et al.* (2018) explored the agarose gel system with varied solid contents and/or reactant solution concentrations. Based on these previous studies of the group, in section 2.4, a discussion is given on the influence of hybrid gelatin-agarose hydrogel on calcium carbonate crystallization with and without magnesium in the growth medium by using double diffusion system. Calcite aggregates that formed in Mg-free hybrid gels have blocky, elongated rhombohedral morphologies. An increase of agarose in the gel mixture does not affect much the size of the calcite precipitates but homogenized the pattern of gel occlusion within the aggregates. The aggregate is almost a single crystal that consists of mainly one large mineral unit and has a stronger crystal co-orientation strength compared to the reference aggregate grown in the hybrid gel that contained 1 wt% agarose and 1 wt% gelatin. On the other hand, the enhancement of gelatin content reduces the size of the aggregates, localizes the gel occlusion, and leads to the formation of membranes within the aggregates. The aggregate develops more subunits and has a weaker crystal co-orientation strength relative to that of the control set. The addition of Mg into the hydrogel mixture brought remarkable changes to all investigated cases. Spherical aggregates were obtained in all three experimental sets, increasing the concentration of either agarose or gelatin both reduced the aggregates sizes and induced the formation of various subunits with different crystallographic orientation. The enrichment of agarose resulted in an archetypical spherulite that has numerous differently sized subunits. However, in the case of more gelatin addition, the multitudinous subunits have a structured distribution according to their size, as the size steadily increases from the centre towards the rim of the composite. Compared to the reference set, the addition of agarose or gelatin both decreases the crystal co-orientation.

Although hydrogels provide adequate model systems as organic matrices in biomimetic experiments, the commercially available gel-forming substances are biologic substances that have been denaturalized during the production process and lack attributes of native biopolymers. The incorporation of bacterial extracellular polymeric substance (EPS) into the growth gels was intended to compensate for the synthetic deficiency of the artificial hydrogels. The Gram-negative bacterium *Pseudomonas putida* EPS was used in the pilot experiment (section 2.5). The Gram-positive bacteria *Bacillus subtilis* and the two bacteria belonging to the *Mycobacterium* genus, *Mycobacterium phley* and *Mycobacterium smagmatis* EPS were used in further experiments (section 2.6).

The addition of a small amount of bacterial EPS tremendously changed the morphology of aggregates, modes of polymer occlusion, texture and microstructure of the calcite crystal aggregates in a species-specific manner. The calcite aggregate sizes are reduced in all four cases with bacterial EPS, compared to the reference crystal grown in the pure 0.5 wt% agarose gel without EPS. The composite crystals that formed with *M. phley* EPS have a blocky morphology and consist of a small number of slightly misoriented, rhombohedron-shaped subunits. The aggregate is well co-aligned in all three dimensions like a single crystal. The occluded polymers are present as membranes. In the case of *M. smagmatis* and *B. subtilis*, the aggregates both have sheaf like morphologies which are composed of two spherulitic units that each occupies approximately half of the space of the aggregate ("half-spherulites"). The occluded polymers are mainly developed as networks of fibrils, and the distribution pattern of the organic matrixed is structured in both cases: two centrosymmetric quadrants of the aggregate subunits pervasively incorporate the EPS/hydrogel mixture, whilst the other two quadrants have very little polymer integration according to the EBSD local kernel misorientation analysis. For *P. putida*, aggregates are spherical polycrystalline solids that consist of numerous irregular-shaped, different-sized, highly-misoriented subunits. The polymer distribution is inhomogeneous and mainly present as membranes. On nanometre scale level, the pattern and strength of calcite crystal co-orientation are similar for all aggregates, however, on sub-micrometre and micrometre-scale levels the co-orientation pattern and strength are distinct from one specific bacterial to another. The observed microstructure and texture characteristics are discernible individual biosignatures that can potentially be developed to an identification tool for the recognition of bacterially mediated calcification.

As mentioned in section 2.3, calcium carbonate biominerals are hierarchical structured materials that comprise of both biopolymers and minerals and extend over several scale levels (Fratzl & Weinkamer 2007; Bar-On & Wagner 2013; Dunlop & Fratzl 2013). In the case of gastropod, bivalve and brachiopod shells, the compliant organic component is an insoluble silk-like protein which forms the basic matrix structures-like membranes, and provide a scaffolded environment where the carbonate crystal entities such as platelets, prisms and fibres can nucleate, orient, and grow (Blank *et al.* 2003; Marin & Luquet 2004; Marin *et al.* 2008; Gries *et al.* 2011). These membranes are often a few nanometres thick and porous, since they have to facilitate the carbonate mineral transportation and crystallographic orientation information from one mineral compartment to the other (Marin & Luquet 2004; Marin *et al.* 2008). Within the compartment unit, a biopolymer network of fibrils can be distinguished, which infiltrate the space between the nanoparticles of a compartment unit and cause misorientation between the nanoparticles (Griesshaber *et al.* 2013; Nindiyasari *et al.* 2015; Casella *et al.* 2017). Cartwright & Checa (2007) proposed a self-organization formation mechanism of the organic matrix through the self-assembly of a liquid-crystalline core that consisting of chitin fibres in nacre of bivalve and gastropod shells, which yields a chitin fibre-polymer composite which regulates the morphology of nacre tables during their growth.

The hydrogel crystal growth experiments were able to produce hybrid composites and thus they mimic biogenic matrix environments to a certain extent, due to their ability to provide confined space like the natural organic matrix and they control the diffusion rates, local concentrations and supersaturation of solutes. Crystal growth by nanoparticle accretion is unlikely to occur in such gel-like matrices, as they are too viscous and inhibiting any particle transport by the network structure, nevertheless a “nanoparticulate” structure of the growing crystal surfaces is visible (Figs. 2.3-8 and 2.4-2). This is a strong indication that the frequently observed 50–100 nm scale “nanoparticulate structure” of biomineral carbonates is a result of an ion-by-ion crystal growth process in the presence of organic matrix rather than the result of a particle assembly process. This conjecture is supported by the fact that the EBSD results show that the crystal structure is coherent over distances much larger than those “nanoparticles”, and the 50–100 nm “nanoparticles” which are supposed to form before they assemble have not been convincingly observed so far, which means they either do not exist or they successfully managed to evade detection. Crystal growth rate (which is related to the supersaturation) and gel strength are the two parameters that influence the amount of gel incorporated into the crystal (Li & Estroff 2007, 2009; Asenath-Smith *et al.* 2012). For physical gels such as agarose and gelatin used in the present work, the gel strength is directly related to their solid content (Asenath-Smith *et al.* 2012; Nindiyasari *et al.* 2015; Greiner *et al.* 2018). Fast crystal growth rate and strong gel strength result in the entire gel network to be incorporated within the crystal without any critical damage of the hydrogel network, while low gel strengths and low growth rates facilitate the formation of practically gel-free crystals (Asenath-Smith *et al.* 2012; Nindiyasari *et al.* 2015; Greiner *et al.*

2018). During the crystal growth process, the hydrogel networks will be both occluded into the crystal and/or accumulated at the growth front depending on the growth rate and gel strength (Fig. 2.3-8). As long as the gel networks accumulation at the growth front is small and contains pores, crystal growth can proceed homoepitaxially. However, when gel accumulation leads to a dense surface film, which significantly blocks the access of further ions from the solution, crystal growth under the film will stop. At the same time, in the type of experiment performed here, the diffusion from the reservoirs will continuously feed ions into the system and built up supersaturation. At a certain threshold, heterogeneous nucleation will occur on the outside of the accumulated gel film, such that a new crystal with a random crystallographic orientation with respect to the underlying crystal will start to grow. Therefore, the membrane-like gel accumulations found in the crystal aggregates can be randomly distributed, which, together with the occluded gel networks fibres, do not resemble those membrane structures that are present in carbonate biominerals, but they resemble the intra-crystalline organic matrix in the biominerals. Although the hydrogel systems do not actively control the mineralization process such as the organisms usually do, the features they provide in the current mimetic experiments could help to understand how the organisms forms the shape of the calcite biominerals that they produce.

3.2 Outlook

The carbonate biomineralization process is complex and still far from fully understood. Although the observations of biological calcium carbonate specimens and the mimetic crystallization experiments based on hydrogels have progressed to provide some answers to a very small part of the field as given in Chapter 2, many questions are still left open. New research perspectives could cover the following points:

Regarding the study of coccolithophores, the investigation/detection of phosphorus concentrations within the cell should be considered, as Sviben *et al.* (2016) reported a Ca-P-rich compartment in their coccolith calcium transportation pathway. Further single cell analysis can be conducted to identify nature and function(s) of the densely stained nanoparticles that form seams at the inner side of the membranes within the reticular body, within peripheral cisternae of the Golgi body, and Golgi vesicles as described in section 2.1. Besides, the methods established could be applied to other popular coccolithophores species i.e. *Florisphaera profunda*, genus *Umbilicosphaera*, and genus *Gephyrocapsa*.

It is very interesting to observe the dendritic-fractal twinned biocalcite in foraminifera. Further calculation is needed to solve the systematic misorientation of 78°, which points to another twin type that does not correspond to any known twin-laws of calcite for the moment. Besides, further projects could investigate the other group of foraminiferal tests, for example, the planktonic species or the imperforate/porcelaneous species. It will be interesting to know whether the twinning also exists in other species or not. As the EBSD technique is widely established by now, it is possible to develop crystal orientation measurements and analyses as a tool to distinguish between the different calcifying foraminiferal groups.

For the biomimetic calcite crystal growth experiments with agarose/gelatin hybrid hydrogels, gel strength is an important parameter to influence the gel incorporation into the calcite crystals as discussed in section 1.3.3, measurements and quantification of the gel strength will bring a better explanation of the observed results. The occlusion of the gel network and the addition of Magnesium can both bring local misorientation to the crystals. STEM investigation combined with EDX on the continuous thin sections of the Mg containing aggregates may visualize the Mg and gel network distribution three-dimensionally, which may help to differentiate the contributions between Mg and gel network and help to understand the Mg cooperation mode within the calcium carbonate (calcite) growth when organic matrices exist. Besides, statistical evaluations (e.g., misorientation angle distribution analysis) of EBSD measurements of the Mg containing crystals could be considered to understand the Mg influence in the artificial hydrogel biomimetic experiments.

Regarding the calcite crystal biomimetic experiments with bacterial EPS doped hydrogels, the exact chemical composition of the EPS is still unclear. Further chemical characterization to determine the biomolecular compositions of the bacterial EPS should be carried out (e.g., high-performance liquid chromatography analysis, Wang *et al.* 2013). The experiments conducted so far containing agarose as a supporting material help to jellify the gel matrix. To better understand the influences of pure bacterial EPS on the calcite mineralization, it is important to try new experimental protocols and/or setups to minimize or even exclude the addition of agarose. The EPS during the extraction procedures are differentiated as soluble EPS, loosely bound EPS, and tightly bound EPS. However, those three EPSs had to be combined as “a total EPS” due to the limitation of extracted materials in our pilot experiments. Further experiments could be designed to conduct crystal growth with each of those three EPS and explore the difference. The current bacterial extraction protocol avoids the metabolism contribution of the bacterial species or intracellular components to the calcite crystal growth. However, both of them are interesting aspects that needed to be investigated further. The nature of bacterial EPS was greatly affected by the nutritional and physical conditions in which the biofilm was generated (Stoodley *et al.* 1999; Flemming *et al.* 2016b). It will be interesting to explore the influence of different nutritional (e.g., bacterial growing culture) to the extracted EPS and the further crystal growth experiments, and also to involve the bacterial intracellular components or bacterial metabolism into the further experiments. The mimetic experiments up to now are only partially able to reproduce some of the natural carbonate composite materials. To fully achieve and reproduce the hierarchical structure of biological calcite, more aspects, such as orientational order like in cholesteric liquid phases, e.g., chitin, need to be considered in further research projects. Further features should be designed and integrated into the current system, e.g., to introduce a self-assembly feature in the artificial matrix, in which the crystals are grown.

A Investigated Samples

A.1 Biological Calcium Carbonate Samples

As mentioned in previous chapters, biomineralization is an extremely widespread phenomenon that involves members from all taxonomic kingdoms (Lowenstam & Weiner 1989; Cuif *et al.* 2018). The biological samples, which have been involved in this study, are summarized as follows (Table A.1-1). Most of them belong to the species in the kingdom Animalia: shells formed by mollusks and brachiopods. Nevertheless, the taxonomic position of coralline algae, coccolithophores, and foraminifera and are still in a state of flux. The table here is mainly following the online taxonomic database *Catalogue of Life* (Roskov *et al.* Date Accessed: 14.05.2020), which attempts to list every documented species.

Table A.1-1. Summary of the species included in this work

Kingdom	Phylum	Class	Order	Species
Chromista	Haptophyta	Coccolithophyceae	Isochrysidales	*Emiliania huxleyi*
	Foraminifera	Globothalamea	Rotaliida	*Amphistegina lobifera*
			Rotaliida	*Amphistegina lessonii*
			Rotaliida	*Ammonia tepida*
Animalia	Mollusca	Gastropod	Lepetellida	*Haliotis asinina*
			Lepetellida	*Haliotis laevigata*
		Bivalvia	Mytilida	*Mytilus edulis*
			Pectinida	*Propeamussium jeffreysii*
			Venerida	*Arctica islandica*
			Unionida	*Cristaria plicatus*
			Unionida	*Elliptio crassidens*
		Cephalopoda	Octopoda	*Argonauta argo*
	Brachiopod	Rhynchonellata	Terebratulida	*Magellania venosa*
			Terebratulida	*Gryphus vitreus*

A.2 Biomimetic Calcium Carbonate Samples

The biomimetic experiment on calcium carbonate crystal growth by using hydrogel single/double diffusion systems is a big and comprehensive project in our research group. It involves several doctoral/master students whose studies focus on different subtopics in the past a few years. The table A.2-2 here below listed all related subprojects.

Table A.2-2. Summary of the hydrogel-calcite growing experiments in our research group

Authors	Reactant Solutions	Hydrogels	Gel Length	Temp.	Mg/ Sr	Publication
Nindiyasari	$CaCl_2$ 0.5M + Na_2CO_3 0.5M	Gelatin 2.5 wt%	70 mm	15°C	/	*Cryst. Growth Des. 2014a*
	$CaCl_2$ 0.5M + Na_2CO_3 0.5M	Gelatin 5 wt%	70 mm	15°C	/	
	$CaCl_2$ 0.5M + Na_2CO_3 0.5M	Gelatin 10 wt%	70 mm	15°C	/	
	$CaCl_2$ 0.5M + Na_2CO_3 0.5M	Gelatin 2.5 wt%	70 mm	15°C	0.01M	*Cryst. Growth Des. 2014b*
	$CaCl_2$ 0.5M + Na_2CO_3 0.5M	Gelatin 10 wt%	70 mm	15°C	0.01M	
	$CaCl_2$ 0.5M + Na_2CO_3 0.5M	Gelatin 10 wt%	120 mm	15°C	/	*Cryst. Growth Des. 2015*
	$CaCl_2$ 0.5M + Na_2CO_3 0.5M	Gelatin 10 wt%	120 mm	15°C	0.1M	
	$CaCl_2$ 0.5M + Na_2CO_3 0.5M	Agarose 1 wt%	120 mm	15°C	/	
	$CaCl_2$ 0.5M + Na_2CO_3 0.5M	Agarose 1 wt%	120 mm	15°C	0.1M	
	$CaCl_2$ 0.5M + Na_2CO_3 0.5M	Silica	120 mm	15°C	/	
	$CaCl_2$ 0.5M + Na_2CO_3 0.5M	Silica	120 mm	15°C	0.1M	
	$CaCl_2$ 0.5M + Na_2CO_3 0.5M	Gelatin 10 wt%	120 mm	15°C	0.01M	*Eur. J. Mineral. 2019*
	$CaCl_2$ 0.5M + Na_2CO_3 0.5M	Agarose 1 wt%	120 mm	15°C	0.01M	
	$CaCl_2$ 0.5M + Na_2CO_3 0.5M	Silica	120 mm	15°C	0.01M	
Greiner	$CaCl_2$ 0.5M + Na_2CO_3 0.5M	Agra 0.5 wt%	120 mm	7°C	/	*Cryst. Growth Des. 2018*
	$CaCl_2$ 0.1M + Na_2CO_3 0.1M	Agra 0.5 wt%	120 mm	7°C	/	
	$CaCl_2$ 0.5M + Na_2CO_3 0.5M	Agra 2 wt%	120 mm	7°C	/	
	$CaCl_2$ 0.1M + Na_2CO_3 0.1M	Agra 2 wt%	120 mm	7°C	/	
Yin	$CaCl_2$ 0.5M + Na_2CO_3 0.5M	Agarose 1 wt% + Gelatin 1 wt%	70 mm	15°C	/	*Cryst. Growth Des. 2019*
	$CaCl_2$ 0.5M + Na_2CO_3 0.5M	Agarose 1 wt% + Gelatin 1 wt%	70 mm	15°C	0.01M	
	$CaCl_2$ 0.5M + Na_2CO_3 0.5M	Agarose 1 wt% + Gelatin 2 wt%	70 mm	15°C	/	
	$CaCl_2$ 0.5M + Na_2CO_3 0.5M	Agarose 1 wt% + Gelatin 2 wt%	70 mm	15°C	0.01M	
	$CaCl_2$ 0.5M + Na_2CO_3 0.5M	Agarose 2 wt% + Gelatin 1 wt%	70 mm	15°C	/	
	$CaCl_2$ 0.5M + Na_2CO_3 0.5M	Agarose 2 wt% + Gelatin 1 wt%	70 mm	15°C	0.01M	
Yin & Weitzel	$CaCl_2$ 0.1M + Na_2CO_3 0.1M	Agarose 0.5 wt%	15 mm	13°C	/	*Cryst. Growth Des. 2020a*
	$CaCl_2$ 0.1M + Na_2CO_3 0.1M	Agarose 0.5 wt% + EPS A	15 mm	13°C	/	
	$CaCl_2$ 0.1M + Na_2CO_3 0.1M	Agarose 0.5 wt% + EPS B	15 mm	13°C	/	*Cryst. Growth Des. 2020b*
	$CaCl_2$ 0.1M + Na_2CO_3 0.1M	Agarose 0.5 wt% + EPS C	15 mm	13°C	/	
	$CaCl_2$ 0.1M + Na_2CO_3 0.1M	Agarose 0.5 wt% + EPS D	15 mm	13°C	/	
Rudin & Thümmler	$CaCl_2$ 0.5M + Na_2CO_3 0.5M	Agar 0.5 wt%	120 mm	7°C	0.01M	Master thesis 2018/2019
	$CaCl_2$ 0.5M + Na_2CO_3 0.5M	Agar 0.5 wt%	120 mm	7°C	0.1M	
	$CaCl_2$ 0.5M + Na_2CO_3 0.5M	Agra 2 wt%	120 mm	7°C	0.01M	
	$CaCl_2$ 0.5M + Na_2CO_3 0.5M	Agra 2 wt%	120 mm	7°C	0.1M	
	$CaCl_2$ 0.1M + Na_2CO_3 0.1M	Agar 0.5 wt%	120 mm	7°C	0.01M	
	$CaCl_2$ 0.1M + Na_2CO_3 0.1M	Agar 0.5 wt%	120 mm	7°C	0.1M	
	$CaCl_2$ 0.1M + Na_2CO_3 0.1M	Agra 2 wt%	120 mm	7°C	0.01M	
	$CaCl_2$ 0.1M + Na_2CO_3 0.1M	Agra 2 wt%	120 mm	7°C	0.1M	
Rudin & Thümmler	$CaCl_2$ 0.5M + Na_2CO_3 0.5M	Agar 0.5 wt%	120 mm	7°C	0.01M	Master thesis 2018/2019
	$CaCl_2$ 0.5M + Na_2CO_3 0.5M	Agar 0.5 wt%	120 mm	7°C	0.1M	
	$CaCl_2$ 0.5M + Na_2CO_3 0.5M	Agra 2 wt%	120 mm	7°C	0.01M	
	$CaCl_2$ 0.5M + Na_2CO_3 0.5M	Agra 2 wt%	120 mm	7°C	0.1M	
	$CaCl_2$ 0.1M + Na_2CO_3 0.1M	Agar 0.5 wt%	120 mm	7°C	0.01M	
	$CaCl_2$ 0.1M + Na_2CO_3 0.1M	Agar 0.5 wt%	120 mm	7°C	0.1M	
	$CaCl_2$ 0.1M + Na_2CO_3 0.1M	Agra 2 wt%	120 mm	7°C	0.01M	
	$CaCl_2$ 0.1M + Na_2CO_3 0.1M	Agra 2 wt%	120 mm	7°C	0.1M	

Notes:

- EPS A, self-produced extracellular polymeric substances (EPS) of *Pseudomonas putida*; EPS B–D, EPS of *Bacillus subtilis*, *Mycobacterium phley*, and *Mycobacterium smegmatis*
- Shaded table cell in "Reaction solution" column: lower concentration of reaction solutions
- Shaded table cell in "Gel length" column: single diffusion experimental set up
- Shaded table cell in "Mg/Sr" column: experiments containing strontium in growth medium

B Applied Methods

B.1 X-ray Powder Diffraction

The polycrystalline or ‘powder’ X-ray diffraction technique is a scientific technique for material characterization. Max von Laue carried out his famous X-ray diffraction experiments in 1912. Afterwards, the Braggs who provided the beautifully simple expression (the Bragg’s Law, for crystal structure analysis, Eq. B.1-1) founded the field of X-ray crystallography. In 1915, Debye and Scherrer investigated polycrystalline specimens and took the first X-ray powder photographs of lithium fluoride at the University of Göttingen.

$$n\lambda = 2d_{hkl}sin\theta \qquad \text{B.1-1}$$

The intensity (I_{hkl}) of X-ray diffraction peaks related to a lattice plane hkl is given by the square of the structure factor F_{hkl}

$$I_{hkl} = P \cdot F_{hkl} \cdot F^{*}_{hkl} \qquad \text{B.1-2}$$

where P compose of a number of geometrical factors that depend on the details of experiments.

$$F_{hkl} = \langle \sum_{j} f_j e^{2\pi i \vec{H}\vec{x_j}} \rangle \qquad \text{B.1-3}$$

where the sum is over all atoms in the unit cell, f_j is the scattering power of atom j (Fourier transform of electron density distribution of atom j), $\vec{H}$ is the scattering vector (hkl), $\vec{x_j}$ is the position of atom j, and $\langle\rangle$ denotes the average over time and space.

The degree of texture in the prepared sample is the most distinguishing feature between powder and single-crystal diffraction. Powder diffraction operates under the assumption that every possible crystalline orientation is randomly arranged in a powdered sample, the isotropic case. From a practical perspective, the sample is commonly rotated to eliminate the effects of texture.

The most widespread use of powder X-ray diffraction is to identify the unknown phase(s) of crystalline solid(s). Both peak positions (corresponding to the lattice spacings) and their relative intensity in a diffraction pattern are indicative of a particular phase, which serve as a ‘fingerprint’ or ‘genetic strand’ (Hammond 2015) for comparison with those of identified phases in crystallographic databases (e.g. Crystallography Open Database (COD); Inorganic Crystal Structure Database (ICSD); International Centre for Diffraction Data (ICDD)).

The other common applications of powder X-ray diffraction are:

- crystal (grain) size and internal elastic strain estimation
- preferred orientation (texture or fabric) analysis
- crystal structure determination and refinement

In this work, X-ray powder diffractograms were recorded on a Debye-Scherrer geometry STOE diffractometer with Mo-Kα_1 radiation (λ = 0.7093 Å) at 50 kV and 30 mA. samples were sealed in ∅0.3 mm glass capillaries and were kept in rotation during the measurement. More details can be found in sections 2.4, 2.5, and 2.6.

B.2 Electron Microscopy

An electron microscope uses electrons for imaging which is analogous to the way that a light microscope uses visible light. Ruska and Knoll built the first transmission electron microscope (TEM) with two electromagnetic lenses in 1931 (Ruska 1987). This great invention brought Ruska the Nobel Prize 55 years later. The first application of a scanning electron microscope (SEM) happened afterwards in 1937, as von Ardenne added scanning coils to a TEM and acquired the first scanning image (von Ardenne 1938). Modern electron microscopes nowadays often integrate different methods/techniques that could provide specific information about the specimen, including morphology, topology, chemical composition, crystallographic orientation, etc. Diverse imaging and spectroscopic methods based on the variety of electron matter interactions are essential tools for the characterization. New insights into many materials properties are gained by the unprecedented up-to-date analytical techniques, and the advancement in electron op-tics enables the imaging and spectroscopy with atomic resolution (Muller 2009). In this section, I will describe the basics, and discuss the techniques that have been involved in the mentioned studies.

B.2.1 Fundamental of SEM, TEM, and STEM

A scanning electron microscope (SEM) permits the observation and characterization of the specimen surface (traditionally used for examining bulk materials) and near-surface structures on a nanometre to micrometre scale. A typical configuration of an SEM that including electrons

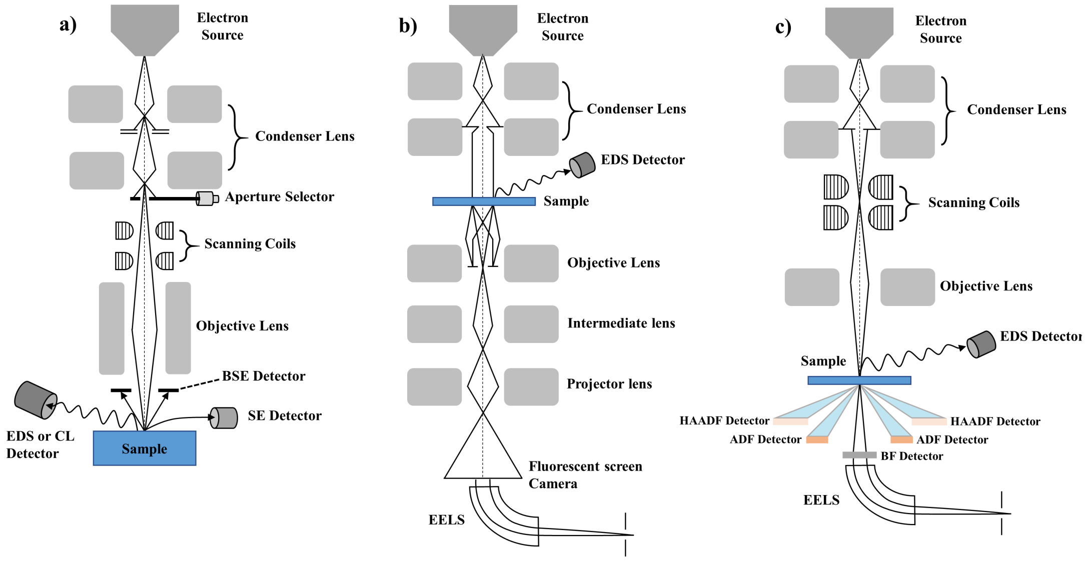

Figure B.2-1. Simplified schematic cross-sections of an (a) SEM, (b) TEM and (c) STEM instrument, from Bell & Erdman 2012 source, lenses, scanning coil, sample chamber, and detectors is shown in Figure B.2-1a. The area or the microvolume that needs to be investigated is irradiated with a finely focused electron beam by a raster scan, as the name of the microscope suggests. The instrument can collect (depending on the detector configuration) secondary, backscattered, and transmitted electron signals (if the specimen is sufficiently thin). Moreover, signals like X-ray emission (can be used for energy-dispersive X-ray spectroscopy, EDX analysis; and wavelength dispersive X-ray spectroscopy, WDX analysis), cathodoluminescence (CL), and electron backscatter diffraction (EBSD) can also be detected.

In a transmission electron microscope (TEM), an ultrathin section (typically < 150 nm thick) is irradiated by a beam of high-energy electrons (typically $\sim$100–300kV). A schematic sketch of a contemporary TEM is presented in Figure B.2-1b. A TEM allows the investigation of a thin specimen has a higher resolution than an SEM by a factor of 10 or more. Crystallographic information can be obtained in TEM by using selecting area mode; elemental characterization can be achieved by either energy-dispersive X-ray spectroscopy (EDS) or electron energy loss spectroscopy (EELS).

A scanning transmission electron microscope (STEM) is a combination of TEM and SEM, in which the beam is finely convergent and scans across the sample area (as SEM does), while the image is generated by the transmitted electrons (like in TEM). STEM can be applied to both SEM or TEM systems with proper affiliations devices and detectors, which enable the microscopes can be switched to “STEM mode”. High-angle annular dark field (HAADF), annular dark field (ADF) plus bright and dark field (BF/DF) signals can be collected through the corresponding detectors. HAADF signal contrast is indicative of the atomic number (also called Z-contrast). The addition of EDS and EELS spectrometers further enhances the microscope. The electron tomography technique allows the detailed 3D structures reconstruction of the specimen. A schematic of a typical STEM is shown in Figure B.2-1c.

As mentioned above, the interaction between the primary electron beam and the specimen can generate several different signals (Fig. B.2-2): secondary (SE) and backscatter electrons (BSE), transmitted electrons (if the specimen is sufficiently thin), Auger electrons, characteristic X-rays and photons. Depending upon the accelerating voltage and sample density, the signals come from different penetration depths.

Auger electrons come from the very thin layer of the sample surface. It is a useful tool to probe chemical and compositional surface environments, especially for conducting specimens. After Auger electrons, secondary electrons (SE) come from the next most shallow penetration depth and produce surface topography contrasts in a SEM image. Backscattered electrons (BSE) are those electrons that reflected after elastic interactions between the primary beam and the sample. The backscattered electrons are highly sensitive to the elements since heavy elements backscatter electrons more strongly than light elements. Therefore, the backscattered electrons produce the chemical composition contrast in a SEM image. Besides, backscattered electrons can also be used to determine the crystallographic orientation of the specimen through the electron backscatter diffraction (EBSD) measurements and analysis. During the primary beam bombardment, two types of X-rays could emit, the continuum X-rays (Bremsstrahlung) and the characteristic X-rays. Energy-dispersive X-ray spectroscopy (EDX) and wavelength dispersive X-ray spectroscopy (WDX) are both based on the detection of characteristic X-rays, which can map the distribution and estimate the abundance of elements that existing on the prepared sample surface. Cathodoluminescence is the phenomenon that some material emits visible light under the irradiation of an electron beam. It provides general information on the trace element distribution and mechanically induced defeats of the sample, which brings fundamental insights to understand the process as such growth, replacement, deformation, and provenance in minerals, especially informative for the geologists.

In present work, SEM, TEM and STEM are extensively involved in all research projects, the details results were discussed in Chapter 2.

B.2.2 Electron Backscatter Diffraction (EBSD) Analysis

Electron backscatter diffraction (EBSD) is an SEM-based technique, which provides crystallographic information about the microstructure of the specimen. The understanding of the crystallography of the material is essential to interpret the relationship between its internal structures and physical properties/material behaviour. Although the BSE image can offer crystallographic contrast in the micrograph as well (as backscattered electrons intensities are influenced by the grain orientations, e.g. Lloyd 1987), this contrast tells nothing about the crystallographic orientation of each grain within the image. EBSD enables this important quantitative information.

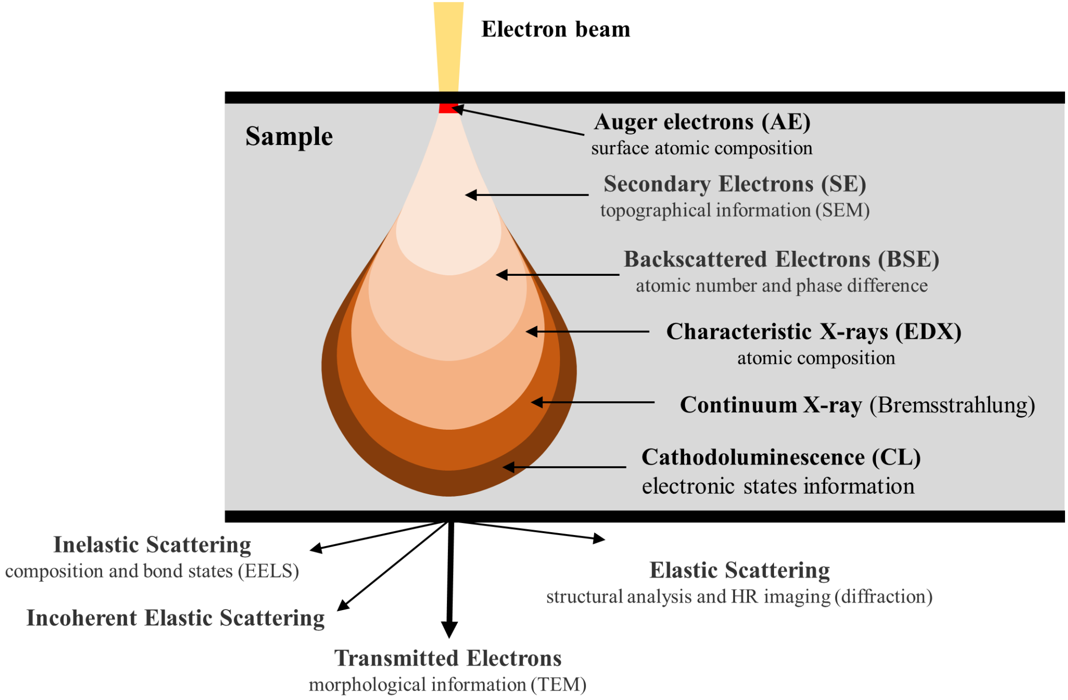

Figure B.2-2. Overview of the signals generated when an electron beam interacts with a (relatively) thin specimen. In the case of a thick specimen, there are no transmitted electrons and the signal gets absorbed within the material, from Nanakoudis (2019).

EBSD patterns are obtained by illuminating a highly tilted crystalline specimen with a stationary electron beam in the SEM. A typical EBSD pattern consists of a large number of parallel lines, Kikuchi lines (Nishikawa & Kikuchi 1928) as the example shown in Figure B.2-3a which can be interpreted as a gnomonic projection of the crystal lattice on the flat phosphor screen (Fig. B.2-3b). Each Kikuchi band can be indexed by the Miller indices of the diffracting crystal plane which forms it. The intersections of the Kikuchi bands correspond to zone axes and are related to specific crystallographic directions in the crystal.

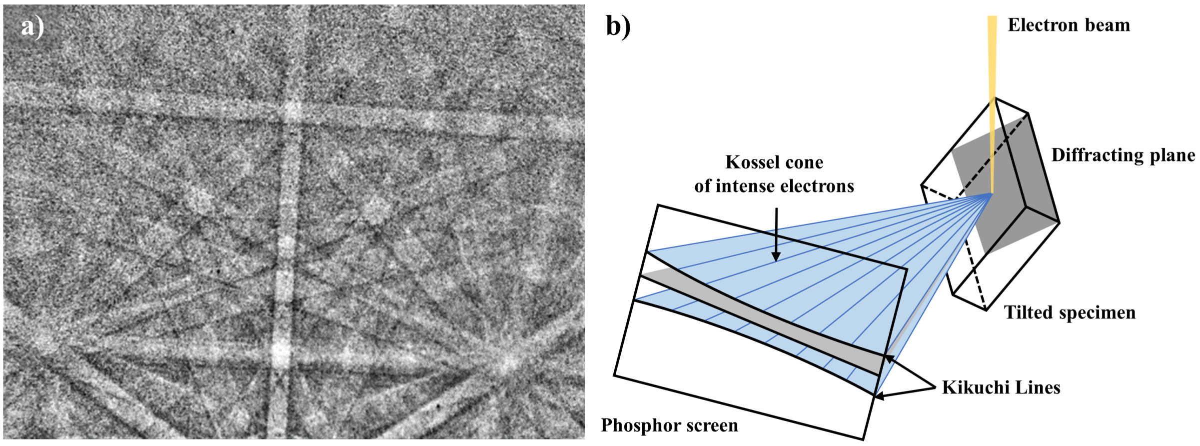

Figure B.2-3. (a) A backscatter Kikuchi pattern from *Megerlia truncata* brachiopod shell calcite at 20 kV, acquired with Hitachi SU5000 FE-SEM. (b)Schematic diagram showing the diffracting cones concerning the reflecting plane, the specimen, and the phosphor screen (modified after Prior et al., 1999)

An EBSD pattern is characteristic of the crystal structure and its orientation of the sample region/spot where it is generated. Accordingly, this diffraction pattern can be used as a tool to identify different crystalline phases, determine individual grain orientation, characterize grain boundaries, and provide local information about the crystalline perfection. When a raster scan is performed on the selected region of the specimen and the diffraction pattern is collected at each point, the resulting EBSD map can reveal the grain size, orientations and boundaries. This data can be further processed to present the texture and microstructure of the selected region, as various statistical distributions can also be obtained through the quantitative analysis. This helps the material scientist/crystallographer to better understand recrystallization, grain boundary structure and properties, grain growth, and many other important physical phenomena that are orientation dependent.

B.2.3 Energy-dispersive X-ray Spectroscopy (EDS) Analysis

A set of EDS systems is a very common affiliation to a SEM, which can provide the chemical composition and/or elements distribution information of the specimens. With the advancement in both hardware and software of the technique, EDS analysis is now considered to be one of the most convenient and accurate methods for (semi) quantitative elemental analysis on the micron or nano level. Nowadays, EDS is also possible to give high-quality quantitative results, which is comparable with that obtained from electron probe microanalysis (EPMA) (Han *et al.* 2018).

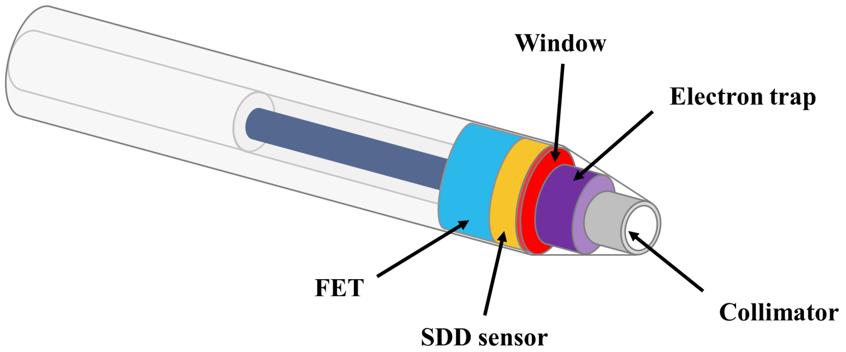

Figure B.2-4. Cutaway diagram showing the construction of a large area silicon drift detector. The collimator ensures X-rays from the area being excited by the primary electron beam are detected; the electron trap deflects any passing electrons that could cause background artefacts; a window isolates the detector crystal under high vacuum; a FET converts electric charges to a voltage pulse and passes it to the pulse processor.

In general, an EDS system consists of three basic parts: an X-ray detector, a pulse processor, and an analyser. In the detector (Fig. B.2-4), the core component is a crystal, which is a semiconductor device that converts X-ray photons into electric charges. These charges will be further converted to voltage output by a field-effect transistor (FET) just behind the crystal. A thin beryllium film could be used as a window material to seal the crystal from the outside, which is robust and well maintains the vacuum of a semiconductor detector. However, the beryllium film heavily absorbs low energy X-rays, which limits the detection of elements lighter than sodium (Na). The modern EDS detectors on SEMs are now using ultra-thin polymer films, which enables the detection of X-rays down to less than 100 eV (Be). Silicon or lithium drifted silicon was the first and the most common material used as the detector crystal in the conventional EDS system. The modern EDS systems nowadays are always equipped with silicon drift detectors (SDD). The development of SDD enables to achieve a liquid-nitrogen-free EDS detector with a much better performance and higher productivity than the Si (Li) detector in SEMs.

The fundamental job of the pulse processor is to remove the noise present on the original X-ray signal, quickly and accurately discriminate energies of X-ray from the incoming voltage pulse, and give a digital count in the corresponding channel to the multi-channel analyser (computer), which is mainly used to display and further interpret the collected EDS data.

B.2.4 Cryo-SEM Imaging

Cryo-SEM imaging is a technique that combines the high-performance imaging ability of a SEM and the cryogenic sample preparation method. It allows the user to investigate the ultrastructure of sample material in their native hydrated state with minimal artefacts or interference from sample preparation procedures. In comparison to the conventional “wet processing”, the advantages of using cryo-SEM are reducing the shrinkage or distortion from the sample preparation, retaining the soluble materials, decreasing the relocation of highly diffusible elements, minimizing the mechanical damage, avoiding toxic reagents (fixatives, buffers), etc.

During cryo preparation, specimens are frozen rapidly and brought to a preparation chamber with a proper transfer toolset. The preparation chamber is under high vacuum conditions and equipped with a cold stage on which the sample can be sublimed or fractured and sputter-coated with metal/carbon. Finally, the specimen is then transferred to the SEM chamber for further analysis under cryogenic conditions. Figure B.2-5 gives a sketch of the main components of a cryo-SEM. The details of the sample preparation will be described in appendix C, and the results were discussed in section 2.1 and section 2.3.

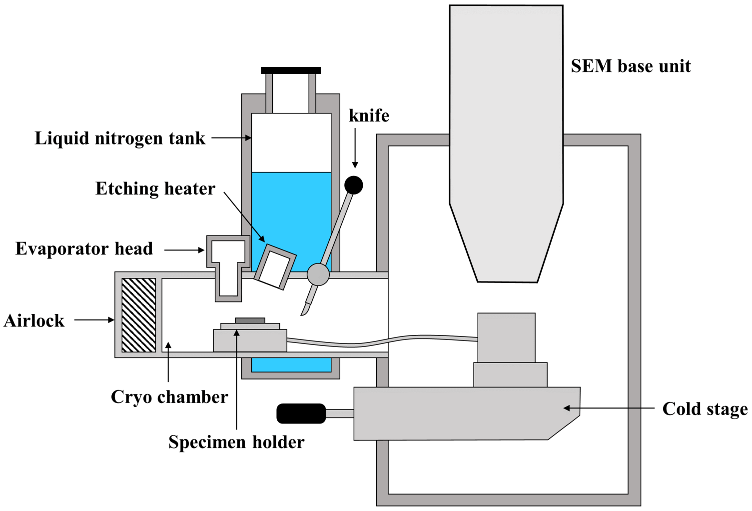

Figure B.2-5. A Schematic sketch of the main components of a cryo-SEM, in which the cryo chamber and the cold stage are integrated. Modified after JEOL application data sheet (SM-B-004-00E).

B.2.5 TEM/STEM Tomography

Tomography is a method of imaging by sections or sectioning. In SEMs, TEMs or STEMs, it offers unparalleled opportunities to explore three-dimensional (3D) cellular ultra-architectures in

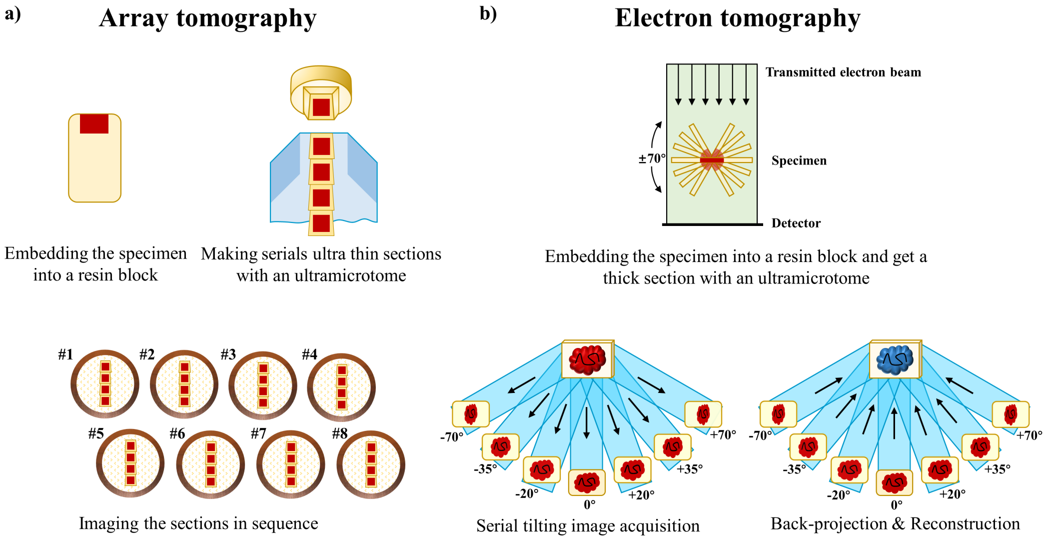

Figure B.2-6. Schematic diagram of two 3D reconstruction methods: a) Array tomography: serial sections are prepared with an ultramicrotome and mounted on a copper TEM grid. These serial sections are imaged and stacked in sequence for the final reconstruction. b) Electron tomography: tomography takes serial-tilting projection images by TEM/STEM and reconstructs the internal 3D structure by back projection of these images.

extremely fine detail for the biologists, or to obtain exhaustive information of internal structure, composition, and physico-chemical properties for the material scientists. Array tomography and electron tomography are the most widely used 3D structure reconstruction and analysis techniques in TEM/STEMs, while focused ion beam (FIB tomography) is very common for the SEMs. The project involved in present work produced tomograms only with TEM and STEMs.

In array tomography, the specimen is first prepared as ultra-thin section ribbon(s) by an ultramicrotome, and serial sections are mounted on the conductive substrate like a copper TEM grid. These serial sections are examined in sequence by a TEM, and 3D images are reconstructed to stack the images in order (Fig. B.2-6a). The advantages of this technique include low initial cost, as the method needs only a conventional TEM and an ultramicrotome; suppression sample charging problem, as the sections are very thin and mounted on the copper grid. However, this technique requires a lot of manual efforts for the segmentation of the section series. Specialized training is necessary for the user to be competent at sectioning. A technical schematic illustration of the sample preparation is presented in Figure B.2-7.

In electron tomography, micrographs are taken from a serial of tilting images of the specimen, and reconstruction is made by the back-projections of the obtained image series. This technique provides high-resolution 3D micrographs; however, it has a thickness limitation defined by the transmission of the electron beam. Therefore, it is difficult to obtain the 3D structure of the whole specimen by electron tomography (Fig. B.2-6b).

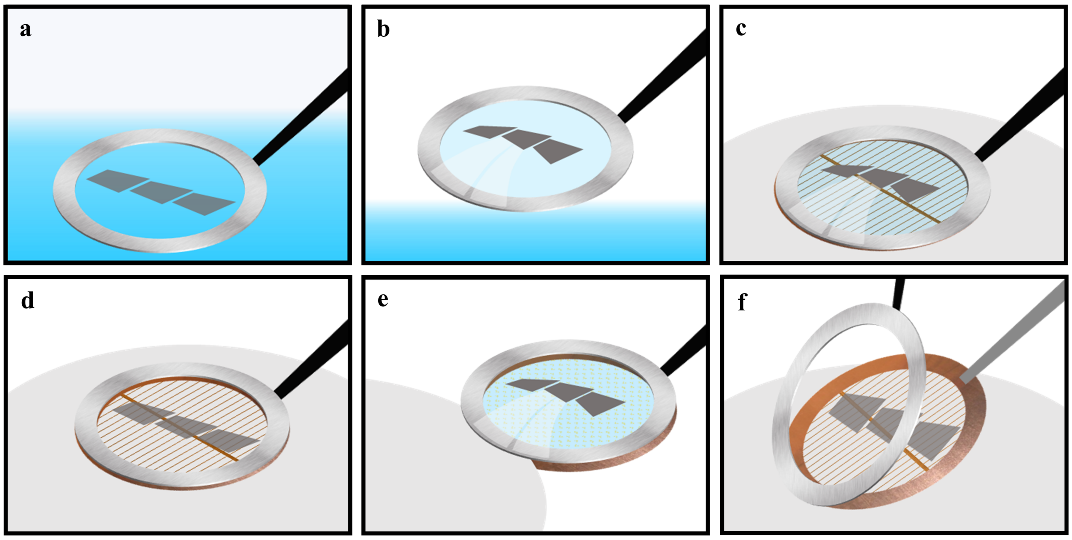

Figure B.2-7. Technical illustration of how to pick-up thin sections onto a TEM grid. a) Centre the “fishing loop” above the section ribbon and slowly lower the loop to touch the water surface. b) Gently lift the loop with the sections and ensure the ribbon does not stick onto the loop. c) Bring the loop above a TEM grid on a filter paper. d) The grid will stick to the loop by surface tension and the filter paper removes the water. e) For the coated TEM girds, use the filter paper to carefully absorb the water between the loop and grid. f) Separate the grid from the loop with a proper tool, for instance, an eyelash or a set of specialized forceps.

C Sample Preparation

C.1 Procedure for Chemical Surface Etching and Decalcification

Chemical etching is commonly used to reveal the microstructure morphology of the material, which is a very important feature in biogenetical hard tissues. A polished and deformation free surface is required. Etching may result in either a uniform removal of substance over the entire exposed surface, or fast dissolution at preferential areas, e.g. grain boundaries, and specific crystal faces or axes. Decalcification here refers to the technique for removing the mineral from calcified hard tissue or mimetic artificial aggregates so that good-quality organic matrices can be preserved with all essential microscopic elements.

To visualize the organic component within the samples, biogenetic specimens were fixed on aluminium rods using super glue. Polished surfaces were prepared in ultramicrotome using a diamond knife (Fabritius *et al.* 2005). The surfaces were then etched superficially in a stirred solution containing 0.1 mol·L^{-1} HEPES and 2.5% glutaraldehyde as a fixative at pH of 6.5 for either 90s or 180s depends on specimens. Decalcification was conducted with a solution containing 0.25 mol·L^{-1} HEPES, 0.05 mol·L^{-1} EDTA, and 2.5% glutaraldehyde stabilized at a pH of 7.8 for several hours or a few days depends on the size of the specimen. Aggregates obtained in biomimetic experiments were first embedded in EPON if their size is smaller than 500 μm. Otherwise, they were prepared the same as the biogenetic specimens as described above.

The etching was stopped by 100% isopropanol and followed with washing. Decalcification was following by washing with double distilled water and dehydration in isopropanol. The specimens were finally critical point dried in a BAL-TEC CPD 030 (Liechtenstein), coated with platinum and carbon, and investigated with a Hitachi SU5000 FE-SEM or a Hitachi S5200 FE-SEM. More details can be found in sections 2.3, 2.4, 2.5 and 2.6.

C.2 Chemical Fixation

Electron microscopy is widely used in the field of modern structural biology. As a high vacuum condition is essential for accelerated electrons propagation, investigations of liquid water containing samples are impossible at room temperature because of the evaporation. In the standard sample preparation procedure, biological samples are usually chemically fixed by aldehyde, dehydrated, embedded, and then thin sections are sliced and further stained with heavy metal ions (Luft 1961; Pease & Porter 1981).

In the present work, the coccolithophore species *Emiliania huxleyi* was fixed in a 0.2M cacodylate buffer solution containing 2.5% glutaraldehyde, and 4% paraformaldehyde at pH 7.6. Samples were gently centrifuged and washed, centrifuged again, postfixed with osmium tetroxide, dehydrated and embedded in EPON resin. Ultrathin sections between 20 to 50 nm thick were then prepared, stained with lead citrate and investigated viewed with a Zeiss 912 TEM (Zeiss, Jena, Germany). More details can be found in section 2.1.

For bacterial EPS, the four bacteria cultures were grown overnight at 28 °C with constant shaking (180 rpm) in a 5 mL test tube containing LB medium. Then, 10 μL droplets of the bacterial suspension were deposited on Petri dishes supplemented with 20 mL of LB culture medium containing 2% agar-agar, 0.5% KH_2PO_4, 0.5% NaCl, 1% glucose and 0.5% yeast extract at pH 7. The dishes were incubated at 28 °C for 4 days. 5×5 mm square blocks were dissected from the growth area and then transferred into the 0.1M sodium cacodylate buffer solution containing 2.5% glutaraldehyde as the fixative at pH 7.3. The specimens were washed, dehydrated, and critical point dried in a BAL-TEC CPD 030 (Liechtenstein). The dried samples were rotary coated with 3-4 nm of platinum (BAF 100, Balzers) at a tilt angle of 45 and imaged with a Hitachi SU5000 FE-SEM (Hitachi Ltd, Tokyo, Japan) at an acceleration voltage of 20 kV. More details can be found in section 2.6.

C.3 Cryo-fixation by High-pressure Freezing

The essential condition for a successful EM investigation is, however, a well-prepared sample. In our biogenetic samples, i.e. the coccolithophores, one would like to resemble the cell living state as closely as possible, for better understanding its biomineralization process. Although chemical fixation is widely accepted as a standard procedure for biological EM sample preparation as described above, artifacts that can be introduced by any steps, e.g. proteins aggregation and lipid loss caused by fixation and dehydration (Cope & Williams 1968), imprecise cell structure interpretation due to heavy metal staining (Kellenberger *et al.* 1992; North *et al.* 1999), push the researchers to find better solutions. Currently, the best approach to preserve the cellular structure and its integrity is cryo-fixation.

Cryo-fixation has two distinct advantages over chemical fixation: the fixation is completed much faster and it instantaneously immobilizes all the macromolecular components. A successful cryo-fixation transforms liquid water into amorphous (vitreous) ice (Escaig 1982; Dubochet 2007) under high cooling rate, without inducing the nucleation of ice crystals which always bring disastrous effects on cellular structure (Meryman 2007). The most common cryo-fixation methods are cold metal block freezing, plunge freezing, spray freezing, propane jet freezing, and high-pressure freezing. The first four methods have their inherent limitations that only a few/dozens μm depth from the sample surface can be well vitrified (Gilkey & Staehelin 1986); only high-pressure freezing enables well-frozen samples up to 200 μm thick (Studer *et al.* 2008). Moor & Riehle (1968) are the pioneers introduced the idea of freezing biological specimens under pressure, and their further alternatives which increased pressure to 210 MPa during cooling (Riehle & Hoechli 1973; Moor *et al.* 1980) laid the foundation of the commercial high-pressure freezing device in 1985.

Specimens that have been cryo-fixed by high-pressure freezing can be processed in follow up procedures: directly investigation on EM cryo-stage; freeze fracturing, which is commonly used for membrane studies (Shotton *et al.* 1978); freeze drying, as a low temperature dehydration process (Edelmann 1986); and freeze substitution, which replaces the ice in a frozen specimen by an organic solvent and crosslinks the stabilized (frozen, solid) framework chemically (van Harreveld & Crowell 1964).

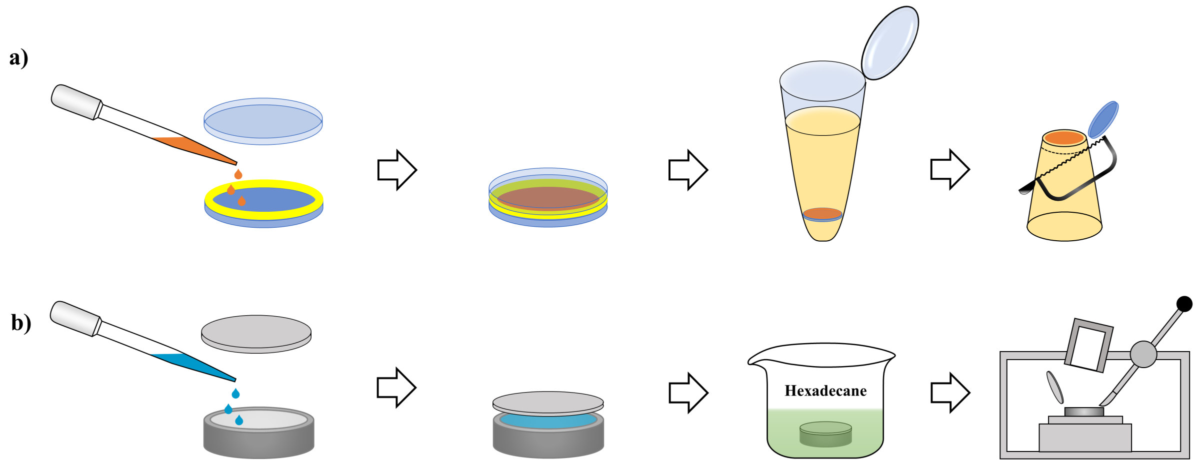

Figure C.3-1. Technical illustration of sample preparation procedures for cryo-fixed (a) coccolithophore samples and (b)hydrogel samples, respectively. a) A few small droplets of the coccolithophore suspension were placed on the centre of a sapphire disk, which is sandwiched of the other sapphire disc and having a 50 μm thick gold ring as a spacer. The sandwich is high-pressure frozen, opened, freeze substituted, and embedded in Epon. The sapphire disc is then removed so that the coccolithophores remain at the surface of the Epon block. The Epon block is sawed with a jigsaw to a height of about 2mm and further sliced with an ultramicrotome for the tomography preparation. b) A few hydrogel droplets were dropped into the cavity of an aluminium planchette and covered by a flat aluminium lid. The sandwich was immersed in hexadecane which severs as the cryoprotectant here. The sandwich is high-pressure frozen, cryo-transferred to a freeze-etching device, opened by a cold knife, and the sample surface was further freeze etched by water sublimation. Then the frozen samples were coated and examined with a cryo-SEM.

To get a better understanding of the cell ultrastructure, the coccolithophores species *Emiliania huxleyi* was cryo-fixation by high-pressure freezing following the protocol developed by Höhn *et al.* (2011), freeze substituted overnight (Walther & Ziegler 2002), and embedded in EPON. Ultrathin sections (20-50 nm thick) for TEM imaging were sliced using an “ultra”-type diamond knife (Diatome, Liechtenstein) in a Reichert Ultracut S microtome (Leica, Wetzlar, Germany), and examined with a Zeiss 912 TEM. Semi-thin sections (500-700 nm) for STEM tomography were prepared using a “semi”-type diamond knife (Diatome, Liechtenstein) in ultramicrotome, and recorded by a Jeol FEM 2100F field-emission microscope (Jeol Ltd, Tokyo, Japan). Cryo-SEM images were performed on high-pressure frozen and freeze fractured samples using a Hitachi S5200 FE-SEM. More details can be found in section 2.1.

To obtain qualitative information (i.e. porosity) of the pristine hydrogel before aggregates crystallization, small volumes (20-30 mL) of hydrogel with different contents were prepared by the identical procedure described for crystal growth experiments (Nindiyasari *et al.* 2015; Greiner *et al.* 2018; Yin *et al.* 2019). A small droplet of the hydrogel was high-pressure frozen between two aluminium planchettes, having a total diameter of 3 mm, and a central cavity of 2 mm in diameter and 300 μm deep, as a sandwich. The sandwiches were frozen fractured and etched further by water sublimation, and subsequently coated with platinum and carbon. Etched samples were cryo-transferred and imaged with a Hitachi S5200 FE-SEM at a temperature of -100 °C and an accelerating voltage of 10 kV. Imaging was performed by using analysis mode and the backscattered electron signal. More details can be found in section 2.4.

C.4 Surface Preparation for EBSD Measurement

Electron backscatter diffraction (EBSD) is a microstructural crystallographic characterization technique, which allows the identification of individual grain orientations boundaries, phases, and morphologies (Adams *et al.* 1993). It is also possible to provide internal stresses and defects information (Wilkinson *et al.* 2006) in the material. Since the backscattered electrons come from the near subsurface of the sample, typically the first micrometers or even less, the specimen surface preparation is critical for the success and quality of the EBSD measurements.

In this work, the highly polished surfaces were prepared by microtome cutting. Biogenetic specimens were fixed on aluminum rods in the desired direction using superglue. The specimens were first cut to the desired depth using a Leica Ultracut ultramicrotome with glass knives. The section planes were further polished using an "Ultra 35°" diamond knife by stepwise removal of material in a series of sections with successively decreasing thicknesses (90, 70, 50, 30, 10 and 5 nm). Each step was repeated 15 times (Fabritius *et al.* 2005). Aggregates obtained in biomimetic experiments were first embedded in EPON if their size is smaller than 500 μm. Otherwise, they were prepared the same as the biogenetic specimens as described above.

The samples were then coated with 4 nm of carbon. EBSD maps were measured with a field emission SEM, SU5000, equipped with a Nordlys II EBSD detector. Data were evaluated with AZtec and CHANNEL 5 HKL software. More details can be found in sections 2.2, 2.4, 2.5 and 2.6.

Bibliography

Adams, B.L., Wright, S.I., & Kunze, K. 1993. Orientation Imaging: The Emergence of a New Microscopy. *Metall. Trans. A*, **24**(4), 819–831.

Addadi, L., & Weiner, S. 2014. Biomineralization: Mineral Formation by Organisms. *Phys. Scr.*, **89**(9), 098003.

Addadi, L., Berman, A., & Weiner, S. 1991. Intracrystalline Proteins from a Sea Urchin and a Mollusk: A Comparison. Mechanisms and Phylogeny of Mineralization in Biological Systems. Springer Japan.

Addadi, L., Raz, S., & Weiner, S. 2003. Taking Advantage of Disorder: Amorphous Calcium Carbonate and Its Roles in Biomineralization. *Adv. Mater.*, **15**(12), 959–970.

Addadi, L., Joester, D., Nudelman, F., & Weiner, S. 2006. Mollusk Shell Formation: A Source of New Concepts for Understanding Biomineralization Processes. *Chem. Eur. J.*, **12**(4), 980–987.

Addadi, L., Gal, A., Faivre, D., Scheffel, A., & Weiner, S. 2016. Control of Biogenic Nanocrystal Formation in Biomineralization. *Isr. J. Chem.*, **56**(4), 227–241.

Agudo J., L., Eggeler, G., & Dlouhy, A. 2012. Advanced Scanning Transmission Stereo Electron Microscopy of Structural and Functional Engineering Materials. *Ultramicroscopy*, **122**, 48–59.

Aguilar, C., Vlamakis, H., Losick, R., & Kolter, R. 2007. Thinking About Bacillus Subtilis as a Multicellular Organism. *Curr. Opin. Microbiol.*, **10**(6), 638–643.

Ahearn, G.A., Mandal, P.K., & Mandal, A. 2004. Calcium Regulation in Crustaceans During the Molt Cycle: A Review and Update. *Comp. Biochem. Physiol., Part A: Mol. Integr. Physiol.*, **137**(2), 247–257.

Aizenberg, J., Hanson, J., Koetzle, T.F., Weiner, S., & Addadi, L. 1997. Control of Macromolecule Distribution within Synthetic and Biogenic Single Calcite Crystals. *J. Am. Chem. Soc.*, **119**(5), 881–886.

Aksay, I.A., Trau, M., Manne, S., Honma, I., Yao, N., Zhou, L., Fenter, P., Eisenberger, P.M., & Gruner, S.M. 1996. Biomimetic Pathways for Assembling Inorganic Thin Films. *Science*, **273**(5277), 892–898.

Albeck, S., Weiner, S., & Addadi, L. 1996. Polysaccharides of Intracrystalline Glycoproteins Modulate Calcite Crystal Growth in Vitro. *Chem. Eur. J.*, **2**(3), 278–284.

Albéric, M., Stifler, C.A., Zou, Z., Sun, C.-Y., Killian, C.E., Valencia, S., Mawass, M.-A., Bertinetti, L., Gilbert, P.U.P.A., & Politi, Y. 2019. Growth and Regrowth of Adult Sea Urchin Spines Involve Hydrated and Anhydrous Amorphous Calcium Carbonate Precursors. *J. Struct. Biol.: X*, **1**, 100004.

Almagro, I., Drzymała, P., Berent, K., Sainz-Díaz, C.I., Willinger, M.G., Bonarski, J., & Checa, A.G. 2016. New Crystallographic Relationships in Biogenic Aragonite: The Crossed-Lamellar Microstructures of Mollusks. *Cryst. Growth Des.*, **16**(4), 2083–2093.

Anderson, Valerie J., & Lekkerkerker, Henk N.W. 2002. Insights into Phase Transition Kinetics from Colloid Science. *Nature*, **416**(6883), 811–815.

Andreassen, J.P., & Lewis, A.E. 2017. Classical and Nonclassical Theories of Crystal Growth. *Pages 137–154 of:* van Driessche, A. E. S., Kellermeier, M., Benning, L. G., & Gebauer, D. (eds), *New Perspectives on Mineral Nucleation and Growth: From Solution Precursors to Solid Materials*. Cham: Springer International Publishing.

Angell, Robert W. 1967. The Process of Chamber Formation in the Foraminifer *Rosalina floridana* (Cushman). *J. Journal of Protozool.*, **14**(4), 566–574.

Angell, Robert W. 1979. Calcification During Chamber Development in *Rosalina floridana*. *J. Foraminiferal Res.*, **9**(4), 341–353.

Angell, R.W. 1980. Test Morphogenesis (Chamber Formation) in the Foraminifer *Spiroloculina hyalina* Schulze. *J. Foraminiferal Res.*, **10**(2), 89–101.

Anning, T., Nimer, N., Merrett, M.J., & Brownlee, C. 1996. Costs and Benefits of Calcification in Coccolithophorids. *J. Mar. Syst.*, **9**(1-2), 45–56.

Araki, Y., & Gonzáles, E.L. 1998. V-and P-Type Ca^{2+}-Stimulated ATPases in a Calcifying Strain of *Pleurochrysis* sp. (Haptophyceae). *J. Physiol.*, **34**, 79–88.

Arias, D., Cisternas, L.A., & Rivas, M. 2017. Biomineralization of Calcium and Magnesium Crystals from Seawater by Halotolerant Bacteria Isolated from Atacama Salar (Chile). *Desalination*, **405**, 1–9.

Arp, G., Thiel, V., Reimer, A., Michaelis, W., & Reitner, J. 1999. Biofilm Exopolymers Control Microbialite Formation at Thermal Springs Discharging into the Alkaline Pyramid Lake, Nevada, USA. *Sediment. Geol.*, **126**(1), 159–176.

Asenath-Smith, E., Li, H.Y., Keene, E.C., Seh, Z.W., & Estroff, L.A. 2012. Crystal Growth of Calcium Carbonate in Hydrogels as a Model of Biomineralization. *Adv. Funct. Mater.*, **22**(14), 2891–2914.

Astilleros, J.M., Fernández-Díaz, L., & Putnis, A. 2010. The Role of Magnesium in the Growth of Calcite: An AFM Study. *Chem. Geol.*, **271**(1-2), 52–58.

Atlas, R.M., Bartha, R., & Atlas, D. 1998. *Microbial Ecology: Fundamentals and Applications*. 4 edn. Benjamin/Cummings.

Bach, L.T., Mackinder, L.C.M., Schulz, K.G., Wheeler, G., Schroeder, D.C., Brownlee, C., & Riebesell, U. 2013. Dissecting the Impact of CO_2 and pH on the Mechanisms of Photosynthesis and Calcification in the Coccolithophore *Emiliania huxleyi*. *New Phytol.*, **199**(1), 121–134.

Balch, W.M., Holligan, P.M., & Kilpatrick, K.A. 1992. Calcification, Photosynthesis and Growth of the Bloom-Forming Coccolithophore, *Emiliania huxleyi*. *Cont. Shelf Res.*, **12**(12), 1353–1374.

Banfield, J.F., & Zhang, H.Z. 2001. Nanoparticles in the Environment. *Rev. Mineral. Geochem.*, **44**, 1–58.

Bar-On, B., & Wagner, H.D. 2013. The Emergence of an Unusual Stiffness Profile in Hierarchical Biological Tissues. *Acta Biomater.*, **9**(9), 8099–8109.

Barber, D.J., & Wenk, H.R. 1979. Deformation Twinning in Calcite, Dolomite, and Other Rhombohedral Carbonates. *Phys. Chem. Miner.*, **5**(2), 141–165.

Baumann, K.H., Andruleit, H., Böckel, B., Geisen, M., & Kinkel, H. 2005. The Significance of Extant Coccolithophores as Indicators of Ocean Water Masses, Surface Water Temperature, and Palaeoproductivity: A Review. *Palaontol. Z.*, **79**(1), 93–112.

Becker, R., & Döring, W. 1935. Kinetische Behandlung Der Keimbildung in Ubersattigten Dampfen. *Ann. Phys.*, **24**(5), 719–752.

Bell, D.C., & Erdman, N. 2012. Introduction to the Theory and Advantages of Low Voltage Electron Microscopy. *Low Voltage Electron Microscopy*, 1–30.

Bentov, S., & Erez, J. 2006. Impact of Biomineralization Processes on the Mg Content of Foraminiferal Shells: A Biological Perspective. *Geochem. Geophys. Geosyst.*, **7**, 1–11.

Bentov, S., Brownlee, C., & Erez, J. 2009. The Role of Seawater Endocytosis in the Biomineralization Process in Calcareous Foraminifera. *Proc. Natl. Acad. Sci.*, **106**(51), 21500–21504.

Bentov, Shmuel, & Erez, Jonathan. 2005. Novel Observations on Biomineralization Processes in Foraminifera and Implications for Mg/Ca Ratio in the Shells. *Geology*, **33**(11), 841–844.

Benzerara, K., Menguy, N., Guyot, F., Dominici, C., & Gillet, P. 2003. Nanobacteria-Like Calcite Single Crystals at the Surface of the Tataouine Meteorite. *Proc. Natl. Acad. Sci.*, **100**(13), 7438–7442.

Benzerara, K., Menguy, N., López-García, P., Yoon, T.-H., Kazmierczak, J., Tyliszczak, T., Guyot, F., & Brown, G.E. 2006. Nanoscale Detection of Organic Signatures in Carbonate Microbialites. *Proc. Natl. Acad. Sci.*, **103**(25), 9440–9445.

Beveridge, T.J. 1989. Role of Cellular Design in Bacterial Metal Accumulation and Mineralization. *Annu. Rev. Microbiol.*, **43**(1), 147–171.

Bewernitz, M.A., Gebauer, D., Long, J., Cölfen, H., & Gower, L.B. 2012. A Metastable Liquid Precursor Phase of Calcium Carbonate and Its Interactions with Polyaspartate. *Faraday Discuss.*, **159**(0), 291–312.

Beyenbach, K.W., & Wieczorek, H. 2006. The V-Type H_+ ATPase: Molecular Structure and Function, Physiological Roles and Regulation. *J. Exp. Biol.*, **209**(4), 577–589.

Bischoff, W.D., Sharma, S.K., & Mackenzie, F.T. 1985. Carbonate Ion Disorder in Synthetic and Biogenic Magnesian Calcites - a Raman Spectral Study. *Am. Mineral.*, **70**(5-6), 581–589.

Blank, S., Arnoldi, M., Khoshnavaz, S., Treccani, L., Kuntz, M., Mann, K., Grathwohl, G., & Fritz, M. 2003. The Nacre Protein Perlucin Nucleates Growth of Calcium Carbonate Crystals. *J. Microsc.-Oxford*, **212**, 280–291.

Boran, G., Mulvaney, S.J., & Regenstein, J.M. 2010. Rheological Properties of Gelatin from Silver Carp Skin Compared to Commercially Available Gelatins from Different Sources. *J. Food Sci.*, **75**(8), E565–E571.

Borman, A.H., Dejong, E.W., Huizinga, M., Kok, D.J., Westbroek, P., & Bosch, L. 1982. The Role in $CaCO_3$ Crystallization of an Acid Ca^{2+}-Binding Polysaccharide Associated with Coccoliths of *Emiliania huxleyi*. *Eur. J. Biochem.*, **129**(1), 179–183.

Borrelli, C., Panieri, G., Dahl, T.M., & Neufeld, K. 2018. Novel Biomineralization Strategy in Calcareous Foraminifera. *Sci. Rep.*, **8**(1), 10201.

Boskey, A.L., Maresca, M., Ullrich, W., Doty, S.B., Butler, W.T., & Prince, C.W. 1993. Osteopontin-Hydroxyapatite Interactions in-Vitro - Inhibition of Hydroxyapatite Formation and Growth in a Gelatin-Gel. *Bone and Mineral*, **22**(2), 147–159.

Braissant, O., Verrecchia, E.P., & Aragno, M. 2002. Is the Contribution of Bacteria to Terrestrial Carbon Budget Greatly Underestimated? *Naturwissenschaften*, **89**(8), 366–370.

Braissant, O., Cailleau, G., Dupraz, C., & Verrecchia, E.P. 2003. Bacterially Induced Mineralization of Calcium Carbonate in Terrestrial Environments: The Role of Exopolysaccharides and Amino Acids. *J. Sediment. Res.*, **73**, 485.

Braissant, O., Decho, A.W., Dupraz, C., Glunk, C., Przekop, K.M., & Visscher, P.T. 2007. Exopolymeric Substances of Sulfate-Reducing Bacteria: Interactions with Calcium at Alkaline pH and Implication for Formation of Carbonate Minerals. *Geobiology*, **5**(4), 401–411.

Brookes, S.J., Robinson, C., Kirkham, J., & Bonass, W.A. 1995. Biochemistry and Molecular Biology of Amelogenin Proteins of Developing Dental Enamel. *Arch. Oral Biol.*, **40**(1), 1–14.

Brooks, R., Clark, L.M., & Thurston, E.F. 1950. Calcium Carbonate and Its Hydrates. *Philos. Trans. R. Soc. London, A*, **243**(861), 145–167.

Brown, C.H. 1952. Some Structural Proteins of *Mytilus edulis*. *Q. J. Microsc. Sci.*, **s3-93**(24), 487–502.

Brownlee, C., & Taylor, A. 2004. Calcification in Coccolithophores: A Cellular Perspective. *Pages 31–49 of:* Thierstein, H. R., & Young, J. R. (eds), *Coccolithophores. From molecular processes to global impact*. Berlin, Heidelberg: Springer.

Brownlee, C., Wheeler, G.L., & Taylor, A.R. 2015. Coccolithophore Biomineralization: New Questions, New Answers. *Semin. Cell Dev. Biol.*, **46**, 11–16.

Bruno, Marco, Massaro, Francesco Roberto, Rubbo, Marco, Prencipe, Mauro, & Aquilano, Dino. 2010. (10.4), (01.8), (01.2), and (00.1) Twin Laws of Calcite ($CaCO_3$): Equilibrium Geometry of the Twin Boundary Interfaces and Twinning Energy. *Cryst. Growth Des.*, **10**(7), 3102–3109.

Bueble, S., & Schmahl, W. W. 1999. Mechanical Twinning in Calcite Considered with the Concept of Ferroelasticity. *Physics and Chemistry of Minerals*, **26**(8), 668–672.

Burkhard, Martin. 1993. Calcite Twins, Their Geometry, Appearance and Significance as Stress-Strain Markers and Indicators of Tectonic Regime: A Review. *J. Struct. Geol.*, **15**(3), 351–368.

Burton, W.K., Cabrera, N., & Frank, F.C. 1949. Role of Dislocations in Crystal Growth. *Nature*, **163**(4141), 398–399.

Burton, W.K., Cabrera, N., Frank, F.C., & Mott, Nevill Francis. 1951. The Growth of Crystals and the Equilibrium Structure of Their Surfaces. *Philos. Trans. R. Soc. London, A*, **243**(866), 299–358.

Bäuerlein, E. 2003. Biomineralization of Unicellular Organisms: An Unusual Membrane Biochemistry for the Production of Inorganic Nano- and Microstructures. *Angew. Chem., Int. Ed.*, **42**(6), 614–641.

Bé, Allan W.H., Hemleben, C., Anderson, O.R., & Spindler, M. 1979. Chamber Formation in Planktonic Foraminifera. *Micropaleontology*, **25**(3), 294–307.

Bé, A.W.H. 1982. Biology of Planktonic Foraminifera. *Notes for a Short Course: Studies in Geology*, **6**, 51–89.

Bé, A.W.H., & Hemleben, C. 1970. Calcification in a Living Planktonic Foraminifer, *Globigerinoides sacculifer* (Brady). *N. Jb. Geol. Paläont. Abh.*, 221–234.

Bøggild, O.B. 1930. The Shell Structure of the Mollusks. *Kgl. Danske Videnskab. Selskabs, Skrifter Naturvidenskab. Math. Afdel.*, **2**, 233–325.

Caccavo, D., Cascone, S., Lamberti, G., & Barba, A.A. 2018. Hydrogels: Experimental Characterization and Mathematical Modelling of Their Mechanical and Diffusive Behaviour. *Chem. Soc. Rev.*, **47**(7), 2357–2373.

Cantaert, B., Kim, Y.Y., Ludwig, H., Nudelman, F., Sommerdijk, Najm, & Meldrum, F.C. 2012. Think Positive: Phase Separation Enables a Positively Charged Additive to Induce Dramatic Changes in Calcium Carbonate Morphology. *Adv. Funct. Mater.*, **22**(5), 907–915.

Carter, J.G. 1980. Guide to Bivalve Shell Microstructures. *Pages 645–673 of:* Rhoads, D., & Lutz, R. A. (eds), *Skeletal Growth of Aquatic Organisms*. New York: Springer US.

Carter, J.G., & Clark II, G.R. 1985. Classification and Phylogenetic Significance of Molluscan Shell Microstructure. *Pages 50–71 of:* Broadhead, T. W. (ed), *Mollusks : notes for a short course / organized by D. J. Bottjer, C. S. Hickman, P. D. Ward.* Tennessee: University of Tennessee, Department of Geological Sciences.

Carter, J.G., Harries, P., Malchus, N., Sartori, A., Anderson, L., Bieler, R., Bogan, A., Coan, E., Cope, J., Cragg, S., Garcia-March, J., Hylleberg, J., Kelley, P., Kleemann, K., Kriz, J., McRoberts, C., Mikkelsen, P., John Pojeta, J., Skelton, P.W., Temkin, I., Yancey, T., & Zieritz, A. 2012. Illustrated Glossary of the Bivalvia. *Treatise Online no. 48: Part N, Revised, Volume 1, Chapter 31*, 1–209.

Cartwright, J.H.E., & Checa, A.G. 2007. The Dynamics of Nacre Self-Assembly. *J. R. Soc. Interface*, **4**(14), 491–504.

Cartwright, J.H.E., Checa, A.G., Escribano, B., & Sainz-Díaz, C.I. 2009. Spiral and Target Patterns in Bivalve Nacre Manifest a Natural Excitable Medium from Layer Growth of a Biological Liquid Crystal. *Proc. Natl. Acad. Sci.*, **106**(26), 10499–10504.

Cartwright, J.H.E., Checa, A.G., Gale, J.D., Gebauer, D., & Sainz-Díaz, C.I. 2012. Calcium Carbonate Polyamorphism and Its Role in Biomineralization: How Many Amorphous Calcium Carbonates Are There? *Angew. Chem., Int. Ed.*, **51**(48), 11960–11970.

Casella, L.A., Griesshaber, E., Yin, X., Ziegler, A., Mavromatis, V., Muller, D., Ritter, A.C., Hippler, D., Harper, E.M., Dietzel, M., Immenhauser, A., Schone, B.R., Angiolini, L., & Schmahl, W.W. 2017. Experimental Diagenesis: Insights into Aragonite to Calcite Transformation of *Arctica islandica* Shells by Hydrothermal Treatment. *Biogeosciences*, **14**(6), 1461–1492.

Castanier, S., Le Métayer-Levrel, G., & Perthuisot, J.P. 1999. Ca-Carbonates Precipitation and Limestone Genesis – the Microbiogeologist Point of View. *Sediment. Geol.*, **126**(1), 9–23.

Castanier, S., Le Métayer-Levrel, G., Orial, G., Loubière, J.F., & Perthuisot, J.P. 2000. Bacterial Carbonatogenesis and Applications to Preservation and Restoration of Historic Property. *Pages 203–218 of:* Ciferri, O., Tiano, P., & Mastromei, G. (eds), *Of Microbes and Art: The Role of Microbial Communities in the Degradation and Protection of Cultural Heritage*. Boston, MA: Springer US.

Caulle, C., Koho, K.A., Mojtahid, M., Reichart, G.J., & Jorissen, F.J. 2014. Live (Rose Bengal Stained) Foraminiferal Faunas from the Northern Arabian Sea: Faunal Succession within and Below the Omz. *Biogeosciences*, **11**(4), 1155–1175.

Cavalier-Smith, T. 2018. Kingdom Chromista and Its Eight Phyla: A New Synthesis Emphasising Periplastid Protein Targeting, Cytoskeletal and Periplastid Evolution, and Ancient Divergences. *Protoplasma*, **255**(1), 297–357.

Chapman, A.D. 2009. *Numbers of Living Species in Australia and the World.*

Chateigner, D., Hedegaard, C., & Wenk, H.R. 2000. Mollusc Shell Microstructures and Crystallographic Textures. *J. Struct. Geol.*, **22**(11-12), 1723–1735.

Checa, A.G. 2018. Physical and Biological Determinants of the Fabrication of Molluscan Shell Microstructures. *Front. Mar. Sci.*, **5**(353).

Checa, A.G., Rodríguez-Navarro, A.B., Delgado, F.J.E., & Esteban-Delgado, F.J. 2005. The Nature and Formation of Calcitic Columnar Prismatic Shell Layers in Pteriomorphian Bivalves. *Biomaterials*, **26**(32), 6404–6414.

Checa, A.G., Cartwright, J.H.E., & Willinger, M.G. 2009. The Key Role of the Surface Membrane in Why Gastropod Nacre Grows in Towers. *Proc. Natl. Acad. Sci.*, **106**(1), 38–43.

Checa, A.G., Cartwright, J.H.E., & Willinger, M.G. 2011. Mineral Bridges in Nacre. *J. Struct. Biol.*, **176**(3), 330–339.

Checa, A.G., Mutvei, H., Osuna-Mascaró, A.J., Bonarski, J.T., Faryna, M., Berent, K., Pina, C.M., Rousseau, M., & Macías-Sánchez, E. 2013. Crystallographic Control on the Substructure of Nacre Tablets. *J. Struct. Biol.*, **183**(3), 368–376.

Checa, A.G., Salas, C., Harper, E.M., & Bueno-Pérez, J. de D. 2014. Early Stage Biomineralization in the Periostracum of the 'Living Fossil' Bivalve *Neotrigonia*. *PLOS ONE*, **9**(2), e90033.

Checa, A.G., Cartwright, J.H.E., Sánchez-Almazo, I., Andrade, J.P., & Ruiz-Raya, F. 2015. The Cuttlefish *Sepia officinalis* (Sepiidae, Cephalopoda) Constructs Cuttlebone from a Liquid-Crystal Precursor. *Sci. Rep.*, **5**, 11513.

Checa, A.G., Macías-Sánchez, E., Harper, E.M., & Cartwright, J.H.E. 2016. Organic Membranes Determine the Pattern of the Columnar Prismatic Layer of Mollusc Shells. *Proceedings of the Royal Society B: Biological Sciences*, **283**(1830).

Checa, A.G., Harper, E.M., & González-Segura, A. 2018. Structure and Crystallography of Foliated and Chalk Shell Microstructures of the Oyster *Magallana*: The Same Materials Grown under Different Conditions. *Sci. Rep.*, **8**(1), 7507.

Checa, A.G., Salas, C., Rodríguez-Navarro, A.B., Grenier, C., & Lagos, N.A. 2019. Articulation and Growth of Skeletal Elements in Balanid Barnacles (Balanidae, Balanomorpha, Cirripedia). *R. Soc. Open Sci.*, **6**(9), 190458.

Checa, A.G., González-Segura, A., Rodríguez-Navarro, A.B., & Lagos, N.A. 2020. Microstructure and Crystallography of the Wall Plates of the Giant Barnacle *Austromegabalanus psittacus*: A Material Organized by Crystal Growth. *J. R. Soc. Interface*, **17**(164), 20190743.

Chekroun, K.B., Rodríguez-Navarro, C., González-Muñoz, M.T., Arias, J.M., Cultrone, G., & Rodríguez-Gallego, M. 2004. Precipitation and Growth Morphology of Calcium Carbonate Induced by Myxococcus Xanthus: Implications for Recognition of Bacterial Carbonates. *J. Sediment. Res.*, **74**(6), 868–876.

Cheng, X., & Gower, L.B. 2006. Molding Mineral within Microporous Hydrogels by a Polymer-Induced Liquid-Precursor (PILP) Process. *Biotechnol. Prog.*, **22**(1), 141–149.

Chernov, A.A. 1984. *Modern Crystallography III: Crystal Growth.* Springer Series in Solid-State Sciences, no. 36. Springer-Verlag Berlin Heidelberg.

Comte, S., Guibaud, G., & Baudu, M. 2006. Relations between Extraction Protocols for Activated Sludge Extracellular Polymeric Substances (EPS) and EPS Complexation Properties: Part I. Comparison of the Efficiency of Eight EPS Extraction Methods. *Enzyme Microb. Technol.*, **38**(1), 237–245.

Connolly, J., Kaufman, M., Rothman, A., Gupta, R., Redden, G., Schuster, M., Colwell, F., & Gerlach, R. 2013. Construction of Two Ureolytic Model Organisms for the Study of Microbially Induced Calcium Carbonate Precipitation. *J. Microbiol. Methods*, **94**(3), 290–299.

Cope, G.H., & Williams, M.A. 1968. Quantitative Studies on Neutral Lipid Preservation in Electron Microscopy. *J. R. Microsc. Soc.*, **88**(2), 259–277.

Corstjens, P.L.A.M., van der Kooij, A., Linschooten, C., Brouwers, G.J., Westbroek, P., & de Vrind-de Jong, E.W. 1998. GPA, a Calcium-Binding Protein in the Coccolithophorid *Emiliania huxleyi* (Prymnesiophyceae). *J. Phycol.*, **34**(4), 622–630.

Corstjens, P.L.A.M., Araki, Y., & González, E.L. 2001. A Coccolithophorid Calcifying Vesicle with a Vacuolar-Type ATPase Proton Pump: Cloning and Immunolocalization of the V_0 Subunit c. *J. Phycol.*, **37**, 71–78.

Costa, O.Y.A., Raaijmakers, J.M., & Kuramae, E.E. 2018. Microbial Extracellular Polymeric Substances: Ecological Function and Impact on Soil Aggregation. *Front. Microbiol.*, **9**(1636).

Costerton, J.W., Lewandowski, Z., Caldwell, D.E., Korber, D.R., & Lappin-Scott, H.M. 1995. Microbial Biofilms. *Annu. Rev. Microbiol.*, **49**(1), 711–745.

Crippa, G., Pasinetti, G., & Dapiaggi, M. 2020a. How Did the Carrier Shell *Xenophora crispa* (König, 1825) Build Its Shell? Evidence from the Recent and Fossil Record. *Lethaia*, **000**(1-13).

Crippa, G., Griesshaber, E., Checa, A.G., Harper, E., Simonet Roda, M., & Schmahl, W.W. 2020b. Orientation Patterns of the Aragonitic Crossed-lamellar, Myostracal and Fibrous Microstructures of Modern *Glycymeris* Shells. *J. Struct. Biol*, submitted.

Cuif, J.P., Dauphin, Y., & Sorauf, J.E. 2018. *Biominerals and Fossils Through Time*. Cambridge University Press.

Currey, J.D. 1977. Mechanical Properties of Mother of Pearl in Tension. *Proc. Royal Soc. B*, **196**(1125), 443–463.

Cusack, M., & Freer, A. 2008. Biomineralization: Elemental and Organic Influence in Carbonate Systems. *Chem. Rev.*, **108**(11), 4433–4454.

Czaczyk, K., & Myszka, K. 2007. Biosynthesis of Extracellular Polymeric Substances (EPS) and Its Role in Microbial Biofilm Formation. *Pol. J. Environ. Stud.*, **16**(6), 799–806.

Côté, A.S., Darkins, R., & Duffy, D.M. 2015. Deformation Twinning and the Role of Amino Acids and Magnesium in Calcite Hardness from Molecular Simulation. *Phys. Chem. Chem. Phys.*, **17**(31), 20178–20184.

Cölfen, H. 2001. Double-Hydrophilic Block Copolymers: Synthesis and Application as Novel Surfactants and Crystal Growth Modifiers. *Macromol. Rapid Commun.*, **22**(4), 219–252.

Cölfen, H., & Antonietti, M. 2008. *Mesocrystals and Nonclassical Crystallization*. John Wiley & Sons, Ltd.

Daskalakis, M.I., Magoulas, A., Kotoulas, G., Catsikis, I., Bakolas, A., Karageorgis, A.P., Mavridou, A., Doulia, D., & Rigas, F. 2013. *Pseudomonas*, *Pantoea* and *Cupriavidus* Isolates Induce Calcium Carbonate Precipitation for Biorestoration of Ornamental Stone. *J. Appl. Microbiol.*, **115**(2), 409–423.

De Jong, A.S.H., Hak, T.J., & Duijn, P.V. 1980. The Dynamics of Calcium Phosphate Precipitation Studied with a New Polyacrylamide Steady State Matrix-Model: Influence of Pyrophosphate, Collagen and Chondroitin Sulfate. *Connect. Tissue Res.*, **7**(2), 73–79.

de Nooijer, L.J., Langer, G., Nehrke, G., & Bijma, J. 2009. Physiological Controls on Seawater Uptake and Calcification in the Benthic Foraminifer *Ammonia tepida*. *Biogeosciences*, **6**(11), 2669–2675.

de Nooijer, L.J., Spero, H.J., Erez, J., Bijma, J., & Reichart, G.J. 2014. Biomineralization in Perforate Foraminifera. *Earth Sci Rev.*, **135**, 48–58.

De Yoreo, J.J., & Vekilov, P.G. 2003. Principles of Crystal Nucleation and Growth. *Biomineralization*, **54**, 57–93.

De Yoreo, J.J., Gilbert, P.U.P.A., Sommerdijk, N.A.J.M., Penn, R.L., Whitelam, S., Joester, D., Zhang, H., Rimer, J.D., Navrotsky, A., Banfield, J.F., Wallace, A.F., Michel, F.M., Meldrum, F.C., Cölfen, H., & Dove, P.M. 2015. Crystallization by Particle Attachment in Synthetic, Biogenic, and Geologic Environments. *Science*, **349**(6247).

De Yoreo, J.J., Sommerdijk, N.A.J.M., & Dove, P.M. 2017. Nucleation Pathways in Electrolyte Solutions. *Pages 1–24 of:* Van Driessche, A. E. S., Kellermeier, M., Benning, L. G., & Gebauer, D. (eds), *New Perspectives on Mineral Nucleation and Growth: From Solution Precursors to Solid Materials*. Cham: Springer International Publishing.

Debenay, J.P., & Guillou, J.J. 2002. Ecological Transitions Indicated by Foraminiferal Assemblages in Paralic Environments. *Estuaries*, **25**(6), 1107–1120.

Debenay, J.P., Guillou, J.J., Redois, F., & Geslin, E. 2000. Distribution Trends of Foraminiferal Assemblages in Paralic Environments. *Pages 39–67 of:* Martin, R. E. (ed), *Environmental Micropaleontology: The Application of Microfossils to Environmental Geology*. Boston, MA: Springer US.

Decho, A.W. 1990. Microbial Exopolymer Secretions in Ocean Environments: Their Role(s) in Food Webs and Marine Processes. *Pages 73–153 of:* Barnes, M. (ed), *Oceanography and Marine Biology: An Annual Review*, vol. 28. Aberdeen University Press.

Decho, A.W. 2000. Microbial Biofilms in Intertidal Systems: An Overview. *Cont. Shelf Res.*, **20**(10-11), 1257–1273.

Decho, A.W. 2010. Overview of Biopolymer-Induced Mineralization: What Goes on in Biofilms? *Ecol. Eng.*, **36**(2), 137–144.

Demichelis, R., Raiteri, P., Gale, J.D., Quigley, D., & Gebauer, D. 2011. Stable Prenucleation Mineral Clusters Are Liquid-Like Ionic Polymers. *Nat. Commun.*, **2**, 1–8.

Di Martino, P. 2018. Extracellular Polymeric Substances, a Key Element in Understanding Biofilm Phenotype. *AIMS Microbiology*, **4**(2), 274–288.

Di Profio, G., Salehi, S.M., Caliandro, R., Guccione, P., Nico, G., Curcio, E., & Fontananova, E. 2016. Bioinspired Synthesis of $CaCO_3$ Superstructures through a Novel Hydrogel Composite Membranes Mineralization Platform: A Comprehensive View. *Adv. Mater.*, **28**(4), 610–616.

Diaz, M.R., Eberli, G.P., Blackwelder, P., Phillips, B., & Swart, P.K. 2017. Microbially Mediated Organomineralization in the Formation of Ooids. *Geology*, **45**(9), 771–774.

Didymus, J.M., Young, J.R., & Mann, S. 1994. Construction and Morphogenesis of the Chiral Ultrastructure of Coccoliths from the Marine Alga *Emiliania huxleyi*. *Proc. Royal Soc. B*, **258**(1353), 237–245.

Donald, A.M., & Windle, A.H. 1992. *Liquid Crystalline Polymers*. Cambridge: Cambridge University Press.

Dorvee, J.R., Boskey, A.L., & Estroff, L.A. 2012. Rediscovering Hydrogel-Based Double-Diffusion Systems for Studying Biomineralization. *CrystEngComm*, **14**(18), 5681–5700.

Douglas, S., & Beveridge, T.J. 1998. Mineral Formation by Bacteria in Natural Microbial Communities. *FEMS Microbiol. Ecol.*, **26**(2), 79–88.

Dubey, D.K., & Tomar, V. 2010. Role of Molecular Level Interfacial Forces in Hard Biomaterial Mechanics: A Review. *Ann. Biomed. Eng.*, **38**(6), 2040–2055.

Dubochet, J. 2007. The Physics of Rapid Cooling and Its Implications for Cryoimmobilization of Cells. *Pages 7–21 of: Methods in Cell Biology*, vol. 79. Academic Press.

Dunlop, J.W.C., & Fratzl, P. 2010. Biological composites. *Pages 1–24 of:* Clarke, D. R., Ruhle, M., & Zok, F. (eds), *Annual Review of Materials Research, Vol 40*. Annual Review of Materials Research, vol. 40. Palo Alto: Annual Reviews.

Dunlop, J.W.C., & Fratzl, P. 2013. Multilevel Architectures in Natural Materials. *Scr. Mater.*, **68**(1), 8–12.

Dupraz, C., & Visscher, P.T. 2005. Microbial Lithification in Marine Stromatolites and Hypersaline Mats. *Trends Microbiol.*, **13**(9), 429–438.

Dupraz, C., Reid, R.P., Braissant, O., Decho, A.W., Norman, R.S., & Visscher, P.T. 2009. Processes of Carbonate Precipitation in Modern Microbial Mats. *Earth Sci Rev.*, **96**(3), 141–162.

Durak, G.M., Laumann, M., Wolf, S.L.P., Pawar, A., Gebauer, D., & Böttcher, T. 2019. Pseudo-Biomineralization: Complex Mineral Structures Shaped by Microbes. *ACS Biomaterials Science & Engineering*, **5**(10), 5088–5096.

Eboigbodin, K.E., & Biggs, C.A. 2008. Characterization of the Extracellular Polymeric Substances Produced by *Escherichia coli* Using Infrared Spectroscopic, Proteomic, and Aggregation Studies. *Biomacromolecules*, **9**(2), 686–695.

Edelmann, L. 1986. Freeze-Dried Embedded Specimens for Biological Microanalysis. *Scan Electron Microsc*, 1337–1356.

Edvardsen, B., Eikrem, W., Green, J.C., Andersen, R.A., Moon-van der Staay, S.Y., & Medlin, L.K. 2000. Phylogenetic Reconstructions of the Haptophyta Inferred from 18S Ribosomal DNA Sequences and Available Morphological Data. *Phycologia*, **39**(1), 19–35.

Elhadj, S., De Yoreo, J.J., Hoyer, J.R., & Dove, P.M. 2006. Role of Molecular Charge and Hydrophilicity in Regulating the Kinetics of Crystal Growth. *Proc. Natl. Acad. Sci.*, **103**(51), 19237–19242.

Elwell, D., & Scheel, H.J. 1975. *Crystal Growth from High-Temperature Solutions*. Academic Press.

Ercole, C., Cacchio, P., Botta, A.L., Centi, V., & Lepidi, A. 2007. Bacterially Induced Mineralization of Calcium Carbonate: The Role of Exopolysaccharides and Capsular Polysaccharides. *Microsc. Microanal.*, **13**(1), 42–50.

Ercole, C., Bozzelli, P., Altieri, F., Cacchio, P., & Del Gallo, M. 2012. Calcium Carbonate Mineralization: Involvement of Extracellular Polymeric Materials Isolated from Calcifying Bacteria. *Microsc. Microanal.*, **18**(4), 829–839.

Erez, J. 1978. Vital Effect on Stable-Isotope Composition Seen in Foraminifera and Coral Skeletons. *Nature*, **273**(5659), 199–202.

Erez, J. 2003. The Source of Ions for Biomineralization in Foraminifera and Their Implications for Paleoceanographic Proxies. *Rev. Mineral. Geochem.*, **54**(1), 115–149.

Escaig, J. 1982. New Instruments Which Facilitate Rapid Freezing at 83 K and 6 K. *J. Microsc.*, **126**(3), 221–229.

Evans, D., Müller, W., & Erez, J. 2018. Assessing Foraminifera Biomineralisation Models through Trace Element Data of Cultures under Variable Seawater Chemistry. *Geochim. Cosmochim. Acta*, **236**, 198–217.

Fabritius, H., Walther, P., & Ziegler, A. 2005. Architecture of the Organic Matrix in the Sternal $CaCO_3$ Deposits of *Porcellio scaber* (Crustacea, Isopoda). *J. Struct. Biol.*, **150**(2), 190–199.

Fagerbakke, K.M., Heldal, M., Norland, S., Heimdal, B.R., & Båtvik, H. 1994. *Emiliania huxleyi*. Chemical Composition and Size of Coccoliths from Enclosure Experiments and a Norwegian Fjord. *Sarsia*, **79**(4), 349–355.

Falini, G., Albeck, S., Weiner, S., & Addadi, L. 1996. Control of Aragonite or Calcite Polymorphism by Mollusk Shell Macromolecules. *Science*, **271**(5245), 67–69.

Falini, G., Weiner, S., & Addadi, L. 2003. Chitin-Silk Fibroin Interactions: Relevance to Calcium Carbonate Formation in Invertebrates. *Calcif. Tissue Int.*, **72**(5), 548–554.

Fehrenbacher, J.S., Russell, A.D., Davis, C.V., Gagnon, A.C., Spero, H.J., Cliff, J.B., Zhu, Z., & Martin, P. 2017. Link between Light-Triggered Mg-Banding and Chamber Formation in the Planktic Foraminifera *Neogloboquadrina dutertrei*. *Nat. Commun.*, **8**(1), 15441.

Fernández-Díaz, L., Astilleros, J.M., & Pina, C.M. 2006. The Morphology of Calcite Crystals Crown in A Porous Medium Doped with Divalent Cations. *Chem. Geol.*, **225**(3), 314–321.

Ferrill, D.A., Morris, A.P., Evans, M.A., Burkhard, M., Groshong, R.H., & Onasch, C.M. 2004. Calcite Twin Morphology: A Low-Temperature Deformation Geothermometer. *J. Struct. Geol.*, **26**(8), 1521–1529.

Fincham, A.G., & Simmer, J.P. 2007. Amelogenin Proteins of Developing Dental Enamel. *Pages 118–134 of:* Chadwick, D. J., & Cardew, G. (eds), *Ciba Foundation Symposium 205 - Dental Enamel*.

Fishman, M.R., Giglio, K., Fay, D., & Filiatrault, M.J. 2018. Physiological and Genetic Characterization of Calcium Phosphate Precipitation by *Pseudomonas* Species. *Sci. Rep.*, **8**, 14.

Flemming, H.C., & Wingender, J. 2010. The Biofilm Matrix. *Nat. Rev. Microbiol.*, **8**(9), 623–633.

Flemming, H.C., Leis, A., & Wingender, J. 2004. Biofilm and the Role of Extracellular Polymeric Substance. *Pages 86–142 of:* Jordan, R., Williams, D., & Charaf, U. (eds), *Advances in Biofilm Science and Engineering*. Bozeman, MT: Cytergy.

Flemming, H.C., Neu, T.R., & Wozniak, D.J. 2007. The EPS Matrix: The "House of Biofilm Cells". *J. Bacteriol.*, **189**(22), 7945–7947.

Flemming, H.C., Wingender, J., Szewzyk, U., Steinberg, P., Rice, S.A., & Kjelleberg, S. 2016a. Biofilms: An Emergent Form of Bacterial Life. *Nat. Rev. Microbiol.*, **14**, 563.

Flemming, H.C., Neu, T.R., & Wingender, J. 2016b. *The Perfect Slime: Microbial Extracellular Polymeric Substances (EPS)*. IWA Publishing.

Floquet, N., & Vielzeuf, D. 2011. Mesoscale twinning and crystallographic registers in biominerals. *American Mineralogist*, **96**(8-9), 1228–1237.

Fortin, D., Ferris, F.G., & Beveridge, T.J. 1997. Surface-Mediated Mineral Development by Bacteria. *Rev. Mineral. Geochem.*, **35**, 161–180.

Frank, F.C. 1949. The Influence of Dislocations on Crystal Growth. *Discuss. Faraday Soc.*, **5**(0), 48–54.

Frankel, R.B., & Bazylinski, D.A. 2003. Biologically Induced Mineralization by Bacteria. *Biomineralization*, **54**, 95–114.

Fratzl, P., & Weinkamer, R. 2007. Nature's Hierarchical Materials. *Prog. Mater. Sci.*, **52**(8), 1263–1334.

Frenkel, J. 1939. A General Theory of Heterophase Fluctuations and Pretransition Phenomena. *J. Chem. Phys.*, **7**(7), 538–547.

Frølich, S., Sørensen, H.O., Hakim, S.S., Marin, F., Stipp, S.L.S., & Birkedal, H. 2015. Smaller Calcite Lattice Deformation Caused by Occluded Organic Material in Coccoliths Than in Mollusk Shell. *Cryst. Growth Des.*, **15**(6), 2761–2767.

Gal, A., Habraken, W., Gur, D., Fratzl, P., Weiner, S., & Addadi, L. 2013. Calcite Crystal Growth by a Solid-State Transformation of Stabilized Amorphous Calcium Carbonate Nanospheres in a Hydrogel. *Angew. Chem., Int. Ed.*, **52**(18), 4867–4870.

Gal, A., Kahil, K., Vidavsky, N., DeVol, R.T., Gilbert, P.U.P.A., Fratzl, P., Weiner, S., & Addadi, L. 2014. Particle Accretion Mechanism Underlies Biological Crystal Growth from an Amorphous Precursor Phase. *Adv. Funct. Mater.*, **24**(34), 5420–5426.

Gallagher, K.L., Dupraz, C., Braissant, O., Norman, R.S., Decho, A.W., & Visscher, P.T. 2010. Mineralization of Sedimentary Biofilms: Modern Mechanistic Insights. *In:* Bailey, WIlliam C. (ed), *Biofilms: Formation, Development and Properties*. Biotechnology in Agriculture, Industry and Medicine. Nova Science Publishers.

García-Ruiz, J.M.and Otálora, F. 1992. Concentration Distribution around a Crystal Growing under Diffusional Control; a Computer Simulation. *J. Cryst. Growth*, **118**(1), 160–162.

García-Ruiz, J.M. 1991. The Uses of Crystal Growth in Gels and Other Diffusing-Reacting Systems. *Key Eng. Mater.*, **58**, 87–106.

García-Ruiz, J.M., & Otálora, F. 1993. Fluid Patterns in the Diffusive Field around a Growing Crystal. *J. Cryst. Growth*, **128**(1), 163–166.

Gaspard, D., Marin, F., Guichard, N., Morel, S., Alcaraz, G., & Luquet, G. 2007. Shell Matrices of Recent Rhynchonelliform Brachiopods: Microstructures and Glycosylation Studies. *Earth Environ. Sci. Trans. R. Soc. Edinb.*, **98**(3-4), 415–424.

Gaspard, D., Marie, B., Luquet, G., & Marin, F. 2008. Biochemical Characteristics of the Soluble Organic Matrix from the Shell of Three Recent Terebratulid Brachiopod Species. *Fossils and Strata*, **54**, 269–275.

Gavira, J.A., & Garcia-Ruiz, J.M. 2002. Agarose as Crystallisation Media for Proteins Ii: Trapping of Gel Fibres into the Crystals. *Acta Crystallogr., Sect. D*, **58**(10 Part 1), 1653–1656.

Gebauer, D., & Cölfen, H. 2011. Prenucleation Clusters and Non-Classical Nucleation. *Nano Today*, **6**(6), 564–584.

Gebauer, D., Volkel, A., & Cölfen, H. 2008. Stable Prenucleation Calcium Carbonate Clusters. *Science*, **322**(5909), 1819–1822.

Gebauer, D., Gunawidjaja, P.N., Ko, J.Y.P., Bacsik, Z., Aziz, B., Liu, L.J., Hu, Y.F., Bergstrom, L., Tai, C.W., Sham, T.K., Eden, M., & Hedin, N. 2010. Proto-Calcite and Proto-Vaterite in Amorphous Calcium Carbonates. *Angew. Chem., Int. Ed.*, **49**(47), 8889–8891.

Gebauer, D., Kellermeier, M., Gale, J.D., Bergström, L., & Cölfen, H. 2014. Pre-Nucleation Clusters as Solute Precursors in Crystallisation. *Chem. Soc. Rev.*, **43**(7), 2348–2371.

Gebauer, D., Raiteri, P., Gale, J.D., & Cölfen, H. 2018. On Classical and Non-Classical Views on Nucleation. *Am. J. Sci.*, **318**(9), 969–988.

Gerasimenko, O.V., Gerasimenko, J.V., Tepikin, A.V., & Petersen, O.H. 1996. Calcium Transport Pathways in the Nucleus. *Eur. J. Phycol.*, **432**(1), 1–6.

Gibbs, J.W. 1876. On the Equilibrium of Heterogeneous Substances. *Transactions of the Connecticut Academy of Arts and Sciences*, **3**, 108–248.

Gibbs, J.W. 1878. On the Equilibrium of Heterogeneous Substances. *Transactions of the Connecticut Academy of Arts and Sciences*, **3**, 343–524.

Gilkey, J.C., & Staehelin, L.A. 1986. Advances in Ultrarapid Freezing for the Preservation of Cellular Ultrastructure. *J. Electron Microsc. Tech.*, **3**(2), 177–210.

Glas, M.S., Fabricius, K.E., de Beer, D., & Uthicke, S. 2012. The C_2, pH and Ca^{2+} Microenvironment of Benthic Foraminifera in a High CO_2 World. *PLOS ONE*, **7**(11), e50010.

Gliko, O., Neumaier, N., Pan, W., Haase, I., Fischer, M., Bacher, A., Weinkauf, S., & Vekilov, P.G. 2005. A Metastable Prerequisite for the Growth of Lumazine Synthase Crystals. *J. Am. Chem. Soc.*, **127**(10), 3433–3438.

Goetz, A.J., Steinmetz, D.R., Griesshaber, E., Zaefferer, S., Raabe, D., Kelm, K., Irsen, S., Sehrbrock, A., & Schmahl, W.W. 2011. Interdigitating Biocalcite Dendrites Form a 3-D Jigsaw Structure in Brachiopod Shells. *Acta Biomater.*, **7**(5), 2237–2243.

Goetz, A.J., Griesshaber, E., Abel, R., Fehr, T., Ruthensteiner, B., & Schmahl, W.W. 2014. Tailored Order: The Mesocrystalline Nature of Sea Urchin Teeth. *Acta Biomater.*, **10**(9), 3885–98.

Goldstein, S.T. 1999. Foraminifera: A Biological Overview. *Pages 37–55 of:* Sen G., Barun K. (ed), *Modern Foraminifera*. Dordrecht: Springer Netherlands.

Goleń, J., Tyszka, J., Bickmeyer, U., & Bijma, J. 2020. SiR-Actin-Labelled Granules in Foraminifera: Patterns, Dynamics, and Hypotheses. *Biogeosciences*, **17**(4), 995–1011.

González-Muñoz, M.T., Rodríguez-Navarro, C., Martínez-Ruiz, F., Arias, J.M., Merroun, M.L., & Rodríguez-Gallego, M. 2010. Bacterial Biomineralization: New Insights from *Myxococcus*-Induced Mineral Precipitation. *Geol. Soc. Spec. Publ.*, **336**(1), 31–50.

Gooday, A.J. 2003. Benthic Foraminifera (Protista) as Tools in Deep-Water Palaeoceanography: Environmental Influences on Faunal Characteristics. *Pages 1–90 of: Advances in Marine Biology*, vol. 46. Academic Press.

Gower, L.B., & Odom, D.J. 2000. Deposition of Calcium Carbonate Films by a Polymer-Induced Liquid-Precursor (PILP) Process. *J. Cryst. Growth*, **210**(4), 719–734.

Grasby, S.E. 2003. Naturally Precipitating Vaterite ($\mu CaCO_3$) Spheres: Unusual Carbonates Formed in an Extreme Environment. *Geochim. Cosmochim. Acta*, **67**(9), 1659–1666.

Grassmann, O., Müller, G., & Löbmann, P. 2002. Organic-Inorganic Hybrid Structure of Calcite Crystalline Assemblies Grown in a Gelatin Hydrogel Matrix: Relevance to Biomineralization. *Chem. Mater.*, **14**(11), 4530–4535.

Greiner, M., Yin, X., Fernández-Díaz, L., Griesshaber, E., Weitzel, F., Ziegler, A., Veintemillas-Verdaguer, S., & Schmahl, W.W. 2018. Combined Influence of Reagent Concentrations and Agar Hydrogel Strength on the Formation of Biomimetic Hydrogel-Calcite Composites. *Cryst. Growth Des.*, **18**(3), 1401–1414.

Gries, K., Heinemann, F., Gummich, M., Ziegler, A., Rosenauer, A., & Fritz, M. 2011. Influence of the Insoluble and Soluble Matrix of Abalone Nacre on the Growth of Calcium Carbonate Crystals. *Cryst. Growth Des.*, **11**(3), 729–734.

Griesshaber, E., Schmahl, W.W., Neuser, R., Pettke, T., Blum, M., Mutterlose, J., & Brand, U. 2007. Crystallographic Texture and Microstructure of Terebratulide Brachiopod Shell Calcite: An Optimized Materials Design with Hierarchical Architecture. *Am. Mineral.*, **92**(5-6), 722–734.

Griesshaber, E., Schmahl, W.W., Ubhi, H.S., Huber, J., Nindiyasari, F., Maier, B., & Ziegler, A. 2013. Homoepitaxial Meso- and Microscale Crystal Co-orientation and Organic Matrix Network Structure in *Mytilus edulis* Nacre and Calcite. *Acta Biomater.*, **9**(12), 9492–9502.

Griesshaber, E., Yin, X., Ziegler, A., Kelm, K., Checa, A., Eisenhauer, A., & Schmahl, W.W. 2017. Patterns of Mineral Organization in Carbonate Biological Hard Materials. *Pages 245–272 of:* Heuss-Aßbichler, S., Amthauer, G., & John, M. (eds), *Highlights in Applied Mineralogy*. Berlin, Boston: De Gruyter.

Grube, M., Gapes, J.R., & Schuster, K.C. 2002. Application of Quantitative IR Spectral Analysis of Bacterial Cells to Acetone–Butanol–Ethanol Fermentation Monitoring. *Anal. Chim. Acta*, **471**(1), 127–133.

Gupta, P., & Diwan, B. 2017. Bacterial Exopolysaccharide Mediated Heavy Metal Removal: A Review on Biosynthesis, Mechanism and Remediation Strategies. *Biotechnol. Rep.*, **13**, 58–71.

Gussone, N., Langer, G., Thoms, S., Nehrke, G., Eisenhauer, A., Riebesell, U., & Wefer, G. 2006. Cellular Calcium Pathways and Isotope Fractionation in *Emiliania huxleyi*. *Geology*, **34**(8), 625–628.

Gussone, N., Filipsson, H.L., & Kuhnert, H. 2016. Mg/Ca, Sr/Ca and Ca Isotope Ratios in Benthonic Foraminifers Related to Test Structure, Mineralogy and Environmental Controls. *Geochim. Cosmochim. Acta*, **173**, 142–159.

Gómez-Morales, J., Torrent-Burgués, J., & Rodríguez-Clemente, R. 1996. Nucleation of Calcium Carbonate at Different Initial pH Conditions. *J. Cryst. Growth*, **169**(2), 331–338.

Hagino, K., & Okada, H. 2006. Intra- and Infra-Specific Morphological Variation in Selected Coccolithophore Species in the Equatorial and Subequatorial Pacific Ocean. *Mar. Micropaleontol.*, **58**(3), 184–206.

Hallam, A., & Perch-Nielsen, K. 1990. The Biotic Record of Events in the Marine Realm at the End of the Cretaceous - Calcareous, Siliceous and Organic-Walled Microfossils and Macroinvertebrates. *Tectonophysics*, **171**(1-4), 347–357.

Hammes, F., & Verstraete, W. 2002. Key Roles of Ph and Calcium Metabolism in Microbial Carbonate Precipitation. *Rev. Environ. Sci. Biotechnol.*, **1**(1), 3–7.

Hammes, F., Boon, N., de Villiers, J., Verstraete, W., & Siciliano, S.D. 2003. Strain-Specific Ureolytic Microbial Calcium Carbonate Precipitation. *Appl. Environ. Microbiol.*, **69**(8), 4901–4909.

Hammond, C. 2015. *The Basics of Crystallography and Diffraction*. Oxford University Press.

Han, W., Jiao, H., & Fox, D. 2018. Scanning Electron Microscopy. *Pages 35–68 of:* Wang, R., Wang, C., Zhang, H., Tao, J., & Bai, X. (eds), *Progress in Nanoscale Characterization and Manipulation*. Singapore: Springer Singapore.

Hansen, H.J. 1999. Shell Construction in Modern Calcareous Foraminifera. *Pages 57–70 of:* Sen G., Barun K. (ed), *Modern Foraminifera*. Dordrecht: Springer Netherlands.

Harper, E.M., & Checa, A. 2017. Physiological Versus Biological Control in Bivalve Calcite Prisms: Comparison of Euheterodonts and Pteriomorphs. *Biol. Bull.*, **232**(1), 19–29.

Hartman, P., & Perdok, W.G. 1955a. On the Relations between Structure and Morphology of Crystals. I. *Acta Crystallogr.*, **8**(1), 49–52.

Hartman, P., & Perdok, W.G. 1955b. On the Relations between Structure and Morphology of Crystals. II. *Acta Crystallogr.*, **8**(9), 521–524.

Hartman, P., & Perdok, W.G. 1955c. On the Relations between Structure and Morphology of Crystals. III. *Acta Crystallogr.*, **8**(9), 525–529.

Harvey, W.R., & Wieczorek, H. 1997. Animal Plasma Membrane Energization by Chemiosmotic H^+ V-ATPases. *J. Exp. Biol.*, **200**, 203–216.

Heijnen, W.M.M. 1985. The Morphology of Gel Grown Calcite. *N. Jb. Miner. Mh.*, 357–371.

Heinemann, F., Launspach, M., Gries, K., & Fritz, M. 2011. Gastropod Nacre: Structure, Properties and Growth - Biological, Chemical and Physical Basics. *Biophys. Chem.*, **153**(2-3), 126–153.

Hemleben, C., Bé, A.W.H., Anderson, O.R., & Tuntivate, S. 1977. Test Morphology, Organic Layers and Chamber Formation of the Planktonic Foraminifer *Globorotalia menardii* (D'orbigny). *J. Foraminiferal Res.*, **7**(1), 1–25.

Hemleben, C., Erson, O.R., Berthold, W., & Spindler, M. 1986. Calcification and Chamber Formation in Foraminifera - a Brief Overview. *In:* Leadbeater, B. S. C., & Riding, R. (eds), *Biomineralization in Lower Plants and Animals*. Oxford: Clarendon Press.

Hemleben, C., Spindler, M., & Anderson, O.R. 1989. *Modern Planktonic Foraminifera*. New York, NY: Springer New York.

Henisch, H.K. 1988. *Crystals in Gels and Liesegang Rings*. New York: Cambridge University Press.

Henisch, H.K., & García-Ruiz, J.M. 1986a. Crystal-Growth in Gels and Liesegang Ring Formation 1. Diffusion Relationships. *J. Cryst. Growth*, **75**(2), 195–202.

Henisch, H.K., & García-Ruiz, J.M. 1986b. Crystal-Growth in Gels and Liesegang Ring Formation 2.Crystallization Criteria and Successive Precipitation. *J. Cryst. Growth*, **75**(2), 203–211.

Henriksen, K., Stipp, S.L.S., Young, J.R., & Marsh, M.E. 2004. Biological Control on Calcite Crystallization: AFM Investigation of Coccolith Polysaccharide Function. *Am. Mineral.*, **89**(11-12), 1709–1716.

Henzler, K., Fetisov, E.O., Galib, M., Baer, M.D., Legg, B.A., Borca, C., Xto, J.M., Pin, S., Fulton, J.L., Schenter, G.K., Govind, N., Siepmann, J.I., Mundy, C.J., Huthwelker, T., & De Yoreo, J.J. 2018. Supersaturated Calcium Carbonate Solutions Are Classical. *Sci. Adv.*, **4**(1), eaao6283.

HobleyHobley, L., Harkins, C., MacPhee, C.E., & Stanley-Wall, N.R. 2015. Giving Structure to the Biofilm Matrix: An Overview of Individual Strategies and Emerging Common Themes. *FEMS Microbiol. Rev.*, **39**(5), 649–669.

Hoffmann, R., Wochnik, A.S., Betzler, S.B., Matich, S., Griesshaber, E., Schmahl, W.W., & Scheu, C. 2014a. TEM Preparation Methods and Influence of Radiation Damage on the Beam Sensitive $CaCO_3$ Shell of *Emiliania huxleyi*. *Micron*, **62**, 28–36.

Hoffmann, R., Wochnik, A.S., Heinzl, C., Betzler, S.B., Matich, S., Griesshaber, E., Schulz, H., Kucera, M., Young, J.R., Scheu, C., & Schmahl, W.W. 2014b. Nanoprobe Crystallographic Orientation Studies of Isolated Shield Elements of the Coccolithophore Species *Emiliania huxleyi*. *Eur. J. Mineral.*, **26**(4), 473–483.

Hoffmann, R., Kirchlechner, C., Langer, G., Wochnik, A.S., Griesshaber, E., Schmahl, W.W., & Scheu, C. 2015. Insight into *Emiliania huxleyi* Coccospheres by Focused Ion Beam Sectioning. *Biogeosciences*, **12**(3), 825–834.

Holtz, L.M., Thoms, S., Langer, G., & Wolf-Gladrow, D.A. 2013. Substrate Supply for Calcite Precipitation in *Emiliania huxleyi*: Assessment of Different Model Approaches. *J. Phycol.*, **49**(2), 417–426.

Holzmann, M., & Pawlowski, J. 2002. Freshwater Foraminiferans from Lake Geneva: Past and Present. *J. Foraminiferal Res.*, **32**(4), 344–350.

Holzmann, M., Habura, A., Giles, H., Bowser, S.S., & Pawlowski, J. 2003. Freshwater Foraminiferans Revealed by Analysis of Environmental DNA Samples. *J. Eukaryot. Microbiol.*, **50**(2), 135–139.

Hottinger, L. 2006. The Depth-Depending Ornamentation of Some Lamellar-Perforate Foraminifera. *Symbiosis*, **42**, 141–151.

Huang, Y.X., Buder, J., Cardoso-Gil, R., Prots, Y., Carrillo-Cabrera, W., Simon, P., & Kniep, R. 2008. Shape Development and Structure of a Complex (Otoconia-Like?) Calcite-Gelatine Composite. *Angew. Chem., Int. Ed.*, **47**(43), 8280–8284.

Huber, J., Griesshaber, E., Nindiyasari, F., Schmahl, W.W., & Ziegler, A. 2015. Functionalization of Biomineral Reinforcement in Crustacean Cuticle: Calcite Orientation in the Partes Incisivae of the Mandibles of *Porcellio scaber* and the Supralittoral Species *Tylos europaeus* (Oniscidea, Isopoda). *J. Struct. Biol.*, **190**(2), 173–191.

Hunter, G.K., Allen, B.L., Grynpas, M.D., & Cheng, P.T. 1985. Inhibition of Hydroxyapatite Formation in Collagen Gels by Chondroitin Sulfate. *Biochem. J.*, **228**(2), 463–469.

Höhn, K., Sailer, M., Wang, L., Lorenz, M., Schneider, M.E., & Walther, P. 2011. Preparation of Cryofixed Cells for Improved 3D Ultrastructure with Scanning Transmission Electron Tomography. *Histochem. Cell Biol.*, **135**, 1–9.

Iglesias-Rodríguez, M.D., Halloran, P.R., Rickaby, R.E.M., Hall, I.R., Colmenero-Hidalgo, E., Gittins, J.R., Green, D.R.H., Tyrrell, T., Gibbs, S.J., von Dassow, P., Rehm, E., Armbrust, E.V., & Boessenkool, K.P. 2008. Phytoplankton Calcification in a High-CO_2 World. *Science*, **320**(5874), 336–340.

Jacob, D. E., Wirth, R., Agbaje, O. B. A., Branson, O., & Eggins, S. M. 2017. Planktic Foraminifera Form Their Shells Via Metastable Carbonate Phases. *Nature Communications*, **8**(1), 1265.

Jones, B., & Peng, X. 2012. Amorphous Calcium Carbonate Associated with Biofilms in Hot Spring Deposits. *Sediment. Geol.*, **269-270**, 58–68.

Jope, M. 1967a. The Protein of Brachiopod Shell-I. Amino Acid Composition and Implied Protein Taxonomy. *Comp. Biochem. Physiol.*, **20**(2), 593–600.

Jope, M. 1967b. The Protein of Brachiopod Shell-II. Shell Protein from Fossil Articulates: Amino Acid Composition. *Comp. Biochem. Physiol.*, **20**(2), 601–605.

Kashchiev, D. 2020. Classical Nucleation Theory Approach to Two-Step Nucleation of Crystals. *J. Cryst. Growth*, **530**, 125300.

Kashchiev, D., & van Rosmalen, G.M. 2003. Review: Nucleation in Solutions Revisited. *Cryst. Res. Technol.*, **38**(7-8), 555–574.

Kellenberger, E., Johansen, R., Maeder, M., Bohrmann, B., Stauffer, E., & Villiger, W. 1992. Artefacts and Morphological Changes During Chemical Fixation. *J. Microsc.*, **168**(2), 181–201.

Kelly, A., & Knowles, K.M. 2012. Twinning. *Pages 335–361 of:* Kelly, A., & Knowles, K.M. (eds), *Crystallography and Crystal Defects*. Wiley Online Books.

Kennedy, W.J., Taylor, J.D., & Hall, A. 1969. Environmental and Biological Controls on Bivalve Shell Mineralogy. *Biol. Rev.*, **44**(4), 499–530.

Kim, Y.-Y., Semsarilar, M., Carloni, J.D., Cho, K.R., Kulak, A.N., Polishchuk, I., Hendley IV, C.T., Smeets, P.J.M., Fielding, L.A., Pokroy, B., Tang, C.C., Estroff, L.A., Baker, S.P., Armes, S.P., & Meldrum, F.C. 2016. Structure and Properties of Nanocomposites Formed by the Occlusion of Block Copolymer Worms and Vesicles within Calcite Crystals. *Adv. Funct. Mater.*, **26**(9), 1382–1392.

Kim, Y.Y., Ribeiro, L., Maillot, F., Ward, O., Eichhorn, S.J., & Meldrum, F.C. 2010. Bio-Inspired Synthesis and Mechanical Properties of Calcite-Polymer Particle Composites. *Adv. Mater.*, **22**(18), 2082–2086.

Kim, Y.Y., Schenk, A.S., Ihli, J., Kulak, A.N., Hetherington, N.B.J., Tang, C.C., Schmahl, W.W., Griesshaber, E., Hyett, G., & Meldrum, F.C. 2014. A Critical Analysis of Calcium Carbonate Mesocrystals. *Nat. Commun.*, **5**, 1–14.

Klaveness, D. 1972. *Coccolithus huxleyi* (Lohmann) Kamptn. I. Morphological Investigations on the Vegetative Cell and the Process of Coccolith Formation. *Protistologica*, **8**(3), 335–346.

Klock, J.-H., Wieland, A., Seifert, R., & Michaelis, W. 2007. Extracellular Polymeric Substances (EPS) from Cyanobacterial Mats: Characterisation and Isolation Method Optimisation. *Mar. Biol.*, **152**(5), 1077–1085.

Knoll, A.H. 2003. Biomineralization and Evolutionary History. *Biomineralization*, **54**, 329–356.

Kobayashi, I., & Akai, J. 1994. Twinned Aragonite Crystals Found in the Bivalvian Crossed Lamellar Shell Structure. *J. Geol. Soc. Japan.*, **100**(2), 177–180.

Kogure, T., Suzuki, M., Kim, H., Mukai, H., Checa, A.G., Sasaki, T., & Nagasawa, H. 2014. Twin Density of Aragonite in Molluscan Shells Characterized Using X-Ray Diffraction and Transmission Electron Microscopy. *J. Cryst. Growth*, **397**, 39–46.

Koide, T., & Nagata, K. 2005. Collagen Biosynthesis. *Pages 85–114 of:* Brinckmann, J., Notbohm, H., & Müller, P. K. (eds), *Collagen - Primer in Structure, Processing and Assembly*, 1 edn. Springer-Verlag Berlin Heidelberg.

Konhauser, K.O. 1998. Diversity of Bacterial Iron Mineralization. *Earth Sci Rev.*, **43**(3), 91–121.

Konhauser, K.O. 2007. *Introduction to Geomicrobiology*. UK: Blackwell Publishing.

Kossel, W. 1927. Zur Theorie des Kristallwachstums. *Nachrichten von der Gesellschaft der Wissenschaften zu Göttingen, Mathematisch-Physikalische Klasse*, 135–143.

Kralj, D., Brečević, L., & Nielsen, A.E. 1994. Vaterite Growth and Dissolution in Aqueous Solution II. Kinetics of Dissolution. *J. Cryst. Growth*, **143**(3), 269–276.

Kulak, A.N., Iddon, P., Li, Y.T., Armes, S.P., Cölfen, H., Paris, O., Wilson, R.M., & Meldrum, F.C. 2007. Continuous Structural Evolution of Calcium Carbonate Particles: A Unifying Model of Copolymer-Mediated Crystallization. *J. Am. Chem. Soc.*, **129**(12), 3729–3736.

Kumar, M.R., Merschrod S, E.F., & Poduska, K.M. 2011. Collagen-Membrane-Induced Calcium Phosphate Electrocrystallization. *Cryst. Growth Des.*, **11**(1), 26–28.

Kunitake, Miki E., Mangano, Lauren M., Peloquin, John M., Baker, Shefford P., & Estroff, Lara A. 2013. Evaluation of Strengthening Mechanisms in Calcite Single Crystals from Mollusk Shells. *Acta Biomater.*, **9**(2), 5353–5359.

Langer, G., Sadekov, A., Thoms, S., Mewes, A., Nehrke, G., Greaves, M., Misra, S., Bijma, J., & Elderfield, H. 2015. Li Partitioning in the Benthic Foraminifera *Amphistegina lessonii*. *Geochem. Geophys. Geosyst.*, **16**(12), 4275–4279.

Langer, M.R. 2008. Assessing the Contribution of Foraminiferan Protists to Global Ocean Carbonate Production. *J. Eukaryot. Microbiol.*, **55**(3), 163–169.

Lee, J.J., & Anderson, O.R. 1991. Symbiosis in Foraminifera. *Pages 157–220 of:* Lee, J. J., & Anderson, O. R. (eds), *Biology of Foraminifera*. London: Academic Press.

Lejzerowicz, F., Pawlowski, J., Fraissinet-Tachet, L., & Marmeisse, R. 2010. Molecular Evidence for Widespread Occurrence of Foraminifera in Soils. *Environ. Microbiol.*, **12**(9), 2518–2526.

Levi, A., Müller, W., & Erez, J. 2019. Intrashell Variability of Trace Elements in Benthic Foraminifera Grown under High CO_2 Levels. *Front. Earth Sci.*, **7**(247).

Levi, A.C., & Kotrla, M. 1997. Theory and Simulation of Crystal Growth. *J. Phys.: Condens. Matter*, **9**(2), 299–344.

Levi-Kalisman, Y., Falini, G., Addadi, L., & Weiner, S. 2001. Structure of the Nacreous Organic Matrix of a Bivalve Mollusk Shell Examined in the Hydrated State Using Cryo-TEM. *J. Struct. Biol.*, **135**(1), 8–17.

Li, H.Y., & Estroff, L.A. 2007. Porous Calcite Single Crystals Grown from a Hydrogel Medium. *CrystEngComm*, **9**(12), 1153–1155.

Li, H.Y., & Estroff, L.A. 2009. Calcite Growth in Hydrogels: Assessing the Mechanism of Polymer-Network Incorporation into Single Crystals. *Adv. Mater.*, **21**(4), 470–473.

Li, H.Y., Xin, H.L., Kunitake, M.E., Keene, E.C., Muller, D.A., & Estroff, L.A. 2011a. Calcite Prisms from Mollusk Shells (*Atrina rigida*): Swiss-Cheese-Like Organic-Inorganic Single-Crystal Composites. *Adv. Funct. Mater.*, **21**(11), 2028–2034.

Li, H.Y., Fujiki, Y., Sada, K., & Estroff, L.A. 2011b. Gel Incorporation inside of Organic Single Crystals Grown in Agarose Hydrogels. *CrystEngComm*, **13**(4), 1060–1062.

Li, L., & Ortiz, C. 2014. Pervasive Nanoscale Deformation Twinning as a Catalyst for Efficient Energy Dissipation in a Bioceramic Armour. *Nat. Mater.*, **13**(5), 501–507.

Li, M., & Dincă, M. 2015. On the Mechanism of MOF-5 Formation under Cathodic Bias. *Chem. Mater.*, **27**(9), 3203–3206.

Lian, B., Hu, Q., Chen, J., Ji, J., & Teng, H.H. 2006. Carbonate Biomineralization Induced by Soil Bacterium *Bacillus megaterium*. *Geochim. Cosmochim. Acta*, **70**(22), 5522–5535.

Lin, A., & Meyers, M.A. 2005. Growth and Structure in Abalone Shell. *Mater. Sci. Eng.: A*, **390**(1), 27–41.

Lippmann, F. 1973. *Sedimentary Carbonate Minerals*. Minerals, Rocks and Mountains, no. 6. Springer-Verlag Berlin Heidelberg.

Lipps, J.H. 1973. Test Structure in Foraminifera. *Annu. Rev. Microbiol.*, **27**(1), 471–486.

Lloyd, G.E. 1987. Atomic Number and Crystallographic Contrast Images with the SEM: A Review of Backscattered Electron Techniques. *Mineral. Mag.*, **51**(359), 3–19.

Loaëc, M., Olier, R., & Guezennec, J. 1997. Uptake of Lead, Cadmium and Zinc by a Novel Bacterial Exopolysaccharide. *Water Res.*, **31**(5), 1171–1179.

Loeblich, A.R., & Tappan, H. 1988. Systematic Descriptions. *Pages 7–691 of: Foraminiferal Genera and Their Classification*. Boston, MA: Springer US.

Lohbeck, K.T., Riebesell, U., & Reusch, T.B.H. 2012. Adaptive Evolution of a Key Phytoplankton Species to Ocean Acidification. *Nat. Geosci.*, **5**(5), 346–351.

Lohbeck, K.T., Riebesell, U., & Reusch, T.B.H. 2014. Gene Expression Changes in the Coccolithophore *Emiliania huxleyi* after 500 Generations of Selection to Ocean Acidification. *Proc. Royal Soc. B*, **281**(1786), 7.

Lopez-Berganza, J.A., Song, R., Elbanna, A., & Espinosa-Marzal, R.M. 2017. Calcium Carbonate with Nanogranular Microstructure Yields Enhanced Toughness. *Nanoscale*, **9**(43), 16689–16699.

Lopez-Berganza, J.A., Chen, S., & Espinosa-Marzal, R.M. 2019. Tailoring Calcite Growth through an Amorphous Precursor in a Hydrogel Environment. *Cryst. Growth Des.*, **19**(6), 3192–3205.

Lowenstam, H.A. 1981. Minerals Formed by Organisms. *Science*, **211**(4487), 1126–1131.

Lowenstam, H.A., & Abbott, D.P. 1975. Vaterite: A Mineralization Product of the Hard Tissues of a Marine Organism (Ascidiacea). *Science*, **188**(4186), 363–365.

Lowenstam, H.A., & Weiner, S. 1989. *On Biomineralization*. New York: Oxford University Press.

Luft, J.H. 1961. Improvements in Epoxy Resin Embedding Methods. *J. Biophys. Biochem. Cytol.*, **9**(2), 409–414.

Mackinder, L., Wheeler, G., Schroeder, D., Riebesell, U., & Brownlee, C. 2010. Molecular Mechanisms Underlying Calcification in Coccolithophores. *Geomicrobiol. J.*, **27**(6-7), 585–595.

Mackinder, L., Wheeler, G., Schroeder, D., von Dassow, P., Riebesell, U., & Brownlee, C. 2011. Expression of Biomineralization-Related Ion Transport Genes in *Emiliania huxleyi*. *Environ. Microbiol.*, **13**(12), 3250–3265.

Mackinnon, D.I., & Williams, A. 1974. Shell Structure of Terebratulid Brachiopods. *Palaeontology*, **17**(1), 179–202.

Macías-Sánchez, E., Checa, A.G., & Willinger, M.G. 2015. The Transport System of Nacre Components through the Surface Membrane of Gastropods. *Key Eng. Mater.*, **672**, 103–112.

Maier, B.J., Griesshaber, E., Alexa, P., Ziegler, A., Ubhi, H.S., & Schmahl, W.W. 2014. Biological Control of Crystallographic Architecture: Hierarchy and Co-Alignment Parameters. *Acta Biomater.*, **10**(9), 3866–74.

Mandel, G.S., Halverson, P.B., Rathburn, M., & Mandel, N.S. 1990. Calcium Pyrophosphate Crystal Deposition: A Kinetic Study Using a Type I Collagen Gel Model. *Scanning Microsc.*, **4**(1), 175–180.

Mann, S. 1983. Mineralization in Biological Systems. Inorganic Elements in Biochemistry. Berlin, Heidelberg: Springer Berlin Heidelberg.

Mann, S. 1988. Molecular Recognition in Biomineralization. *Nature*, **332**(6160), 119–124.

Mann, S. 2001. *Biomineralization: Principles and Concepts in Bioinorganic Materials Chemistry*. 1 edn. Oxford Chemistry Masters. New York: Oxford University Press.

Mann, S., Didymus, J.M., Sanderson, N.P., Heywood, B.R., & Samper, E.J.A. 1990. Morphological Influence of Functionalized and Non-Functionalized α, ω-Dicarboxylates on Calcite Crystallization. *J. Chem. Soc. Faraday Trans.*, **86**(10), 1873–1880.

Marin, F., & Luquet, G. 2004. Molluscan Shell Proteins. *C. R. Palevol*, **3**(6-7), 469–492.

Marin, F., Luquet, G., Marie, B., & Medakovic, D. 2008. Molluscan Shell Proteins: Primary Structure, Origin, and Evolution. *Curr. Top. Dev. Biol.*, **80**, 209–276.

Marsh, M.E. 1994. Polyanion-Mediated Mineralization - Assembly and Reorganization of Acidic Polysaccharides in the Golgi System of a Coccolithophorid Alga During Mineral Deposition. *Protoplasma*, **177**(3-4), 108–122.

Marsh, M.E. 1999. Coccolith Crystals of Pleurochrysis Carterae: Crystallographic Faces, Organization, and Development. *Protoplasma*, **207**(1-2), 54–66.

Marsh, M.E. 2003. Regulation of $CaCO_3$ Formation in Coccolithophores. *Comp. Biochem. Physiol., Part B: Biochem. Mol. Biol.*, **136**(4), 743–754.

Marsh, M.E., Ridall, A.L., Azadi, P., & Duke, P.J. 2002. Galacturonomannan and Golgi-Derived Membrane Linked to Growth and Shaping of Biogenic Calcite. *J. Struct. Biol.*, **139**(1), 39–45.

Marvasi, M., Visscher, P.T., & Casillas Martinez, L. 2010. Exopolymeric Substances (EPS) from *Bacillus subtilis*: Polymers and Genes Encoding Their Synthesis. *FEMS Microbiol. Lett.*, **313**(1), 1–9.

Marxen, J.C., Hammer, M., Gehrke, T., & Becker, W. 1998. Carbohydrates of the Organic Shell Matrix and the Shell-Forming Tissue of the Snail *Biomphalaria glabrata* (Say). *Biol. Bull.*, **194**(2), 231–240.

Marxen, J.C., Becker, W., Finke, D., Hasse, B., & Epple, M. 2003. Early Mineralization in Biomphalaria Glabrata: Microscopic and Structural Results. *J. Molluscan Stud.*, **69**, 113–121.

McLean, R.J.C., Nickel, J.C., Beveridge, T.J., & Costerton, J.W. 1989. Observations of the Ultrastructure of Infected Kidney Stones. *J. Med. Microbiol.*, **29**(1), 1–7.

Meldrum, F.C. 2003. Calcium Carbonate in Biomineralisation and Biomimetic Chemistry. *Int. Mater. Rev.*, **48**(3), 187–224.

Meldrum, F.C., & Cölfen, H. 2008. Controlling Mineral Morphologies and Structures in Biological and Synthetic Systems. *Chem. Rev.*, **108**(11), 4332–4432.

Meldrum, F.C., & Sear, R.P. 2008. Now You See Them. *Science*, **322**(5909), 1802–1803.

Meryman, H.T. 2007. Cryopreservation of Living Cells: Principles and Practice. *Transfusion*, **47**(5), 935–945.

Metzler, R.A., Tribello, G.A., Parrinello, M., & Gilbert, P.U.P.A. 2010. Asprich Peptides Are Occluded in Calcite and Permanently Disorder Biomineral Crystals. *J. Am. Chem. Soc.*, **132**(33), 11585–11591.

Meyers, M.A., Chen, P.Y., Lin, A.Y.M., & Seki, Y. 2008. Biological Materials: Structure and Mechanical Properties. *Prog. Mater. Sci.*, **53**(1), 1–206.

Miller, A., Parker, S.B., Miller, A., Phillips, D.C., & Williams, R.J.P. 1984. Collagen: The Organic Matrix of Bone. *Philos. Trans. R. Soc. London, B*, **304**(1121), 455–477.

Milliman, J.D. 1993. Production and Accumulation of Calcium-Carbonate in the Ocean - Budget of a Nonsteady State. *Global Biogeochem. Cycles*, **7**(4), 927–957.

Mishra, A., & Jha, B. 2013. Microbial Exopolysaccharides. *Pages 179–192 of:* Rosenberg, E., DeLong, E. F., Lory, S., Stackebrandt, E., & Thompson, F. (eds), *The Prokaryotes: Applied Bacteriology and Biotechnology*. Berlin, Heidelberg: Springer Berlin Heidelberg.

Misogianes, M.J., & Chasteen, N.D. 1979. A Chemical and Spectral Characterization of the Extrapallial Fluid of *Mytilus edulis*. *Anal. Biochem.*, **100**(2), 324–334.

Mitov, M. 2017. Cholesteric Liquid Crystals in Living Matter. *Soft Matter*, **13**(23), 4176–4209.

Monteiro, F.M., Bach, L.T., Brownlee, C., Bown, P., Rickaby, R.E.M., Poulton, A.J., Tyrrell, T., Beaufort, L., Dutkiewicz, S., Gibbs, S., Gutowska, M.A., Lee, R., Riebesell, U., Young, J., & Ridgwell, A. 2016. Why Marine Phytoplankton Calcify. *Sci. Adv.*, **2**(7).

Moor, H., & Riehle, U. 1968. Snap Freezing under High Pressure: A New Fixation Technique for Freeze Etching. vol. 2.

Moor, H., Bellin, G., Sandri, C., & Akert, K. 1980. The Influence of High Pressure Freezing on Mammalian Nerve Tissue. *Cell Tissue Res.*, **209**(2), 201–216.

Mor Khalifa, G., Weiner, S., & Addadi, L. 2011. Mineral and Matrix Components of the Operculum and Shell of the Barnacle *Balanus amphitrite*: Calcite Crystal Growth in a Hydrogel. *Cryst. Growth Des.*, **11**(11), 5122–5130.

Mor Khalifa, G., Kahil, K., Erez, J., Kaplan Ashiri, I., Shimoni, E., Pinkas, I., Addadi, L., & Weiner, S. 2018. Characterization of Unusual Mgca Particles Involved in the Formation of Foraminifera Shells Using a Novel Quantitative Cryo SEM/EDS Protocol. *Acta Biomaterialia*, **77**, 342–351.

Moura, G., Vilarinho, L., Santos, A.C., & Machado, J. 2000. Organic Compounds in the Extrapalial Fluid and Haemolymph of *Anodonta cygnea* (L.) with Emphasis on the Seasonal Biomineralization Process. *Comp. Biochem. Physiol., Part B: Biochem. Mol. Biol.*, **125**(3), 293–306.

Muller, David A. 2009. Structure and Bonding at the Atomic Scale by Scanning Transmission Electron Microscopy. *Nat. Mater.*, **8**(4), 263–270.

Mullin, J.W. 2001. *Crystallization*. Elsevier Science.

Mutvei, H. 1978. Ultrastructural Characteristics of the Nacre in Some Gastropods. *Zool. Scr.*, **7**(1–4), 287–296.

Nagai, Y., Uematsu, K., Chen, C., Wani, R., Tyszka, J., & Toyofuku, T. 2018a. Weaving of Biomineralization Framework in Rotaliid Foraminifera: Implications for Paleoceanographic Proxies. *Biogeosciences*, **15**(22), 6773–6789.

Nagai, Y., Uematsu, K., Wani, R., & Toyofuku, T. 2018b. Reading the Fine Print: Ultra-Microstructures of Foraminiferal Calcification Revealed Using Focused Ion Beam Microscopy. *Front. Mar. Sci.*, **5**(67).

Nakahara, H. 1983. Calcification of Gastropod Nacre. *Pages 225–230 of:* Westbroek, P., & de Jong, E. W. (eds), *Biomineralization and Biological Metal Accumulation: Biological and Geological Perspectives Papers presented at the Fourth International Symposium on Biomineralization, Renesse, The Netherlands, June 2–5, 1982*. Dordrecht: Springer Netherlands.

Nakahara, H. 1991. Nacre Formation in Bivalve and Gastropod Molluscs. *Pages 343–350 of:* Suga, S., & Nakahara, H. (eds), *Mechanisms and Phylogeny of Mineralization in Biological Systems*. Tokyo: Springer Japan.

Nanakoudis, A. 2019. SEM: Types of Electrons and the Information They Provide. *Thermo Fisher Scientific, Microscopy Blog*.

Nehrke, G., Keul, N., Langer, G., de Nooijer, L.J., Bijma, J., & Meibom, A. 2013. A New Model for Biomineralization and Trace-Element Signatures of Foraminifera Tests. *Biogeosciences*, **10**(10), 6759–6767.

Neu, T.R., & Lawrence, J. R. 2016. The Extracellular Matrix - an Intractable Part of Biofilm Systems. *In:* Flemming, H. C., Neu, T. R., & Wingender, J. (eds), *The Perfect Slime: Microbial Extracellular Polymeric Substances (EPS)*. IWA Publishing.

Neville, A.C., & Luke, B.M. 1971. A Biological System Producing a Self-Assembling Cholesteric Protein Liquid Crystal. *J. Cell Sci.*, **8**(1), 93–109.

Nickl, H.J., & Henisch, H.K. 1969. Growth of Calcite Crystals in Gels. *J. Electrochem. Soc.*, **116**(9), 1258–1260.

Niederberger, M., & Cölfen, H. 2006. Oriented Attachment and Mesocrystals: Non-Classical Crystallization Mechanisms Based on Nanoparticle Assembly. *Phys. Chem. Chem. Phys.*, **8**(28), 3271–3287.

Nielsen, M.H., Aloni, S., & De Yoreo, J.J. 2014. In Situ TEM Imaging of $CaCO_3$ Nucleation Reveals Coexistence of Direct and Indirect Pathways. *Science*, **345**(6201), 1158–1162.

Nimer, N.A., & Merrett, M.J. 1992. Calcification and Utilization of Inorganic Carbon by the Coccolithophorid *Emiliania huxleyi* Lohmann. *New Phytol.*, **121**(2), 173–177.

Nimer, N.A., Brownlee, C., & Merrett, M.J. 1994. Carbon-Dioxide Availability, Intracellular pH and Growth-Rate of the Coccolithophore *Emiliania huxleyi*. *Mar. Ecol. Prog. Ser.*, **109**(2-3), 257–262.

Nindiyasari, F., Griesshaber, E., Fernández-Díaz, L., Astilleros, J.M., Sanchez-Pastor, N., Ziegler, A., & Schmahl, W.W. 2014a. Effects of Mg and Hydrogel Solid Content on the Crystallization of Calcium Carbonate in Biomimetic Counter-Diffusion Systems. *Cryst. Growth Des.*, **14**(9), 4790–4802.

Nindiyasari, F., Fernández-Díaz, L., Griesshaber, E., Astilleros, J.M., Sanchez-Pastor, N., & Schmahl, W.W. 2014b. Influence of Gelatin Hydrogel Porosity on the Crystallization of $CaCO_3$. *Cryst. Growth Des.*, **14**(4), 1531–1542.

Nindiyasari, F., Ziegler, A., Griesshaber, E., Fernández-Díaz, L., Huber, J., Walther, P., & Schmahl, W.W. 2015. Effect of Hydrogel Matrices on Calcite Crystal Growth Morphology, Aggregate Formation, and Co-orientation in Biomimetic Experiments and Biomineralization Environments. *Cryst. Growth Des.*, **15**(6), 2667–2685.

Nindiyasari, F., Fernández-Díaz, L., Yin, X., Greiner, M., Griesshaber, E., Tsige, M., Ziegler, A., & Schmahl, W.W. 2019. Influence of Gel-Strength and Magnesium Doping on the Organization of Calcite/Hydrogel Mesocrystal Composites. *Eur. J. Mineral.*, **31**(2), 217–229.

Nishikawa, S., & Kikuchi, S. 1928. Diffraction of Cathode Rays by Mica. *Nature*, **121**(3061), 1019–1020.

Nixon, H.R.F.M., Nixon, M., Young, J.Z., Allen, R.E., Young, J.Z., & Young, E.P.A.J.Z. 2003. *The Brains and Lives of Cephalopods*. OUP Oxford.

Normand, V., Lootens, D.L., Amici, E., Plucknett, K.P., & Aymard, P. 2000. New Insight into Agarose Gel Mechanical Properties. *Biomacromolecules*, **1**(4), 730–738.

North, A.J., Bardsley, W.G., Hyam, J., Bornslaeger, E.A., Cordingley, H.C., Trinnaman, B., Hatzfeld, M., Green, K.J., Magee, A.I., & Garrod, D.R. 1999. Molecular Map of the Desmosomal Plaque. *J. Cell Sci.*, **112**(23), 4325–4336.

Nudelman, F., Gotliv, B.A., Addadi, L., & Weiner, S. 2006. Mollusk Shell Formation: Mapping the Distribution of Organic Matrix Components Underlying a Single Aragonitic Tablet in Nacre. *J. Struct. Biol.*, **153**(2), 176–187.

Nudelman, F., Chen, H.H., Goldberg, H.A., Weiner, S., & Addadi, L. 2007. Spiers Memorial Lecture: Lessons from Biomineralization: Comparing the Growth Strategies of Mollusc Shell Prismatic and Nacreous Layers in *Atrina rigida*. *Faraday Discuss.*, **136**, 9–25.

Nwodo, U.U., Green, E., & Okoh, A.I. 2012. Bacterial Exopolysaccharides: Functionality and Prospects. *Int. J. Mol. Sci.*, **13**(11), 14002–14015.

Obst, M., Dynes, J.J., Lawrence, J.R., Swerhone, G.D.W., Benzerara, K., Karunakaran, C., Kaznatcheev, K., Tyliszczak, T., & Hitchcock, A.P. 2009. Precipitation of Amorphous $CaCO_3$ (Aragonite-Like) by Cyanobacteria: A STXM Study of the Influence of EPS on the Nucleation Process. *Geochim. Cosmochim. Acta*, **73**(14), 4180–4198.

Ohara, M., & Reid, R.C. 1973. *Modeling Crystal Growth Rates from Solution*. Prentice-Hall.

Oppenheimer-Shaanan, Y., Sibony-Nevo, O., Bloom-Ackermann, Z., Suissa, R., Steinberg, N., Kartvelishvily, E., Brumfeld, V., & Kolodkin-Gal, I. 2016. Spatio-Temporal Assembly of Functional Mineral Scaffolds within Microbial Biofilms. *NPJ Biofilms Microbiomes*, **2**, 15031.

Osuna-Mascaró, A.J., Cruz-Bustos, T., Marin, F., & Checa, A.G. 2015. Ultrastructure of the Interlamellar Membranes of the Nacre of the Bivalve *Pteria hirundo*, Determined by Immunolabelling. *PLOS ONE*, **10**(4).

Paasche, E. 1968. Effect of Temperature Light Intensity and Photoperiod on Coccolith Formation. *Limnol. Oceanogr.*, **13**(1), 178–181.

Paasche, E. 2001. A Review of the Coccolithophorid *Emiliania huxleyi* (Prymnesiophyceae), with Particular Reference to Growth, Coccolith Formation, and Calcification-Photosynthesis Interactions. *Phycologia*, **40**(6), 503–529.

Palmer, A.R. 1992. Calcification in Marine Molluscs: How Costly Is It? *Proc. Natl. Acad. Sci.*, **89**(4), 1379–1382.

Pan, J., Zhao, H., Tucker, M.E., Zhou, J., Jiang, M., Wang, Y., Zhao, Y., Sun, B., Han, Z., & Yan, H. 2019. Biomineralization of Monohydrocalcite Induced by the Halophile *Halomonas smyrnensis* WMS-3. *Minerals*, **9**(10), 632.

Paquette, J., & Reeder, R.J. 1995. Relationship between Surface Structure, Growth Mechanism, and Trace Element Incorporation in Calcite. *Geochim. Cosmochim. Acta*, **59**(4), 735–749.

Parker, F.S. 1983. *Applications of Infrared, Raman, and Resonance Raman Spectroscopy in Biochemistry*. New York: Plenum Press.

Parker, S.B., Skarnulis, A.J., Westbroek, P., & Williams, R.J.P. 1983. The Ultrastructure of Coccoliths from the Marine Alga *Emiliania huxleyi* (Lohmann) Hay and Mohler - an Ultrahigh Resolution Electron-Microscope Study. *Proc. Royal Soc. B*, **219**(1215), 111–117.

Pawlowski, J., Holzmann, M., Berney, C., Fahrni, J., Gooday, A.J., Cedhagen, T., Habura, A., & Bowser, S.S. 2003. The Evolution of Early Foraminifera. *Proc. Natl. Acad. Sci.*, **100**(20), 11494–11498.

Pease, D.C., & Porter, K.R. 1981. Electron Microscopy and Ultramicrotomy. *J. Cell Biol.*, **91**, 287s–292s.

Pellicer-Nàcher, C., Domingo-Félez, C., Mutlu, A.G., & Smets, B.F. 2013. Critical Assessment of Extracellular Polymeric Substances Extraction Methods from Mixed Culture Biomass. *Water Res.*, **47**(15), 5564–5574.

Peters, W. 1972. Occurrence of Chitin in Mollusca. *Comp. Biochem. Physiol., B: Comp. Biochem.*, **41**(3), 541–550.

Petersen, O.H., Gerasimenko, O.V., Gerasimenko, J.V., Mogami, H., & Tepikin, A.V. 1998. The Calcium Store in the Nuclear Envelope. *Cell Calcium*, **23**(2-3), 87–90.

Phillips, P.J., Brandes, M.C., Mills, M.J., & De Graef, M. 2011a. Diffraction Contrast Stem of Dislocations: Imaging and Simulations. *Ultramicroscopy*, **111**(9-10), 1483–1487.

Phillips, P.J., Mills, M.J., & De Graef, M. 2011b. Systematic Row and Zone Axis Stem Defect Image Simulations. *Philos. Mag.*, **91**(16), 2081–2101.

Pokroy, B., Kapon, M., Marin, F., Adir, N., & Zolotoyabko, E. 2007. Protein-Induced, Previously Unidentified Twin Form of Calcite. *Proc. Natl. Acad. Sci.*, **104**(18), 7337–7341.

Pokroy, B., Kabalah-Amitai, L., Polishchuk, I., DeVol, R.T., Blonsky, A.Z., Sun, C.Y., Marcus, M.A., Scholl, A., & Gilbert, Pupa. 2015. Narrowly Distributed Crystal Orientation in Biomineral Vaterite. *Chem. Mater.*, **27**(19), 6516–6523.

Politi, Y., Arad, T., Klein, E., Weiner, S., & Addadi, L. 2004. Sea Urchin Spine Calcite Forms Via a Transient Amorphous Calcium Carbonate Phase. *Science*, **306**(5699), 1161–1164.

Politi, Y., Levi-Kalisman, Y., Raz, S., Wilt, F., Addadi, L., Weiner, S., & Sagi, I. 2006. Structural Characterization of the Transient Amorphous Calcium Carbonate Precursor Phase in Sea Urchin Embryos. *Adv. Funct. Mater.*, **16**(10), 1289–1298.

Pouget, E.M., Bomans, P.H.H., Goos, J.A.C. M, Frederik, P.M., de With, G., & Sommerdijk, N.A.J.M. 2009. The Initial Stages of Template-Controlled $CaCO_3$ Formation Revealed by Cryo-TEM. *Science*, **323**(5920), 1455–1458.

Poulton, A.J., Adey, T.R., Balch, W.M., & Holligan, P.M. 2007. Relating Coccolithophore Calcification Rates to Phytoplankton Community Dynamics: Regional Differences and Implications for Carbon Export. *Deep Sea Res. Part II Top. Stud. Oceanogr*, **54**(5), 538–557.

Prieto, M. 2014. Nucleation and Supersaturation in Porous Media (Revisited). *Mineral. Mag.*, **78**(6), 1437–1447.

Prieto, M., Fernández-Diaz, L., López-Andrés, L., & López-Andrés, S. 1989. Supersaturation Evolution and First Precipitate Location in Crystal Growth in Gels; Application to Barium and Strontium Carbonates. *J. Cryst. Growth*, **98**(3), 447–460.

Prieto, M., Fernández-Diaz, L., & López-Andrés, S. 1991. Spatial and Evolutionary Aspects of Nucleation in Diffusing-Reacting Systems. *J. Cryst. Growth*, **108**(3), 770–778.

Prieto, M., Putnis, A., Fernández-Díaz, L., & López-Andrés, S. 1994. Metastability in Diffusing-Reacting Systems. *J. Cryst. Growth*, **142**(1), 225–235.

Putnis, A., Prieto, M., & Fernandez-Diaz, L. 1995. Fluid Supersaturation and Crystallization in Porous Media. *Geol. Mag.*, **132**(1), 1–13.

Radha, A.V., & Navrotsky, A. 2013. Thermodynamics of Carbonates. *Pages 73–121 of:* DePaolo, D. J., Cole, D. R., Navrotsky, A., & Bourg, I. C. (eds), *Rev. Mineral. Geochem.* Reviews in Mineralogy & Geochemistry, vol. 77. Chantilly: Mineralogical Soc Amer.

Raz, S., Hamilton, P.C., Wilt, F.H., Weiner, S., & Addadi, L. 2003. The Transient Phase of Amorphous Calcium Carbonate in Sea Urchin Larval Spicules: The Involvement of Proteins and Magnesium Ions in Its Formation and Stabilization. *Adv. Funct. Mater.*, **13**(6), 480–486.

Redmile-Gordon, M.A., Brookes, P.C., Evershed, R.P., Goulding, K.W.T., & Hirsch, P.R. 2014. Measuring the Soil-Microbial Interface: Extraction of Extracellular Polymeric Substances (EPS) from Soil Biofilms. *Soil Biol. Biochem.*, **72**, 163–171.

Reiss, Z. 1957. The Bilamellidea, nov. superfam., and Remarks on *Cretaceous globorotaliids*. *Contributions from the Cushman Foundation for Foraminiferal Research*, **8**(127–145).

Reiss, Z. 1960. Structure of So-Called Eponides and Some Other Rotaliiform Foraminifera. *Israel. Geol. Survey. Bull.*, **29**, 1–28.

Rey, A.D., Herrera-Valencia, E.E., & Murugesan, Y.K. 2014. Structure and Dynamics of Biological Liquid Crystals. *Liq. Cryst.*, **41**(3), 430–451.

Rey, Alejandro D. 2010. Liquid Crystal Models of Biological Materials and Processes. *Soft Matter*, **6**(15), 3402–3429.

Richards, R.P. 1999. The Four Twin Laws of Calcite and How to Recognize Them. *Rocks & Minerals*, **74**(5), 308–317.

Riehle, U., & Hoechli, M. 1973. The Theory and Technique of High Pressure Freezing. *Pages 31–61 of:* Benedetti, E. L., & Favard, P. (eds), *Freeze Etching, Techniques and Applications*. Paris: Société Française de Microscopie Electronique.

Rivadeneyra, M.A., Ramos-Cormenzana, A., Delgado, G., & Delgado, R. 1996. Process of Carbonate Precipitation by *Deleya halophila*. *Curr. Microbiol.*, **32**(6), 308–313.

Rivadeneyra, M.A., Delgado, G., Ramos-Cormenzana, A., & Delgado, R. 1998. Biomineralization of Carbonates by *Halomonas eurihalina* in Solid and Liquid Media with Different Salinities: Crystal Formation Sequence. *Res. Microbiol.*, **149**(4), 277–287.

Robinson, R.A. 1952. An Electron Microscope Study of Cartilage and Bone and Its Relationship to the Organic Matrix. *J. Bone Joint Surg.*, **34**(2), 389–476.

Rodríguez-Navarro, A.B., Checa, A., Willinger, M.G., Bolmaro, R., & Bonarski, J. 2012. Crystallographic Relationships in the Crossed Lamellar Microstructure of the Shell of the Gastropod *Conus marmoreus*. *Acta Biomater.*, **8**(2), 830–835.

Rodríguez-Navarro, C., Jimenez-Lopez, C., Rodríguez-Navarro, A., González-Muñoz, M.T., & Rodríguez-Gallego, M. 2007. Bacterially Mediated Mineralization of Vaterite. *Geochim. Cosmochim. Acta*, **71**(5), 1197–1213.

Rodríguez-Navarro, C., Kudlacz, K., Cizer, O., & Ruiz-Agudo, E. 2015. Formation of Amorphous Calcium Carbonate and Its Transformation into Mesostructured Calcite. *CrystEngComm*, **17**(1), 58–72.

Rodríguez-Navarro, C., Burgos Cara, A., Elert, K., Putnis, C.V., & Ruiz-Agudo, E. 2016. Direct Nanoscale Imaging Reveals the Growth of Calcite Crystals Via Amorphous Nanoparticles. *Cryst. Growth Des.*, **16**(4), 1850–1860.

Rosenberg, G. 2014. A New Critical Estimate of Named Species-Level Diversity of the Recent Mollusca. *Am. Malacol. Bull.*, **32**(2), 308–322, 15.

Roskov, Y., Ower, G., Orrell, T., Nicolson, D., Bailly, N., Kirk, P.M., Bourgoin, T., DeWalt, R.E., Decock, W., Nieukerken, E. van, Zarucchi, J., & Penev, L. Date Accessed: 14.05.2020. Species 2000 & ITIS Catalogue of Life, 2019 Annual Checklist.

Rousseau, M., Lopez, E., Coute, A., Mascarel, G., Smith, D.C., Naslain, R., & Bourrat, X. 2005. Sheet Nacre Growth Mechanism: A Voronoi Model. *J. Struct. Biol.*, **149**(2), 149–157.

Rousseau, M., Meibom, A., Geze, M., Bourrat, X., Angellier, M., & Lopez, E. 2009. Dynamics of Sheet Nacre Formation in Bivalves. *J. Struct. Biol.*, **165**(3), 190–195.

Ruggiero, M.A., Gordon, D.P., Orrell, T.M., Bailly, N., Bourgoin, T., Brusca, R.C., Cavalier-Smith, T., Guiry, M.D., & Kirk, P.M. 2015. A Higher Level Classification of All Living Organisms. *PLOS ONE*, **10**(4), e0119248.

Ruska, E. 1987. The Development of the Electron Microscope and of Electron Microscopy (Nobel Lecture). *Angew. Chem., Int. Ed.*, **26**(7), 595–605.

Rybacki, E., Konrad, K., Renner, J., Wachmann, M., Stöckhert, B., & Rummel, F. 2003. Experimental Deformation of Synthetic Aragonite Marble. *J. Geophys. Res. Solid Earth*, **108**(B3).

Saleuddin, A.S.M., & Petit, H.P. 1983. The Mode of Formation and the Structure of the Periostracum. *Pages 199–234 of:* Saleuddin, A. S. M., & Wilbur, K. M. (eds), *The Mollusca*. Academic Press.

Sanchez-Pastor, N., Gigler, A.M., Cruz, J.A., Park, S.H., Jordan, G., & Fernandez-Diaz, L. 2011. Growth of Calcium Carbonate in the Presence of Cr(VI). *Cryst. Growth Des.*, **11**(7), 3081–3089.

Santomauro, G., Sun, W.L., Brummer, F., & Bill, J. 2016. Incorporation of Zinc into the Coccoliths of the Microalga *Emiliania huxleyi*. *BioMetals*, **29**(2), 225–234.

Sardari, R.R.R., Kulcinskaja, E., Ron, E.Y.C., Björnsdóttir, S., Friðjónsson, Ó.H., Hreggviðsson, G. Ó., & Karlsson, E.N. 2017. Evaluation of the Production of Exopolysaccharides by Two Strains of the Thermophilic Bacterium *Rhodothermus marinus*. *Carbohydr. Polym.*, **156**, 1–8.

Saruwatari, K., Ozaki, N., Nagasawa, H., & Kogure, T. 2008. Comparison of Crystallographic Orientations between Living (*Emiliania huxleyi* and *Gephyrocapsa oceanica*) and Fossil (*Watznaueria barnesiae*) Coccoliths Using Electron Microscopes. *Am. Mineral.*, **93**(10), 1670–1677.

Saruwatari, K., Tanaka, Y., Nagasawa, H., & Kogure, T. 2011. Crystallographic Variability and Uniformity in Cretaceous Heterococcoliths. *Eur. J. Mineral.*, **23**(4), 519–528.

Schedl, A. 2006. Applications of Twin Analysis to Studying Meteorite Impact Structures. *Earth Planet. Sci. Lett.*, **244**(3), 530–540.

Schenk, A.S., & Kim, Y.Y. 2015. Unraveling the Internal Microstructure of Biogenic and Bioinspired Calcite Single Crystals. *MRS Bull.*, **40**(6), 499–508.

Schenk, A.S., Cantaert, B., Kim, Y.-Y., Li, Y., Read, E.S., Semsarilar, M., Armes, S.P., & Meldrum, F.C. 2014. Systematic Study of the Effects of Polyamines on Calcium Carbonate Precipitation. *Chem. Mater.*, **26**(8), 2703–2711.

Schlüter, L., Lohbeck, K.T., Gutowska, M.A., Groger, J.P., Riebesell, U., & Reusch, T.B.H. 2014. Adaptation of a Globally Important Coccolithophore to Ocean Warming and Acidification. *Nat. Clim. Change*, **4**(11), 1024–1030.

Schmahl, W.W., Griesshaber, E., Neuser, R., Lenze, A., Job, R., & Brand, U. 2004. The Microstructure of the Fibrous Layer of Terebratulide Brachiopod Shell Calcite. *Eur. J. Mineral.*, **16**(4), 693–697.

Schmahl, W.W., Griesshaber, E., Kelm, K., Goetz, A., Jordan, G., Ball, A., Xu, D.Y., Merkel, C., & Brand, U. 2012. Hierarchical Structure of Marine Shell Biomaterials: Biomechanical Functionalization of Calcite by Brachiopods. *Z. Kristallogr.*, **227**(11), 793–804.

Seidl, B.H.M., Griesshaber, E., Fabritius, H.-O., Reisecker, C., Hild, S., Taiti, S., Schmahl, W.W., & Ziegler, A. 2018. Tailored Disorder in Calcite Organization in Tergite Cuticle of the Supralittoral Isopod *Tylos europaeus* Arcangeli, 1938. *J. Struct. Biol.*, **204**(3), 464–480.

Seknazi, E., & Pokroy, B. 2018. Residual Strain and Stress in Biocrystals. *Adv. Mater.*, **30**(41), 1707263.

Sethmann, I., Putnis, A., Grassmann, O., & Löbmann, P. 2005. Observation of Nano-Clustered Calcite Growth Via a Transient Phase Mediated by Organic Polyanions: A Close Match for Biomineralization. *Am. Mineral.*, **90**(7), 1213–1217.

Sethmann, I., Hinrichs, R., Worheide, G., & Putnis, A. 2006. Nano-Cluster Composite Structure of Calcitic Sponge Spicules - a Case Study of Basic Characteristics of Biominerals. *J. Inorg. Biochem.*, **100**(1), 88–96.

Sethmann, I., Wang, J.W., Becker, U., & Putnis, A. 2010. Strain-Induced Segmentation of Magnesian Calcite Thin Films Growing on a Calcite Substrate. *Cryst. Growth Des.*, **10**(10), 4319–4326.

Shin, Y.A., Yin, S., Li, X., Lee, S., Moon, S., Jeong, J., Kwon, M., Yoo, S.J., Kim, Y.-M., Zhang, T., Gao, H., & Oh, S.H. 2016. Nanotwin-Governed Toughening Mechanism in Hierarchically Structured Biological Materials. *Nat. Commun.*, **7**(1), 10772.

Shirakawa, M.A., Cincotto, M.A., Atencio, D., Gaylarde, C.C., & John, V.M. 2011. Effect of Culture Medium on Biocalcification by *Pseudomonas putida*, *Lysinibacillus sphaericus* and *Bacillus subtilis*. *Braz. J. Microbiol.*, **42**(2), 499–507.

Shotton, D., Thompson, K., Wofsy, L., & Branton, D. 1978. Appearance and Distribution of Surface Proteins of the Human Erythrocyte Membrane. An Electron Microscope and Immunochemical Labeling Study. *J. Cell Biol.*, **76**(2), 512–531.

Simkiss, K., & Wilbur, K.M. 1989. *Biomineralization. Cell Biology and Mineral Deposition*. San Diego, CA: Academic Press.

Simon, P., Carrillo-Cabrera, W., Formánek, P., Göbel, C., Geiger, D., Ramlau, R., Tlatlik, H., Buder, J., & Kniep, R. 2004. On the Real-Structure of Biomimetically Grown Hexagonal Prismatic Seeds of Fluorapatite-Gelatine-Composites: TEM Investigations Along [001]. *J. Mater. Chem.*, **14**(14), 2218–2224.

Simon, P., Carrillo-Cabrera, W., Huang, Y.X., Buder, J., Borrmann, H., Cardoso-Gil, R., Rosseeva, E., Yarin, Y., Zahnert, T., & Kniep, R. 2011. Structural Relationship between Calcite-Gelatine Composites and Biogenic (Human) Otoconia. *Eur. J. Inorg. Chem.*, 5370–5377.

Simoneit, B.R.T. 2002. Molecular Indicators (Biomarkers) of Past Life. *Anat. Rec.*, **268**(3), 186–195.

Simoneit, B.R.T. 2004. Biomarkers (Molecular Fossils) as Geochemical Indicators of Life. *Adv. Space Res.*, **33**(8), 1255–1261.

Simonet Roda, M., Griesshaber, E., Ziegler, A., Rupp, U., Yin, X., Henkel, D., Häussermann, V., Laudien, J., Brand, U., Eisenhauer, A., Checa, A.G., & Schmahl, W.W. 2019a. Calcite Fibre Formation in Modern Brachiopod Shells. *Sci. Rep.*, **9**(1), 598.

Simonet Roda, M., Ziegler, A., Griesshaber, E., Yin, X., Rupp, U., Greiner, M., Henkel, D., Häussermann, V., Eisenhauer, A., Laudien, J., & Schmahl, W.W. 2019b. Terebratulide Brachiopod Shell Biomineralization by Mantle Epithelial Cells. *J. Struct. Biol.*

Smeets, P.J.M., Finney, A.R., Habraken, W.J.E.M., Nudelman, F., Friedrich, H., Laven, J., De Yoreo, J.J., Rodger, P.M., & Sommerdijk, N.A.J.M. 2017. A Classical View on Nonclassical Nucleation. *Proc. Natl. Acad. Sci.*, **114**(38), E7882–E7890.

Sommerdijk, N.A.J.M., & Cölfen, H. 2010. Lessons from Nature – Biomimetic Approaches to Minerals with Complex Structures. *MRS Bull.*, **35**(2), 116–121.

Spanos, N., & Koutsoukos, P.G. 1998. The Transformation of Vaterite to Calcite: Effect of the Conditions of the Solutions in Contact with the Mineral Phase. *J. Cryst. Growth*, **191**(4), 783–790.

Spero, H.J. 1988. Ultrastructural Examination of Chamber Morphogenesis and Biomineralization in the Planktonic Foraminifer *Orbulina universa*. *Mar. Biol.*, **99**(1), 9–20.

Stadelmann, P.A. 2012. *JEMS (Java Version of Electron Microscopy Software).*

Staudt, W.J., Reeder, R.J., & Schoonen, M.A.A. 1994. Surface Structural Controls on Compositional Zoning of SO_4^{2-} and SeO_4^{2-} in Synthetic Calcite Single Crystals. *Geochim. Cosmochim. Acta*, **58**(9), 2087–2098.

Stoodley, P., Boyle, J.D., DeBeer, D., & Lappin-Scott, H.M. 1999. Evolving Perspectives of Biofilm Structure. *Biofouling*, **14**(1), 75–90.

Stranski, I.N. 1928. Zur Theorie des Kristallwachstums. *Z. Phys. Chem.*, **136U**(1), 259–278.

Studer, D., Humbel, B.M., & Chiquet, M. 2008. Electron Microscopy of High Pressure Frozen Samples: Bridging the Gap between Cellular Ultrastructure and Atomic Resolution. *Histochem. Cell Biol.*, **130**(5), 877–889.

Subba, R.M. 1973. Kinetics and Mechanism of the Transformation of Vaterite to Calcite. *Bull. Chem. Soc. Jpn.*, **46**(5), 1414–1417.

Suffrian, K., Schulz, K.G., Gutowska, M.A., Riebesell, U., & Bleich, M. 2011. Cellular pH Measurements in *Emiliania huxleyi* Reveal Pronounced Membrane Proton Permeability. *New Phytol.*, **190**(3), 595–608.

Sugawara, A., Ishii, T., & Kato, T. 2003. Self-Organized Calcium Carbonate with Regular Surface-Relief Structures. *Angew. Chem., Int. Ed.*, **42**(43), 5299–5303.

Sun, J.Y., & Bhushan, B. 2012. Hierarchical Structure and Mechanical Properties of Nacre: A Review. *RSC Adv.*, **2**(20), 7617–7632.

Sunagawa, I. 1981. Characteristics of Crystal Growth in Nature as Seen from the Morphology of Mineral Crystals. France: Bull. Mineral.

Sunagawa, I. 1987. Morphology of Minerals. *Pages 509–587 of:* Sunagawa, I. (ed), *Morphology of Crystals, Part B*. Terra Sci. Pub., Tokyo/ D. Reidel, Dordrecht.

Sunagawa, I. 2005. *Crystals: Growth, Morphology and Perfection*. 1 edn. Cambridge University Press.

Sutherland, I.W. 2001. Biofilm Exopolysaccharides: A Strong and Sticky Framework. *Microbiology (Reading, UK)*, **147**, 3–9.

Suzuki, M., Kim, H., Mukai, H., Nagasawa, H., & Kogure, T. 2012. Quantitative XRD Analysis of {110} Twin Density in Biotic Aragonites. *J. Struct. Biol.*, **180**(3), 458–468.

Sviben, S., Gal, A., Hood, M.A., Bertinetti, L., Politi, Y., Bennet, M., Krishnamoorthy, P., Schertel, A., Wirth, R., Sorrentino, A., Pereiro, E., Faivre, D., & Scheffel, A. 2016. A Vacuole-Like Compartment Concentrates a Disordered Calcium Phase in a Key Coccolithophorid Alga. *Nat. Commun.*, **7**, 1–9.

Sze, H., Li, X., & Palmgren, M.G. 1999. Energization of Plant Cell Membranes by H^+ -Pumping ATPases: Regulation and Biosynthesis. *Plant Cell*, **11**, 677–689.

Sánchez-Román, M., Rivadeneyra, M.A., Vasconcelos, C., & McKenzie, J.A. 2007. Biomineralization of Carbonate and Phosphate by Moderately Halophilic Bacteria. *FEMS Microbiol. Ecol.*, **61**(2), 273–284.

Taylor, A.R., Russell, M.A., Harper, G.M., Collins, T.F.T., & Brownlee, C. 2007. Dynamics of Formation and Secretion of Heterococcoliths by *Coccolithus pelagicus* ssp. *braarudii*. *Eur. J. Phycol.*, **42**(2), 125–136.

Taylor, A.R., Brownlee, C., & Wheeler, G.L. 2012. Proton Channels in Algae: Reasons to Be Excited. *Trends Plant Sci.*, **17**(11), 675–684.

Taylor, J.D., & Layman, M. 1972. The Mechanical Properties of Bivalve (Mollusca) Shell Structures. *Palaeontology*, **15**(1), 73–87.

ten Wolde, P.R., & Frenkel, D. 1997. Enhancement of Protein Crystal Nucleation by Critical Density Fluctuations. *Science*, **277**(5334), 1975–1978.

Teng, H.H., & Dove, P.M. 1997. Surface Site-Specific Interactions of Aspartate with Calcite During Dissolution; Implications for Biomineralization. *Am. Mineral.*, **82**(9-10), 878–887.

Thierstein, H.R., Geitzenauer, K.R., & Molfino, B. 1977. Global Synchroneity of Late Quaternary Coccolith Datum Levels - Validation by Oxygen Isotopes. *Geology*, **5**(7), 400–404.

Thompson, J.B., Paloczi, G.T., Kindt, J.H., Michenfelder, M., Smith, B.L., Stucky, G., Morse, D.E., & Hansma, P.K. 2000. Direct Observation of the Transition from Calcite to Aragonite Growth as Induced by Abalone Shell Proteins. *Biophys. J.*, **79**(6), 3307–3312.

Tourney, J., & Ngwenya, B.T. 2009. Bacterial Extracellular Polymeric Substances (EPS) Mediate $CaCO_3$ Morphology and Polymorphism. *Chem. Geol.*, **262**(3), 138–146.

Tourney, J., & Ngwenya, B.T. 2014. The Role of Bacterial Extracellular Polymeric Substances in Geomicrobiology. *Chem. Geol.*, **386**, 115–132.

Towe, K.M., & Lowenstam, H.A. 1967. Ultrastructure and Development of Iron Mineralization in the Radular Teeth of *Cryptochiton stelleri* (Mollusca). *J. Ultrastruct. Res.*, **17**(1), 1–13.

Toyofuku, T., Matsuo, M.Y., De Nooijer, L.J., Nagai, Y., Kawada, S., Fujita, K., Reichart, G.-J., Nomaki, H., Tsuchiya, M., Sakaguchi, H., & Kitazato, H. 2017. Proton Pumping Accompanies Calcification in Foraminifera. *Nat. Commun.*, **8**(1), 14145.

Tyszka, J., Bickmeyer, U., Raitzsch, M., Bijma, J., Kaczmarek, K., Mewes, A., Topa, P., & Janse, M. 2019. Form and Function of F-Actin During Biomineralization Revealed from Live Experiments on Foraminifera. *Proc. Natl. Acad. Sci.*, **116**(10), 4111–4116.

Urmos, J., Sharma, S.K., & Mackenzie, F.T. 1991. Characterization of Some Biogenic Carbonates with Raman-Spectroscopy. *Am. Mineral.*, **76**(3-4), 641–646.

van der Wal, P., Dejong, E.W., Westbroek, P., Debruijn, W.C., & Mulderstapel, A.A. 1983. Polysaccharide Localization, Coccolith Formation, and Golgi Dynamics in the Coccolithophorid *Hymenomonas carterae*. *J. Ultrastruct. Res.*, **85**(2), 139–158.

van Dijk, I., Mouret, A., Cotte, M., Le Houedec, S., Oron, S., Reichart, G.J., Reyes-Herrera, J., Filipsson, H.L., & Barras, C. 2019. Chemical Heterogeneity of Mg, Mn, Na, S, and Sr in Benthic Foraminiferal Calcite. *Front. Earth Sci.*, **7**(281).

van Emburg, P.R., de Jong, E.W., & Daems, W. Th. 1986. Immunochemical Localization of a Polysaccharide from Biomineral Structures (Coccoliths) of *Emiliania huxleyi*. *J. Ultrastruct. Mol. Struct. Res.*, **94**(3), 246–259.

van Harreveld, A., & Crowell, J. 1964. Electron Microscopy after Rapid Freezing on a Metal Surface and Substitution Fixation. *Anat. Rec.*, **149**(3), 381–385.

Vielzeuf, D., Floquet, N., Chatain, D., Bonnete, F., Ferry, D., Garrabou, J., & Stolper, E.M. 2010. Multilevel Modular Mesocrystalline Organization in Red Coral. *Am. Mineral.*, **95**(2-3), 242–248.

Vijayaraghavan, K., & Yun, Y.S. 2008. Bacterial Biosorbents and Biosorption. *Biotechnol. Adv.*, **26**(3), 266–291.

Vincent, J. 2012. *Structural Biomaterials*. New Jersey, USA: Princeton University Press.

Visscher, P.T., & Stolz, J.F. 2005. Microbial Mats as Bioreactors: Populations, Processes, and Products. *Palaeogeogr. Palaeoclimatol. Palaeoecol.*, **219**(1), 87–100.

Volmer, M., & Schultze, W. 1931. Kondensation an Kristallen. *Z. Phys. Chem.*, **156A**(1), 1.

Volmer, M., & Weber, A. 1926. Nucleus Formation in Supersaturated Systems. *Z. Phys. Chem.*, **119**, 277–301.

von Ardenne, M. 1938. Das Elektronen-Rastermikroskop. *Z. Phys.*, **109**(9), 553–572.

Wada, K. 1960. Crystal Growth on the Inner Shell Surface of *Pinctada martensii* (Dunker) I. *J. Electron Microsc.*, **9**(1), 21–23.

Wada, K. 1962. Crystal Growth of Molluscan Shell. *Bull. Natl. Pearl Res. Lab.*, **7**, 703–828.

Wada, Y., Fujisawa, R., Nodasaka, Y., & Kuboki, Y. 1996. Electrophoretic Gels of Dentin Matrix Proteins as Diffusion Media for in Vitro Mineralization. *J. Dent. Res.*, **75**(6), 1381–1387.

Walther, P., & Ziegler, A. 2002. Freeze Substitution of High-Pressure Frozen Samples: The Visibility of Biological Membranes Is Improved When the Substitution Medium Contains Water. *J. Microsc.*, **208**, 3–10.

Wang, R.Z., Suo, Z., Evans, A.G., Yao, N., & Aksay, I.A. 2001. Deformation Mechanisms in Nacre. *J. Mater. Res.*, **16**(9), 2485–2493.

Wang, T., Cölfen, H., & Antonietti, M. 2005. Nonclassical Crystallization: Mesocrystals and Morphology Change of $CaCO_3$ Crystals in the Presence of a Polyelectrolyte Additive. *J. Am. Chem. Soc.*, **127**(10), 3246–3247.

Wang, Z., Choi, O., & Seo, Y. 2013. Relative Contribution of Biomolecules in Bacterial Extracellular Polymeric Substances to Disinfection Byproduct Formation. *Environ. Sci. Technol.*, **47**(17), 9764–9773.

Watanabe, J., & Akashi, M. 2008. An Electrophoretic Approach Provides Tunable Mineralization inside Agarose Gels. *Cryst. Growth Des.*, **8**(2), 478–482.

Wei, S., Cui, H., Jiang, Z., Liu, H., He, H., & Fang, N. 2015. Biomineralization Processes of Calcite Induced by Bacteria Isolated from Marine Sediments. *Braz. J. Microbiol.*, **46**(2), 455–464.

Weibel, E.R. 1969. Stereological Principles for Morphometry in Electron Microscopic Cytology. *Pages 235–302 of:* Bourne, G. H., Danielli, J. F., & Jeon, K. W. (eds), *International Review of Cytology*, vol. 26. Academic Press.

Weiner, S. 1984. Organization of Organic Matrix Components in Mineralized Tissues. *Am. Zool.*, **24**(4), 945–951.

Weiner, S., & Addadi, L. 1997. Design Strategies in Mineralized Biological Materials. *J. Mater. Chem.*, **7**(5), 689–702.

Weiner, S., & Addadi, L. 2011. Crystallization Pathways in Biomineralization. *Pages 21–40 of:* Clarke, D. R., & Fratzl, P. (eds), *Annual Review of Materials Research, Vol 41*. Annual Review of Materials Research, vol. 41. Palo Alto: Annual Reviews.

Weiner, S., & Dove, P.M. 2003. An Overview of Biomineralization Processes and the Problem of the Vital Effect. *Rev. Mineral. Geochem.*, **54**, 1–29.

Weiner, S., & Traub, W. 1984. Macromolecules in Mollusk Shells and Their Functions in Biomineralization. *Philos. Trans. R. Soc. London, B*, **304**(1121), 425–434.

Weiner, S., & Wagner, H.D. 1998. The Material Bone: Structure-Mechanical Function Relations. *Annu. Rev. Mater. Sci.*, **28**(1), 271–298.

Weiss, I.M., & Schonitzer, V. 2006. The Distribution of Chitin in Larval Shells of the Bivalve Mollusk *Mytilus galloprovincialis*. *J. Struct. Biol.*, **153**(3), 264–277.

Westbroek, P., Dejong, E.W., van der Wal, P., Borman, A.H., Devrind, J.P.M., Kok, D., Debruijn, W.C., & Parker, S.B. 1984. Mechanism of Calcification in the Marine Alga *Emiliania huxleyi*. *Philos. Trans. R. Soc. London, B*, **304**(1121), 435–444.

Westbroek, P., Young, J.R., & Linschooten, K. 1989. Coccolith Production (Biomineralization) in the Marine Alga *Emiliania huxleyi*. *J. Journal of Protozool.*, **36**(4), 368–373.

Westbroek, P., Brown, C.W., Vanbleijswijk, J., Brownlee, C., Brummer, G.J., Conte, M., Egge, J., Fernandez, E., Jordan, R., Knappertsbusch, M., Stefels, J., Veldhuis, M., van der Wal, P., & Young, J. 1993. A Model System Approach to Biological Climate Forcing - the Example of *Emiliania huxleyi*. *Glob. Planet. Change*, **8**(1-2), 27–46.

Whitfield, C. 1988. Bacterial Extracellular Polysaccharides. *Can. J. Microbiol.*, **34**(4), 415–420.

Whittaker, R.H. 1969. New Concepts of Kingdoms of Organisms. *Science*, **163**(3863), 150–160.

Wiercigroch, E., Szafraniec, E., Czamara, K., Pacia, M.Z., Majzner, K., Kochan, K., Kaczor, A., Baranska, M., & Malek, K. 2017. Raman and Infrared Spectroscopy of Carbohydrates: A Review. *Spectrochim. Acta A*, **185**, 317–335.

Wilbur, K.M., & Watabe, N. 1963. Experimental Studies on Calcification in Molluscs and Alga *Coccolithus huxleyi*. *Ann. N. Y. Acad. Sci.*, **109**(1), 82–112.

Wilkinson, A.J., Meaden, G., & Dingley, D.J. 2006. High-Resolution Elastic Strain Measurement from Electron Backscatter Diffraction Patterns: New Levels of Sensitivity. *Ultramicroscopy*, **106**(4), 307–313.

Williams, A. 1967. Evolution of the Shell Structure of Articulate Brachiopods. *Special Papers in Palaeontology*, **2**, 1–55.

Wingender, J., Neu, T.R., & Flemming, H.C. 1999. *Microbial Extracellular Polymeric Substances: Characterization, Structure and Function*. 1 edn. Springer, Berlin, Heidelberg.

Wolf, D., Yamakov, V., Phillpot, S.R., Mukherjee, A., & Gleiter, H. 2005. Deformation of Nanocrystalline Materials by Molecular-Dynamics Simulation: Relationship to Experiments? *Acta Mater.*, **53**(1), 1–40.

WoRMS, Editorial Board. Date accessed: 30.09.2020. *World Register of Marine Species. Available from http://www.marinespecies.org at VLIZ.*

Wählisch, F.C., Peter, N.J., Abad, O.T., Oliveira, M.V., Schneider, A.S., Schmahl, W.W., Griesshaber, E., & Bennewitz, R. 2014. Surviving the Surf: The Tribomechanical Properties of the Periostracum of *Mytilus* sp. *Acta Biomater.*, **10**(9), 3978–85.

Ye, F., Crippa, G., Angiolini, L., Brand, U., Capitani, G., Cusack, M., Garbelli, C., Griesshaber, E., Harper, E., & Schmahl, W.W. 2018a. Mapping of Recent Brachiopod Microstructure: A Tool for Environmental Studies. *J. Struct. Biol.*, **201**(3), 221–236.

Ye, F., Crippa, G., Garbelli, C., & Griesshaber, E. 2018b. Microstructural Data of Six Recent Brachiopod Species: SEM, EBSD, Morphometric and Statistical Analyses. *Data Brief*, **18**, 300–318.

Yin, X., Griesshaber, E., Fernández-Díaz, L., Ziegler, A., García-García, F.J., & Schmahl, W.W. 2019. Influence of Gelatin–Agarose Composites and Mg on Hydrogel-Carbonate Aggregate Formation and Architecture. *Cryst. Growth Des.*, **19**(10), 5696–5715.

Yin, X., Weitzel, F., Griesshaber, E., Fernández-Díaz, L., Jimenez-Lopez, C., Ziegler, A., Rodríguez-Navarro, A.B., & Schmahl, W.W. 2020a. Bacterial EPS in Agarose Hydrogels Directs Mineral Organization in Calcite Precipitates: Species-Specific Biosignatures of *Bacillus subtilis*, *Mycobacterium phley*, *Mycobacterium smagmatis*, and *Pseudomonas putida* EPS. *Cryst. Growth Des.*, **20**(7), 4402–4417.

Yin, X., Weitzel, F., Jiménez-López, C., Griesshaber, E., Fernández-Díaz, L., Rodríguez-Navarro, A., Ziegler, A., & Schmahl, W.W. 2020b. Directing Effect of Bacterial Extracellular Polymeric Substances (EPS) on Calcite Organization and EPS–Carbonate Composite Aggregate Formation. *Cryst. Growth Des.*, **20**(3), 1467–1484.

Yin, X.F., Ziegler, A., Kelm, K., Hoffmann, R., Watermeyer, P., Alexa, P., Villinger, C., Rupp, U., Schluter, L., Reusch, T.B.H., Griesshaber, E., Walther, P., & Schmahl, W.W. 2018. Formation and Mosaicity of Coccolith Segment Calcite of the Marine Algae *Emiliania huxleyi*. *J. Phycol.*, **54**(1), 85–104.

Young, J.R. 1994. Variation in *Emiliania huxleyi* Coccolith Morphology in Samples from the Norwegian EHUX Experiment, 1992. *Sarsia*, **79**(4), 417–425.

Young, J.R., & Henriksen, K. 2003. Biomineralization within Vesicles: The Calcite of Coccoliths. *Rev. Mineral. Geochem.*, **54**(1), 189–215.

Young, J.R., Didymus, J.M., Bown, P.R., Prins, B., & Mann, S. 1992. Crystal Assembly and Phylogenetic Evolution in Heterococcoliths. *Nature*, **356**(6369), 516–518.

Young, J.R., Geisen, M., Cros, L., Kleijne, A., Sprengel, C., Probert, I., & J, Østergaard. 1997. A Guide to Extant Coccolithophore Taxonomy. *J. Nanoplancton, Special Issue*, **1**, 1–125.

Young, J.R., Davis, S.A., Bown, P.R., & Mann, S. 1999. Coccolith Ultrastructure and Biomineralisation. *J. Struct. Biol.*, **126**(3), 195–215.

Yourdkhani, M., Pasini, D., & Barthelat, F. 2011. Multiscale Mechanics and Optimization of Gastropod Shells. *J. Bionic Eng.*, **8**(4), 357–368.

Zahn, D. 2004. Atomistic Mechanism of NaCl Nucleation from an Aqueous Solution. *Phys. Rev. Lett.*, **92**(4), 040801.

Zhu, T., & Gao, H. 2012. Plastic Deformation Mechanism in Nanotwinned Metals: An Insight from Molecular Dynamics and Mechanistic Modeling. *Scr. Mater.*, **66**(11), 843–848.

Acknowledgement

First of all, I would like to sincerely thank "meinem Doktorvater" Prof. Dr. Wolfgang W. Schmahl and also Dr. Erika Griesshaber, "meiner Doktormutter", for their constant support, patient guidance and "great parenting" through the past years. I owe earnest thankfulness for all their contributions of time, ideas, and funding, which allowed me to complete this dissertation.

I am especially grateful for the encouragement, kind help and great support from Prof. Dr. Lurdes Fernández-Díaz, Madrid, who helped me to move on when I was in times of trouble and at the brim of giving up.

Special thanks are given to Dr. Andreas Ziegler who has been always there to help, with him the great collaboration between Munich and Ulm always works well and moves towards the right direction.

I would like to thank our collaborators from Granada, Prof. Dr. Concepción Jiménez-López and Prof. Dr. Alejandro Rodríguez-Navarro introduced the bacteria EPS into the crystal growth system I have worked with, which brought very interesting outcomes and inspired for further research projects.

I owe further thanks to Prof. Antonio G. Checa González from University of Granada for his valuable ideas and fruitful discussions in the foraminifera project.

Thanks to all my current and past colleagues in the working group, Dr. Fitriana Nindiyasari-Behal, Dr. Martina Greiner, María del Mar Simonet Roda, Dr. Laura Antonella Casella, Viola Mages, our beloved "Pluto" and all the Master students. Also, thanks to my colleagues and friends in the department Geo- und Umweltwissenschaften in LMU and all my collaborating laboratories. This inspiring group has been a constant source of friendship, good advice and accompany, which made the last six years to a delightful and pleasant experience: Prof. Dr. SoHyun Park (together with Luna), Prof. Dr. Peter Gille, Prof. Dr. Guntram Jordan, Dr. Michael Lindner, Dr. Ulf Gattermann, Dr. Benedikt Röska, Dr. Mirtha Pillaca Quispe, Elnaz Raghami, Kristian Bader, Alexander Reul, Michael Hahne, Balázs Kocsis, Stefanie Hoser, Moritz Zenkert, Detlef Körner, Max Häberle, Karin Kleinstück, Barbara Jaeger, Prof. Dr. Paul Walther, Dr. Clarissa Read (Villinger), Julia Huber and Ulrich Rupp.

I really enjoyed and learned a lot from this multidisciplinary group, and some of the friendships developed will be cherished for the rest of my life.

I am appreciative of my parents for their unconditional love and support during good and difficult times throughout this work. I would like to thank my husband Chen for his constant love and support during my whole doctoral life.

List of Publications

Peer-reviewed Articles

Yin, X.; Griesshaber, E.; Checa, A.G.; Nindiyasari-Behal, F.; Sánchez-Almazo, I.; Ziegler, A. and Schmahl, W.W. (2020): Calcite crystal orientation patterns in the bilayers of laminated shells of benthic rotaliid foraminifera. *J. Struct. Biol.*, **213**, 107707.

Yin, X.; Weitzel, F.; Griesshaber, E.; Fernández-Díaz, L.; Jimenez-Lopez, C.; Ziegler, A.; Rodriguez-Navarro, A.B.; Schmahl, W.W. (2020): Bacterial EPS in agarose hydrogels directs mineral organization in calcite precipitates: species-specific biosignatures of *Bacillus subtilis*, *Mycobacterium phley*, *Mycobacterium smagmatis*, and *Pseudomonas putida* EPS. *Cryst. Growth Des.*, **20**, 4402–4417.

Yin, X.; Weitzel, F.; Jimenez-Lopez, C.; Griesshaber, E.; Fernández-Díaz, L.; Rodriguez-Navarro, A.B.; Ziegler, A. and Schmahl, W.W. (2020): Directing effect of bacterial extracellular polymeric substances (EPS) on calcite organization and EPS-carbonate composite aggregate formation. *Cryst. Growth Des.*, **20**, 1467–1484.

Yin, X.; Griesshaber, E.; Fernández-Díaz L.; Ziegler A.; García-García F.J. and Schmahl W.W. (2019): Influence of gelatin-agarose composites and Mg on hydrogel-carbonate aggregate formation and architecture. *Cryst. Growth Des.*, **19**, 5696–5715.

Yin, X.; Ziegler, A.; Kelm, K.; Hoffmann, R.; Watermeyer, P.; Alexa, P.; Villinger, C.; Rupp, U.; Schluter, L.; Reusch, T.B.H.; Griesshaber, E.; Walther, P. and Schmahl, W.W. (2018): Formation and mosaicity of coccolith segment calcite of the marine algae *Emiliania huxleyi*. *J. Phycol.*, **54**, 85–104.

Schenk, A.; Goll, M.; Reith, L.; Roussel, M.; Blaschkowski, B.; Rosenfeldt, S.; **Yin, X.**; Schmahl, W.W.; Ludwigs, S. (2020): Hierarchically Structured Spherulitic Cobalt Hydroxide Carbonate as a Precursor to Ordered Nanostructures of Electrocatalytically Active Co_3O_4. *Cryst. Growth Des.*, **20**, 6407–6420.

Simonet Roda, M.; Ziegler, A.; Griesshaber, E.; **Yin, X.**; Rupp, U.; Greiner, M.; Henkel, D.; Häussermann, V.; Eisenhauer, A.; Laudien, J. and Schmahl, W.W. (2019): Terebratulide brachiopod shell biomineralization by mantle epithelial cells. *J. Struct. Biol.*, **207**, 136–157.

Simonet Roda, M.; Griesshaber, E.; Ziegler, A.; Rupp, U.; **Yin, X.**; Henkel, D.; Häussermann, V.; Laudien, J.; Brand, U.; Eisenhauer, A.; Checa, A.G. and Schmahl, W.W. (2019): Calcite fibre formation in modern brachiopod shells. *Scientific Reports*, **9**, 598.

Nindiyasari, F.; Fernández-Díaz, L.; **Yin, X.**; Greiner, M.; Griesshaber, E.; Tsige, M.; Ziegler, A. and Schmahl, W.W. (2019): Influence of gel-strength and magnesium doping on the organization of calcite/hydrogel mesocrystal composites. *Eur. J. Mineral.*, **31**, 217–229.

Greiner, M.; Férnandez-Díaz, L.; Griesshaber, E.; Zenkert, M.; **Yin, X.**; Ziegler, A.; Veintemillas-Verdaguer, S. and Schmahl, W.W. (2018): Biomineral Reactivity: The kinetics of the replacement reaction of biological aragonite to apatite. *Minerals*, **8**, 315.

Greiner, M.; **Yin, X.**; Fernández-Díaz, L.; Griesshaber, E.; Weitzel, F.; Ziegler, A.; Veintemillas-Verdaguer, S. and Schmahl, W.W. (2018): Combined influence of reagent concentrations and agar hydrogel strength on the formation of biomimetic hydrogel-calcite composites. *Cryst. Growth Des.*, **18**, 1401–1414.

Casella, L.A.; Griesshaber, E.; **Yin, X.**; Ziegler, A.; Mavromatis, V.; Muller, D.; Ritter, A.C.; Hippler, D.; Harper, E.M.; Dietzel, M.; Immenhauser, A.; Schone, B.R.; Angiolini, L. and Schmahl, W.W. (2017): Experimental diagenesis: insights into aragonite to calcite transformation of *Arctica Islandica* shells by hydrothermal treatment. *Biogeosciences*, **14**, 1461–1492.

Book Chapters

Schmahl, W.W.; Schiebel, K.; Kadletz, P.M.; **Yin, X.** and Hoelzel, M. (2017): Crystallographic symmetry analysis in NiTi shape memory alloys. in “Highlights in Applied Mineralogy”, S. Heuss-Aßbichler, G. Amthauer & M. John, eds., De Gruyter, Berlin, Boston, 113–134.

Griesshaber, E.; **Yin, X.**; Ziegler, A.; Kelm, K.; Checa, A.; Eisenhauer, A. and Schmahl, W.W. (2017): Patterns of mineral organization in carbonate biological hard materials. in “Highlights in Applied Mineralogy”, S. Heuss-Aßbichler, G. Amthauer & M. John, eds., De Gruyter, Berlin, Boston, 245–272.

Oral Presentations at Conferences

Influence of bacterial EPS on mineral organization in EPS-hydrogel-calcite composite aggregates: the effect of *Bacillus subtilis*, *Mycobacterium phley*, *Mycobacterium smegmatis*, and *Pseudomonas putida* EPS
Yin, X.; Weitzel, F.; Jiménez-López, C.; Férnandez-Díaz, L.; Griesshaber, E.; Ziegler, A.; Rodríguez-Navarro, A. and Schmahl, W.W.
15th International Symposium on Biomineralization (BIOMIN XV), Munich, Germany, 9–13 September 2019

The directing effects of bacterial EPS and artificial hydrogel matrices on calcite crystal organization in EPS-hydrogel-calcite composite aggregates
Yin, X.; Weitzel, F.; Griesshaber, E.; Jiménez-López, C.; Fernández-Díaz, L.; Ziegler, A.; Rodríguez-Navarro, A. and Schmahl, W.W.
31st European Crystallography Meeting (ECM-31), Oviedo Spain, 22–27 August 2018

Calcite organization, Ca^{2+} transport and mineral formation in scales of the marine algae *Emiliania huxleyi*
Yin, X.; Ziegler, A.; Kelm, K.; Hofmann R.; Watermeyer; P.; Alexa; P.; Villinger; C.; Rupp, U.; Schlüter, L.; Reusch, T.B.H.; Griesshaber, E.; Walther, P. and Schmahl, W.W.
14th International Symposium on Biomineralization (BIOMIN XIV), Tsukuba Japan, 9–13 October 2017

Biomimetic formation of calcite in intermixed gelatin/agarose hydrogels: Aggregate co-orientation and Mg content
Yin, X.; Nindiyasari, F.; Griesshaber, E.; Fernández-Díaz, L.; Ziegler, A.; Walther, P.; García-García, F.J. and Schmahl, W.W.
The Granada-Münster Discussion Meeting (GMDM4), Münster Germany, 24–25 November 2016

Biomimetic formation of calcite in intermixed gelatin/agarose hydrogels: Aggregate co-orientation and Mg content
Yin, X.; Nindiyasari, F.; Griesshaber, E.; Fernández-Díaz, L.; Ziegler, A. and Schmahl, W.W.
30th European Crystallography Meeting (ECM-30), Basel Switzerland, 28 August–1 September 2016

Formation and mosaicity of coccolith segment calcite of the marine algae *Emiliania huxleyi*
Yin, X.; Alexa, P.; Ziegler, A.; Kelm, K.; Miersch, L.; Reusch, T.B.H.; Griesshaber, E. and Schmahl, W.W.
3rd Euro Bio-inspired Materials, Potsdam Germany, 22–25 February 2016

Formation and mosaicity of coccolith segment calcite of the marine algae *Emiliania huxleyi*
Yin, X.; Alexa, P.; Ziegler, A.; Kelm, K.; Miersch, L.; Reusch, T.B.H.; Griesshaber, E. and Schmahl, W.W.
13th International Symposium on Biomineralization (BIOMIN XIII), Granada Spain, 16–19 September 2015

First Author Posters at Conferences

Formation and mosaicity of coccolith segment calcite of the marine algae *Emiliania huxleyi*
Yin, X.; Ziegler, A.; Kelm, K.; Hoffmann, R.; Watermeyer, P.; Alexa, P.; Villinger, C.; Rupp, U.; Schluter, L.; Reusch, T.B.H.; Griesshaber, E.; Walther, P. and Schmahl, W.W.
15th International Symposium on Biomineralization (BIOMIN XV), Munich, Germany, 9–13 September 2019

The directing effect of bacterial EPS on calcite organization and EPS-carbonate composite aggregate formation
Yin, X.; Weitzel, F.; Griesshaber, E.; Jiménez-López, C.; Fernández-Díaz, L.; Rodríguez-Navarro, A.; Ziegler, A. and Schmahl, W.W.
15th International Symposium on Biomineralization (BIOMIN XV), Munich, Germany, 9–13 September 2019

Patterns of mineral assembly in hybrid gelatin/agarose hydrogels: Similarities and/or discrepancies between bioinspired and biological biopolymer-carbonate composite materials
Yin, X.; Griesshaber, E.; Fernández-Díaz, L.; Ziegler, A.; García-García, F.J. and Schmahl, W.W.
14th International Symposium on Biomineralization (BIOMIN XIV), Tsukuba Japan, 9–13 October 2017

Formation of biomimetic calcite-gelatin/agarose composites: Gel occlusion, aggregate co-orientation and Mg content
Yin, X.; Fernández-Díaz, L.; Griesshaber, E.; Ziegler, A.; Walther, P.; García-García, F.J. and Schmahl, W.W.
XXXVI Reunión Científica de la Sociedad Española de Mineralogía, Oviedo Spain, 4–7 July 2017.